ZANCO Journal of Pure and Applied Sciences
The official scientific journal of Salahaddin University-Erbil
https://zancojournals.su.edu.krd/index.php/JPAS

ISSN (print):2218-0230**, ISSN (online):** 2412-3986**, DOI: http://dx.doi.org/10.21271/zjpas**

RESEARCH PAPER

Seepage through earthen dams under different dam geometries and conditions

Jehan M. Sheikh Suleimany[1]

1-Department of Water Resource Eng., College of Engineerin, Salahaddin University-Erbil, Kurdistan Region, Iraq.

A B S T R A C T:
The study presents a method to carry out a new equation for the seepage rate of homogeneous earth fill dam with clay core using various geometry conditions. For this purpose the Slide 6.0 software has been used. The proposed program runs for (85) different geometrical cases of dam body to determine the seepage rate. The aim of the study is to examine the capabilities of slide 6.0 software in computing the rate of seepage and to find the impact of different structure geometry (e.g., upstream horizontal blanket length and thickness and, cutoff depth) on the reduction of the rate of seepage through the proposed earth dam.
Dimensional analysis is conducted using Buckingham π theorem to find the dependent and non-dependent variables. Artificial Neural Network (ANN) model is developed that relates the output variables with the input variables which govern the rate of the seepage through homogenous earth dam with clay core. The results are analyzed using SPSS software.
Three different heights of the dam, three different lengths of the upstream blanket with four different thickness of the blanket and four different cutoff depths with different conditions were used in this study and the results showed that the rate of the seepage decreased as the upstream blanket length, the cutoff depth and the thickness of the blanket are increased. Also, the impact of the upstream blanket length is greater than the cutoff depth and then the thickness of the blanket in decreasing the rate of seepage. While, the rate of the seepage were increased as the top width of the dam were decreased.
The seepage rate obtained by the Slide 6.0 program was compared with its quantity calculated from an empirical equation developed in this study. This relation has a determination coefficient of (R^2 = 0.8842).

KEY WORDS: Seepage; earth dam; Phi theorem; Slide software; Artificial Neural Network (ANN).
DOI: http://dx.doi.org/10.21271/ZJPAS.32.2.1
ZJPAS (2020) , 32(2);1-6 .

1.INTRODUCTION

The seepage rate can be decreased by using materials with low hydraulic conductivity such as clay, setting cutoffs, and increase the length of the upstream blanket those can cause to increase the seepage path (Fattah et al., 2014). Most of the dam failure is due to seepage through earth dam, for this reason, it should be controlled to eliminate those effects by using sheet pile, upstream horizontal blanket, cutoff trench (Aboelela, 2016).

The seepage of flow through earth dams was studied numerically. Zomorodian and Abodollahzadeh, (2010) used SEEP/W software to investigate the effect of horizontal drains on upstream slope of earth fill dams during rapid drawdown conditions. Olonade et al., (2013) have employed to study seepage through Oba dam using finite element method. Hasani et al., (2013) reported seepage analysis in Ilam earth fill dam that was done using SEEP/W software. Jamel, (2016) used Casagrandi and Dupuits assumptions to estimate seepage through homogeneous earth dam without a filter. Çalamak et al.,(2016) investigated the suitability and the effectiveness of blanket and chimney drains in earth fill dams for various properties of the

* **Corresponding Author:**
Jehan M. Sheikh Suleimany
E-mail: jehanmohammed.sheikhsuleimany@su.edu.krd
Article History:
Received: 16/03/2019
Accepted: 22/09/2019
Published: 22/04 /2020

drainage system. (Irzooki, 2016) was used SEEP/W code to run on homogenous earth dam models with horizontal toe drain, a new equation was found for computing the quantity of seepage. Omofunmi et al., (2017) reviewed on effects and control of seepage through earth-fill dams.
In this study, the Slide 6.0 program was used with the helpful of dimensional analysis method and the statistics software program SPSS, for evaluating seepage rate through homogenous earth dams with clay core for different dam geometries and conditions to find out their impacts on the seepage rate. Artificial Neural Network (ANN) model was used to predict the rate of seepage through earth dams for different geometries and conditions.

2. MATERIALS AND METHODS

In this study, a dimensional analysis using Buckingham π theorem was applied to predict an empirical equation for determining the seepage quantity through the proposed homogenous earth dam with clay core as shown in Figure 1.

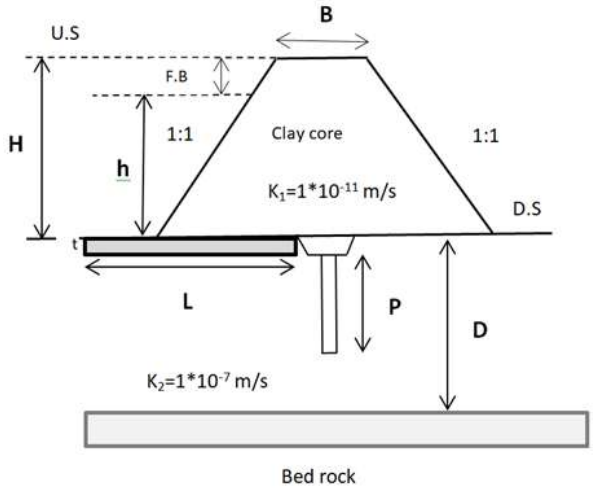

Figure 1: General section of homogenous earth dam with clay core.

The variables that might have an impact on the seepage rate are:
Q: rate of the seepage (L^3/T),
L: upstream length of the blanket (L),
P: cutoff depth (L),
H: dam height (L),
h: reservoir height (L),
t: blanket thickness (L),
B: top width (L), which was taken as a function of the height of the dam.

ρ: density of water (M/L^3), and
g: gravity acceleration(L/T^2).

$B=5/3\ H^{0.5}$ …….... (1)

Q =f (L, P, t, B, h, H, ρ, g)…….…… (2)

Using π theorem, the following dimensionless terms were carried out from equation (2)

$$\frac{Q}{g^{1/2}H^{5/2}} = f(\frac{L}{H}, \frac{P}{H}, \frac{t}{H}, \frac{B}{h}) \text{ …….. (3)}$$

An empirical equation of calculating the rate of seepage through earth dam with clay core was obtained using the dimensionless parameters of equation (3) with the SPSS program.

$$Yk = f\left[\sum_{j=1}^{m}\left(Wk_j fh(\sum_{i-1}^{n}(Wj, ixi) + bj)\right) + bk\right] \text{…….. (4)}$$

Where:

Yk: is the output, x: is the input variable, n: is the number of the input layer, and m: is the hidden layer.

The discharge quantities were computed for (85) various geometrical shapes and conditions of the dam, with a slope of 1:1 for both u/s and d/s are considered. Additionally, the hydraulic conductivity of the clay core and the foundation of the dam are considered to be 1x10^11, 1x10^7, and 7.5 x 10^7 m/s, respectively. The depth of the foundation soil (D) was considered to be 60 m.

3. RESULTS AND DISCUSSION

Using three to four different values for each of the dimensionless parameters in equation (3) that have impacts on the rate of the seepage, it concludes that the total runs applied in the Slide 6.0 program were 85 tests. These tests were repeated for three different dam heights (H) (20, 25 and 30 m, respectively). With two conditions first, the upstream blanket length (L) was considered to be constant and secondly, the cutoff depth (P) was considered to be constant.

The tests of each group were carried out with three different lengths of the upstream blanket (L) (0, 5 and 10 m), three different top width (B) as a function of the heights of the dam (7.45, 8.33 and 9.129 m) given in equation (1). Four different cutoff depths (P) (0, 5.10 and 20 m), and four different thickness of the blanket (0, 1, 1.5 and 2 m) were considered for testing of each group.
Figure 2-a, demonstrates a case in the slide 6.0 program, where L=0 m, P=0 m, H=20 m, h=18 m, t=0 m and B =7.45 m. Figure 2-b, illustrates the seepage rate in m^3/s through the Slide.6 program for the same case.

For each run in the Slide 6.0 program, the seepage rate (Q) was obtained and then the dimensionless parameters, given in equation (3), were computed and tabulated in a results table. From these results, the impact of each variable on the seepage rate through homogenous earth dams can be seen as the following:

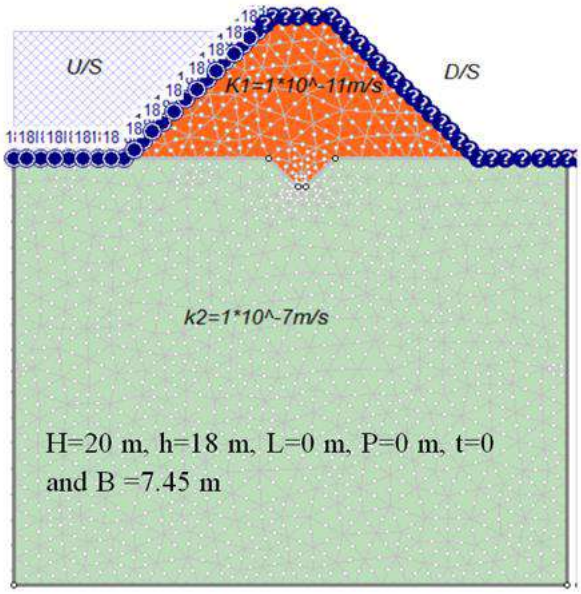

Figure 2-a: The geometrical shape of the earth using Slide program.

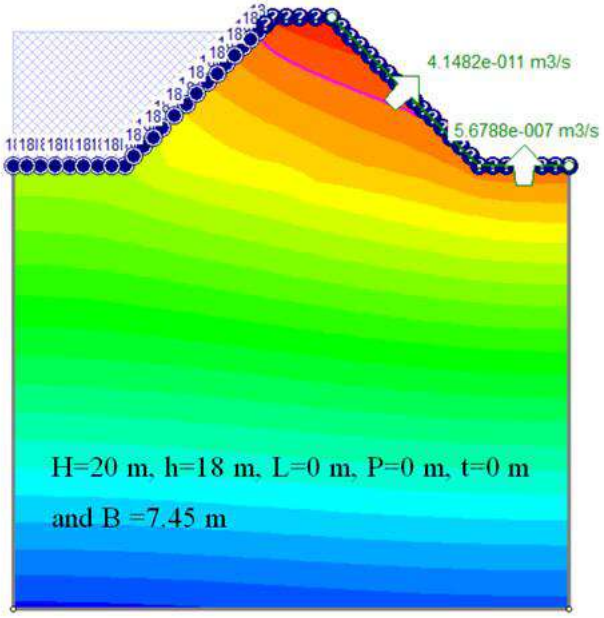

Figure 2-b: Seepage rate of the earth dam through Slide program.

3.1 Impact of the upstream blanket length (L).

Figure 3-a and Figure3-b illustrates the variation of the dimensionless parameter ($Q/g^{1/2}H^{5/2}$) with the dimensionless parameter (L/H) for some testing cases and for the condition where the height of the dam (H) and the cutoff depth (P) are constants and the upstream length of the blanket (L) is variable. From these figures, it can be seen that the rate of the seepage is decreased when the length of the blanket and the cutoff depth are increased if the other affecting parameters are constant. Also, the rates of the seepage increased as the height of the dam (H) are increased. It's worth to mention that all other cases and conditions were given the same results.

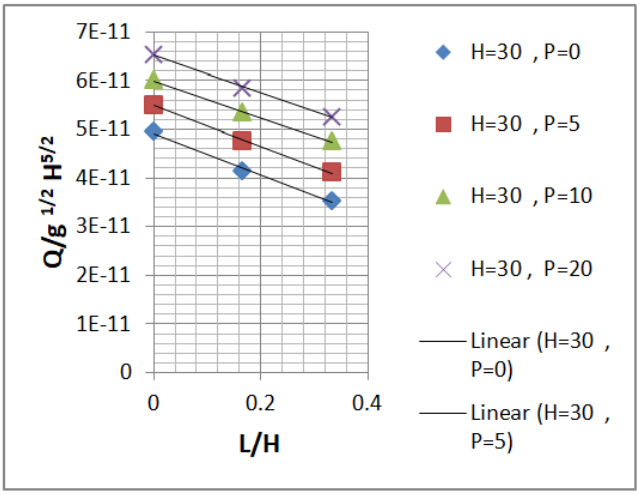

Figure 3-a: Relation of $(Q/g^{1/2} H^{5/2})$ with (L/H) for a constant height (H) of the earth dam.

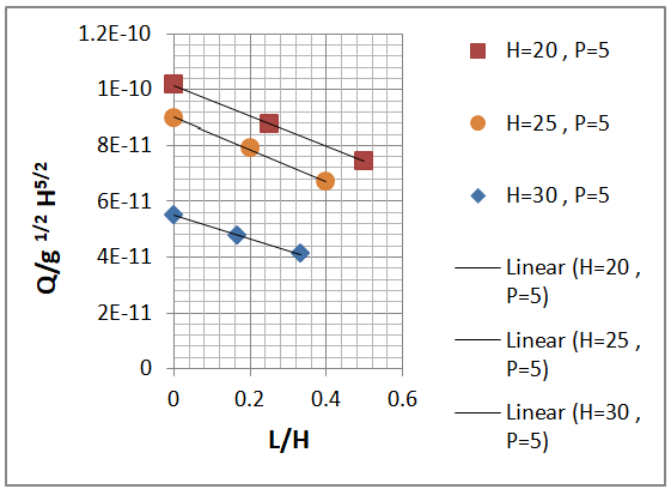

Figure3-b: Relation of $(Q/g^{1/2} H^{5/2})$ with (L/H) for different heights (H) of the earth dam.

3.2 Impact of the cutoff depth (P)

Figure 4-a and Figure 4-b represents the relation between $(Q/g^{1/2}H^{5/2})$ and (P/H) for some testing cases and a condition where the height of the dam (H) and the upstream length of the blanket (L) are constants and the cutoff depth (P) is variable.

From these figures it can be seen that, if the other affecting parameters are constant the rate of seepage will be decreased as the cutoff depths increased. As a comparison between the impacts of the upstream blanket length (L) and the cutoff depth (P). From the steep slopes of the lines in(Figure's 3-a and 3-b), it concludes that the impact of the upstream blanket length is more significant and greater than the impact of the cuttoff depth represented by the flat slopes of the lines in (Figures 4-a and 4-b). It's worth to mention that all other cases and conditions were given the same results.

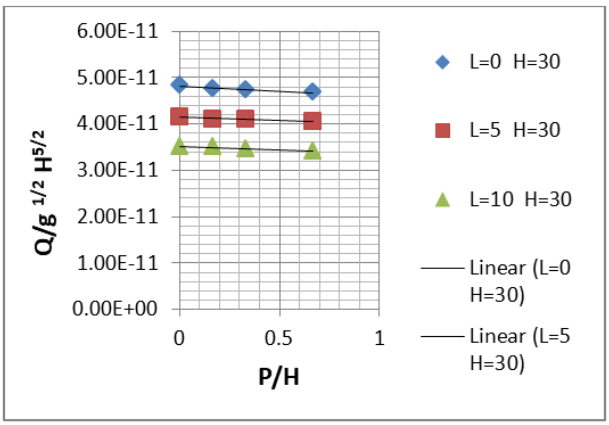

Figure 4-a: Relation of $(Q/g^{1/2} H^{5/2})$ with (P/H) for a constant height (H) of the earth dam.

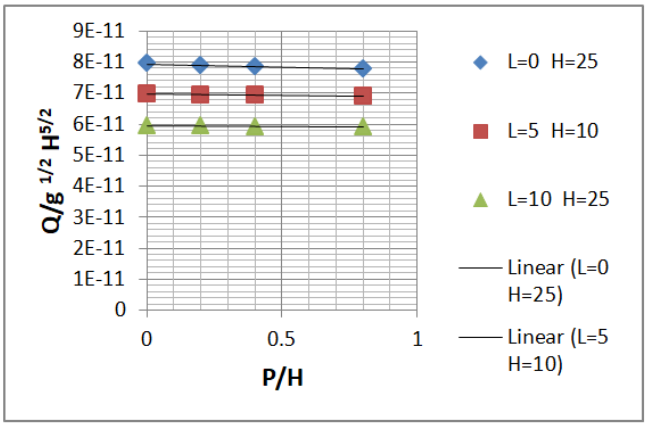

Figure 4-b: Relation of $(Q/g^{1/2} H^{5/2})$ with (P/H) for different heights (H) of the earth dam.

3.3 Impact of thickness of the upstream blanket (t)

Figure 5 shows the relation of the dimensionless parameter $(Q/g^{1/2}H^{5/2})$ with the dimensionless parameter (t/H) for some testing cases and for the conditions where the cutoff depth (P) or the upstream blanket depth (L) were constants. The figure concludes that the rate of the seepage is decreased when the thickness of the blanket (t) is

increased if the other affecting parameters are constant. But still, the impact of the blanket thickness (t) is less than the impact of the upstream blanket length as explained in section (3.1) It's worth to mention that all other cases and conditions were given the same results.

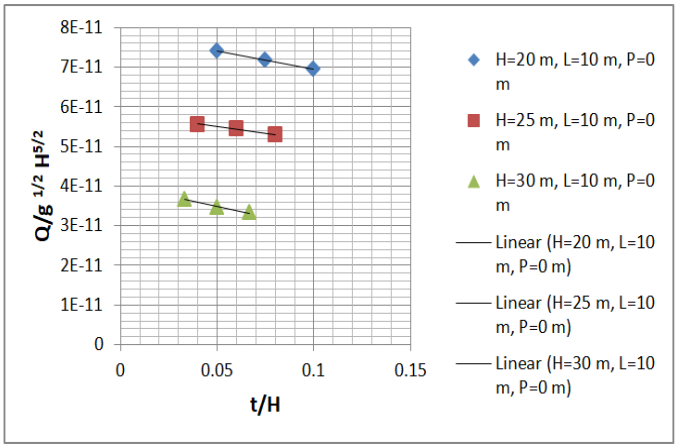

Figure 5: Relation of the parameter ($Q/g^{1/2} H^{5/2}$) with the parameter (t/H).

3.4 Impact of the top width (B).

Figure 6 shows the relation between the dimensionless parameter ($Q/g^{1/2}H^{5/2}$) with the dimensionless parameter (B/h), the figure concludes that the rate of seepage increased as the top width decreasing.

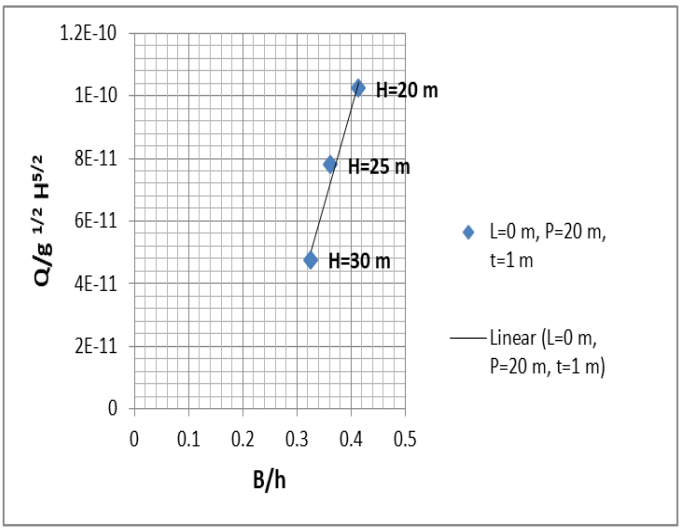

Figure 6: Relation of the parameter ($Q/g^{1/2} H^{5/2}$) with the parameter (B/h).

3.5 Artificial Neural Network (ANN) Model.

An empirical equation of calculating the rate of seepage through earth dam with clay core was obtained using the dimensionless parameters of equation (3) with the SPSS program as given in equation (4).

The database that has been created by using the Slide 6.0 program was employed to create the artificial neural network (ANN), model. The input variables were the most geometrical dimensions of the earth dam that has impacts on the rate of the seepage: as the height of the dam (H), the cutoff depth (P), the upstream blanket length (L), the blanket thickness (t) and the reservoir height (h) and the output variable was the rate of seepage(Q).

The base structure of this model was selected as (9-12-1) which is the most effective selected data set in agreement with results, which means among 85 data sets, 61% was for training and 17% were for testing. By trending the discharge values of both ANN and Slide 6.0 data in excel program SPSS, a new relation is obtained. Figure 7 shows the computed rate of the seepage by ANN and Slide 6.0 program. It is observed that the coefficient of determination (R^2) is about (0.8842), which is considered good.

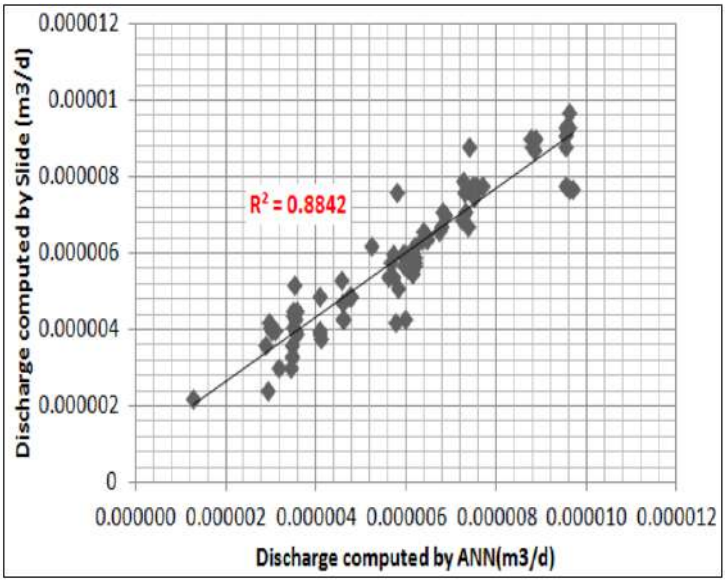

Figure 7: Rate of the seepage computed by ANN and Slide 6.0 program.

4. CONCLUSIONS

In the conducted research, the Slide 6.0 program used to estimate the rate of the seepage of homogeneous earth fill dam with clay core using various geometry conditions. The Slide 6.0 program shows very good performance in estimating the rate of the

seepage. The result shows that the seepage quantity through homogenous earth dams decreased with increasing the upstream blanket length (L), the cutoff depth (P) and the thickness of the blanket (t). Also, the result shows that the length of the upstream blanket length (L) is the more affecting geometrical variable on the seepage rate. The seepage rate through the earth dam increased with the decreasing of the top width (B) of the dam. The comparison between the predicted results by (ANN) model and those computed from the Slide 6.0 program for the different geometries and conditions were very good.

5. REFERENCES

Aboelela, M.M (2016)," Control of Seepage through Earth Dams Based on Pervious Foundation Using Toe Drainage Systems", Journal of Water Resource and Protection, 8, 1158-1174, ISSN Online: 1945-310.

Fattah, Y.M, et .al (2014)" Seepage Analysis of a Zoned Earth Dam by Finite Elements", International Journal of Civil Engineering and Technology (IJCIET), Vol.5, Issue8, pp.128-139, ISSN (online):0976-6316.

Gopal ,P and Kumar.K (2014), "slope stability and seepage analysis of earthen dam of a summer storage tank: a case study by using different methods "International Journal of Innovative Research in Advanced Engineering (IJIRAE) ISSN: 2349-2163Volume 1.

H. Hasani, j. et.al (2013), "Stability of Slope and Seepage Analysis in Earth Fills Dams Using Numerical Models" World Applied Science Journal21 (9):1398-1402.

Irzooki, H.R., (2016), "Computation of Seepage through Homogenous Earth Dams with Horizontal Toe Drain" Eng. & Tech. Journal, Vol. 34, Part (A), No.3.

Jamel A.A. (2016) ,"Analysis and Estimation of Seepage through Homogeneous Earth Dam without Filter", Diyala Journal of Engineering Sciences, Vol. 9, No. 2, pp. 38-49.

Omofunmi O. E., et.al, (2017), "A Review on Effects and Control of Seepage through Earth-fill Dam"Journal of Applied Science and Technology, Vol. 22, No. 5, pp.1-11.

Olonade, et. al, (2013),"A Study of Seepage through Oba Dam Using Finite Element Method", Civil and Environmental Research, Vol. 3, No 3

S.M. Zomorodian and S.M. Abodollahzadeh (2010)," Effect of Horizontal Drains on Upstream Slope Stability During Rapid Drawdown Condition" Shiraz University, Iran, International Journal of Geology, Issue 4,Volume 4.

U.S.B.R (1987),"Design of Small Dams" A Water Resources Technical Publication Washington, DC 20402-9323Third Edition.

ZANCO Journal of Pure and Applied Sciences
The official scientific journal of Salahaddin University-Erbil
https://zancojournals.su.edu.krd/index.php/JPAS

ISSN (print):2218-0230**, ISSN (online):** 2412-3986**, DOI: http://dx.doi.org/10.21271/zjpas**

RESEARCH PAPER

Comparing pumping test between Boulton and Neuman in unconfined aquifer

Srwa Othman Ismail[1] ,Dana khider Mawlood[2]

[1&2]Department of Civil, College of Engineering, Salahaddin University-Erbil , Kurdistan Region, Iraq.

A B S T R A C T:
Groundwater is known as a crucial source of water in the history of human, as it less contaminated, it has more preferable than surface water. Analyzing data of pumping test for evaluating aquifer parameters specific yield (Sy), transmissivity (T) and storativity (S) are usually using standard procedures like Theis or Jacob method. Boulton was the first to present the delayed response concept of unconfined aquifers under pumping conditions. Then Neuman used a different method than Boulton to develop an analytical model for a fully penetrating well in unconfined aquifers. The Neuman's model is depended on physical parameters which are well defined in aquifer system that is the main difference comparing to Boulton model. The main objective of this research on understanding water table aquifers in the Xabat area is to analyze the two main Boulton and Neuman methods by using aquifer test pro 2016 software and to see which of them are most appropriate for this area, which is the main reason for applying and comparing the two methods. The results of the layer property (specific yield, transmissivity, and storativity) are similar depending on the user and the availability of the methods, as well as the future development of the program analysis.

KEY WORDS: Aquifer test pro 2016, Boulton method, Neuman method, water table aquifer parameters.
DOI: http://dx.doi.org/10.21271/ZJPAS.32.2.2
ZJPAS (2020) , 32(2);7-14 .

1.INTRODUCTION :

Groundwater hydrologists for their quantitative studies usually conduct pumping test and analyze data to get aquifer parameters. Analyzing data of pumping test for an unconfined aquifer is known to be a marginally complex due to the curve of transient drawdown, which displays three segments in the response to the pumping. At the beginning of the pumping time and during the first segment, the storage water is released immediately.

* **Corresponding Author:**
Srwa Othman Ismail
E-mail: srwa.ismail@su.edu.krd
Article History:
Received: 26/06/2019
Accepted: 06/10/2019
Published: 22/04 /2020

The vertical gradient close to water table produces porous matrix drainage throughout second segment, as a result, rate of hydraulic head would drop and then slowing down and it might lead to stop after an amount of time. Lastly, when the flow is fundamentally horizontal, nearly all of pumping is provided by the specific yield, Sy, in the last segment. Parameters of aquifer could be estimated at a specific site through a pumping test, after collecting data different method could be used to analyze these data for example Jacob or Theis. The simple graphical method to estimate storativity and transmissivity of the aquifer which is based on Theis's formula is proposed by Chenini *et al.*, (2008). In confined aquifers, standard methods have been used to analyze pumping test data. The expectations in Jacob or Theis methods were resulting to meet the most

cases in confined aquifers. While, generally these methods are not suited for unconfined aquifers and the reason might back to two points: first is phenomenon of delayed yield, the second is drawdowns being that occasionally bigger to the aquifer's primary saturated thickness. Boulton (1954 and 1963) through introducing delayed yield's concept, he established an analytical solution for the unconfined aquifer flow equation. Depend on Boulton method by using graphical procedures Prickett (1965) introduced systematic approach to determine hydraulic parameter. Cooley and Case (1973) point to the Boulton's equation that defined a flow system with a rigid phreatic aquitard on top of the main aquifer which the effect of the unsaturated zone above the phreatic surface was neglected. A solution is developed by Neuman (1972, 1974) to consider elastic storage affection and aquifer's anisotropy on the behavior of drawdown. Another development of procedure graphical type curve match was showed by Neuman (1975) for determination unconfined aquifer's parameters. A combination of two models Boulton and Neuman for flow directed to well in an unconfined aquifer was documented by Moench (1995).

There are many articles provided to demonstrate the flow through the water table aquifers, for instance Grimestad (2002) found that a part of the water pumped from aquifers had been obtained from other sources. Zhan and Zlotnik (2002) addressed how a solution can be found for flow to a horizontal or slanted well in an unconfined aquifer. Hunt (2006) used a significant aquifer parameter instead of an empiric constant in the Zhan and Zlotnik (2002) equation to describe the flow to a well when a number of overlying aquitards exist between the pumped aquifer and the free surface. Mishra and Neuman (2011) determined saturated and unsaturated flow to a well with storage in a compressible unconfined aquifer. And also Malama (2011) proposed alternative linearization of water table kinematic condition (Moench, 2004; Tartakovsky and Neuman, 2007; Ni et al., 2015). Until then, there is rarely water table (Phreatic) aquifer investigation in Kurdistan of Iraq.

Waterloo Hydrogeological Incorporated used computer and developed software for aquifer test, then all parameters for pumping test are calculated by this software (Hui, 2011). Also, this software can be specially used for processing data, analyzing data, obtain graphical parameters, and data analyzing of pumping test.

This software can be used for calculating data, display results and then printing results of parameters. The Aquifer Test pro-2016 software was used to determine aquifer parameters based on formula of two models Boulton and Neuman through using pumping test data.

1.1 AREA OF STUDY

This study was conducted in Kabat/Khabat district (Kurdish: Qazay Xabat). It is located in the west of Erbil Governorate Iraq. Khabat district includes 64 villages and three main sub-districts, which are Darashekran, Rizgary and Kewrgosk. Geographically, Khabat situated longitude (36∘16′20.48 ″), latitude (43°40′ 23.99″) and 37 km far from Erbil city. The elevation of this location varies between (200 to 400 m) above sea level as shown in Figure 1.

The pumping test exercise was carried out on a single well within the Kabat area, with a constant discharge of 267 Gpm (1730.2 m^3/day). The pumping well is 250 m depth. The aquifer saturation thickness is 214 m and the original static water level is 36 m and other data presented in Table 1.

2. METHODOLOGY

2.1 Boulton (1963) Type-curve Method

Boulton (1963) supposed that derived water volume from storage in unconfined aquifer contain 2 modules. The first component the amount of water release instantly from storage at this situation aquifer acting like confined. The last factor is the amount of water release as delayed yield. In unconfined aquifers the formula is written basically with 2 components (Batu, 1998). The assumptions are given below (Boulton, 1954):

1. The aquifer is homogeneous and anisotropic, infinitely lateral and underlined by an impermeable horizontal bed.
2. Well completely penetrates the aquifer and is unlined.
3. The specific yield (Sy) is constant.
4. The flow in the aquifer obeys Darcy's law.
5. The water table is initially horizontal.
6. The well is pumped from the moment t=0 at a steady pace.
7. The contribution to the flow by water and aquifer compression may be neglected, except during the very early period of pumping.

8. The drawdown of the water table is small compared with the saturated thickness of the aquifer.

The general solution of that equation is complex which symbolically, and in analogy to the Theis equation, may be written as:

$$s = \frac{Q}{4\pi T} W(U_{AB}, r/D) \quad (1)$$

$$\alpha = \frac{T}{Sy\ D^2} \quad (2)$$

$$\frac{r}{D} = r\sqrt{\left(\frac{\alpha\ Sy}{T}\right)}, \qquad \alpha t = \left(\frac{r}{D}\right)^2 \frac{1}{4\ U_B}$$

Equation (1) defines the first section of the time drawdown curve under early stages and is converted to:

$$s = \frac{Q}{4\pi T} W(U_A, r/D) \quad (3)$$

Where

$U_A = \frac{r^2 S}{4Tt}$, [unit less]

Equation (1) discusses the third section of the time-drawdown curve under late-time criteria and decreases it to:

$$s = \frac{Q}{4\pi T} W(U_B, r/D) \quad (4)$$

Where

$U_B = \frac{r^2 Sy}{4Tt}$, [unit less]

Boulton provided W (U_{AB}, r / D) values for the practical U_A, U_B, and r / D ranges. Parameters of W (U_{AB}, r / D) were graphed on logarithmic paper against values of l/U_u and $1/U_B$ and two types of curves were built. The type curves on the left side of the r/D values are called "Type A curves." Early time-drawdown information is analyzed using them. The type curves on the right side of the r/D values are called "Type B curves" and are used to evaluate delayed time-drawdown information.

2.2 Neuman (1975) solution

Neuman (1972, 1974, 1975, and 1987) documented water table aquifer solution and consist of two main parts: the first part related to the time when pumping just started, the second part is for time after pumping. This solution occurs when water flows below gravity drainage (Fetter, 2001). Depending on these assumptions of (Batu, 1998) this method increases to:

1. The (Q) pumping rate is constant for well.
2. Well's diameter significantly small, and the well fully penetrates the aquifer thickness.
3. The aquifer stays saturated at all periods, and the law of Darcy applies.
4. The unconfined aquifer is lateral infinite and sits on a horizontal layer that is impermeable.
5. The aquifer is homogeneous but anisotropic and its main hydraulic material.
6. Water expansion and gravity drainage water is removed from free surface storage by compaction of the aquifer.
7. The well can be handled as a sink in the row, meaning that the face of the sink is ignored.
8. It is possible to neglect the capillarity impacts above the water table. This implies that water is released from the unsaturated zone immediately.
9. The water table drawdown is low compared to the aquifer's saturated thickness.

Conductivity is parallel to the axes of the coordinates. The suggested water table aquifer equation is the well-functioning W (U_A, U_B, /) for three distinct stages and the equation drawdown:

$$s = \frac{Q}{4\pi T}\ W(u_A, u_B, \Gamma) \quad (5)$$

Initial period: This acts as an elastic storage and is equal to the value u:

$$u_A = \frac{r^2\ S}{4Tt} \quad (6)$$

Time of transition: This operates as an aquifer known as Leaky by:

$$\Gamma = \frac{r^2}{b^2}\frac{Kv}{Kh} \quad (7)$$

Late time: this acts as drainage of gravity:

$$u_B = \frac{r^2\ Sy}{4Tt} \quad (8)$$

In the early stages, water is removed from elastic storage (S) when drawdown follows a matching Theis type curve, and then a flat curve and a gap in the derivative changes. A second Theis curve corresponds to the water released from the drainage of the unsaturated zone (Sy) for the subsequent moment as shown in Figure 2.

2.3 Applying of Boulton and Neuman solution throughout Aquifer test program

Aquifer test software package known as a simple to use for visualizing pumping test, data analysis, and interpreting. It has been designed for hydro-geologists. This test is provided nearly all essential tools to get accurate results and interpret data under different conditions, types of test, and aquifer types.

Boulton and Neuman have created a technique that can be helpful in determining water table (Phreatic) aquifers ' elastic storage coefficient (S), transmissivity (T), specific yield (Sy), and horizontal and vertical hydraulic conductivity. This solution involves matching drawdown information gathered during the pumping test.

3. Result and discussion

Formula of Neuman well contains unconfined aquifer or aquifer's basement. The aquifer is constant gravity specific yield, homogeneous, and anisotropic. The formula of Boulton well needs the weathered aquifer to be isotropic and homogeneous. The pumping test results data analyzed by Neuman and Boulton methods that are showed in Fig. 3 and Fig. 4. The result of specific yield (Sy), Storage Coefficient (S) and transmissivity (T) are in Table 2. Both Neuman (1975) and Boulton (1963) solutions are applied for analyzing pumping test data of unconfined aquifer, as it is in Xabat area, and the solution required to monitoring drawdown form observation well, since, the test was conducted on the pumped well (single well test), may cause to get unreliable values of the particular yield, which is out of the range of (0.01 to 0.3).

The solution gives the transmissivity values of (213 m^2/day) by Boulton method and (236 m^2/day) by Neuman method which can be classified according to (Table 3) from high to intermediate.

4. Conclusion

Pumping test data from Xabat area was evaluated by Boulton and Neuman methods. Neuman and Boulton methods gave values of transmissivities and specific yield that are relatively close to each other. The delayed water table response process in homogeneous anisotropic unconfined aquifer can be simulated by using constant values of specific storage S, and specific yield Sy. The delay process mathematical model is found without using unsaturated flow theory, simply through treating the unconfined aquifer as a compressible stem and the phreatic surface as a moving material boundary. Boulton's integral transformation as used as a free-surface condition in three-dimensional, axisymmetric boundary value problems for water table aquifer flow.

The development of Boulton equation lead to analyze Neuman equation, the major different is the application program and the software has the major impact of giving different results, however another reason forgetting different value of parameters is the location and the equipment measure at the site. And the hydrogeological formation of the area has another impact, and the main point of the thickness of the aquifer application is always suitable for unconfined aquifers of high thickness. There are many difficulties with a water table of a few meters thickness, so Neuman's program recommended for northern Iraq, since most of unconfined aquifers and reservoirs of high thickness, in fact, Neuman carried out and developed an analysis based on Boulton's principle of unconfined aquifer analysis.

Table 1 Pumping test data results obtained from Ministry of Agriculture and Water Resource/ Directorate of Erbil Groundwater.

Name of abstraction well: well no.(55) in Mamsinjy city					
Place of well: Qazay Xabat			Date of test: 27/8/2017		
Well depth: 250 m			Length of pipe test: 120 m		
Static water level: 36 m			Radius of pipe test: 3 in		
Dynamic water level: 45 m			Type of test equipment: 22-SP46 4 in		
Discharge: 267 (g/min), 1.2015 (m^3/min)			Inside raduis of pipes: 8 in		
Time (min)	**Depth to water level (m)**	**Drawdown (m)**	**Time (min)**	**Depth to water level (m)**	**Drawdown (m)**
0	36	0	9	44.9	8.9
0.5	38	2	10	45	9
1	40	4	15	45	9
1.5	42	6	20	45	9
2	44	8	25	45	9
3	44.2	8.2	30	45	9
4	44.4	8.4	40	45	9
5	44.6	8.6	50	45	9
6	44.7	8.7	60	45	9
7	44.8	8.8	80	45	9
8	44.9	8.9	100	45	9

Table 2 Results of both Neuman and Boulton solution

Aquifer parameter	Neuman	Boulton
Transmissivity (T) (m^2/day)	$2.36x10^{2}$	$2.13x10^{2}$
Storativity (S)	$2.67x10^{-5}$	$2.93x10^{-5}$
specific yield (Sy)	$2.67x10^{-3}$	$2.93x10^{-3}$
Kv/Kh	$1x10^{-2}$	$1x10^{-2}$

Table 3 Classification of Transmissivity value according to (Krásný, 1993).

Coefficient of Transmissivity (m^2/day)	Classification of Transmissivity magnitude	Designation of Transmissivity magnitude
>1000	I	Very high
100 to 1 000	II	High
10 to 100	III	Intermediate
1 to 10	V	Low
0.1 to 1	IV	Very low
<0.1	VI	Imperceptible

Figure 1 Satellite image of Khabat Sub-district from Google earth.

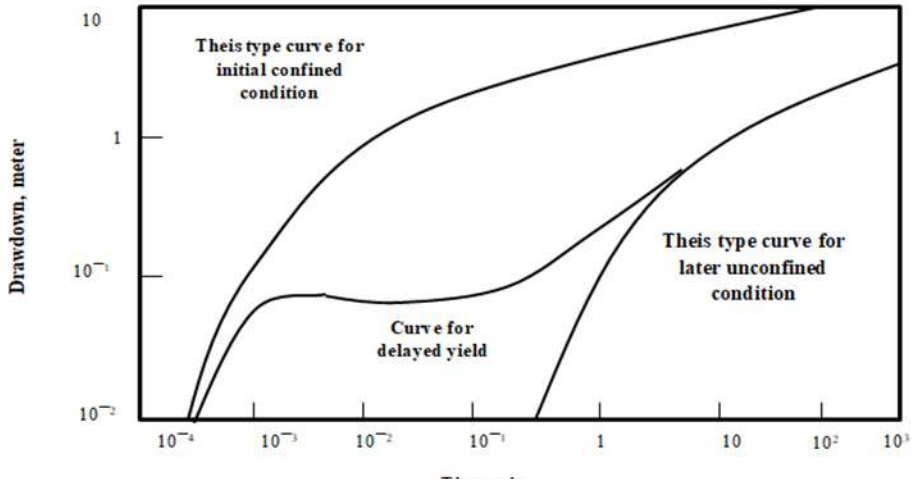

Figure 2 Type curves of drawdown versus time illustrating the effect of delayed yield for pumping tests in unconfined aquifers.

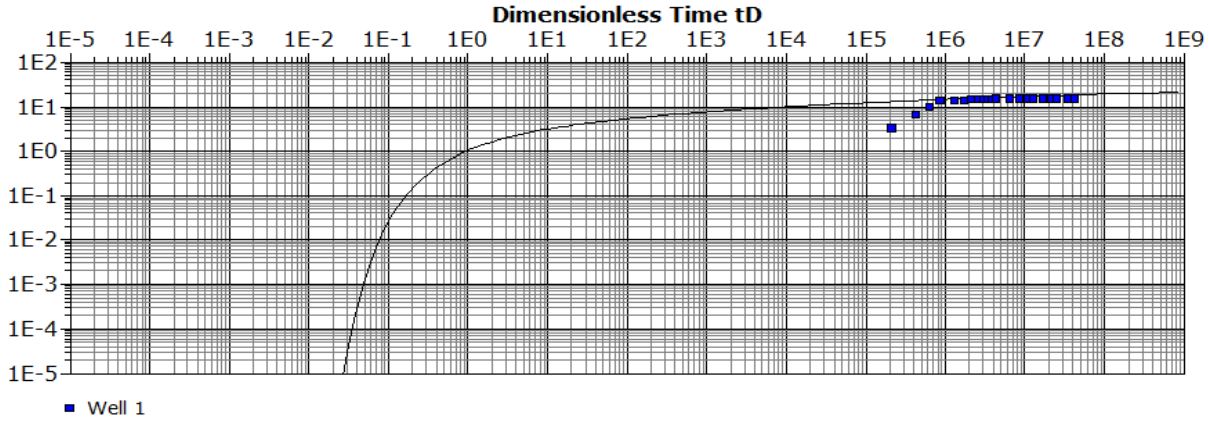

Figure 3 Neuman's solution by aquifer test program

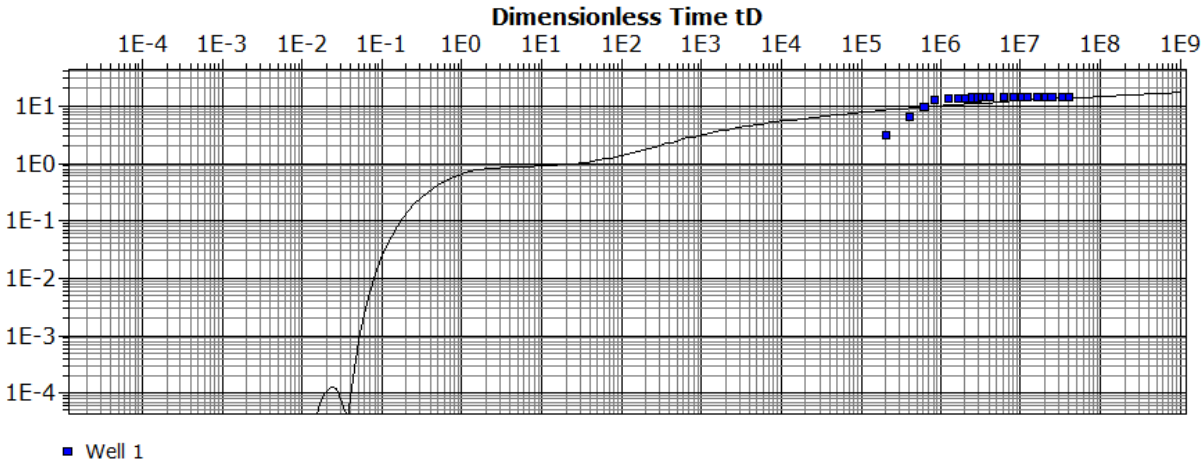

Figure 4 Boulton's solution by aquifer test program

Notation:

s: Drawdown, [L]
Q: Flow rate, [L^3 /T]
T: Aquifer Transmissivity, [L^2 / T]
W (U_{AB}, r/D) = Boulton's well-function [unit less]
α is Boulton delay index curve.
S: Storativity, [unit less]
T: Time, [T]
Sy: Specific yield [unit less].
W (u_A, u_B, Γ): is Neuman well function.
Γ: Neuman parameter of type curve [unit less].
r: radial distance from pumping well, [L].
b: is the initial saturated thickness of aquifer, [L].
Kh: Horizontal hydraulic conductivity, [L / T].
Kv: Vertical hydraulic conductivity, [L / T].

REFERENCES

BATU, V. 1998. *Aquifer hydraulics: a comprehensive guide to hydrogeologic data analysis*, John Wiley & Sons.

BOULTON, N. 1954. Unsteady radial flow to a pumped well allowing for delayed yield from storage. *Int. Assoc. Sci. Hydrol. Publ,* 2**,** 472-477.

BOULTON, N. S. 1963. Analysis of data from non-equilibrium pumping tests allowing for delayed yield from storage. *Proceedings of the Institution of Civil Engineers,* 26**,** 469-482.

CHENINI, I., SILVAIN, R. & BEN-MAMMOU, A. 2008. A simple method to estimate Transmissibility and Storativity of Aquifer Using Specific Capacity of Wells. *J. Applied Sci,* 8**,** 2640-2643.

COOLEY, R. L. & CASE, C. M. 1973. Effect of a water table aquitard on drawdown in an underlying pumped aquifer. *Water Resources Research,* 9**,** 434-447.

GRIMESTAD, G. 2002. A reassessment of ground water flow conditions and specific yield at Borden and Cape Cod. Groundwater, 40, 14-24.

HUI, J. 2011. An analysis of parameter calculation through pumping tests based on the aquifer test. *Hydrogeology and Engineering Geology,* 38**,** 35-38.

HUNT, B. 2006. Characteristics of unsteady flow to wells in unconfined and semi-confined aquifers. Journal of hydrology, 325, 154-163.

KRÁSNÝ, J. 1993. Classification of transmissivity magnitude and variation. *Groundwater,* 31**,** 230-236.

MALAMA, B. 2011. Alternative linearization of water table kinematic condition for unconfined aquifer pumping test modeling and its implications for specific yield estimates. Journal of hydrology, 399, 141-147.

MISHRA, P. K. & NEUMAN, S. P. 2011. Saturated-unsaturated flow to a well with storage in a compressible unconfined aquifer. Water Resources Research, 47.

MISHRA, P. K. & NEUMAN, S. P. 2011. Saturated-unsaturated flow to a well with storage in a compressible unconfined aquifer. Water Resources Research, 47.

MOENCH, A. F. 1995. Combining the Neuman and Boulton models for flow to a well in an unconfined aquifer. *Groundwater,* 33**,** 378-384.

MOENCH, A. F. 2004. Importance of the vadose zone in analyses of unconfined aquifer tests. Groundwater, 42, 223-233.

NEUMAN, S. P. 1972. Theory of flow in unconfined aquifers considering delayed response of the water table. *Water Resources Research,* 8**,** 1031-1045.

NEUMAN, S. P. 1974. Effect of partial penetration on flow in unconfined aquifers considering delayed gravity response. *Water resources research,* 10**,** 303-312.

NEUMAN, S. P. 1975. Analysis of pumping test data from anisotropic unconfined aquifers considering delayed gravity response. *Water Resources Research,* 11**,** 329-342.

NI, C.-F., HUANG, Y.-J., DONG, J.-J. & YEH, T.-C. 2015. Sequential hydraulic tests for transient and highly permeable unconfined aquifer systems-model development and field-scale implementation. Hydrology & Earth System Sciences Discussions, 12.

PRICKETT, T. A. 1965. Type-curve solution to aquifer tests under water-table conditions. *Groundwater,* 3**,** 5-14.

TARTAKOVSKY, G. D. & NEUMAN, S. P. 2007. Three-dimensional saturated-unsaturated flow with axial symmetry to a partially penetrating well in a compressible unconfined aquifer. Water Resources Research, 43.

ZHAN, H. & ZLOTNIK, V. A. 2002. Groundwater flow to a horizontal or slanted well in an unconfined aquifer. Water Resources Research, 38, 13-1-13-11.

ZANCO Journal of Pure and Applied Sciences
The official scientific journal of Salahaddin University-Erbil
https://zancojournals.su.edu.krd/index.php/JPAS

ISSN (print):2218-0230**, ISSN (online):** 2412-3986**, DOI: http://dx.doi.org/10.21271/zjpas**

RESEARCH PAPER

Synthesis, Characterization, and Antibacterial Activity of Ni(II), Pd(II), and Pt(II) Complexes with 2-benzoylthiobenzimidazole

Karwan O. Ali[1], and Hikmat A. Mohamad[2]

[1]Department of Physics, College of Science, Halabja University, Halabja, Kurdistan Region, Iraq
[2]Department of Chemistry, College of Education, Salahaddin University-Erbil, Kurdistan Region, Iraq

A B S T R A C T:

The thioester compound of 2-benzoylthiobenzimidazole was prepared by S-acylation of 2-mercaptobenzimidazole with benzoyl chloride and reactions of divalent Ni, Pd, and Pt salts with one equivalent of thioester compound a new complexes were isolated in a high percentage. A tetradentate thioester compound and a bivalent metal complexes were identified by CHNS analysis, IR, magnetic susceptibility, molar conductivity, UV-Vis, and ^{1}H, ^{13}C NMR spectroscopies. The anti-bacterial activity of the thioester compound and the bivalent metal complexes were studied using disk diffusion test method against the bacterial species, Staphylococcus aureus, and Pseudomonas aeruginosa. The divalent metal complexes demonstrated a greater activities compared to thioester compound a lone. Structural analysis showed that 2-benzoylthiobenzimidazole L behaves as a neutral four coordination modes compound and bonds to the bivalent metals cation through two nitrogen, sulfur and oxygen atoms. Our study informed the formation of four-coordinate square planar complexes structure around divalent metal salts of Ni, Pd, and Pt.

KEY WORDS: 2-benzoylthiobenzimidazole; Square planar geometry; Divalent metal ions complexes; Antibacterial activity, Structural study.
DOI: http://dx.doi.org/10.21271/ZJPAS.32.2.3
ZJPAS (2020) , 32(2);15-23 .

INTRODUCTION :

Transition coordination compounds were analyzed and get more significant in coordination chemistry for a numerous analyst around the world since of their molecular structure bind together by the interactions in a single structure, such as acid to base interaction, metal to ligand and ligand to metal charge transfer (Steed and Atwood, 2000; Sauvage, 1999).

* **Corresponding Author:**
Karwan Omer Ali
E-mail: karwan.ali@uoh.edu.iq
Article History:
Received: 29/05/2019
Accepted: 13/10/2019
Published: 22/04 /2020

Inorganic compounds and coordination chemistry have been comprehensively used in catalysts, drug chemistry and biochemical application (Gupta and Sutar, 2008). Derivatives of 2-benzimidazolethiol are a significant part of heterocyclic chemistry as a result of their extensive play in biochemical and pharmaceutical studies such as antibacterial (Mavrova et al., 2010), antimicrobial (Gurrala et al., 2011) antitubercular (Gupta and Pancholi, 2011), antifungal (Huang et al., 2007), antagonist and antihistamine (Okamoto et al., 2008). Thioester consisting of heterocyclic compound one of the most essential organosulfur compounds that are the main constituent of biological ester and pharmaceutical compounds (Neumann and Walsh, 2008; Schwarzer et al., 2011). Thiol derivatives reacts with acyl chloride one of the

significant method for the preparation of heterocyclic thioester compounds (Kazemi and Shiri, 2015). The acylation of a sulfur atom of heterocyclic thiols (S-acylation) gives a sufficient and competitive way to keep SH group in the preparation progress (Ko et al., 2006; Goux et al., 1994). Thioester compounds have been effectively used as a raw material for the synthesis of a new drug, and cosmetic. Mixed ligand complexes of thioester compounds with tertiarydiphosphine ligand were also been identified and published (Ali et al., 2017). In this study, the newly thioester ligand have been currently prepared by the S-acylation of 2-benzimidazolethiol with benzoyl chloride. In this report, a newly three bivalent metal complexes of this ligand were investigated, and these complexes showed a significant activity against the P. *aeruginosa and S. aureus* bacteria.

1. MATERIALS AND INSTRUMENTATION

Anhydrous divalent, palladium and platinum salt and 2-benzimidazolethiol was achieved and obtained from Suzhou Yacoo Science Co. $NiCl_2.6H_2O$ from Sigma Aldrich Company. All solvents were brought from Sigma Aldrich. Elemental investigation was taken by a EURUEA 300 CHNS analyzer. FTIR Shimadzu 8400S spectrophotometer was used by using CsI disc and KBr discs from 4000-200 cm^{-1} and 4000-400 cm^{-1} respectively. Burkeir 400 MHz spectrometer was used to record ^1H and ^{13}C NMR spectra in $CDCl_3$ as solvent and TMS as an internal standard. AE-UV1609 (UK) CO., LTD Shimadzu spectrometer was used to measure UV-Vis spectra using a chloroform solvent. Magnetic moment of synthesized transition compounds was measured at 25 °C on Johnson Brukeir Magnet BM6. Digital Senz mSiemen conductivity meter was used on 10^3M solution to measure conductivity of complexes. MPD-200 pixel Melting point, apparatus was used to record melting point of prepared compounds.

1.1 2-benzoylthiobenzimidazole

A mixture of 2-benzimidazolethiol (9.02g, 0.06 mol) and potassium carbonate (8.3g, 0.06 mol) was added to acetone (125ml) in distilling flask (250ml) and then the solution mixture was for about 10 min after that added benzoyl chloride (8.434g, 0.06mole) by droops and refluxed for another 4 hr., left a mixture to cool at room temperature and add 100 ml of water, and acidified with dilute acetic acid, then isolate product and rinse by water several times. Yield: 11.296 g (74%), m.p.: (197 °C). M.Wt: 254.307 g/mol. IR spectrum: 3057 (Ar), 1618 (CN), 1712 (CO), 3151 (N-H), 657 (C-S), 1350 (C-N). UV-Vis spectrum, $\lambda_{max,}$ nm: 238.8, 307.8 and 383. ^1H NMR spectrum, δ, ppm: 10.72 s (1H, NH), 7.26-7.52 t (2H, Ar), 7.42-7.91 d (2H, Ar), 7.69 t (1H, Ar).^{13}C NMR spectrum, δC, ppm: 169.18 (C=O), 109.95 (C9, Ph), 112.67 (C10, Ph), 124.02 (C11, Ph), 125.11 (C3, Ph), 128.86 (C4, Ph), 130.87 (C5, Ph),131.04 (C2, Ph), 132.20 (C8, Ph), 132.71 (C7, Ph), 134.5 (C6, Ph), 169.18 (C1, Ph).

1.2 Synthesis of the complexes

In general manner, Bivalent metal complexes were synthesized by add $NiCl_2.6H_2O$, $PdCl_2$ and $PtCl_2$ (2.0 mmol) in methanol (20 mL) to the 2-benzoylthiobenzimidazole ligand (1 mmol) in methanol (20 ml). The resulting mixtures were refluxed for 4 h., allow the mixtures to evaporate at room temperature and purified the product by washing three times with diethyl ether.

$[Ni_2LCl_4].2H_2O$: yellow green solid, yield 82%, mp 166°C, M.Wt: 419.96 g/mol.. IR spectrum: 3381 (OH), 3163 (NH), 3052 $(CH)_{Ar}$, 1612 (CN), 1691(CO), 482 (Ni-O), 582 (Ni-N), 428 (Ni-Cl). UV–Vis spectrum, $\lambda_{max,}$ nm: 254, 310, and 524.

$[Pd_2LCl_4]$: Orange brown solid, yield 73%, mp 292°C, M.Wt: 609.14 g/mol. IR spectrum: 3162 (NH), 3056 $(CH)_{Ar}$, 1616 (CN), 1701(CO), 507 (Pd-N), 553 (Pd-NH), 451 (Pd-S), 470 (Pd-O), 343 (Pd-Cl). UV–Vis spectrum, $\lambda_{max,}$ nm: 248, 350, and 426.

$[Pt_2LCl_4]$: Brown yellow solid, yield 72%, mp >310°C, M.Wt: 786.46 g/mol. IR spectrum: 3159 (NH), 3059 $(CH)_{Ar}$, 1608 (CN), 1699 (CO), 514 (Pd-N), 534 (Pd-NH), 443 (Pd-S), 472 (Pd-O), 337 (Pd-Cl). UV–Vis spectrum, $\lambda_{max,}$ nm: 256, 308, and 435.

1.3 Bacterial species

In the study we used one gram negative bacterium and one gram positive bacterium. The standard strains of the following microorganism were used as test organisms: Pseudomonas aeruginosa (ATCC15442) and Staphylococcus aureus (MTCC1144).

2. RESULTS AND DISCUSSION

Physical properties and analysis data of 2-benzoylthiobenzimidazole and bivalent

coordination compounds are collected in the Table 1. A new 2-benzoylthiobenzimidazole ligand was synthesized by the esterification of thiol 2-mercaptobenzimidazole with benzoyl chloride 1:1 M ratio in acetone (Scheme 1) (Heralagi, et al., 2012). A 2-benzoylthiobenzimidazole have four donor atoms (O, 2N, S) that capable to the formation of binuclear bivalent metal complexes. Spectroscopic studies and CHNS analysis data showed that the complexes structures are $[Ni_2LCl_4].2H_2O$ and $[M_2LCl_4]$ (where M= Pd(II), Pt(II) and L= 2-benzoylthiobenzimidazole ligand). An expected complexes structures are comparable with data taken by spectroscopic techniques, magnetic moment and molar conductivity. The conductivity value of bivalent nickel, palladium, and platinum complexes in dimethyl sulfoxide (DMSO) were 17.3, 12 and 10.6 ($mol^{-1}.cm^2.ohm^{-1}$) that declares the complexes are nonelectrolyte since all chloride atoms is coordinated to bivalent metal ions and no chlorine is present outside the coordination sphere. A complexes expected structure is in the (Scheme 2).

Table 1. Analytical and physical data of the ligand and their complexes

Compound	m.p °C	μ_{eff}, BM	Colour	Analysis found (calculated), %				Λ_m, Ω^{-1} mol^{-1} cm^2
				C	H	N	S	
[L] $C_{14}H_{10}N_2OS$	197		light yellow	66.31 (66.12)	3.86 (3.96)	11.11 (11.02)	12.70 (12.61)	4.8
$C_{14}H_{10}N_2OSNi_2Cl_4$	166	0.48	yellow green	40.00 (39.73)	3.43 (3.39)	6.66 (6.57)	7.62 (7.94)	17.3
$C_{14}H_{10}N_2OSPd_2Cl_4$	292	0.34	orange brown	27.42 (27.57)	1.53 (1.64)	4.53 (4.59)	5.23 (5.25)	12
$C_{14}H_{10}N_2OSPt_2Cl_4$	>310	0.38	Brown yellow	22.09 (21.36)	1.24 (1.27)	3.46 (3.56)	4.11 (4.06)	10.6

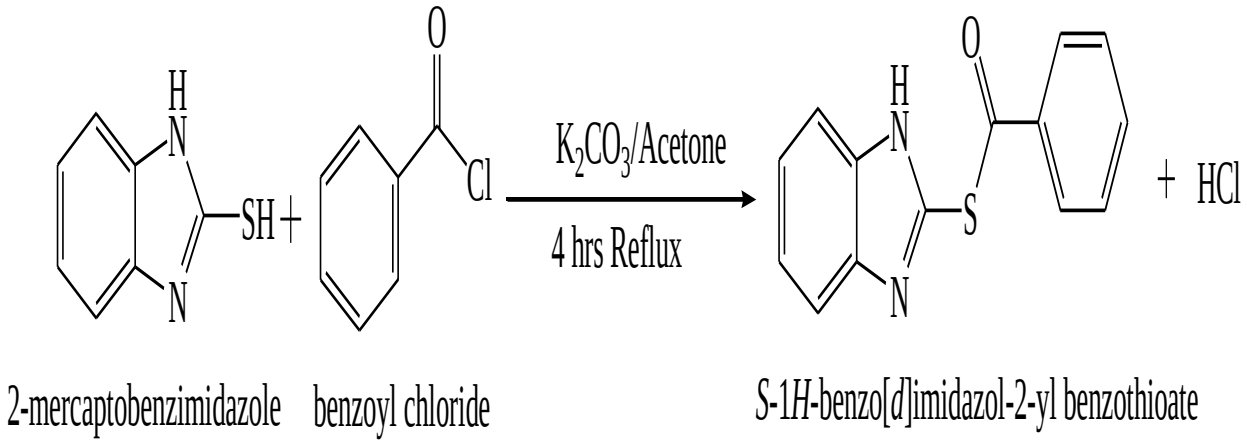

Scheme 1. **Synthesis of the 2-benzoylthiobenzimidazole ligand.**

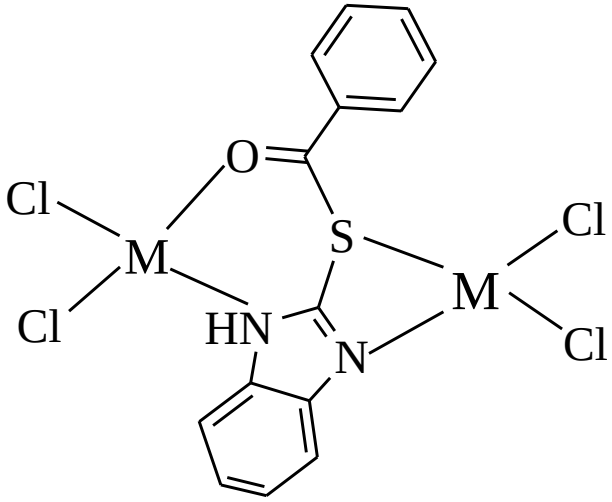

M= Ni(II), Pd(II), and Pt(II)

Scheme 2. The proposed geometrical structure of the complexes.

2.1 The IR Spectra

Table 2 shows a many bands of 2-benzoylthiobenzimidazole ligand and its bivalent metal complexes. In the IR spectrum of thioester ligand the strong absorption peak at 1712 cm^{-1} due to the ν(C=O) carbonyl group (Rao, et al., 2013; Awaz, 2015). In the Ni(II), Pd(II), and Pt(II) complexes, the strong band of ν(C=O) carbonyl groups shifted to the lower frequency to 1691, 1701 and 1699 cm^{-} respectively, by complexation through carbonyl Oxygen to metal atoms (Uçan, 2014). The ligand showed a strong band at 1618 cm^{-1} related to ν(C=N) azomethine group (Hamad, et al., 2016), and the strong peaks at 1612, 1616 and 1608 cm^{-1} attributed to ν(C=N) azomethine group in the bivalent Ni, Pd, and Pt complexes respectively after complexation through the nitrogen of azomethine group (Pessoa, et al., 1998). In addition, the new broad peaks at 3350 cm^{-1} contributed to uncoordinated water molecules was appeared in the Ni(II) complex with the ligand (Al-Jibori, et al., 2002). Also, The bands at 560, 514, and 507 cm^{-1} due to ν (M-N) and the bands at 428, 482, and 470 cm^{-1} related to ν (M-O) have been appeared in the Ni, Pd and Pt complexes respectively (Amin, et al., 2004; Apenysheva, et al., 2006). A new ν (M-S) have been observed at 482, 451, and 443 cm^{-1} in the Ni, Pd, and Pt complexes respectively (Matin and Khojasteh, 2015). Similarly, new ν (M-NH) bands at 560, 553, and 534 cm^{-1} have been created in the Ni, Pd, and Pt complexes respectively (Khan, et al., 2000). In the complexes the bands at 368, 349 and 343 cm^{-1} belong to metal-halogen (M-Cl) coordination (Buttrus, et al., 2003).

Table 2. IR spectral data of the thioester ligand and its complexes.

Compounds	ν (OH)	ν (N-H)	ν (C=N)	ν (C=O)	ν (M-NH)	ν (M-N)	ν (M-S)	ν (M-O)	ν (M-Cl)
[L] $C_{14}H_{10}N_2OS$		3151	1618	1712					
$C_{14}H_{10}N_2OSNi_2Cl_4$	3350	3163	1612	1691	560	560	482	428	368
$C_{14}H_{10}N_2OSPd_2Cl_4$		3161	1616	1701	553	514	451	482	349
$C_{14}H_{10}N_2OSPt_2Cl_4$		3159	1608	1699	534	507	443	470	343

2.2 The NMR spectra

Figure 1 and 2 displays the ^{1}H and ^{13}C NMR signals of thioester ligand. A ^{1}H NMR. Showed singlet signal at 10.72 ppm for one proton attached to the (N-H) group (Ceylan, et al., 2017). The protons of benzene ring connected to the carbonyl group appeared at 7.91 ppm (2d, 2H), 7.52 ppm (t, 2H) and 7.68 ppm (t, 1H). The protons of 2-benzimidazolethiol ring showed a (d, 2H) at 7.42 ppm, (t, 2H) at 7.27 ppm (Kotovskaya, et al., 2001). The structure of the thioester ligand was evaluated further using ^{13}C NMR that exhibited signal at 169.18 ppm corresponding to the carbon of (C=O) group (Farouq, 2018). The ligand also displayed signals at 109.95, 112.67, 124.02, 125.11, 128.86, 130.87, 131.04, 132.20, 132.71 and 134.5 ppm. The formation of these signals is a good confirmation for the thioester ligand formation (Karaoglu, et al., 2009).

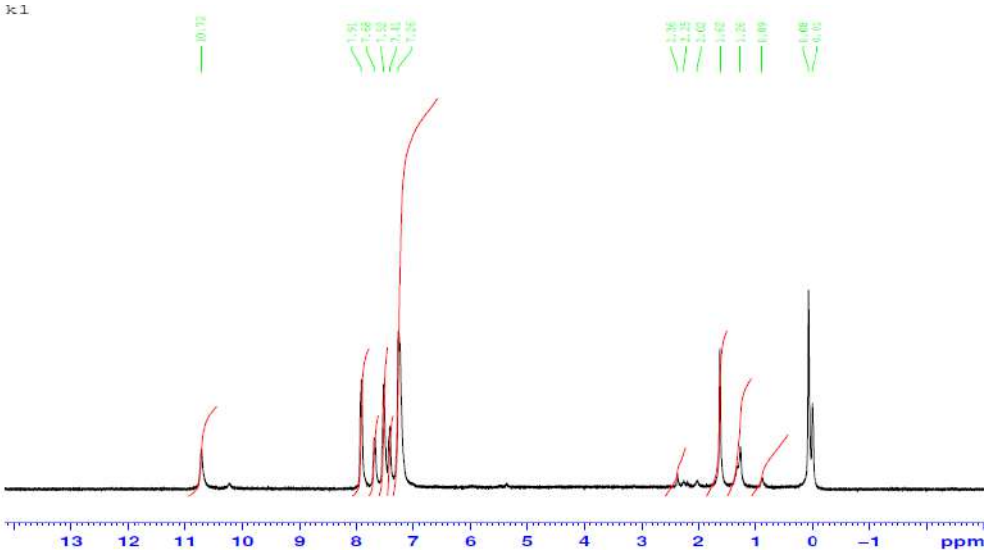

Figure 1. ^{1}H-NMR spectrum of 2-benzoylthiobenzimidazole ligand

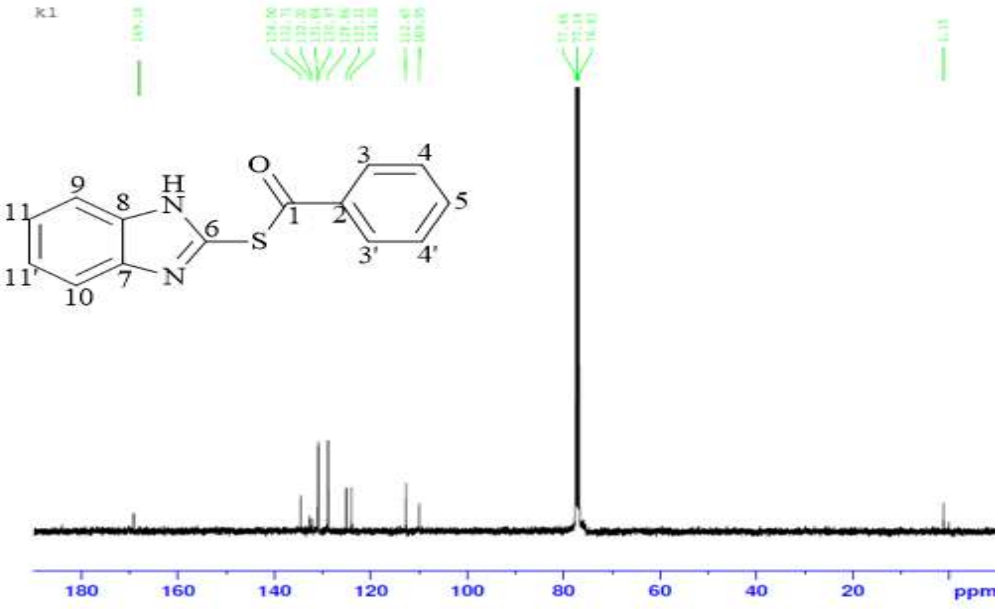

Figure 2. ^{13}C-NMR spectrum of 2-benzoylthiobenzimidazole ligand

2.3 Magnetic and conductivity study

Table 1 displays the value of magnetic susceptibility that carry out at 25°C. The values of magnetic susceptibility are of 0.48, 0.34, and 0.38 BM for the Ni, Pd, and Pt binuclear metal complexes respectively. These values of magnetic moment are in agreement with the formation of diamagnetic metal complexes (Ferenc, et al., 2018). The conductivity study of the metal complexes was measured in DMSO for 10^{-3} M at 25°C. The values of molar conductance was 17.3, 12.0, and 10.6 $cm^2.ohm^{-1}.mol^{-1}$ for Ni, Pd, and Pt complexes respectively. The values of electrical conductivity indicated that the binuclear metal complexes are non-electrolytic since chlorine atoms are coordinated to the metal ions and no one outside the coordination sphere (Geary, 1971) (Table 1).

2.4 UV-Vis study

Figure 3 shows the UV-Vis peaks of the 2-benzoylthiobenzimidazole ligand and it's their binuclear metal complexes which measured in $CHCl_3$ in the range 200–800 nm. The carbonyl group of the thioester ligand showed a peak at 238.8, 307.8 nm and imidazole ring nitrogen has peaks at 348.8, 383 nm assigned to π to π^* (Aziz, et al., 2012) and n to π^* transition (Buyukuslu, et al., 2010). The $[Ni_2LCl_4].2H_2O$ complex displays, peaks at 19083, 32258, and 39370 cm^{-1} a first one was related to ^1A_1g to ^1A_2g transition and the other two peaks were contributed to MLC transfer transition (Mihalache, et al., 2018). The $[Pd_2LCl_4]$ complex have bands at 23474, 28571 and 40322 cm^{-1} which were attributed to ^1A_1g to ^1B_1g, ^1A_1g to 1Eg, and charge transfer transition respectively (Howlader, et al., 2019). The $[Pt_2LCl_4]$ complex shows bands at 22988, 32467 and 39062 cm^{-1}, the first one peak was referred to $^1A_1g \rightarrow {}^1B_1g$ and the other two peaks which were indicated C.T transition (Alsalihi, et al., 2017).

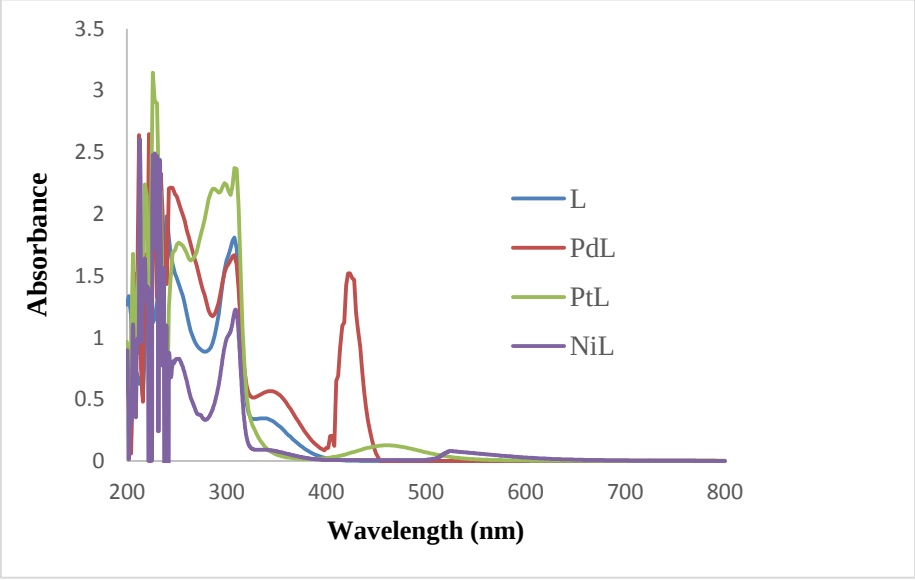

Figure3. UV-Vis spectra of ligand (L) and (Ni(II), Pd(II), Pt(II) complexes.

2.5 Biological activity

The antibacterial properties of ligand 2-benzoylthiobenzimidazole and it's their divalent metal complexes was measured on two kinds of bacteria *Pseudomonas aeruginosa* and *Staphylococcus aureus* by using an inhibition technique according to the literature (De Graaf, et al., 2013; Ramezan, et al., 2012). Figure 4 and table 3 illustrates the inhibition zone in (mm) against bacterial for one day. It is clear from the results that the binuclear metal complexes have more biological activity than the thioester ligand itself under the same condition. The chelation theory can answer the enhancement of the biological activity of coordination compounds (Bermejo, et al., 1999). The ligands increased their biological activity and growth their inhibition area due to chelation in complexes than free ligand. The $[Ni_2LCl_4].2H_2O$ complex has a high activity against the two types of bacteria compared to Pd and Pt complexes. The results of $[Pt_2LCl_4]$ complex displaced remarkable activity for both microorganisms. The nickel and platinum complexes have high activity against *P. aeruginosa and S. aureus* microorganisms in contrast to $[Pd_2LCl_4]$ complex.

Table 3. Antibacterial activity results of ligand and its metal complexes

Compound	Growth Inhibition zone against Bacteria In (mm)	
	P.aeruginosa	***S.aureus***
KBr	0	0
Ligand (L)	5	4
$[Ni_2(L)Cl_4].2H_2O$	29	23
$[Pd_2(L)Cl_4]$	15	12
$[Pt_2(L)Cl_4]$	26	24

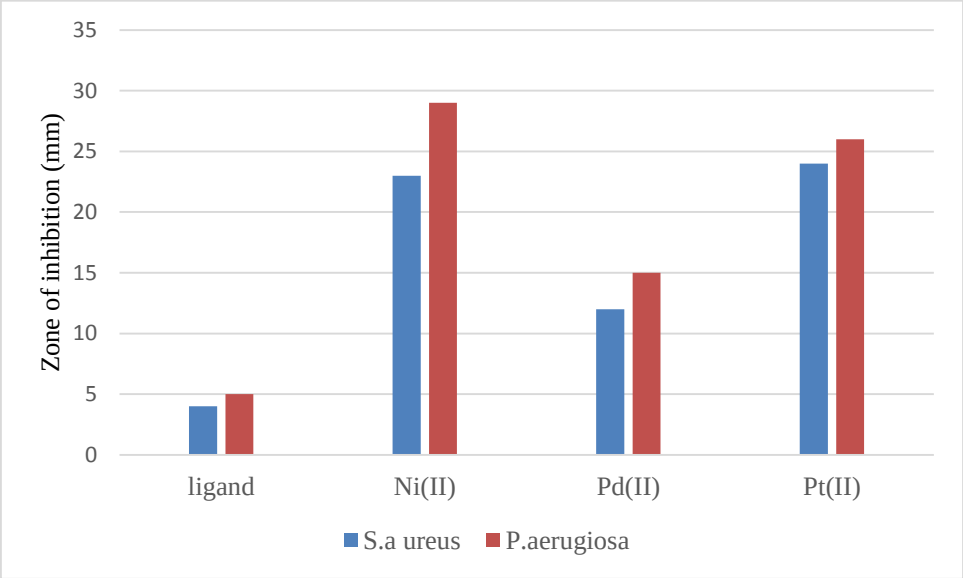

Figure 4. Antibacterial activity of the ligand and complexes

3. CONCLUSIONS

This research has shown the 2-benzoylthiobenzimidazole that contain imidazole group forms binuclear Ni(II), Pd(II) and Pt(II) complexes and these complexes were investigated by spectroscopic and analytical methods. The compound, 2-benzoylthiobenzimidazole was acting as tetradentate ligand in the formation of binuclear metal ion complexes. The magnetic data showed that the bivalent metal complexes of thioester ligand are diamagnetic. The complexes of, 2-benzoylthiobenzimidazole have a good activity against microorganism *P. aeruginosa and S. aureus*.

Acknowledgements

We wish to thank the Salahaddin University for supporting this work. The authors also thank the Halabja University for limited help of this work.

Conflict of Interest

There is no conflict of interest

REFERENCES

Ali, K.O., Ali, H.M., Gerber, T. and Hosten, E. 2017. Mixed Ligand, Palladium (II) and Platinum (II) Complexes of Tertiary DiphosphineswithS-1H Benzo[d] Imidazole-2-yl Benzothioate. *Oriental Journal of Chemistry*, 33 (2), 584-592.

Al-Jibori, S.A., Al-Nassiri, I.N., Al-Hayaly, L.J. and Jassim, A.H. 2002. Mixed ligand transition metal complexes of tertiary phosphines and 5-phenyl-l, 3, 4-oxadiazole-2-thione. *Transition Metal Chemistry*, 27, 191-195.

Alsalihi, E. I. and Al-Fahdawi, A. S. and Meena, B. A. 2017. Synthesis and Characterization of Sodium Diphenylcarbamodithioate Ligand [L] and its Cobalt, Nickel, and Copper Complexes. *Aro-The Scientific Journal of Koya University*, 5(2), 1-5.

Amin, O.H., Al-Hayaly, L.J., and Al-Jibori S.A. 2004. Heterobimetallic complexes of palladium (II) and platinum (II) bridged by the ligand 5-phenyl-1, 3, 4-oxadiazole-2-thione. *Polyhedron*, 23, 2013-2020.

Apenysheva, T.E., Pushkareva, K.S., Bolotin, S.N., Frolov, V.Y., Kolokolov, F.A., Gromachevskaya, E.V., Borodavko, A.A. and Kosulina, T.P. 2006. Synthesis and study of copper(II), nickel(II), and cobalt(II) complex compounds with dihydrobenzoxazine derivatives, *Russian Journal of General Chemistry*, 76, 641-644.

Aziz, A.A., A., Salem, A. N., Sayed, M.A. and Aboaly, M.M. 2012. Synthesis, structural characterization, thermal studies, catalytic efficiency and antimicrobial activity of some M (II) complexes with ONO tridentate Schiff base N-salicylidene-o-aminophenol ($saphH_2$). *Journal of Molecular Structure*, 1010, 130-138.

Bermejo, E., Carballo, R., Castiñeiras, A., Domínguez, R., Maichle-Mössmer, C., Strähle, J. and West, D.X. 1999. Synthesis, characterization and antifungal activity of group 12 metal complexes of 2-acetylpyridine-4 N-ethylthiosemicarbazone (H4EL) and 2-acetylpyridine-N-oxide-4 N-ethylthiosemicarbazone (H4ELO). *Polyhedron*, 18(27), 3695-3702.

Buttrus, N.H., Hussain, A.K. and Talal, A.K. 2003. Synthesis and characterization of new trinuclear palladium (II) and platinum (II) complexes containing Phosphorus-Sulphur ligands. *Asian Journal of Chemistry*, 15(3), 1617.

Buyukuslu, H., Akdogan, M., Yildirim, G. and Parlak, C. 2010. Ab initio Hartree-Fock and density functional theory study on characterization of 3-(5-methylthiazol-2-yldiazenyl)-2-phenyl-1H-indole. *Spectrochimica Acta. Part A, Molecular and Biomolecular Spectroscopy*, 75(4), 1362-1369.

Ceylan, Ü., Çapan, A., Yalçın, Ş.P., Sönmez, M. and Aygün, M. 2017. Vibrational spectroscopic and thermo dynamical property studies, Fukui functions, HOMO-LUMO, NLO, NBO and crystal structure analysis of a new Schiff base bearing phenoxy-imine group. *Journal of Molecular Structure*, 1136, 222-230.

De Graaf, D.C., Alippi, A.M., Antúnez, K., Aronstein, K.A., Budge, G., De Koker, D., De Smet, L., Dingman, D.W., Evans, J.D., Foster, L.J. and Fünfhaus, A. 2013. Standard methods for American foulbrood research. *Journal of Apicultural Research*, 52(1), 1-28.

Ferenc, W., Osypiuk, D., Sarzyński, J. and Głuchowska, H. 2018. The New Complexes of Selected Transition Metal Ions with a Ligand Formed by Condensation of Isatin with Amino Acid: Spectral, Thermal, and Magnetic Properties. *Russian Journal of General Chemistry*, 88, 1525-1532.

Geary, W.J. 1971. The Use of Conductivity Measurements in Organic Solvents for the Characterisation of Coordination Compounds. *Coordination Chemistry Reviews*, 7, 81-122.

Goux, C., Lhoste, P., and Sinou, D. 1994. Palladium (O)-catalyzed alkylation of thiols. *Tetrahedron*, 50, 10321-10330.

Gupta, K.C. and Sutar, A.K. 2008. Catalytic activities of Schiff base transition metal complexes. *Coordination Chemistry Reviews*, 254, 1420-1550.

Gupta, S.K. and Pancholi, S.S. 2011. Synthesis and evaluation of antitubercular activity of some thiobenzimidazolyl derivatives. *Der Pharma Chemica*, 3(1), 274-279.

Gurrala, S., Babu, Y.R., Rao, M.V. and Latha, B.M. 2011. Symmetrical coupling of 2-mercapto Benzimidazole derivatives and their antimicrobial activity. *Journal of Pharmacy and Pharmaceutical Sciences*, 3(2), 217-220.

Hamad, A.N., Briem, R.R. and Nooraddin, S.M. 2016. Synthesis, structure elucidation and antibacterial screening of some new 1, 3-imidazolinone derivatives using micro broth dilution assay. ZANCO Journal of Pure and Applied Sciences, 27(6), 19-30.

Hawaiz, F.E. 2018. Design, Synthesis and Antibacterial Evaluation of Some New Pyrazolinyl Bromophenylthiazoles. ZANCO Journal of Pure and Applied Sciences, 29(6), 28-37.

Heralagi, R., Jayaveera, I. and Shivkumar, B. 2012. Synthesis of some novel bis type 2-mercapto benzimidazole derivatives. *Research Journal of Pharmaceutical, Biological and Chemical Sciences*, 3(2), 407-414.

Howlader, M.B., Tarafder, M.T. and Islam, M.A. 2009. Palladium (II) complexes of hydrazones derived from 4-dodecyloxybenzoylhydrazine with some aliphatic and aromatic aldehydes and their

mesogenic behaviour. *Indian Journal of Chemistry*, 48A, 1078-1084.

Huang, W., Zhao, P.L., Liu, C.L., Chen, Q., Liu, Z.M. and Yang, G.F. 2007. Design, Synthesis, and Fungicidal Activities of New Strobilurin Derivatives. *Journal of Agricultural and Food Chemistry*, 55(8), 3004-3010.

Hussein, A.J. 2015. Synthesis and characterization of some new pyrazoline compounds derived from azo-benzaldehyde. ZANCO Journal of Pure and Applied Sciences, 27(1), 51-58.

Karaoglu, K., Baran, T., Serbest, K., Er, M. and Degirmencioglu, I. 2009. Two novel macroacyclic schiff bases containing bis-N_2O_2 donor set and their binuclear complexes: synthesis, spectroscopic and magnetic properties. *Journal of Molecular Structure*, 922, 39-45.

Kazemi, M. and Shiri, L. 2015. Thioesters synthesis: recent adventures in the esterification of thiols. *Journal of Sulfur Chemistry*, 36, 613-623.

Khan, S.R.A., Guzman-Jimenez, I., Whitmire, K.H. and Khokhar, A.R. 2000. Synthesis and characterize ation of piperidine platinum (II) complexes with dicarboxylates: crystal and molecular structure of cis-[Pt (piperidine)$_2$Cl$_2$]· H_2O. *Polyhedron*, 19(8), 975-981.

KO, J., Ham, J., Yang, I., Chin, J., Nam, S.J. and Kang, H. 2006. A simple one-pot synthesis of hydroxylated and carboxylated aryl alkyl sulfides from various bromobenzenes. *Tetrahedron Letters*, 47, 7101-7106.

Kotovskaya, S.K., Perova, N.M., Baskakova, Z.M., Romanova, S.A., Charushin, V.N. and Chupakhin, O.N. 2001. Fluoro-containing heterocycles. IV. Synthesis of benzimidazole derivatives. *Russian Journal of Organic Chemistry*, 37(4), 564-569.

Matin, S.J. and Khojasteh, R.R. 2015. Synthesis, characterization, and antibacterial activities of Cr(III), Co(III), Ni(II), and Mn(III) complexes of heptadentate Schiff base ligand derived from tris(2-aminoethyl)amine. *Russian Journal of General Chemistry*, 85, 1763-1767.

Mavrova, A.T., Vuchev, D., Anichina, K. and Vassilev, N. 2010. Synthesis, antitrichinnellosis and antiprotozoal activity of some novel thieno [2,3-d]pyrimidin-4(3H)-ones containing benzimidazole ring. *European Journal of Medicinal Chemistry*, 45, 5856-5861.

Mihalache, M., Negreanu-Pirjol, T., Dumitrașcu, F., Drăghici, C. and Călinescu, M. 2018. Synthesis, characterization and biological activity of new Ni (II), Pd (II) and Cr (III) complex compounds with chlorhexidine. *Journal of the Serbian Chemical Society*, 83(3), 271-284.

Neumann, C.S. and Walsh, C.T. 2008. Biosynthesis of (-)-(1S, 2R)-allocoronamic acyl thioester by an FeII-dependent halogenase and a cyclopropane-forming flavoprotein. *Journal of the American Chemical Society*, 130(43), 14022-1423.

Okamoto, O., Kobayashi, K., Kawamoto, Ito, H., Satoh, A., Kato, T., Yamamoto, I., Mizutani, S., Hashimoto, M., Shimizu, A. and Sakoh, H. 2008. Identification of novel benzimidazole series of potent and selective ORL1 antagonists. *Bioorganic and Medicinal Chemistry Letters*, 18, 3278-3281.

Pessoa, J.C., Duarte, M.T., Gillard, R.D., Madeira, C., Matias, P.M. and Tomaz, I. 1998. Preparation of [VO (sal-L-Trp)(H 2 O)](sal-L-Trp= N-salicylidene-L-tryptophanate) and characterisation of an unusual product obtained from its solutions in water pyridine. *Journal of the Chemical Society, Dalton Transactions*, 23, 4015-4020.

Ramezan, A. A., Ali, M.T., Mohammad, J. H., Khadijeh, M. and Mahdi, G.Z. 2012. A method for antibiotic susceptibility testing: applicable and accurate. *Jundishapur Journal of Microbiology*, 2012, 341-345.

Rao, S.S., Dubey, P.K. and Kumari Y.B. 2013. A green and simple synthesis of N-substituted-2-mercaptobenzimidazoles. *Indian Journal of Chemistry*, 52B, 1210-1213.

Sauvage, J.P. 1999. *Transition Metals in Supramolecular Chemistry*. New York: John Wiley.

Schwarzer, D., Ludwig, C., Thiel, I.V. and Mootz, H.D. 2011. Probing intein-catalyzed thioester formation by unnatural amino acid substitutions in the active site. *Biochemistry*, 51(1), 233-242.

Steed, J.W. and Atwood, J.L. 2000. *Supramolecular Chemistry*. 2nd ed. New York: John Wiley.

Uçan, S.Y. 2014. Synthesis, Spectral, thermal, and Magnetic Studies of Cobalt(II), Nickel(II), Copper(II), Zinc(II), and Cadmium(II) Complexes With N_2O_2donor groups. *Russian Journal of General. Chemistry*, 84, 1819-1824.

ZANCO Journal of Pure and Applied Sciences
The official scientific journal of Salahaddin University-Erbil
https://zancojournals.su.edu.krd/index.php/JPAS

ISSN (print):2218-0230**, ISSN (online):** 2412-3986**, DOI: http://dx.doi.org/10.21271/zjpas**

RESEARCH PAPER

The use of pixel-based algorithm for automatic change detection of 3D Building from Aerial and Satellite Imagery: Erbil city as a case study

Sitav H. Abdullah[1], Haval Abduljabbar Sadeq[2], Dleen Mohammed Salih[2]

[1]Department of Civil, Collage of Engineering, Salahaddin University- Erbil , Kurdistan Region, Iraq
[2] Geomatics (Surveying) Department, Collage of Engineering, Salahaddin University- Erbil, Kurdistan Region, Iraq

A B S T R A C T:

Detection of Three Dimension (3D) changes and monitoring urban areas using photogrammetric and remotely sensed data is becoming an important research topic for monitoring the city development, disaster assessment, earthquake monitoring, and updating geo-database. In practice, identifying 3D changes manually in urban areas, specifically when dealing with a large number of buildings is considered to be a very time-consuming task, in such cases, automatic 3D change detection is considered to be very cost-effective. This paper presents an algorithm which is based on using pixels differencing to automatically detect 3D change of the buildings that occurred in the selected study area (Erbil city) for the periods from 2012 to 2017 by subtracting two digital surface models (DSMs) generated from two different datasets that has been captured from two different sensors. The first dataset is from stereo aerial imagery captured in (2012) and the second dataset is based on Very High Resolution (VHR) stereo satellite imagery captured in (2017). The proposed method is applied to three study areas (Ankawa, Dream city and 32 park) in Erbil city. Prior to applying change detection algorithm, the vertical accuracy of the DSMs is checked, through field point measurements by Differential GPS (DGPS).

The presented work in this article deals with building change detection. The changes that refer to differences in size and shape of buildings are considered significant, while changes in other urban objects, such as roads, ground and vegetation, are considered insignificant and needs to be removed. Through some post-processing steps that performed to preserve only the real changes and eliminate the virtual ones.

The outcome of this study revealed that for study area one (Ankawa), 105 out of 157 changed buildings are detected correctly. While in the study area two (Dream city) 74 out of 106 changed buildings are detected correctly, and for study area three (32 park) the result was more accurate and 28 out of 31 changed buildings are detected correctly.

KEY WORDS: DSM, stereo aerial imagery, 3D building change detection, very high-resolution stereo satellite imagery
DOI: http://dx.doi.org/10.21271/ZJPAS.32.2.4
ZJPAS (2020) , 32(2);24-38 .

1.INTRODUCTION :

The process of identifying differences in the state of an object or phenomenon by observing it at different times is known as change detection (CD) (Singh, 1989).

The most dynamically changing areas on earth are specified to be in urban areas. Detection of urban changes is significant for a large number of organizations, such as local governments and municipalities, for various applications including updating maps and managing emergency issues, such as earthquakes or floods.

Generally, remote sensing data is primary sources that is widely used for detecting changes. Recently, because of the steady technology development of sensors, platforms, and algorithms

* **Corresponding Author:**
Sitav Hiwa Abdullah
E-mail: Sitav.abdullah@su.edu.krd
Article History:
Received: 01/06/2019
Accepted: 24/10/2019
Published: 22/04 /2020

for 3D data acquisition and generation, the decision-makers can quickly identify the changes in the area of interest.

Monitoring the changes in Earth's surface features is a significant task, therefore, change detection techniques are an active topic by researchers. Various techniques have been developed to accommodate user requirements in an attempt to overcome the difficulties that arises during the process and provide accurate results for change detection (Lu et al., 2004).

Kurdistan Region of Iraq and particularly Erbil city has a significant urban growth since the year 2000, and the total cultivated land decreases annually, because land transformed to relevant build-up area due to urban growth Erbil city (Ibrahim, 2015). Therefore, automatically detecting building changes is a critical need to measure the amount of changes rapidly.

Different researchers focused only on 2D data that extracted from satellite images for change detection purposes such as (Im et al., 2008, Sadeq, 2009, Bouziani et al., 2010, Champion et al., 2010). However, 2D change detection can extract horizontal changes in planimetric direction, especially in order to detect the object's changing size in planimetric space These results are not sufficient for applications where the vertical change are required, such as progress monitoring for building construction and quantitative estimation of landslides volume (Qin et al., 2016).

3D change detection is considered to be more robust than 2D change detection, because 2D change detection strongly affected by illumination and atmospheric conditions(Tian, 2013). For example, two satellite images are available for the locations where no changes have occurred. One is from the (early summer) where fields and bare soil are visible, while the other is from the (winter) that most of the unsealed area is snow-covered. In such cases when 2D change detection algorithms are adopted by comparing only the spectral images, it would lead to large areas of change because they share different radiometric resolution coming from seasonal differences, which make a false positive in change detection process. Therefore, height is a very important feature in such cases for highlighting the vertical changes. In this research the height information is addressed in change detection which is extracted from the DSMs to determine 3D changes.

Various researcher used 3D change detection based on using Digital Surface Model that derived from Light Detection and Ranging (LiDAR) such as (Murakami et al., 1999, Benedek and Szirányi, 2009, Choi et al., 2009). The 3D change detection is considered to be more accurate but has the limitation of being more expensive and exhibit a low temporal repetition rate. While, in most situations, satellite stereo data are usually much faster, easier, and less expensive to acquire.

Most of the previous studies used only one type of the optical sensor to determine 3D changes (Krauß et al., 2007, d'Angelo et al., 2008, Tian, 2013, Tian et al., 2014). In this research work two different optical sensors used to determine the building changes, one is specified to be derived from aerial sensors which provide 0.1 m Ground Sample Distance (GSD) resolution and satellite sensor which has 0.5 m GSD. The data are captured at two epochs (approximately 5 years difference). Thus, two different DSMs are generated and then subtracted from each other using pixel based images differencing algorithm to determine building changes. The applied techniques in this research can be implemented for municipality works such as illegal housing detection when building structures are constructed in forbidden areas, or during the war when government needs a rapid damage assessment of the impacted areas. As well as it can be used for planning purposes.

2. METHODOLOGY AND MEASUREMENTS

2.1 Study area and Dataset

A study area of 5× 5 km square that had a significant urban development in Erbil city is selected. The methodology is examined in three test areas located within that selected area: Area 1 (ankawa), Area 2 (dream city) and Area 3 (32 park). The first group of the data set consists of a very high resolution stereo satellite imagery of world view-02 (WV02) in year (2017). As shown in the figure (1)

The WV02 satellite was launched by DigitalGlobe at 2009, the images consisted of eight band multi-spectral images, where a set of four new bands (coastal, yellow, red edge and NIR2) are added to the usual four bands (red,

green, blue, and NIR1) with resolution 2 m and one panchromatic band with resolution 0.5m (Konstantinidis, 2017).

The second group of data set is a very high resolution aerial imageries of Erbil city at year (2012) with 0.10m GSD resolution were provided by the photogrammetric labs of Geomatics (surveying) engineering department-college of Engineering. The aerial imageries were acquired by Ultracam Xp sensor with 100.5mm focal length at an altitude of 2195m above MSL, and table-1 presents the characteristic of used aerial images in each case study.

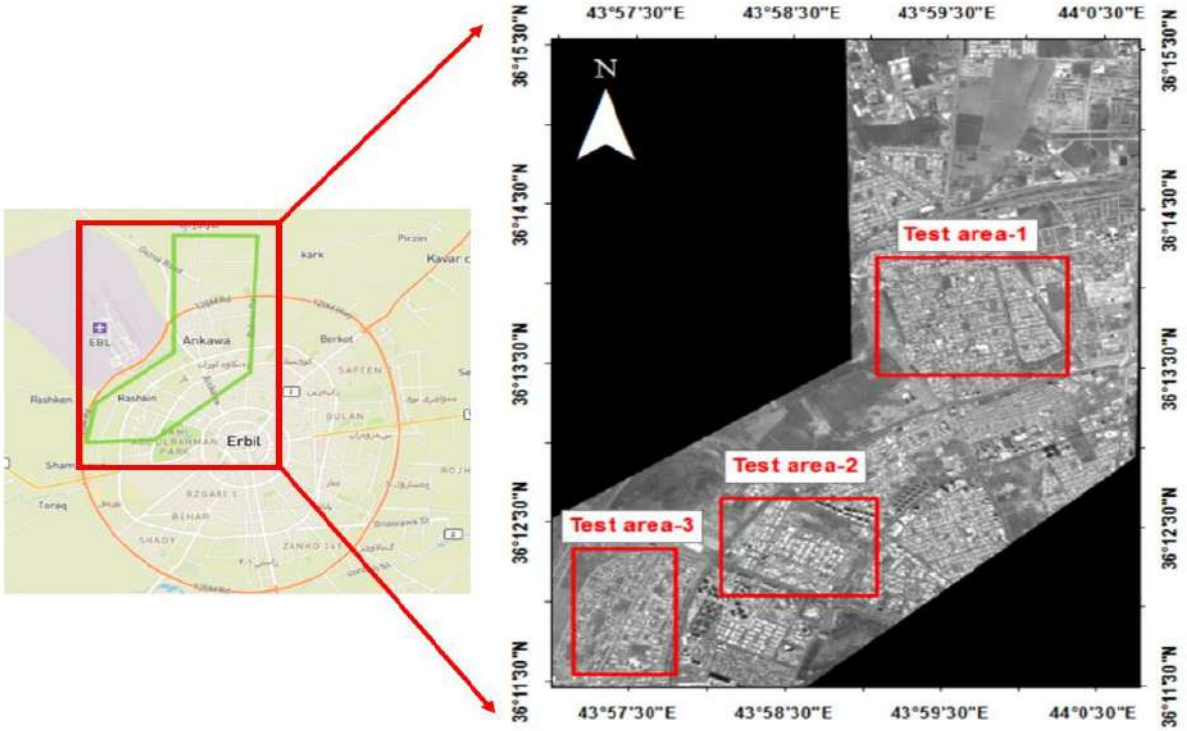

Figure (1): The location of three test areas on the VHR stereo satellite images

Table (1) technical characteristic of the aerial image data used in this research

Test areas	Image ID	Xs	Ys	Zs	OMEGA	PHI	KAPPA	Overlapped Area	GSD
Test area.1	10_0521 10_0522	409642.0549 409640.0010	4009941.9519 4010422.5094	2587.7359 2587.7704	-0.1444 -0.0904	-0.1094 -0.0819	-179.7243 -179.8258	%60 %30	10cm
Test area.2	09_0442 09_0442	408386.4046 408385.4408	4007322.6850 4006840.4430	2593.9523 2594.1559	-0.0100 0.0223	0.1988 0.1600	0.1317 0.1486	%60 %30	10cm
Test area.3	08_0390 08_0391	407118.1138 407116.7327	4006727.4551 4007214.2485	2593.3563 2592.9113	-0.0564 -0.0706	-0.0817 -0.0859	-179.8687 -179.8242	%60 %30	10cm

2.2 Measuring Ground Control Point (GCP)

A set of GCPs is measured for the processing purpose of the satellite and aerial imagery and for the purpose of evaluating the accuracy. The data are collected by using Leica-1200 GPS instrument, at the beginning one hour observation for the base station was carried out via a static method. Then the GCPs were observed through the GPS post processing kinematic (PPK) technique. This technique is used to locate positions whereby received signals from a movable location (rover) to the receiving device (base) then stores position data that can be adjusted by the use of corrections from a reference station after the data collection process. During the observation, the base station took a measurement consciously for seven hours, and the required observation for each rover stations is approximately three minutes. The GCPs are acquired with Universal Transverse Mercator (UTM) zone 38N projection and WGS 84 datum, later the GPS points are imported to Leica geo-office software for post processing purpose and they are processed based on the nearest Continuously Operating Reference Station (CORS), which was Iraq Survey Erbil (ISER) as a source of GPS corrections the result, relative to the base station, was thirty GCPs within millimeters accuracy. Based on the study areas several GCPs are used as checkpoints to assess the accuracy of generated DSMs, figure (2) presented location of GCPs with green dots.

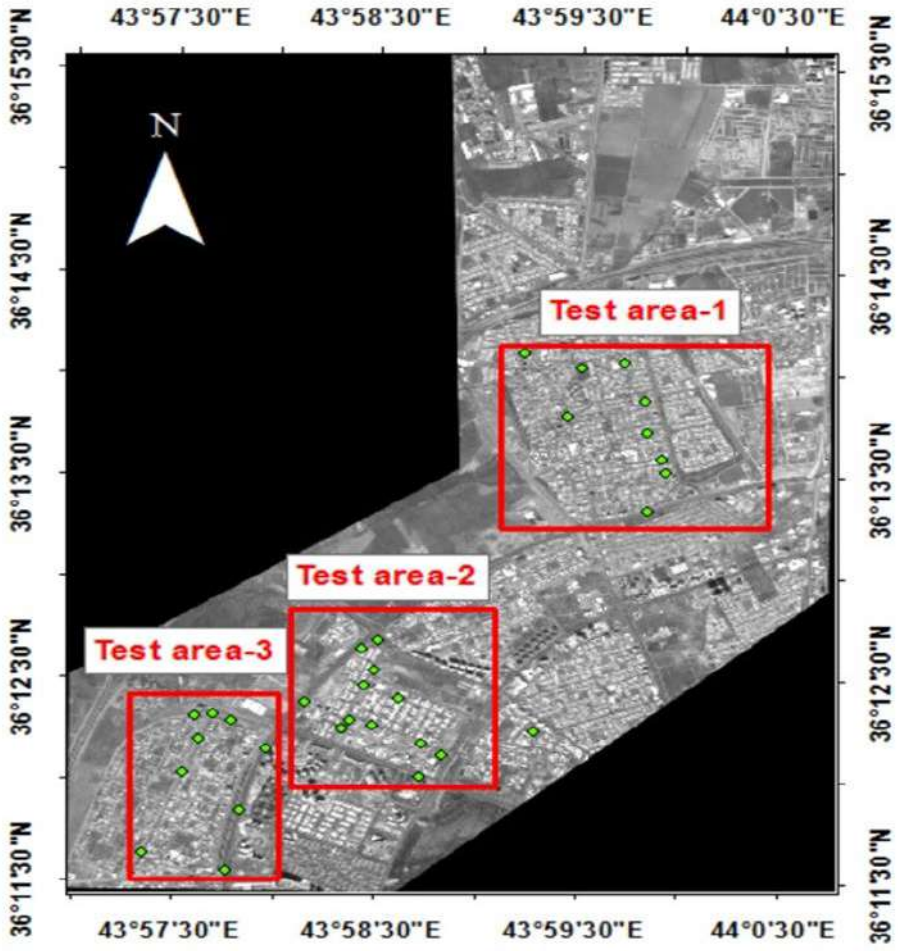

Figure (2): location of the GCPs presented by green dots

2.3 Data Processing and DSM generation

In this study the stereo aerial and satellite imageries are processed through the use of a full featured remote sensing software known as ERDAS Imagine. The package includes Leica photogrammetry suite (LPS) with all the basic photogrammetric tools, it is used to generate DSM from worldview-2 stereo pair data and Aerial images for all three test areas. The flow charts of generating DSM in LPS for both data sets are described in figure (3).

The first step of generating DSM in LPS starts by describe a block file, for the stereo pair satellite images which defining the geometric model of the image through Rational Polynomial Coefficient (RPC) model and the projection. As Worldview-2 stereo images are provided with RPC within Rational Function (RF) sensor model. RPC file contains information about the interior and exterior orientations. The accompanied files are considered to be very useful since it minimizes the time for image processing due to not having to embark on the interior and exterior orientation processes (Sadeq, 2015). Then the block project is assigned by the vertical and horizontal coordinates with UTM projection and WGS 84 datum zone 38N. The two stereo images are added to the block file.

For the aerial images the block file creation starts with adding the parameters of the geometric model of the camera to define the interior orientation. The interior orientation describes the internal geometry of the sensor as it was during image capture while exterior orientation is the sensor position and its orientation, at the time of image capturing (Sadeq, 2015). Followed by, assigning the coordinate system to the UTM zone 38N projection and WGS 84 datum to the block file, the parameters are defined from the camera calibration Report, which is provided by the Manufacturer: Vexcel Imaging GmbH, A-8010 Graz, Austria. Then for each study area, one stereo pair which consisted from two aerial images are added to the block file.

Later, start the tie point generation and bundle block adjustment which lead to the completion of exterior orientation, all these processes are achieved in the LPS software environment. The LPS software supports both manual and automatic tie points generation. The ground coordinates of tie points are not known, but the points are visually recognizable within the overlapping areas of image pairs. LPS selects a matching point in one image, finding its conjugate point in the other (stereomate) image, to measure the similarity between the image points appearing in the overlapped area (Saha, 2014). The Ground coordinates for tie points are computed during block (or aerial) triangulation, where LPS offers the use of different models to optimize the result of aerial triangulation, such as bundle block adjustment (BBA). The BBA uses the collinearity condition as the basis for formulating the relationship between image space and ground space (Geosystems and Mapping, 2003).

A bundled solution is computed including exterior orientation parameters of each image in a block and the X, Y and Z coordinate of tie points.

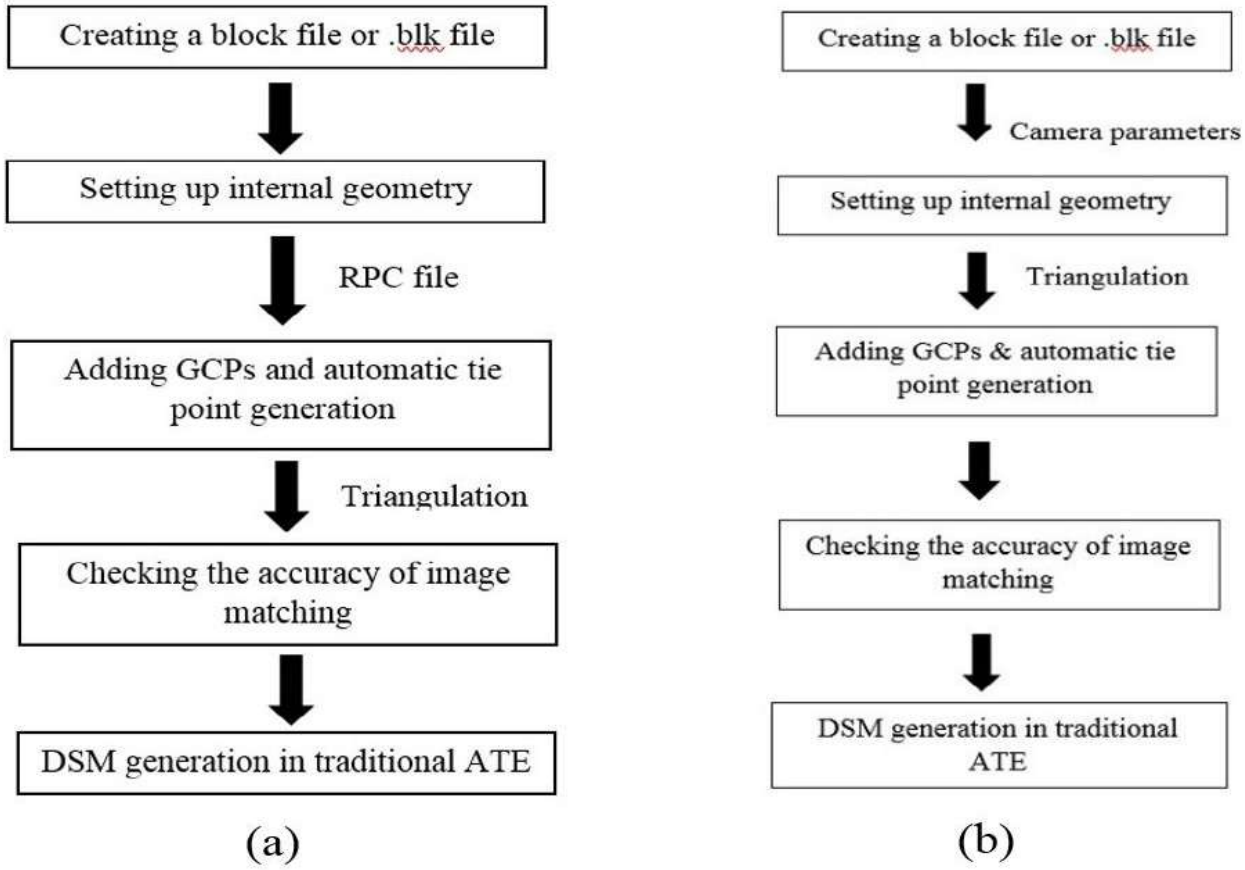

Figure (3): flow charts showing the steps of generation DSM (a) for stereo satellite and (b) for Aerial images

2.4 DSM generation

The DSM is obtained by using classical photogrammetric approach in LPS which is done by image matching process using least square (LS) matching algorithm. It is idea is based on minimizing the differences in grey values between the reference window and search window in an adjustment process where geometric (location, size, and shape of the search window) and radiometric (pixel gray values) corrections of one of matching windows are determined (Schenk, 1999). Least squares correlation is iterative process. The parameters calculated during the initial pass are used in the calculation of the second pass and so on, until an optimum solution is determined. Least square matching technique is the most accurate image matching technique, and the location of the match can be estimated with an accuracy of up to 0.01 pixels(Geosystems and Mapping, 2003).

Finally, the obtained results from LPS processing were six DSMs with 0.30m grid cell size, produced from optical stereo aerial and stereo satellite images. Later the produced DSMs are resampled to 1m grid cell size in order to have the same cell resolution with Normalized Differenced Vegetation Index (NDVI) mask that mentioned in the section 3, because when there is a processing between multiple raster datasets, they need to be stored with the same cell resolution.

Hence, the DSMs from aerial and satellite images for three selected study areas have been generated and shown in figure (4).

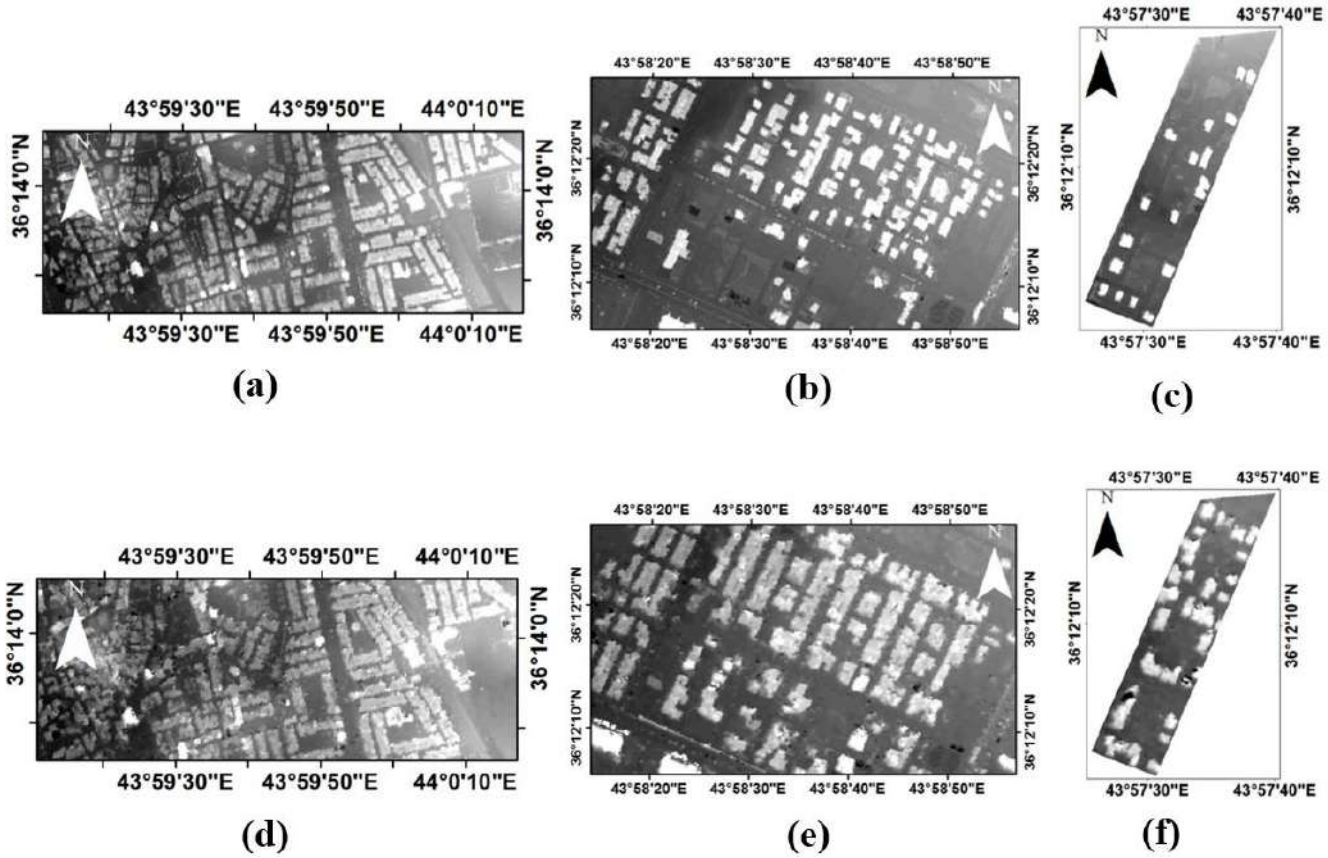

Figure (4) DSMs have been produced for the three study areas, (a, b and c) represents Arial DSMs - 2012 for test area (1, 2&3) respectively, while satellite DSMs-2017 represented by (d, e and f).

3. APPLYING CHANGE DETECTION

Pixel-based image differencing algorithm determines the magnitude of change per pixel between two compared images independently without taking into consideration the pixel neighborhoods. Pixel-based algorithms are fast and easy to implement but suffer from the effect of noise, shadows and illumination variations(Konstantinidis, 2017).

In this study, to perform change detection process, an image differencing algorithm by MATLAB is used to apply on the generated DSMs from date (2012) to the (2017). The flow chart of this pixel-based 3D change detection algorithm is illustrated in figure (5).

The elevation values from the generated DSMs are subtracted, pixel by pixel for computing new binary change map to determine building heights as follow:

$$\text{If } DSM_2(i,j) - DSM_1(i,j) \geq T \quad BC(i,j) = 1 \text{ (changed pixel)} \qquad (1)$$

$$\text{If } DSM_2(i,j) - DSM_1(i,j) < T \quad BC(i,j) = 0 \text{ (Unchanged pixel)} \qquad (2)$$

Where: DSM_2 is satellite DSM-2017, DSM_1 is Aerial DSM-2012, i and j are line and pixel numbers in the DSM images, T is the threshold value, BC is the new binary change map

The obtained binary change map is given in Figure (6) as it shows BC for all test areas.

By subtracting the generated DSMs form each other, the differences in the height of the buildings or urban features are detected. However, some virtual changes that are not belong to the buildings have appeared also. These objects are removed through three steps. First, thresholding is applied as T=2m determines so that height differences less than a threshold value T are considered as computation errors and removed. afterward, the obtained thresholded map is binarized into black and white, where black pixel represents unchanged area while white pixel represents changed area that there changed value is more than 2m.

From the result, it is noticed that the thresholding step succeeds to eliminate most of the virtual changes resulting from DSM computation errors. Nevertheless, some virtual changes do still remain and need to be removed, since the main interest of this paper is only on 3D building changes so the elimination of the vegetation from the 3D change detection scheme is essential. Therefore, in the second step, NDVI mask is calculated from the near-infrared and visible light reflected by vegetation from stereo satellite images as it is given in equation (3). Then NDVI mask subtracted from the binary change map.

$$NDVI = (NIR — VIS) / (NIR + VIS) \quad (3)$$

Where: NIR and VIS stand for the spectral reflectance measurements acquired in the near-infrared and visible (red) regions, respectively (Herring, 2000).

Spurious change in altitude can also be caused by other land covers or DSM computation errors. Building change extraction results will be affected by this type of changes, as they are displayed often around the buildings, therefore, more adaptive post-processing steps are required to keep only the real changes. The final step is applying some mathematical morphology operations, opening followed by closing. Where the mathematical morphology is a non-linear process that commonly used in image analysis which is based on modifying the geometrical shapes within the image, rather than pixel values (Sadeq, 2015).

Based on the test areas the choice of the kernels size for opening and closing operation are carefully done to keep most of the real changes and remove most of the virtual ones, in order to make the real changes more compact and the virtual ones thinner. Figure (6) shows a cleaner final change map.

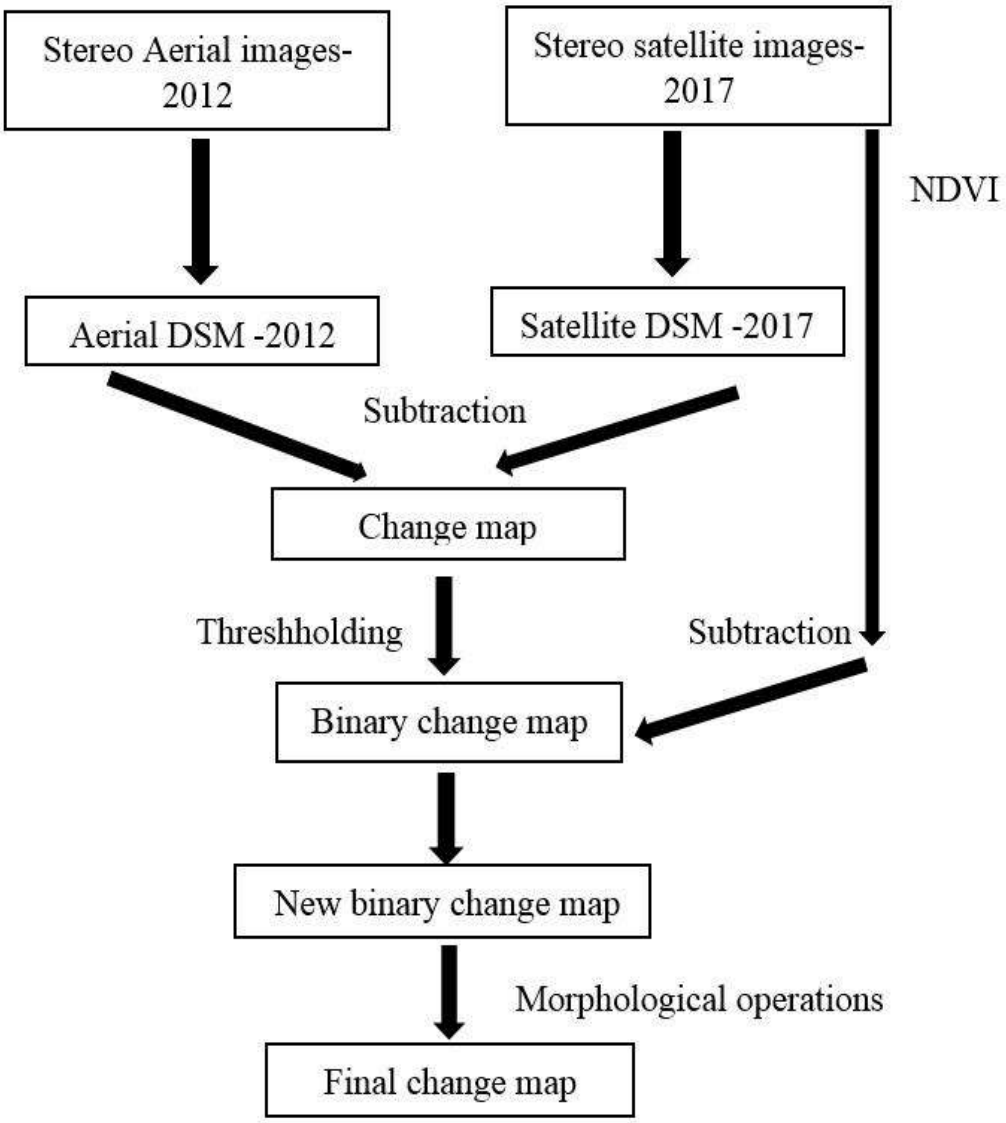

Figure (5) flowchart of the pixel based 3D change detection approach

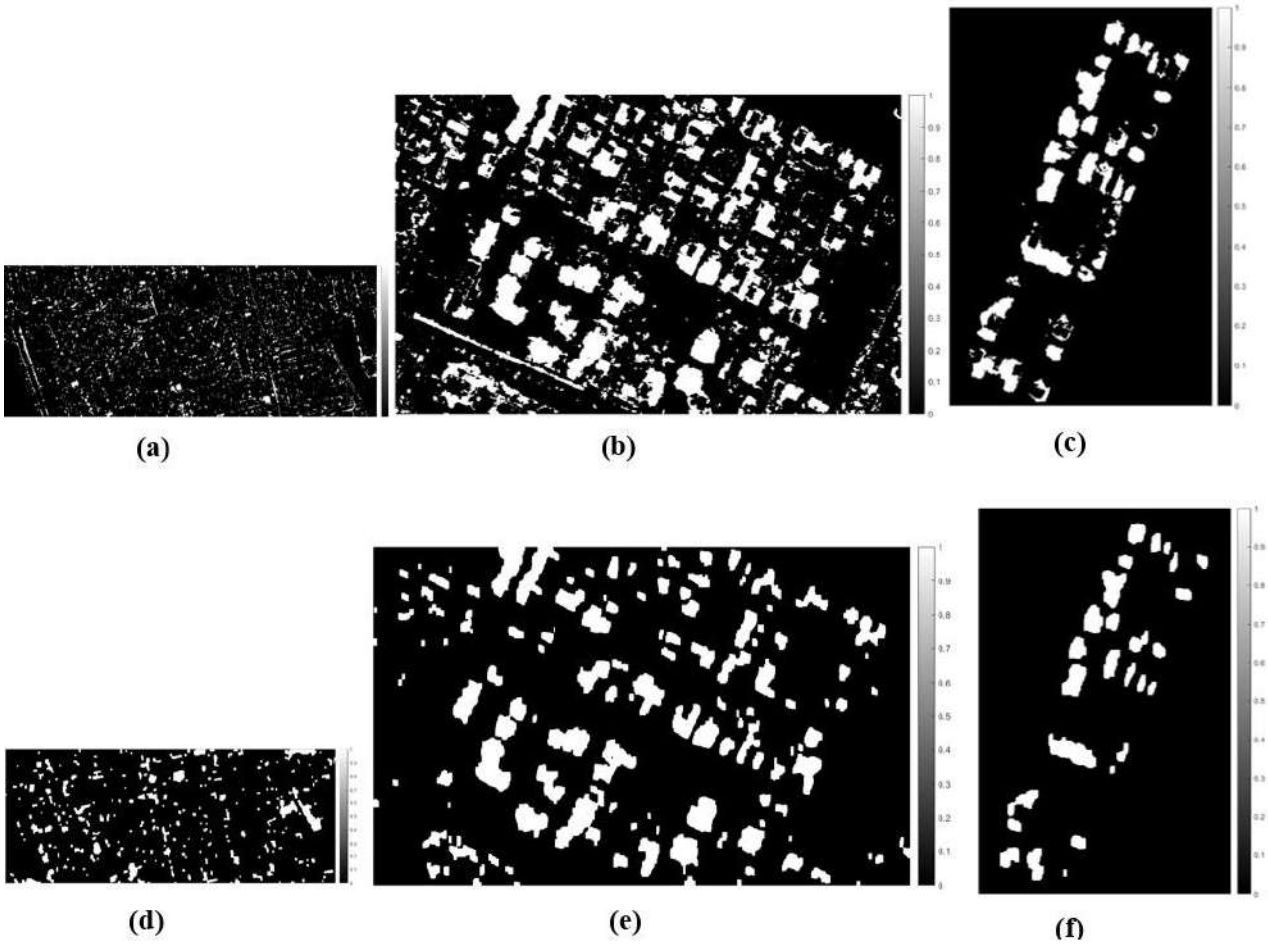

Figure(6) only image differencing pixel based change detection algorithm applied for all test areas presented by (a, b ,c),while after subtracting NDVI mask and applying morphological operation final change map presented by (d ,e, f).A cleaner map is obtained.

4. RESULTS AND DISCUSSION

The change detection results based on the pixel-based image differencing algorithm was examined on three areas (1, 2 and 3). For selected study areas, the building outlines are appeared sharp in the aerial DSMs, while they are quite smooth in the satellite DSMs and showed fewer details than the aerial DSM as it's shown in Figure (4), the reason is the GSD resolution of the aerial DSM is (0.1m) which is higher than the satellite DSM as its (0.50m), so its effect the quality of generated DSMs. Also, a simple difference between generated DSMs at different times is not sufficiently robust to detect the real changes as it is presented by (a, b and c) from figure (6).From the change detection result the vegetation growths are detected as 3D changes, therefore NDVI mask is applied to eliminate the vegetation from the change map. It's seen in figure (7). Also, the existed noise coming from sensor variations and different resolutions are already eliminated by applying some post processing steps in MATLAB software and a cleaner change map obtained as presented in figure (6-d, e, f).

It can be seen from figure (8-a) that a concrete foundation is obviously visible in the center of aerial image 2012. While figure (8-b) a new building can be recognized in the satellite image 2017, which was built on the concrete area, so there is the possibility that the roof top of a new building and the previous concrete floor consist of similar material: therefore, they will share similar radiometric characteristics and even similar texture. In such a cases if only 2D information extracted from satellite and aerial images used to determine changes, the changes in vertical direction are easily overlooked. Thus the height information from a DSM plays an important role in this domain.

For test area two (dream city) from figure (6-e), there is larger urban growth than the test area one, and study area three (32 park), as it's presented in figure (6-f), a smaller area selected in order to show building changes clearly. The outcome result presented in Table-2 shows a good performance for the test area (3) and medium performance for the test area (2). The reason is that in this test area, with 5 years of time difference, some buildings have been reconstructed with a similar height at nearly the same place as the former buildings. In this case, height change is not really helpful.

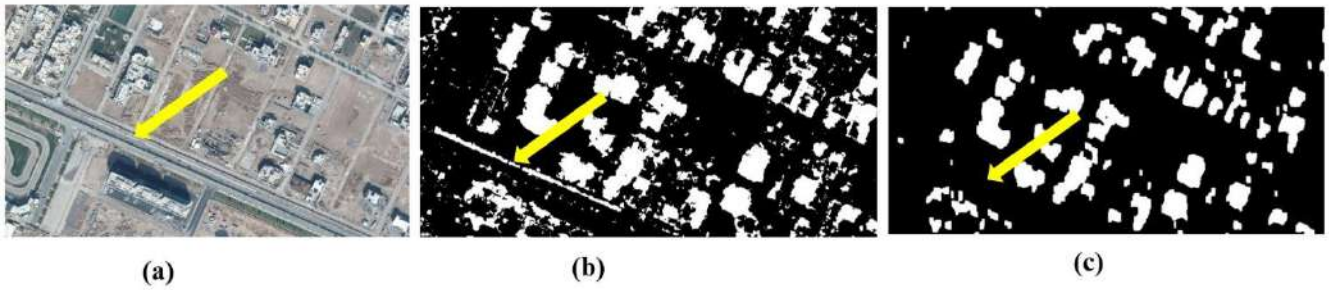

Figure (7) (a) vegetation location in Aerial image marked by the yellow arrow (b) pixel base change map result (c) vegetation removed after subtracting NDVI from the change map

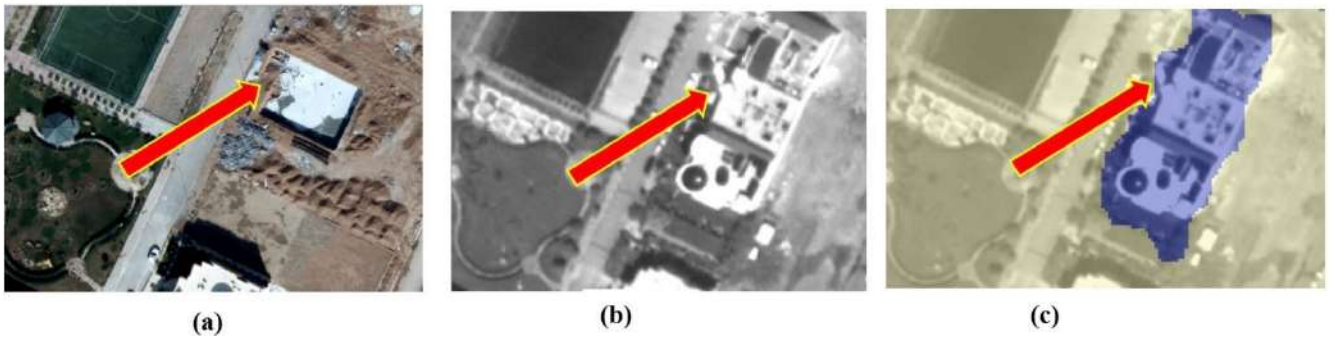

Figure (8) (a) a concrete foundation on Aerial image from (2012), (b) a constructed building on satellite image from (2017) .Also (c) represents the correctly detected 3D building changes without being overlooked.

Table (2) accuracy assessment of each study area based on pixel based change detection algorithm

Test areas	True detected number(TDN)	False detected number(FDN)	Total changed object number(N_T)	True detected rate	False detected rate
Test area-1	105	52	157	%67	%33
Test area-2	74	32	106	%70	%30
Test area-3	28	3	31	%90	%10

4.1 Accuracy assessment

The vertical accuracy of the aerial and satellite DSMs are checked prior to applying change detection it is achieved by comparing the computed Z-coordinate values at checkpoints with the same points on generated DSMs the root mean square error (RMSE) were calculated for each test areas. The result for study area (1,2,3) from aerial DSM were (0.23 m,0.39 m,0.52 m) respectively, and from satellite DSMs were (0.41 m,0.48 m,0.23 m) respectively.

Also, for change detection accuracy assessment, quantitative analysis is applied to check the success rate by overlay the final change map result with the ortho-images generated from aerial DSMs and projected satellite images using arc map software to compare and analysis the result as shown in figure (9) . Moreover, for evaluation pixel based change detection result four indices are measured:

1. True detected number (TDN): The changed objects number that correctly detected as changed.

2-True detected rate (TD): The percentage of the true detected objects number is given in equation (4).

$$TD = TDN/N_T \times 100 \qquad (4)$$

3. False detected number (FDN): The unchanged objects number that incorrectly detected as changed.

4. False detected rate (FD): The percentage of the false detected objects number is given in equation (5).

$$FD = FDN/N_T \times 100 \qquad (5)$$

Where N_T is the total changed objects number. The evaluation result for all test areas presented in table-2.

From the visual inspection of the achieved results, it has shown that DSMs generated from optical stereo imageries could be reliable sources for efficient 3D change detection. However most of the changes are correctly detected, some wrongly detected building changes appeared within the study areas, and they are eliminated through the post processing steps. An example of false and truly detected change result is illustrated in figure (10).

Figure (9) (a) satellite image, (b) ortho image generated from Aerial images, (c) binary change map layer. All layers are overlaid using arc map software

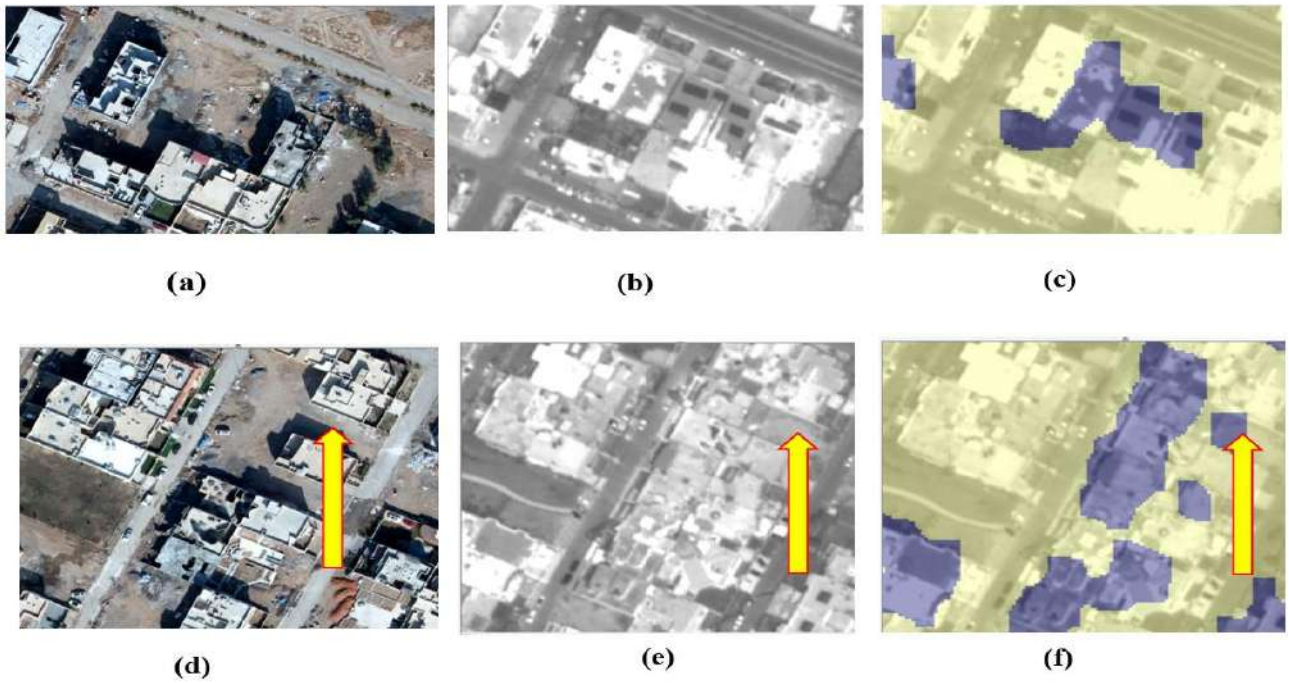

Figure (10) (a) ortho aerial images-2012,(b) satellite image-2017,(c) truly detected change detection result ,(d) ortho Aerial image-2012,(e) satellite imag-2017,(f) false detected change area where selected area by yellow arrow on the images(d,e) is unchanged, while its considered as changed in (f)

5. CONCLUSIONS

Height information plays an important role in monitoring city development, especially, it is helpful for detecting building changes. Most of the previous 3D change detection approaches prefer LiDAR data, which are more accurate but have the drawback of being more expensive and exhibit a low temporal repetition rate. While, in most situations, satellite stereo data are usually much faster, easier, and less expensive to acquire.

Height information from DSM is particularly crucial for change detection of objects exhibiting height values above the ground such as tree or buildings, and the quality of the generated DSMs will be influenced based on the used datasets. However, most of the studies used to determine 3D changes, are addresses only one type of optical sensor used as mentioned in section 1(introduction). In this research two different optical sensors are used. One is specified to be from an aerial optical sensor which provides 0.1 GSD resolution and the other is from the satellite sensor with 0.50 GSD resolution. The generated DSM from aerial images provide more detailed information than the DSM from stereo data.

In this research, the obtained result for test area one (Ankawa) out of 157, the changed buildings that are detected correctly were 105. While in the test area two (Dream city) 74 out of 106 changed buildings are detected correctly, and for test area three (32 park) the result was more accurate and 28 out of 31 changed buildings are detected correctly.

Finally, it can be concluded that manually selecting the threshold value for the change map should be carefully done, which affects the results in several procedures. Also it is noticed that a simple DSM differencing at different times is not sufficiently robust to identify the real changes, therefore, some post-processing steps are required to keep the real changes and eliminate the virtual ones caused by the DSM computation error and also from different nature of the DSM sources.

REFERENCES

BENEDEK, C. & SZIRÁNYI, T. 2009. Change detection in optical aerial images by a multilayer conditional mixed Markov model. *IEEE Transactions on Geoscience and Remote Sensing*, 47**,** 3416-3430.

BOUZIANI, M., GOÏTA, K. & HE, D.-C. 2010. Automatic change detection of buildings in urban environment from very high spatial resolution images using existing geodatabase and prior knowledge. *ISPRS Journal of Photogrammetry and Remote Sensing*, 65**,** 143-153.

CHAMPION, N., BOLDO, D., PIERROT-DESEILLIGNY, M. & STAMON, G. 2010. 2D building change detection from high resolution satelliteimagery: A two-step hierarchical method based on 3D invariant primitives. *Pattern Recognition Letters*, 31**,** 1138-1147.

CHOI, K., LEE, I. & KIM, S. 2009. A feature based approach to automatic change detection from LiDAR data in urban areas. *Int. Arch. Photogramm. Remote Sens. Spat. Inf. Sci*, 18**,** 259-264.

D'ANGELO, P., LEHNER, M., KRAUSS, T., HOJA, D. & REINARTZ, P. Towards automated DEM generation from high resolution stereo satellite images. International Society for Photogrammetry and Remote Sensing, 2008. 1137-1342.

GEOSYSTEMS, L. & MAPPING, L. 2003. Leica photogrammetry suite orthoBASE and orthoBASE Pro user's guide. *Leica Geosystems GIS and Mapping, LLC, Atlanta, GA, USA*.

HERRING, J. W. A. D. 2000. *earthobservatory* [Online]. Available: https://earthobservatory.nasa.gov/features/MeasuringVegetation/measuring_vegetation_2.php [Accessed 18th may 2019].

IBRAHIM, G. R. F. 2015. *Urban Expansion Monitoring in Erbil City. Utilizing Remote Sensing tools in the Kurdistan Region*, GRIN Verlag.

IM, J., JENSEN, J. & TULLIS, J. 2008. Object-based change detection using correlation image analysis and image segmentation. *International Journal of Remote Sensing*, 29**,** 399-423.

KONSTANTINIDIS, D. 2017. Building detection for monitoring of urban changes.

KRAUß, T., REINARTZ, P., STILLA, U., MAYER, H., SCHMITT, M., JUTZI, B. & ROTTENSTEINER, F. 2007. Extracting orthogonal building objects in urban areas from high resolution stereo satellite image pairs. *Int. Arch. Photogrammetry, Remote Sens., Spatial Information Sc*, 36**,** 3.

LU, D., MAUSEL, P., BRONDIZIO, E. & MORAN, E. 2004. Change detection techniques. *International journal of remote sensing*, 25**,** 2365-2401.

MURAKAMI, H., NAKAGAWA, K., HASEGAWA, H., SHIBATA, T. & IWANAMI, E. 1999. Change detection of buildings using an airborne laser scanner. *ISPRS Journal of Photogrammetry and Remote Sensing*, 54**,** 148-152.

QIN, R., TIAN, J. & REINARTZ, P. 2016. 3D change detection–approaches and applications. *ISPRS Journal of Photogrammetry and Remote Sensing*, 122**,** 41-56.

SADEQ, H. A. 2009. City Growth Monitoring Using Map and Remote Sensing: Case Study Arbil-Kurdistan. *ZANCO Journal of Pure and Applied Sciences.*, 21**,** 8.

SADEQ, H. A. 2015. *Merging digital surface models sourced from multi-satellite imagery and their consequent application in automating 3D building modelling*. University of Glasgow.

SAHA, K. 2014. DSM extraction and evaluation from Cartosat-1 stereo data for Bhopal city, Madhya Pradesh. *International Journal of Scientific and Research Publication*, 4**,** 1-5.

SCHENK, T. 1999. *Digital photogrammetry: Vol. I: Background, fundamentals, automatic orientation produceres*, TerraScience.

SINGH, A. 1989. Review article digital change detection techniques using remotely-sensed data. *International journal of remote sensing*, 10**,** 989-1003.

TIAN, J. 2013. *3D change detection from high and very high resolution satellite stereo imagery*. Universität Osnabrück.

TIAN, J., CUI, S. & REINARTZ, P. 2014. Building change detection based on satellite stereo imagery and digital surface models. *IEEE Transactions on Geoscience and Remote Sensing*, 52**,** 406-417.

ZANCO Journal of Pure and Applied Sciences
The official scientific journal of Salahaddin University-Erbil
https://zancojournals.su.edu.krd/index.php/JPAS

ISSN (print):2218-0230**, ISSN (online):** 2412-3986**, DOI: http://dx.doi.org/10.21271/zjpas**

RESEARCH PAPER

Free vibration analysis of multi-cracked nanobeam using nonlocal elasticity theory

Nazhad A. Hussein [*1], Hardi A. M. Rasul [1], Sardar S. Abdullah [1,2],

[1] Department of Mechanical, College of Engineering, Salahaddin University-Erbil, Erbil, Iraq
[2] School of Mechanical Engineering, Iran University of Science and Technology, Narmak, Tehran, Iran

A B S T R A C T:

The aim of this paper is to study the free lateral vibration of multi-cracked nanobeams, and consequently finding the natural frequencies of the cracked nanobeams using two methods. The model of the beam is Euler-Bernoulli in which shear effect has been neglected. Crack is assumed to divide the beam into two segments and these segments are connected to each other by a linear spring and a rotational spring. The crack induces more flexibility to the beam and reduces the stiffness of the beam and consequently influences the dynamic response and the natural frequencies of the beam. Cases of double-cracked and triple-cracked nanobeams are studied. It is observed that when the number of the cracks are increased, the natural frequencies will be decreased. Nonlocal elasticity theory is exposed to the equation of motion. Nonlocal parameter and number of the cracks affect the natural frequencies of the nanobeams. For the case of cantilever, the results are slightly different in contrast to simply supported and clamped-clamped cases. It has been shown that some frequency modes remain constant when the crack severity increases, because of the location of the crack which is a node for a certain mode of vibration.

Keywords: Free vibration, Multi-cracked nanobeams, Euler-Bernoulli, Nonlocal elasticity theory.
DOI: http://dx.doi.org/10.21271/ZJPAS.32.2.5
ZJPAS (2020) , 32(2);39-54 .

1. INTRODUCTION

Nano-sized structures are being applied to highly sensitive and very fine devices, sensors and electromechanical systems. These nanostructures could be plates, beams, or other membranes [1, 2]. When structure is in nano-dimension, the word of size effect will be highlighted and it could not be neglected during analysis of the micro- or nano-sized structures.

* **Corresponding Author:**
Nazhad A. Hussein
E-mail: nazhad6@gmail.com
Article History:
Received: 29/07/2019
Accepted: 28/10/2019
Published: 22/04 /2020

There are several theories of continuum mechanics that have paid attention to the size effect. These theories are size dependent such as modified couple stress theory (MCST), couple stress theory(CST), strain gradient theory, and nonlocal elasticity theory that could be used for analysis of micro and nanostructures [3-6]. Among these continuum theories, nonlocal elasticity theory is one of the widely used theories [7]. In nonlocal theory the size effect is an important factor and it enters the equations for analyzing the wave propagation, crack, and dislocation problems [8, 9].

Nonlocal continuum theory has simpler calculations in contrast to molecular dynamics and discrete atomic simulations. For the first time, Peddieson et al. [10] used nonlocal continuum

theory in nanotechnology and derived the equations of the nonlocal Euler- Bernoulli beam for the case of static. Later, Zhang et al.[11] extended the derived equations to the dynamic problems. Lu et al. [12] has proposed the general expression of the shear force and bending moment for Euler-Bernoulli beam using nonlocal elasticity. Wang [13], Wang et al. [14], and Wang and Varadan [15], have obtained equations for Timoshenko beam using nonlocal elasticity based on the nonlocal bending moment and the local shear force, in which the distributed transverse force was not considered. Reddy [16] derived equations of motion for all kinds of the well-known beam theories such as Euler-Bernoulli, Timoshenko, and Reddy, in order to obtain analytical and numerical solutions on static deflections, buckling loads, and natural frequencies by using the nonlocal elasticity theory relations.

There are several researchers that have used the different continuum theories for linear and nonlinear vibration analysis of nanorods and nanobeams including several parameter effects [17-21].

Loya et al. [22] proposed two methods to analyze free vibration of the nanobeams. They obtained the natural frequencies of the single cracked Euler nanobeams using nonlocal elasticity. Their two proposed methods give the same results the first one has longer calculations but second one leads to shorter equations to find natural frequencies.

Torabi and Nafar Dastgerdi [23] studied the free vibration of cracked Timoshenko nanobeams to find the natural frequencies of the single-cracked nanobeams using nonlocal elasticity. Their results of Timoshenko well agreed with the Euler-Bernoulli beam results.

Roostai and Haghpanahi [24] studied the free vibration of multi-cracked nanobeams by a different method in which the induced flexibility due to the crack, was used instead of crack severity in calculations. Loghmani and Yazdi [25] studied free lateral vibration of Euler-Bernoulli nanobeam with multiple discontinuities. Cracks and steps were considered as discontinuities. Based on wave approach, vibrations were assumed as moving waves along the structure. Mahdi Soltanpour and co-worker's [26] studied free transverse vibration analysis of size dependent Timoshenko FG cracked nanobeams resting on elastic medium. Ebrahimi and Mahmoodi [27] studied the thermal loading effect on free vibration characteristics of carbon nanotubes (CNTs) with multiple cracks. Furthermore, a noticeable amount of studies has been conducted on the case of forced vibration analysis. Akbaş [28] worked on the forced vibration responses of functionally graded Timoshenko nanobeam using modified couple stress theory with damping effect.

2. THEORY AND FORMULATION

2.1. Governing equations for the Eringen nonlocal elasticity theory

According to the nonlocal elasticity theory [7], the nonlocal stress-tensor (σ_{ij}) at point x in a body is not only a function of the strain at the same point (local theory), but it is also a function of strains at all other points of the structure. As for the case of homogenous and isotropic nonlocal elastic solid, the general form of equations is written as

$$\sigma_{ij}(x) = \int \alpha(|\acute{x} - x|, T) t_{ij}(x) dV(\acute{x}) \quad (1)$$

The kernel $\alpha|\acute{x} - x|$ is the nonlocal modulus which incorporates into the constitutive relation the nonlocal effect of the stress at point x created by local strain at the point $\acute{x}$. $|\acute{x} - x|$is the Euclidean distance. The expressions t_{ij} are the components of the classical local stress tensor at point x. These components have a relation with the local linear strain tensor components ε_{ij} for the materials that obey Hook's law as:

$$t_{ij}(x) = \lambda \varepsilon_{ss}(x) \delta_{ij} + 2G\varepsilon_{ij}(x) \quad (2)$$

T is the ratio between a characteristic internal length a and characteristic external l length, and $e_o$is a constant which depends on the material and it has to be obtained experimentally or by matching dispersion curves of plane waves with those of atomic-lattice dynamics. T is given by

$$T = \frac{e_o a}{l} \quad (3)$$

The integral form of the relation given by Eq. (1) can be represented as a differential form as

$$[1 - (e_o a)^2 \nabla^2]\sigma_{ij} = [1 - (Tl)^2 \nabla^2]\sigma_{ij} = E\varepsilon(x) = t_{ij} \quad (4)$$

2.2. Nonlocal Euler-Bernoulli beam equations

The displacements for a beam with length L along its axial direction and its vertical directions are:

$$u_1 = u(x,t) - z\frac{\partial w}{\partial x} \quad u_2 = w(x,t) \quad u_3 = 0 \quad (5)$$

Where u and w are displacements of the beam along the axial and the transvers directions respectively and there is not any motion along third direction (i.e. $u_3 = 0$). Strain in x direction (axial) is given as

$$\varepsilon_{xx} = \frac{\partial u}{\partial x} - z\,\frac{\partial w^2}{\partial x^2} \quad (6)$$

Equations of motion for the beam in axial and transverse directions where rotary inertia is neglected will be

$$\frac{\partial P}{\partial x} + Q(x,t) = \rho A\,\frac{\partial u^2}{\partial t^2} \quad (7)$$

$$\frac{\partial M}{\partial x} + f(x,t) = \rho A\,\frac{\partial w^2}{\partial t^2} \quad (8)$$

where P is the axial force, Q is the horizontal distributed force along the axial direction, M is the resultant bending moment, f is the vertical distributed force, ρ is the density, and A is the cross-sectional area of the beam. Where I is the second moment of inertia and V is the shear force. Where $P, M, V,$ and I are defined as

$$P = \int_A \sigma_{xx}\,dA \qquad M = \int_A -\sigma_{xx}\,z\,dA$$

$$V = \int_A \sigma_{xy}\,dA \qquad I = \int_A z^2 dA \quad (9)$$

According to Reddy [16] and Reddy and Pang [3], the nonlocal form of axial force, the bending moment and the shear force can be written as:

$$P(x) = EA\frac{\partial u}{\partial x} + (e_o a)^2\left[\frac{\partial}{\partial x}\left(\rho A\,\frac{\partial^2 u}{\partial t^2}\right) - \frac{\partial Q}{\partial x}\right]$$

$$M(x) = EI\frac{\partial^2 w}{\partial x^2} + (e_o a)^2(\rho A\,\frac{\partial^2 w}{\partial t^2} - f\,)$$

$$V(x) = -EI\frac{\partial^3 w}{\partial x^3} + (e_o a)^2\left[\frac{\partial}{\partial x}\left(\rho A\,\frac{\partial^2 w}{\partial t^2}\right) - \frac{\partial f}{\partial x}\right] \quad (10)$$

Equations of motion of the nonlocal nanobeam for the axial and the lateral displacements according to Reddy [16] and Reddy and Pang [3], are respectively as

$$EA\frac{\partial^2 u}{\partial x^2} + Q - (e_o a)^2\frac{\partial^2 Q}{\partial x^2} = \rho A\,\frac{\partial^2 u}{\partial t^2} \quad (11)$$

$$EI\frac{\partial^4 w}{\partial x^4} + \rho A\left[\frac{\partial^2 w}{\partial t^2} - (e_o a)^2\frac{\partial^2}{\partial x^2}\left(\frac{\partial^2 w}{\partial t^2}\right)\right] = f - (e_o a)^2\frac{\partial^2 f}{\partial x^2} \quad (12)$$

For the case of free lateral vibration, all of the external forces must be zero, so Eq. (12) will be changed and used for lateral vibration as

$$EI\frac{\partial^4 w}{\partial x^4} + \rho A\left[\frac{\partial^2 w}{\partial t^2} - (e_o a)^2\frac{\partial^2}{\partial x^2}\left(\frac{\partial^2 w}{\partial t^2}\right)\right] = 0 \quad (13)$$

The well-known separation method will be used to solve the above differential equation as

$$w(x,t) = W(x)T(t) \quad (14)$$

Let's assume $c^2 = \frac{\rho A}{EI}$ and ω is the natural frequency of non-cracked beam, then substituting Eq. (14) in Eq. (13) gives

$$\frac{\partial^4 W(x)}{\partial x^4} * \frac{1}{c^2[\,W - (e_o a)^2\frac{\partial^2 W(x)}{\partial x^2}\,]} = \omega^2 \quad (15)$$

Using following dimensionless variables and constants given by

$$\varsigma = \frac{x}{L} \qquad \mu = \frac{e_o a}{L} \qquad \lambda^4 = c^2\omega^2 L^4 = \frac{\rho A\,L^4}{EI}\omega^2$$

$$\bar{W} = \frac{W}{L} \quad (16)$$

Substituting Eq. (16) in Eq. (15) leads to reform Eq. (15) to a spatial equation as

$$\bar{W}^{IV} + \lambda^4(\mu^2\,\bar{W}'' - \bar{W}) = 0 \quad (17)$$

Where $(.)'$ is the derivative with respect to ς. We assume $\bar{W} = me^{st}$ to solve the above differential equation and find its roots as

$$s^4 + \lambda^4(\mu^2 s^2 - 1) = 0 \quad (18)$$

The roots will be as following

$$s_1 = -\beta_1 \qquad s_2 = \beta_1 \qquad s_3 = i\beta_2$$

$$s_4 = -i\beta_2 \quad (19)$$

The general solution of Eq. (17) by using Eq. (19) will be as

$$\bar{W}(\varsigma) = A_1 e^{-i\beta_2 x} + A_2 e^{i\beta_2 x} + A_3 e^{-\beta_1 x} + A_4 e^{\beta_1 x}$$

$$\bar{W}(\varsigma) = C_1\sinh(\beta_1\varsigma) + C_2\cosh(\beta_1\varsigma) + C_3\sin(\beta_2\varsigma) + C_4\cos(\beta_2\varsigma) \quad (20)$$

Where

$$\beta_1 = \lambda^2\,\mu\sqrt{\frac{\sqrt{1+4/\mu^4\,\lambda^4}-1}{2}}$$

$$\beta_2 = \lambda^2\,\mu\sqrt{\frac{\sqrt{1+4/\mu^4\,\lambda^4}+1}{2}} \quad (21)$$

When the lateral dimensionless displacement is obtained from Eq. (20), the bending slope, the dimensionless bending moment, and the shear force can be obtained respectively form Eq. (10) as

$$\theta(\varsigma) = \bar{W}'(\varsigma)$$

$$\bar{M}(\varsigma) = \frac{M(\varsigma)\,L}{EI} = \bar{W}''(\varsigma) + \mu^2\,\lambda^4\,\bar{W}(\varsigma)$$

$$\bar{V}(\varsigma) = \frac{V(\varsigma)\,L^2}{EI} = \bar{W}'''(\varsigma) + \mu^2\,\lambda^4\,\bar{W}'(\varsigma) \quad (22)$$

Constants C_1, C_2, C_3 and C_4 in Eq. (20) can be determined through the boundary conditions.

2.3. Nonlocal cracked Euler-Bernoulli beam equations

In this case, it is assumed that a beam has one open edge crack of length d located at a distance $\bar{L}$ from the left end and b= $\bar{L}/L$ (b is dimensionless crack distance from the left end of the beam). For the case of the cracked nanobeam as shown Fig. 1, the method which was used by Loya et al. [29],

and has been extended by J. Loya et al. [22]. Now it is being used in this paper.

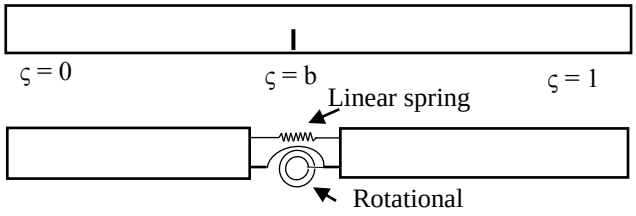

Fig.1 The model of the cracked beam

Crack induces more flexibility to the beam and reduces the stiffness of the beam, therefore, a crack can be modeled as a linear and a rotational spring while the crack induces an additional strain energy to the beam. According to Loya et al. [22], the additional strain energy due to the crack is as

$$\Delta \mathcal{U}_c = \frac{1}{2}\, M\, \Delta\theta + \frac{1}{2}\, P\, \Delta u \qquad (23)$$

Where $\Delta\theta$ and Δu are the angle of rotation of the rotational spring and the axial displacement of the linear spring respectively. In this work, because there is not any axial force acting on the beam, the amount of Δu will be zero. Thus, there is only a rotational spring, and parameter $\Delta\theta$ is given by

$$\Delta\theta = k_{MM}\, \frac{\partial^2 w}{\partial x^2} + k_{MV}\, \frac{\partial u}{\partial x} \qquad (24)$$

The crossover flexibility constant k_{MV} is neglected because it is small enough. Now the slope increment $\Delta\theta$ will be rewritten in the form of dimensionless

$$\Delta\theta = \frac{k_{MM}}{L}\, \frac{\partial^2 \bar{W}(\varsigma)}{\partial \varsigma^2}\Big|_{\varsigma=b} = K\, \frac{\partial^2 \bar{W}(\varsigma)}{\partial \varsigma^2}\Big|_{\varsigma=b} = K\ \bar{W}''(b) \qquad (25)$$

where $K = \frac{k_{MM}}{L}$ and it is a dimensionless form. For nanobeams, $\Delta \mathcal{U}_c$ has to be obtained from either molecular dynamics or "ab initio studies".

2.3.1. First method for cracked nanobeam

Each crack divides the beam into two parts, so if the number of the cracks is increased, the number of parts will be increased too. Each part has its own equation of motion as

$$\bar{W}_1^{IV} + \Lambda^4(\mu^2\, \bar{W}_1'' - \bar{W}_1) = 0 \quad 0 \le \varsigma \le b$$
$$\bar{W}_2^{IV} + \Lambda^4(\mu^2\, \bar{W}_2'' - \bar{W}_2) = 0 \quad \mathrm{b} \le \varsigma \le 1 \qquad (26)$$

The above equation shows the beam has only one crack because there are two equations of motion. Parameter Λ is the frequency parameter of the cracked beam, and its relation with natural frequency of the cracked nanobeam (ω_c) is written as

$$\Lambda^4 = c^2\, \omega_c^2\, L^4 = \frac{\rho A\, L^4}{EI}\omega_c^2 \qquad (27)$$

The same process has been taken in order to find the solution for the case of non-cracked beam, is necessary to be exposed to find the general solution for the case of the cracked beam. Thus, the solution for differential Eq. (26) will be as

$$\bar{W}_1(\varsigma) = C_1 \sinh(\beta_s \varsigma) + C_2 \cosh(\beta_s \varsigma) + C_3 \sin(\beta_f \varsigma) + C_4 \cos(\beta_f \varsigma)$$
$$0 \le \varsigma \le b$$
$$\bar{W}_2(\varsigma) = C_5 \sinh(\beta_s \varsigma) + C_6 \cosh(\beta_s \varsigma) + C_7 \sin(\beta_f \varsigma) + C_8 \cos(\beta_f \varsigma)$$
$$\mathrm{b} \le \varsigma \le 1 \qquad (28)$$

where coefficients β_s and β_f for the cracked beam are similar to Eq. (21) and are given as

$$\beta_s = \Lambda^2\, \mu \sqrt{\frac{\sqrt{1+4/\mu^4\, \Lambda^4}-1}{2}}$$
$$\beta_f = \Lambda^2\, \mu \sqrt{\frac{\sqrt{1+4/\mu^4\, \Lambda^4}+1}{2}} \qquad (29)$$

There are eight unknown constants in Eq. (28), which have to be obtained by exposing the boundary conditions to Eq. (28) and from the following compatibility equations at the crack position.

- Continuity of the vertical displacement

$$\bar{W}_1(\mathrm{b}) = \bar{W}_2(\mathrm{b}) \qquad (30)$$

- Jump in Bending slope

$$\Delta\theta = \bar{W}_2'(\mathrm{b}) - \bar{W}_1'(\mathrm{b}) = K\, \bar{W}_1''(\mathrm{b}) \qquad (31)$$

- Continuity of the bending moment

$$\bar{W}_1''(\mathrm{b}) + \Lambda^4\mu^2\, \bar{W}_1(\mathrm{b}) = \bar{W}_2''(\mathrm{b}) + \Lambda^4\mu^2\, \bar{W}_2(\mathrm{b}) \qquad (32)$$

- Continuity of the shear force

$$\bar{W}_1'''(\mathrm{b}) + \Lambda^4\mu^2\, \bar{W}_1'(\mathrm{b}) = \bar{W}_2'''(\mathrm{b}) + \Lambda^4\mu^2\, \bar{W}_2'(\mathrm{b}) \qquad (33)$$

2.3.2. Second method for cracked beam

There is another method proposed by Loya et al. [22], in which the number of the constants, for all cases of single cracked and multi-cracked nanobeams, for all types of beam supports and boundary conditions will be only four unknown constants, and this method gives the same results as the last method. These constants are: vertical displacement W_o, bending slope θ_o, bending moment M_o, and shear force V_o at $\varsigma = 0$.

$$\bar{W}_1(\varsigma) = W_o\, j_1(\varsigma) + \theta_o\, j_2(\varsigma) + M_o\, j_3(\varsigma) + V_o\, j_4(\varsigma) \qquad 0 \le \varsigma \le b$$

$$\bar{W}_2(\varsigma) = \bar{W}_1(\varsigma) + \Delta\theta\, j_2(\varsigma - b) \quad b \le \varsigma \le 1 \quad (34)$$

Now functions $j_i(\varsigma)$ for all cases, according to Loya [22], are given as

$$j_1(\varsigma) = \cosh(\beta_s\varsigma) + \frac{(\Lambda^4\mu^2+\beta_s{}^2)\,[\cos(\beta_f\varsigma)-\cosh(\beta_s\varsigma)]}{\beta_f{}^2+\beta_s{}^2} \quad (35)$$

$$j_2(\varsigma) = \frac{\sin(\beta_f\varsigma)}{\beta_f} - \frac{(\beta_f{}^3-\Lambda^4\mu^2\beta_f)\,[\beta_s\sin(\beta_f\varsigma)-\beta_f\sinh(\beta_s\varsigma)]}{\beta_f{}^2\beta_s(\beta_f{}^2+\beta_s{}^2)} \quad (36)$$

$$j_3(\varsigma) = \frac{\cosh(\beta_s\varsigma)-\cos(\beta_f\varsigma)}{\beta_f{}^2+\beta_s{}^2} \quad (37)$$

$$j_4(\varsigma) = \frac{-\beta_f\sinh(\beta_s\varsigma)+\beta_s\sin(\beta_f\varsigma)}{\beta_f\beta_s(\beta_f{}^2+\beta_s{}^2)} \quad (38)$$

In this method, for all types of beam supports and boundary conditions, there will be only four constants that two of them could be determined by the boundary conditions at $\varsigma = 0$. The other two constants are determined by the boundary conditions at $\varsigma = 1$. Then a coefficient matrix will be obtained. Determinant of this coefficient matrix will be set equal to zero and a new equation with only one variable is obtained, then the roots of this equation will give the frequency parameters of the cracked nanobeam.

2.4. Nonlocal double-cracked Euler-Bernoulli beam equations

In this section, the equations are derived for double-cracked nanobeam using both methods have been mentioned in last section. A general form is presented for a multi-cracked beam. Equations of the both methods are derived for three different types of supports having different boundary conditions. According to Eq. (28) and Eq. (34) the equations for both methods are derived respectively.

First method to obtain the general equations, and consequently the coefficient matrix, as well as the frequency parameters, is as

$$\bar{W}_1(\varsigma) = C_1\sinh(\beta_s\varsigma) + C_2\cosh(\beta_s\varsigma) + C_3\sin(\beta_f\varsigma) + C_4\cos(\beta_f\varsigma) \qquad 0 \le \varsigma \le b_1$$

$$\bar{W}_2(\varsigma) = C_5\sinh(\beta_s\varsigma) + C_6\cosh(\beta_s\varsigma) + C_7\sin(\beta_f\varsigma) + C_8\cos(\beta_f\varsigma) \qquad b_1 \le \varsigma \le b_2$$

$$\bar{W}_3(\varsigma) = C_9\sinh(\beta_s\varsigma) + C_{10}\cosh(\beta_s\varsigma) + C_{11}\sin(\beta_f\varsigma) + C_{12}\cos(\beta_f\varsigma) \qquad b_2 \le \varsigma \le 1 \quad (39)$$

The boundary conditions for simply supported beam are, as

First B.C.:

$$\varsigma = 0 \rightarrow \bar{W}_1(0) = 0, \quad \bar{M}_1(0) = \bar{W}_1''(0) + \mu^2\lambda^4\bar{W}_1(0) = 0 \quad (40)$$

Second B.C.:

$$\varsigma = 1 \rightarrow \bar{W}_3(1) = 0, \quad \bar{M}_3(1) = \bar{W}_3''(1) + \mu^2\lambda^4\bar{W}_3(1) = 0 \quad (41)$$

The boundary conditions for clamped-clamped beam are, as

First B.C.:

$$\varsigma = 0 \rightarrow \bar{W}_1(0) = 0, \qquad \bar{W}_1'(0) = 0 \quad (42)$$

Second B.C.:

$$\varsigma = 1 \rightarrow \bar{W}_3(1) = 0, \qquad \bar{W}_3'(1) = 0 \quad (43)$$

The boundary conditions for cantilever beam are, as

First B.C.:

$$\varsigma = 0 \rightarrow \bar{W}_1(0) = 0, \qquad \bar{W}_1'(0) = 0 \quad (44)$$

Second B.C.:

$$\varsigma = 1 \rightarrow \bar{M}_3(1) = \bar{W}_3''(1) + \mu^2\lambda^4\bar{W}_3(1) = 0, \quad \bar{V}_3(1) = \bar{W}_3'''(1) + \mu^2\lambda^4\bar{W}_3'(1) = 0 \quad (45)$$

For all three different types of the beams mentioned above, the following conditions will be the same.

Continuity of the vertical displacements:

$$\varsigma = b_1 \rightarrow \bar{W}_1(b_1) = \bar{W}_2(b_1) \quad (46)$$

$$\varsigma = b_2 \rightarrow \bar{W}_2(b_2) = \bar{W}_3(b_2) \quad (47)$$

Jump in Bending slopes:

$$\varsigma = b_1 \rightarrow \Delta\theta_1 = \bar{W}_2'(b_1) - \bar{W}_1'(b_1) = K_1\bar{W}_1''(b_1) \quad (48)$$

$$\varsigma = b_2 \rightarrow \Delta\theta_2 = \bar{W}_3'(b_2) - \bar{W}_2'(b_2) = K_2\bar{W}_2''(b_2) \quad (49)$$

Continuity of the bending moments:

$$\varsigma = b_1 \rightarrow \bar{W}_1''(b_1) + \Lambda^4\mu^2\,\bar{W}_1(b_1) = \bar{W}_2''(b_1) + \Lambda^4\mu^2\,\bar{W}_2(b_1) \quad (50)$$

$$\varsigma = b_2 \rightarrow \bar{W}_2''(b_2) + \Lambda^4\mu^2\,\bar{W}_2(b_2) = \bar{W}_3''(b_2) + \Lambda^4\mu^2\,\bar{W}_3(b_2) \quad (51)$$

Continuity of the shear forces:

$$\varsigma = b_1 \rightarrow \bar{W}_1'''(b_1) + \Lambda^4\mu^2\,\bar{W}_1'(b_1) = \bar{W}_2'''(b_1) + \Lambda^4\mu^2\,\bar{W}_2'(b_1) \quad (52)$$

$$\varsigma = b_2 \rightarrow \bar{W}_2'''(b_2) + \Lambda^4\mu^2\,\bar{W}_2'(b_2) = \bar{W}_3'''(b_2) + \Lambda^4\mu^2\,\bar{W}_3'(b_2) \quad (53)$$

There are twelve equations and twelve unknown constants for simply supported and clamped-clamped nanobeams. Two of these constants are zero, thus only ten constants remain. Finally, ten equations will be obtained. As for the clamped-free (i.e. cantilever) nanobeam, none of the constants are zero but two of them are related to each other, that is the reason why the number of unknown constants will be reduced to ten and there will be a coefficient matrix of 10×10 and its determinant can give the frequencies of the double-cracked nanobeam. For the case of more than two cracks, all of the procedures are the same but, only the number of unknown constants will be increased according to the number of the cracks. If the crack severities are different, then it is necessary to write them into the equations by different names. For example, in the above equations K_1 and K_2 are independent from another, and each of them is assigned to a particular crack as shown in Fig. 2. The expressions b_1 and b_2 are positions of the first and the second crack respectively

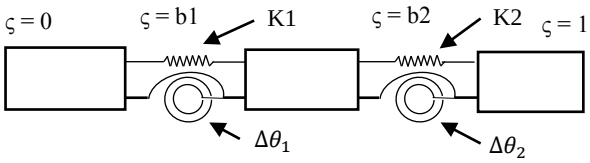

Fig. 2. Doubled-cracked beam

The second method will give simpler and faster calculations in contrast to the first method that was mentioned above. The second method to obtain the general equations, and consequently coefficient matrix, as well as the frequency parameters, is as

$$\bar{W}_1(\varsigma) = W_o\,j_1(\varsigma) + \theta_o\,j_2(\varsigma) + M_o\,j_3(\varsigma) + V_o\,j_4(\varsigma) \quad 0 \le \varsigma \le b_1$$
$$\bar{W}_2(\varsigma) = \bar{W}_1(\varsigma) + \Delta\theta_1\,j_2(\varsigma - b_1) \quad b_1 \le \varsigma \le b_2$$
$$\bar{W}_3(\varsigma) = \bar{W}_2(\varsigma) + \Delta\theta_2\,j_2(\varsigma - b_2) \quad b_2 \le \varsigma \le 1 \quad (54)$$

The first boundary condition for simply supported beam is as

$$\varsigma = 0 \rightarrow W_o = 0,\ and\ M_o = 0 \rightarrow \bar{W}_1(\varsigma) = \theta_o\,j_2(\varsigma) + V_o\,j_4(\varsigma) \quad (55)$$

First boundary condition for clamped-clamped beam is as

$$\varsigma = 0 \rightarrow W_o = 0,\ and\ \theta_o = 0 \rightarrow \bar{W}_1(\varsigma) = M_o\,j_3(\varsigma) + V_o\,j_4(\varsigma) \quad (56)$$

First boundary condition for cantilever beam is as

$$\varsigma = 0 \rightarrow W_o = 0,\ and\ \theta_o = 0 \rightarrow \bar{W}_1(\varsigma) = M_o\,j_3(\varsigma) + V_o\,j_4(\varsigma) \quad (57)$$

As shown in Eqns. (55), (56) and (57), two of the unknown constants out of four constants will be determined by the type of support at $\varsigma = 0$ and two other unknown constants will be obtained by a system of two equations from the boundary condition at $\varsigma = 1$. The second method is better to be used because in all of the cases such as non-cracked, single –cracked, double cracked, and more than two cracks, the coefficient matrix will be 2×2. The determinant of this coefficient matrix sometimes will be a very long formula that has to be solved numerically to obtain its roots.

2.4. Nonlocal triple-cracked Euler-Bernoulli beam equations

This case is similar to the case of the double-cracked nanobeam. It is only needed to expand the equations of the double-cracked nanobeams to the triple-cracked nanobeams as

$$\bar{W}_1(\varsigma) = W_o\,j_1(\varsigma) + \theta_o\,j_2(\varsigma) + M_o\,j_3(\varsigma) + V_o\,j_4(\varsigma) \quad 0 \le \varsigma \le b_1$$
$$\bar{W}_2(\varsigma) = \bar{W}_1(\varsigma) + \Delta\theta_1\,j_2(\varsigma - b_1) \quad b_1 \le \varsigma \le b_2$$
$$\bar{W}_3(\varsigma) = \bar{W}_2(\varsigma) + \Delta\theta_2\,j_2(\varsigma - b_2) \quad b_2 \le \varsigma \le b_3$$
$$\bar{W}_4(\varsigma) = \bar{W}_3(\varsigma) + \Delta\theta_3\,j_2(\varsigma - b_3) \quad b_3 \le \varsigma \le 1$$
$$\Delta\theta_3 = K_3\,\bar{W}_3''(b_3) \quad (58)$$

3. Results and discussion

3.1. Simply supported beam

In this paper the simply supported beam is analyzed for the cases of double-cracked and triple-cracked. When the cracks are introduced to the beam, the natural frequencies will be decreased and as much as the crack severities are increased the natural frequencies become smaller, and there is an exception in this expression. The exception is the crack location. When the crack location locates on a node of a certain mode of vibration, that mode will not experience any changes by the presence of the crack and increasing the crack severity, consequently there will not be any changes in the frequency of the same mode. This is due to the fact that the amount of the bending slope at both sides of the point on which the crack is located, will be the same, and there will not be any changes in the bending slope and there will not be any jumps in the bending slope. According to Eq. (31), the crack can affect the beam when there is a jump in the bending slope. When both angles at both sides of a point are equal to each other, so amount of $\Delta\theta$ will be zero and this causes the crack effect to be canceled at a mode of vibration in which the crack and one of the nodes of this mode have the same location.

Another factor, which plays an important role in decreasing the natural frequencies, is the size effect introduced by scale effect parameter μ. As μ is increased, the natural frequencies will be reduced. The results that have already been obtained for simply supported beam as non-cracked beam by Lu et al. [12], are calculated again and completely coincide, then, they are used to be compared with the cases of the double cracked and the triple-cracked. Fig.3 shows the first four frequencies of the non-cracked simply supported beam (i.e. $K_1 = K_2 = K_3 = 0$), and starting from the first mode, the successive odd and even vibration modes approach each other and are suppressed with the increase of μ .When the number of the cracks is increased, the frequencies of all of the modes will be decreased, except the cases in which one or more cracks are located on the nodes of the certain modes. The results of the double-cracked simply supported beams are tabulated in Table 1.a and b. and are shown in Fig. 4 (a, b, c and d), in which both of the crack severities are changed in accordance with one another. However, it will be possible that each crack severity differs from the other crack severities that is the reason why the crack severity for each crack is named by a different expression such as $K_1$and K_2. As for the case of double-cracked, the fourth frequency remains constant while the crack severities are changed, this is because both points $b_1 = 0.25$ and $b_2 = 0.5$ are the nodes of the fourth mode. The same phenomenon occurs for the case of triple-cracked, where all three cracks are located at the nodes of mode four. The results of the triple-cracked simply supported beams are tabulated in Table 2.a and b. and are shown in Fig. 5 (a, b, c and d). The fourth mode remains constant while the crack severities are increased because all cracks are located on the nodes of the fourth mode as shown in Fig. 6. As the scale effect parameter is increased the frequencies of all modes are decreased. The highest amount of decreasing of the frequencies of all modes for any amount of the nonlocal parameter, is observed when the third crack is introduced to the beam.

Table 1. a. and b. Frequencies of double-cracked simply supported beam with different nonlocal parameter μ and crack severities K_1 and K_2. Crack positions $\varsigma = 0.25$ and $\varsigma = 0.5$.

$\mu = 0$				
Λ	$K_1 = 0$ $K_2 = 0$	$K_1 = 0.065$ $K_2 = 0.065$	$K_1 = 0.35$ $K_2 = 0.35$	$K_1 = 2$ $K_2 = 2$
1	3.1416	3.0044	2.6226	1.9256
2	6.2832	6.1007	5.5522	4.2553
3	9.4248	9.0315	8.1721	7.4180
4	12.5664	12.5664	12.5664	12.5664
$\mu = 0.4$				
Λ	$K_1 = 0$ $K_2 = 0$	$K_1 = 0.065$ $K_2 = 0.065$	$K_1 = 0.35$ $K_2 = 0.35$	$K_1 = 2$ $K_2 = 2$
1	2.4790	2.3694	2.0584	1.4983
2	3.8204	3.7015	3.2600	2.3268
3	4.7722	4.5563	4.1199	3.8918
4	5.5509	5.5509	5.5509	5.5509

a.

$\mu = 0.2$			
$K_1 = 0$ $K_2 = 0$	$K_1 = 0.065$ $K_2 = 0.065$	$K_1 = 0.35$ $K_2 = 0.35$	$K_1 = 2$ $K_2 = 2$
2.8908	2.7639	2.4074	1.7604
4.9581	4.8071	4.2799	3.1046
6.4520	6.1629	5.5422	5.1663
7.6407	7.6407	7.6407	7.6407
$\mu = 0.6$			
$K_1 = 0$ $K_2 = 0$	$K_1 = 0.065$ $K_2 = 0.065$	$K_1 = 0.35$ $K_2 = 0.35$	$K_1 = 2$ $K_2 = 2$
2.1507	2.0552	1.7830	1.2949
3.1815	3.0820	2.7056	1.9236
3.9329	3.7548	3.4032	3.2282
4.5565	4.5565	4.5565	4.5565

b.

Table 2.a and b. Frequencies of a triple-cracked simply supported beam with different nonlocal parameter μ with three similar cracks of severity K at $\varsigma = 0.25$, $\varsigma = 0.5$, and $\varsigma = 0.75$.

$\mu = 0$				
Λ	$K = 0$	$K = 0.065$	$K = 0.35$	$K = 2$
1	3.1416	2.9652	2.5239	1.8136
2	6.2832	5.9295	5.0418	3.6171
3	9.4248	8.8807	7.4775	5.2977
4	12.5664	12.5664	12.5664	12.5664
$\mu = 0.4$				
Λ	$K = 0$	$K = 0.065$	$K = 0.35$	$K = 2$
1	2.4790	2.3390	1.9862	1.4221
2	3.8204	3.5974	3.0148	2.1232
3	4.7722	4.4659	3.6264	2.4910
4	5.5509	5.5509	5.5509	5.5509

a.

$\mu = 0.2$			
$K = 0$	$K = 0.065$	$K = 0.35$	$K = 2$
2.8908	2.7281	2.3195	1.6640
4.9581	4.6719	3.9320	2.7828
6.4520	6.0459	4.9386	3.4051
7.6407	7.6407	7.6407	7.6407
$\mu = 0.6$			
$K = 0$	$K = 0.065$	$K = 0.35$	$K = 2$
2.1507	2.0290	1.7218	1.2317
3.1815	2.9953	2.5071	1.7633
3.9329	3.6793	2.9837	2.0478
4.5565	4.5565	4.5565	4.5565

b.

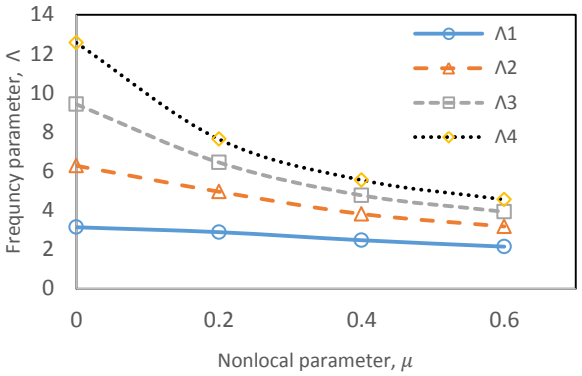

Fig. 3. Change of four eigenvalues of non-cracked simply supported beam versus nonlocal parameter μ.

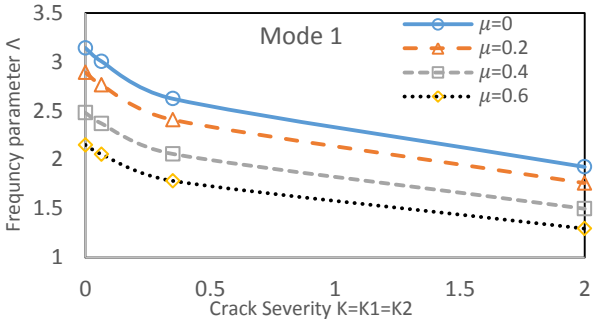

a.

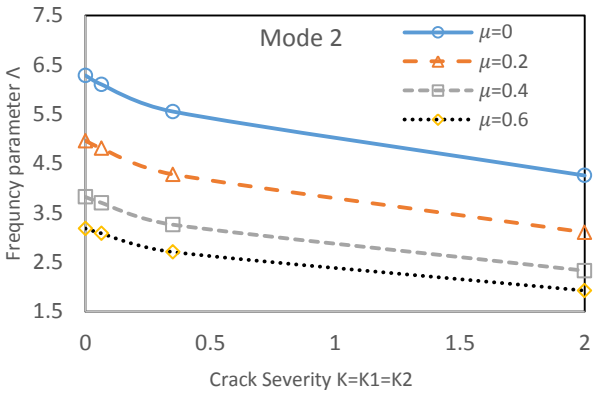

b.

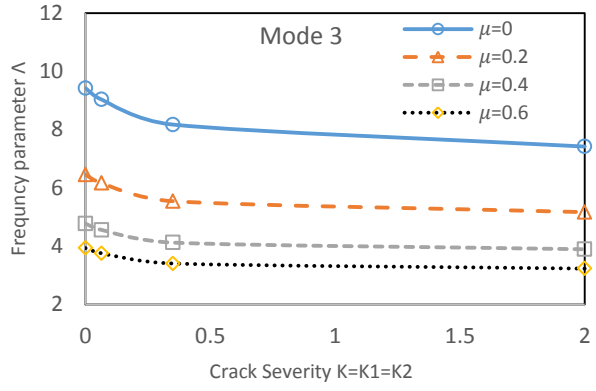

c.

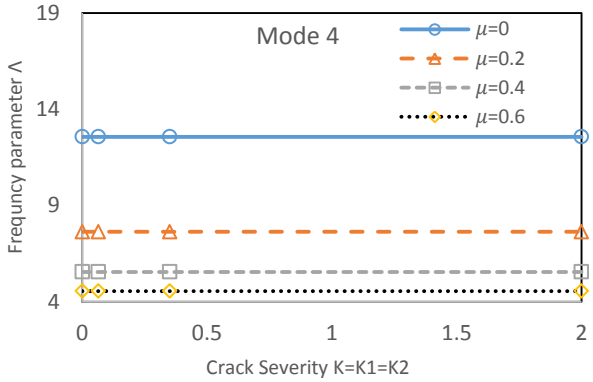

d.

Fig. 4. Frequencies of a double-cracked simply supported beam with crack positions $\varsigma = 0.25$ and $\varsigma = 0.5$.

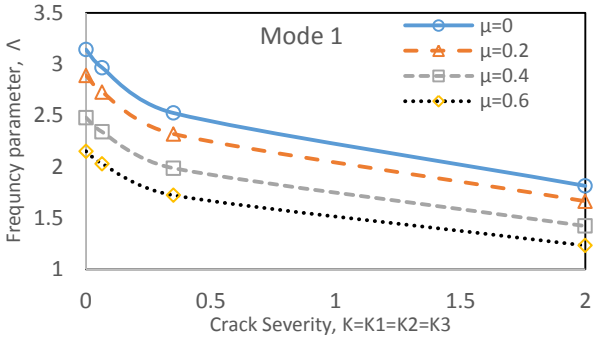

a.

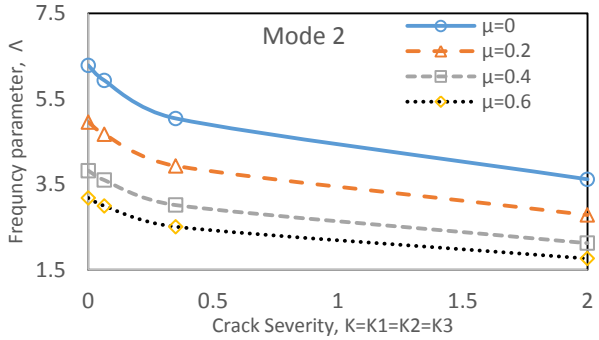

b.

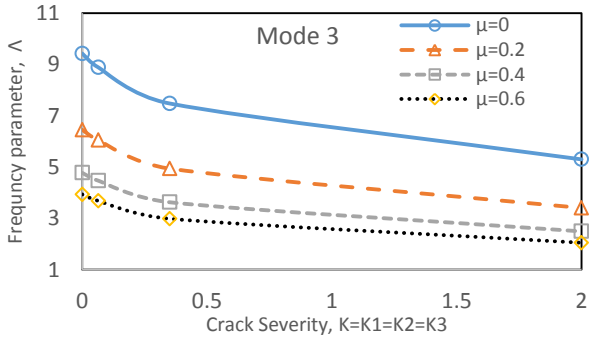

c.

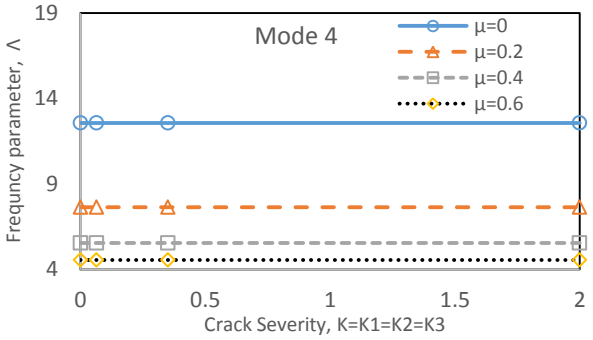

d.

Fig. 5. Frequencies a triple-cracked simply supported beam with crack positions $\varsigma = 0.25$, $\varsigma = 0.5$, and $\varsigma = 0.75$.

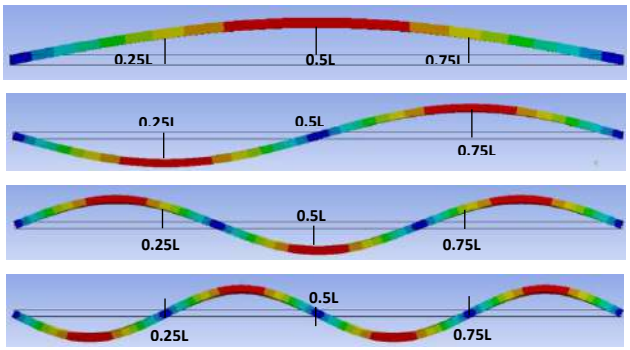

Fig.6. Mode shapes of simply supported beam and position of the nodes.

3.2. Clamped-Clamped beam

Non-cracked simply supported beam frequencies are obtained for different nonlocal parameter values. (i.e. $K_1 = K_2 = K_3 = 0$) and the non-cracked case results are shown in Fig. 7. The first four frequency parameters of the clamped-clamped beam are presented in Table 3 (a and b) and in Fig. 8 (a, b, c, and d) for the double-cracked beams and in Table 4 (a and b) and graphically in Fig. 9 for the triple-cracked beams. When the nonlocal parameter is increased the frequencies of all modes are decreased. When the clamped-clamped beam has two cracks at $b_1 = 0.25$ and $b_2 = 0.5$, the frequencies will be decreased more in contrast to the non-cracked beam, and this is due to the presence of the more flexibility in the beam as shown in Fig. 8. In this case, the frequencies of all modes are decreased

by increasing the crack severities of the cracks and in fact only the crack severity K_1 of the first crack is the reason of decreasing the second and the fourth frequencies, and K_2 which belongs to the second crack, does not have any effect on decreasing them because the second crack is located on the nodes of the second and the fourth modes and the amount of $\Delta\theta_2 = 0$ as shown in Fig. 10. Increasing the nonlocal scale effect parameter is another factor for decreasing the frequencies of the double-cracked beam. Third crack decreases all mode frequencies and the lowest amount of the frequencies belongs to the case of the triple-cracked beam as shown in Fig. 9 (a, b, c, and d). In this case only the first and the third cracks are the reason of decreasing the second and the fourth modes. The third crack location is not the node for any modes.

Table 3. Frequencies of a double-cracked clamped-clamped beam with different nonlocal parameter μ and crack severities K_1 and K_2. Crack positions $\varsigma = 0.25$ and $\varsigma = 0.5$.

$\mu = 0$				
Λ	$K_1 = 0$ $K_2 = 0$	$K_1 = 0.065$ $K_2 = 0.065$	$K_1 = 0.35$ $K_2 = 0.35$	$K_1 = 2$ $K_2 = 2$
1	4.7300	4.6276	4.3531	3.8350
2	7.8532	7.6974	7.2501	6.5217
3	10.9956	10.4769	9.5173	8.8476
4	14.1372	14.0909	14.0119	13.9498
$\mu = 0.4$				
Λ	$K_1 = 0$ $K_2 = 0$	$K_1 = 0.065$ $K_2 = 0.065$	$K_1 = 0.35$ $K_2 = 0.35$	$K_1 = 2$ $K_2 = 2$
1	3.5923	3.4947	3.1864	2.5767
2	4.5978	4.4938	4.0780	3.6656
3	5.4738	5.1691	4.7791	4.6427
4	6.1504	6.0837	5.8674	5.6307

a.

$\mu = 0.2$			
$K_1 = 0$ $K_2 = 0$	$K_1 = 0.065$ $K_2 = 0.065$	$K_1 = 0.35$ $K_2 = 0.35$	$K_1 = 2$ $K_2 = 2$
4.2766	4.1735	3.8721	3.2575
6.0352	5.9028	5.3861	4.7371
7.3840	6.9713	6.3598	6.1174
8.4624	8.3863	8.1469	7.8308
$\mu = 0.6$			
$K_1 = 0$ $K_2 = 0$	$K_1 = 0.065$ $K_2 = 0.065$	$K_1 = 0.35$ $K_2 = 0.35$	$K_1 = 2$ $K_2 = 2$
3.0837	2.9949	2.7068	2.1586
3.8165	3.7298	3.3905	3.0745
4.5231	4.2743	3.9691	3.8669
5.0505	4.9932	4.8082	4.6154

b.

Table 4. frequencies of a triple-cracked clamped-clamped beam with different nonlocal parameter μ with three similar cracks of severity K at $\varsigma = 0.25$, $\varsigma = 0.5$, and $\varsigma = 0.75$.

$\mu = 0$				
Λ	$K = 0$	$K = 0.065$	$K = 0.35$	$K = 2$
1	4.7300	4.6268	4.3497	3.6513
2	7.8532	7.5618	6.9381	6.3018
3	10.9956	10.2411	8.6693	7.0230
4	14.1372	14.0397	13.8556	13.7059
$\mu = 0.4$				
Λ	$K = 0$	$K = 0.065$	$K = 0.35$	$K = 2$
1	3.5923	3.4946	3.1619	2.3325
2	4.5978	4.4193	3.9742	3.5209
3	5.4738	5.0222	4.2248	3.7754
4	6.1504	6.0048	5.7356	5.5906

a.

$\mu = 0.2$			
$K = 0$	$K = 0.065$	$K = 0.35$	$K = 2$
4.2766	4.1734	3.8595	3.0030
6.0352	5.8021	5.2461	4.6762
7.3840	6.7818	5.6246	4.7921
8.4624	8.2964	7.9512	7.7323
$\mu = 0.6$			
$K = 0$	$K = 0.065$	$K = 0.35$	$K = 2$
3.0837	2.9946	2.6795	1.9443
3.8165	3.6683	3.2940	2.9138
4.5231	4.1520	3.5236	3.1947
5.0505	4.9253	4.7018	4.5864

b.

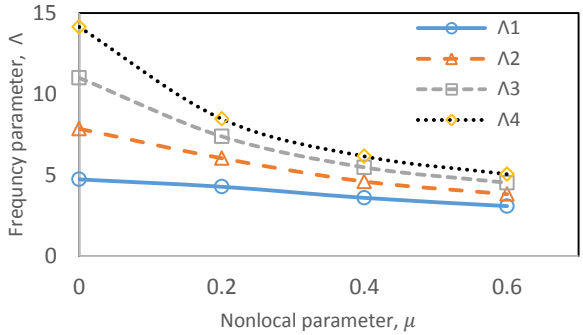

Fig. 7. Change of four eigenvalues of non-cracked clamped-clamped beam versus nonlocal parameter μ.

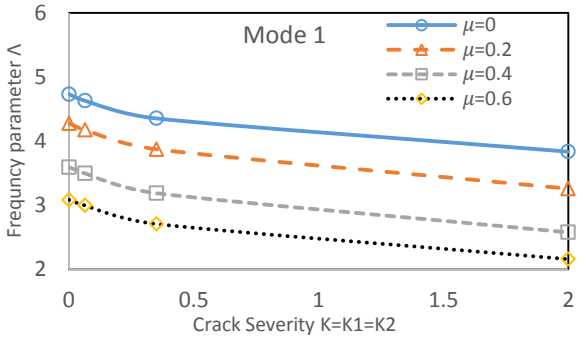

a.

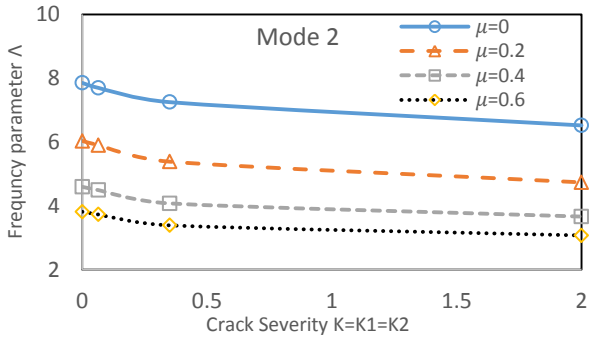

b.

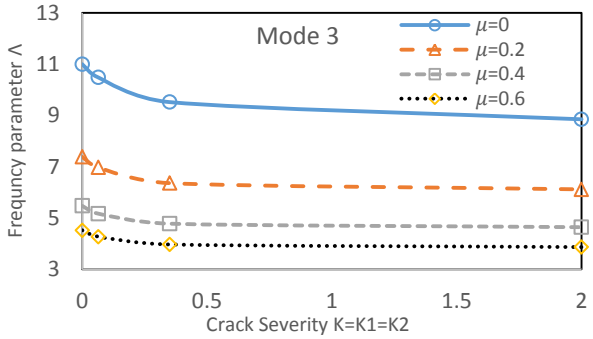

c.

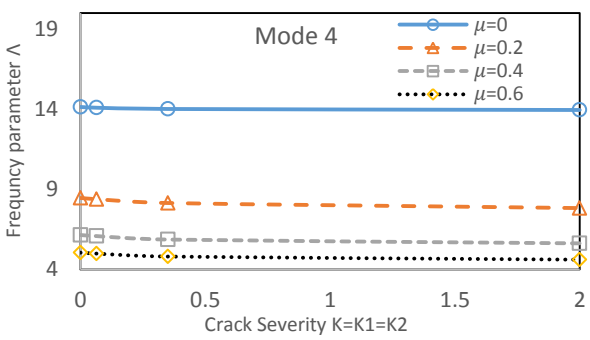

d.

Fig. 8. Frequencies of a double-cracked clamped-clamped beam with crack positions $\varsigma = 0.25$ and $\varsigma = 0.5$.

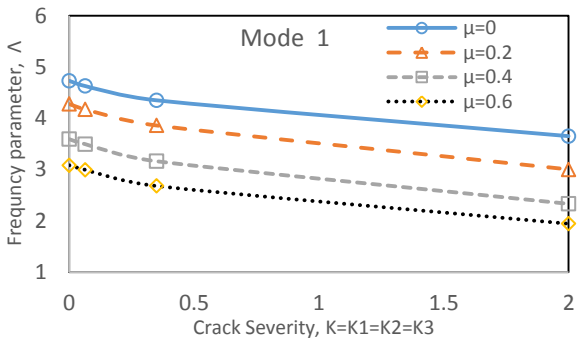

a.

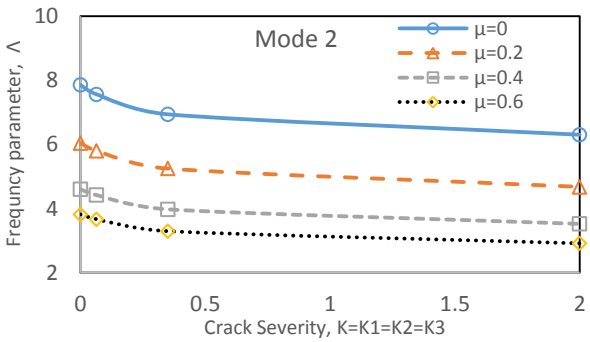

b.

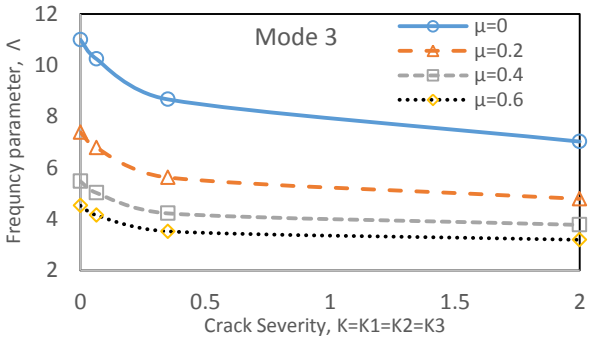

c.

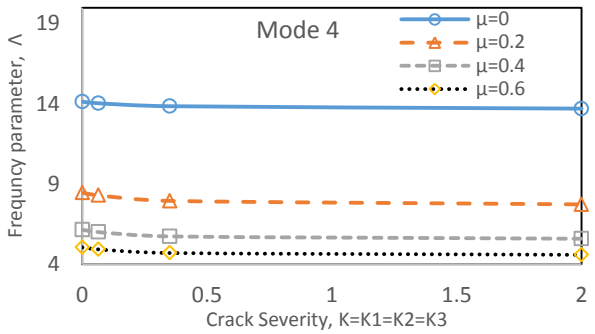

d.

Fig. 9. Frequencies of a triple-cracked clamped-clamped beam with crack positions $\varsigma = 0.25$, $\varsigma = 0.5$, and $\varsigma = 0.75$.

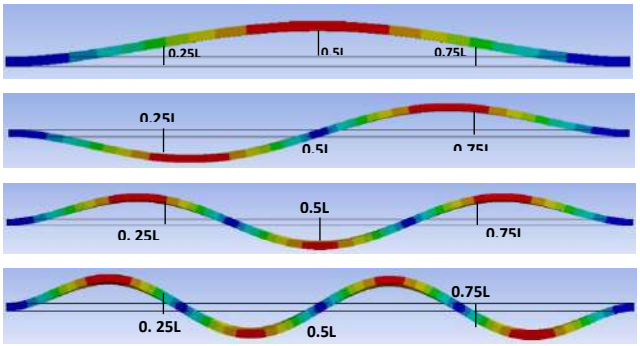

Fig. 10. Mode shapes of clamped-clamped beam and position of the nodes

3.3. Cantilever beam

The results of the cantilever beam for the non-cracked case are shown in Fig. 11. Other results of the cantilever are presented in Table 5 and in Fig. 12 (a, b, c, and d) for the double-cracked beams, and in Table 6 and in Fig. 13 (a, b, c, and d) for the triple-cracked beams. General mode shapes of a cantilever beam are shown in Fig. 14. It can be observed from the results that the natural frequencies are very sensitive to the nonlocal parameter in contrast to the simply supported and the clamped-clamped beams, especially for the cases in which the nonlocal parameter (μ) increases. The cantilever beam is not suitable to be used in the design of the resonators in nanoscale. As for the case of non-cracked (i.e. $K_1 = K_2 = K_3 = 0$), only the first frequency increases by an increase in the nonlocal parameter, whereas the others decrease by increasing the parameter μ and the frequencies approach each other in pairs as shown in Fig. 11. When $\mu > 0.62$, one even cannot find nontrivial real eigenvalues. This means that starting from the first mode, the successive odd and even vibration modes approach each other and are suppressed with the increase of μ. Thus, for the cantilever beam vibration mode, the magnitude of the exponential terms increases dramatically with the nonlocal parameter comparing with the traveling wave terms, and eventually, it restrains the vibration. For the cantilever as the cracks are introduced to the beam, the frequencies of all modes are reduced, and as the crack severities are increased the rate of decreasing the frequencies becomes more. The doubled-cracked cantilever beam results are presented in Table 5 and they are shown in Fig. 12 (a, b, c, and d), and when they are compared with the other cases, it is observed that all of the frequencies are decreased except the fourth mode frequency of case $K_1 = K_2 = 2$ for $\mu = 0.6$, where it is increased. It is one of the abnormal results happened here. Third crack does not have any great effect on the first frequency of the cantilever beam, then the first frequency in both double-cracked and triple-cracked beam have approximately the same value for all the amounts of the nonlocal parameter, but frequencies of the other modes are decreased by introducing the third crack to the beam. There are some abnormal results obtained in the cantilever cases which have not been happened for the simply supported and the clamped-clamped beam cases. The reason is the fact that the higher value of μ has more complex effect on the frequencies, especially when both μ and K are increased simultaneously and it is sometimes unpredictable to know what will be happened for a case in which the amount of the nonlocal parameter is high.

Table 5. First four frequency parameters for a double-cracked cantilever beam with different nonlocal parameter μ and crack severities K_1 and K_2. Crack positions $\varsigma = 0.25$ and $\varsigma = 0.5$.

$\mu = 0$				
Λ	$K_1 = 0$ $K_2 = 0$	$K_1 = 0.065$ $K_2 = 0.065$	$K_1 = 0.35$ $K_2 = 0.35$	$K_1 = 2$ $K_2 = 2$
1	1.8751	1.8136	1.6255	1.2287
2	4.6941	4.5518	4.1572	3.2994
3	7.8548	7.6994	7.2454	6.5074

4	10.9955	10.4809	9.5378	8.8927
$\mu = 0.4$				
Λ	$K_1 = 0$ $K_2 = 0$	$K_1 = 0.065$ $K_2 = 0.065$	$K_1 = 0.35$ $K_2 = 0.35$	$K_1 = 2$ $K_2 = 2$
1	1.9543	1.8906	1.6909	1.2690
2	3.3456	3.2155	2.8479	2.1148
3	4.8370	4.7655	4.1575	3.6429
4	5.2399	4.9629	4.8385	4.8043

a.

$\mu = 0.2$			
$K_1 = 0$ $K_2 = 0$	$K_1 = 0.065$ $K_2 = 0.065$	$K_1 = 0.35$ $K_2 = 0.35$	$K_1 = 2$ $K_2 = 2$
1.8919	1.8299	1.6394	1.2374
4.1924	4.0460	3.6277	2.7481
6.0674	5.9395	5.4040	4.7359
7.3617	6.9726	6.4311	6.2394
$\mu = 0.6$			
$K_1 = 0$ $K_2 = 0$	$K_1 = 0.065$ $K_2 = 0.065$	$K_1 = 0.35$ $K_2 = 0.35$	$K_1 = 2$ $K_2 = 2$
2.1989	2.1380	1.8903	1.3706
2.4809	2.3731	2.1291	1.6387
…	…	3.5533	3.0490
…	…	3.9588	4.0261

b.

Table 6. Frequencies of a triple-cracked cantilever beam with different nonlocal parameter μ with three similar cracks of severity K at $\varsigma = 0.25$, $\varsigma = 0.5$ and $\varsigma = 0.75$.

$\mu = 0$				
Λ	$K = 0$	$K = 0.065$	$K = 0.35$	$K = 2$
1	1.8751	1.8121	1.6206	1.2214
2	4.6941	4.4054	3.6597	2.5515
3	7.8548	6.9997	5.2577	3.8570
4	10.9955	9.9345	8.1246	6.6601
$\mu = 0.4$				
Λ	$K = 0$	$K = 0.065$	$K = 0.35$	$K = 2$
1	1.9543	1.8950	1.7050	1.2886
2	3.3456	3.1834	2.7516	2.0012
3	4.8370	…	3.8404	2.5818
4	5.2399	…	4.0351	3.6505

a.

$\mu = 0.2$			
$K = 0$	$K = 0.065$	$K = 0.35$	$K = 2$
1.8919	1.8299	1.6392	1.2371
4.1924	4.0155	3.5370	2.6288
6.0674	5.7618	4.9197	3.4561
7.3617	6.7084	5.5042	4.7355
$\mu = 0.6$			
$K = 0$	$K = 0.065$	$K = 0.35$	$K = 2$
2.1989	…	…	…
2.4809	…	…	…
…	…	…	…
…	…	…	…

b.

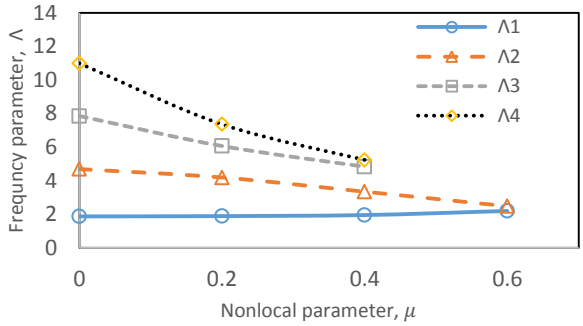

Fig. 11. Change of four eigenvalues of non-cracked cantilever beam versus nonlocal parameter μ

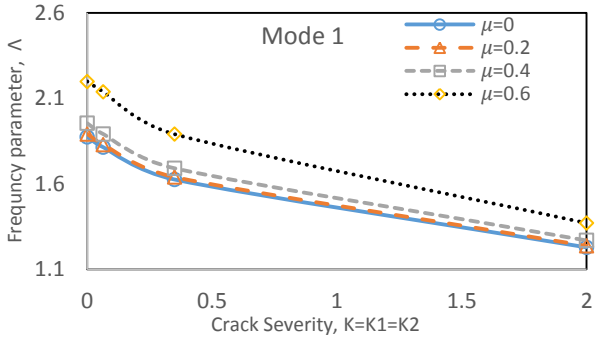

a.

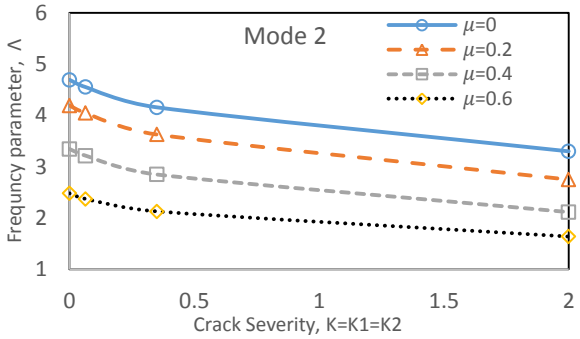

b.

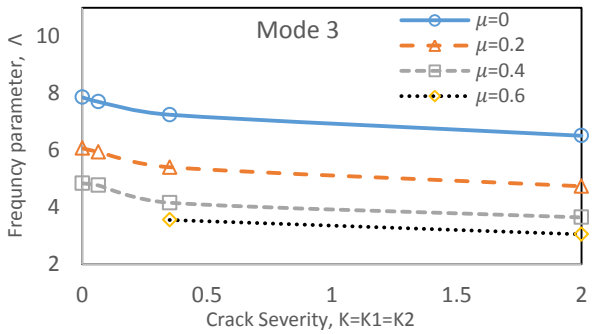

c.

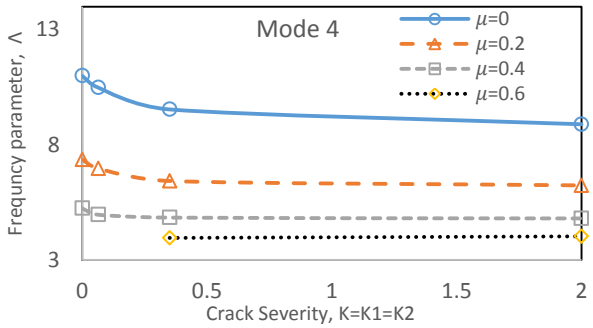

d.

Fig. 12. Frequencies of a double-cracked cantilever beam with crack positions $\varsigma = 0.25$ and $\varsigma = 0.5$.

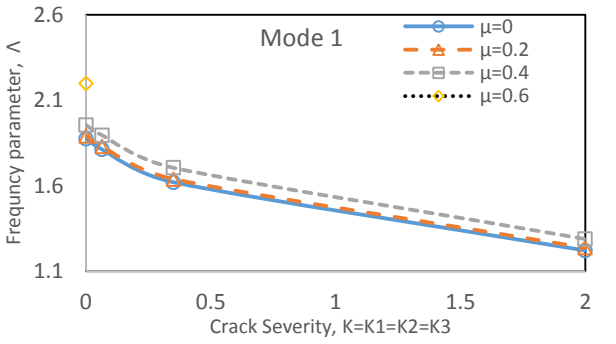

a.

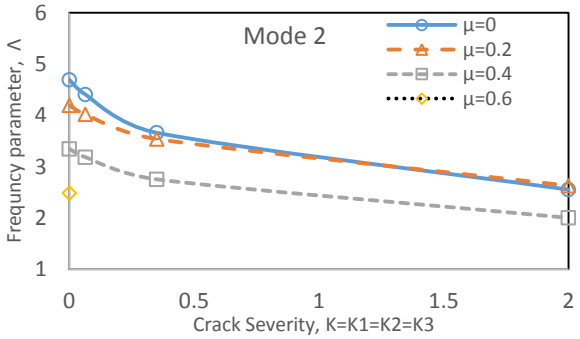

b.

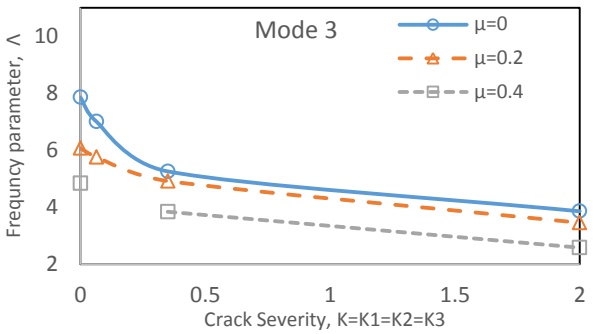

c.

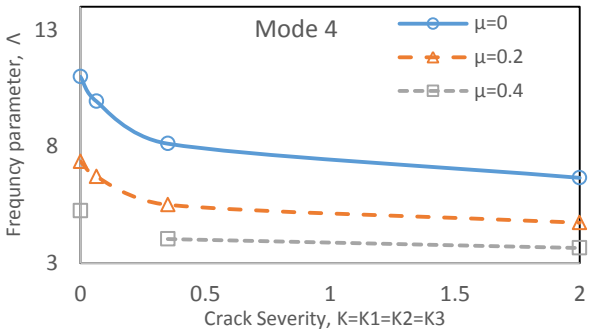

d.

Fig. 13. Frequencies of a triple-cracked cantilever beam with crack positions $\varsigma = 0.25$, $\varsigma = 0.5$, and $\varsigma = 0.75$.

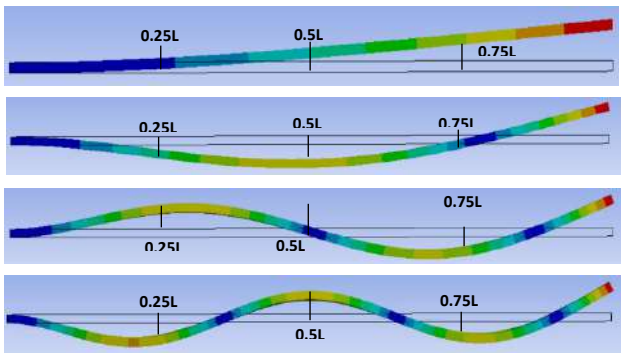

Fig. 14. Mode shapes of cantilever beam and position of the nodes.

4. Conclusions

In this paper, free vibration analysis of double-cracked and triple-cracked nanobeams for three different types of beam supports, including simply supported, clamped-clamped, and cantilever is exposed to find the natural frequencies. The crack is modeled as a rotational spring and the value of the crack severities are calculated using molecular dynamics for the nanobeams. The effect of the crack severities, number of the cracks, and the nonlocal parameter are checked in this paper. The nonlocal parameter is considered in the equations and its effect on the frequencies of all studied

cases is determined. The Following conclusions have been made based on the results obtained throughout this paper:

- In the cases of the simply supported and the clamped-clamped as the crack severity increases, the frequencies decrease for all values of the nonlocal parameter.
- As the position of the crack gets near the fixed end, the crack effect decreases. As the number of the cracks is increased, there will be a reduction in the frequencies.
- As for the cantilever nanobeam, the results are somehow complicated. When the crack position is closer to the free end, the frequencies of some modes increase and this is a new phenomenon that was observed here.
- For the cantilever nanobeam, the small size effect parameter (nonlocal parameter) has the greatest effect among three cases of support nanobeams.
- The first mode frequency of the cantilever beam increases by an increase in the nonlocal parameter.

References

[1] K. Ekinci, M. Roukes, Nanoelectromechanical systems, Review of scientific instruments, 76 (2005) 061101. https://doi.org/10.1063/1.1927327
[2] N.V. Lavrik, M.J. Sepaniak, P.G. Datskos, Cantilever transducers as a platform for chemical and biological sensors, Review of scientific instruments, 75 (2004) 2229. https://doi.org/10.1063/1.1763252
[3] J. Reddy, S. Pang, Nonlocal continuum theories of beams for the analysis of carbon nanotubes, Journal of Applied Physics, 103 (2008) 023511. https://doi.org/10.1063/1.2833431
[4] L. Sudak, Column buckling of multiwalled carbon nanotubes using nonlocal continuum mechanics, Journal of applied physics, 94 (2003) 7281-7287. https://doi.org/10.1063/1.1625437
[5] C. Wang, Y. Zhang, S.S. Ramesh, S. Kitipornchai, Buckling analysis of micro-and nano-rods/tubes based on nonlocal Timoshenko beam theory, Journal of Physics D: Applied Physics, 39 (2006) 3904. https://doi.org/10.1088/0022-3727/39/17/029
[6] L. Wang, H. Hu, Flexural wave propagation in single-walled carbon nanotubes, Physical Review B, 71 (2005) 195412. https://doi.org/10.1103/PhysRevB.71.195412
[7] A.C. Eringen, D. Edelen, On nonlocal elasticity, International Journal of Engineering Science, 10 (1972) 233-248. https://doi.org/10.1016/0020-7225(72)90039-0
[8] C. Sun, H. Zhang, Size-dependent elastic moduli of platelike nanomaterials, Journal of Applied Physics, 93 (2003) 1212-1218. https://doi.org/10.1063/1.1530365
[9] H. Zhang, C. Sun, Nanoplate model for platelike nanomaterials, AIAA journal, 42 (2004) 2002-2009. https://doi.org/10.2514/1.5282
[10] J. Peddieson, G.R. Buchanan, R.P. McNitt, Application of nonlocal continuum models to nanotechnology, International Journal of Engineering Science, 41 (2003) 305-312. https://doi.org/10.1016/S0020-7225(02)00210-0
[11] Y. Zhang, G. Liu, X. Xie, Free transverse vibrations of double-walled carbon nanotubes using a theory of nonlocal elasticity, Physical Review B, 71 (2005) 195404. https://doi.org/10.1103/PhysRevB.71.195404
[12] P. Lu, H. Lee, C. Lu, P. Zhang, Dynamic properties of flexural beams using a nonlocal elasticity model, Journal of applied physics, 99 (2006) 073510. https://doi.org/10.1063/1.2189213
[13] Q. Wang, Wave propagation in carbon nanotubes via nonlocal continuum mechanics, Journal of Applied physics, 98 (2005) 124301. https://doi.org/10.1063/1.2141648
[14] Q. Wang, G. Zhou, K. Lin, Scale effect on wave propagation of double-walled carbon nanotubes, International Journal of Solids and Structures, 43 (2006) 6071-6084. https://doi.org/10.1016/j.ijsolstr.2005.11.005
[15] Q. Wang, V. Varadan, Vibration of carbon nanotubes studied using nonlocal continuum mechanics, Smart Materials and Structures, 15 (2006) 659. https://doi.org/10.1088/0964-1726/15/2/050
[16] J. Reddy, Nonlocal theories for bending, buckling and vibration of beams, International Journal of Engineering Science, 45 (2007) 288-307. https://doi.org/10.1016/j.ijengsci.2007.04.004
[17] M. Şimşek, Large amplitude free vibration of nanobeams with various boundary conditions based on the nonlocal elasticity theory, Composites Part B: Engineering, 56 (2014) 621-628. https://doi.org/10.1016/j.compositesb.2013.08.082
[18] M. Şimşek, Nonlinear free vibration of a functionally graded nanobeam using nonlocal strain gradient theory and a novel Hamiltonian approach, International Journal of Engineering Science, 105 (2016) 12-27. https://doi.org/10.1016/j.ijengsci.2016.04.013
[19] R. Nazemnezhad, R. Mahoori, A. Samadzadeh, Surface energy effect on nonlinear free axial vibration

and internal resonances of nanoscale rods, European Journal of Mechanics-A/Solids, 77 (2019) 103784. https://doi.org/10.1016/j.euromechsol.2019.05.001
[20] S. Hosseini-Hashemi, R. Nazemnezhad, H. Rokni, Nonlocal nonlinear free vibration of nanobeams with surface effects, European Journal of Mechanics-A/Solids, 52 (2015) 44-53. https://doi.org/10.1016/j.euromechsol.2014.12.012
[21] R. Hamza-Cherif, M. Meradjah, M. Zidour, A. Tounsi, S. Belmahi, T. Bensattalah, Vibration analysis of nano beam using differential transform method including thermal effect, in: Journal of Nano Research, Trans Tech Publ, 2018, pp. 1-14. https://doi.org/10.4028/www.scientific.net/JNanoR.54.1
[22] J. Loya, J. López-Puente, R. Zaera, J. Fernández-Sáez, Free transverse vibrations of cracked nanobeams using a nonlocal elasticity model, Journal of Applied Physics, 105 (2009) 044309. https://doi.org/10.1063/1.3068370
[23] K. Torabi, J.N. Dastgerdi, An analytical method for free vibration analysis of Timoshenko beam theory applied to cracked nanobeams using a nonlocal elasticity model, Thin Solid Films, 520 (2012) 6595-6602. https://doi.org/10.1016/j.tsf.2012.06.063
[24] H. Roostai, M. Haghpanahi, Vibration of nanobeams of different boundary conditions with multiple cracks based on nonlocal elasticity theory, Applied Mathematical Modelling, 38 (2014) 1159-1169. https://doi.org/10.1016/j.apm.2013.08.011
[25] M. Loghmani, M.R.H. Yazdi, An analytical method for free vibration of multi cracked and stepped nonlocal nanobeams based on wave approach, Results in Physics, 11 (2018) 166-181. https://doi.org/10.1016/j.rinp.2018.08.046
[26] M. Soltanpour, M. Ghadiri, A. Yazdi, M. Safi, Free transverse vibration analysis of size dependent Timoshenko FG cracked nanobeams resting on elastic medium, Microsystem Technologies, 23 (2017) 1813-1830. https://doi.org/10.1007/s00542-016-2983-3
[27] F. Ebrahimi, F. Mahmoodi, Vibration analysis of carbon nanotubes with multiple cracks in thermal environment, Advances in nano research, 6 (2018) 57-80. https://doi.org/10.12989/anr.2018.6.1.057
[28] Ş.D. Akbaş, Forced vibration analysis of functionally graded nanobeams, International Journal of Applied Mechanics, 9 (2017) 1750100. http://dx.doi.org/10.1142/S1758825117501009
[29] J. Loya, L. Rubio, J. Fernández-Sáez, Natural frequencies for bending vibrations of Timoshenko cracked beams, Journal of Sound and Vibration, 290 (2006) 640-653. https://doi.org/10.1016/j.jsv.2005.04.005

ZANCO Journal of Pure and Applied Sciences
The official scientific journal of Salahaddin University-Erbil
https://zancojournals.su.edu.krd/index.php/JPAS

ISSN (print):2218-0230**, ISSN (online):** 2412-3986**, DOI: http://dx.doi.org/10.21271/zjpas**

RESEARCH PAPER

Periodic Solutions Bifurcating From a Curve of Singularity of the Jerk System

Niazy H. Hussein[1, 2]

[1]Department of Mathematics, Faculty of Science, Soran University-Erbil, Kurdistan Region, Iraq
[2]Department of Mathematics, College of Basic Education, University of Raparin, Ranya, Kurdistan Region, Iraq

A B S T R A C T:

We investigate a periodic solution which bifurcates from a curve of the singularity of the jerk system in R^3.More precisely, we give the explicit states for the existence of a periodic solution of the jerk system with a nonisolated singular point, where for each singular point has a simple pair of purely imaginary and one zero eigenvalues. We recall for this point of singularity as a zero-Hopf (z-H) singular point. The coefficients in the jerk system are described for which the z-H singularity occur at each point of that curve of singularity. We show that for each point at that curve of singularity there is only one family of parameters which exhibits such type of singular points. The method of averaging in the second order is utilized to determine one periodic solution which bifurcates from any point of that curve of singularity. As far as, we realize that this investigation is the study on bifurcations from a curve of nonisolated z-H singularity to provide a periodic solution via the method of averaging. Under a generic small perturbation at the parameters, we prove that a periodic solution will be bifurcated at any point that located on a curve of a singularity of the jerk system.

KEY WORDS: Jerk system, periodic orbit, zero-Hopf singularity, the method of averaging
DOI: http://dx.doi.org/10.21271/ZJPAS.32.2.6
ZJPAS (2020) , 32(2);55-61 .

INTRODUCTION

Time derivative of acceleration in physics is called the jerk. It can be defined in dynamical system by $\dddot{x} = f(x, \dot{x}, \ddot{x})$, see (Gottlieb, 1998). This equation, by changing the variables, can be remold into a general 3D differential system

$$\dot{x} = y,\ \dot{y} = z,\ \dot{z} = g(x, y, z). \qquad (1)$$

System (1) is very remarkable in nonlinear dynamic systems. For instance, the simplest possible chaotic system is in this form studying in (Sprott, 1997).

* **Corresponding Author:**
Niazy Hady Hussein
E-mail: Niazy.hussein@soran.edu.iq or Niazy.hady@yahoo.com
Article History:
Received: 25/06/2019
Accepted: 31/10/2019
Published: 22/04 /2020

$$g(x, y, z) = a_0 + a_1x + a_2y + a_3z + a_4x^2 + a_5y^2 + a_6z^2 + a_7xy + a_8xz + a_9yz,$$

where a_i for $i = 0, \ldots, 9$ are real parameters. This system has only one singular point when

$$a_0 = \frac{a_1^2}{4a_4},\ a_4 \neq 0 \quad \text{or} \quad a_4 = 0.$$

The case $a_0 = \frac{a_1^2}{4a_4}, a_4 \neq 0$ was considered by Wei et al. in (Wei, Sprott, &Chen, 2015). They addressed a periodic solution which bifurcates from one single non-hyperbolic singular point. The other case $a_4 = 0$ was considered by Molaie, et al. in (Molaie, Jafari, Sprott, & Golpayegani, 2013). They found 23 simple chaotic flows of system (1). Here, the case $a_4 = 0$ with extra conditions will be considered (see Propositions 1 and 2) to determine nonisolated zero–Hopf

singularity which fill the curve passing through the origin of coordinates.

A zero-Hopf singular point of a polynomial differential system in the 3-dimentions is an isolated singular point which owns a zero and a simple pair of purely imaginary eigenvalues. This type of singular point is an interesting topic and it considered by (John, 1981; John & Philip, 2013; Kuznetsov, 2013; Rizgar, 2017) and others. Generally, a zero– Hopf bifurcation is a 2-parameter unfolding of a polynomial systems in the 3-dimensions which has an isolated z-H singular point. It has realized that several intricate sets of invariant of the unfolding maybe bifurcate in a neighborhood of an isolated z-H singular point under some generic states, for example a local birth of "chaos" could be implied from the z-H bifurcation, see (Baldom´a & Seara, 2006; Broer & Vegter, 1984).

In general, there is no theory to determine when some periodic solutions are bifurcated by perturbing the parameters of the 3D systems from the z-H singular point. Some authors are investigated on zero–Hopf singular point, see (Garc´ıa, Llibre, & Maza, 2014; Llibre, 2014; Llibre, Makhlouf, & Badi, 2009; Euz´ebio, Llibre, & Vidal, 2015; Euz´ebio & Llibre, 2017; Llibre &P´erez-Chavela, 2014; Castellanos, Llibre, & Quilantan, 2013; Llibre, Oliveira, & Valls, 2015; Rizgar, 2017). They studied the periodic solutions bifurcating in a neighborhood of the isolated z-H singular point. Only the two works (Llibre & Xiao, 2014; Cˆandido & Llibre, 2018), they studied the periodic solutions bifurcating in a neighborhood of a nonisolated zero–Hopfpoint located only at $(0,0,0)$-point. However, a case where system (1) has infinitely many (actually a continuum of) zero-Hopf singularity will be studded. This is explained in Proposition 1. By linear algebra the following result can be obtained.

System (1) has a curve of a singularity which passes through $(0,0,0)$-point if and only if

$$a_0 = a_1 = a_4 = 0.$$

From now, we consider the condition $a_0 = a_1 = a_4 = 0$. So, we modify the general case in system (1) into following one

$$\dot{x} = y,\ \dot{y} = z, \dot{z} = f(x,y,z), \qquad (2)$$

$$f(x,y,z) = a_2 y + a_3 z + a_5 y^2 + a_6 z^2 + a_7 xy + a_8 xz + a_9 yz,$$

where there are no x and x^2 terms in the $\dot{z}$ equation to guarantee that there is a curve of singularity. We see that any singular point (p_0, p_1, p_2) of system (2) must have $p_1 = p_2 = 0$, and eigenvalues λ that satisfy

$$\lambda^3 - f_z\lambda^2 - f_y\lambda - f_x$$

in which $f_x = 0, f_y = a_2 + a_7 p_0$ and $f_z = a_3 + a_8 p_0$. Using the Routh–Hurwitz stability criterion, for the singular point (p_0, p_1, p_2) to be asymptotically stable, we need

$$f_z < 0,\ f_y f_z + f_x > 0, \text{ and } f\_x < 0.$$

Therefore, the quadratic jerk system (2) cannot have the stable equilibria. As shown in (Llibre & Xiao, 2014), we can easily find that system (2) has infinitely many (actually a continuum of) singular points which are at the following curve (curve of a singularity)

$$C_x = \{(p_0, 0,0) : p_0 \in \mathbb{R}\}. \qquad (3)$$

An analysis is made on the polynomial system (1) such that each point of the curve C_x becomes a nonisolated z-H singular point which is the main purpose in this work. This is described in following proposition. It has shown that there is only one family of parameters in the jerk system in which any singular point at the curve$C_x$becomes the z-H singular point. Furthermore, we use the method of averaging in the second order to estimate a periodic solution of the jerk system which bifurcates at the line of singularity.

Proposition 1. System (2) has the z-H singular points which are localized at the curveC_x, if the following conditions are satisfied

$$a_3 = -a_8 p_0, \text{ and } a_2 + a_7 p_0 < 0. \qquad (4)$$

We prove this proposition in Section 2.

In Section 1, we describe the method of averaging in the second order. It explains the accurate conditions for the existence of a periodic solution which bifurcates from the nonisolated z-H singular point. In Section 2, the bifurcations

with nonisolated z-H singular points are studied using a small perturbation of system (2) keeping the nonisolated singular points at the curve C_x which obtains a perturbation system. In the neighborhood of any point, the given perturbation system is reduced to a 2π-periodic system in a type of cylindrical coordinates, and the re-scaling of variables is needed to prove the main result (Theorem 1).

The following theorem is our main result to obtain a periodic solution which bifurcates from one family of parameters for the jerk system with a curve of z-H singularity.

Theorem 1 Let $(a_2, a_3, a_5, a_6, a_7, a_8, a_9) = (b_2 + \epsilon\, c_2, \epsilon c_3, b_5 + \epsilon\, c_5, b_6 + \epsilon\, c_6, \epsilon\, c_7, \epsilon\, c_8, b_9 + \epsilon\, c_9)$ be a vector and $c_3 = 0, b_5 = -\omega^2 b_6$, with a sufficiently small parameterϵ. If $b_6 b_7 \neq 0$. Then, system (2) has a z-H bifurcation at the nonisolated singular point which localizes at the curve of singularity, and a periodic solution can be produced for each point at that curve of a singularity when $\epsilon = 0$.

We prove Theorem 1 in Section 2. The method of averaging of second order is the main tool to prove Theorem 1. The method of averaging is made a history and for a new explanation of this method, one can see the work of (Sanders et al, 2007). In the following section (Section 1), we recall the method of averaging of second order as was described in (Buica, Fran¸coise, & Llibre, 2007; Pi & Zhang, 2009).

1. THE METHOD OF AVERAGING OF THE SECOND ORDER FOR PEIRODIC SOLUTIONS

The purpose of this section is to describe basic results from the method of averaging. This method requires to prove the bifurcating periodic solutions from nonisolated z-H singular points of system (2), for a proof of the method of averaging on can found in Theorem 2.6.1 of Sanders and Verhulst (O'Malley Jr, 1987) also Theorem 11.5 of Verhulst. The averaging method of second order was described clearly in (Buica et al., 2007; Llibre et al., 2009). Also, in (Marsden & McCracken, 2012; Chow & Hale, 2012; Buica et al., 2007; Sanders, Verhulst, & Murdock, 1987) the researchers have devoted their attempt to determine a periodic solution using the method of averaging.

The following theorem is summarized the method of averaging of second order.

Theorem 2 Consider the Differential equation

$$\dot{\mathrm{x}} = \epsilon\, f_1(\mathrm{t}, \mathrm{x}) + \epsilon^2 f_2(\mathrm{t}, \mathrm{x}, \epsilon) + \epsilon\, \mathrm{R}(\mathrm{t}, \mathrm{x}, \epsilon) \qquad (6)$$

where $f_1, f_2 : \mathbb{R} \times \mathrm{Y} \to \mathbb{R}^n$, $\mathrm{R}: \mathbb{R} \times \mathrm{U} \times (-\epsilon_0, \epsilon_0) \to \mathbb{R}^n$ are continuous functions, T-periodic in the variable t and $U \subset \mathbb{R}^n$ is an open subset. Assume that the following conditions satisfy

i. $f_1(t, .) \in C^1(U), \forall t \in \mathbb{R}$, f_2, R and $\frac{\partial f_1}{\partial x}$ are locally Lipschitz with respect to variable x, and R is twice differentiable with respect to x .

ii. Define $F_{i0} : U \to \mathbb{R}^n$ for $i = 1,2$ by

$$\mathrm{F}_{10} = \frac{1}{T}\int_0^T f_1(s, z)\, ds$$

$$\mathrm{F}_{20} = \frac{1}{T}\int_0^T [\, D_z f_1(s, z) \int_0^s f_1(s, z)\, ds + f_2(s, z)]\, ds$$

where $D_z f_1\,(s, z)$ is the Jacobian determinant matrix of the components of $f_1$with respect to z.

iii. For V bounded and an open set in U, for $\epsilon \in (-\epsilon_0, \epsilon_0)\backslash\{0\}$ there is $r_\epsilon \in V$ such that$F_{10} + \epsilon\, F_{20} = 0$ and$d_B(F_{10} + \epsilon\, F_{20})$ is not equal to zero.

Hence, for a sufficiently small$|\epsilon| > 0$, a T-periodic solution $\phi(\Delta, \epsilon)$ of system (6) is existed such that $\phi(0, \epsilon) = r_\epsilon$.

The term$d_B(F_{10} + \epsilon\, F_{20}) \neq 0$ denotes the Brouwer degree of the function$F_{10} + \epsilon\, F_{20}: V \to \mathbb{R}^n$ at the singular point r which is not finish. A sufficient condition for the inequality to be true is that the Jacobian of$(F_{10} + \epsilon\, F_{20})$ at r_ϵ is notfinish. If$F_{10} \neq 0$, then the zeros of$(F_{10} + \epsilon\, F_{20})$ are mainly the zeros of $F_{10}$for $0 \ll \epsilon$. In this situation, the previous result uses the method of averaging of first order. If$F_{10} = 0$and$F_{20} \neq 0$, then the zeros of$F_{10} + \epsilon\, F_{20}$are mainly the zeros of F_{20} for$0 \ll \epsilon$. In this situation, the previous result gives the method of averaging of second order.

2. PROOF OF THE MAIN RESULT

Proof of Proposition 1. The characteristic equation of system (2) for each singular point, say $(p_0, 0,0)$, which is at the curve L is

$$\lambda^3 - (a_3 + a_8 p_0)\lambda^2 - (a_2 + a_7 p_0)\lambda = 0.$$

Putting this in $\lambda(\lambda^2 + \omega^2) = 0$where $\omega > 0$, we obtain only one family of condition, that is $a_3 = -a_8 p_0$ and $a_2 + a_7 p_0 < 0$.

Therefore, for any nonisolated singular point $(p_0, 0,0) \in L$ of system (2) has the eigenvalues$\lambda_1 = 0$ and $\lambda_{2,3} = \pm\sqrt{a_2 + a_7 p_0}$. This means that each singular point is in the z-H singular type.

Proof of Theorem 1. If we perturb the parameters $(a_2, a_3, a_5, a_6, a_7, a_8, a_9) = (b_2 + \epsilon\, c_2, \epsilon c_3, b_5 + \epsilon\, c_5, b_6 + \epsilon\, c_6, \epsilon\, c_7, \epsilon\, c_8, b_9 + \epsilon\, c_9)$ with $0 \ll \epsilon < 1$.Then system (2) becomes

$$\begin{aligned}
&\dot{x} = y,\\
&\dot{y} = z,\\
&\dot{z} = (b_2 + \epsilon\, c_2)y + \epsilon c_3 z + (b_5 + \epsilon\, c_5)y^2 + (b_6 + \epsilon\, c_6)z^2 + (b_7 + \epsilon\, c_7)xy + \epsilon\, c_8 xz + (b_9 + \epsilon\, c_9)\, yz.
\end{aligned} \tag{7}$$

Re-scaling variables $(x, y, z) = (\epsilon X, \epsilon Y, \epsilon Z)$ system (7) in variables (X, Y, Z) becomes

$$\begin{aligned}
&\dot{X} = Y,\\
&\dot{Y} = Z,\\
&\dot{Z} = (b_2 + \epsilon\, c_2)Y + \epsilon c_3 Z + (\epsilon\, b_7 + \epsilon^2 c_7)XY + \epsilon^2 c_8 XZ + (c_5\epsilon^2 + b_5\epsilon)Y^2 + (c_9\epsilon^2 + b_9\epsilon)ZY + (\epsilon b_6 + \epsilon^2 c_6)Z^2.
\end{aligned} \tag{8}$$

The above system has also a line of singular points (X = X, Y = 0, Z = 0). Thus, the linear part at each of nonisolated singular point of system (8) when $\epsilon = 0$ shall be transformed to its real Jordan form, which is as

$$\begin{pmatrix} 0 & -\omega & 0 \\ \omega & 0 & 0 \\ 0 & 0 & 0 \end{pmatrix},$$

where $\omega^2 = -b_2$. For doing that changing of variables

$$\begin{pmatrix} X \\ Y \\ Z \end{pmatrix} = \begin{pmatrix} 1 & 0 & 1 \\ 0 & -\omega & 0 \\ -\omega^2 & 0 & 0 \end{pmatrix} \begin{pmatrix} U \\ V \\ W \end{pmatrix}, \tag{9}$$

can be used. In the new variables (U, V, W), system (8) writes

$$\begin{aligned}
&\dot{U} = -\omega V + \Big(V^2 b_5 - c_3\omega U + b_9\omega\, UV + \omega^2 b_6 U^2 - \tfrac{1}{\omega} V\,(c_2 + b_7 U + b_7 W)\Big)\epsilon + \Big(-\omega^2 U^2 c_6 - c_5 V^2 - \omega\, c_9 VU + c_8 U(U + W) + \tfrac{1}{\omega} c_7 V(U + W)\Big)\epsilon^2,\\
&\dot{V} = \omega U,\\
&\dot{W} = \Big(c_5 V^2 - c_8 U(U + W) + \omega U(c_6\omega U + c_9 V) - \tfrac{1}{\omega} c_7 V(U + W)\Big)\epsilon^2 + \Big(-c_3 U + b_5 V^2 + \omega(b_9 UV + \omega b_6 U^2) - \tfrac{1}{\omega}(b_7 VW + b_7 UV + c_2 V)\Big)\epsilon.
\end{aligned} \tag{10}$$

Using the cylindrical coordinates (r, θ, W)defining by

$$(U, V, W) = (r\cos(\theta), r\sin(\theta), W),$$

and suggesting θ as the independent variable. System (10) can be expressed as

$$\begin{aligned}
&\frac{dr}{d\theta} = \epsilon\, f_{1,1} + \epsilon^2 f_{1,2} + O(\epsilon),\\
&\frac{dW}{d\theta} = \epsilon\, f_{2,1} + \epsilon^2 f_{2,2} + O(\epsilon),
\end{aligned} \tag{11}$$

where

$$\begin{aligned}
f_{1,1} = {} & \tfrac{r\cos(\theta)}{\omega^2}(r\omega(\omega^2 b_6 - b_5)\cos^2(\theta) + (r\sin(\theta)(b_9\omega^2 - b_7) - \omega c_3)\cos(\theta) + (-b_7 W - c_2)\sin(\theta) + r\omega b_5),\\
f_{1,2} = {} & \tfrac{r\cos(\theta)}{\omega^2}(-(r\cos(\theta)(\omega^2 r\cos(\theta)\sin(\theta)c_9 + r\omega c_5 - (\cos(\theta))^2 r\omega c_5 + \omega^3 r(\cos(\theta))^2 c_6 - c_8\,\omega\cos(\theta)W - c_8\omega r(\cos(\theta))^2 - r\sin(\theta)c_7\cos\theta - \sin(\theta)c_7 W) + r\cos\tfrac{\theta}{\omega^2}\Big(r\,\omega b_5 - (\cos(\theta))^2 r\,\omega b_5 + r\,\omega^2\cos(\theta)\sin(\theta)b_9 - \sin(\theta)b_7 W - \sin(\theta)c_2 - c_3\,\omega\cos(\theta) - r\sin(\theta)b_7\cos(\theta) + r\omega^3(\cos(\theta))^2 b_6\Big)\Big(rb_7\cos(\theta) +
\end{aligned}$$

$sin(\theta)\left(cos(\theta)\right)^2 r\omega b_5 - r\,\omega\, b_5\, sin\,(\theta) - r\,\omega^2 cos(\theta) b_9 - sin(\theta) r\omega^3 \left(cos(\theta)\right)^2 b_6 + sin(\theta) c_3 \omega\, cos(\theta) + b_7 W - \left(cos(\theta)\right)^2 b_7 W + c_2 + \left(cos(\theta)\right)^3 r\,\omega^2\, b_9 - \left(\, cos\,(\theta)\right)^3 r b_7 - \left(cos(\theta)\right)^2 c_2\Big)\,\omega^2),$

$f_{2,1} = \frac{r}{\omega^3}(r\,\omega\,(\omega^2 b_6 - b_5)(\,cos(\theta))^2 + (r(-b_7 + \omega^2 b_9) sin(\theta) - c_3\,\omega)\,cos(\theta) + (\,-b_7 W - c_2) sin(\theta) + r\,\omega b_5),$

$f_{22} = \Big(\, r\,\Big(\,\omega^2 r cos(\theta) sin(\theta) c_9 + r\omega c_5 - \left(cos(\theta)\right)^2 r\omega c_5 + \omega^3 r\left(cos(\theta)\right)^2 c_6 c_8 \omega cos(\theta) W - c_8 \omega r\left(cos(\theta)\right)^2 - r sin(\theta) c_7 cos(\theta) - sin(\theta) c_7 W\Big) - \frac{r}{\omega}\Big(\, r\omega b_5 - \left(cos(\theta)\right)^2 r\omega b_5 + r\omega^2 cos(\theta) sin(\theta) b_9 - sin(\theta) b_7 W - sin(\theta) c_2 - c_3 \omega cos(\theta) - r sin(\theta) b_7 cos(\theta) + r\omega^3 \left(cos(\theta)\right)^2 b_6\Big)\Big(\, -r b_7 cos(\theta) - sin(\theta)\left(cos(\theta)\right)^2 r\omega b_5 + r\omega b_5 sin(\theta) + r\omega^2 cos(\theta) b_9 + sin(\theta) r\omega^3 \left(cos(\theta)\right)^2 b_6 sin(\theta) c_3 \omega cos(\theta) - b_7 W + \left(cos(\theta)\right)^2 b_7 W - c_2 - \left(cos(\theta)\right)^3 r\omega^2 b_9 \left(cos(\theta)\right)^3 r b_7 + \left(cos(\theta)\right)^2 c_2\,\Big)\omega^2\Big) - \frac{r}{\omega^2}\Big(\, r\omega b_5 - \left(cos(\theta)\right)^2 r\omega b_5 + r\omega^2\, cos(\theta) sin(\theta) b_9 - sin(\theta) b_7 W - sin(\theta) c_2 - c_3 \omega cos(\theta) - r sin(\theta) b_7 cos(\theta) + r\omega^3 \left(cos(\theta)\right)^2 b_6\Big)\Big(-r b_7 cos(\theta) - sin(\theta)\left(cos(\theta)\right)^2 r\omega b_5 + r\omega b_5 sin(\theta) + r\omega^2 cos(\theta) b_9 + sin(\theta) r\omega^3 \left(cos(\theta)\right)^2 b_6 - sin(\theta) c_3 \omega cos(\theta) - b_7 W\left(cos(\theta)\right)^2 b_7 W - c_2 - \left(cos(\theta)\right)^3 r\omega^2 b_9 + \left(cos(\theta)\right)^3 r b_7 + \left(cos(\theta)\right)^2 c_2\Big)\omega^3\,.$

The two systems (11) and (6) are equivalent by taking the notation in Theorem 2, that is, letting $t = \theta,\ T = 2\pi,\ x = (r, W) \in (0, \infty) \times R,\ x_0 = (ro, Wo)$ and

$$F_{10}(t,x) = \frac{1}{2\pi}\int_0^{2\pi} f_1(\theta, r, W)\, d\theta = \begin{bmatrix} \frac{1}{2\pi}\int_0^{2\pi} f_{1,1}(\theta, r, W)\, d\theta \\ \frac{1}{2\pi}\int_0^{2\pi} f_{2,1}(\theta, r, W)\, d\theta \end{bmatrix} = \begin{bmatrix} f_{1,1}^{\circ}(r, W) \\ f_{2,1}^{\circ}(r, W) \end{bmatrix}. \quad (12)$$

Computing equation (12), we obtain

$$f_{1,1}^{\circ}(r, W) = -\frac{1}{2}\frac{r\, c_3}{\omega},\ \ f_{2,1}^{\circ}(r, W) = \frac{r^2(\omega^2 b_6 + b_5)}{2\omega}. \quad (13)$$

From (Buica et al., 2007) the non-zero solution of system (13) gives a periodic solution which bifurcates in the neighborhood of the each point at the curve *L*for system (2). In other word, for $r > 0$, the method of averaging of first order characterized by (Llibre & P´erez Chavela, 2014) does not give the possible periodic solutions bifurcating from the z-H singular point. Therefore, the averaged function of the first order $(f_{1,1}^{\circ}(r, W), f_{2,1}^{\circ}(r, W))$ is equal to zero if and only if

$$c_3 = 0, \text{ and } b_5 = -\omega^2 b_6\ (\omega^2 = -b_2). \quad (14)$$

For using the Brouwer degree of second order, we now consider the conditions in equation (14) to use the method of averaging of second order. Therefore, the following expression must be computed:

$$\begin{bmatrix} \frac{\partial f_{1,1}}{\partial r} & \frac{\partial f_{1,1}}{\partial W} \\ \frac{\partial f_{2,1}}{\partial r} & \frac{\partial f_{2,1}}{\partial W} \end{bmatrix} \begin{bmatrix} \int_0^{\theta} f_{1,1}(\theta, r, W)\, d\theta \\ \int_0^{\theta} f_{2,1}(\theta, r, W)\, d\theta \end{bmatrix} + \begin{bmatrix} f_{2,1} \\ f_{22} \end{bmatrix}. \quad (15)$$

We integrate the above expression from 0 to 2π with respect θ and divide by 2π to obtain the following equation

$$F_{20}(t,x) = \begin{bmatrix} F_{2,0,1}^{*} \\ F_{2,0,2}^{*} \end{bmatrix} + \begin{bmatrix} \frac{r}{8\omega}(r^2 b_7 b_6 + 4 c_8 W) \\ \frac{-r^2}{2\omega}(c_8 - c_5 - \omega^2 c_6 + c_2 b_6 + b_6 b_7 W) \end{bmatrix}. \quad (16)$$

To look for a periodic solution, we solve the following system of equation (We keep away for the zero solution with $r \geq 0$),

$$F_{20}(t,x) = 0 \rightarrow \begin{bmatrix} F_{2,0,1}^{\circ} = 0 \\ F_{2,0,2}^{\circ} = 0 \end{bmatrix}. \quad (17)$$

That is

(r, W)
$= (\frac{2\sqrt{c_8(c_2b_6 - c_5 + c_8 - c_6\omega^2)}}{b_7b_6}, \frac{c_5 + c_6\omega^2 - c_2b_6 - c_8}{b_7b_6})$

Let (r^*, W^*) be a solution of system (17). In order to have a periodic solution according with Theorem 2, we must have

$$J(F_{2,0}(r, W))|_{(r,w)=(r^*,W^*)} \neq 0. \quad (18)$$

We then compute the Jacobian matrix of (17) to obtain

$$-\frac{2c_8^2}{b_7^2b_6^2}(\omega^2c_6 - b_6c_2)^2,$$

which is not equal to zero when $b_7b_6 \neq 0$, where c_8, c_2 and c_6 are arbitrary, then we can chose that $c_8(\omega^2c_6 - b_6c_2)^2 \neq 0$.

Shortly, the solution (r^*, W^*) of system (17) which confirms condition (18) satisfies the assumptions (i) and (ii) of Theorem 2. So, for utilizing the method of averaging of second order we deduce that system (11) has the periodic solution bifurcating at each point at the curve L. Therefore, due to the re-scaling in system (8) with generic conditions (5) and (14), the periodic solution of system (2) is obtained which bifurcates from the nonisolated z-H singularity.

Therefore, for $\epsilon > 0$ sufficiently small, Theorem 2 guaranties that there is a periodic solution $(r(\theta, \epsilon), W(\theta, \epsilon))$ of system (11) such that$\big(r(0, \epsilon), W(0, \epsilon)\big) \to (r^*, W^*)$ when $\epsilon \to 0$.
Thus, for $\epsilon \gg 0$

$(U(\theta, \epsilon), V(\theta, \epsilon), W(\theta, \epsilon)) =$
$(r\cos(\theta), r\sin(\theta), W(\theta, \epsilon)), \quad (19)$

is the periodic solution of system (10). Consequently, system (8) under the change of variables in equation (9) has the periodic solution $(X(\theta), Y(\theta), Z(\theta))$ which obtains from (19). Finally, for $\epsilon > 0$sufficiently small, we have
$(x(\theta), y(\theta), z(\theta)) = (\epsilon X(\theta), \epsilon Y(\theta), \epsilon Z(\theta))$,

Thus, system (2) has the periodic solution tending to the point at the curve L when $\epsilon \to 0$. It is the periodic solution which starts at the z-H singular point localized at the curve L when $\epsilon \to 0$. Hence, we complete the proof this theorem.

3. CONCLUSIONS

In this work, the jerk system has been considered which was suggested by Gottlieb in (Gottlieb, H. P. 1998). We put conditions on parameters in which the jerk system has a curve of singularity. We have then described the values of the parameters for which a zero-Hopf singular point occurs at the point of that curve of singularity. Moreover, we have used the averaging method of second order (see Theorem 2) to estimate of a periodic solution which bifurcates from the zero–Hopf equilibrium point. This theorem obtained a periodic solution $\big(r(\theta, \epsilon), W(\theta, \epsilon)\big)$ of the jerk system such that

$$\big(r(0, \epsilon), W(0, \epsilon)\big) = (r^*, W^*) + O(\epsilon),$$

where

$(r^*, W^*) =$
$\left(\frac{2\sqrt{c_8(c_2b_6 - c_5 + c_8 - c_6\omega^2)}}{b_7b_6}, \frac{c_5 + c_6\omega^2 - c_2b_6 - c_8}{b_7b_6}\right).$

In coordinates (r, θ, ω), we can write this periodic solution as

$$\big(r\,(t, \epsilon), \theta(t, \epsilon), \omega(t, \epsilon)\big)$$

which satisfies

$$\big(r\,(0, \epsilon), \theta(0, \epsilon), W(0, \epsilon)\big) = (r^*, 0, W^*) + O(\epsilon).$$

Now, in the coordinates (U, V, W) the periodic solution becomes

$$(U(t, \epsilon), V\,(t, \epsilon), W(t, \epsilon))$$

which satisfies

$$(U(0, \epsilon), V(0, \epsilon), W(0, \epsilon)) = (r^*, 0, W^*) + O(\epsilon).$$

Also, the above periodic solution in the variables (X, Y, Z) becomes $(X(t, \epsilon), Y(t, \epsilon), Z(t, \epsilon))$ which satisfies

$$(X(0, \epsilon), Y(0, \epsilon), Z(0, \epsilon)) = (r^* + W^*, 0, -\omega^2r^*) + O(\epsilon).$$

Finally, in the variables (x, y, z) this periodic solution becomes

$$(x(t, \epsilon), y(t, \epsilon), z(t, \epsilon))$$

which satisfies

$$\big(x(0, \epsilon), y(0, \epsilon), z(0, \epsilon)\big) = \epsilon(r^* + W^*, 0, -\omega^2r^*) + O(\epsilon).$$

Acknowledgements

We would like to thank Dr. Azad I. Amen for offering a number of valuable suggestions as well as for fruitful discussions. Also, we would like to express our gratitude to the referee for their comments and valuable suggestions to improve the display of this work.

References

BALDOM'A, I. & SEARA, T. 2006. Breakdown of heteroclinic orbits for some analytic unfoldings of the Hopf-zero singularity, 16(6), 543-582.

BROER, H., W. & VEGTER, G. 2006. Subordinate Sil'nikov bifurcations near some singularities of vector fields having low codimension. Ergodic Theory and Dynamical Systems. 4(4), 509-525.

BUICA, A., FRAN,COISE, J., P. & LLIBRA, J. 2007. Periodic solutions of nonlinear periodic differential systems with a small parameter. Communications on Pure and Applied Analysis, 6 (1), 103.

C^ANDIDO, M. R. & LLIBRA, L. 2018. Periodic Orbits Bifurcating from a Nonisolated Zero-Hopf Equilibrium of Three-Dimensional Differential Systems Revisited. International Journal of Bifurcation and Chaos. 28(05), 1850058.

CASTELLANOS, V., LLIBRA, L. & QUILANTAN, I. 2003. Simultaneous periodic orbits bifurcating from two z-H equilibria in a tritrophic food chain model. Journal of Applied Mathematics and Physics, 1 (07), 31.

CHOW, S.-N & HALE, J., K. 2012 Methods of bifurcation theory Vol. 251. Springer Science and Business Media.

EUZ'EBIO, R., D. & LLIBRA, L. 2017. Zero-Hopf bifurcation in a chua system. Nonlinear Analysis: Real World Applications, 37, 31–40.

EUZ'EBIO, R., D., LLIBRA, L. & VIDAL, C. 2015. Zero-Hopf bifurcation in the fitzhughnagumo system. Mathematical Methods in the Applied Sciences, 38 (17), **42**89–4299.

GARC'IA, I., LLIBRA, L. & MAZA, S. 2014. On the periodic orbit bifurcating from a zero hopf bifurcation in systems with two slow and one fast variables. Applied Mathematics and Computation, 232, 84–90.

GOTTLIEB,H. P. 1990. Simple nonlinear jerk functions with periodic solutions.American Journal of Physics. 66(10), 903-906.

JOHN, G. 1981. On a codimension two bifurcation. In Dynamical systems and turbulence, Warwick 1980 (pp. 99–142). Springer.

JOHN, G. & PHILIP, H. 2013. Nonlinear oscillations, dynamical systems, and bifurcations of vector fields (Vol. 42). Springer Science and Business Media.

KUZNETSOV, Y. A. 2013. Elements of applied bifurcation theory (Vol. 112). Springer Science and Business Media.

LLIBRA, L. 2014. Periodic orbits in the zero-hopf bifurcation of the r¨ossler system'. Romanian Astronomical Journal, 24 (1), 49–60.

LLIBRA, L., MAKHOUF, A. & BADI, S. 2009. 3-dimensional hopf bifurcation via averaging theory of second order. Discrete and Continuous Dynamical Systems A, 25 (4), 1287–1295.

LLIBRA, L., OLIVERIRA, R. D. & VALLS, C. 2015. On the integrability and the zero-hopf bifurcation of a chen–wang differential system. Nonlinear Dynamics, 80 (1-2), 353–361.

LLIBRA, L., & P´EREZ-CHAVELA, E. 2014. Zero-hopf bifurcation for a class of Lorenz type systems. Discrete and Continuous Dynamical Systems-Series B, 19(6), 1731–1736.

LLIBRA, L. & XIAO, D. 2014. Limit cycles bifurcating from a non-isolated zero-hopf equilibrium of three-dimensional differential systems. Proceedings of the American Mathematical Society, 142 (6), 2047–2062.

MARSDEN, J. E. & McCRACKEN, M. 2012. The hopf bifurcation and its applications (Vol. 19). Springer Science and Business Media.

MOLAIE, M., JAFARI, S., SPROTT, J. C. & GOLPAYEGANI, S. M. 2013. Simple chaotic flows with one stable equilibrium. International Journal of Bifurcation and Chaos, 23 (11), 1350188.

RIZGAR, H. 2017. Zero-Hopf Bifurcation in the Rössler's Second System. ZANCO Journal of Pure and Applied Sciences, 29(5), 66-75.

O'MALLEY, Jr. R. 1987. Averaging methods in nonlinear dynamical systems. (jasanders and f. verhulst). Society for Industrial and Applied Mathematics.

PI, D., H. & and ZHANG, X. 2009. Limit cycles of differential systems via the averaging methods. Canadian Appl. Math. Quarterly. 17, 243-269.

SANDERS, J. A., VERHULST, F. & MURDOCK, J. 2007. Averaging methods in nonlinear dynamical systems. Society for Industrial and Applied Mathematics. (Vol. 59). Springer

SPROTT, J. C. 1997. Simplest dissipative chaotic low. Physics letters A. 228(4-5), 271-274.

WEI, Z., SPROTT, J. & CHEN, H. 2015. Elementary quadratic chaotic flows with a single non-hyperbolic equilibrium. Physics Letters A, 379 (37), 2184 - 2187.

ZANCO Journal of Pure and Applied Sciences
The official scientific journal of Salahaddin University-Erbil
https://zancojournals.su.edu.krd/index.php/JPAS

ISSN (print):2218-0230**, ISSN (online):** 2412-3986**, DOI: http://dx.doi.org/10.21271/zjpas**

RESEARCH PAPER

Centre Bifurcations for a Three Dimensional System with Quadratic Terms

Rizgar H. Salih[1], Mohammad S. Hasso[2], Surma H. Ibrahim[3]

[1]Department of Mathematics, College of Basic Education, University of Raparin, Kurdistan Region-Iraq
[2]Department of Mathematics, Faculty of Science and Health, Koya University, Kurdistan Region-Iraq
[3]Department of Mathematics, Koya University, Faculty of Science and Health, Kurdistan Region-Iraq

A B S T R A C T:

This article is devoted to study the bifurcated periodic orbits from centre for a differential equation of third order. Sufficient conditions for the existence of a centre are obtained by using inverse Jacobi multiplier. As a result, we found four sets of centre conditions on the centre manifold. For a given centre, it is shown that three periodic orbits can be bifurcated from the origin under two sets of condition and four periodic orbits under the other sets of condition. The cyclicityes are obtained by considering the linear parts of the corresponding Liapunov quantities of the perturbed system.

KEY WORDS: Hopf and Centre Bifurcation; Periodic Solutions; Inverse Jacobi Multiplier.
DOI: http://dx.doi.org/10.21271/ZJPAS.32.2.7
ZJPAS (2020) , 32(2);62-71 .

INTRODUCTION

We consider the following third order differential equation

$$\dddot{x} - \alpha\,\ddot{x} - \beta\,\dot{x} - \gamma\,x - H(x\,,\dot{x},\ddot{x}) = 0, \qquad (1)$$

where $\alpha\,,\beta\,,\gamma \in \mathbb{R}$ and $H(x\,,\dot{x},\ddot{x})$ is an analytic quadratic function. When $\alpha = \beta = \gamma = -1$, the centre problem on a local centre manifold of equation (1) is studied in (Mahdi, 2013). By eliminating two coefficients of the quadratic function H, he has found the necessary and conditions for the existence of a centre on the centre manifold for the three 4-parameter families of equation (1). Mahdi et al. (2017) have constructed a hybrid approach using numerical algebraic geometry to the center-focus problem. They applied their technique to have centre conditions for equation (1) (Mahdi, et al., 2017).

Equation (1) can be transformed into a system of nonlinear equations. This can be introducing $\dot{x} = y,\ \ddot{x} = z$ to obtain

$$\begin{aligned} \dot{x} &= y && = P_1(x,y,z), \\ \dot{y} &= z && = P_2(x,y,z), \\ \dot{z} &= \alpha\,z + \beta\,y + \gamma\,x + H(x\,,y\,,z) && = P_3(x,y,z), \end{aligned} \qquad (2)$$

where $H(x,y,z) = a_1x^2 + a_2y^2 + a_3z^2 + a_4\,xy + a_5xz + a_6yz$. System above has an isolated critical point at the origin, the Jacobian matrix of system (2) at that point has a zero and

* **Corresponding Author:**
Rizgar H. Salih
E-mail: rizgar.salih@uor.edu.krd or rizgarmath4@gmail.com
Article History:
Received: 17/05/2019
Accepted: 31/10/2019
Published: 22/04 /2020

two pure imaginary eigenvalues under some conditions on the parameters. In that case, the origin is called zero-Hopf critical point (for more information see (Salih, 2017)). Furthermore, under some other conditions on the parameters, the Jacobian matrix of system (2) at the origin has a non-zero and a pair of pure imaginary eigenvalues, in such case the origin is called Hopf point. For the three dimensional systems (2), a sufficient condition for a Hopf bifurcation is explained below. The characteristic polynomial for system (2) is given by

$$\lambda^3 - T\,\lambda^2 - K\,\lambda - D = 0, \tag{3}$$

such that

i. $T = \sum_{i=1}^{3} b_{i,i}$ (trace of the Jacobian matrix of system (2) at the origin),
ii. $D =$ determinant of the Jacobian matrix of system (2) at the origin,
iii. $K = -(B_1 + B_2 + B_3)$,

where $B_1 = b_{2,2}b_{3,3} - b_{2,3}b_{3,2}$, $B_2 = b_{1,1}b_{3,3} - b_{1,3}b_{3,1}$, $B_3 = b_{2,2}b_{1,1} - b_{2,1}b_{1,2}$ and $b_{i,j}$, $i,j = 1,2,3$ are elements of the Jacobian matrix of system (2) at the origin (for more detail on Hopf bifurcation also reader can consult (Ameen, et al., 2009), (Salih, 2009) and (Salih & Ameen, 2008)). Then the Hopf bifurcation take place at a point, Hopf point, on the surface

$$TK + D = 0\,; \quad K < 0 \quad \text{and} \quad T \neq 0\,. \tag{4}$$

Using the following change of variables with Hopf conditions

$$\begin{bmatrix} x \\ y \\ z \end{bmatrix} = \begin{bmatrix} 0 & 1 & \frac{1}{\alpha^2} \\ \omega & 0 & \frac{1}{\alpha} \\ 0 & -\omega^2 & 1 \end{bmatrix} \begin{bmatrix} y_1 \\ y_2 \\ y_3 \end{bmatrix}, \tag{5}$$

we can write system (2) as

$$\begin{aligned} \dot{y}_1 &= -\omega y_2 + G(y_1, y_2, y_3), \\ \dot{y}_2 &= \omega y_1 + \frac{\omega}{\alpha} G(y_1, y_2, y_3), \\ \dot{y}_3 &= \alpha y_3 - \alpha\omega\, G(y_1, y_2, y_3), \end{aligned} \tag{6}$$

where $\omega = \sqrt{-\beta}$ and

$$G(y_1,y_2,y_3) = -\frac{\alpha\omega a_2 {y_1}^2}{\omega^2+\alpha^2} + \frac{(\omega^2 a_6 - a_4)\alpha\, y_1 y_2}{\omega^2+\alpha^2} - \frac{(\alpha^2 a_6 + 2\alpha a_2 + a_4) y_1 y_3}{\alpha(\omega^2+\alpha^2)} + \frac{1}{\alpha\,\omega(\omega^2+\alpha^2)}(-\alpha^2(\omega^4 a_3 - \omega^2 a_5 + a_1)\, {y_2}^2 + (2\alpha^2\omega^2 a_3 + \alpha\omega^2 a_6 + \omega^2 a_5 - \alpha^2 a_5 - \alpha a_4 - 2a_1) y_3 y_2 - \frac{1}{\alpha^3\omega(\omega^2+\alpha^2)}(\alpha^4 a_3 + \alpha^3 a_6 + \alpha^2 a_2 + \alpha^2 a_5 + \alpha a_4 + a_1) y_3^2.$$

There are two methods to solve the centre problems of system (6) at the Hopf point. The classical method which is called Lyapunov Centre Theorem (for more detail see (Bibikov, 1979)) and the inverse Jacobi multiplier is the modern method (for more detail on this method see (Berrone & Giacomini, 2003) and (Buica, et al., 2012)). The nonzero smooth function V is called inverse Jacobi multiplier of system (6), if it satisfies the following partial differential equation:

$$\chi(V) = V\, div(\chi), \tag{7}$$

where χ is a vector field associated to (6) and div refers to the divergence operator. Using inverse Jacobi multiplier, Buică, et al. (2012) solves the centre problem by the following theorem.

Theorem 1. System (6) has a centre at the origin if and only if it admits a local analytic inverse Jacobi multiplier of the form $V(y_1, y_2, y_3) = y_3 + \cdots$ in a neighborhood of the origin in $\mathbb{R}^3$. Moreover, when such V exists, the local analytic centre manifold, W^c, lies in $V^{-1}(0)$.

Remark 1. The Hopf critical point $u^* \in \mathbb{R}^3$ is a centre of system (2) if and only if there is an inverse Jacobi multiplier V at the Hopf point where $\nabla V(u^*) \neq 0$.

Mahdi (2013) has studied the center problem of system (2) which has quadratic nonlinearities. For the existence of a center, the necessary and sufficient conditions were found. In this article, the inverse Jacobi multiplier is used to find centre conditions on the centre manifold of system (2). Then, we perturbed the parameters to obtain a number of bifurcated periodic orbits.

The layout of the article is as follows. The sufficient conditions for the existence of a centre are studied in section one. The summery of the cyclicity technique is presented in section two. Section Three is devoted to apply the cyclicity technique to find number of periodic orbits bifurcating from centre for the third order differential equation. The conclusions are finally made. Throughout this paper, MAPLE software is used to verify calculations and also to plot figures.

1. CENTRE CONDITIONS

The primary purpose of this section is to present sufficient conditions for the existence of the Hopf bifurcation and the centre on the centre manifold in the three dimensional system (2). The Hopf critical point is called centre if there exists a neighborhood U of the point such that all orbits are periodic on it. Furthermore, if all the orbits have the same period, it is called isochronous center (Ameen, 2015).

Proposition 1. System (2) has a Hopf point at the origin if and only if the following conditions are satisfied:

$$\gamma = -\alpha\,\beta\ ,\ \alpha \neq 0 \text{ and } \beta < 0\,. \tag{8}$$

Proof: First, we shall prove the necessary conditions (8) and let the origin be a Hopf point. The characteristic equation of the Jacobian matrix of system (2) at the origin is given by

$$\lambda^3 - \alpha\,\lambda^2 - \beta\,\lambda - \gamma = 0\,. \tag{9}$$

If we compare the equation above with equation (3), the following values of T, K and D are obtained:

$$T = \alpha\ ,\ K = \beta \text{ and } D = \gamma. \tag{10}$$

Since the origin is a Hopf point, then the parameters in equation (10) satisfy equation (4):

$$TK + D = 0\ \Rightarrow\ \alpha\beta + \gamma = 0\ \Rightarrow\ \gamma = -\alpha\beta,$$
$$T \neq 0 \text{ and } K < 0\ \Rightarrow\ \alpha \neq 0 \text{ and } \beta < 0\,.$$

Therefore, the conditions are held.

Conversely: We shall prove sufficiency. Assume that $\gamma = -\alpha\beta$, $\alpha \neq 0$ and $\beta < 0$. Since $\beta < 0$, we can assume that $\beta = -\omega^2$. The Jacobian matrix of system (2) at the origin becomes

$$\begin{bmatrix} 0 & 1 & 0 \\ 0 & 0 & 1 \\ \gamma & -\omega^2 & \alpha \end{bmatrix}, \tag{11}$$

and its eigenvalues are $\lambda_{1,2} = \pm\omega i$ and $\lambda_3 = \alpha$. This means that the Jacobian matrix of system (2) at the origin has a pair of purely imaginary and a nonzero eigenvalues. Thus, the origin is a Hopf point. □

Now, we are looking for the inverse Jacobi multiplier function for system (2). The vector field of the system is denoted by χ :

$$\chi = \big(P_1(x,y,z), P_2(x,y,z), P_3(x,y,z)\big) \tag{12}$$

which is a quadratic vector field and we let V be an inverse Jacobi multiplier for system (2), which is defined by

$$V = \sum_{k=0}^{2}\sum_{j=0}^{k}\sum_{i=0}^{j} C_{(k-j,j-i,i)}\, x^{k-j}\, y^{j-i}\, z^{i}$$

$$= C_{2,0,0}x^2 + C_{1,1,0}\,xy + C_{1,0,1}\,xz + C_{0,2,0}y^2 + C_{0,1,1}\,yz$$

$$+ C_{0,0,2}z^2 + C_{1,0,0}x + C_{0,1,0}y + C_{0,0,1}z + C_{0,0,0}, \tag{13}$$

where $C_{i,j,k} \in \mathbb{R}\,, i,j,k = 0,1,2\,.$

Proposition 2. System (2) has an inverse Jacobi multiplier if and only if one of the following conditions are satisfied:

$$i.\,\tau_1 = \{a_1 = \omega^2\alpha(\omega^2 - 1), a_2 = a_3 = \alpha, a_4 = a_6 = 0, a_5 = 2\alpha(\omega^2 - 1)\},$$
$$ii.\,\tau_2 = \{a_1 = a_5\omega^2, a_2 = a_3 = 0, a_4 = \omega^2 a_6\},$$
$$iii.\,\tau_3 = \left\{a_1 = \tfrac{-1}{2}\,\alpha a_4\,, a_2 = a_3 = a_5 = a_6 = 0\right\},$$

$iv.\tau_4 = \{a_1 = -\alpha\omega^2, a_2 = \alpha, a_5 = -2\alpha,\ a_3 = a_4 = a_6 = 0\ \}$,
where $\omega = \sqrt{-\beta}$.

Proof. First, we shall prove that the conditions τ_1, τ_2, τ_3 and τ_4 are necessary. Assume that system (2) has an inverse Jacobi multiplier, V, which is defined in (13). Then it satisfies the following partial differential equation

$$\chi(V) = V\ \mathrm{div}(\chi),$$

where χ is a vector field of (2) which is defined in (12):

$$\begin{aligned}\chi(V) = \frac{\partial V}{\partial x}P_1(x,y,z) + \frac{\partial V}{\partial y}P_2(x,y,z) \\ + \frac{\partial V}{\partial z}P_3(x,y,z) \\ = (C_{1,0,1}z + C_{1,1,0}y + 2C_{2,0,0}x + C_{1,0,0})y \\ + (C_{0,1,1}z \\ +2C_{0,2,0}y + C_{1,1,0}x + C_{0,1,0})z \ + (2C_{0,0,2}z \\ + C_{0,1,1}y \\ +C_{1,0,1}x, +C_{0,0,1})(\alpha\, z + \beta\, y + \gamma\, x \\ + H(x\,, y\,, z))\end{aligned}$$

and

$$\begin{aligned}\mathrm{div}\,(\chi) = \frac{\partial P_1(x,y,z)}{\partial x} + \frac{\partial P_2(x,y,z)}{\partial y} \\ + \frac{\partial P_3(x,y,z)}{\partial z} \\ = \alpha + a_5 x + a_6 y + 2a_3 z\ .\end{aligned}$$

After solving $\chi(\mathrm{V}) - \mathrm{div}(\chi)\mathrm{V} = 0$, the set of solutions τ_1, τ_2, τ_3 and τ_4 can be obtained.

Conversely: We shall now prove sufficiency. Assume that condition τ_1 holds. Thus, we consider the vector field of system (2)

$$\chi = (y, z, \alpha\,\omega^2 x - \omega^2 y + \alpha\, z + \omega^2\alpha\,(\omega^2 - 1)x^2 \\ +2\alpha\,(\omega^2 - 1)\,xz + \alpha\, y^2 + \alpha\, z^2).$$

From

$$\chi(\mathrm{V}) = \mathrm{V}\,\mathrm{div}(\chi)\ ,$$

where

$$V = \sum_{k=0}^{2}\sum_{j=0}^{k}\sum_{i=0}^{j} C_{(k-j,j-i,i)}\ x^{k-j}\ y^{j-i}\ z^{i}$$

and $\mathrm{div}\chi = 2\alpha(\omega^2 - 1)\mathrm{x} + 2\alpha\,\mathrm{z} + \alpha$ is divergent of the vector field χ, the following function is obtained

$$V = \omega^2 x + z + (\omega^4 - \omega^2)x^2 + 2(\omega^2 - 1)xz \\ + y^2 + z^2$$

which is the inverse Jacobi multiplier of system (2).

Assume condition τ_2 holds. The vector field of system (2) becomes:

$$\chi = (y, z, \alpha\omega^2 x - \omega^2 y + \alpha z + \omega^2 a_5 x^2 + \omega^2 a_6 xy \\ + a_5 xz + a_6 yz)$$

from $\chi(\mathrm{V}) = \mathrm{V}\,\mathrm{div}\chi$, where V defined above and $\mathrm{div}\chi = \mathrm{a_5x} + \mathrm{a_6y} + \alpha$ is divergent of χ, the following inverse Jacobi multiplier is obtained

$$V = \omega^2 x + z. \tag{14}$$

Assume condition τ_3 holds. Then the vector field of system (2) is given by

$$\chi = (y, z, (\alpha z - \omega^2 y + \alpha\omega^2 x - \tfrac{1}{2}\alpha a_4 x + a_4 xy))$$

from $\chi(\mathrm{V}) = \mathrm{V}\,\mathrm{div}\chi$ where $div\chi = \alpha$ and V defined above, we obtain the following inverse Jacobi multiplier for system (2)

$$V = \omega^2 x + z - \tfrac{1}{2}a_4 x^2.$$

Assume condition τ_4 holds. Then, we consider the vector field of system (2)

$$\chi = (y, z, \alpha\omega^2 x - \omega^2 y + \alpha z - \alpha\,\omega^2 x^2 + \alpha\, y^2 \\ - 2\,\alpha\, xz)$$

from $\chi(\mathrm{V}) = \mathrm{V}\,\mathrm{div}\chi$ where $\mathrm{div}\chi = \alpha - 2\alpha x$ and V defined above, the following inverse Jacobi multiplier is obtained

$$V = \omega^2 x + z - \omega^2 x^2 - 2xz + y^2.$$

□

The inverse Jacobi multiplier is used to find sufficient conditions for a critical point to be a centre for the three dimensional system (2). The

explicit formula for the inverse Jacobi multiplier for system (2) is given by the following propositions.

Proposition 3. The Hopf critical point at the origin is center of system (2) if the parameters satisfy the following conditions

$i.\tau_1 = \{a_1 = \omega^2\alpha(\omega^2-1), a_2 = a_3 = \alpha, a_4 = a_6 = 0, a_5 = 2\alpha(\omega^2-1)\}$,

$ii.\tau_2 = \{a_1 = a_5\omega^2, a_2 = a_3 = 0, a_4 = \omega^2 a_6\}$

$iii.\tau_3 = \{a_1 = \frac{-1}{2}\alpha a_4, a_2 = a_3 = a_5 = a_6 = 0\}$

$iv.\tau_4 = \{a_1 = -\alpha\omega^2, a_2 = \alpha, a_5 = -2\alpha, a_3 = a_4 = a_6 = 0\}$.

Proof. It is easy to prove the above proposition by finding the inverse Jacobi multiplier corresponding to each set of conditions (Buica, et al., 2012). The inverse Jacobi multiplier corresponding to each set of conditions and passing through the origin are

- $V = \omega^2 x + z + (\omega^4 - \omega^2)x^2 + 2(\omega^2 - 1)xz + y^2 + z^2$ Corresponding to τ_1 (see Figure 1 (a)),
- $V = \omega^2 x + z$ Corresponding to τ_2 (see Figure 2 (a)),
- $V = \omega^2 x + z - \frac{1}{2}a_4 x^2$ Corresponding to τ_3 (see Figure 2 (b)),
- $V = \omega^2 x + z - \omega^2 x^2 - 2xz + y^2$ Corresponding to τ_4 (see Figure 1 (b)).

Since $\nabla V(0,0,0) = \omega^2 + 1 \neq 0$ for each case, then Theorem 1 indicates that the Hopf critical point at the origin is a centre.

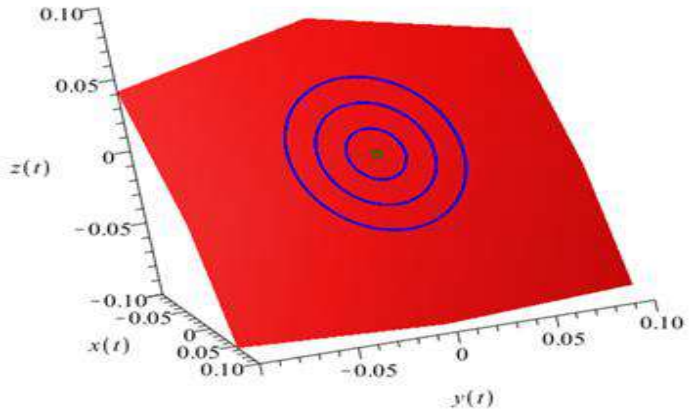

Figure 1. (a): Phase portrait of system (2) satisfying conditions τ_1 , $\omega = a_3 = 1$, with initial points (0.01, 0.01, -0.0102), (0.02, 0.02, -0.0208), (0.03, 0. 03, -0.0318). The green point is the critical point and the red plane is the inverse Jacobi multiplier $V(x,y,z) = (\omega^4 - \omega^2)x^2 + 2(\omega^2 - 1)xz + y^2 + z^2 + \omega^2 x + z$.

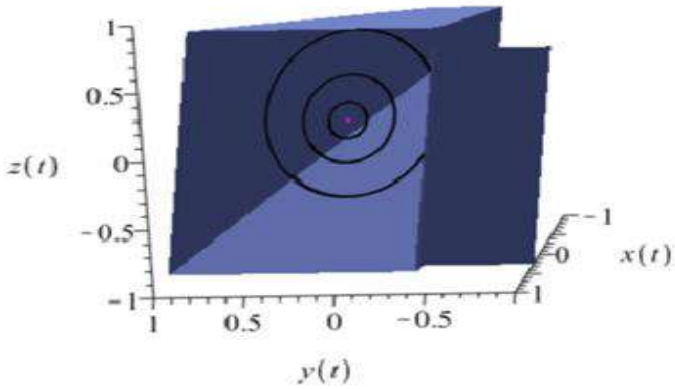

(b) Phase portrait of system (2) satisfying conditions τ_3 , $\omega = a_4 = \alpha = 1$, with initial points (0.01, 0.01, -0.00995), (0.02, 0.02, -0.0198), (0.03, 0. 03, -0.02955). The magenta point is the critical point and the Niagara Azure plane is the inverse Jacobi multiplier $V(x,y,z) = -\frac{1}{2}a_4 x^2 + \omega^2 x + z$.

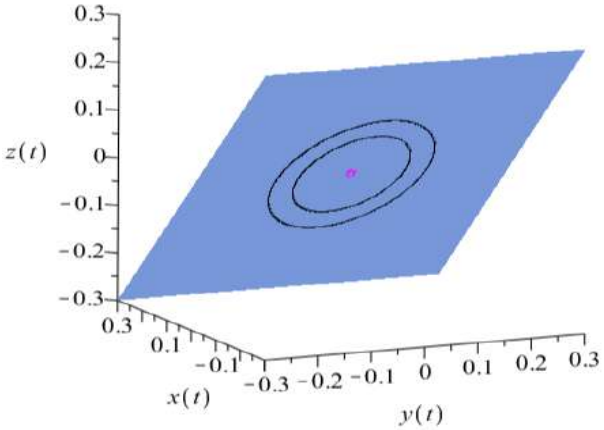

Figure 2. (a): Phase portrait of system (2) satisfying conditions τ_2 , $\omega = a_5 = a_6 = \alpha = 1$, with initial points (0, 0.1, 0), (0.1, 0.1, -0.1). The magenta point is the critical point and the Niagara Azure plane is the inverse Jacobi multiplier $V(x,y,z) = \omega^2 x + z$.

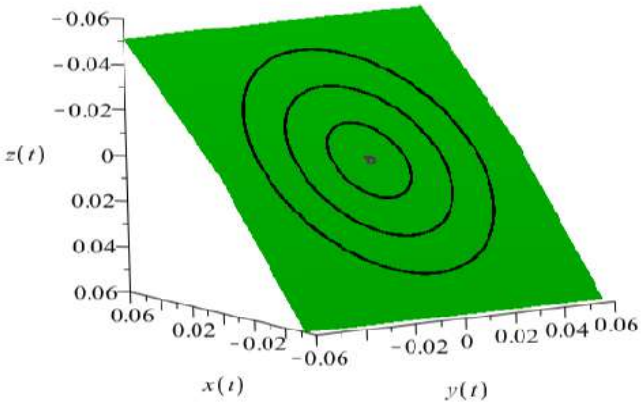

(b) Phase portrait of system (2) satisfying conditions τ_4 , $\omega = a_5 = 1$, with initial points (0., 0.1, 0), (0.1, 0.2, -0.125), 0.2, 0. 3, -0.3333333333). The magenta point is the critical point and the Niagara Azure plane is the inverse Jacobi multiplier $V(x,y,z) = -\omega^2 x^2 + y^2 - 2xz + \omega^2 x + z$.

2. A CYCLICITY TECHNIQUE IN $\mathbb{R}^3$

In the bifurcation theory, one of the contemporary research areas is the bifurcation of limit cycles from centre. They are obtained by perturbing a focus or centre. Here, we consider system (6), the set of all parameters in $G(y_1, y_2, y_3)$ and the corresponding parameter space is denoted by Λ and $\boldsymbol{K}$, respectively.

In two dimensional systems, for the first time Christopher (2005) has explored a useful technique for examining the cyclicity bifurcating from the centre by linearizing the Liapunov quantities (Christopher, 2005). Salih (2015) has generalized the technique to three dimensional systems to examine the cyclicity bifurcating from centres (Salih, 2015). In addition, Salih and Hasso, have used the same technique to study the bifurcated periodic orbits in a three dimensional system and the L$\ddot{u}$ system (Salih & Hasso, 2017). We summarize the technique which is used to estimate the cyclicity in three dimensional system as follows.

1. A point will be selected for a centre variety.
2. We linearize the Liapunov quantities around this point.
3. We check the codimension of the point. If the codimension of the point be r where the first r linear terms of Liapunov quantities are linearly independent, then $r-1$ limit cycles can be bifurcated by small perturbation.

Composing the Liapunov function and finding its Liapunov quantities is a way to determine the number and stability of the limit cycles. In this method, we define a function of the form

$$F(x,y,z) = y_1^2 + y_2^2 + \sum_{k=3}^{\infty} F_k(y_1, y_2, y_3), \qquad (15)$$

where

$$F_k = \sum_{i=0}^{k} \sum_{j=0}^{j} C_{(k-i,i-j,j)} y_1^{k-i}\, y_2^{i-j} y_3^{j}.$$

For system (6) and the coefficients of F_k satisfy

$$\chi(F) = L_1(y_1^2 + y_2^2) + L_2(y_1^2 + y_2^2)^2 + L_3(y_1^2 + y_2^2)^3 + \cdots, \qquad (16)$$

where $L_i, i = 1,2,\ldots$ are polynomials and the L_i is the i^{th} Liapunov constant. We assume that $0 \in K$ corresponds to the centre of system (6). Using a perturbation technique, the following are obtained

$$\chi = \chi_o + \chi_1 + \cdots, \quad F = F_o + F_1 + \cdots, \quad L_i = L_{io} + L_{i1} + \cdots, \quad i = 1,2,\ldots, \qquad (17)$$

where χ_o, F_o and L_{io} are calculated at the unperturbed terms and χ_1, F_1 and L_{1i} are obtained at the perturbed terms of first order (the terms of degree one in Λ), and so forth. Both the Liapunov function F_i and the Liapunov quantity L_i have same degree in parameters which is i. Substituting equation (17) into equation (16), the following equations are obtained

$$\chi_o F_o = 0,$$
$$\chi_o F_1 + \chi_1 F_o = L_{11}(y_1^2 + y_2^2) + L_{21}(y_1^2 + y_2^2)^2 + \cdots \qquad (18)$$

and more general,

$$\chi_o F_i + \cdots + \chi_i F_o = L_{1i}(y_1^2 + y_2^2) + L_{2i}(y_1^2 + y_2^2)^2 + \cdots \qquad (19)$$

Solving the pair equations (18) simultaneously, the linear terms of the Liapunov quantities L_k (modulo the $L_i, i < k$) will be obtained. To obtain the higher order terms of the Liapunov quantities, equation (19) is used.

3. CENTRE BIFURCATION FOR SYSTEM (2)

In this section, the technique which is presented in the previous section is applied to examine the cyclicity bifurcating from the center at the origin of system (2) where the parameters fulfill the

conditions in Proposition 3. The main outcome of this section are the theorems below.

Theorem 2. Four limit cycles can bifurcate from the critical point at the origin when the parameters in system (2) satisfy conditions τ_1 or τ_4 of Proposition 3, proved that $\omega \geq 1$.

Proof. When condition τ_1 hold, system (2) reduces to

$$\dot{x} = y,$$
$$\dot{y} = z,$$
(20)
$$\dot{z} = \alpha\omega^2 x - \omega^2 y + \alpha z + \omega^2\alpha(\omega^2 - 1)x^2 + \alpha y^2 + \alpha z^2 + 2\alpha(\omega^2 - 1)xz,$$

and the transformed system (6) is obtained where

$$G(y_1, y_2, y_3) = -\frac{\alpha^2\omega {y_1}^2}{\alpha^2+\omega^2} - 2\frac{\alpha y_1 y_3}{\alpha^2+\omega^2} - \frac{\alpha^2\omega {y_2}^2}{\alpha^2+\omega^2} + 2\frac{\alpha^2 y_2 y_3}{\omega(\alpha^2+\omega^2)} - \frac{(\alpha^2+\omega^2-1){y_3}^2}{\alpha^2\omega}$$.
(21)

It is easy to define the Liapunov function of F_o of equation (6) which it satisfies $\chi_o F_o = 0$:

$$\chi_o = \left(-\omega y_2 + G(y_1, y_2, y_3), \omega y_1 + \frac{\omega}{\alpha}G(y_1, y_2, y_3), \alpha y_3 - \alpha\omega G(y_1, y_2, y_3)\right),$$

where $G(y_1, y_2, y_3)$ is defined in (21) and

$$F_o = {y_1}^2 + {y_2}^2 + \sum_{k=3}^{N}\sum_{j=0}^{k}\sum_{i=0}^{j} C_{(k-j,j-i,i)}\, {y_1}^{k-j} {y_2}^{j-i} {y_3}^{i}$$

We choose a point from center variety,
$(a_1, a_2, a_3, a_4, a_5, a_6, \alpha, \beta, \gamma) = (\omega^2(\omega^2 - 1), 1, 1, 0, 2(\omega^2 - 1), 0, 1, -\omega^2, \omega^2)$
and we let
$a_1 = \omega^2(\omega^2 - 1) + \epsilon_1$, $a_2 = 1 + \epsilon_2$, $a_3 = 1 + \epsilon_3$, $a_4 = 0 + \epsilon_4$, $a_5 = 2(\omega^2 - 1) + \epsilon_5$, $a_6 = 0 + \epsilon_6$, $\alpha = 1 + \epsilon_7$, $\beta = -\omega^2 + \epsilon_8$, $\gamma = \omega^2 + \epsilon_9$,
where $\epsilon_1, \epsilon_2, \epsilon_3, \epsilon_4, \epsilon_5, \epsilon_6, \epsilon_7, \epsilon_8$ and ϵ_9 are parameters after perturbation in the system.

Transformation (5) is also used for perturbed part of vector field of system (6). Using MAPLE software and solving equation (18), the following linear independent terms of Liapunov quantities are obtained:

1. $L_1 = \frac{1}{\omega^2+1}(\omega^2\epsilon_7 - \epsilon_8 - \epsilon_9)$

2. $L_2 = \frac{-1}{4\omega^6+9\omega^4+6\omega^2+1}(3\,\omega^6\epsilon_3 + 4\,\omega^6\epsilon_5 + 2\omega^6\epsilon_6 - 16\,\omega^6\epsilon_7 - 8\omega^6\epsilon_8 - 8\omega^4\epsilon_1 - 3\omega^4\epsilon_2 + 3\omega^4\epsilon_3 - 6\omega^4\epsilon_4 + 2\omega^4\epsilon_5 + \omega^4\epsilon_6 + 26\omega^4\epsilon_7 + 14\omega^4\epsilon_8 + 16\omega^4\epsilon_9 - 7\omega^2\epsilon_1 - 3\omega^2\epsilon_2 - 6\omega^2\epsilon_4 - 2\omega^2\epsilon_5 - \omega^2\epsilon_6 + 9\omega^2\epsilon_7 - 21\omega^2\epsilon_8 - 26\omega^2\epsilon_9 + \epsilon_1 - 10\epsilon_8 - 9\epsilon_9)$,

3. $L_3 = \frac{1}{(16\omega^2+1)(9\omega^2+1)(\omega^2+4)(4\omega^2+1)^2(\omega^2+1)^4}\big((3456\epsilon_3 - 2304\epsilon_5 + 4608\epsilon_8)\omega^{20} + (4608\epsilon_1 - 3456\epsilon_2 + 13560\epsilon_3 - 2304\epsilon_4 - 28048\epsilon_5 - 8064\epsilon_6 + 32256\epsilon_7 + 44576\epsilon_8)\omega^{18} + (-32256\epsilon_9 + 52640\epsilon_1 - 13560\epsilon_2 + 994\epsilon_3 + 1904\epsilon_4 - 78976\epsilon_5 - 36344\epsilon_6 + 125408\epsilon_7 + 45936\epsilon_8)\omega^{16} + (-125408\epsilon_9 + 144392\epsilon_1 - 994\epsilon_2 + 36522\epsilon_3 + 43824\epsilon_4 + 29685\epsilon_5 + 2752\epsilon_6 - 251808\epsilon_7 - 331158\epsilon_8)\omega^{14} + (251808\epsilon_9 - 60364\epsilon_1 - 36522\epsilon_2 + 146634\epsilon_3 - 66261\epsilon_4 + 207565\epsilon_5 + 92376\epsilon_6 - 214784\epsilon_7 - 176002\epsilon_8)\omega^{12} + (214784\epsilon_9 - 451652\epsilon_1 - 146634\epsilon_2 + 145406\epsilon_3 - 326072\epsilon_4 + 114886\epsilon_5 + 62042\epsilon_6 + 878586\epsilon_7 + 143396\epsilon_8)\omega^{10} + (-878586\epsilon_9 - 376406\epsilon_1 - 145406\epsilon_2 + 49356\epsilon_3 - 310350\epsilon_4 - 34566\epsilon_5 - 10210\epsilon_6 + 741694\epsilon_7 - 723860\epsilon_8)\omega^8 +$

$(-741694\epsilon_9 - 76274\epsilon_1 - 49356\epsilon_2 + 5112\epsilon_3 - 99372\epsilon_4 - 28015\epsilon_5 - 12474\epsilon_6 + 207298\epsilon_7 - 708102\epsilon_8)\omega^6 + (-207298\epsilon_9 + 6674\epsilon_1 - 5112\epsilon_2 + 160\epsilon_3 - 9493\epsilon_4 - 3319\epsilon_5 - 1622\epsilon_6 + 20182\epsilon_7 - 217558\epsilon_8)\omega^4 + (-20182\epsilon_9 + 1526\epsilon_1 - 160\epsilon_2 - 276\epsilon_4 - 108\epsilon_5 - 56\epsilon_6 + 568\epsilon_7 - 21812\epsilon_8)\omega^2 - 568\epsilon_9 + 56\epsilon_1 - 624\epsilon_8)$,

4. $L_4 = \frac{F}{G(\omega)}$, where
   - F is a polynomial of $\epsilon_1, \epsilon_2, \epsilon_3, \epsilon_4, \epsilon_5, \epsilon_6, \epsilon_7, \epsilon_8, \epsilon_9$ and ω which has 192 different monomials.
   - $G(\omega)$ is an even polynomial of degree 40 which has 21 different monomials.
5. $L_5 = \frac{F}{G(\omega)}$, where
   - F is a polynomial of $\epsilon_1, \epsilon_2, \epsilon_3, \epsilon_4, \epsilon_5, \epsilon_6, \epsilon_7, \epsilon_8, \epsilon_9$ and ω which has 336 different monomials.
   - $G(\omega)$ is an even polynomial of degree 70 which has 36 different monomials.

The origin critical point of system (2) is weak focus of order 4 if and only if

1. $\epsilon_7 = \frac{1}{\omega^2}(\epsilon_8 + \epsilon_9)$,
2. $\epsilon_1 = \frac{1}{8\,\omega^2-1}(\,3\omega^4\epsilon_3 + 4\omega^5\epsilon_5 + 2\omega^4\epsilon_6 - 4\omega^4\epsilon_8 - 3\omega^2\epsilon_2 - 6\omega^2\epsilon_4 - 2\omega^2\epsilon_5 - \omega^2\epsilon_6 + 6\omega^2\epsilon_8 - \epsilon_8\,)$,
3. $\epsilon_2 = \frac{1}{2(324\omega^6-315\omega^4+70\omega^2+1)}\,(648\omega^8\,\epsilon_3 + 144\omega^8\,\epsilon_6 - 630\omega^6\,\epsilon_3 - 720\omega^6\,\epsilon_4 - 324\omega^6\,\epsilon_5 - 488\omega^6\,\epsilon_6 - 648\omega^6\,\epsilon_8 + 140\omega^4\,\epsilon_3 + 604\omega^4\,\epsilon_4 + 315\omega^4\,\epsilon_5 + 364\omega^4\,\epsilon_6 + 630\omega^4\,\epsilon_8 + 2\omega^2\,\epsilon_3 - 119\omega^2\,\epsilon_4 - 70\omega^2\,\epsilon_5 - 60\omega^2\,\epsilon_6 - 140\omega^8\,\epsilon_8 - 15\,\epsilon_4 - \epsilon_5 - 2\,\epsilon_8\,)$
4. $\epsilon_4 = \frac{2(31104\omega^{14}+3218\omega^{12}-216174\omega^{10}+250611\omega^8-116161\omega^6+20813\omega^4-959\omega^2+82)\omega^2\epsilon_6}{311040\omega^{14}-984528\omega^{12}+1188420\omega^{10}-680538\omega^8+188699\omega^6-24554\omega^4+1526\omega^2-15}$

Since

$$\begin{vmatrix} \frac{\partial L_1}{\partial\,\epsilon_7} & \frac{\partial L_1}{\partial\,\epsilon_1} & \frac{\partial L_1}{\partial\,\epsilon_2} & \frac{\partial L_1}{\partial\,\epsilon_4} \\ \frac{\partial L_2}{\partial\,\epsilon_7} & \frac{\partial L_2}{\partial\,\epsilon_1} & \frac{\partial L_2}{\partial\,\epsilon_2} & \frac{\partial L_2}{\partial\,\epsilon_4} \\ \frac{\partial L_3}{\partial\,\epsilon_7} & \frac{\partial L_3}{\partial\,\epsilon_1} & \frac{\partial L_3}{\partial\,\epsilon_2} & \frac{\partial L_3}{\partial\,\epsilon_4} \\ \frac{\partial L_4}{\partial\,\epsilon_7} & \frac{\partial L_4}{\partial\,\epsilon_1} & \frac{\partial L_4}{\partial\,\epsilon_2} & \frac{\partial L_4}{\partial\,\epsilon_4} \end{vmatrix}$$

$$= \frac{2\omega^6}{(\omega^2+1)^4(4\omega^2+1)^3(9\omega^2+1)^2(16\omega^2+1)}(311040\omega^{14} - 984528\omega^{12} + 1188420\omega^{10} - 680538\omega^8 + 188699\omega^6 - 24554\omega^4 + 1526\omega^2 - 15)$$

and is not equal to zero, then by perturbing the coefficients of Liapunov quantities, in the neighborhood of the critical point, four limit cycles can be bifurcated from the critical point at the origin of system (2).

Remark 2. By the same way, four limit cycles can be bifurcated from the origin of system (2) when the parameters satisfy condition τ_4 of Proposition 3.

Theorem 3. Three limit cycles can bifurcate from the critical point at the origin when the parameters in system (2) satisfy the conditions τ_2 or τ_3 of Proposition 3.

Proof. We suppose that parameters satisfy condition τ_2 of Proposition 3. When condition τ_2 holds, system (2) reduces to

$$\dot{x} = y$$
$$\dot{y} = z$$
(22)
$$\dot{z} = -\alpha\omega^2 x + \omega^2 y + \alpha z + a_5\omega^2 x^2 + \omega^2 a_6 xy + a_5 xz + a_6 yz,$$

and the transformed system (6) is obtained where

$$G(y_1, y_2, y_3) = -\frac{a_6}{\alpha} y_1 y_3 - \frac{a_5}{\alpha\omega} y_2 y_3 - \frac{(\alpha a_6 + a_5)}{\alpha^3 \omega} y_3^2 \quad (23)$$

It is easy to define the Liapunov function of F_o of system (6) which satisfies $\chi_o F_o = 0$:

$$\chi_o = (-\omega y_2 + G(y_1, y_2, y_3), \omega y_1 + \frac{\omega}{\alpha} G(y_1, y_2, y_3), \alpha y_3 - \alpha\omega G(y_1, y_2, y_3)),$$

where $G(y_1, y_2, y_3)$ is defined in (23) and

$$F_o = {y_1}^2 + {y_2}^2 + \sum_{k=3}^{N} \sum_{j=0}^{k} \sum_{i=0}^{j} C_{(k-j,j-i,i)} {y_1}^{k-j} {y_2}^{j-i} {y_3}^i.$$

We choose a point from center variety

$$(a_1, a_2, a_3, a_4, a_5, a_6, \alpha, \beta, \gamma) = (\omega^2, 0, 0, \omega^2, 1, 1, 1, -\omega^2, \omega^2)$$

We let
$a_1 = \omega^2 + \epsilon_1,\ a_2 = 0 + \epsilon_2,\ a_3 = 0 + \epsilon_3,$
$a_4 = \omega^2 + \epsilon_4,\ a_5 = 1 + \epsilon_5, a_6 = 1 + \epsilon_6,$
$\alpha = 1 + \epsilon_7,\ \beta = -\omega^2 + \epsilon_8,\ \gamma = \omega^2 + \epsilon_9,$

where $\epsilon_1, \epsilon_2, \epsilon_3, \epsilon_4, \epsilon_5, \epsilon_6, \epsilon_7, \epsilon_8$and ϵ_9 are parameters after perturbation in the system. Transformation (5) is also used for perturbed part of vector field of system (6). Using MAPLE software and solving equation (18), the following linear independent terms of Liapunov quantities are obtained:

1. $L_1 = \frac{1}{\omega^2+1}(\omega^2\epsilon_7 - \epsilon_8 - \epsilon_9)$,
2. $L_2 = \frac{1}{4(4\omega^4+5\omega^2+1)}(18\,\omega^6\epsilon_3 + 14\omega^4\epsilon_2 + 6\omega^4\epsilon_3 - 18\omega^4\epsilon_5 - \omega^4\epsilon_6 + 14\omega^4\epsilon_7 + 18\,\omega^2\epsilon_1 + 2\omega^2\epsilon_2 + \omega^2\epsilon_4 - 6\omega^2\epsilon_5 - \omega^2\epsilon_6 + 8\omega^2\epsilon_7 + 5\omega^2\epsilon_8 - 14\omega^2\epsilon_9 + 6\epsilon_1 + \epsilon_4 - \epsilon_8 - 8\epsilon_9)$,
3. $L_3 = \frac{1}{8(36\omega^6+49\omega^4+14\omega^2+1)}(111\,\omega^8\epsilon_3 + 51\,\omega^6\epsilon_2 + 112\omega^6\epsilon_3 - 111\,\omega^6\epsilon_5 + 29\omega^6\epsilon_6 + 51\omega^6\epsilon_7 + 111\omega^4\epsilon_1 + 68\omega^4\epsilon_2 + 17\omega^4\epsilon_3 - 29\omega^4\epsilon_4 - 112\omega^4\epsilon_5 + 12\omega^4\epsilon_6 + 70\omega^4\epsilon_7 + 31\omega^4\epsilon_8 - 51\omega^4\epsilon_9 + 112\omega^2\epsilon_1 + \omega^2\epsilon_2 - 12\omega^2\epsilon_4 - 17\omega^2\epsilon_5 - \omega^2\epsilon_6 + 19\omega^2\epsilon_7 + 30\omega^2\epsilon_8 - 70\omega^2\epsilon_9 + 17\epsilon_1 + \epsilon_4 - \epsilon_8 - 19\epsilon_9)$,
4. $L_4 = \frac{5}{64(576\omega^6+244\omega^4+29\omega^2+1)}(388\,\omega^8\epsilon_3 + 124\,\omega^6\epsilon_2 + 300\omega^6\epsilon_3 - 388\,\omega^6\epsilon_5 + 175\omega^6\epsilon_6 + 124\omega^6\epsilon_7 + 388\omega^4\epsilon_1 + 244\omega^4\epsilon_2 + 32\omega^4\epsilon_3 - 175\omega^4\epsilon_4 - 300\omega^4\epsilon_5 + 54\omega^4\epsilon_6 + 158\omega^4\epsilon_7 + 89\omega^4\epsilon_8 - 124\omega^4\epsilon_9 + 300\omega^2\epsilon_1 - 54\omega^2\epsilon_4 - 32\omega^2\epsilon_5 - \omega^2\epsilon_6 + 34\omega^2\epsilon_7 + 88\omega^2\epsilon_8 - 158\omega^2\epsilon_9 + 32\epsilon_1 + \epsilon_4 - \epsilon_8 - 34\epsilon_9))$.

The origin critical point of system (2) is weak focus of order 3 if and only if

1. $\epsilon_7 = \frac{1}{\omega^2}(\epsilon_8 + \epsilon_9)$,

2. $\epsilon_1 = \frac{-1}{6(3\omega^2+1)}\ (18\omega^6\epsilon_3 + 14\omega^4\epsilon_2 + 6\omega^4\epsilon_3 - 18\omega^4\epsilon_5 - \omega^4\epsilon_6 + 2\omega^2\epsilon_2 + \omega^2\epsilon_4 - 6\omega^2\epsilon_5 - \omega^2\epsilon_6 + 19\omega^2\epsilon_8 + \epsilon_4 + 7\epsilon_8)$,
3. $\epsilon_2 = \frac{1}{4\omega^2(159\omega^6+65\omega^4+9\omega^2+7)}\ (633\omega^8\epsilon_6 - 633\omega^6\epsilon_4 + 613\omega^6\epsilon_6 - 633\omega^6\epsilon_8 - 613\omega^4\epsilon_4 + 183\omega^4\epsilon_6 - 613\omega^4\epsilon_8 - 183\omega^2\epsilon_4 + 11\omega^2\epsilon_6 - 183\omega^2\epsilon_8 - 11\epsilon_4 - 11\epsilon_8\ )$.

Since

$$\begin{vmatrix} \frac{\partial L_1}{\partial\ \epsilon_7} & \frac{\partial L_1}{\partial\ \epsilon_1} & \frac{\partial L_1}{\partial\ \epsilon_2} \\ \frac{\partial L_2}{\partial\ \epsilon_7} & \frac{\partial L_2}{\partial\ \epsilon_1} & \frac{\partial L_2}{\partial\ \epsilon_2} \\ \frac{\partial L_1}{\partial\ \epsilon_7} & \frac{\partial L_1}{\partial\ \epsilon_1} & \frac{\partial L_1}{\partial\ \epsilon_2} \end{vmatrix} = \frac{-\omega^4(159\omega^5 + 65\omega^4 + 9\omega^2 + 7)}{8(\omega^2+1)(4\omega^4+5\omega^2+1)(36\omega^6+49\omega^4+14\omega^2+1)}$$

and it is not equal to zero, then by perturbing the coefficients of Liapunov quantities, in the neighborhood of the critical point, three limit cycles can be bifurcated from the critical point at the origin of system (2).

Remark 3. By the same way, three limit cycles can be bifurcated from the origin of system (2) when the parameters satisfy condition τ_3 of Proposition 3.

4. CONCLUSIONS

The centre bifurcation of a third order differential equation (1) is studied by using a simple technique to estimate the cyclisity bifurcating from centre (see (Salih, 2015) and (Salih & Hasso, 2017)). Four sets of sufficient condition of parameters for the existence of a centre are obtained. When we perturbed the parameters, by taking the linear parts of the corresponding Liapunov quantities of the perturbed system, a number of bifurcated periodic orbits have appeared. As a result, four limit cycles can be bifurcated from two sets of condition and three limit cycles from the other two sets of condition.

REFERENCES

Ameen, A. I., 2015. Computing Isochronous Center Conditions for Polynomial Differential Systems. ZANCO Journal of Pure and Applied Sciences, 27(1), pp. 41--50.

Ameen, A. I., Salih, R. H. & Aziz, W., 2009. Hopf Bifurcation Analysis for Stablity Nontrivial Critical Points of the Rössler's Second System. Journal of Koya University, Volume 12, pp. 77-95.

Berrone, L. R. & Giacomini, H., 2003. Inverse Jacobi multipliers. Rendiconti del Circolo Matematico di Palermo, 52(1), pp. 77-130.

Bibikov, Y. N., 1979. Local Theory of Nonlinear Analytic Ordinary Differential Equations. s.l.:Springer.

Buică, A., Garc´ıa, I. & Maza, S., 2012. Existence of inverse Jacobi multipliers around Hopf points in Emphasis on the center problem. Journal of Differential Equation, pp. 6324- 6336.

Christopher, C., 2005. Estimating Limit Cycle Bifurcations from Centers. Differential Equation with symbolic computation, pp. 23-35.

Mahdi, A., 2013. Center problem for third-order ODEs. International Journal of Bifurcation and Chaos, Volume 23, p. 1350078.

Mahdi, A., Pessoa, C. & Hauenstein, . J., 2017. A hybrid symbolic-numerical approach to the center-focus problem. Journal of Symbolic Computation, Volume 82, pp. 57--73.

Salih, R. H., 2009. Studying the Stability of Origin Point for the Rossler's Second System. Journal of Koya University, Volume 10, pp. 29-44.

Salih, R. H., 2015. HOPF BIFURCATION AND CENTRE BIFURCATION IN THREE DIMENSIONAL LOTKA-VOLTERRA SYSTEMS. s.l.:PhD thesis, Plymouth University.

Salih, R. H., 2017. Zero-Hopf Bifurcation in the Rössler's Second System. ZANCO Journal of Pure and Applied Sciences, 29(5), pp. 66-75.

Salih, R. H. & Ameen, A. I., 2008. Limit Cycles of Lorenz System With Hopf Bifurcation. AL-Rafidain Journal of Computer Sciences and Mathematics, pp. 81-99.

Salih, R. H. & Hasso, M. S., 2017. Centre bifurcations of periodic orbits for some special three dimensional systems. Electronic Journal of Qualitative Theory of Differential Equations, Issue 19, pp. 1-10.

ZANCO Journal of Pure and Applied Sciences
The official scientific journal of Salahaddin University-Erbil
https://zancojournals.su.edu.krd/index.php/JPAS

ISSN (print):2218-0230**, ISSN (online):** 2412-3986**, DOI: http://dx.doi.org/10.21271/zjpas**

RESEARCH PAPER

Determination of the Astrophysical S-factor and Thermonuclear Reaction Rates of the (α,n) Medium Elements Reactions

Mohammed Issa Hussein[1] and Ramadhan Hayder Abdullah[2]

[1&2]Department of Physics, College of Science, Salahaddin University-Erbil, Kurdistan Region, Iraq

A B S T R A C T:

Cross-sections of the (α,n) medium elements reactions as a function of energies of alpha (α)-particle such as $^{45}Sc(\alpha,n)^{48}V$, $^{48}Ti(\alpha,n)^{51}Cr$, $^{51}V(\alpha,n)^{54}Mn$, $^{50}Cr(\alpha,n)^{53}Fe$, $^{55}Mn(\alpha,n)^{58}Co$, $^{54}Fe(\alpha,n)^{57}Ni$, $^{59}Co(\alpha,n)^{62}Cu$, $^{62}Ni(\alpha,n)^{65}Zn$, $^{63}Cu(\alpha,n)^{66}Ga$, and $^{66}Zn(\alpha,n)^{69}Ge$ have been interpolated from threshold to 10 MeV in step of 0.05 MeV by using the Program of MATLAB. Weighted averages of the Cross-sections in (mb) have been utilized to calculate the astrophysical S-factor and thermonuclear reaction rates as a function of the energy of the center of mass, $E_{c.m.}$ and T_9 Which is the temperature in units of $10^9 K$ ($T_9 = 10^{-9}T$)

respectively. Polynomial relationships have been utilized to fit the computed astrophysical S-factor and thermonuclear reaction rates to determine the astrophysical S-factor at various $E_{c.m.}$ and thermonuclear reaction rates at various T_9 from best fitting equations with the minimum Chi-Square. Empirical formulae of set of reactions $^{45}Sc(\alpha,n)^{48}V$, $^{48}Ti(\alpha,n)^{51}Cr$, $^{51}V(\alpha,n)^{54}Mn$, $^{55}Mn(\alpha,n)^{58}Co$, $^{59}Co(\alpha,n)^{62}Cu$, and $^{45}Sc(\alpha,n)^{48}V$, $^{48}Ti(\alpha,n)^{51}Cr$, $^{51}V(\alpha,n)^{54}Mn$, $^{55}Mn(\alpha,n)^{58}Co$, $^{62}Ni(\alpha,n)^{65}Zn$, $^{66}Zn(\alpha,n)^{69}Ge$ have been utilized to compute astrophysical S-factor as a function of $E_{c.m.}$ and Z and thermonuclear reaction rates as a function of T_9 and the target nucleus atomic number Z. The results have been compared with the embraced astrophysical S-factor and thermonuclear reaction rates that have been calculated from the fitting equations which have a good agreement.

KEY WORDS: Cross-sections; astrophysical S-factor; thermonuclear reaction rates; Gamow factor; Gamow energy; Sommerfeld parameter.
DOI: http://dx.doi.org/10.21271/ZJPAS.32.2.8
ZJPAS (2020) , 32(2);72-86 .

INTRODUCTION :

The astrophysical S-factor, S(E), has covered a large area which used in the field to remove the energy dependence of the Coulomb barrier penetration from the cross-section, $\sigma(E)$ (Jose, 2016). As stellar energies are much lower than the Coulomb barrier, the cross sections hardly depend on energy (Descouvemont, 2011).

Thermonuclear reactions play an important role in supplying the major source of energy in stars in particular during hydrogen burning. This burning process in the stellar interiors consists of the proton-proton (pp) chain and the carbon-nitrogen-oxygen (CNO) cycle (Abdul Aziz, 2008). The quantity of interest in computing thermonuclear reaction rates for astrophysical aims is $N_A<\sigma v>$, which is the product of Avogadro's number with the average value of the cross section times velocity, averaged over a Maxwell-Boltzmann distribution of temperature (Roughton *et al.*, 1983). Total Cross-sections of

* **Corresponding Author:**
Mohammed Issa Hussein
E-mail: m_issa76@yahoo.com
Article History:
Received: 30/09/2019
Accepted: 03/11/2019
Published: 22/04 /2020

the (α,n) medium element reactions, that is a function of center of mass energy, have been calculated by a few authors, which are reminded by various references such as ^{45}Sc(α,n)^{48}V(Vlieks, Morgan and Blatt, 1974; Hansper *et al.*, 1989; Haider, 2012) , ^{48}Ti(α,n)^{51}Cr(Chang *et al.*, 1973; Vonach, Haight and Winkler, 1983; Levkovski, 1991; Morton *et al.*, 1992; Baglin, Coral *et al.*, 2004), ^{51}V(α,n)^{54}Mn (Levkovski, 1991; Hansper *et al.*, 1993; Sonzogni *et al.*, 1993; Peng, He and Long, 1999; Noori, 2008; Haider, 2012), ^{50}Cr(α,n)^{53}Fe(Vlieks, Morgan and Blatt, 1974; Morton *et al.*, 1994; Haider, 2012) , ^{55}Mn(α,n)^{58}Co(Rizvi *et al.*, 1989; Levkovski, 1991; Tims *et al.*, 1993; Haider, 2012) , ^{54}Fe(α,n)^{57}Ni (Houck and Miller, 1961; Vlieks, Morgan and Blatt, 1974; Tims *et al.*, 1991; Haider, 2012) , ^{59}Co(α,n)^{62}Cu(Stelson and McGowan, 1964; D`auria *et al.*, 1968; Zhukova *et al.*, 1972; Tims *et al.*, 1988; Noori, 2008) , ^{62}Ni(α,n)^{65}Zn (Stelson and McGowan, 1964; Levkovski, 1991; Haider, 2012) , ^{63}Cu(α,n)^{66}Ga(Stelson and McGowan, 1964; Zhukova *et al.*, 1970; Haider, 2012) , and ^{66}Zn(α,n)^{69}Ge(Stelson and McGowan, 1964; Levkovski, 1991) respectively. The goal of this work is to determine the empirical formulae to compute the astrophysical S-factor, S(E), and thermonuclear reaction rates, $N_A\langle\sigma v\rangle$, utilizing the altered cross- sections of the reactions of the medium elements. The outcomes were compared with those published in the previous work.

2. Theory

Atomic masses of each medium element and isotopes related to this present work have been taken from the nuclear wallet cards published by the National Nuclear Data Center (NNDC) (Tuli, 2011). The Q-Value of the reaction $X(\alpha,n)Y$, is defined as the difference between the initial and the final rest mass energies (Meyerhof, 1967):

$$Q = [M_\alpha + M_X - (M_Y + M_n]c^2 \qquad (1)$$

Where (M_α , M_X , M_Y , *and* M_n) are the atomic masses of the incident, target particles, product nucleus and neutron (outgoing particle), respectively and (c^2 = 931.494013 MeV/u; where u=atomic mass unit (amu) =1.66×10^{-27} kg). This equation is called the Q-value equation. If Q is + ive, the reaction called exoergic; if Q is - ive, it is endoergic.

The amount of energy needed for an endoergic reaction is called the *threshold energy* and can be calculated easily (Kaplan, 1962).

$$E_{th} = -Q(1 + \frac{M_\alpha}{M_X}) \qquad (2)$$

Fusion requires two (or more) interacting particles to approach closely enough, within the short range of the (attractive) strong nuclear force, $\lesssim 10^{-15}$ m, to construct a new nucleus with A = A_1+A_2. The so-called height V_C of the barrier is its maximum value, which occurs at the nuclear radius, and is (Evans, 1955).

$$V_C = \frac{Z_1 Z_2 e^2}{R} \qquad (3)$$

Where $Z_1$and Z_2 are the charges of the projectile and target nuclei, and R and $(R = R_1 + R_2)$ is their separation, e is the charge of electron ($e^2 = 1.44\ MeV\ fm$), and the radius of the nucleus is given by $R = 1.3 \times 10^{-13} A^{1/3}$ cm, where A is the mass number (atomic weight) (Shaviv, 2012). Then Eq. (3) leads to

$$V_C = E_C = \frac{1.44}{1.3}\left(\frac{Z_1 Z_2}{A_1^{1/3}+A_2^{1/3}}\right) \qquad (4)$$

Where E_C is the coulomb barrier (Coulomb energy) in MeV, $A_1^{1/3}$ *and* $A_2^{1/3}$ are the mass numbers of the charges of bombarding and targeting nuclei respectively.

The astrophysical S-factor, *S*(*E*), in the unit (MeV-b) is related to the cross-section by (Li, J. *et al.*, 2012):

$$S(E) = E\sigma(E)\exp(2\pi\eta) \qquad (5)$$

Where E *is* the center-of-mass energy ($E_{c.m.}$) in MeV, $\sigma(E)$ is the cross-section of the reaction in (mb), $2\pi\eta$ is the Gamow factor, and η is Sommerfeld parameter (Angulo *et al.*, 1999):

$$\eta = \frac{Z_1 Z_2 e^2}{\hbar v} = 0.1575 Z_1 Z_2 \sqrt{\frac{\mu(u)}{E(MeV)}} \qquad (6)$$

, $\hbar$ is Planck's constant over 2π (1.0546 × 10^{-27} ergs), v is the relative velocity, μ is the reduced mass. The Gamow factor G (E) or $2\pi\eta$ can be written as in (Jose, 2016):

$$2\pi\eta = 0.98951 Z_1 Z_2 \sqrt{\frac{\mu(u)}{E(MeV)}} \qquad (7)$$

The reduced mass μ in u (amu) is determined by the relationship (Clayton, 1968):

$$\mu = \frac{m_1 m_2}{m_1 + m_2} \quad (8)$$

Where $m_1$and m_2 represent the masses of the bombarding and target nucleus in units of (amu), respectively. The energy of the center of mass of pair of particles $E_{c.m.}$ is related to the laboratory energy, $E_{Lab.}$ of the projectile particle by the equation (Meyerhof, 1967):

$$E_{c.m.} = \frac{m_2}{m_1 + m_2} E_{lab.} \quad (9)$$

The Gamow energy E_G , in MeV (Brown, 2015):

$$E_G = 2\pi^2 \mu u C^2 \alpha^2 (Z_1 Z_2)^2 = 0.979 \mu (Z_1 Z_2)^2 \quad (10)$$

Where $\alpha = \frac{1}{137} = \frac{e^2}{\hbar c}$ is the fine-structure constant. The thermonuclear reaction rates, $N_A\langle\sigma v\rangle$ in unit $(cm^3 mol^{-1} s^{-1})$ (Angulo *et al.*, 1999):

$$N_A\langle\sigma v\rangle = \left(\frac{8}{\mu\pi}\right)^{1/2} \frac{1}{(k_B T)^{3/2}} N_A \int_0^\infty E\sigma(E) \exp(-E/k_B T)\, dE \quad (11)$$

Where N_A is the Avogadro's number ($6.022 \times 10^{23} mol^{-1}$), k_B is the Boltzmann's constants ($1.38 \times 10^{-16} erg/K$), and $T\ is\ the\ temperature$ respectively. Eq. (11) leads to (Angulo *et al.*, 1999):

$$N_A\langle\sigma v\rangle = 3.7313 \times 10^7 \mu^{-1/2} T_9^{-3/2} \int_0^\infty E\sigma(E) \exp(-11.605E/T_9)\, dE \quad (12)$$

Where T_9 is the temperature in units of $10^9 K$ ($T_9 = 10^{-9} T$)
The weighted averages of the Cross-sections of medium elements $\sigma_0(mb)$ and the uncertainty (errors) $\Delta\sigma_0(mb)$ are expressed by the following Eqs. (Bevington and Robinson, 2003):

$$\sigma_0(mb) = \frac{\sum_i (\sigma_i / {\delta_i}^2)}{\sum_i (1/{\delta_i}^2)} \quad (13)$$

Where σ_i and δ_i $(\Delta\sigma_i)$ are the cross-section and the uncertainties of i^{th} reference, relating to each value of σ_i,

$$\Delta\sigma_0(mb) = \pm \frac{1}{\sqrt{\sum_i (1/\delta_i^2)}} \quad (14)$$

The considered formalism type is the polynomial fit expression of the shape:

$$Y = C_0 + C_1 X + C_2 X^2 + C_3 X^3 + \cdots + C_N X^N = \sum_{i=0}^{M} C_i X^i \quad (15)$$

This polynomial is obtained by the Excel computer program (Format Trendline). Where $(C_0, C_1, C_2, C_3, \dots)$ are free parameters (coefficients of polynomial), and $(i = 0, 1, 2, 3, \dots, M)$, and

$$C_i = \sum_{j=0}^{N} C_{ij} K^j \quad (16)$$

Are considered in this work, then by combining the Eqs. (15) & (16), the following relation has been acquired:

$$Y = \sum_{i=0}^{M} \left(\sum_{j=0}^{N} C_{ij} K^j\right) X^i \quad (17)$$

Where Y=ln[S(E)] or ln[N_A<σv>], (i=0,1,2,…M), (j=0,1,2,…N), (C_{00},C_{01},C_{02},….) are coefficients of polynomials, K is the energy of the center of mass

or T_9 according to the S(E) or N_A<σv>, and X is atomic number Z. The Excel computer program has been utilized to acquire the best fit relationship corresponding to various energies ranges near threshold up to 10 MeV in the center of mass system or T_9 ranges from (1 to 10) 10^9K. The data of these extents were avoided in each step, till a possible value of the determination coefficient $R^2 \approx 1$ was come to. The best fit adopted data was acquired with increasing order to supply the minimum value of Chi-Square (χ^2) by using the Eq. (Belgaid *et al.*, 2005):

$$\chi^2 = \frac{1}{(N - M)} \sum_i^N \left(\frac{Y_{exp}^i - Y_{cal}^i}{\Delta Y_{exp}^i}\right)^2 \quad (18)$$

Where N is the data points' number, M is the fitting coefficients number, Y_{exp}^i and ΔY_{exp}^i are the experimental (adopted value) of $ln[S(E)]$ or $ln[N_A\langle\sigma v\rangle]$ and its error (uncertainty) respectively, Y_{cal}^i is the calculated $ln[S(E)]$ or $ln[N_A\langle\sigma v\rangle]$.

3. Data Reduction and Analysis

The Atomic masses have been taken into consideration to determine the Q-Value, threshold energy, Coulomb barrier, reduced mass, and the ratio between ($E_{c.m.}/E_{lab.}$) of (α, n) medium elements reactions using the Eqs. (1, 2, 4, 8, and 9); the results have been shown in the table (1). Eqs. (6,7,10, and 5) taken into consideration to

determine the Sommerfeld parameter(η), Gamow factor G(E), Gamow energy (E_G), and the S-factor of astrophysical, S(E) of the (α,n) medium element reactions. The results are shown in table (2). The cross-sections of (α,n) reactions of medium elements in present work such as (^{45}Sc, ^{48}Ti, ^{51}V, ^{50}Cr, ^{55}Mn, ^{54}Fe, ^{59}Co, ^{62}Ni, ^{63}Cu, and ^{66}Zn), which are available in the literature review has been taken and plotted again, and using the MATLAB software to interpolate to acquire the cross-sections in fine step of 0.05 MeV. The weighted average of the altered Cross-sections of ith references for the medium elements which cross-section (σ_0) and uncertainty ($\Delta\sigma_0$) have been computed by using Eqs. (13) and (14) respectively[7]. The acquired results have been utilized to calculate the astrophysical S-factor and thermonuclear reaction rates of (α,n) reactions as a function of the center of mass energies $E_{c.m.}$ by using eq. (5) and (12). The acquired equations to compute the S-factor of the reminded reactions are shown in Table 2.

The final formula for each astrophysical S-factor, $S(E)$ and thermonuclear reaction rates $N_A\langle\sigma v\rangle$ is shown in Eq. (17) where $Y = \ln[S(E)]$ or $Y = \ln[N_A\langle\sigma v\rangle]$.

Table 1. Q-Value, threshold energy ($E_{threshold}$), Coulomb barrier E_c, reduced mass (**μ**), and the ratio between ($E_{c.m.}/_{Elab.}$) of (α, n) medium elements reactions.

(α,n) Medium Element Reaction	Q-value (MeV)	$E_{threshold}$ (MeV)		Coulomb Barrier E_c (MeV)	Reduced Mass (**μ**) (amu)	Ec.m./Elab.
		Lab. System	C.M. System			
^{45}Sc(α,n)^{48}V	-2.241E+00	2.440E+00	2.241E+00	9.044E+00	3.675E+00	9.182E-01
^{48}Ti(α,n)^{51}Cr	-2.687E+00	2.911E+00	2.687E+00	9.334E+00	3.694E+00	9.230E-01
^{51}V(α,n)^{54}Mn	-2.294E+00	2.474E+00	2.294E+00	9.622E+00	3.711E+00	9.272E-01
^{50}Cr(α,n)^{53}Fe	-4.961E+00	5.359E+00	4.961E+00	1.009E+01	3.706E+00	9.258E-01
^{55}Mn(α,n)^{58}Co	-3.512E+00	3.767E+00	3.512E+00	1.027E+01	3.731E+00	9.321E-01
^{54}Fe(α,n)^{57}Ni	-5.817E+00	6.249E+00	5.817E+00	1.073E+01	3.726E+00	9.309E-01
^{59}Co(α,n)^{62}Cu	-5.089E+00	5.434E+00	5.089E+00	1.091E+01	3.748E+00	9.364E-01
^{62}Ni(α,n)^{65}Zn	-6.480E+00	6.899E+00	6.480E+00	1.119E+01	3.760E+00	9.393E-01
^{63}Cu(α,n)^{66}Ga	-7.502E+00	7.979E+00	7.502E+00	1.154E+01	3.763E+00	9.402E-01
^{66}Zn(α,n)^{69}Ge	-7.445E+00	7.897E+00	7.445E+00	1.181E+01	3.774E+00	9.428E-01

Table 2. The Sommerfeld parameter(η), Gamow factor G(E), Gamow energy (E_G), and the astrophysical S-factor, S(E) of the (α,n) medium elements reactions

(α,n) Medium Element Reaction	Sommerfeld Parameter η	Gamow factor G(E)	Gamow Energy Eg(MeV)	Astrophysical S-factor S(E)
^{45}Sc(α,n)^{48}V	$1.268E+01/\sqrt{E_{c.m.}}$	$7.967E+01/\sqrt{E_{c.m.}}$	6.348E+03	$E_{c.m.}\sigma(E)Exp(7.967E+01/\sqrt{E_{c.m.}})$
^{48}Ti(α,n)^{51}Cr	$1.331E+01/\sqrt{E_{c.m.}}$	$8.368E+01/\sqrt{E_{c.m.}}$	7.003E+03	$E_{c.m.}\sigma(E)Exp(8.368E+01/\sqrt{E_{c.m.}})$
^{51}V(α,n)^{54}Mn	$1.395E+01/\sqrt{E_{c.m.}}$	$8.769E+01/\sqrt{E_{c.m.}}$	7.689E+03	$E_{c.m.}\sigma(E)Exp(8.769E+01/\sqrt{E_{c.m.}})$
^{50}Cr(α,n)^{53}Fe	$1.455E+01/\sqrt{E_{c.m.}}$	$9.143E+01/\sqrt{E_{c.m.}}$	8.360E+03	$E_{c.m.}\sigma(E)Exp(9.143E+01/\sqrt{E_{c.m.}})$
^{55}Mn(α,n)^{58}Co	$1.520E+01/\sqrt{E_{c.m.}}$	$9.556E+01/\sqrt{E_{c.m.}}$	9.132E+03	$E_{c.m.}\sigma(E)Exp(9.556E+01/\sqrt{E_{c.m.}})$
^{54}Fe(α,n)^{57}Ni	$1.580E+01/\sqrt{E_{c.m.}}$	$9.932E+01/\sqrt{E_{c.m.}}$	9.865E+03	$E_{c.m.}\sigma(E)Exp(9.932E+01/\sqrt{E_{c.m.}})$
^{59}Co(α,n)^{62}Cu	$1.646E+01/\sqrt{E_{c.m.}}$	$1.034E+02/\sqrt{E_{c.m.}}$	1.070E+04	$E_{c.m.}\sigma(E)Exp(1.034E+02/\sqrt{E_{c.m.}})$
^{62}Ni(α,n)^{65}Zn	$1.709E+01/\sqrt{E_{c.m.}}$	$1.074E+02/\sqrt{E_{c.m.}}$	1.154E+04	$E_{c.m.}\sigma(E)Exp(1.074E+02/\sqrt{E_{c.m.}})$
^{63}Cu(α,n)^{66}Ga	$1.771E+01/\sqrt{E_{c.m.}}$	$1.113E+02/\sqrt{E_{c.m.}}$	1.240E+04	$E_{c.m.}\sigma(E)Exp(1.113E+02/\sqrt{E_{c.m.}})$
^{66}Zn(α,n)^{69}Ge	$1.835E+01/\sqrt{E_{c.m.}}$	$1.153E+02/\sqrt{E_{c.m.}}$	1.330E+04	$E_{c.m.}\sigma(E)Exp(1.153E+02/\sqrt{E_{c.m.}})$

4. Results and Discussion

In general, we can write Eq. (15), and instead of X insert center of mass energies $E_{c.m.}$. Then the Eq. (15) becomes

$$Y = C_0 + C_1K + C_2K^2 + C_3K^3 + \cdots + C_NK^N = \sum_{i=0}^{M} C_iK^i \qquad (19)$$

Where (C_0, C_1, C_3 …) are free parameters, K are parameters that represent the C.M energy or T_9, (i=0, 1, 2, 3… M), and Y=ln[S-factor (MeV-b)] or Y=ln[N_A<σv> ($cm^3mol^{-1}s^{-1}$)].

4.1. Astrophysical S-factor Empirical Formulae

The adopted astrophysical S-factor has been used to acquire the fitting parameters by using the expressions of the polynomial (18), (20) and (19) as shown in the steps:

1. The polynomial relations which are utilized in eq. (19) to fit the computed astrophysical S-factor, S(E) in the natural logarithm of the calculated elements to compute the adopted (taken on) natural logarithm of astrophysical S-factor from the best fitting with a minimum (χ^2) using Eq. (20). The acquired best fitting relations of the reminded reactions were presented in Eqs. (20, 21, 22, 23, 24, 25, 26, 27, 28, and 29) for the reactions $^{45}Sc(\alpha,n)^{48}V$, $^{48}Ti(\alpha,n)^{51}Cr$, $^{51}V(\alpha,n)^{54}Mn$, $^{50}Cr(\alpha,n)^{53}Fe$, $^{55}Mn(\alpha,n)^{58}Co$, $^{54}Fe(\alpha,n)^{57}Ni$, $^{59}Co(\alpha,n)^{62}Cu$, $^{62}Ni(\alpha,n)^{65}Zn$, $^{63}Cu(\alpha,n)^{66}Ga$, and $^{66}Zn(\alpha,n)^{69}Ge$ respectively.

$^{45}Sc(\alpha,n)^{48}V \qquad x^2 = 0.0247$

$$ln[S-factor(MeV-b)] = 0.0062E^3 - 0.2075E^2 + 1.0183E + 30.7 \qquad (20)$$

$^{48}Ti(\alpha,n)^{51}Cr \qquad x^2 = 0.086$

$$ln[S-factor\ (MeV-b)] = -0.0867E^4 + 2.5599E^3 - 28.125E^2 + 135.15E - 206.65 \qquad (21)$$

$^{51}V(\alpha,n)^{54}Mn \qquad x^2 = 0.041$

$$ln[S-factor\ (MeV-b)] = -0.0261E^3 + 0.4478E^2 - 3.1956E + 41.906 \qquad (22)$$

$^{50}Cr(\alpha,n)^{53}Fe \qquad x^2 = 0.682$

$$ln[S-factor\ (MeV-b)] = 0.0763E^3 - 1.9295E^2 + 15.185E - 5.9137 \qquad (23)$$

$^{55}Mn(\alpha,n)^{58}Co \qquad x^2 = 0.0015$

$$ln[S-factor\ (MeV-b)] = 0.0153E^3 - 0.4515E^2 + 3.3053E + 28.436 \qquad (24)$$

$^{54}Fe(\alpha,n)^{57}Ni \qquad x^2 = 0.051$

$$ln[S-factor\ (MeV-b)] = 0.2583E^3 - 6.0359E^2 + 45.678E - 78.034 \qquad (25)$$

$^{59}Co(\alpha,n)^{62}Cu \qquad x^2 = 0.112$

$$ln[S-factor\ (MeV-b)] = 0.0872E^3 - 2.205E^2 + 17.564E - 8.1943 \qquad (26)$$

$^{62}Ni(\alpha,n)^{65}Zn \qquad x^2 = 0.0056$

$$ln[S-factor\ (MeV-b)] = 0.1946E3E^3 - 4.9013E^2 + 40.02E - 69.093 \qquad (27)$$

$^{63}Cu(\alpha,n)^{66}Ga \qquad x^2 = 0.027$

$$ln[S-factor\ (MeV-b)] = 2.2587E^3 - 57.223E^2 + 480.3E - 1299.5 \qquad (28)$$

$^{66}Zn(\alpha,n)^{69}Ge \qquad x^2 = 0.685E\text{-}03$

$$ln[S-factor\ (MeV-b)] = 0.7816E^3 - 20.777E^2 + 183.26E - 498.11 \qquad (29)$$

2. At fixed values of energy in center-of-mass, the change of the S-factor in natural logarithm with the Z has been fitted to the polynomial relation utilizing Eq. (19). The acquired results were used to determine the free parameters (coefficients of polynomial) (C_i).

3. The free parameters C_i, were plotted against each value of the center of mass energies and fitted to sufficient the polynomial relation were shown in Eq. (16).

4. The last formula of a set of reactions has been calculated by utilizing the combination of the two polynomials to show the systematic manner of the reactions which are shown in Eq. (17). The Y Variable is the astrophysical S-factor.

4.1.1 The Empirical Formulae Relating the Astrophysical S-factor to Center of Mass Energy and the Atomic Number Z of the Target Nucleus

The empirical formulae related to the astrophysical S-factor (MeV-b) with both of center of mass energy $E_{c.m.}$, and the atomic number Z were performed as the steps below:

1- At fixed values of the center of mass energies from 5.5 to 10 MeV in steps of 0.25 MeV for the $^{45}Sc(\alpha,n)^{48}V$, $^{48}Ti(\alpha,n)^{51}Cr$, $^{51}V(\alpha,n)^{54}Mn$,$^{55}Mn(\alpha,n)^{58}Co$, and $^{59}Co(\alpha,n)^{62}Cu$ reactions, the astrophysical S- factor in natural logarithm will vary with the atomic number(Z), as shown in Fig. (1). The data was fitted into the accompanying polynomial expression:

$$Y = \sum_{i=0}^{2} C_iX^i \qquad (30)$$

Where $Y = \ln[S(E)]$, and X=Z, with free parameters C_i (C_0, C_1, and C_2).

2- The S-factor, S(E), which is was adopted, has been utilized as a function of atomic number Z of target nucleus at the fixed center of mass energies using the computer program Excel to acquire the fitting relations and then it was utilized to

compute the fitting parameters. The acquired results are shown in Table 3.

3- The obtained free parameters C_i (C_0, C_1, and C_2), presented in Table (3) are plotted against with the fixed values of center of mass energies from 5.5 to 10 MeV in step of 0.25 MeV as shown in Fig.(2), and then the acquired coefficients of polynomials C_i have been fitted to the polynomial expression below:

$$C_i = \sum_{j=0}^{2} C_{ij} E^j \qquad (31)$$

The combination of the two polynomials Eq. (30) and Eq. (31) takes the form of the formula below of energy ranged from 5.5 to 10 MeV in the step of 0.25 MeV:

$$Y = \sum_{i=0}^{2} (\sum_{j=0}^{2} C_{ij} E^j) X^i \qquad (32)$$

Where Y=ln[S(E)], X=atomic number Z

$$Y = \sum_{i=0}^{2} (C_{i0}E^0 + C_{i1}E^1 + C_{i2}E^2) X^i$$

$$Y = C_{00}E^0X^0 + C_{01}E^1X^0 + C_{02}E^2X^0 + C_{10}E^0X^1 + C_{11}E^1X^1 + C_{12}E^2X^1 + C_{20}E^0X^2 + C_{21}E^1X^2 + C_{22}E^2X^2 \qquad (33)$$

Where (C_{00}, C_{01}, C_{02}, C_{10}, C_{11}…. C_{22}) are free parameters and their values are shown in the matrix below:

$$\begin{bmatrix} C_{00} & C_{01} & C_{02} \\ C_{10} & C_{11} & C_{12} \\ C_{20} & C_{21} & C_{22} \end{bmatrix} = \begin{bmatrix} -2.0079 & -14.163 & 1.4295 \\ 2.5083 & 1.1719 & -0.1305 \\ -0.0466 & -0.0217 & 0.0027 \end{bmatrix}, \begin{bmatrix} R^2 = 0.6757 \\ R^2 = 0.7426 \\ R^2 = 0.7585 \end{bmatrix}$$

The acquired formula of a set of reactions such as $^{45}Sc(\alpha,n)^{48}V$, $^{48}Ti(\alpha,n)^{51}Cr$, $^{51}V(\alpha,n)^{54}Mn$,$^{55}Mn(\alpha,n)^{58}Co$, and $^{59}Co(\alpha,n)^{62}Cu$ has been used to calculate the astrophysical S-factor S(E) for each of the above reactions and compared with the adopted astrophysical S-factor calculated from the fitting expressions and shown to be in a good agreement and the comparison of the two results are shown in Table (4).

Table 3. Free parameters C_i (C_0, C_1, and C_2) as a function of the energy of the center of mass .

Ec.m. (MeV)	C0	C1	C2
5.5	-49.997	6.1814	-0.1106
5.75	-41.303	5.3931	-0.093
6	-34.449	4.7574	-0.0787
6.25	-29.331	4.2685	-0.0675
6.5	-25.812	3.9172	-0.0593
6.75	-23.719	3.6906	-0.0538
7	-22.843	3.5724	-0.0508
7.25	-22.944	3.5423	-0.0497
7.5	-23.743	3.5767	-0.0501
7.75	-24.928	3.6484	-0.0515
8	-26.154	3.7264	-0.053
8.25	-27.038	3.7763	-0.054
8.5	-27.164	3.7599	-0.0535
8.75	-26.081	3.6355	-0.0508
9	-23.304	3.3579	-0.0446
9.25	-18.311	2.8781	-0.0339
9.5	-10.548	2.1436	-0.0176
9.75	0.5769	1.0983	0.0057
10	15.687	-0.3175	0.0374

Table 4. Comparison between polynomial fitting expression (Best Fitting) of the adopted astrophysical S-Factor of (α,n) medium element reactions with those computed from Eq. (33).

Ec.m	$^{45}Sc(\alpha,n)^{48}V$	$^{48}Ti(\alpha,n)^{51}C$	$^{51}V(\alpha,n)^{54}Mn$	$^{55}Mn(\alpha,n)^{58}Co$	$^{59}Co(\alpha,n)^{62}Cu$

. (MeV)	ln[S-factor(MeV-b)] (Best Fitting) 4.04%	ln[S-factor(MeV-b)] (Formula)	ln[S-factor(MeV-b)] (Best Fitting) 4.215%	ln[S-factor(MeV-b)] (Formula)	ln[S-factor(MeV-b)] (Best Fitting) 3.801%	ln[S-factor(MeV-b)] (Formula)	ln[S-factor(MeV-b)] (Best Fitting) 3.028%	ln[S-factor(MeV-b)] (Formula)	ln[S-factor(MeV-b)] (Best Fitting) 1.974%	ln[S-factor(MeV-b)] (Formula)
5.5	31.055±1.255	31.301	32.461±1.368	32.684	33.534±1.275	33.897	35.503±1.075	35.819	36.214±0.715	37.067
5.75	30.873±1.247	31.182	32.466±1.368	32.584	33.375±1.269	33.821	35.422±1.073	35.803	36.473±0.720	37.128
6	30.679±1.239	31.048	32.325±1.363	32.467	33.216±1.263	33.727	35.319±1.069	35.769	36.645±0.723	37.174
6.25	30.473±1.231	30.899	32.087±1.352	32.334	33.054±1.256	33.615	35.193±1.066	35.716	36.737±0.725	37.203
6.5	30.255±1.222	30.735	31.791±1.340	32.183	32.886±1.250	33.484	35.046±1.061	35.645	36.758±0.726	37.217
6.75	30.026±1.213	30.556	31.472±1.327	32.016	32.712±1.243	33.336	34.881±1.056	35.556	36.715±0.725	37.216
7	29.787±1.203	30.362	31.154±1.313	31.832	32.527±1.236	33.170	34.698±1.051	35.449	36.618±0.723	37.198
7.25	29.539±1.193	30.152	30.853±1.300	31.631	32.329±1.229	32.986	34.498±1.045	35.324	36.474±0.720	37.165
7.5	29.281±1.183	29.928	30.577±1.289	31.413	32.117±1.221	32.784	34.284±1.038	35.180	36.292±0.716	37.117
7.75	29.015±1.172	29.689	30.328±1.278	31.179	31.887±1.212	32.564	34.056±1.031	35.019	36.079±0.712	37.052
8	28.741±1.161	29.434	30.096±1.269	30.928	31.637±1.203	32.326	33.816±1.024	34.839	35.844±0.708	36.972
8.25	28.459±1.150	29.165	29.865±1.259	30.659	31.365±1.192	32.070	33.566±1.016	34.641	35.595±0.703	36.876
8.5	28.171±1.138	28.880	29.613±1.248	30.374	31.068±1.181	31.796	33.306±1.009	34.424	35.340±0.698	36.764
8.75	27.877±1.126	28.581	29.306±1.235	30.072	30.744±1.169	31.504	33.039±1.000	34.190	35.088±0.693	36.637
9	27.577±1.114	28.266	28.903±1.218	29.754	30.391±1.155	31.195	32.766±0.992	33.937	34.846±0.688	36.494
9.25	27.272±1.102	27.937	28.357±1.195	29.418	30.005±1.140	30.867	32.488±0.984	33.666	34.622±0.683	36.335
9.5	26.963±1.089	27.592	27.611±1.164	29.066	29.584±1.124	30.521	32.206±0.975	33.377	34.426±0.680	36.161
9.75	26.649±1.077	27.232	26.600±1.121	28.696	29.127±1.107	30.157	31.923±0.967	33.070	34.264±0.676	35.971
10	26.333±1.064	26.858	25.250±1.064	28.310	28.630±1.088	29.776	31.639±0.958	32.745	34.146±0.674	35.765

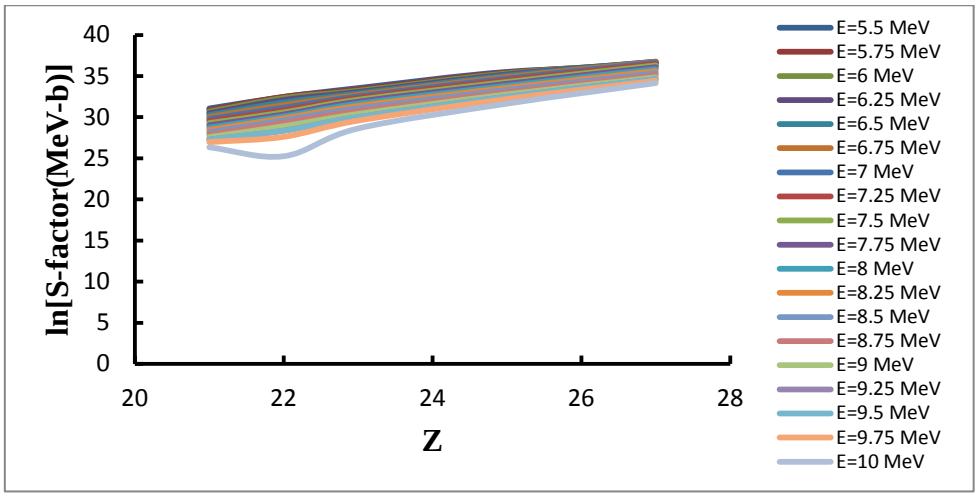

Fig. 1. The variation of the natural logarithm of the astrophysical S-factor S(E) with the atomic number (Z) for the $^{45}Sc(\alpha,n)^{48}V$, $^{48}Ti(\alpha,n)^{51}Cr$, $^{51}V(\alpha,n)^{54}Mn$,$^{55}Mn(\alpha,n)^{58}Co$, and $^{59}Co(\alpha,n)^{62}Cu$ reactions at fixed values of center of mass energies.

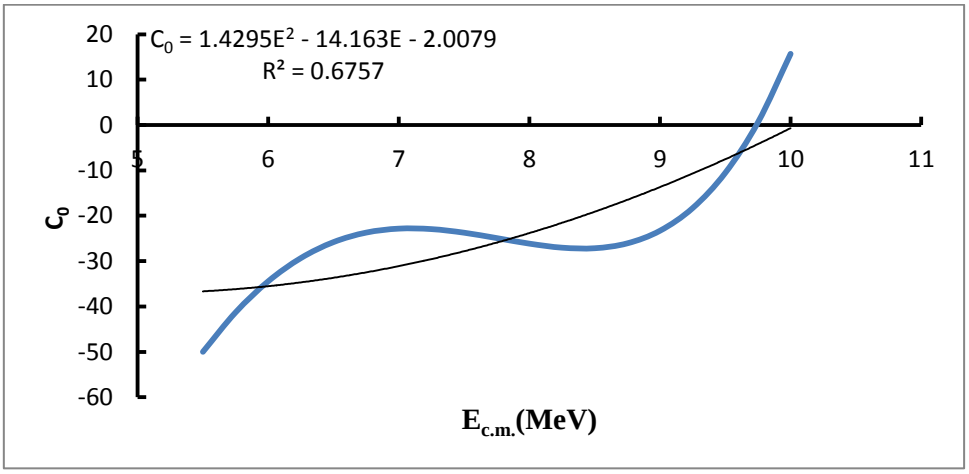

(a)

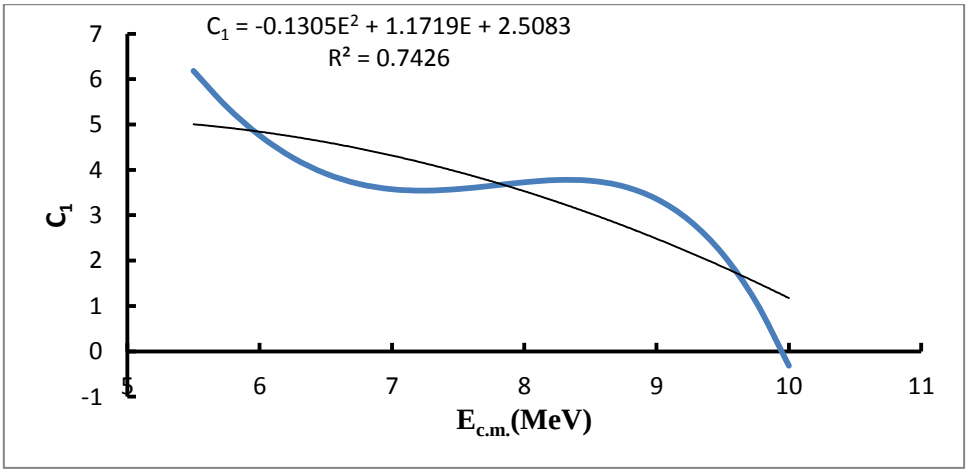

(b)

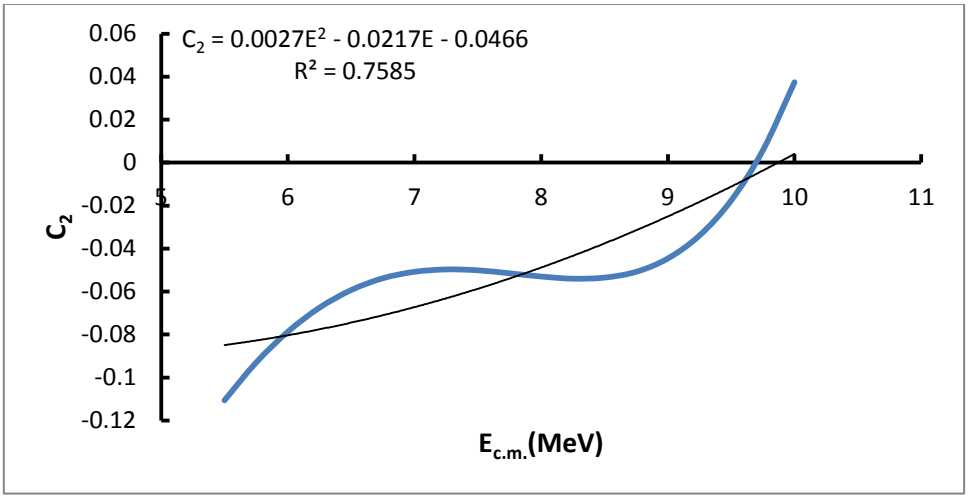

(c)

Fig. 2. C_i coefficients against the center of mass energy, for C_0 ,C_1, and C_2 respectively. The solid line represents the fitted curve through the data.

4.2. Thermonuclear Reaction Rates Empirical Formulae

The adopted thermonuclear reaction rates $N_A\langle\sigma v\rangle$ have been utilized to acquire the fitting parameter by utilizing the polynomial expressions (16), (18) and (19) by the steps below:

1. Polynomial expressions were utilized in eq. (19) to fit the computed thermonuclear reaction rates natural logarithm $N_A\langle\sigma v\rangle$ of the thoughtful medium elements to set the embraced natural logarithm of thermonuclear reaction rates $N_A\langle\sigma v\rangle$ from the best fitting with a minimum (χ^2) utilizing Eq. (18). The acquired best fitting relationships of the remembered reactions are shown in Eqs. (34, 35, 36, 37, 38, 39, 40, 41, 42, and 43) for the reactions $^{45}Sc(\alpha,n)^{48}V$, $^{48}Ti(\alpha,n)^{51}Cr$, $^{51}V(\alpha,n)^{54}Mn$, $^{50}Cr(\alpha,n)^{53}Fe$, $^{55}Mn(\alpha,n)^{58}Co$, $^{54}Fe(\alpha,n)^{57}Ni$, $^{59}Co(\alpha,n)^{62}Cu$, $^{62}Ni(\alpha,n)^{65}Zn$, $^{63}Cu(\alpha,n)^{66}Ga$, and $^{66}Zn(\alpha,n)^{69}Ge$ respectively.

$^{45}Sc(\alpha,n)^{48}V \quad x^2 = 1.064$

$$\ln[N_A\langle\sigma v\rangle(cm^3\ s^{-1}\ mol^{-1})] = 0.0018T^5 - 0.0636T^4 + 0.9094T^3 - 6.7134T^2 + 27.463T - 42.483 \quad (34)$$

$^{48}Ti(\alpha,n)^{51}Cr \quad x^2=1.216$

$$ln[N_A\langle\sigma v\rangle(cm^3\ s^{-1}\ mol^{-1})] = -0.0156T^4 + 0.4584T^3 - 5.103T^2 + 26.92T - 48.328 \quad (35)$$

$^{51}V(\alpha,n)^{54}Mn \quad x^2=0.979$

$$ln[N_A\langle\sigma v\rangle(cm^3\ s^{-1}\ mol^{-1})] = -0.01T^4 + 0.299T^3 - 3.4636T^2 + 19.663T - 37.011 \quad (36)$$

$^{50}Cr(\alpha,n)^{53}Fe \quad x^2=0.445$

$$ln[N_A\langle\sigma v\rangle(cm^3\ s^{-1}\ mol^{-1})] = 0.0281T^3 - 0.8253T^2 + 8.9513T - 24.344 \quad (37)$$

$^{55}Mn(\alpha,n)^{58}Co \quad x^2=0.318$

$$ln[N_A\langle\sigma v\rangle(cm^3\ s^{-1}\ mol^{-1})] = -0.0053T^4 + 0.1798T^3 - 2.4157T^2 + 16.122T - 34.73 \quad (38)$$

$^{54}Fe(\alpha,n)^{57}Ni \quad x^2=0.57$

$$ln[N_A\langle\sigma v\rangle(cm^3\ s^{-1}\ mol^{-1})] = -0.0093T^4 + 0.2984T^3 - 3.7055T^2 + 22.31T - 47.654 \quad (39)$$

$^{59}Co(\alpha,n)^{62}Cu \quad x^2=0.849$

$$ln[N_A\langle\sigma v\rangle(cm^3\ s^{-1}\ mol^{-1})] = 0.0013T^5 - 0.0504T^4 + 0.7943T^3 - 6.5501T^2 + 30.053T - 55.065 \quad (40)$$

$^{62}Ni(\alpha,n)^{65}Zn \quad x^2=0.597$

$$ln[N_A\langle\sigma v\rangle(cm^3\ s^{-1}\ mol^{-1})] = -0.0103T^4 + 0.3309T^3 - 4.1158T^2 + 24.749T - 53.036 \quad (41)$$

$^{63}Cu(\alpha,n)^{66}Ga \quad x^2 = 1.475$

$$ln[N_A\langle\sigma v\rangle(cm^3\ s^{-1}\ mol^{-1})] = 0.0048T^5 - 0.1684T^4 + 2.3605T^3 - 16.76T^2 + 63.115T - 100.95 \quad (42)$$

$^{66}Zn(\alpha,n)^{69}Ge \quad x^2 = 0.422$

$$ln[N_A\langle\sigma v\rangle(cm^3\ s^{-1}\ mol^{-1})] = 0.0048T^5 - 0.1689T^4 + 2.3715T^3 - 16.888T^2 + 63.973T - 102.72 \quad (43)$$

2. At fixed values of T_9, the variation of the natural logarithm of the thermonuclear reaction rates with the physical parameter atomic number Z has been fitted to the polynomial expression utilizing Eq. (19). The acquired outcomes are contemplated to set the coefficients of polynomials (C_i).

3. The coefficients of polynomials C_i, are plotted versus each value of T_9 and fitted to satisfactory

the polynomial expression were shown in Eq. (16).

4. The last formula of a set of reactions has been determined by utilizing the combination of the two polynomials to show the systematic manner of the reactions, which is shown in Eq. (17). The Y Variable is the thermonuclear reaction rates.

4.2.1. The Empirical Formulae Relating the Thermonuclear Reaction Rates to T_9 and the Atomic Number Z of the Target Nucleus

The empirical formulae relating to the thermonuclear reaction rates $N_A\langle\sigma v\rangle$ ($cm^3\ s^{-1}\ mol^{-1}$) with both T_9 and Z were performed as the steps below:

1- At fixed values of the T_9 from 6 to 10 10^9 K in steps of 0.25 10^9 K for the $^{45}Sc(\alpha,n)^{48}V$, $^{48}Ti(\alpha,n)^{51}Cr$, $^{51}V(\alpha,n)^{54}Mn$, $^{55}Mn(\alpha,n)^{58}Co$, $^{62}Ni(\alpha,n)^{65}Zn$, and $^{66}Zn(\alpha,n)^{69}Ge$ reactions, the natural logarithm of the thermonuclear reaction rates will vary with the atomic number Z this shown in Fig. (3). The data fitted to the polynomial expression as the same as Eq. (30), Where $Y = \ln[N_A\langle\sigma v\rangle]$, X=Z, with free parameters C_i (C_0, C_1, and C_2).

2- The adopted thermonuclear reaction rates have been used as a function of Z at fixed T_9 utilizing the computer program Excel to acquiring the fitting expressions and then used to calculate the fitting parameters. The obtained results are presented in Table (5).

3- The obtained free parameters C_i (C_0, C_1, and C_2), as presented in Table (5) are plotted versus with the fixed values of T_9 from 6 to 10 10^9K in steps of 0.25 10^9K as presented in Fig.(4),and then the acquired coefficients of polynomials C_i have been fitted to the polynomial expression:

$$C_i = \sum_{j=0}^{2} C_{ij} {T_9}^j \qquad (44)$$

The combination of the two polynomials Eq. (30) and Eq. (44) takes the shape of the following formula range T_9 from 6 to 10 10^9K in steps of 0.25 10^9K:

$$Y = \sum_{i=0}^{2} \left(\sum_{j=0}^{2} C_{ij} {T_9}^j \right) X^i \qquad (45)$$

Where $Y=\ln[N_A\langle\sigma v\rangle]$, T_9 is the temperature in 10^9K, and X=atomic numberZ

$$Y = \sum_{i=0}^{2} (C_{i0}T_9^0 + C_{i1}T_9^1 + C_{i2}T_9^2)X^i$$

$$Y = C_{00}T_9^0X^0 + C_{01}T_9^1X^0 + C_{02}T_9^2X^0 + C_{10}T_9^0X^1 + C_{11}T_9^1X^1 + C_{12}T_9^2X^1 + C_{20}T_9^0X^2 + C_{21}T_9^1X^2 + C_{22}T_9^2X^2 \qquad (46)$$

Where (C_{00}, C_{01}, $C_{02,}$, C_{10}, C_{11}…. C_{22}) are free parameters and their values are shown in the matrix below**:**

$$\begin{bmatrix} C_{00} & C_{01} & C_{02} \\ C_{10} & C_{11} & C_{12} \\ C_{20} & C_{21} & C_{22} \end{bmatrix} =$$

$$\begin{bmatrix} 42.691 & -16.998 & 1.7602 \\ -3.0522 & 1.4998 & -0.145 \\ 0.0375 & -0.0265 & 0.0027 \end{bmatrix}, \begin{bmatrix} R^2 = 0.9717 \\ R^2 = 0.9645 \\ R^2 = 0.9643 \end{bmatrix}$$

The acquired formula of a set of reactions such as $^{45}Sc(\alpha,n)^{48}V$, $^{48}Ti(\alpha,n)^{51}Cr$, $^{51}V(\alpha,n)^{54}Mn$, $^{55}Mn(\alpha,n)^{58}Co$, $^{62}Ni(\alpha,n)^{65}Zn$, and $^{66}Zn(\alpha,n)^{69}Ge$ has been used to calculate the thermonuclear reaction rates $N_A\langle\sigma v\rangle$ for each of the above reactions and compared with the adopted thermonuclear reaction rates calculated from the fitting expressions and shown to be in a good agreement and the comparison of the two results are shown in Table (6).

Table 7 presents the comparison of thermonuclear reaction rates of some (α,n) medium elements reactions with other works as Roughton et.al. (Roughton *et al.*, 1983)

Table 5. Free parameters C_i (C_0, C_1, and C_2) as a function of T_9.

T9 (109 K)	C0	C1	C2
6	1.8494	0.9114	-0.0281
6.25	3.9765	0.7593	-0.0247
6.5	6.3605	0.5865	-0.021
6.75	8.9003	0.4013	-0.017
7	11.488	0.2126	-0.013

7.25	14.021	0.0288	-0.0091
7.5	16.418	-0.1433	-0.0056
7.75	18.627	-0.2998	-0.0023
8	20.644	-0.4404	0.0006
8.25	22.523	-0.5696	0.0032
8.5	24.388	-0.6979	0.0058
8.75	26.451	-0.8427	0.0086
9	29.02	-1.0295	0.0124
9.25	32.512	-1.2928	0.0176
9.5	37.472	-1.6774	0.0253
9.75	44.58	-2.2392	0.0366
10	54.667	-3.0466	0.0528

Comparison between polynomial fitting expression (Best Fitting) of the adopted astrophysical S-Factor of (α,n) medium element reactions with those computed from Eq. (46).

T9 (109 K)	$^{45}Sc(\alpha,n)^{48}V$		$^{48}Ti(\alpha,n)^{51}Cr$		$^{51}V(\alpha,n)^{54}Mn$		$^{55}Mn(\alpha,n)^{58}Co$		$^{62}Ni(\alpha,n)^{65}Zn$		$^{66}Zn(\alpha,n)^{69}Ge$	
	ln[Na<σv> (cm3 s-1 mol-1)] (Best Fitting) 4.04%	ln[Na<σv> (cm3 s-1 mol-1)] (Formula)	ln[Na<σv> (cm3 s-1 mol-1)] (Best Fitting) 4.215%	ln[Na<σv> (cm3 s-1 mol-1)] (Formula)	ln[Na<σv> (cm3 s-1 mol-1)] (Best Fitting) 3.801%	ln[Na<σv> (cm3 s-1 mol-1)] (Formula)	ln[Na<σv> (cm3 s-1 mol-1)] (Best Fitting) 3.028%	ln[Na<σv> (cm3 s-1 mol-1)] (Formula)	ln[Na<σv> (cm3 s-1 mol-1)] (Best Fitting) 3.785%	ln[Na<σv> (cm3 s-1 mol-1)] (Formula)	ln[Na<σv> (cm3 s-1 mol-1)] (Best Fitting) 9.071%	ln[Na<σv> (cm3 s-1 mol-1)] (Formula)
6	8.614±0.348	8.613	8.281±0.349	8.294	7.901±0.300	7.927	7.005±0.212	7.048	5.415±0.205	5.364	3.824±0.347	3.998
6.25	9.060±0.366	9.027	8.696±0.367	8.710	8.325±0.316	8.348	7.479±0.226	7.488	5.941±0.225	5.858	4.459±0.404	4.545
6.5	9.485±0.383	9.430	9.091±0.383	9.111	8.724±0.332	8.751	7.916±0.240	7.907	6.427±0.243	6.330	5.057±0.459	5.072
6.75	9.889±0.400	9.821	9.471±0.399	9.497	9.101±0.346	9.136	8.323±0.252	8.303	6.879±0.260	6.779	5.620±0.510	5.580
7	10.275±0.415	10.201	9.841±0.415	9.867	9.461±0.360	9.502	8.701±0.263	8.677	7.301±0.276	7.205	6.148±0.558	6.067
7.25	10.643±0.430	10.568	10.202±0.430	10.222	9.804±0.373	9.850	9.054±0.274	9.029	7.699±0.291	7.608	6.642±0.602	6.534
7.5	10.994±0.444	10.924	10.556±0.445	10.561	10.134±0.385	10.179	9.385±0.284	9.359	8.076±0.306	7.989	7.100±0.644	6.981
7.75	11.331±0.458	11.268	10.904±0.460	10.885	10.450±0.397	10.490	9.697±0.294	9.667	8.435±0.319	8.346	7.523±0.682	7.409
8	11.653±0.471	11.600	11.243±0.474	11.193	10.751±0.409	10.783	9.990±0.302	9.952	8.777±0.332	8.681	7.912±0.718	7.816
8.25	11.964±0.483	11.921	11.571±0.488	11.487	11.036±0.419	11.058	10.266±0.311	10.216	9.102±0.345	8.992	8.269±0.750	8.203
8.5	12.266±0.496	12.230	11.882±0.501	11.764	11.302±0.430	11.314	10.526±0.319	10.457	9.411±0.356	9.281	8.600±0.780	8.570
8.75	12.563±0.508	12.527	12.171±0.513	12.027	11.547±0.439	11.552	10.770±0.326	10.676	9.702±0.367	9.547	8.911±0.808	8.918
9	12.860±0.520	12.812	12.431±0.524	12.274	11.765±0.447	11.772	10.997±0.333	10.873	9.973±0.377	9.790	9.215±0.836	9.245
9.25	13.164±0.532	13.085	12.652±0.533	12.506	11.953±0.454	11.973	11.207±0.339	11.047	10.220±0.387	10.010	9.525±0.864	9.553
9.5	13.483±0.545	13.347	12.824±0.541	12.722	12.102±0.460	12.156	11.399±0.345	11.200	10.440±0.395	10.207	9.860±0.894	9.840
9.75	13.826±0.559	13.597	12.935±0.545	12.923	12.207±0.464	12.321	11.571±0.350	11.330	10.626±0.402	10.382	10.245±0.929	10.108
10	14.207±0.574	13.835	12.972±0.547	13.109	12.259±0.466	12.467	11.720±0.355	11.439	10.774±0.408	10.533	10.710±0.972	10.355

Table 7. comparison of the thermonuclear reaction rates in natural logarithm ln[Na<σv> (cm^3 s^{-1} mol^{-1})] of some (α,n) medium element reactions with other works.

T9 (109 K)	$^{48}Ti(\alpha,n)^{51}Cr$		$^{51}V(\alpha,n)^{54}Mn$		$^{50}Cr(\alpha,n)^{53}Fe$		$^{55}Mn(\alpha,n)^{58}Co$	
	Roughton et al. 1983	Present Work	Roughton et al. 1983	Present Work	Roughton et al. 1983	Present Work	Roughton et al. 1983	Present Work
2	-10.054	-11.904	-10.680	-9.599	-15.936	-16.080	-12.652	-13.626

3	-1.347	-2.179	-2.120	-1.796	-5.655	-5.707	-3.507	-3.953
4	3.401	2.918	2.708	2.723	-0.211	-0.181	1.629	1.283
5	6.446	6.098	5.914	5.780	3.258	3.313	5.011	4.654
6	8.556	8.290	8.189	7.973	5.670	5.728	7.378	7.015
7	10.127	9.894	9.903	9.607	7.496	7.490	9.116	8.755
8	11.327	11.117	11.184	10.860	8.882	8.826	10.491	10.081
9	12.301	12.076	12.206	11.845	9.999	9.869	11.608	11.120
10	13.102	12.846	13.060	12.636	10.897	10.700	12.506	11.952
T9 (109 K)	$^{54}Fe(\alpha,n)^{57}Ni$		$^{59}Co(\alpha,n)^{62}Cu$		$^{63}Cu(\alpha,n)^{66}Ga$		$^{66}Zn(\alpha,n)^{69}Ge$	
	Roughton et al. 1983	Present Work	Roughton et al. 1983	Present Work	Roughton et al. 1983	Present Work	Roughton et al. 1983	Present Work
2	-18.526	-18.474	-16.811	-17.051	-25.945	-25.653	-25.759	-26.138
3	-6.908	-6.867	-5.991	-6.195	-10.871	-11.147	-10.820	-11.238
4	-0.968	-0.942	-0.174	-0.380	-3.270	-3.901	-3.244	-3.708
5	2.708	2.699	3.526	3.311	1.335	0.427	1.386	0.826
6	5.193	5.179	6.131	5.865	4.431	3.291	4.522	3.841
7	7.003	6.978	8.039	7.726	6.659	5.317	6.791	5.979
8	8.434	8.339	9.547	9.134	8.343	6.821	8.517	7.568
9	9.547	9.401	10.714	10.231	9.680	7.975	9.852	8.789
10	10.519	10.248	11.695	11.104	10.736	8.887	10.951	9.753

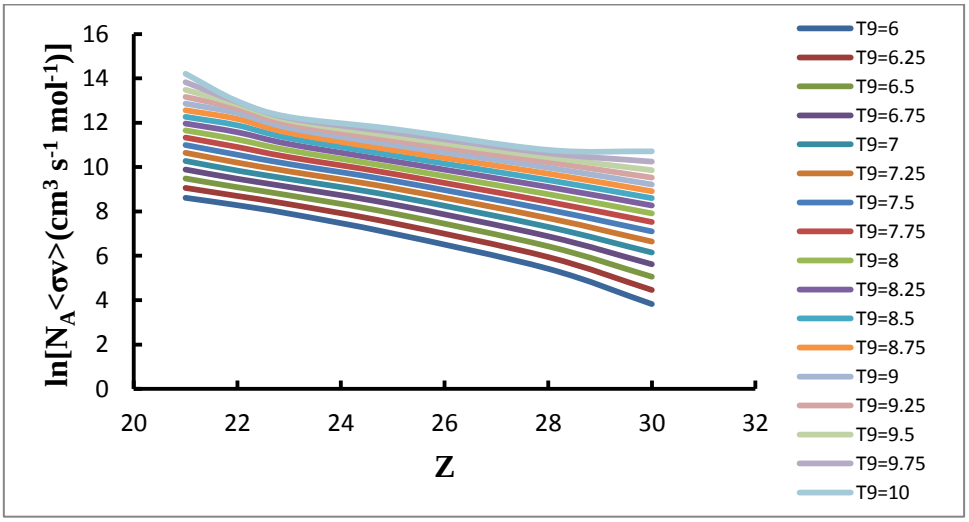

Fig. 3. The variation of the natural logarithm of the thermonuclear reaction rates with the atomic number Z for the $^{45}Sc(\alpha,n)^{48}V$, $^{48}Ti(\alpha,n)^{51}Cr$, $^{51}V(\alpha,n)^{54}Mn$, $^{55}Mn(\alpha,n)^{58}Co$, $^{62}Ni(\alpha,n)^{65}Zn$, and $^{66}Zn(\alpha,n)^{69}Ge$ reactions at fixed values of T_9.

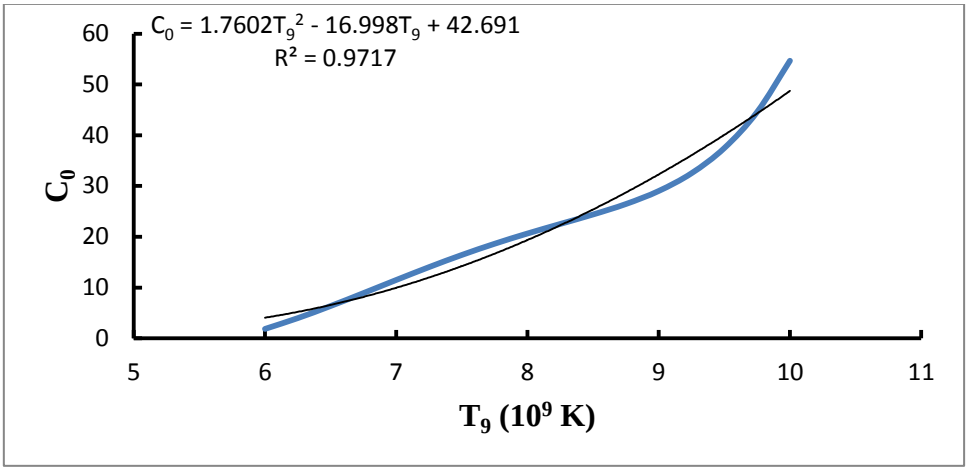

(a)

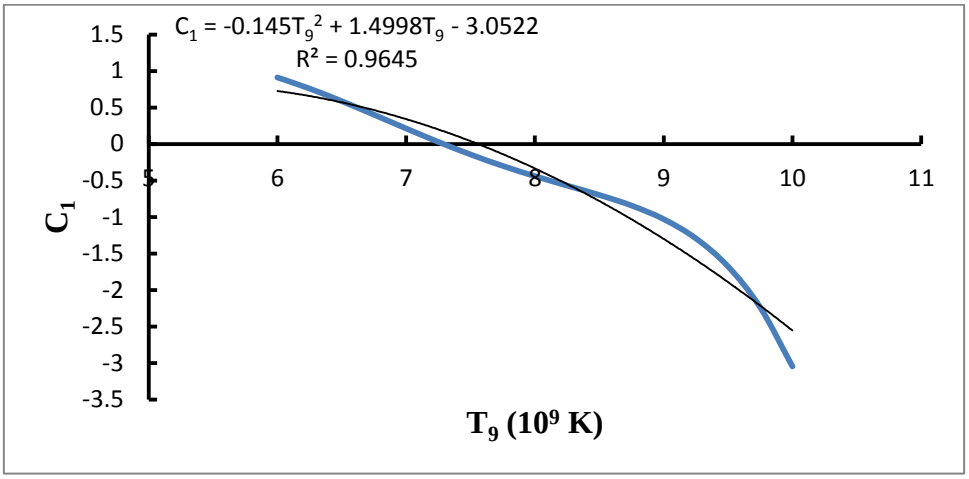

(b)

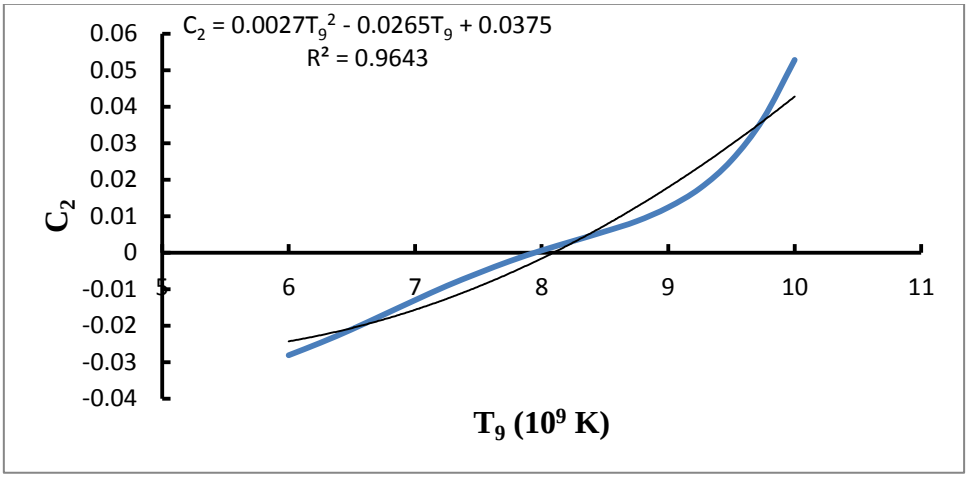

(c)

Fig. 4. C_i coefficients against T_9, for C_0, C_1, and C_2 respectively. The solid line represents the fitted curve through the data.

5. Conclusions

1-The astrophysical S-factor, S(E), was starting with an increase and then decreased irregularly by increasing the center of mass energy, this because of Coulomb barrier penetration $\exp(2\pi\eta)$.

2-The astrophysical S-factor increased with increasing atomic number Z of target nuclei at a fixed center of mass energy.

3-The thermonuclear reaction rates, $N_A\langle\sigma v\rangle$, were increased with increasing T_9 because by increasing the T_9 the charged interacting particles need to overcome the existing Coulomb barrier.

4-The thermonuclear reaction rates decreased with increasing atomic number Z of target nuclei at fixed T_9 because as Z increased Coulomb barrier increased.

5-The astrophysical S-factor and Thermonuclear reaction rates calculated in the present work are in good agreement with those measured previously by other works.

References

Abdul Aziz, A. (2008) *Charged-Particle Induced Thermonuclear Reaction Rates of Light Nuclei. (M.Sc. Thesis)*. University of Malaya, Malaysia.

Angulo, C. *et al.* (1999) 'A compilation of charged-particle induced thermonuclear reaction rates', *Nuclear Physics A*, 656(1), pp. 3–183. doi: 10.1016/S0375-9474(99)00030-5.

Baglin, Coral, M. *et al.* (2004) 'Measurement of 107 Ag (α , γ) 111 In Cross Sections', *Conf.on Nucl.Data for Sci.and Techn., Santa Fe 2004*, 2, p. 1370.

Belgaid, M. *et al.* (2005) 'Semi-empirical systematics of (n, p) reaction cross sections at 14.5 MeV neutron energy', *Nuclear Instruments and Methods in Physics Research, Section B: Beam Interactions with Materials and Atoms*, 239(4), pp. 303–313. doi: 10.1016/j.nimb.2005.05.053.

Bevington, P. R. and Robinson, D. K. (2003) *Data Reduction and Error Analysis for the Physical Sciences. McGraw-Hill Companies, Inc.*

Brown, E. (2015) *stellar astrophysics. Edward Brown*.

Chang, C. N. *et al.* (1973) 'Total cross section measurements by x-ray detection of electron-capture residual activity', *Nuclear Instrum.and Methods in Physics Res.*, 109(January), pp. 327–331.

Clayton, D. D. (1968) *Principles of Stellar Evolution and Nucleosynthesis. McGraw-Hill Book Company*.

D`auria, J. M. *et al.* (1968) 'Reaction Cross Section for Low-Energy Alpha Particles on 59Co', *Physical Review*, 168, p. 1224.

Descouvemont, P. (2011) 'Theoretical Models in Nuclear Astrophysics PoS, p.008.'

Haider, R. D. (2012) *The Empirical Formulae to Determine the Astrophysical S-Factor of (α,n) Reactions for some Medium Elements. (M.Sc. Thesis)*. University of Salahaddin, Kurdistan Region, Iraq.

Hansper, V. Y. *et al.* (1989) 'The 45Sc(a, p)48Ti and 45Sc(a,n)48V Cross Sections', 504, pp. 605–620.

Hansper, V. Y. *et al.* (1993) 'Cross sections and thermonuclear reaction rates for 51V(alpha,n)54Mn and 51V(alpha,p)54Cr', *Nuclear Physics, Section A*, 551, p. 158.

Houck, F. S. and Miller, J. M. (1961) 'Reactions of Alpha Particles with Iron-54 and Nickel-58', *Physical Review*, 123(1), pp. 231–240.

Jose, J. (2016) *Stellar Explosions Hydrodynamics and Nucleosynthesis. Taylor & Francis Group, LLC, Science*. doi: 10.1126/science.218.4576.992.

Kaplan, I. (1962) *Nuclear Physics. Addison-Wesley Publishing Company, Inc.*

Levkovski, V. N. (1991) 'Cross sections of medium mass nuclide activation (A=40-100) by medium energy protons and alpha-particles (E=10-50 MeV)', *Levkovskij,Act.Cs.By Protons and Alphas,Moscow*.

Li, J., Y. *et al.* (2012) 'New determination of the astrophysical 13C(p, γ) 14N S(E) factors and reaction rates via the 13C(7Li, 6He) 14N reaction', *European Physical Journal A*, 48(2), pp. 1–7. doi: 10.1140/epja/i2012-12013-x.

Meyerhof, W. E. (1967) *Elements of Nuclear Physics. McGraw-Hill Book Company*.

Morton, A. J. *et al.* (1992) 'The 48Ti(a, n)51Cr and 48Ti(a,p)51V Cross Sections', *Nuclear Physics A*, 537, pp. 167–182.

Morton, A. J. *et al.* (1994) 'The 50Cr(a, n)53Fe and 50Cr(a, p)53 Mn cross sections', *Nuclear Physics, Section A*, 573(2), pp. 276–290. doi: 10.1016/0375-9474(94)90171-6.

Noori, B. M. (2008) *Empirical Formulae to calculate Neutron Yields for (α,n) Reactions Using Medium Elements and Various Alpha Emitters. (M.Sc. Thesis)*. University of Salahaddin, Kurdistan Region, Iraq.

Peng, X., He, F. and Long, X. (1999) 'Excitation functions for α-induced reactions on vanadium', *Nuclear Instruments and Methods in Physics Research, Section B: Beam Interactions with Materials and Atoms*, 152(4), pp. 432–436. doi: 10.1016/S0168-583X(99)00179-2.

Rizvi, I. A. *et al.* (1989) ' Preequilibrium emission of multiparticles in α-induced reactions with 55 Mn nucleus ', *Canadian Journal of Physics*, 67(11), pp. 1091–1096. doi: 10.1139/p89-188.

Roughton, N. A. *et al.* (1983) 'Thick-Target Measurements and Astrophysical Thermonuclear Reaction Rates: Alpha-Induced Reactions', *Atomic Data and Nuclear Data Tables*, 28(November), pp. 341–353.

Shaviv, G. (2012) *The Synthesis of the Elements, The Astrophysical Quest for Nucleosynthesis and What It Can Tell Us About the Universe. Springer-Verlag Berlin Heidelberg*.

Sonzogni, A. A. *et al.* (1993) 'Alpha and deuteron induced reactions on vanadium', *Journal of Radioanalytical and Nuclear Chemistry Articles*, 170(1), pp. 143–156. doi: 10.1007/BF02134585.

Stelson, P. H. and McGowan, F. K. (1964) 'Cross Sections for (a,n) Reactions for Medium-Weight Nuclei', *Physical Review*, 133(February), pp. B911–B919.

Tims, S. G. *et al.* (1988) 'The 59Co(a,n)62Ni and 59Co(a,n)62Cu Cross Sections', *Nuclear Physics A*, 483(December), pp. 354–370.

Tims, S. G. *et al.* (1991) 'The 54Fe(a, n)57Ni and 54Fe(a, P)57Co Cross Sections', *Nuclear Physics A524*, 524, pp. 479–494.

Tims, S. G. *et al.* (1993) 'Cross sections of the reactions 58Fe (p , y) 59Co,58Fe(p,n)58Co,55Mn(a,n)58Co,55Mn(a,n)58Fe and 57Fe (p , n) 57Co', *Nuclear Physics A*, 563, pp. 473–493.

Tuli, J. K. (2011) 'Nuclear Wallet Cards', *National Nuclear Data Center*. doi: 10.1080/03632415.2011.626737.

Vlieks, A. E., Morgan, J. F. and Blatt, S. L. (1974) 'Total cross sections for some (α, n) and (α, p) reactions in medium-weight nuclei', *Nuclear Physics, Section A*, 224(3), pp. 492–502. doi: 10.1016/0375-9474(74)90551-X.

Vonach, H., Haight, R. C. and Winkler, G. (1983) '(alpha,n) and total alpha-reaction cross sections for Ti-48 and V-51', *Physical Review, Part C, Nuclear Physics*, 28, p. 2278.

Zhukova, O. A. *et al.* (1970) 'Excitation functions of reactions induced by alpha particles with maximum energy of 38 MeV on copper isotopes.', *Izvestiya Akademii Nauk KazSSSR,Ser.Fiz.-Mat.*, 1970(4), p. 1.

Zhukova, O. A. *et al.* (1972) 'Nuclear Reactions Produced Y Alpha Particles on Co-59', *Yadernaya Fizika*, 16, p. 242.

ZANCO Journal of Pure and Applied Sciences
The official scientific journal of Salahaddin University-Erbil
https://zancojournals.su.edu.krd/index.php/JPAS

ISSN (print):2218-0230**, ISSN (online):** 2412-3986**, DOI: http://dx.doi.org/10.21271/zjpas**

RESEARCH PAPER

Optical Analysis of 1300 nm GaInNAsSb/GaAs Vertical Cavity Semiconductor Optical Amplifier

*Faten Adel Ismael Chaqmaqchee, Shawbo Abdulsamad Abubekr Salh, Mohammed Faeq Mohammed Sabri

Department of Physics, Faculty of Science and Health, Koya University, University Park, Danielle Mitterrand Boulevard, Koya KOY45, Kurdistan Region-F.R. Iraq

A B S T R A C T:
Vertical cavity semiconductor optical amplifiers (VCSOAs) based on GaInNAsSb active region is designed to operate in reflection mode at wavelength of 1300 nm. Addition of antimony Sb to the GaInNAs has dramatically improve the performance of VCSOAs, where the wavelength shifts to longer wavelength. This study is aimed to design GaInNAsSb/GaAs quantum wells (QWs) enclosed between various periods of front and 25-periods of back of AlGaAs/GaAs distributed Bragg mirrors (DBRs) by using MATLAB. GaInNAsSb can be grown and lattice matched to GaAs with a very small band gap and it can be grown monolithically on high quality GaAs/AlGaAs distributed Bragg reflector. Peak reflection gain at around of 53.2 dB at single pass gain of 1.076 is observed. In addition, amplifier bandwidth at various front back mirrors reflectivities is simulated to achieve high gain and wide optical bandwidth at low reflectivity of front mirrors.

KEY WORDS: Vertical cavity semiconductor optical amplifier (VCSOA), distributed Bragg reflectors (DBRs), quantum wells (QWs), gain, amplifier bandwidth, mirror reflectivity.
DOI: http://dx.doi.org/10.21271/ZJPAS.32.2.9
ZJPAS (2020) , 32(2);87-92

1. INTRODUCTION:

Dilute nitride III-V-N materials have been successfully employed in optoelectronic devices. The first optically pumped was demonstrated in 1972 under using III-nitride materials (Pankove *et al.* 1972). In 1996, the InGaAs was discovered by Kondow and co-workers (Kondow *et al.* 1997).
gap. Additionally, incorporating antimony (Sb) into GaInNAs/GaAs is pushing the vertical cavity surface emitting lasers VCSEL/VCSOA devices to the longer wavelengths ranges between 1300 to 1500 nm (Wistey *et al.* 2006; Aho *et al.* 2016).

* **Corresponding Author:**
Faten Adel Ismael Chaqmaqchee
E-mail: faten.chaqmaqchee@koyauniversity.org
Article History:
Received: 17/02/2019
Accepted: 07/11/2019
Published: 22/04/2020

decrease the lattice constant and decrease the band

Antimony controls atom diffusion length and allows more nitrogen incorporation that lowers the band gap and improves material and optical quality (Braza *et al.* 2017; Rahman *et al.* 2018). Therefore, Sb affects the valence band and likely the quinary of five component alloy will not only control of band gap and lattice match, but also affect the band offset ratio (Yang *et al.* 1999; Gambin *et al.* 2002; Harris Jr 2005; Yuen *et al.* 2006).

The first surface emitting laser was demonstrated in 1979 (Soda *et al.* 1979), which then led to the development of the vertical cavity surface emitting lasers VCSELs (Haghighi *et al.* 2018, Chaqmaqchee 2019, Liu *et al.* 2019). Since then, extensive work has been done on both types of the devices. Thus, the first VCSOAs was demonstrated in 1991 by koyama, Kubota and Iga at Tokyo institute of technology that present the first VCSEL (Koyama *et al.* 1991). The vertical

geometry of VCSOAs are essentially VCSELs are operated below lasing threshold, and the design for VCSELs can be directly applied in VCSOA devices. The main difference is that strong feedback is desired in VCSELs in order to minimize the threshold current. While in VCSOAs, reduced feedback is useful so as to allow high gain. VCSOAs can be operated in reflection mode, depending on the reflectivity from the DBR mirrors, therefore VCSOAs require higher single pass gain and lower mirror reflectivity than VCSELs (Karim *et al.* 2000; Song *et al.* 2007; Chaqmaqchee and Balkan, 2014; Spiewak 2018).

Vertical cavity semiconductor optical amplifiers (VCSOAs) are an interesting alternative to conventional amplifier technologies for long wavelengths optical fiber communications systems, data storage and access network applications. Furthermore, VCSOA devices have been used as optical preamplifiers, and interconnect in applications such as optical routing, signal regeneration, and wavelength shifting. Such devices have a number of advantages over edge emitting lasers (EEL) and semiconductor optical amplifier (SOA), including low cost manufacturing, compact size, wafer scale fabrication and testing processes (Bjorlin *et al.* 2001).

In this article, VCSOA are designed using Fabry Perot (FP) models. The cavity of $3\lambda/2n_c$ long is based on GaInNAsSb/GaAs multi quantum wells (MQWs), where a recombination process occurs to produce photons of light. The model includes reflectivity spectra, material gain, optical gain and amplifier bandwidth in reflection mode.

2. VCSOA Design and modelling

To improve the performance of present vertical cavity semiconductor optical amplifiers (VCSOAs), several extensive researches have been done and still under investigation (Piprek *et al.* 2001; Chaqmaqchee 2015). VCSOAs are usually made by a thin layer of quantum well (QW) lying between two DBRs to improve the recombination efficiency of the active region and to obtain high optical gain. The electrons and holes can be trapped near each other by using a QW structure. The most important device aspect in VCSOAs is the choice of gain material, which affect all device parameter and defines achievable wavelength range (Ilroy *et al.* 1985; Li and Chua 2010).

In this study, the VCSOA device consist of an active region of nine $Ga_{0.61}In_{0.39}N_{0.0033}As_{0.9876}Sb_{0.016}$ QWs bounded between 9-periods of front and 25-periods of back DBRs mirrors to make a VCSOA amplifying, and the layers structure is depicted in Table 1. The QWs are grouped together in three sets of three wells each positioned on standing wave of $3\lambda/2n_c$ with the total layer thickness of 10 µm QWs to provide high periodic gain and matches the standing wave pattern within the cavity as indicated in Fig.1. However, using the large number of QWs in active region leads to the lack of uniform carrier distribution over each well due to energy barriers of adjacent QWs in the device, whereas the gain enhancement increases with decreasing the number of QWs per standing wave peak (Chaqmaqchee and Balkan, 2012).

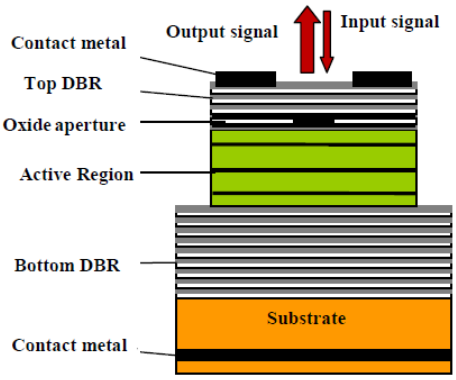

Figure 1: Typical VCSOA structures of top emitting mesa. To make a VCSOA amplifying, it requires mirrors with less reflectivity typically less than 99 % using DBRs.

Table (1) Design of VCSOA structure with GaInNAsSb QWs.

Materials	Thickness (nm)	Notes
GaAs cap	10	9 pairs top DBR with total layer thickness 1837 nm
GaAs	94.4	
$Al_{0.9}Ga_{0.1}As$	108.6	
AlAs	20000	Oxide aperture
GaAs	566.9	Active region 3 QWs per three stuck with total layer thickness 10092.4 nm
$Ga_{0.61}In_{0.39}N_{0.0033}As_{0.9876}Sb_{0.016}$	554	
GaAs	566.9	
$Al_{0.9}Ga_{0.1}As$	108.6	25 pairs bottom DBR with total layer thickness 5075 nm
GaAs	94.4	
GaAs substrate		

The gain and bandwidth spectrum of a VCSOA can be modeled using equations namely

Fabry- Perot (FP) and photon rate equations. The amplifier gain in reflection mode (G_r) can be calculated using (Adams *et al.*1985):

$$G_r = \frac{(\sqrt{R_f}-\sqrt{R_b}g_s)^2+4\sqrt{R_fR_b}g_s sin^2\emptyset}{(1-\sqrt{R_fR_b}g_s)^2+4\sqrt{R_fR_b}g_s sin^2\emptyset} \quad (1)$$

where R_b, R_f and g_s are the back mirror reflectivity, the front mirror reflectivity, and the single pass gain, respectively. The maximum amplification gain is achieved when $\emptyset = 0°$ whereas the minimum gain occurs when $\emptyset = 90°$.

The DBR peak reflectivities can also stimulated as a fixed mirror positioned at a distance from the boundary with the incident medium and given by (Karim *et al.* 2000):

$$R = \left(\frac{1-qap^{N-1}}{1+qap^{N-1}}\right)^2 \quad (2)$$

where *q*, *a*, and *p* are refractive indices that characterize the incident and exist media. Factor q is the ratio of the first medium and first DBR section refractive indices. Factor *a* is the ratio of exist medium and final DBR section refractive indices. Factor *p* is the ratio of low and high index mirror period refractive indexes and finally *N* is the number of mirror layer for bottom DBR or top DBRs.

The material gain provided dependence carrier density *N* can be modelled as (Coldren and Corzine, 1995):

$$g = g_o \ln\left(\frac{N+N_s}{N_{tr}+N_s}\right) \quad (3)$$

where N_{tr} is the transparence carrier density, fitting parameters, and g_o and N_s can be taken from the calculated results.

The gain bandwidth is mainly measured by the line width of Fabry Perod (FP) modes. Additionally, an optical amplifier in reflection mode can be obtained using (Piprek *et al.* 2001; Connelly, 2002):

$$\Delta f_r = \frac{c}{\pi n_c L_c} \times arcsin\left\{4\sqrt{R_fR_b}g_s\left[(1-\sqrt{R_fR_b}g_s)^{-2}-2\sqrt{R_f}-\sqrt{R_b}\,g_s)^{-2}\right]\right\}^{-1/2} \quad (4)$$

where c, L_c, n_c, g_s, R_f, R_b are the velocity of light in vacuum, the effective cavity length, the cavity refractive index, the single pass gain, the top mirror and bottom mirror reflectivities, respectively.

3. RESULTS AND DISCUSSION

The structure of VCSOAs is optically designed (Piprek 2002, Chaqmaqchee 2016, Karim *et al.* 2017) to operate at wavelength of 1300 nm using many important simulation steps. Eq. 2 has been used for plotting Fig. 2 by Matlab program. The mirror reflectivity of $Al_xGa_{1-x}As$ increases as a result of increasing the number of front of back distributed brag mirrors layers, and the mirror reflectivity increases with the concentration of aluminum (Al).

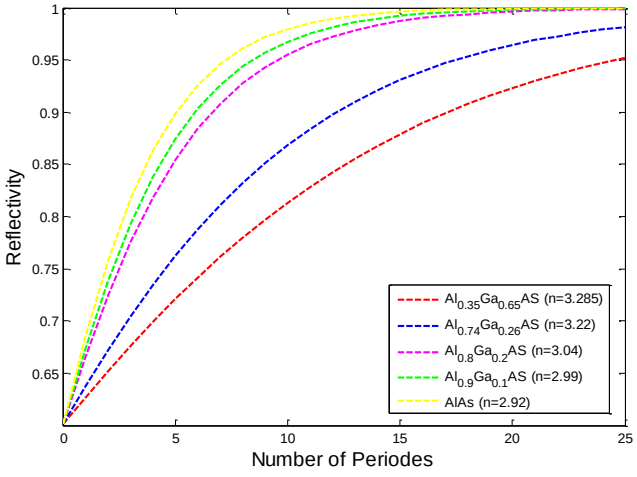

Figure 2: Distributed Bragg reflectors versus number of periods for different concentration of Al.

Figure 3, shows the reflectivity spectrum of the GaInNAsSb VCSOA structure versus wavelength for different front mirrors of 9, 12, 14 and 16 periods and fixed back mirrors of 25 periods along with the assumed refractive index values used for the various layers within the structure. The center dip of the mirror stop band represents the position of cavity resonance at emission wavelength of 1300 nm. This increase in transmissivity at the resonance frequency helps to couple light out of the structure, as the number of front mirror increased, the reflectivity of the mirrors increased greater than 99% for high gain bandwidth, while low mirror reflectivity causes a lower gain, and high saturation power.

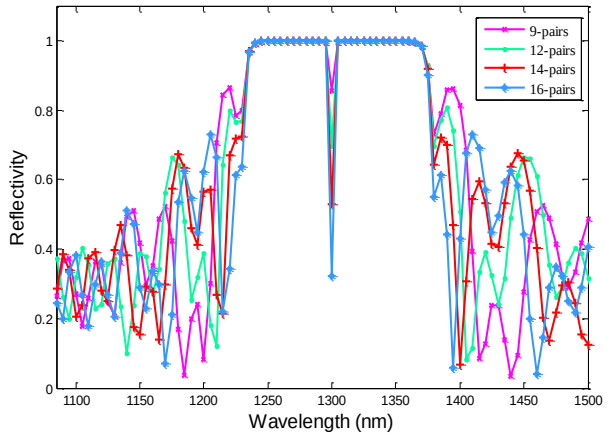

Figure 3: Reflectivity spectra for a cavity GaInNAsSb/GaAs VCSOAs placed between varied periods of front DBRs and 25-periods of back DBRs.

The relationship between material gain and carrier density is illustrated in Fig. 4. The material gain can be calculated using Eq. 3. The material gain was calculated according to a parameter transparency of carrier density of $1.8 \times 10^{18}\ cm^{-3}$, and fitting parameters of $4200\ cm^{-1}$ $and - 0.21 \times 10^{18}\ cm^{-3}$ (Björlin *et al.* 2003; Laurand *et al.* 2005). The material gain depends on carrier density of QW and their precise description at low carrier densities.

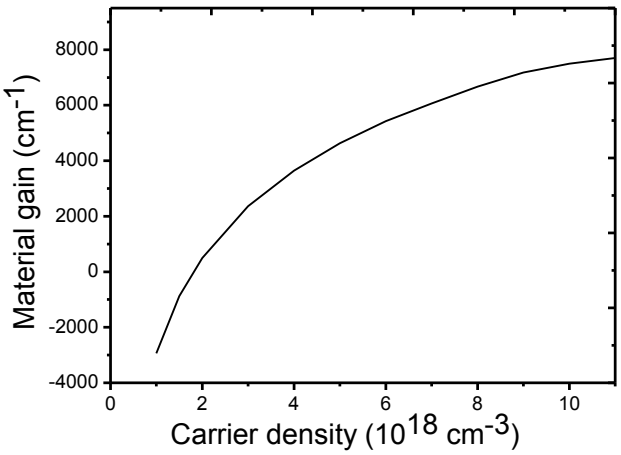

Figure 4: Material gain versus carrier density modeled using a three-parameter logarithmic function.

Equation 1 was used to calculate the peak gain of the VCSOAs in reflection mode. The peak gain depends on the front mirrors, the back mirrors and the single pass gains. Fig. 5 shows the gain spectra of GaInNAsSb/GaAs in reflection mode by using various single pass gains. The single pass gain G_s required achieving high amplifier gain. When the single pass gain G_s values are increased from 1.064 to 1.076, the peak gain values are also increased from 22.17 to 53.2 dB, while the bandwidth decreased with increased peak gain spectra. The narrow bandwidth of VCSOA reduces bad noise that making it ideal for signal amplifying optical filter (Lisesivdin *et al.*, 2014).

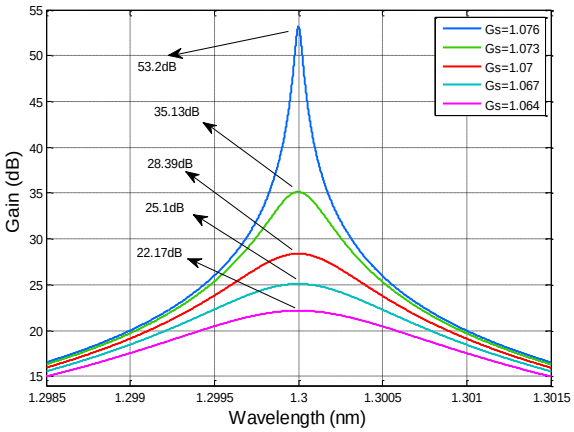

Figure 5: VCSOAs gain spectra in Reflection mode with different value of G_s and fixed R_b=99.9% and R_f=86.6%.

Figure 6 illustrates amplifier bandwidth against peak reflection gain according to Eq.4 with 25- periods of 0.999 back mirrors reflectivity and 9, 10, 11, 12 and 15-periods of 0.939, 0.957, 0.969, 0.978 and 0.985 front mirrors reflectivities, respectively. The amplifier bandwidth in reflection mode for GaInNAsSb/GaAs VCSOA decreases as the peak reflection gain increases. Besides, by reducing the reflectivity of the front Bragg mirror from 0.985 to 0.939 allows for further gain and for wide optical bandwidth. As well as, the reflectivity of the front mirror is decreased to achieve wide optical bandwidth. The narrow bandwidths reduce the signal noise as in filtering application, while the wider bandwidths used in applications with multiple channels (Bjorlin and Bowers, 2002).

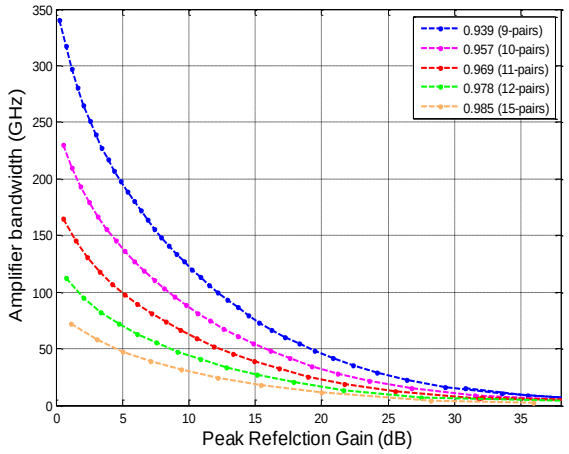

Figure 6: Amplifier bandwidth vs. peak reflection gain for back DBR of 0.999 (25-peiods) and different number of top DBR.

4. CONCLUSIONS

The study was focused on the design, and demonstration of the optically design of VCSOAs devices. The theoretical model had based on Fabry-Perot (FP) SOAs equations and earliest theoretical analysis of the VCSOA design, in which have a potential applications in fiber optic communication systems. GaInNAsSb used as an active region of VCSOAs on GaAs substrate it can be grown monolithically on GaAs/AlGaAs distributed Bragg reflector mirrors with high reflectivity for operation in the 1.3 μm wavelength range. Peak reflection gain at around of 53.2 dB is observed. Moreover, high amplifier bandwidth is achieved at 0.939 front mirrors reflectivity. The optical design of the layer thickness DBRs should redesigned to regulate the emission at 1300 nm and using materials have enough reflectivity for the light to be amplified via internal reflection. The construction of DBR layers essentially governs the operation features of VCSOAs. Therefore, it is very important to select appropriate material system.

Acknowledgements

The authors gratefully acknowledge the department of physics, faculty of science and health at Koya University for enabling this study.

References

Adams, M. J., Collins, J. V., Henning, I. D. 1985. Analysis of semiconductor laser optical amplifiers, *Proc. IEE*, 132 (1), 58-63.

Aho, A., Korpijärvi, V-M., Isoaho, R., Malinen, P., Tukiainen, A., Honkanen, and M., Guina, M. 2016. Determination of composition and energy gaps of GaInNAsSb layers grown by MBE. *Journal of Crystal Growth*, 438, 49-54.

Bjorlin, E. S. 2002. Long-wavelength vertical-cavity semiconductor optical amplifiers, In *Semiconductor Lasers and Optical Amplifiers for Lightwave Communication Systems*, 35-47. International Society for Optics and Photonics.

Bjorlin, E. S., and Bowers, J. E. 2002. Noise figure of vertical-cavity semiconductor optical amplifiers, *IEEE journal of quantum electronics*, 38 (1), 61-66.

Bjorlin, E. S., Kimura, T., and Bowers, J. E. 2003. Carrier-confined vertical-cavity semiconductor optical amplifiers for higher gain and efficiency, *IEEE journal of selected topics in quantum electronics*, 9 (5), 1374-85.

Bjorlin, E. S., Riou. B, Abraham, P., Piprek, J., Chiu Y-Y, Black, K. A., Keating, A., and Bowers, J. E. 2001. Long wavelength vertical-cavity semiconductor optical amplifiers, *IEEE journal of quantum electronics*, 37 (2), 274-81.

Braza, V., Reyes, D. F., Gonzalo, A., Utrilla, A. D., Ben, T., Ulloa, J. M., and González, D. 2017. Sb and N Incorporation Interplay in GaAsSbN/GaAs Epilayers near Lattice-Matching Condition for 1.0-1.16-eV Photonic Applications, *Nanoscale Research Letters*, 356 (12) 1-10.

Chaqmaqchee, F. A. 2015. Optical Amplification in Dilute Nitride Hot Electron Light Emission–VCSOAs Devices, Arabian Journal for Science and Engineering, 40 (7), 2111-2115.

Chaqmaqchee, F. A. 2019. Performance Characteristics of Conventional Vertical Cavity Surface Emitting Lasers VCSELs at 1300 nm, *ZANCO Journal of Pure and Applied Sciences*, 2 (31), 14-18.

Chaqmaqchee, F. A. 2016. Optical Design of Dilute Nitride Quantum Wells Vertical Cavity Semiconductor Optical Amplifiers for Communication Systems, *ARO-The Scientific Journal of Koya University*, 4 (1), 8-12.

Chaqmaqchee, F. A. I. and Balkan, N. 2012. Gain studies of 1.3-mum dilute nitride HELLISH-VCSOA for optical communications. *Nanoscale Res Lett.*, 7(1), 526-529.

Chaqmaqchee, F. A. I. and Balkan, N. 2014. $Ga_{0.35}In_{0.65}N_{0.02}As_{0.08}$/GaAs bidirectional

light-emitting and light-absorbing heterojunction operating at 1.3 μm. *Nanoscale Res Lett.*, 9 (1), 1-5.

Coldren, L. A, Corzine, S. W. 1995. *Diode lasers and photonic integrated circuits*, New York, Wiley.

Cole, G. D., Bjorlin, E. S., Chen, Q., Chan, C.-Y., Wu, S., Wang, C. S., MacDonald, N. C., and Bowers, J. E. 2005. MEMS-tunable vertical-cavity SOAs, *IEEE journal of quantum electronics*, 41 (3), 390-407.

Connely, M. J. 2002. *Semicondctor optical amplifiers*, New York, Kluwer acadamic publishers.

Gambin, V., Ha, W., Wistey, M., Yuen, H., Bank, S.R, Kim, S. M. and Harris Jr, J. S. 2002. GaInNAsSb for 1.3-1.6 m long wavelength lasers grown by molecular beam epitaxy, *IEEE J. Sel. Topics Quantum Electron*, 8 (4), 795-800.

Haghighi, N., Rosales, R., Larisch, G., Marcin, G., Frasunkiewicz, L., Czyszanowski, T., and Lott, J. A. 2018. Simplicity VCSELs, *Proc. SPIE*, 10552, 1-9.

Harris Jr, J. S. 2005. The opportunities, successes and challenges for GaInNAsSb, *Journal of crystal growth*, 278 (1), 3-17.

Ilroy, P. M., Kurobe, A., and Uematsu, Y. 1985. Analysis and application of theoretical gain curves to the design of multi-quantum-well lasers, *IEEE J. Quantum Electron*., 21 (12), 1958-1963.

Karim, A., Bjorlin, S., Piprek, J., and Bowers, J. E. 2000. Long-wavelength vertical-cavity lasers and amplifiers, *IEEE journal of selected topics in quantum electronics*, 6 (6), 1244-53.

Karim, M. R., Rahman, M. A., Akhtar, J., and Reja, M. I. Design and performance analysis of GaInNAsSb/GaAs MQW VCSEL operating at 1550 nm. 2017. *IEEE, 3rd International Conference on Electrical Information and Communication Technology (EICT).*

Kondow, M., Kitatani, T., Nakatsuka, S., Larson, M.C, Nakahara, K., Yazawa, Y., Okai M., and Uomi, K. 1997. GaInNAs: a novel material for long-wavelength semiconductor lasers, *IEEE journal of selected topics in quantum electronics*, 3 (3), 719-30.

Koyama, F., Kubota, S., and Iga, K. 1991. GaAlAs/GaAs active filter based on vertical cavity surface emitting laser, *Electronics Letters*, 27 (12), 1093-95.

Laurand, N., Calvez, S., Dawson, M. D., Bryce, A. C. and Jouhti, T. 2005. Performance comparison of GaInNAs vertical-cavity semiconductor optical amplifiers, *IEEE journal of quantum electronics*, 41 (5), 642-49.

Li, B. J. and Chua, S. J. 2010, "Optical switches: matarial and design", *Woodhead Publishing series in electroinc and optical materials*, UK, pp. 158-180.

Lisesivdin, S. B., Khan, N. A., Mazzucato, S., Balkan, N., Adams, M. J., Korpijärvi, V-M., Guina, M., Mezosi, G., and Sorel, M. 2014. Optical gain in 1.3-μm electrically driven dilute nitride VCSOAs, *Nanoscale Res Lett.*, 9 (1), 1-5.

Liu, A., Wolf, P., Lott, J. A. and Bimberg, D. 2019. Vertical-cavity surface-emitting lasers for data communication and sensing, *Photonics Research*, 7 (2), 121-136.

Pankove, J. I., Miller, E. A. and Berkeyheiser, J. E. 1972. GaN blue light-emitting diodes, Journal of Luminescence, 5 (1), 84-86.

Piprek, J., Björlin, E.S. and Bowers, J. E. 2001. Optical gain-bandwidth product of vertical-cavity laser amplifiers, *Electronics Letters*, 37 (5), 298-299.

\Piprek, J., Bjorlin, S. and Bowers, J. E. 2001. Design and analysis of vertical-cavity semiconductor optical amplifiers, *IEEE journal of quantum electronics*, 37 (1), 127-134.

Rahman, M. A., Karim, M. R., Akhtar, J., Reja, M. I. 2018. Performance Characterization of a GaAs Based 1550 nm $Ga_{0.591}In_{0.409}N_{0.028}As_{0.89}Sb_{0.08}$ MQW VCSEL, International Journal of Photonics and Optical Technology, 4 (1), 14-18.

Soda, H., Iga, K.-i., Kitahara, C., and Suematsu, Y. 1979. GaInAsP/InP surface emitting injection lasers, *Japanese Journal of Applied Physics*, 18 (12), 2329.

Song, D., Gauss, V., Zhang, H., Gross, M., Wen, P., and Esener, S. 2007. All-optical flip-flop based on vertical cavity semiconductor optical amplifiers, *Optics letters*, 32 (20), 2969-2971.

Spiewak, P., Gebski, M., Haghighi, N., Rosales, R., Komar, P., Walczak, J., Wieckowska, M, Sarzala, R.P., Lott, J.A., and Wasiak, M. 2018. Impact of the top DBR in GaAs-based VCSELs on the
threshold current and the cavity photon lifetime. *SPIE Proceedings*, 10552.

Wistey, M. A., Bank, S. R., Bae, H. P., Yuen, H. B., Pickett, E. R., Goddard, L. L., and Harris, J. S. 2006. GaInNAsSb/GaAs vertical cavity surface emitting lasers at 1534nm, *Electronics Letters*, 42 (5), 282-283.

Yang, X., Jurkovic, M. J., Heroux, J. B., and Wang, W. I. 1999. Molecular beam epitaxial growth of InGaAsN: Sb/GaAs quantum wells for long-wavelength semiconductor lasers, *Applied Physics Letters*, 75 (2), 178-180.

Yuen, H. B., Bank, S. R., Bae, H., Wistey, M. A, and Harris Jr, J. S. 2006. The role of antimony on properties of widely varying GaInNAsSb compositions, *Journal of Applied Physics*, 99 (9), 093504.

ZANCO Journal of Pure and Applied Sciences
The official scientific journal of Salahaddin University-Erbil
https://zancojournals.su.edu.krd/index.php/JPAS

ISSN (print):2218-0230**, ISSN (online):** 2412-3986**, DOI: http://dx.doi.org/10.21271/zjpas**

RESEARCH PAPER

A Study of Current situation, Difficulties, and Advantages of implementing BIM in the Construction Sector in Northern Iraq

Nazik Imad Saber*[1] and Khalil Ismail Wali[2]
[1&2]Department of civil, College of Engineering, Salahaddin University- Erbil, Kurdistan Region, Iraq.

A B S T R A C T:

Building Information Modeling (BIM) as an effective Technique of construction projects management has been adopted by the AEC (Architectural, Engineering, and Construction) industry. BIM has substantial benefits over the whole construction lifecycle. In spite of the importance of applying BIM in construction projects, It looks there is fewer study presented to rank the difficulties factors of implementing BIM , also there is less study conducted to show the advantages of using BIM in the construction sector in Northern Iraq. The major objective of this study is to investigate the current situation of applying BIM in the construction sector in Northern Iraq, examine the difficulties of implementing BIM and identify the advantages of implement BIM in the construction industry. A questionnaire was prepared and distributed to 276 engineers in three Governorates (Erbil, Kirkuk, and Sulaymaniyah) in both sectors (private and public). The collected data analyzed using the relative importance index (RII) and mean to rank the difficulties and advantages of implement BIM in Northern Iraq. The analysis results revealed that the most significant difficulties factors in adopting BIM in Northern Iraq are lack of education and syllabus in college regarding the sophisticated package, e.g., ArchiCAD and Revit, there is no training and tutoring for BIM applications in government departments and lack of government supporting and encouraging implementing BIM. The results also revealed the most significant advantages of using BIM are reduce risks in the design stage, improve building design and models, and improve the quality of the building.

KEY WORDS: BIM, difficulties, advantages, current situation, RII
DOI: http://dx.doi.org/10.21271/ZJPAS.32.2.10
ZJPAS (2020) , 32(2);93-106 . .

1.INTRODUCTION

The actual implementation and application of BIM are so far remains challenging for the construction industry. Nevertheless, investigations and studies show a considerable escalation in the percentage of BIM adoption and implementation in typical activities in the construction through the latest five years (Delavar, 2017). BIM is the data and documents process involving information about all stages of the project like planning, design, construction, and operation. It is also useful for extracting estimates such as time, cost, and so on (Kumar and Mukherjee, 2009).

* **Corresponding Author:**
Nazik Imad Saber
E-mail: nazik.saber@su.edu.krd
Article History:
Received:08 /10/2019
Accepted: 11/11/2019
Published: 22/ 04/2020

BIM is not only a technology or a software tool that can be learned and applied. It is rather a model that joins and merges technology with people and progression problems in the construction industry (Haron et al., 2017).

Some of the software which has work in the field of BIM system technology is Graphisoft's ArchiCAD, Autodesk's Revit, etc. Propositions BIM tools are cooperative in the improvement of the project plan and design and generating enhanced coordinated building information and documents (Gajbhiye, 2011).

BIM technology is reflected in the Architectural, Engineering, and Construction (AEC) Industry. In the earlier ten years, design tools have been developed in the AEC industry

from 2D modeling to 3D modeling (Yan and Demian, 2008).

The unique benefits can be obtainable by BIM is the incorporation of the interested party during entirely project phases and the imposition of a cooperative working condition among them to increase the zone of interest (Hatem et al., 2018b).

The future project design and construction will progressively be dependent on BIM. Nowadays, BIM is being implemented in several phases of the project lifecycle, making substantial advantages for the project parties and society (Sun et al., 2017).

BIM find out integrated progressions during the whole lifecycle of the project. The attention is to produce reliable information by the stakeholders during the lifecycle (Arayici et al., 2012).

Academic investigations and case studies, principally within the construction and post-construction phases, unsuccessful to examine and measure BIM benefits, Therefore, Understanding the positive advantages of BIM is a vital driver for active adaptation (Talebi, 2014).

This paper aims to:

1- Investigate the current situation of Applying BIM in Northern Iraq.

2- Examine the difficulties of implementation BIM in the construction industry.

3- Identify the advantages of implementation BIM in the construction industry.

2. THE LITERATURE REVIEW

BIM has improved the design, construction, and operation stages of the buildings. The applied of BIM has run to better profitability, improved time managing, reduced costs, and enhanced customer-client connections.

Azhar et al. (2012) focused on BIM's core concepts by presenting an overview of BIM uses in the construction life cycle and advantages for the project stakeholders. This study also explains barriers and risks to BIM application and future trends.

Even though the several advantages of BIM were identified, there are difficulties remains to be overcome. The main barriers to BIM implementation in the UK were identified and ranked by Eadie et al. (2014), which were "Scale of Culture Change Required/Lack of Flexibility" came as the first barrier. "Lack of supply Chain Buy-in" and "Doubts about Return on Investment/Lack of Vision of Benefits" are ranked second and third respectively.

Saleh (2015) and Matarneh and Hamed (2017) showed the main barriers to implementing BIM in Libya and Jordan, respectively.

BIM implementation was until 2016 even not were discussed a lot in Ghana and other African developing countries. Therefore, Armah (2016) explored the benefits and barriers faced BIM implementation in the Ghanaian Construction Industry. This study discovered the major benefits of BIM, which were improved constructability, improved Visualization, and improved productivity. Additionally, explored the main barriers which were: Lack of knowledge in the usage of BIM, Software compatibility, and BIM cost setup.

BIM aiding code officials visualize the building project, from selecting items could be extracted essential information, e.g. quantities, allow the tasks to have the best understanding of unique project characteristic and how they relate to other components (Belliard and Shantalle, 2016).

Hamada et al. (2017) and Hamada et al. (2016) and Hatem et al. (2018a) and Hatem et al. (2018b) concentrated on the implementation of BIM technology and identified the benefits desired and challenges that reduce adoption this technique in the Iraqi construction industry.

The differing opinions of BIM implementation obstacles between the owners, designers, and contractors were identified by (Li et al., 2017).

Seed (2015) recognized the important variations of implementation BIM by company type and size in the UK construction industry.

In Germany, the barriers to implement BIM techniques and the current practice regarding BIM were analyzed by (Both, 2012).

Chan (2014) in Hong Kong examined the BIM implementation among the design companies and identified their requirements and obstacles in the BIM application process.

Sreelakshmi et al. (2017) found the challenges in the implementation of BIM and involved studying the situation of BIM knowledge in India's construction projects. Collected data were analyzed using RII. The majority of respondents proposed that the cost of BIM implementation is the main barrier.

Zahrizan et al. (2014) determined the actual barriers that obstruct BIM implementation and the motivating factors that could improve its application in the Malaysian construction industry.

Several group meetings were held in China and Australia by Liu et al. (2015) to identifying, classifying, and ranking the main barriers to implementing BIM through a survey.

Memon et al. (2014) focused on assessing the present situation of BIM application in the Malaysian construction industry. This study also examined advantages and disadvantages with obstacles to implementations of BIM and suggesting practical plans for improving the BIM application in the construction industry.

Azhar (2011) discussed the current trends, benefits, possible risks, and future challenges of BIM applications for the AEC industry. The results of this research provided beneficial information for AEC industry parties considering applying BIM techniques in their projects.

Examination of the present status of BIM applications in the Middle East by discovering the range of BIM adoption among stakeholders in the AEC industry in this region were researched by (Gerges et al., 2017).

In the South African construction industry, Kekana et al. (2014) studied the critical barrier's factors to implement BIM. The study revealed that the major barriers, which are attributed to contractual subjects such as licensing, insurance, and persons lacks in terms of training, education, and skills improvement.

3. MATERIALS AND METHODS

The questionnaire survey prepared and designed with the detailed understandable questions in order to create an easily answered survey for the respondents and distributed to professional engineers who have dealt with project in the northern Iraq construction industry in two departments and in both sectors (public and private), taking the Designers, Owners, Contractors, Consultants, Site engineers and Project Managers ideas that have different years of experience in construction industry with the aim of conclude all the required data to accomplish an effective survey to obtain the objective of the study.

3.1 Data collection

The survey was distributed to 300 engineers in three Governorates (Erbil, Kirkuk, and Sulaymaniyah). From the 300 surveys distributed, 17 rejected because of random and unreliable answering with seven uncompleted. Therefore, the total filled and accepted surveys were 276, so meaning that 92 % of the people who were part of this survey answered.

3.2 Determining the sample size in the governorates

The questionnaire distributed for the target engineers in the three governorates using Stratified Sampling depending on the population size (Civil and Architecture engineers) that registered in the Engineers Syndicate. The population size (N1) in Erbil Governorate is 2932 engineers (Kurdistan Engineers Union/Erbil branch), (N2) in Kirkuk is 2506 engineers (Iraqi Engineers Syndicate/Kirkuk branch), and (N3) in Sulaymaniyah is 3051 engineers (Kurdistan Engineers Union/ Sulaymaniyah branch). The total population size (N) is 8489. BY approving proportional allocation, the sample sizes shall be obtaining asunder for the different strata:
1. Strata with N1 = 2932, we have P1 = 2932/8489, n= Sample size =276

$n1 = n.\ P1$ (1) (Kothari, 2004)

$= 276\ (2932/8489) = 95.3 \approx 95$

2. Strata with N2 = 2506, P2= 2506/8489,

$n2 = n.\ P2 = 276\ (2506/8489) = 81.5 \approx 82$, and

3. Strata with N3 = 3051, P3 =3051/8489

$n3 = n.\ P3 = 276\ (3051/8489) = 99.1 \approx 99$.

Therefore, by using proportional allocation, the sample sizes for different strata are 95, 82, and 99, respectively.

3.3 The questionnaire design

The questionnaire designed to cover four main parts:

Part 1 (Personal information): This part includes Personal information regarding the respondent (Work Sector, Gender, Age group, Engineering Department, Experience, Educational level, Type of construction work, Position and Governorate).

Part 2 (BIM technique knowledge Information): This part was prepared to define the current situation of applying BIM in Northern Iraq

construction industry and it's practiced in three governorates (Erbil, Kirkuk, and Sulaymaniyah) as a case study, which comprised questions about the software or tool that the engineer is using in his/her work, how much he/she knows about BIM, number of projects implemented by BIM that he/she has worked on and how did he/she train for using BIM.

Part 3 (the difficulties of implementing BIM in the construction industry): This part is carrying out to identify the obstacles of implementing BIM in the construction industry, and it contains a list of the key obstacles factors that are facing the BIM. It includes 28 questions designed by the five-point Likert scale. The scale is (1: Strongly disagree 2: Disagree 3: Neural 4: Agree 5: Strongly agree). Each respondent was requested to provide a degree of agreement to each question according to what he/she believes within the environment of the Northern Iraq construction sector.

Part 4 (Advantages of using BIM in the construction industry): This part consists of the critical factors of the advantages of using BIM by the five-point Likert scale. The scale is (1: Not important 2: Less Important 3: Fair 4: Important 5: Very important). This part is carrying out to gather with the level of importance of appliance BIM in the construction industry.

3.4 Pilot study

A pilot study was conducted in this study to test and refine their questionnaires using a pilot study before implementing it in a formal survey that is considerably more recommended from several researchers(Saleh, 2015), (Hatem et al., 2018a), (Li et al., 2017). A pilot study is a small sample done for the complete survey to assess and improve the questionnaires. It is as well-known as a 'feasibility' study (Calitz, 2009).

Blaxter (2010) mentioned that "You may think that you know well enough what you are doing, but the value of pilot research cannot be overestimated. Things never work quite the way you envisage, even if you have done them many times before, and they have a nasty habit of turning out very differently from how you expected". When the questionnaire is conducted and prepared, the information should be recorded and prearranged. Pilot test for the survey should be performed by the researcher "with a small set of respondents" that are like those in the final study (Neuman, 2011). Therefore, the collected pilot study's size in this research is ten surveys.

3.4 The participate respondent's sectors

The respondents were specialists in construction sectors are from following public and private sectors:

1. Salahaddin University/ college of engineering.
2. Kirkuk University/ college of engineering.
3. Sulaymaniyah University/ college of engineering.
4. Tishik University/ college of engineering.
5. Ministry of Construction & Housing.
6. General Directorate of the Municipality- Erbil.
7. General Directorate of Road & Bridge- Construction & Housing- Erbil.
8. Directorate of Construction & Housing- Erbil.
9. General Directorate of Roads - Construction & Housing- Sulaymaniyah.
10. General Directorate of the Municipality- Sulaymaniyah.
11. Directory of Roads& Bridge- Sulaymaniyah.
12. Directorate of Reconstruction & Housing- Sulaymaniyah.
13. School buildings department- Kirkuk.
14. Iraqi Engineers Syndicate/ Kirkuk branch.
15. Directorate of Construction & Housing- Kirkuk.
16. General Directorate of the Municipality- Kirkuk.
17. General Directorate of Road & Bridge- Kirkuk.
18. Engineering consultancy offices in Erbil Governorate are Bunyan, Amran, Al-amara, Kurdo and Kapr offices.
19. Engineering consultancy offices in Kirkuk Government are CAD, AL-Ofoq, Solaf and Dar Al-handasy offices.
20. Engineering consultancy offices in Sulaymaniyah Governorate are Design Center, Khanay andazyari Sako , Groupi andazyaran, Asos, and Bahramand offices.

4. Data Analysis

For analyzing the survey questionnaire, the quantitative statistical techniques in SPSS programmer were used. The below techniques have been used in this paper:

1. Frequencies

The Frequencies process is commonly used, particularly with investigation and survey

researches. It is an adequate number to brief the collected data (and is mainly essential with vast data collections). Through using the Frequencies method, other analyses can be generated (e.g., generating descriptive statistics, such as the mean or mode). Also making separate frequency tables (e.g., to compare the number of course taken by male vs. female students) (Arkkelin, 2014)

2. Reliability analysis

Reliability is one of the most desirable technical merits in any educational research through its meaning differs in quantitative and qualitative research. Quantitative research assures the possibility of replication (Oluwatayo, 2012). The Cronbach Alpha coefficient is the furthermost used internal consistency measure. It is viewed as the most appropriate measure of reliability when making use of Likert scales. No absolute rules exist for internal consistencies. However, most agree on a minimum Cronbach Alpha coefficient is .70 (Taherdoost, 2016). The four cut-off points that recommended by (Hinton et al., 2004) for the reliability test are:

Excellent reliability is 0.90 and above.
High reliability is 0.70 to 0.90.
Moderate reliability is 0.50 to 0.70
Low reliability is 0.50 and below.

3. Relative Importance Index (RII)

The techniques method used to analyze the questionnaires and data that employ Likert scales to capture respondents' self-reported attitudes the surveys commonly used by Construction Management Research (CMR) (Holt, 2014). The object of using RII is to rank each factor in a specific part in the survey.

The equation of RII: (Abubakar et al., 2014)

$$RII = \frac{\Sigma w}{(A \times N)} \quad (1) \quad 0 \leq RII \leq 1$$

$$RII = \frac{5(n5)+4(n4)+3(n3)+2(n2)+n1}{5(n5+n4+n3+n2+n1)} \quad (2)$$

W = the weighting given for each item by the respondents and ranges from 1 to 5.

A = highest weight (in this case is 5)

N = respondents' total number.

4. One-Way ANOVA test.

Analysis of variance (known as "ANOVA") "can examine differences between any number of means. This small change not only enables researchers to investigate designs with three or more groups but also allows them to make conceptual leaps, such as from comparing group means defined by one independent variable (IV)" (Berkman and Reise, 2011).

5. RESULTS AND DISCUSSION

5.1 Respondents Personal Information

The survey showed the profile of respondents for five items in **Table 1**.

Table 1: **The profile of respondents**

Personal information	Categories	Percent
1. Work Sector	Public	65.6
	Private	12
	Both sectors (public and private)	22.5
2. Gender	Male	64.1
	Female	35.9
3. Age Group (years)	18-24	3.3
	25-34	33.3
	35-44	36.2
	Over 45	27.2
4. Engineering department	Civil Engineer	74.3
	Architect Engineer	25.7
5. Experience (years)	Under 5	7.6
	5_9	30.4
	10_19	40.9
	Over 20	21
6. Educational level	BSc	76.8
	High Diploma	2.5
	MSc	13.8
	PhD	6.9
7. The main type of construction work	Highway	12.7
	Building	84.1
	sanitary work	1.4
	Others	1.8
8. Position	Designer	26.1
	Owner	8.3
	Contractor	2.2
	Consultant	9.4
	Site engineer	44.9
	Project manager	9.1
9. Governorate distribution	Erbil	34.4
	Kirkuk	30.1
	Sulaymaniyah	35.5

5.2 BIM technique knowledge Information

This paper has studied all the required data to perform an effective questionnaire, the survey

designed and prepared to take the respondents' knowledge about the BIM. The respondents asked four questions related to their implementing of BIM and knowing the extent of applying BIM in the Northern Iraq region.

Figure.1 illustrates the percent of BIM users which 13.41% of the respondents do not use any software, 58.70% used 2D CAD software or that not based-BIM (like AutoCAD) only, 2.17% using 3D CAD or software that based-BIM (like Revit, ArchiCAD) only, 23.29% used both 2D CAD and 3D CAD (BIM), and 2.54% using other software.

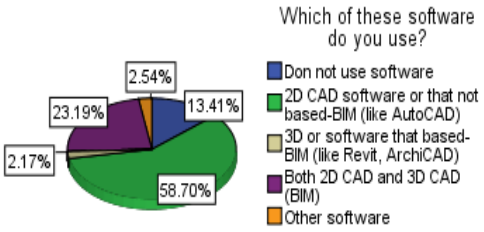

Figure 2: The percent of BIM users.

The result shows that a minor percent of engineers are far from computer's software using. In contrast, a more significant percentage of respondents are using 2D CAD (like AutoCAD). The total percent of BIM users in these three governorates is 25.73%, and that is a progressive point towards BIM's future in Northern Iraq.

Figure.2 shows the level of BIM skills for the respondents where expert users are only 3.99%. While 37.32% have no expertise or they do not know anything about the BIM.

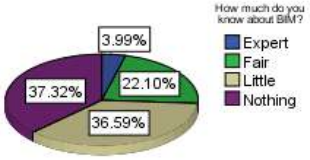

Figure 2: Respondents knowledge about BIM

The result reveals that the experts in BIM skills in the Northern Iraq construction industry are very low.

Figure.3 demonstrated the number of projects that involved or implemented by the respondents, where 9.06% are implemented 2-5

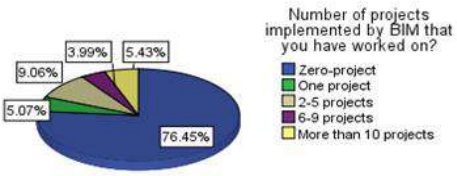

Figure 1: The number of projects that implemented by the respondents.

projects using BIM techniques. On the other hand, 79.45% do not perform any project.

This result shows the project implementing by the BIM techniques in Northern Iraq is low and maybe most of them performed by the private sector.

Figure.4 shows how the respondents gained their BIM skills. The result illustrated that the engineers who know using BIM they taught themselves and dependent on themselves to learn this technique with 20.65%, and the high percent is 59.42% for respondents who do not train to use BIM.

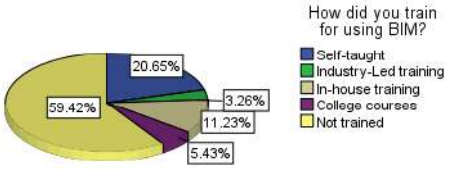

Figure 3: The training method of respondent use BIM techniques

5.3 RII analysis and mean for ranking the difficulties of implementing BIM in Northern Iraq.

Statistical analysis of collected data using mean and RII were performed to rank the main 28 factors that effected on implement BIM in Northern Iraq, as presented in **Table 2.**

Table 2: Ranking of the difficulties of implementing BIM in Northern Iraq using RII and mean.

Factors		1	2	3	4	5	∑W	RII	Mean	Rank
D1	There is no training and tutoring for BIM applications in government departments.	4	13	35	125	99	1130	0.819	4.09	2
D2	Lack of government supporting and encouraging implementing BIM.	4	18	36	120	98	1118	0.810	4.05	3
D3	Lack of standards and guidelines for BIM implementation in projects.	7	16	48	124	81	1084	0.786	3.93	6
D4	Organizations are not sufficiently familiar with BIM use.	3	19	77	114	63	1043	0.756	3.79	9
D5	There are no practical solutions to implement BIM at an adequate level in spite of many studies find the theoretical requests of BIM application.	5	29	76	130	36	991	0.718	3.59	11
D6	Benefits from carrying out BIM do not balance the costs to appliance it.	35	81	91	51	18	764	0.554	2.77	25
D7	No demands for BIM use from owners, contractors, government and other parties.	4	23	40	123	86	1092	0.791	3.96	5
D8	The high cost of training on the BIM tools.	11	53	109	79	24	880	0.638	3.19	18
D9	Lack of clear benefits of BIM.	17	62	63	83	51	917	0.664	3.32	17
D10	Lack of skilled BIM tools operators.	12	43	67	114	40	955	0.692	3.46	14
D11	Current tools are enough (AutoCAD, Excel sheets, and other)	45	96	52	66	17	742	0.538	2.69	26
D12	BIM is unsuitable for small projects.	40	85	89	52	10	735	0.533	2.66	28
D13	Engineers refuse to learn especially the senior engineers .	26	67	88	75	20	824	0.597	2.99	23
D14	People comparing BIM to CAD (They think it is same).	13	57	96	96	14	869	0.630	3.15	21
D15	Contractor and engineers look at BIM as a waste of money, time, and human resource.	13	55	99	91	18	874	0.633	3.17	20
D16	BIM needs collaboration between parties, particularly in organizing change management situations.	6	12	81	143	34	1015	0.736	3.68	10
D17	The engineers use the software just that familiar to them (like Auto CAD, Excel, etc.)	4	19	45	145	63	1072	0.777	3.88	7
D18	Lack of cooperation between engineers from a different department to implement an integrated BIM system.	4	19	65	131	57	1046	0.758	3.79	8
D19	Lack of education and syllabus in college regarding the sophisticated package e.g. ArchiCAD and Revit.	3	13	37	112	111	1143	0.828	4.14	1
D20	Lack of managers' and owners' awareness and support.	5	9	48	129	85	1108	0.803	4.01	4
D21	BIM requests to professionals to use and implement it.	2	17	108	121	28	984	0.713	3.57	12
D22	Lack of BIM tools interoperability.	7	26	127	93	23	927	0.672	3.36	15
D23	Requirements of BIM contracts frame.	5	28	128	93	22	927	0.672	3.36	16
D24	The high cost of BIM software and its updates.	11	52	108	86	19	878	0.636	3.18	19
D25	The additional time needed to implement BIM.	9	77	100	74	16	839	0.608	3.04	22
D26	The future of the BIM is not clear.	24	91	98	50	13	765	0.554	2.77	26

D27	Lack of BIM applications currently.	8	38	75	105	50	979	0.709	3.55	13
D28	Engineers think BIM is losing of process documents, information, and productivity.	21	76	112	58	9	786	0.570	2.85	24

According to the RII and mean ranking analysis the results revealed the top ten significant factors causes the difficulties of implementing BIM in Northern Iraq construction sector, in the first rank comes lack of education and syllabus in college regarding the sophisticated package, e.g., ArchiCAD and Revit, followed by there is no training and tutoring for BIM applications in government departments, lack of government supporting and encouraging implementing BIM, lack of managers' and owners' awareness and support, no demands for BIM use from owners, contractors, government and other parties, lack of standards and guidelines for BIM implementation in projects, the engineers use the software just that familiar to them (like Auto CAD, Excel, etc.), lack of clear benefits of BIM, organizations are not sufficiently familiar with BIM use, and BIM needs collaboration between parties, particularly in organizing change management situations with RIIs of 0.828, 0.819, 0.810, 0.803, 0.791, 0.786, 0.777, 0.758, 0.756, and 0.736 respectively. The means are 4.14, 4.09, 4.05, 4.01, 3.96, 3.93, 3.88, 3.79, 3.79, and 3.68 respectively.

5.4 RII analysis and mean for ranking the advantages of using BIM in the construction industry in Northern Iraq.

Statistical analysis of collected data using mean and RII were performed to rank the main 30 factors of the advantages of using BIM in the construction industry, as presented in **Table 3**.

Table 3: Ranking of the advantages of using BIM in Northern Iraq using RII and mean.

Factors		1	2	3	4	5	∑W	RII	Mean	Rank
A1	Reduced construction cost.	8	14	89	117	48	1011	0.733	3.66	23
A2	Minimizing of time needed to complete the project.	7	12	66	124	67	1060	0.768	3.84	10
A3	Improve the quality of the building. of the building.	3	7	53	134	79	1107	0.802	4.01	3
A4	manage operation and maintenance of constructions during their operating lifecycle.	2	17	56	129	72	1080	0.783	3.91	6
A5	Reduce risks in the design stage.	1	20	39	117	99	1121	0.812	4.06	1
A6	Extract estimates from BIM models e.g. quantities and so on.	6	10	48	142	70	1088	0.788	3.94	5
A7	Improve visualization.	3	13	74	132	54	1049	0.760	3.80	12
A8	Provide accurate cost, time, and relevant information throughout the lifecycle management	4	15	56	144	57	1063	0.770	3.85	9
A9	Improve communication.	8	28	85	120	35	974	0.706	3.53	28
A10	Clash detection.	2	17	58	116	83	1089	0.789	3.95	4
A11	Minimizing rework and change order.	3	13	82	135	43	1030	0.746	3.73	20
A12	Maximizing productivity.	3	19	59	148	47	1045	0.757	3.79	13
A13	Improve document management and integration.	1	14	58	149	54	1069	0.775	3.87	8
A14	Improve distribution of materials during Construction.	4	24	50	151	47	1041	0.754	3.77	16
A15	Improve building design and models.	1	10	39	153	73	1115	0.808	4.04	2
A16	Arrange location and placement of facility elements (like configure, layout, locate, place)	5	21	63	137	50	1034	0.749	3.75	18
A17	Provide a building assembly.	4	19	64	133	56	1046	0.758	3.79	14
A18	Produce as-Built Model	4	18	55	123	76	1077	0.780	3.90	7
A19	Arrange for Construction consequence.	3	17	70	147	39	1030	0.746	3.73	21
A20	Facilitate feasibility studies.	4	13	75	142	42	1033	0.749	3.74	19

A21	Improve the communication between all parties in the construction.	5	16	75	133	47	1029	0.746	3.73	22
A22	Increased efficiency of procurement.	5	19	83	136	33	1001	0.725	3.63	24
A23	Facility management.	5	25	85	128	33	987	0.715	3.58	25
A24	Develop the arrangement in the form of contracts	5	27	78	135	31	988	0.716	3.58	26
A25	Improve Sustainability of the project by analyze models for environmental concerns (energy, day lighting, and other)	5	12	64	134	61	1062	0.770	3.85	10
A26	Reduce Contingencies.	12	40	79	104	41	950	0.688	3.44	29
A27	Improve cooperation skills.	8	24	81	132	31	982	0.712	3.56	27
A28	Analyze models for safety.	5	21	68	120	62	1041	0.754	3.77	17
A29	Reduce human resource.	11	40	77	118	30	944	0.684	3.42	30
A30	All of the shop drawings of the building systems for the fabricators can be more easily and quickly produced.	3	17	72	131	53	1042	0.755	3.78	15

According to the RII and mean ranking analysis the results revealed the top ten significant factors of the advantages of using BIM in the construction industry in the Northern Iraq, in the first rank comes reduce risks in the design stage followed by improve building design and models, Improve quality, clash detection, extract estimates from BIM models e.g. quantities and so on, manage operation and maintenance of constructions during their operating lifecycle, produce as-Built Model, improve document management and integration, Provide accurate cost, time, and relevant information throughout the lifecycle management, and minimizing of time needed to complete the project with RIIs of 0.812, 0.808, 0.802, 0.789, 0.788, 0.783, 0.780, 0.775, 0.770, and 0.768 respectively. The means are 4.06, 4.04, 4.01, 3.95, 3.94, 3.91, 3.90, 3.87, 3.85, and 3.84 respectively.

5.5 Fishbone diagram for the difficulties of implementing BIM in Northern Iraq and the advantages of using BIM in the construction industry in Northern Iraq

The Fishbone diagram, also known as Ishikawa diagram is an analysis tool used to determine the potential root causes of a problem. This analysis also provides a systematic way of examining the effects of the causes that involve those effects (Watson, 2004).

Figure 5 shows the root causes of difficulties of implementing BIM in Northern Iraq which are lack of education and syllabus in college regarding the sophisticated package, e.g., ArchiCAD and Revit come in the first rank, followed by there is no training and tutoring for BIM applications in government departments, lack of government supporting and encouraging implementing BIM, lack of managers' and owners' awareness and support, no demands for BIM use from owners, contractors, government and other parties, and lack of standards and guidelines for BIM implementation in projects.

Figure 6 shows the main advantages of using BIM in the construction industry in Northern Iraq which are reduce risks in the design stage comes in the first rank followed by improve building design and models, Improve quality, clash detection, extract estimates from BIM models e.g. quantities and so on, manage operation and maintenance of constructions during their operating lifecycle, produce as-Built Model and improve document management and integration.

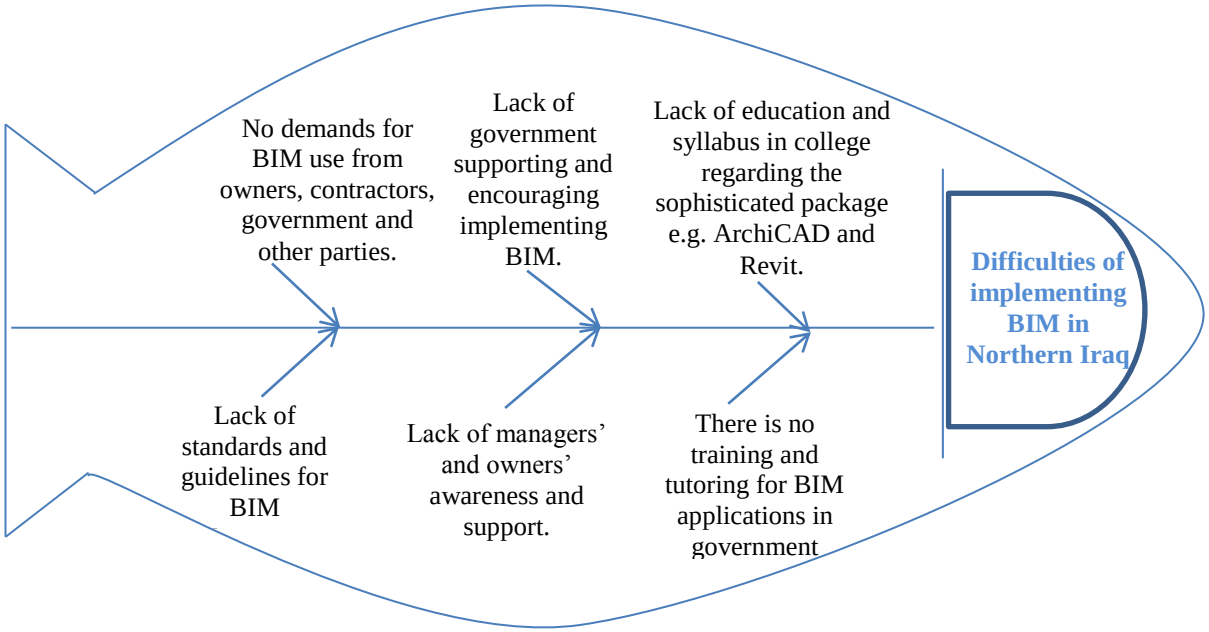

Figure 4: Fishbone diagram for difficulties of implementing BIM in Northern Iraq.

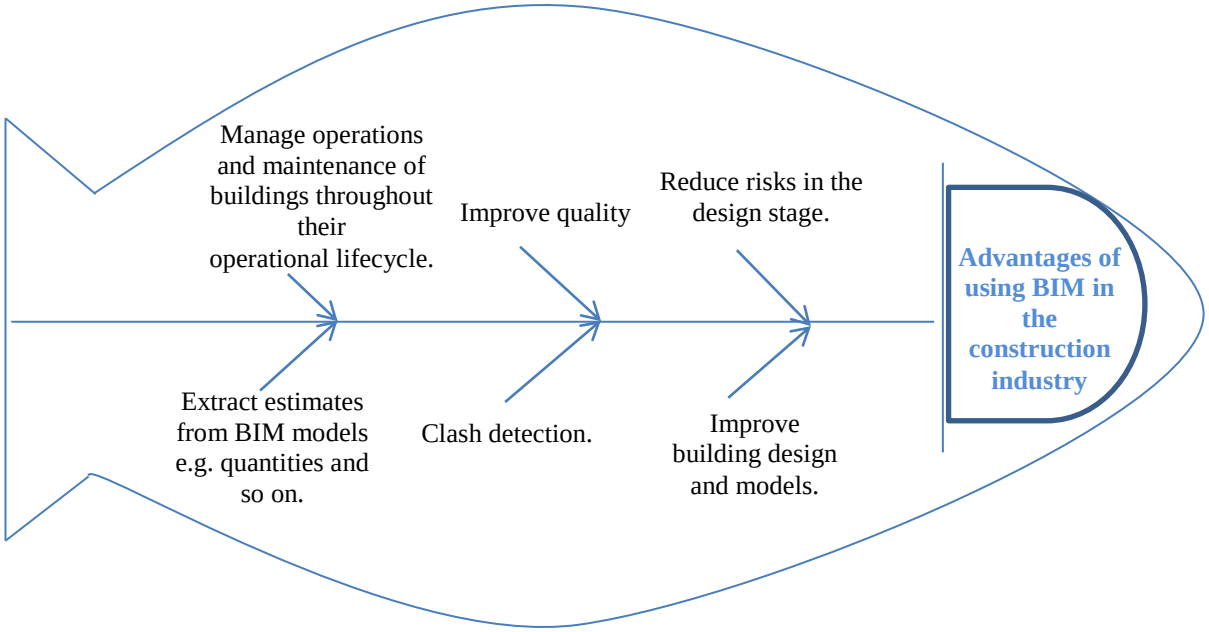

Figure 5: Fishbone diagram for the main advantages of using BIM in the construction industry in Northern Iraq.

5.6 Reliability statistical testing results:

The Cronbach's Alpha result for the difficulties of implementing BIM in Northern Iraq is 0.833, which is within the high reliability and the Cronbach's Alpha result for the advantages of using BIM in Northern Iraq is 0.918 which is within the excellent reliability as shown in **Table 4**.

Table 4: The alpha-Cronbach coefficient degree for the difficulties of implementing BIM in Northern Iraq and for the advantages of using BIM in Northern Iraq.

Reliability Statistics (the difficulties of implementing BIM in Northern Iraq)

Cronbach's Alpha	N of Items
.833	28

Reliability Statistics (the advantages of using BIM in Northern Iraq)

Cronbach's Alpha	N of Items
.918	30

5.7 Statistical analysis of One-Way ANOVA by using SPSS results.

After computing two variables (Mean1 for the means of the 28 difficulties factors of implementing BIM in the Northern Iraq and Mean2 for the means of the 30 advantages factors of using BIM in Northern Iraq), One-Way ANOVA analysis was used to compare the opinions of respondents engineers in the three Governorates.

The Null Hypothesis (Ho): μErbil = μKirkuk = μ Sulaymaniyah

Alternative Hypothesis (Ha): μErbil ≠ μKirkuk ≠ μ Sulaymaniyah

The ANOVA results showed that there is no significant different between means (sig. = .639 > .05) that is proof the engineers opinions regarding the difficulties of implementing BIM in Northern Iraq in the three Governorates and their views were very close to each other as shown in **Table 5**. Therefore, the Null Hypothesis (Ho) was accepted.

Table 5: ANOVA test results Mean1(the means of the 28 difficulties factors of implementing BIM in the Northern Iraq)

	Sum of Squares	df	Mean Square	F	Sig.
Between Groups	.153	2	.076	.448	.639
Within Groups	46.544	273	.170		
Total	46.697	275			

Table 6 shows the means converge in the three Governorate Erbil, Kirkuk, and Sulaymaniyah, which is 3.406, 3.463, and 3.419, respectively.

Table 6: Descriptives for Mean1 (the means of the 28 difficulties factors of implementing BIM in the Northern Iraq)

	N	Mean	Std. Deviation	Std. Error	95% Confidence Interval for Mean		Minimum	Maximum
					Lower Bound	Upper Bound		
Erbil	95	3.406	.46129	.04733	3.3117	3.4996	1.82	4.29
Kirkuk	82	3.463	.35828	.03957	3.3838	3.5413	2.75	4.36
Sulaymaniyah	99	3.419	.40588	.04079	3.3382	3.5001	2.36	5.00
Total	276	3.427	.41208	.02480	3.3786	3.4762	1.82	5.00

The results presented that there is no significant different (sig. = .722 > .05) between respondent ideas regarding the advantages of using BIM in Northern Iraq in the three Governorates and their opinions were same or

near to each other as shown in **Table 7**. Therefore the Null Hypothesis (Ho) was accepted.

Table 7: ANOVA test results Mean2 (the means of the 30 advantages factors of using BIM in Northern Iraq)

	Sum of Squares	df	Mean Square	F	Sig.
Between Groups	.151	2	.076	.325	.722
Within Groups	63.506	273	.233		
Total	63.658	275			

Table 8 illustrates the means converge in the three Governorate Erbil, Kirkuk, and Sulaymaniyah, which is 3.792, 3.733, and 3.770, respectively.

Table 8: Descriptives for Mean2 (the means of the 30 advantages factors of using BIM in Northern Iraq)

	N	Mean	Std. Deviation	Std. Error	95% Confidence Interval for Mean		Minimum	Maximum
					Lower Bound	Upper Bound		
Erbil	95	3.792	.51704	.05305	3.6863	3.8969	2.20	5.00
Kirkuk	82	3.733	.46570	.05143	3.6310	3.8357	2.57	4.63
Sulaymaniyah	99	3.770	.46082	.04631	3.6785	3.8623	2.53	5.00
Total	276	3.767	.48113	.02896	3.7097	3.8237	2.20	5.00

6. Conclusions

This investigation has provided important results in the current situation, difficulties, and advantages of BIM Implementation in the Construction Sector in Northern Iraq.

1. In Northern Iraq there is lacking in BIM implementation and knowledge, 3.99% from respondent engineers are experts in BIM, 25.36% from respondent engineers are using BIM tools, and 76.45% of respondents have not implemented BIM in any of their projects whether in private or public sector.
2. The third part of the questionnaire results of this research identified and ranked the major first five difficulties factors of implementing BIM in Northern Iraq, which is lack of education and syllabus in college regarding the sophisticated package, e.g., ArchiCAD and Revit comes in the first rank, followed by there is no training and tutoring for BIM applications in government departments, lack of government supporting and encouraging implementing BIM, lack of managers' and owners' awareness and support, and no demands for BIM use from owners, contractors, government and other parties respectively.
3. The last part of the questionnaire analysis revealed the significant first five advantages of using BIM in the construction industry, which is reduce risks in the design stage comes in the first rank. Followed by improve building design, models and Improve the quality of the building, clash detection, and extract estimates from BIM models, e.g. quantities and so on, respectively.
4. The Fishbone diagram shows the root causes of difficulties of implementing BIM in Northern Iraq and shows the main advantages of using BIM in the construction industry.
5. ANOVA analysis revealed that the respondent engineers have the same opinion or the close view about the

difficulties and advantages of implement BIM in the three Governorate Erbil, Kirkuk, and Sulaymaniyah and the Null Hypothesis (H_o) is accepted ($\mu_{Erbil} = \mu_{Kirkuk} = \mu_{Sulaymaniyah}$).

REFERENCES

ABUBAKAR, M., IBRAHIM, Y., KADO, D. & BALA, K. Contractors' perception of the factors affecting building information modelling (BIM) adoption in the Nigerian construction industry. International Conference on Computing in Civil and Building Engineering, 2014. 23-25.

ARAYICI, Y., EGBU, C. & COATES, S. 2012. Building information modelling (BIM) implementation and remote construction projects: issues, challenges, and critiques. *Journal of Information Technology in Construction,* 17**,** 75-92.

ARKKELIN, D. 2014. Using SPSS to understand research and data analysis.

ARMAH, N. N. O. 2016. *Assessing the benefits and barriers of the use of building information modeling (BIM) in the Ghanaian Building Construction Industry*.

AZHAR, S. 2011. Building information modeling (BIM): Trends, benefits, risks, and challenges for the AEC industry. *Leadership and management in engineering,* 11**,** 241-252.

AZHAR, S., KHALFAN, M. & MAQSOOD, T. 2012. Building information modelling (BIM): now and beyond. *Construction Economics and Building,* 12**,** 15-28.

BELLIARD, R. & SHANTALLE, L. 2016. Implementation of BIM in the Municipal Plan Review Process.

BERKMAN, E. T. & REISE, S. P. 2011. *A conceptual guide to statistics using SPSS*, Sage.

BLAXTER, L. 2010. *How to research*, McGraw-Hill Education (UK).

BOTH, P. V. 2012. Potentials and barriers for implementing BIM in the German AEC market: results of a current market analysis.

CALITZ, M. 2009. Chapter 5 pilot study. *Retrieved from uir. unisa. ac. za/bitstream/handle/10500/1648/06chapter5. pd*.

CHAN, C. T. 2014. Barriers of implementing BIM in construction industry from the designers' perspective: A Hong Kong experience. *Journal of System and Management Sciences,* 4**,** 24-40.

DELAVAR, M. 2017. BIM Assisted Design Process Automation for Pre-Engineered Buildings (PEB).

EADIE, R., ODEYINKA, H., BROWNE, M., MCKEOWN, C. & YOHANIS, M. 2014. Building information modelling adoption: an analysis of the barriers to implementation. *Journal of Engineering and Architecture,* 2**,** 77-101.

GAJBHIYE, A. D. 2011. *Empirical Study of Macrobim and Conceptual Estimation.* Texas A & M University.

GERGES, M., AUSTIN, S., MAYOUF, M., AHIAKWO, O., JAEGER, M., SAAD, A. & GOHARY, T.-E. 2017. An investigation into the implementation of Building Information Modeling in the Middle East. *Journal of Information Technology in Construction (ITcon),* 22**,** 1-15.

HAMADA, H., HARON, A., ZAKIRIA, Z. & HUMADA, A. 2016. Benefits and Barriers of BIM Adoption in the Iraqi Construction Firms. *International Journal of Innovative Research in Advanced Engineering*, 3**,** 76-84.

HAMADA, H. M., HARON, A., ZAKIRIA, Z. & HUMADA, A. M. Factor Affecting of BIM Technique in the Construction Firms in Iraq. MATEC Web of Conferences, 2017. EDP Sciences, 03003.

HARON, N. A., SOH, R., ANA, R. P. Z. & HARUN, A. N. 2017. Implementation of Building Information Modelling (BIM) in Malaysia: A Review. *Pertanika Journal of Science & Technology*, 25.

HATEM, W. A., ABD, A. M. & ABBAS, N. N. 2018a. Barriers of Adoption Building Information Modeling (BIM) in Construction Projects of Iraq. *Engineering Journal,* 22**,** 59-81.

HATEM, W. A., ABD, A. M. & ABBAS, N. N. 2018b. Testing a Measurement Model of BIM Potential Benefits in Iraqi Construction Projects. *Civil Engineering Journal,* 3**,** 1349-1365.

HINTON, P., BROWNLOW, C., MCMURRAY, I. & COZENS, B. 2004. Using SPSS to analyse questionnaires: Reliability. *SPSS explained***,** 356-366.

HOLT, G. D. 2014. Asking questions, analysing answers: relative importance revisited. *Construction Innovation,* 14**,** 2-16.

KEKANA, T., AIGBAVBOA, C. & THWALA, W. Building information modelling (BIM): Barriers in adoption and implementation strategies in the South Africa construction industry. International Conference on Emerging Trends in Computer and Image Processing, Pattaya, Thailand, 2014.

KOTHARI, C. R. 2004. *Research methodology: Methods and techniques*, New Age International.

KUMAR, J. V. & MUKHERJEE, M. 2009. Scope of building information modeling (BIM) in India. *Journal of Engineering Science and Technology Review,* 2**,** 165-169.

LI, H., NG, S. T., SKITMORE, M., ZHANG, X. & JIN, Z. Barriers to building information modelling in the Chinese construction industry. Proceedings of the Institution of Civil Engineers-Municipal Engineer, 2017. ICE Publishing, 105-115.

LIU, S., XIE, B., TIVENDAL, L. & LIU, C. 2015. Critical barriers to BIM implementation in the AEC industry. *International Journal of Marketing Studies,* 7**,** 162-171.

MATARNEH, R. & HAMED, S. 2017. Barriers to the Adoption of Building Information Modeling in the

Jordanian Building Industry. *Open Journal of Civil Engineering*, 7**,** 325.

MEMON, A. H., RAHMAN, I. A., MEMON, I. & AZMAN, N. I. A. 2014. BIM in Malaysian construction industry: status, advantages, barriers and strategies to enhance the implementation level. *Research Journal of Applied Sciences, Engineering and Technology*, 8**,** 606-614.

NEUMAN, W. L. 2011. Social science methods: Quantitative and qualitative approaches. Boston, MA, Allyn & Bacon.

OLUWATAYO, J. A. 2012. Validity and reliability issues in educational research. *Journal of Educational and Social Research*, 2**,** 391-400.

SALEH, M. A. D. 2015. *Barriers and Driving Factors for Implementing Building Information Modelling (BIM) in Libya.* Eastern Mediterranean University (EMU)-Doğu Akdeniz Üniversitesi (DAÜ).

SEED, L. 2015. *The Dynamics of BIM Adoption: A Mixed Methods Study of BIM as an Innovation within the United Kingdom Construction Industry.* University of Huddersfield.

SREELAKSHMI, S., KANTILAL, B. S. & ROSHAN, M. 2017. A Study on the Barriers to the Implementation of Building Information Modeling. *International Journal of Civil Engineering and Technology*, 8**,** 42–50.

SUN, C., JIANG, S., SKIBNIEWSKI, M. J., MAN, Q. & SHEN, L. 2017. A literature review of the factors limiting the application of BIM in the construction industry. *Technological and Economic Development of Economy*, 23**,** 764-779.

TAHERDOOST, H. 2016. Validity and reliability of the research instrument; how to test the validation of a questionnaire/survey in a research.

TALEBI, S. Exploring advantages and challenges of adaptation and implementation of BIM in project life cycle. 2nd BIM International Conference on Challenges to Overcome, 2014. BIMForum Portugal.

WATSON, G. 2004. The legacy of Ishikawa. *Quality Progress*, 37**,** 54.

YAN, H. & DEMIAN, P. 2008. Benefits and barriers of building information modelling.

ZAHRIZAN, Z., ALI, N. M., HARON, A. T., MARSHALL-PONTING, A. & HAMID, Z. A. 2014. Exploring the barriers and driving factors in implementing building information modelling (BIM) in the Malaysian construction industry: A preliminary study. *Journal Institution of Engineers Malaysia*, 75**,** 1-10.

ZANCO Journal of Pure and Applied Sciences
The official scientific journal of Salahaddin University-Erbil
https://zancojournals.su.edu.krd/index.php/JPAS

ISSN (print):2218-0230**, ISSN (online):** 2412-3986**, DOI: http://dx.doi.org/10.21271/zjpas**

RESEARCH PAPER

Flexural Behavior of Self Compacting Concrete T-Beams Reinforced with AFRP

Sinan A.Yaseen[1]

[1]Department of Civil Engineering, College of Engineering, Salahaddin University-Erbil, Kurdistan Region, Iraq

A B S T R A C T:
In This paper, an experimental work is carried out to study behavior and performance of Self compacted concrete (SCC) T-section beams reinforced with Aramid fiber reinforced polymers (AFRP) bar. Key variables that taken into consideration were flexural reinforcement ratio, different self-compacted concrete mixes having different strengths. Normal strength steel bars for data comparison. 9 samples of T-sections were designed using (AFRP) to be weak in flexure. 3 samples of T-sections were used with normal steel bars as control samples for comparison. The effect of these fiber reinforcement contents on flexural behavior and crack pattern were observed during third-point loading tests. A data comparison was performed between experimental and analytical beam calculation using ACI 440 as an applied design source. The results show that the final deflection was more in AFRP compared with steel reinforced beams indicating to significant enhancement in strength and toughness. The ultimate capacity of AFRP beams increased more than steel reinforced beams by increasing self-compacting concrete strength. The reinforcement ratio improves the final resisting load as the ratio increases. The maximum observed crack-width in beams reinforced with AFRP bars is three to five times that of normal steel reinforced beams. The exactness of the data depends on both the compressive strength and reinforcement ratio for both AFRP and conventional steel bars. It is seen from data comparison between the experimental work and the ACI 440, That the ACI440 is more conservative when AFRP is used in SCC.

KEY WORDS: T-Beam, Aramid fiber reinforced polymer bar, Flexural behavior and Performance, Self-compacted concrete.
DOI: http://dx.doi.org/10.21271/ZJPAS.32.2.11
ZJPAS (2020) , 32(2);107-114 .

INTRODUCTION :

T-beam is produced as a combination slab beam action in reinforced concrete system as they placed monolithically; these two parts acts together to resist flexural and shear stresses (Daia & Thomas, 2002; Guowei et al., 2011; Tiago et al., 2010; Erki & Rizkalla, 1993). Self-Compacted Concrete (SCC) become popular in construction industry.

Because of high flowability and moderate viscosity, no blocking may occur during flow; which has to de-air by itself during casting of SCC. It is used in specific structures instead of the conventional type concrete (Yasser, 2012; Raya & Bilal 2015). Here the most point of concern in concrete structures is the durability. Corrosion of steel reinforcement (main element in casting members) is related to durability problem. Corrosion attacked constructions are chemical industry facilities, coastal structures, bridges, and ports; they are examples of critical structures subject to reinforcement corrosion. Different types of reinforcements are used to fill the tension weakness side of concrete, such as fiber-reinforced polymers (FRP) (Abdullah & Abdul Kadir, 2016), glass fiber reinforced polymers

* **Corresponding Author:**
Sinan Abdulkhaleq Yaseen
E-mail: sinan.yaseen@su.edu.krd
Article History:
Received: 06/102019
Accepted: 11/112019
Published: 22/04 /2020

(GFRP), and aramid fiber reinforced polymers (AFRP). The main advantage of these materials than conventional reinforcement is corrosion resistance, it can be used in magnetic field area, and has high strength-to-weight ratio (Rolland et al., 2014; Efe & Head, 2014; Ola & Jonas, 1993). AFRP bars are made of composite fibers and possess numerous other distinct properties such as excellent fatigue behavior, high tensile strength, and non-conductivity, while their thermal expansion is close to that of concrete. These bars govern structural behavior of casted elements when subjected to flexural stresses. The elastic modulus, tensile strength, and bond properties are the main mechanical properties of AFRP (Rolland et al., 2014; Ola & Jonas 1993; ACI 440.1R, 2006). Up to date, very little work has investigated the flexural behavior and performance of T-beams reinforced with AFRP and casted by Self compacted concrete. Lee et al. (Lee et al., 2011) investigated the externally strengthened T-beam behavior in shear and the performance of these beams. It was concluded that the strengthening length of the sheets, fiber direction combination, and anchorage have significant influence on the shear performance of strengthened deep beams. Tavares et al. (Tavares et al., 2008) studied the behavior of reinforced concrete beams reinforced with GFRP bars. They show that the capacity of the beams was lower than that of the steel-reinforced beam and it seen that similar flexural capacity can be achieved for the steel- and for the GFRP-reinforced concrete beams by controlling the stiffness. Buyukkaragoz et al. (Buyukkaragoz et al., 2013) made a numerical study of concrete beams reinforced with AFRP bars to focus on the flexural behavior. The load on the beams found by finite elements FE was near to those from the effective moment of inertia expressions, the numerical ultimate moments also correlated well with the analytical values of concrete stress-strain models. Numerical analyses, which hardly predict the sudden reduction in the flexural rigidity of FRP-reinforced concrete beams due to the crushing of cover concrete, were shown to provide somewhat conservative deflection estimates.

2. RESEARCH SIGNIFICANT

In the present study, series of T-beams were tested to investigate the flexural behavior of T-section casted with SCC and reinforced with AFRP bars, to show their influence on load carrying capacity, toughness, and changing of properties while comparing with normal concrete with conventional steel bars. A total of 12 T-beams sections (9 reinforced by AFRP and 3 with steel bars) were designed to be deficient in flexure. The behaviors of the tested beams were studied during static third -point loading tests with crack patterns. The flexural behaviors were observed from the load-displacement curves. In addition, a comparative study was made between the present experimental results and theoretical results based on ACI440 (ACI440, 2006).

3. EXPERIMENTAL PROGRAM

The test program include fabrication of T-beams with three different compressive strengths of self-compacted concrete 60, 80, and 100 MPa, and using AFRP as main longitudinal reinforcement with different ratios (less than balance reinforcement, between balance and $1.4\rho_b$ ratio, and more than $1.4\rho_b$). Also three beams were casted using conventional steel bars with balanced reinforcement ratio, as a reference

3.1. Details of Flexural -Deficient T-Beams

A total of 12 reinforced SCC T-beams, 3 normal reinforced with steel bars and the other with AFRP bars was designed and casted. T-beams dimension were: web width 75mm, flange width 200mm, flange thickness 50mm, over all height 200mm, with beam length of 1100mm as shown in Fig.1. The notation (TA) was given for Aramid reinforced samples, while (TS) was given for normal reinforced samples. The reinforcing details of all the group samples are given in Table.1.

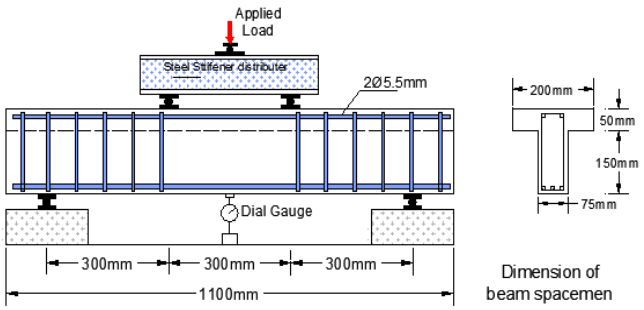

Figure 1: Tested beam geometry

3.2. Details of Self Compacted Concrete

Control specimens' properties of the SCC in fresh state and hardened state were studied through a series of casting and testing of concrete specimens Table (2). Properties of SCC in fresh state which

includes: slump flow test which investigate the filling ability and flow time (T50), The V-funnel test which measures the flow time for SCC needs

Table (1) Tested beam details

G. No.	Sample	SCC strength f_c (MPa)	Rein.Ratio ρ	No. of main bars	Stirrups	Details
1	TS-11	60	0.83	2-Ø8mm	Ø5.5@ 75 mm	ρ_b
	TA-12		0.55	1-Ø5mm		$\rho < \rho_b$
	TA-13		1.09	2-Ø5mm		$\rho_b < \rho < 1.4\rho_b$
	TS-14		1.64	3-Ø5mm		$\rho > 1.4\rho_b$
2	TS-21	80	0.97	2-Ø10mm	Ø5.5@ 75 mm	ρ_b
	TA-22		0.82	2-Ø5mm		$\rho < \rho_b$
	TA-23		1.23	3-Ø5mm		$\rho_b < \rho < 1.4\rho_b$
	TA-24		1.64	4-Ø5mm		$\rho > 1.4\rho_b$
3	TS-31	100	0.78	2-Ø10mm	Ø5.5@ 75 mm	ρ_b
	TA-32		0.66	3-Ø5mm		$\rho < \rho_b$
	TA-33		1.31	4-Ø5mm		$\rho_b < \rho < 1.4\rho_b$
	TA-34		1.64	5-Ø5mm		$\rho > 1.4\rho_b$

to pass a narrow opening that show the filling ability blocking and/or segregation do not take place, and L-box test which measures the reached height of fresh SCC in the formworks, were examined and listed in Table (3). In the hardened state, the compressive strength and modulus of elasticity tests were carried out (Yaseen S.A. et al, 2017) (Hamad Amen, et al, 2018).

Table (2) Self-compacted concrete mix proportion

Mix No.	Cement kg/m3	Gravel kg/m3	Sand kg/m3	Silica Fume kg/m3	Stone Powder kg/m3	%Super plasticizer By weight of cement	Free water kg/m3	SCC strength at 28 day f_c (MPa)
Mix 1	380	850	900	38	57	1.40	155	60
Mix 2	440	800	900	44	66	1.20	165	80
Mix 3	480	900	720	48	72	2.10	139	100

Table (3) Fresh self-compacted concrete test results

Mix No.	Slump Flow (mm)	T_{50} (sec)	V-Funnel (sec)	L-Box (H1/H2)
Mix 1	645	4.45	9.65	0.88
Mix 2	675	3.12	8.4	0.91
Mix 3	565	6.85	12.32	0.8

4. RESULTS EVALUATION

4.1. Outcome Results

The results of all specimens with their 1st cracking load, deflection, ultimate load (P_u), and their final deflections are summarized in Table 4.

Table (4) Tests results of SCC T-Beams

Sp.No.	G.No.	Samples	SCC strength f `c (MPa)	First Crack load kN	Deflection at first crack mm	Failure load kN	Deflection mm
1	G1	TS-11	60	21.07	1.4	52.67	5.99
2		TA-12		7	3.17	33.6	79.11
3		TA-13		8.64	5.9	60.45	87.26
4		TA-14		9.82	6.2	70.7	91.61
5	G2	TS-21	80	22.69	0.91	75.64	5.96
6		TA-22		4.76	2.9	65.03	80.55
7		TA-23		6.86	3.8	84.38	83.06
8		TA-24		10.16	5.27	94	89.15
9	G3	TS-31	100	23.47	0.91	78.25	5.03
10		TA-32		8.08	1.22	95.35	81.98
11		TA-33		9.13	3.2	107.57	85.19
12		TA-34		9.37	3.53	119.93	91.2

4.2. Crack Pattern and Modes of Failure

The flexural crack of the T-beam specimens starts at the bottom close to mid-span of beam when the applied load reached the values shown in Table 4. The first crack load increased slightly when the concrete strength changed from 60 to100MPa for the same reinforcement ratio. Steel reinforced specimens had extremely lesser deflection at first crack at very higher loads compared with aramid reinforced beams. Number of cracks increases by load increasing and extend upward, indicating the neutral axis movement upward as shown in Fig. 2. Further loading on specimens, cracks propagated typically as for ordinary flexural beams. The cracks at the failure stage in the AFRP reinforced beam were mainly vertical cracks under the applied load. These cracks had similar shape but larger width than the cracks in the steel reinforced beam. The final crack spacing approximately was 2.3, 3.4, 5.8 mm for the three ratios respectively. The maximum observed crack-width in beams reinforced with AFRP bars is three to five times with that of normal steel reinforced beams. In contrast, the cracks in the steel-reinforced beam were mainly one vertical and two inclined cracks; all of them started from bottom and moved up to where the load line was imposed. Observation of the cracks shows that the crack propagation was much progressive on the AFRP beams than steel reinforced beam. The number of cracks was much larger in the AFRP specimens compared to the normal T-beams. All beams failed under compression failure at regions close to the loading points. On the normal beam, the failure was initiated by the yielding of the steel reinforcement and followed by the compression failure of the concrete. The final deflections of AFRP beam ranged between 80-90mm more than the steel reinforced beams which was 6 mm.

4.3. Compressive Strength Effects on Ultimate Capacity

A different group of T-beams with same reinforcement ratios are compared for each of the compressive strength of SCC taken in this paper. The increase of ultimate capacity seen to be small in low AFRP ratios and increased when the strength changed from 60MPa, to 80MPa, and then to 100MPa for reinforcement ratios listed in Table 1, respectively as shown in Fig. 3.

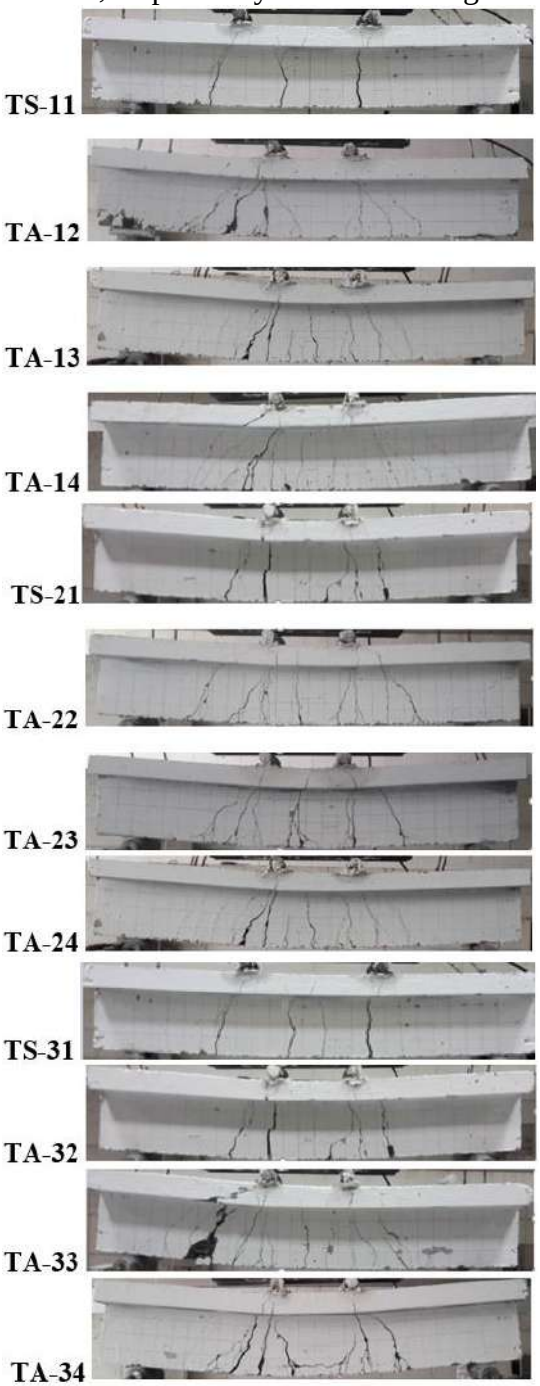

Figure 2: Crack pattern of T-beams

The smooth increase of load carrying capacity is observed for the three samples of each strength indicated. The AFRP and steel reinforced beams that have the same reinforcement ratio were compared, the steel reinforced beams load carrying capacity differs by 56.7%, 15.33%, and -17.93% than aramid reinforced beams respectively for concrete strength's groups. The steel reinforced beams show an increase of 43.6% in load carrying capacity when the concrete strength changed from 60 to 80 MPa and increase of 3.45% when the strength changed from 80 to 100 MPa.

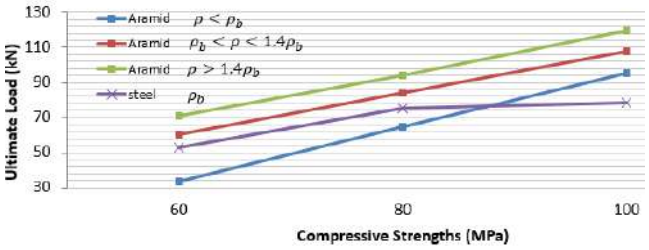

Figure 3: Ultimate load capacity vs SCC strength

4.4. AFRP Reinforcement Ratio Effect

Three beams were reinforced with ratios ($\rho < \rho_b$, $\rho_b < \rho < 1.4\rho_b$ and $\rho > 1.4\,\rho_b$ for each SCC concrete type. Three beams were reinforced with normal strength steel bar having balanced ratio of reinforcement for comparison purposes were tested under static loading conditions. The reinforcement ratio improves the final resisting load as the ratio increase. The increase was 79.9%, 29.7%, and 12.8% for each compressive strength group when the ratio changed from $\rho < \rho_b$ to $\rho_b < \rho < 1.4\rho_b$, and the increase were 16.9%, 11.4%, and 11.4% for each compressive strength when the ratio changed from $\rho_b < \rho < 1.4\rho_b$ to $\rho > 1.4\,\rho_b$ as shown in Fig. 4.

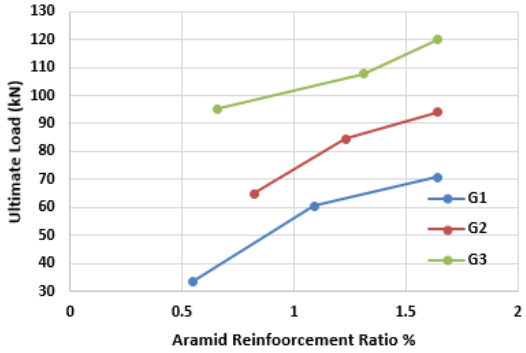

Figure 4: Ultimate load capacity vs AFRP ratio

4.5. Load Displacement Relations

The relationships between applied load stages and their deflection response at the mid span are shown in figs. 5, 6, 7 for AFRP reinforced beams, and Fig.8 for steel reinforced beam. An extensive deformation was noted at failure as shown in Fig.

2 and Figs. 5, 6, 7 in aramid beams and the effect of increasing the AFRP ratio had slight influence on reducing the deflections in the beams; these are due the low elastic modulus of AFRP. The increase of the reinforcement ratio had an effect of increasing the ultimate load capacity of the beams. A very small deflection was seen in normal strength steel reinforced beams with a moderate final load carrying capacity. The deformed Steel bars carry a load better than AFRP because it is stiffer. From a large load carrying intensities shown, it is concluded that the AFRP bars develop high tensile stress like steel bars higher at high strain levels. An increase in load carrying capacity was seen in comparison of similar AFRP ratio groups by changing the concrete strength. For $\rho < \rho_b$ group an increase in load were 93.5% and 46.6% when the strengths changed from 60-80 MPa and 80-100 MPa respectively, for $\rho_b < \rho < 1.4\rho_b$ group an increase in load was 39.58% and 27.4% when the strengths changed from 60-80 MPa and 80-100 MPa respectively, and for $\rho > 1.4\,\rho_b$ group an increase in load was 32.95% and 27.58% when the strengths changed from 60-80 MPa and 80-100 MPa respectively. The displacements in steel reinforced beams were too smaller compared with AFRP beams. The displacements reduced with increasing the concrete strength, but the load carrying capacity increased with increasing the SCC strength as seen in Fig. 8.

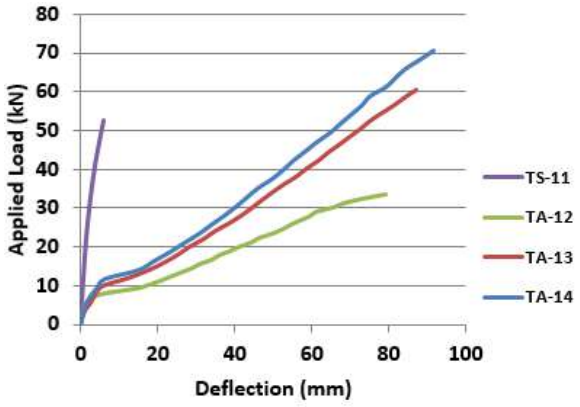

Figure 5: Force-Displacement response for G1- $\acute{f}_c$ = 60MPa Aramid and steel reinforced T-beams

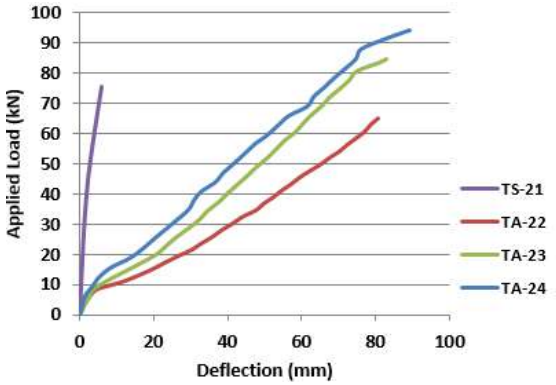

Figure 6: Force-Displacement response for G2- $\acute{f}_c$ = 80MPa Aramid and steel reinforced T-beams

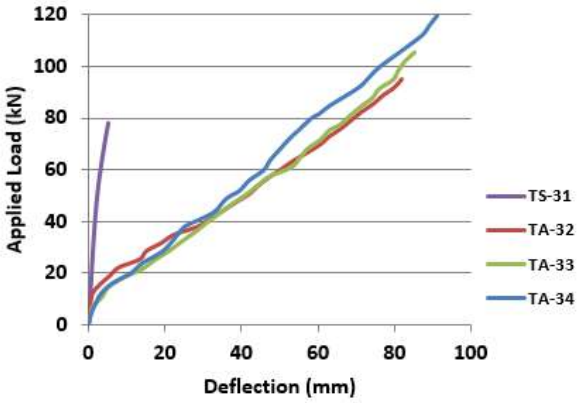

Figure 7: Force-Displacement response for G3- $\acute{f}_c$ = 100MPa Aramid and steel reinforced T-beams

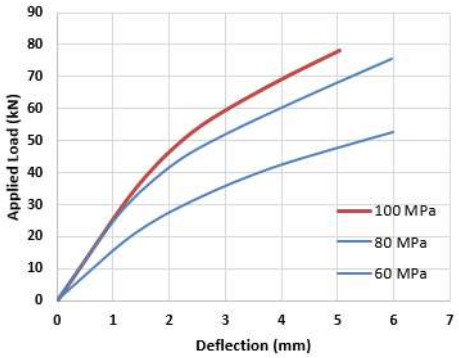

Figure 8: Force-Displacement response for steel reinforced T-beams

5.THEORETICAL STRESS BLOCK EVALUATION

When the neutral axis depth lay within the flange of T-beam ($a \leq$ hf), it means the beam acts as a rectangular section with a width of the concrete compression block is equal to the b_f (flange width), Fig. 9. The neutral axis depth c (and consequently the equivalent stress block evaluated) is found from the axial force and moment equilibrium equations. The value of (a) for the concentric loading cases of T-beam increases as the concrete strength increases

(related to strain value), and vice versa. It can be easily observed from Fig.10 that the SCC compressive strength affects the values of (a) for the same reinforcement ratio groups (Aramid & Steel). An increase in block depth was observed by increasing the strength of concrete for AFRP $\rho < \rho_b$ and steel $\rho = \rho_b$, while it Noted that the depths for AFRP $\rho_b < \rho < 1.4\rho_b$ and $\rho > 1.4\rho_b$ were too large and equal for the same group of reinforcement ratio. The effect of reinforcement ratio on the values of (a) for the same groups of SCC compressive strength is shown in fig.11. It is recorded that there is a significant increase in the depth of compressive stress by increasing the reinforcement ratio for all AFRP samples.

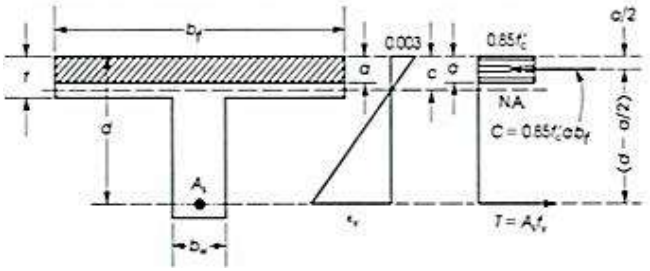

Figure 9: Flanged T-beam ($a \leq h_f$)

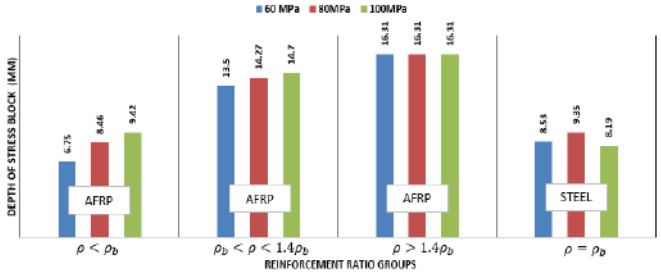

Figure 10: Effect of SCC compressive Strength on Equivalent stress block

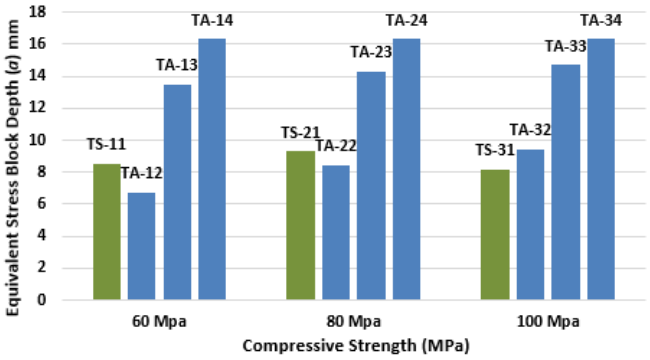

Figure 11: Effect of reinforcement ratio of (Aramid & Steel) on depth of Equivalent stress block

6. ANALYTICAL METHODS FOR COMPARISON USING ACI440-06

The difference in properties of used bars AFRP and normal steel, leads to obtain different strengths and strains which affects the determination of actual and balanced reinforcement ratio, and consequently, affected on equivalent stress block depth. The depth of stress block and the ultimate moment capacity for the under reinforced (for all types of reinforcement) are found by using conventional ACI 440 equations (Eq 1 & 2).

$$\epsilon_s \geq \epsilon_y \;; \quad c = \frac{a}{\beta_1} \;;$$

$$\epsilon_s = \left(\frac{d-c}{c}\right)\epsilon_{cu} \geq \epsilon_y \;;\; a = \frac{A_s f_s}{0.85 f'_c b} \qquad Eq.1$$

$$M = A_s.f_s.\left(d - {}^{a}/_{2}\right) = \alpha_1.f'_c.a.b.\left(d - {}^{a}/_{2}\right) \qquad Eq.2$$

The experimental versus the theoretical data for comparison are presented in figs. 12,13,14,15, &16. Ultimate load capacity versus SCC strength and reinforcement ratio are plotted for AFRP and normal steel reinforced T-beams. The effect of increasing the of self-compacted concrete strength lead to an increasing It is observed that as the SSC strength increases, the load carrying capacity increases, the increasing ratio was 183% for $\rho < \rho_b$, 78% for $\rho_b < \rho < 1.4\rho_b$ and 70% for $\rho > 1.4\,\rho_b$ as the strength change from 60MPa to 100MPa fig.12. The increase in the reinforcement ratio leads to increase the load capacity as well, the load carrying capacity increased by 110.4% for 60MPa, 44.5% for 80MPa, and 25.77% for 100MPa when the reinforcement ratio change from($\rho < \rho_b$ to $\rho > 1.4\,\rho_b$) fig. 13. From the plotted relation it is seen that there is good agreement between the experimental and theoretical results with increasing compression strength. Similar relation is seen between the experimental and theoretical data for conventional steel bars. It is seen that the ACI440 method was more conservative.

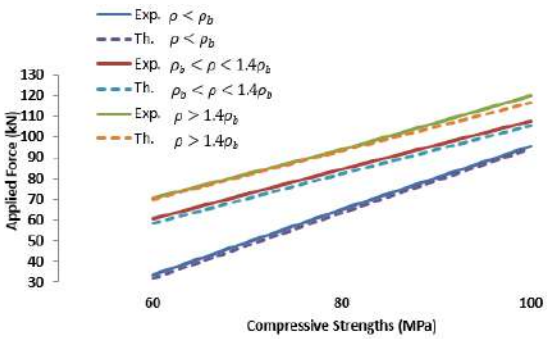

Figure 12: Analytical and experimental beam capacity vs SCC strength

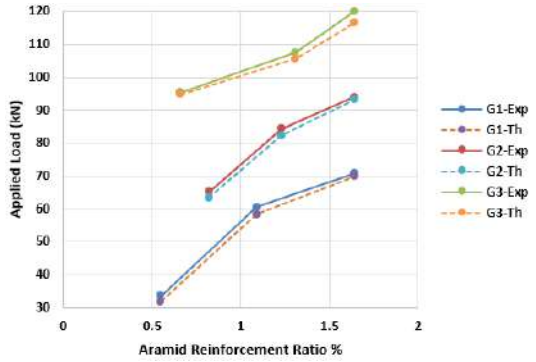

Figure 13: Analytical and experimental beam capacity vs Reinforcement Ratio

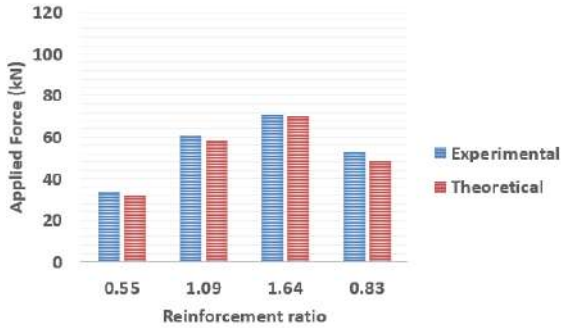

Figure 14: Analytical and experimental beam capacity vs Reinforcement Ratio for G1-$\acute{f}_c$=60MPa

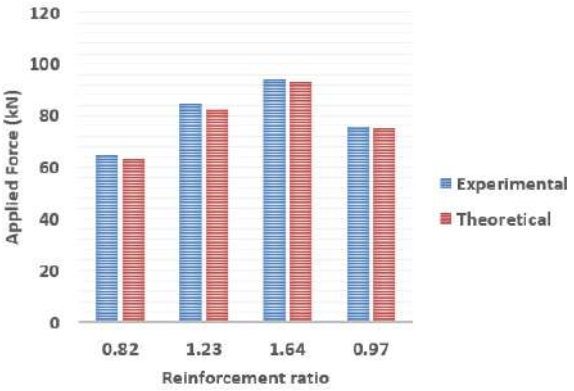

Figure 15: Analytical and experimental beam capacity vs Reinforcement Ratio for G2-$\acute{f}_c$=80MPa

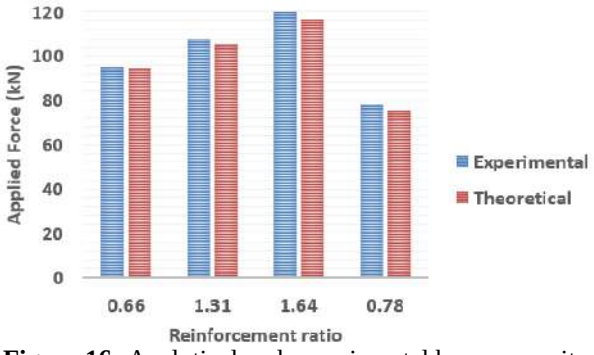

Figure 16: Analytical and experimental beam capacity vs Reinforcement Ratio for G3-$\acute{f}_c$=100MPa

7. CONCLUSION

1-The final deflection increases with the increase of the reinforcement ratio for the three group ($\rho < \rho_b$, $\rho_b < \rho < 1.4\rho_b$ and $\rho > 1.4\,\rho_b$), while the deflection was limited in the deformed normal steel bar reinforced beams, which reflects to toughness enhancement compared with steel bars.

2- An increase in load carrying capacity were seen in comparison of similar AFRP ratio groups by changing the concrete strength, for $\rho < \rho_b$ group an increase in load were 93.5% and 46.6% when the strengths changed from 60-80 MPa and 80-100 MPa respectively, for $\rho_b < \rho < 1.4\rho_b$ group an increase in load were 39.58% and 27.4% when the strengths changed from 60-80 MPa and 80-100 MPa respectively, and for $\rho > 1.4\,\rho_b$ group an increase in load were 32.95% and 27.58% when the strengths changed from 60-80 MPa and 80-100 MPa respectively.

3- The steel reinforced beams load carrying capacity differs by 56.7%, 15.33%, and -17.93% than aramid reinforced beams for all concrete strength's groups for balanced reinforcement ratio.

4-The steel reinforced beams show an increase of 43.6% in load carrying capacity when the concrete strength changed from 60 to 80 MPa and increase of 3.45% when the strength changed from 80 to 100 MPa.

5- The reinforcement ratio improves the final resisting load as the ratio increases. The increase was 79.9%, 29.7%, and 12.8% for each compressive strength when the ratio changed from $\rho < \rho_b$ to $\rho_b < \rho < 1.4\rho_b$. and the increase were 16.9%, 11.4%, and 11.4% for each compressive strength when the ratio changed from $\rho_b < \rho < 1.4\rho_b$ to $\rho > 1.4\,\rho_b$.

6-The final crack spacing approximately were 2.3, 3.4, 5.8 mm for the three ratios respectively. The maximum observed crack-width in beams reinforced with AFRP bars is three to five times that of normal steel reinforced beams.

7- In theoretical calculation, an increase in block depth was obtained when increasing the strength of concrete for AFRP $\rho < \rho_b$ and steel $\rho = \rho_b$, while the depths for AFRP $\rho_b < \rho < 1.4\rho_b$ and $\rho > 1.4\rho_b$ were too large and equal for the same group of reinforcement ratio.

8- It is from data comparison with experimental work that the ACI440 method was more conservative when applied on SCC AFRP reinforced beams.

REFERENCES

ACI 440.1R-06. 2006. *ACI Committee 440 Guide for the Design and Construction of Concrete Reinforced with FRP Bars*, American Concrete Institute, Farmington Hills, Michigan.

ABDULLAH A.H, AND ABDUL KADIR M.R. 2016. NSM FRP Reinforcement for Strengthening Reinforced Concrete Beams-Overview, *ZANCO Journal of Pure and Applied Sciences*, 28(2), 178-200.

BUYUKKARAGOZ, A., KALKAN, I., & LEE, J. H. 2013. A Numerical Study of the Flexural Behavior of Concrete Beams Reinforced with AFRP Bars. *Strength of Materials journal*, 45(6), 716–729.

DAIA, Z., & THOMAS, V.2002. Checking the Limit State of Existing T-Beam Girder Bridges. *6th International Conference on Short & Medium Span Bridges SMSB-VI, Vancouver BC, Canada*, 1, 691-698.

EFE, S., & HEAD, M. 2014. Structural behavior and response analysis of aramid fiber reinforced polymer reinforced bridge columns under combined loading. Tenth U.S. *National Conference on Earthquake Engineering Frontiers of Earthquake Engineering*. Anchorage, Alaska.

ERKI, M. A., & RIZKALLA, S. H. 1993. FRP reinforcement for concrete structures. *A sample of international production*.

GUOWEI, N., BO, L. , XIAO L., & WENSHANG, Y. 2011. Experimental Study on Concrete T-Beams Strengthened with Carbon Fiber Reinforced Polymer (CFRP) Sheets on Three Sides. *Systems Engineering Procedia*, 1, 69–73.

HAMAD AMEN D.K., SABIR M.A, YASEEN S.A. 2018.Size and Shape effects of testing specimens on the compressive Strength of SCC, *ZANCO Journal of Pure and Applied Sciences*, 30(1): 65-72.

LEE, H. K., CHEONG, S. H., HA, S. K., & LEE, C. G. 2011. Behavior and performance of RC T-section deep beams externally strengthened in shear with CFRP sheets. *Journal of Composite Structures*, 93, 911–922.

OLA G., & JONAS H. 1993. Aramid Fiber Rods as Reinforcement in Concrete. *Lund Institute of Technology, Department of Structural Engineering, Report TVBK-5067*, Sweden.

RAYA, H. H., & BILAL, S. H. 2015. Performance of High Strength Self-Compacted Concrete Beams under Different Modes of Failure. *International Journal of Concrete Structures and Materials*, 9(1), 69–88.

ROLLAND, A., CHATAIGNER, S., BENZARTI, K., QUIERTANT, M., ARGOUL, P., & PAUL, J-M. 2014. Mechanical behaviour of aramid fiber reinforced polymer (AFRP) rebar/concrete interfaces. *Transport Research Arena*, Paris.

TAVARES, D. H., GIONGO, J. S., & PAULTRE, P. 2008. Behavior of reinforced concrete beams reinforced with GFRP bars. *IBRACON Structures and Materials Journal*. 1(3), 285 – 295.

TIAGO, C., CARLOS, C., & HUGO, B. 2010. Raquel Fernandes Paula. Flexural Behavior of RC T-Beams Strengthened with Different FRP Materials. *The Third International fib Congress and Exhibition "Think Globally, Build Locally"*.

YASEEN S.A., SABIR M.A., HAMAD AMEN D.K, & ABDULRAZZAQ N.M .2017.Effects of curing types on the strength of high Strength self-compacted concrete.*ZANCO Journal of Pure and Applied Sciences*, 29(5), 22-29.

YASSER, S. 2012. Structural performance of Self-Consolidating Concrete used in reinforced concrete beams. *KSCE Journal of Civil Engineering*, 16(4), 618–626.

ZANCO Journal of Pure and Applied Sciences
The official scientific journal of Salahaddin University-Erbil
https://zancojournals.su.edu.krd/index.php/JPAS

ISSN (print):2218-0230**, ISSN (online):** 2412-3986**, DOI: http://dx.doi.org/10.21271/zjpas**

RESEARCH PAPER

Evaluation of Full-Scale Concrete Frames Exposed to Natural Fires at Early Ages.

Muhammad Ismaiel Omer[1*], Dilshad Kakasoor Jaf [2]

[1&2]Department of Civil, College of Engineering, Salahaddin University-Erbil, Kurdistan Region, Iraq

A B S T R A C T:

This article presents the evaluation of full scale reinforced concrete frames subjected to natural fire at early age. The test program consisted of constructing three large frames of reinforced concrete as well as revealing them to the natural fire by shooting their formwork when the age of concrete achieves three and five days. The evaluation of reinforced concrete frames was done by the load test method as described in the American Concrete Institute (ACI), namely the 24 hrs load test method, which is evaluation criteria that have been in use for several decades. For each frame, the structural evaluation based on deflection criteria is discussed. Results showed that the frame exposed early to natural fire was generally more affected than the other frame, as its midspan deflection was increased to about 109% if compared to frame not exposed to fire.

KEY WORDS: Reinforced concrete structures, Natural fire, Early ages, ACI load test methods
DOI: http://dx.doi.org/10.21271/ZJPAS.32.2.12
ZJPAS (2020) , 32(2);115-128 .

1. INTRODUCTION

Concrete is the composite material widely used in Iraq's structural system and worldwide (Bikhiet et al., 2014). The common material used in Iraq for molding formwork of reinforced concrete structures is timber. Timber is a famous material that burns rapidly, particularly in the summer season, when oiled. Therefore, in recent years, in some developing countries numerous fire accidents occurred in reinforced concrete buildings during the construction stage, due to problems with the construction procedure and on-site management (Lu et al., 2019). The concrete in the mold usually reaches an early age in these conditions (i.e., the "young"), and the inner chemical composition of early-age concrete differs from that in the carrier due to unfinished early-age hydration.

The literature contains overall evaluations of concrete performance at high temperatures (Khoury, 1992, Schneider, 1988, Xiao and König, 2004). An extensive study has revealed that concrete is a multipurpose material and, if properly designed, can be fundamentally fire-resistant. The reaction to a natural fire of the concrete material and structure relies on the kind of fire, which can differ significantly (Khoury et al., 2007).

Available studies have been established either using “time-temperature curve” methods sometimes called “standard fire curves” such as those mentioned in ISO 834 (ISO 834, 2014) and ASTM E119 (ASTM E119, 2000) (based on experimental observations) or using “natural fire”

* **Corresponding Author:**
Muhammad Ismaiel Omer
E-mail: muhammad.omer@su.edu.krd
Article History:
Received: 18/09/2019
Accepted: 17/11/2019
Published: 22/04 /2020

methods (Behnam and Ronagh, 2013). The studies showed that the behavior of structural elements under natural fire is completely different from that observed during the standard fire tests. The standard fire curve is not representative of a real fire in a real building (Li et al., 2015). However, fires in compartments are simulated using natural fire where both heating and cooling phases are taken into consideration, and they provide a realistic illustration of a fire event (Behnam, 2018).

Bisby et al. (2013) results have been reviewed for non-standard large-scale fire test structures. They noted that non-standard fire tests conducted worldwide over the last three decades detected different weaknesses in our knowledge of natural fires; in most cases, standard furnace tests could not identify these weaknesses.

Fire causes heat to flow into the concrete structure. The temperature in the concrete mass will rise, thereby causing thermal expansion of the constituents, evaporation of moisture, the buildup of pore pressure, and the degradation of mechanical properties (Khoury et al., 2007). The deterioration of concrete strength due to short-term exposure to elevated temperature (fire) has attracted attention in the last decades. The nature of the fire, types of structure, and loading system are reasons that the modes of concrete failure under fire exposure will be varied (Bikhiet et al., 2014).

When concrete exposed to high temperatures, the chemical composition and physical structure change considerably, resulting in a significant reduction of the mechanical properties, such as strength, modulus of elasticity, and volume stability. These changes are related to differential thermal expansions between the aggregate and cement paste associated with dehydration of the cement paste due to the decomposition of the calcium silicate hydrate (C-S-H) (Kirchhof et al., 2015). However, when the temperature reaches about 300 °C, some of the combined water from C–S–H and chloraluminite hydrates and the interlayer (C–S–H) water will evaporate. Calcium hydroxide $Ca(OH)_2$, which is one of the essential compounds in cement paste, dissociates at around 530 °C, thereby resulting in the shrinkage of concrete (Chen et al., 2009).

While severe fire can cause significant damage to reinforced concrete structures, reinforced concrete structures failure is rarely caused by fire damage. If a fire accident takes place during the construction stage, then the residual strength of younger reinforced concrete structural elements should be assessed by the engineers so that the safety and reparability of the structure after the fire evaluated (Lu et al., 2019).

An important issue involving researchers and engineers in many countries is the evaluation of existing buildings (Pucinotti, 2015). In-situ load testing is a method widely used for evaluating the strength of the existing structure (ElBatanouny et al., 2015). The U.S. is a century-old tradition that the in-situ load testing of concrete structures where one of the 1890s ' oldest cases with excellent documentation. The most direct evidence of the exclusive and novel performance of construction materials and methods was on-site load testing in the early days. The American Concrete Institute ACI started standardizing load testing processes of concrete structure in 1920. The ACI addresses in-situ load testing in two standards: a) ACI 318 chapter 27 “Building Code Requirements for Structural Concrete” (ACI 318-19, 2019), and b) ACI 437 “Code Requirements for Load Testing of Existing Concrete Structures” (ACI 437.2-13, 2013). The test criteria for passing the stress test focused on maximum deflection under continuous load in combination with deflection recovery following removal of the test load (Galati et al., 2008).

In technical literature, there is almost no relevant study available on assessment of early ages of reinforced concrete frames exposed to natural fire. Thus, an investigational study was performed on the strength assessment of early-age concrete by in situ load test after exposed high-temperature. The consequence of removing the formwork was identified by firing the wood on reinforced concrete frames at an early age.

2. MATERIALS AND METHODS

2.1 Frame Dimensions and Details

The test program consisted of casting three frames of reinforced concrete, which has the same dimensions. These dimensions are shown in Figure 1; the column cross-section was 300×300 mm; the beam width was 300 mm, 300 mm dropped below the slab; and the slab thickness was 120 mm. The span of the frame in both directions between the center of the columns was

4000 mm, and the height of the column was 3000 mm. The test frame was supported on four single column footings built specifically for this purpose.

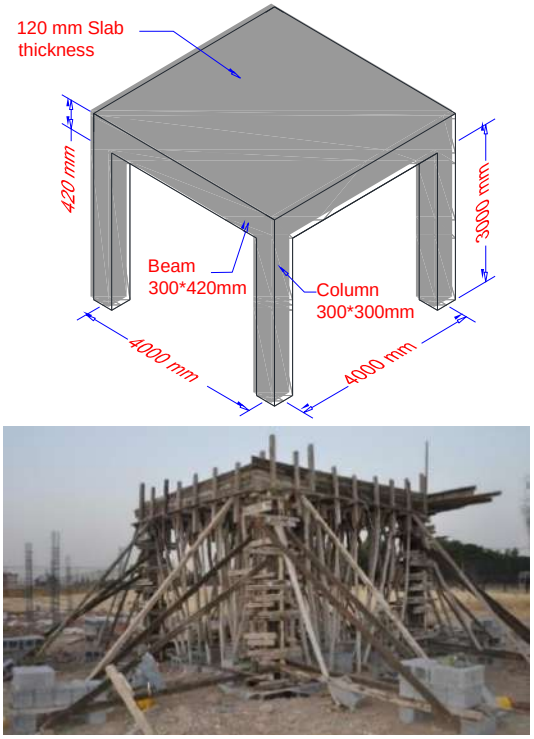

Figure 1: Dimensions of frame structure

The casting of reinforced concrete frames was performed by ready mixed concrete, which was provided by Lafarge Company (a special company for supplying high quality ready mixed concrete). Furthermore, the casting of the test frame occurred in two stages. The footings were cast first on the strong-floor. The columns, beams, and slab of the frame were cast in one stage during the pour of concrete in the structure. Care was taken during mixing and placing operations to ensure consistent concrete properties and consolidation. A sufficient number of control specimens were collected to monitor strength development in the test frame, particularly for determining the strength of concrete in the frame at the time of the load test.

The reinforcement details of the frame are shown in Figure 2 and Figure 3. Table 1 shows the detail of the full-scale reinforced concrete frames and variables. The primary variable used in this investigation is the age of concrete when subjected to fire in order to understand the effect of concrete age on reinforced concrete frame deformation, as presented in Table 1.

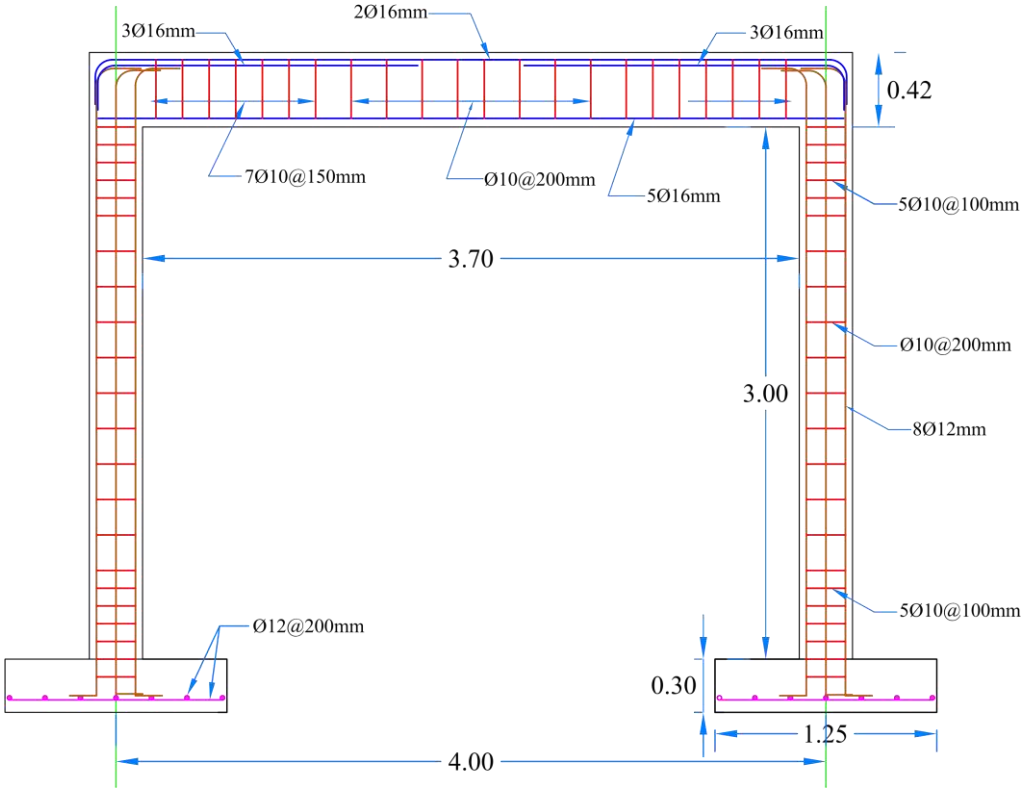

Figure 2: Reinforcement details of column, beam and footing

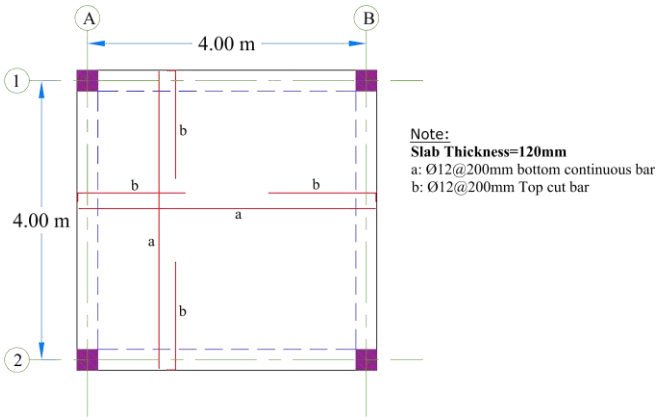

Figure 3: Reinforcement details of slab

Table (1) Frames with variables

Frame No.	f_{cu} (MPa)	Exposed to fire	Age at fire exposure (Days)
FF3	33.5	yes	3
FF5	41.9	yes	5
FN	38.3	no	Nil

2.2 Materials

Three reinforced concrete frames were constructed using ordinary Portland cement / Lafarge OPC, water, fine aggregate, crushed aggregated gravel was locally available used as coarse aggregate with a maximum size of 19 mm. The mix proportion used in fabricating reinforced concrete frames is presented in Table 2.

Table (2) Mix proportion

Specified concrete strength f_{cu} (MPa)	W/C (%)	Cement (kg/m^3)	Water (kg/m^3)	Fine Aggregate (kg/m^3)	Coarse Aggregate (kg/m^3)
35	0.51	356	182	701	1131

2.3 Time–Temperature Curve

In any fire test, it should follow one kind of the time-temperature curve. Furthermore, there are two types of time-temperature curves; standards and natural. However in the current paper we prefer the stance taken by Harmathy and Lie who rightly noted that "it always must be borne in mind that in a strict sense standard fire endurance (testing) is not a measure of the actual performance of an element in fire, and, furthermore, that it is not even a perfect measure for comparison" (Harmathy and Lie, 1970).

After creating a wooden mold for the concrete frame, then cast with concrete. The concrete curing process began and continued until the concrete age was three days for FF3 and five days for FF5. Then the wooden mold of the reinforced concrete frame was burned, as shown in Figure 4. The temperature of the inside concrete was increased after the wooden mold was burned. The measuring temperature inside the concrete was done by inserting k-type thermocouples into the mold before casting, as shown in Figure 5. A total of 11 number of embedded thermocouples were used and secured in place before the casting of concrete. The location of the thermocouples is shown in Figure 6.

Figure 4: Reinforced concrete frame exposed to fire

Figure 5: Insertion of a thermocouple

The average time-temperature curve, as shown in Figure 7, was drawn after all recorded temperatures were collected. Thus, with time, the

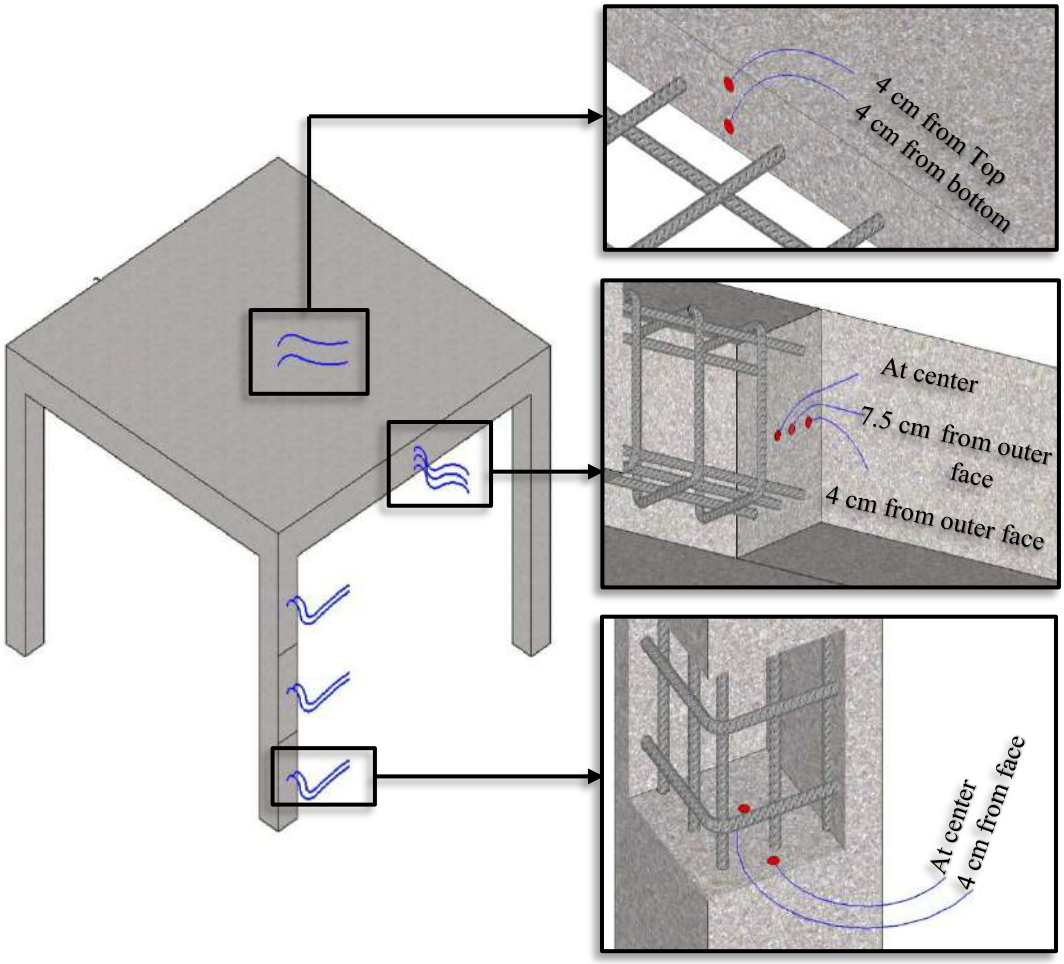

Figure 6: Location of thermocouples

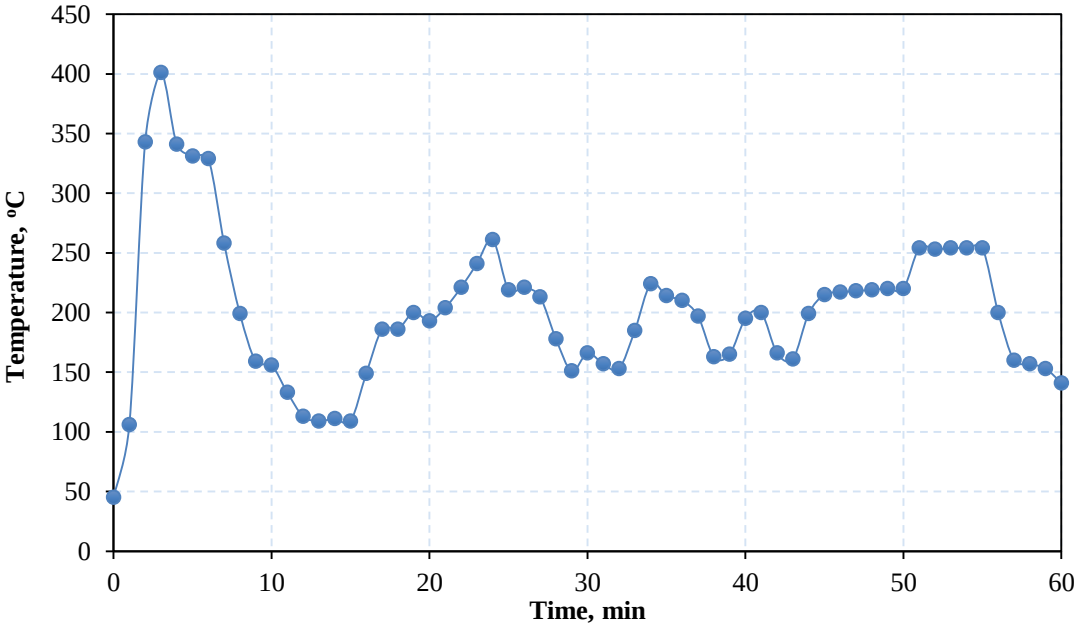

Figure 7: Average time-temperature relationship

temperature was increased. Flashover occurred between four and five minutes, after which, the fire advanced to its fully developed stage. Generally, the temperature rose significantly in the first 10 minutes and reached 400 °C due to the fire in the ignition step. The temperature then dropped to an average of 200 °C until the firing process was completed. The temperature variation inside the elements of the reinforced concrete frame is shown in Figures 8, 9, 10, 11 and 12. After the fire was burned all the wooden formwork of frame, then the frame was cooled in the air without using water.

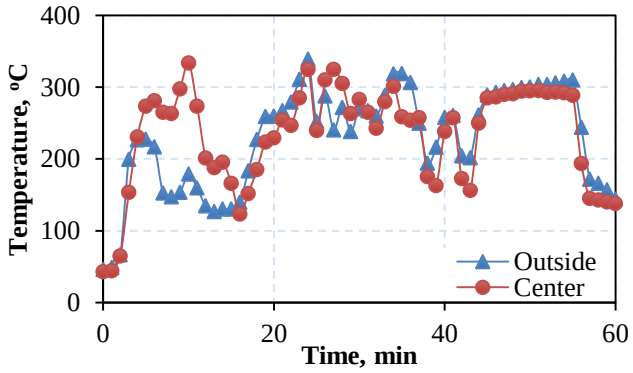

Figure 8: Time-temperature relationship of column at bottom

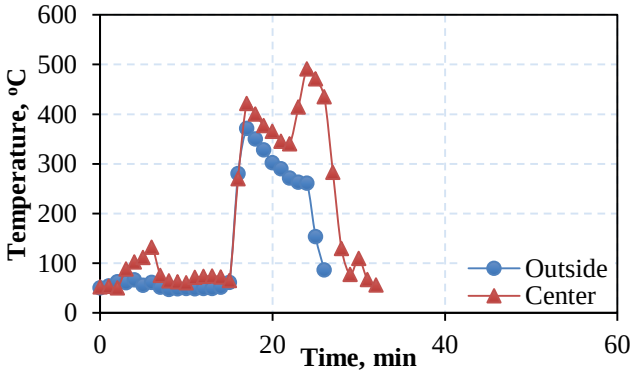

Figure 9: Time-temperature relationship of column at mid height

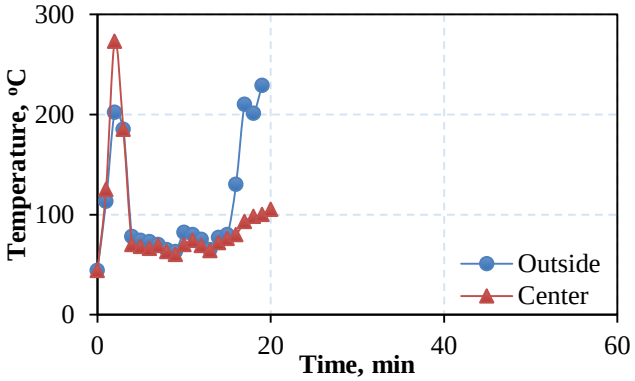

Figure 10: Time-temperature relationship of column at top

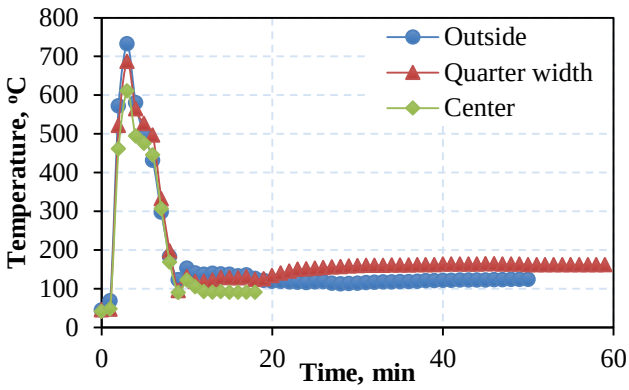

Figure 11: Time-temperature relationship of beam

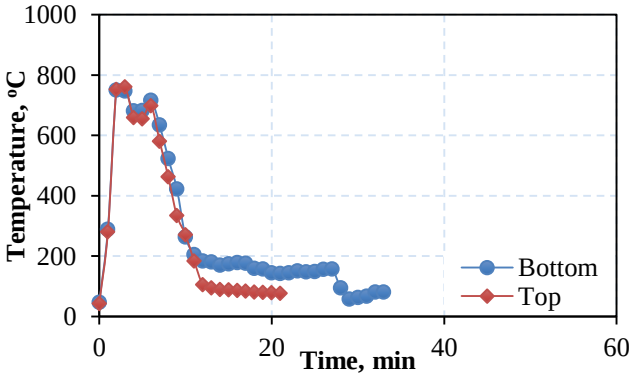

Figure 12: Time-temperature relationship of slab

2.4 Description of the Load Test

In particular, load testing was performed in a download method by uniformly distributing a load of sandbags with known weight over the entire area of the slab to check the deflection of the slab.

The design loads were simulated utilizing sandbags, and the weight of each sandbag was equal to 25 kg in order to be easy to installing and removing it on the structure. To distribute the sandbags on the slab equally, for this purpose, the slab divided into strips of 1m width to set the required load on one m^2. The sandbags were distributed precisely like a real load. These sandbags give the perfect response of the slab system and allow using lighter equipment at a low cost. The load test of the slabs was done in phases, as presented in the following sections.

Deflection measurements were taken in three different locations in the slab and the beams by installing dial gauges, while two locations were selected for column displacement in order monitoring the displacement during the load test, Deflection and displacement measurements were taken by 100-millimeter dial gauge which fixed on

stands and set below the slab & beams and beside of column. The first dial gauges were installed at the center point of the slab, and the second and third dial gauge was mounted in the middle of the two beams, while the fourth and fifth dial gauges were installed beside the column in two directions and at mid-height as shown in Figure 13.

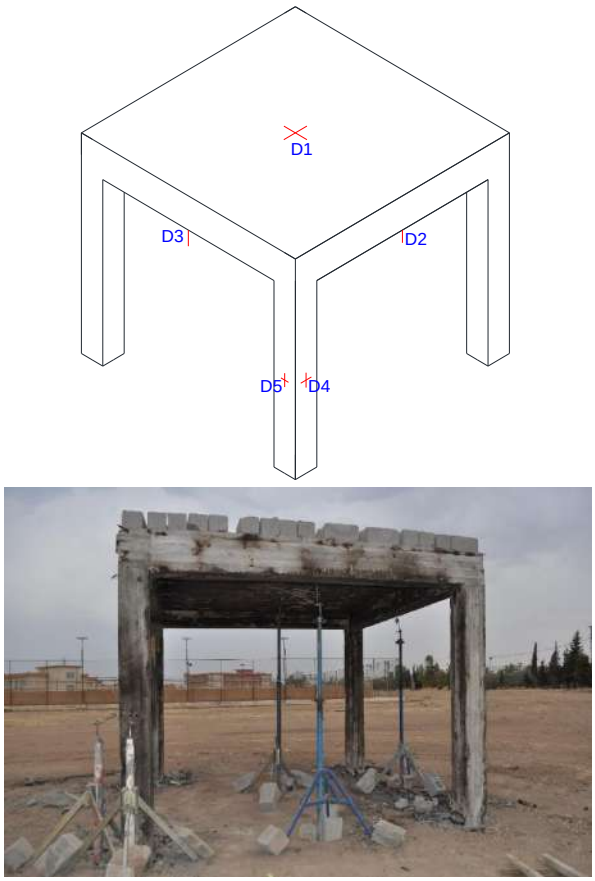

Figure 13: Location of installed dial gauges

2.5 Testing Procedure

The next section shows the conceptual steps followed in order to:

- Determine the value of the total test load magnitude during a preparatory phase.
- Obtain continuous structural assessment during the load test performance.

2.5.1 Protocols of Load Test

Both the ACI 318-19 chapter 27 (ACI 318-19, 2019) and ACI 437.2-13 (ACI 437.2-13, 2013) stated that the age of concrete structure should be higher than 56 days also stated that the 24 hrs load test consists in the monotonic loading of the structure up to the designed load level followed by a phase in which the load is sustained for a time period of at least 24 hrs. The two variables are considered for the principal evaluation, and they are:

- Dead load effect such as self-weight of the slab and superimposed load.
- Live load effect.

Thus, as suggested by ACI 318 (ACI 318-19, 2019) and ACI 437.2 (ACI 437.2-13, 2013), the total load (weight) applied to the slab can be calculated as follows.

Test Load Magnitude (TLM) to be applied is the larger of:

$TLM = 1.3\ (Dw + Ds) - D$ …..……..…….(1)

or $TLM = (1.0\ Dw + 1.1Ds + 1.6\ L + 0.5\ (Lr \text{ or } S \text{ or } R)) - D$ ……. ……(2)

where:

L: Live load = 250 kg / m^2

Ds: Superimposed dead load= 230 kg/m^2

Dw: Self-weight dead load= 288 kg/m^2

Total Dead Load (D) = (Dw + Ds) = 518 kg/m^2

$TLM = ((1.3\ (Dw + Ds)) - D) = 1.3 \times (518) - 518$

= 155 kg/m^2

or $TLM = (1.0\ Dw + 1.1Ds + 1.6\ L + 0.5\ (Lr \text{ or } S \text{ or } R)) - D$

$= (1.0 \times 288 + 1.1 \times 230 + 1.6 \times 250) - 518$

= 423 kg/m^2

TLM = 423 kg/m^2

2.5.2 Load Configuration

The load was applied uniformly throughout the area to the slab. Before installing sandbags, it should apply the superimposed dead load. For this purpose, concrete blocks were used as a superimposed dead load, and the load was 230 kg/m^2. The intensity of the load applied as determined in four layers of the sandbag, and a total load of these four layers is equal to the exactly calculated test load, which is distributed uniformly. In each layer of one square meter contains four sandbags (4×25kg=100 kg/m^2/layer).

The ACI requirements and standards for the structural performance must be considered and limited by two variables that are the maximum deflection and residual deflection. The limits of maximum deflection and the residual deflection are as follows:

$\Delta l \leq lt / 180$ ……..…….. (3)

$\Delta r \leq \Delta l / 4$ ……..... (4)

Where:

Δl: the maximum measured deflection during the test.

Δr: residual deflection measured after the 24 hrs recovery period following complete removal of the load after the load test.

lt: span of slab on the short side taken as the smaller of the distance between the center of supports or clear distance between supports plus thickness h of the member.

If the maximum deflection Δl measured during the test is less than 1.27mm or deflection as a fraction of span length, *lt* is less than *lt/2000*; the residual deflection requirements are given by equation (4) could be ignored.

2.5.3 Load Testing Procedure

1. At first, the concrete blocks were located on the slab as a superimposed dead load.
2. After 24 hrs of installing the concrete blocks, the dial gauges (No. 1 to No. 5) were installed on to the center of the slab and center of two beams and mid-height of the column in two directions are located as shown in Figure 13.
3. The magnetic base was used to install dial gages, as shown in Figure 14.
4. All the initial readings were recorded before the testing.
5. The load (sandbags) were added step by step from 0%, 25%, 50%, 75%, and 100% of the maximum test load, and each load step is held for 2-3 minutes.
6. After each of the loading steps records, all dial gauges reading except for the maximum test load (100%) that has to maintain 24 hrs, as shown in Figure 15.
7. After 24 hrs, the test load should be removed then record all dial gauges reading.

3.RESULTS AND DISCUSSIONS:

3.1 Visual Observations

The visual observation was done for the fire affected reinforced concrete frames. Spalling, cracking, and discoloration status of some components of the structure have recorded.

Figure 14: Installation of dial gage by using the magnetic base

Figure 14: Applying full load by using sandbags

3.1.1 Spalling

Spalling is the violent or non-violent breaking off of layers or pieces of concrete from the surface of a structural element when it is exposed to high and rapidly rising temperatures, as experienced in fires with heating rates typically 20–30 ^{o}C/min. Spalling can be grouped into four categories: (a)aggregate spalling; (b) explosive spalling; (c) surface spalling; (d) corner/sloughing-off spalling. The first three occur during the first 20–30 min into a fire and are influenced by the heating rate, while the fourth occurs after 30–60 min of fire and is influenced by the maximum temperature. Surface and explosive spalling are violent, while corner/sloughing-off spalling is non-violent. It could also be argued that surface spalling is a subset of explosive spalling, which is the most serious, and hence most researched, a form of spalling (Khoury, 2000).

Spalling begins to occur when the concrete reaches an elevated temperature of 250 °C. From 250-420 °C, some spalling occurs. After reaching 300 ^{o}C, concrete starts to lose its strength. Within 550-600 °C, cement-based materials experience creep and lose their load-bearing capacity (Iffat and Bose, 2016). As shown in Figure 16, despite the observed surface spalling at the bottom of the slab, the test frames did not suffer any significant spalling (loss of big chunks) of concrete or loss of cover (exposing reinforcement) at any location in the test frame.

Figure 16: Spalling and change color occurred in slab

3.1.2 Cracking

When reinforced concrete is subjected to high temperatures due to fire, the losses in compressive strength of concrete and the reduction in its stiffness are related to gradual deterioration of the hardened cement paste and the destruction of the bond between the cement paste and the aggregates. Also, thermal expansion causes internal cracking and spalling of concrete, as well as the debonding of the reinforcement bars (Riad et al., 2017).

No deterioration in the strength of the burned frames after load testing was observed. Despite the observed inelastic excursions, the test frames did not suffer any significant structural damage and noticeable cracking.

3.1.3 Discoloration

The color change of concrete is a significant indication of the effect of fire. Color change provides a perfect visual guide to estimating the temperature range to which concrete has been exposed at various depths during the fire. However, the change in color is not directly related to a change in mechanical properties, but the occurrence of a color change indicates a temperature range where the mechanical properties may start to decrease. Concrete may change color from its typical grey to pink or red between 300 – 600 °C, whitish-grey between 600 – 900 °C and buff between 900 – 1000 °C (Short et al., 2001).

After exposing the reinforced concrete frame to the natural fire by burning its wooden formwork, the inner face color of the frame was black due to wood smoke, but no major change in the color of concrete itself was observed as shown in Figure 16.

3.2 Fire Effect on Compressive Strength

The compressive strength of concrete cubes is plotted in Figure 17 as a function of the age of concrete. Before burning the wooden formwork of reinforced concrete frame, the concrete control specimens were put on the iron table, which was under the concrete frame. After burning, the concrete specimens were left in the laboratory environment without curing until the compressive strength test day. However, the test of the compressive strength of mature concrete cubes was done in the laboratory in which concrete cubes were curried totally until the age reached a specified day without being burned.

When the temperature is 150 ^{o}C, the evaporation of free water in the concrete specimens increases capillary pressure, which generates pore and capillary cracks inside the specimens, and then reduces concrete compressive strength (Chen et al., 2009). When the specimens are exposed to 350 ^{o}C, the free water in the specimens is subjected to continuous evaporation. Although the bound water is released from the cementitious substance and enhanced the bonding action (Khoury et al., 2002, Guo and Li, 1993), the continuous development of pores and capillary cracks finally results in a further decrease in concrete's strength.

The significant difference in deformation, the self-expansion, and breakage significantly reduce compressive strength (Liu et al., 2005). Especially in the early phase of curing, concrete has a lower strength and relatively less dense microstructure, which is easy to crack and

intensified the decrease in strength under high temperatures.

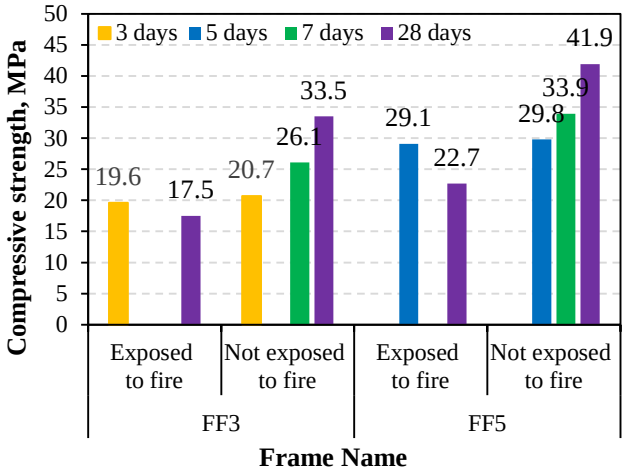

Figure 17: Effect of fire on compressive strength of concrete cubes

As shown in Table 3, the concrete cubes of frame FF3 exposed to high temperatures on the 3rd day have low strength. After being exposed to high temperature, the internal water rapidly evaporates, and many pores and microcracks form, the bonding between paste matrix and aggregate is broke. Nevertheless, the concrete cubes of frame FF5 exposed to high temperatures on the 5th day have a higher hydration degree than that on the 3rd day, but its strength is still lower, because high temperatures break the internal structure of concrete subjected to high temperature on the 5th day, and the hydration in subsequent rest that can offset the strength loss is weaker than the strength loss in the concrete exposed to high temperature on the 3rd day. Therefore, the reduction strength ratio of concrete with initial curing of 5 days is 2.4 and is lower than that of concrete with an initial curing of 3 days is 5.3. However, the reduction in compressive strength of concrete cubes of both frames FF3 and FF5 at age 28 days was 47.8% and 45.8% respectively because when concrete cubes were exposed to fires the curing process of concrete cubes were stopped from age 3 days and 5 days and the hydration process also stopped.

Table (3) Compressive strength of concrete cubes

Age (Days)	Compressive strength, MPa					
	Frame Name					
	FF3			FF5		
	Exposed to Fire	Not Exposed to Fire	Reduction Due to Fire %	Exposed to Fire	Not Exposed to Fire	Reduction Due to Fire %
3	19.6	20.7	5.3	-	-	-
5	-	-	-	29.1	29.8	2.4
7	-	26.1	-	-	33.9	-
28	17.5	33.5	47.8	22.7	41.9	45.8

3.3 Slab Deflection

The main effect of firing the formwork of the concrete frame at an early age is on the slab element because of the slab element wider and more exposed to fire than beams and columns. After firing the formwork of reinforced concrete frame, the slab becomes not having formwork support; therefore, the slab loaded by its self-weight at an early age. In order to find the effect of firing of it is formwork, the load test was done by sandbags, the results of the slab deflection of three reinforced concrete frames shown in Table 4 and Figure 18. According to ACI 437 & ACI 318, the slab deflection after 24 hrs of loading should be less than 21.22 mm while the slab deflection of frame FF3, FF5, FN were 2.4, 1.93 and 1.15 mm respectively and satisfied the ACI limitation. Besides, the three frames satisfied the ACI 437 and ACI 318 limitation of residual slab deflection after 24 hrs of unloading.

As shown in Table 4, the slab deflection of frame FF3 and frame FF5 after 24 hrs of loading was higher by 109% and 68%, respectively, if

compared to slab deflection of frame FN, which not exposed to fire. However, the residual slab deflection of frame FF3 and frame FF5 after 24 hrs of unloading was higher by 175% and 33%, respectively, if compared to slab deflection of frame FN.

The deflection expression is a function of load, span, and end conditions divided by the flexural rigidity (EI) (modulus of elasticity of concrete and moment of inertia of the member) (Darwin et al., 2016). The relation between deflection and the modulus of elasticity is inverse and as known the modulus of elasticity of concrete is depending on the compressive strength of concrete; therefore, the increase in slab deflection of frame FF3 and FF5 is due to decrease in compressive strength of concrete after exposure to fire as shown in Table 3.

Table (4) Slab Deflection

Loading stage	Deflection, mm		
	Frame Name		
	FF3	FF5	FN
Initial	0	0	0
1/4 loading	0.1	0.18	0.16
1/2 loading	0.25	0.31	0.37
3/4 loading	0.74	0.53	0.51
Full loading	1.8	0.95	0.59
After 24 hrs loading	2.4	1.93	1.15
After 24 hrs unloading	0.33	0.16	0.12

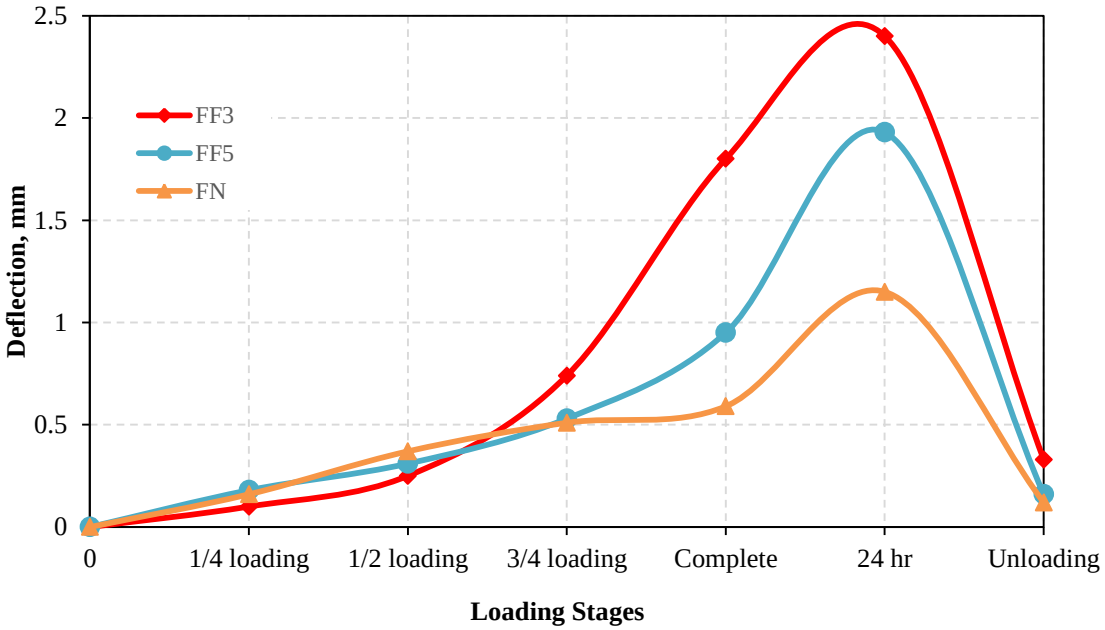

Figure 18: Slab Deflection Curve

3.4 Beam Deflection

Beams in reinforced concrete frames are essential elements that carry loads from the slab. When a building structure sustains a fire accident, a beam with three surfaces and a slab with one surface exposed to fire are the most common working conditions (Guo and Shi, 2011).

The average mid-span deflections of the beam elements, which were loaded by sandbags, are listed in Table 5 and shown in Figure 19. The deflections were recorded at each stage of the load test at mid-span of the beam. As shown in Figure 19, it can be noted that the increase in the midspan deflection of frame FF3 when compared to frame FF5 due to earlier exposed to fire. This increase in midspan can be attributed to the fact that burning causes a reduction in beam stiffness, which is mainly due to the reduction in the modulus of elasticity of concrete. Furthermore, it can be noted from Figure 17 the midspan deflection of beams of two frames FF3 and FF5 for all stages of load test are near to each other and far from frame FN.

The midspan of beam deflection of frame FF3 and frame FF5 after 24 hrs of loading was higher by 71% and 55%, respectively, if compared to beam deflection of frame FN, which not exposed to fire. Also, the residual beam deflection of frame FF3 and frame FF5 after 24 hrs of

unloading was higher by 50% and 38%, respectively, if compared to beam deflection of frame FN, which not exposed to fire.

Table (5) Beam Deflection (Average)

Loading stage	Deflection, mm		
	Frame Name		
	FF3	FF5	FN
Initial	0	0	0
1/4 loading	0.035	0.025	0.015
1/2 loading	0.065	0.06	0.03
3/4 loading	0.13	0.115	0.09
Full loading	0.19	0.165	0.1
After 24 hrs loading	0.325	0.295	0.19
After 24 hrs unloading	0.15	0.12	0.025

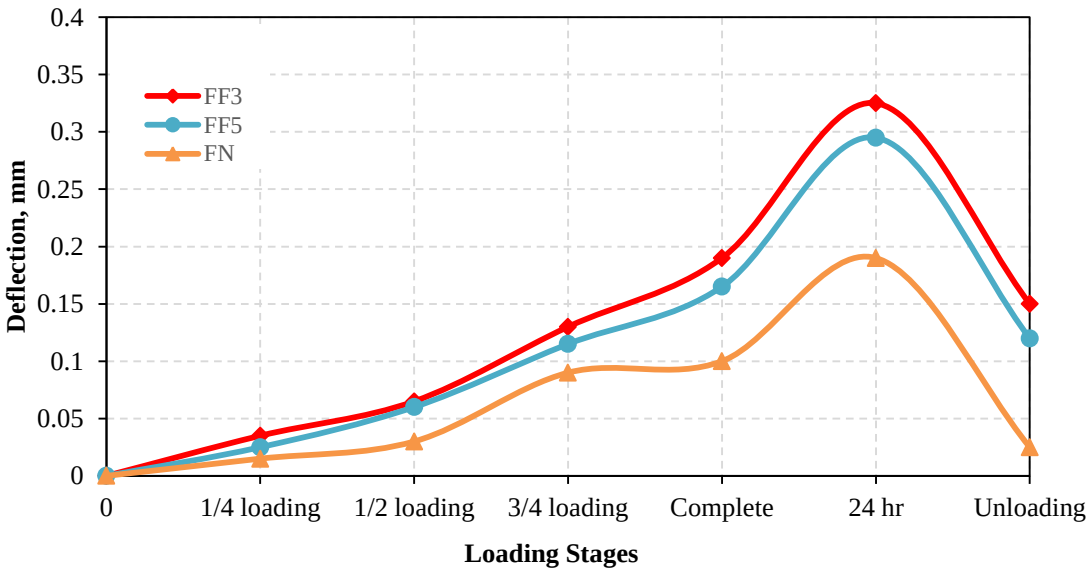

Figure 19: Beam Deflection Curve (Average)

3.5 Column Deflection

Reinforced concrete columns are essential elements because these are primary load-bearing members, and a column could be crucial for the stability of the entire structure. Usually, reinforced concrete columns simultaneously bear the actions of the bending moment and axial compression. When a building sustains a fire accident, four, three, two, or one surface of the rectangular cross-section of an eccentric compressive member may be exposed to high temperature, depending on its position (Guo and Shi, 2011). However, in our experimental investigation, the columns exposed to fire by two faces.

The column displaced at the mid-height of the column into the outside (buckled) after loading. As shown in Table 6 and Figure 20, the column displacement of all frames was near to each other at loading stages, but after 24 hrs of loading, the displacement of FF3 significantly higher than frame FF5 and FN. The Column displacement of frame FF3 and frame FF5 after 24 hrs of loading was higher by 97% and 49%, respectively, if compared to column displacement of frame FN, which not exposed to fire. However, the residual column displacement of frames FF3 and FF5 after 24 hrs of unloading was higher by 113% and 41%, respectively, if compared to column displacement of frame FN, which not exposed to fire.

Table (6) Column Displacement (Average)

Loading stage	Displacement, mm		
	Frame name		
	FF3	FF5	FN
Initial	0	0	0
1/4 loading	0.015	0.025	0.005
1/2 loading	0.045	0.07	0.03
3/4 loading	0.12	0.11	0.105
Full loading	0.26	0.19	0.12
After 24 hrs loading	0.77	0.58	0.39
After 24 hrs unloading	0.17	0.113	0.08

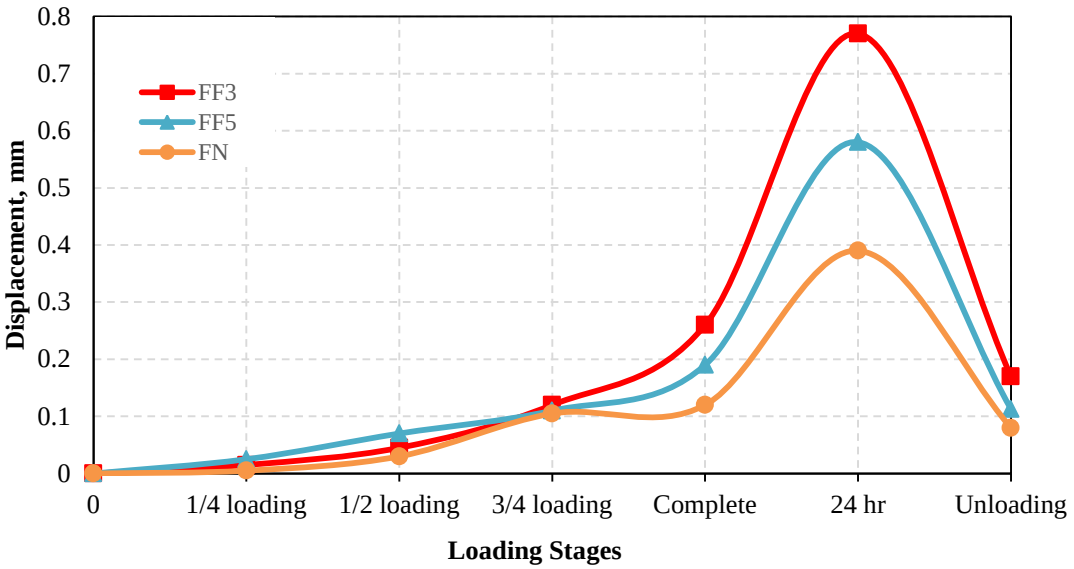

Figure 20: Column Displacement Curve (Average)

4. CONCLUSION:

The following conclusions were drawn based on the observation and analysis of the test results. Using the ACI load test, the concrete quality of early-age structural elements was evaluated under natural fire:

1-The application of the load test does not require special loading devices (hydraulic cylinders, actuators, or others) as the load can be applied using sandbags, However, the structure remains inaccessible for at least 48 hrs during the application of the load test.

2-In general, the frame that was exposed early to natural fire (FF3) was more affected than the frame that was later exposed (FF5), and its slab deflection increased to approximately 109% and 68% respectively compared to the frame that was not exposed to fire (FN), due to earlier firing wooden support of the slab.

3-After comparing the result of the load test of all reinforced concrete structures with limits in ACI criteria, it can be concluded that all reinforced concrete frame verified the ACI limitation.

4-It can be concluded that if a fire accident occurred in any reinforced concrete structure at an early age due to any reason, the structure did not significantly affect by the fire because the time was short and fire exposure was not high.

Conflict of Interest

Authors declare that there is no conflict of interest

References

ACI 318-19 2019. Building code requirements for structural concrete and commentary. Farmington Hills, MI 48331: American Concrete Institute (ACI) Committee 318.

ACI 437.2-13 2013. Code Requirements for Load Testing of Existing Concrete Structures Farmington Hills, MI, 21 pp: American Concrete Institute (ACI) Committee 437.

ASTM E119 2000. Standard Test Methods for Fire Tests of Building Construction and Materials. West Conshohocken, PA: ASTM International.

BEHNAM, B. 2018. On the interaction between span length and opening ratio of RC frames under natural fires. *Proceedings of the Institution of Civil Engineers - Structures and Buildings,* 171**,** 472-486.

BEHNAM, B. & RONAGH, H. 2013. Performance of reinforced concrete structures subjected to fire following earthquake. *European Journal of Environmental and Civil Engineering,* 17**,** 270-292.

BIKHIET, M. M., EL-SHAFEY, N. F. & EL-HASHIMY, H. M. 2014. Behavior of reinforced concrete short columns exposed to fire. *Alexandria Engineering Journal,* 53**,** 643-653.

CHEN, B., LI, C. & CHEN, L. 2009. Experimental study of mechanical properties of normal-strength concrete exposed to high temperatures at an early age. *Fire Safety Journal,* 44**,** 997-1002.

DARWIN, D., DOLAN, C. W. & NILSON, A. H. 2016. *Design of concrete structures*, McGraw-Hill Education.

ELBATANOUNY, M., ZIEHL, P., LAROSCHE, C. & NANNI, A. 2015. Load Testing Techniques for the Strength Evaluation of Existing Reinforced Concrete Structures. *Forensic Engineering 2015*.

GALATI, N., NANNI, A., GUSTAVO TUMIALAN, J. & ZIEHL, P. H. 2008. In-situ evaluation of two concrete slab systems. I: Load determination and loading procedure. *Journal of Performance of Constructed Facilities,* 22**,** 207-216.

GUO, Z. & LI, W. 1993. Deformation testing and constitutive relationship of concrete under different stress-temperature paths. *China Civil Engineering Journal,* 26**,** 58-69.

GUO, Z. & SHI, X. 2011. *Experiment and calculation of reinforced concrete at elevated temperatures*, Elsevier.

HARMATHY, T. & LIE, T. 1970. Fire test standard in the light of fire research. *Fire Test Performance.* ASTM International.

IFFAT, S. & BOSE, B. 2016. A Review on Concrete Structures in Fire. *International Journal of Civil, Environmental, Structural, Construction and Architectural Engineering,* 2**,** 123-128.

ISO 834 2014. Fire resistance tests — Elements of building construction. Geneva, Switzerland: International Standard ISO 834.

KHOURY, G. 1992. Compressive strength of concrete at high temperatures: a reassessment. *Magazine of concrete Research,* 44**,** 291-309.

KHOURY, G., ANDERBERG, Y., BOTH, K., FELLINGER, J., HØJ, N. & MAJORANA, C. 2007. Fib bulletin 38: fire design of concrete structures—materials, structures and modelling, state-of-the art report. *Federation internationale du beton, Lausanne, Switzerland*.

KHOURY, G., MAJORANA, C., PESAVENTO, F. & SCHREFLER, B. 2002. Modelling of heated concrete. *Magazine of concrete research,* 54**,** 77-101.

KHOURY, G. A. 2000. Effect of fire on concrete and concrete structures. *Progress in Structural Engineering and Materials,* 2**,** 429-447.

KIRCHHOF, L. D., LORENZI, A. & SILVA FILHO, L. C. P. 2015. Assessment of Concrete Residual Strength at High Temperatures using Ultrasonic Pulse Velocity. *The e-Journal of Nondestructive Testing,* 20.

LI, Y., LU, X., GUAN, H., YING, M. & YAN, W. 2015. A Case Study on a Fire-Induced Collapse Accident of a Reinforced Concrete Frame-Supported Masonry Structure. *Fire Technology,* 52**,** 707-729.

LIU, L.-X., LV, L., LIU, Z. & WANG, H.-Y. 2005. Investigation on the Mechanical Behavior of Concrete at and after Elevated Temperature [J]. *Building Science,* 3.

LU, L., YUAN, G., SHU, Q., HUANG, Z., ZHONG, C. & XU, B. 2019. Bond behaviour between early age concrete and steel bar subjected to cyclic loading after fire. *Fire Safety Journal,* 105**,** 129-143.

PUCINOTTI, R. 2015. Reinforced concrete structure: Non destructive in situ strength assessment of concrete. *Construction and Building Materials,* 75**,** 331-341.

RIAD, M., GENIDI, M. M., SHOEIB, A. E.-K. & ABD ELNABY, S. F. M. 2017. Effect of discrete glass fibers on the behavior of R.C. Beams exposed to fire. *HBRC Journal,* 13**,** 145-151.

SCHNEIDER, U. 1988. Concrete at high temperatures—a general review. *Fire safety journal,* 13**,** 55-68.

SHORT, N., PURKISS, J. & GUISE, S. 2001. Assessment of fire damaged concrete using colour image analysis. *Construction and Building Materials,* 15**,** 9-15.

XIAO, J. & KÖNIG, G. 2004. Study on concrete at high temperature in China—an overview. *Fire safety journal,* 39**,** 89-103.

ZANCO Journal of Pure and Applied Sciences
The official scientific journal of Salahaddin University-Erbil
https://zancojournals.su.edu.krd/index.php/JPAS

ISSN (print):2218-0230**, ISSN (online):** 2412-3986**, DOI: http://dx.doi.org/10.21271/zjpas**

RESEARCH PAPER

A comparison of empirical equations of Estimating Potential Evapotranspiration (PET) from climatological data in Erbil city

Sardar.M.R.K Al-Jumur *

[1]Department of Physics, College of Science, Salahaddin University-Erbil, Kurdistan Region, Iraq

A B S T R A C T:

Potential evapotranspiration (PET) is an important index of hydrologic budgets at different spatial scales and it is a critical variable for understanding regional hydrological processes. The objective of this study is to find the most suitable method for estimating PET in Erbil city which was done by comparing seven commonly PET methods. Radiation based method: Pristley – Taylor(PT), Turc(TU), Makkink (MK), and temperature based method: Ivanov (IV), Penman–Monteith method (1965) , FAO Penman–Monteith method, and Thornthwaite(TW). The data were collected and used in the models to find PET for the period (1992-2015). The performance indicators were applied by using statistical parameters such as: the Root Mean Square Error (RMSE), Mean Absolute Error (MAE), person correlation coefficient (R2), MBE Mean bias error. The monthly PET results from the models were compared with the actual evaporation. Current work shows that Makkink (MK) model is better than the other models for estimating the potential Evapotranspiration in Erbil depending on the values of statistical parameters.

KEY WORDS: potential evapotranspiration , PET ,Pristley –Taylor(PT) , Turc(TU) Makkink (MK) , Ivanov (IV) , Penman–Monteith , FAO Penman–Monteith Thornthwaite(TW)
DOI: http://dx.doi.org/10.21271/ZJPAS.32.2.13
ZJPAS (2020) , 32(2);129-139 .

1.INTRODUCTION

Evapotranspiration (ET) may be defined as the process of water transfer to the atmosphere, which is consisted of the combined procedures of evaporation from the soil and water surface and transpiration from a vegetated surface; therefore it has a special importance in agricultural, hydrological, meteorological, water and soil conservation research. Evapotranspiration is an important index in Planning and designing any irrigation project in arid and semi-arid regions. Accurate estimation of Evapotranspiration would reduce the wasting of massive quantities of water (Abdullah et al., 2014).

Three terms are normally used in describing evaporation and evapotranspiration: (1) Free water evaporation (E) is used for the amount of evaporation lost from an open water surface (Peterson et al., 1995) (2) Actual evapotranspiration (AET) describes all the processes by which liquid water at or near the land surface becomes atmospheric water vapor under natural condition (Morton, 1983) (3) Potential evapotranspiration (PET) is water loss that will occur if there is no deficiency of water in the soil for use of vegetation at any time (Thornthwaite., 1 944).

The measurement of actual evapotranspiration is so difficult and impractical (Efthimiou et al., 2013; Ahmed Saud et al., 2014).The differences among PET methods are very important to be identified in order to find the most suitable method to predict the actual evapotranspiration

* **Corresponding Author:**
Sardar M. R. Kareem Al-jumur
E-mail: Sardar.kareem @su.edu.krd
Article History:
Received: 11/07//2019
Accepted: 26/11/2019
Published:22/04/ /2020

(AET). Different PET methods give wide different annual values at particular locations as demonstrated in previous studies (Federer et al., 1996). Recent hydrological modeling activities and their results are not quite accurate due to their different assumption and data requirements, and these models were designed for specific climate region. However, it is very important to find a well performed model to predict potential evapotranspiration accurately. During the past 50 years, several empirical models were developed by different scientists and technicians for measuring evapotranspiration based on various climatic variables (Federer et al., 1996). However, PET methods may give different values for evapotranspiration which could not be convenient with specific region. The PET method that requires fewer parameters with high accuracy are the preferred one for regional scale studies (Fennessey and Vogel, 1990).

The effects of climate change on the terrestrial water cycle still unknown parameter in current model calculations. Climate observations of many climate stations report that temperature has increased in the last century while the change in precipitation shows regionally differentiated patterns of increase and decrease. PET methods is subject to many different parameters: atmospheric precipitation, soil water reserve, solar radiation, air and soil temperature, wind speed, depth of groundwater, type of vegetation etc (Bormann, 2011). Therefore it would be necessary to take such an essential parameters in consideration in computing the evapotranspiration which could be expressed as the equivalent amount of water evaporated per unit of time and generally expressed as water depth per unit of time (e.g. mm day-1 (Efthimiou et al., 2013).

Evaporation and transpiration (ET) happen at the same time and there is no easy way to separate them. For example, when the crop is small, the main process for losing water is evaporation, but once the crop completely developed and covered the soil, transpiration becomes the main process (Jahanbani and El-Shafie, 2011). Lu et al. (2005) found a great differences among the temperature based PET methods and radiation based PET methods. He recommended Priestley-Taylor, Turc, and Hamon methods for southeastern United States due to its accurate performing for finding PET in the region of the study.

Previous studies did not focus on the performing of PET methods across our region (Kurdistan region). Therefore, the main objective of this study is to compare and evaluate the performance of seven empirical methods Pristley –Taylor (PT), Turc (TU), Makkink (MK), Ivanov (IV), Penman–Monteith method (1965), FAO Penman–Monteith method, and Thornthwaite (TW) in estimating monthly potential evapotranspiration (PET) compared to the monthly actual evapotranspiration in Erbil Governorate.

1. STUDY AREA

The study area current research is Erbil city which is considered as one of the oldest living city in the world, Erbil is also the capital of the federal Kurdistan region which is about $350 km^2$ north of Baghdad (see figure 1) . It is located 360 km away from Baghdad and it is considered as the fourth city in Iraq in terms of size after Baghdad, Basra, and Mosul.

Fig (1): Erbil Governorate

The climate of Erbil is semi-arid continental. Summer season (June-September) is hot and dry, while winter is cold and wet with a short spring and autumn seasons. Rainfall is limited to the period between October – February with an average of 543 mm. The geographical location of the study area lies between latitude 36.195 ° N, longitude 44.039°E and altitude 420 m (Zohary, 1950).The highest point is the Peak of Hasarost Mountain in Erbil Governorate which is about 3607 m above mean sea level. According to Koppen classification, the climate of Kurdistan region is classified as arid and semi-arid climate (steppe - BSh and Mediterranean – Csa).

2. DATA COLLECTED

Five meteorological parameters are recorded in climate station in Erbil Governorate and used in this research to estimate potential

evapotranspiration by using different models. In order to estimate the potential evapotranspiration, several parameters are used: monthly average temperature, maximum temperature, minimum temperature, solar radiation and relative humidity for the period 1992-2015. The station elevation is about 470 m with latitude 36.12 N° and longitude 44.04 E° fig 2. (kareem et al.,2017,rashed et al.,2017).

Fig (2): Climate station in Erbil Governorate

3. METHODS FOR ESTIMATING THE POTENTIALEVAPORANSPIRATION

There are many scientific models used in previous studies to estimate the Potential Evapotranspiration, each model used different meteorological parameters. In current research we chose seven models that were not used before to estimate PET in Erbil city.

3.1 Thornthwaite Method (1948) (TW):-

The mathematical formula of Thornthwaite method is based on a hypothesis that potential evapotranspiration (PET) is determined by one meteorological parameter which is temperature. However, it does not explicitly reflect the dependency on air humidity and windiness (Kijne 1974, Henderson 2012, Ibrahim et al. 2012, Anderson et al. 2011a). The formula of the model:

$$PET = 1.6 \times L_d \times \left(\frac{10\,T}{I}\right)^{a} \dots (1)$$

La - Monthly correction constant function of latitude.

$$I = \sum_{j=1}^{12} i_j \dots (2)$$

$$i_j = \left(\frac{T_j}{5}\right)^{1.514} \dots (3)$$

$$a = (6.75 \times 10^{-7} I^3 - 7.71 \times 10^{-5} I^2 + 0.49239) \dots (4)$$

Where PET is the potential evapotranspiration (mm/month), I is the annual heat index and can be calculated by using equation (2), T denotes average monthly temperature C°, i_j is the monthly heat index and can be estimated from using equation (3) and a is a constant and can be calculated by equation (4).

3.2 Makkink method (MK):

This model was developed by Makkink in 1957. Makkink method used incoming short-wave radiation Rs and temperature instead of using net radiation, Rn, and temperature (Bakhtiari, 2011). Daily evapotranspiration is calculated as:

$$PET = 0.61 \times \left(\frac{\Delta}{\Delta + \gamma}\right) \times \left(\frac{R_s}{58.5}\right) - 0.12 \dots (5)$$

In equation (5), PET is the daily evapotranspiration (mm /day), and Rs is solar radiation ($MJm^{-2}day^{-1}$); Δ is the slope of the saturation vapor pressure temperature curve ($kPa℃^{-1}$) given by:

$$\Delta = 0.2 \times (0.00738\,T + 0.8072)^7 - 0.000116 \dots (6)$$

And γ is the psychometric constant modified by the ratio of canopy resistance to atmospheric resistance ($kPa℃^{-1}$).

3.3 Turc Method (TU):-

Turc model is modified in 1961 which considers only air humidity under dry conditions, (Bormann, 2011).The equation to estimate PET is given by two formulas:

$$PET = 0.013 \times \left(\frac{T}{T+15}\right) \times (R_S + 50) \times \left(1 + \frac{50-RH}{70}\right) \dots (7) \quad \text{when (RH>50)}$$

$$PET = 0.013 \times \left(\frac{T}{T+15}\right) \times (R_S + 50) \dots (8)$$

when (RH<50)

Where, PET is the daily PET (mm/day); T is the daily mean air temperature (°C); Rs is the daily solar radiation (cal/cm^2/d) and where cal/cm^2/d equals (100/4.1868) MJ/m2/day; and RH is the

daily mean relative humidity (percent) (Lu et al., 2005).

In equations (7) and (8), two different formulas are presented for areas with relative humidity of lower and higher than fifty percent this model depend on the relativity humidity and solar radiation.

3.4 Priestley–Taylor method (PT):-

Priestley–Taylor equation is modified in 1972. Evapotranspiration is expressed as modified Priestley–Taylor model in irrigated maize. (Priestley and Taylor, 1972):

$$PET = \alpha \times \left(\frac{\Delta}{\Delta + \gamma}\right) \times (R_n - G)/\lambda \ldots (9)$$

PET is the daily potential evapotranspiration (mm/day); λ is the latent heat of vaporization (MJ/kg), λ =2.501-0.002361T; T is the daily mean air temperature in (°C); α is the calibration constant (α = 1.26) for wet or humid conditions; Δ is the slope of the saturation vapor pressure temperature curve (kPa/°C) given in equation:

Δ = 0.200 (0.00738 T + 0.8072)7 - 0.000116

3.5 Ivanov method (IV):-

Ivanov had been able to develop an equation estimates the potential evapotranspiration using temperature and relative humidity as an equation parameters.

$$PET = 0.0018 \times (T + 25)^2 \times (100 - RH) \ldots (10)$$

Where PET is the monthly Potential Evapotranspiration mm / month , RH and T stand for monthly relative humidity, and monthly average temperature (°C), respectively (Shakeel et al., 2017).

3.6 Penman –Monteith equation:-

Penman equation is modified by Monteith (1965) to represent the evapotranspiration from vegetation surface by including parameters such as: atmospheric conductance and canopy conductance. The formula is expressed for daily values as:

$$PET = \frac{\Delta(R_n - G) + \rho_a c_p \frac{(e_s - e_a)}{r_a}}{\lambda(\Delta + \gamma\left(1 + \frac{r_s}{r_a}\right))} \ldots (11)$$

Where PET is monthly evapotranspiration (mm/month), Rn is the net radiation (MJ/m2 .month), G is the soil heat flux neglected, es saturation vapour pressure (kPa). ea actual vapour pressure (kPa), ρa is the mean air density at constant pressure ,cp is the specific heat of air ($1.013*10^{-3}$MJk/g °C) , Δ represents the slope of the saturation vapour pressure temperature relationship(kPa/°C), γ is the psyschrometric constant (kPa/°C), λ latent heat of vaporization (2.45 MJ/ kg), rs and ra are the surface and aerodynamic resistance (sm^{-1},sm^{-1}) γ is found by using this equation:-

$$\gamma = 0.665 \times 10^{-3} P \ldots (12)$$

Where P is the atmospheric pressure (kPa):-

$$P = 101.3 \times \left(\frac{293 - 0.0065 \times z}{293}\right)^{5.26} \ldots (13)$$

And z is elevation above sea level (m).

3.7 FAO-56 Penman –Monteith equation

Fao penman equation was derived from three equations: Penman-Monteith equation, Aerodynamic resistance (ra), and surface resistance (rs). The equation depends on meteorological parameters such as solar radiation (sunshine), air temperature, humidity and wind speed. The measurements should be made on a condition that the instrument height should at 2 m above the surface.

The general form of Fao – 56 Penman equations to estimate the evapotranspiration is in the form (Allen et al., 1998):

$$\text{PET} = \frac{0.408\,\Delta(\text{R}_\text{n} - \text{G}) + \gamma \frac{\text{C}_\text{n}}{\text{T}_\text{a}+273} \text{U}_2\,(\text{e}_\text{s} - \text{e}_\text{a})}{\Delta + \gamma(1 + 0.34\,\text{U}_2)} \ldots (14)$$

Where:

ET is evapotranspiration [mm day-1], Rn net radiation at the crop surface [MJ m-2 day-1] , G soil heat flux density [MJ m-2 day-1] , T mean daily air temperature at 2 m height [°C] , u2 wind speed at 2 m height [m s-1] , es saturation vapour pressure [kPa] , ea actual vapour pressure [kPa] , es - ea saturation vapour pressure deficit [kPa] , Δ Slope vapour pressure curve [kPa °C-1] , γ Psychrometric constant [kPa °C-1] and Cn-numerator constant.

3.8 Statistical Parameters

The Root mean square error (RMSE) is the square root of the mean square error (MSE). The mean square error is defined as the expected value of the square of the difference between the estimator and the parameter. It is the sum of variance and squared Bias. By using this relation (Moeletsi et al., 213)

$$\mathrm{RMSE} = \sqrt{\frac{1}{\mathrm{n}}\sum(\mathrm{ET_{Obs.}} - \mathrm{ET_{model}})}$$

Where (n) is the number of observations (month of the year) .

The mean bias error (MBE) is the difference between the mean of the predicted and observed concentrations. It indicates the degree to which the observed concentrations are 'over' or 'under' predicted by the mode (Moeletsi et al., 213).

$$\mathrm{MBE} = \frac{\sum_{\mathrm{i=1}}^{12}(\mathrm{ET_{Obs.}} - \mathrm{ET_{model}})}{12}$$

The mean absolute error (MAE) is a measure of difference between two continuous variables.

$$\mathrm{MAE} = \frac{1}{\mathrm{N}}\sum_{\mathrm{i=1}}^{\mathrm{N}}\left|\frac{\mathrm{ET_{Obs.}} - \mathrm{ET_{model}}}{\mathrm{ET_{Obs.}}}\right| \times 100\ \%$$

4. METHODS

Seven PET models were used in our study in order to compare their results with actual measured data in Erbil government which in turn could help to find out the most suitable method in our region.

Seven commonly PET methods were used, radiation based method: Pristley –Taylor(PT), Turc(TU), Makkink (MK), and temperature based method: Ivanov (IV), Penman–Monteith method (1965) , FAO Penman–Monteith method, and Thornthwaite (TW). The output data of these methods have been compared with the real data of pan evaporation. To evaluate the performance of these method and find out the suitability of them for simulate the potential evapotranspiration, we have made the following assumption:

1. Since our region have very limited green land area and mostly appears during winter, and crop is small which in turn lead to consider the main process for losing water is evaporation, therefore we have neglected the transpiration term from the crops compared to the evaporation term.

2. The second assumption is that the potential evapotranspiration from selected models should exceed measured evaporation.

3.The relationship between potential evapotranspiration and measured evaporation should be linear. Statistical analysis methods were applied for each PET method by using the Root Mean Square Error (RMSE), Mean Absolute Error (MAE), Correlation coefficient (R2), and Mean bias error (MBE) to find the nature of the relationship between measured data and simulated data of each PET method.

5. RESULTS

The performance of PET empirical methods were evaluated and compared to the measured climate data for study models. Several models were used to determine the evapotranspiration in Erbil city. Table (1) shows the potential evapotranspiration values from the models of the study for each month of the year.

The maximum potential evapotranspiration values were 385,300, 476, 258, 342, 214, and 180, in July for Makking, Turc, Ivanov, Priestley-Taylor, Thornthwait, Penman-Monteith and Fao Penman-Monteith methods respectively. In contrast, the minimum values were 39, 43, 60, 53, 5,40, and 33 occurred in January for Makking, Turc, Ivanov, Priestley- Taylor, Thornthwait, Penman-Monteith and Fao Penman-Monteith methods respectively.

Table (1): potential evapotranspiration

month	Erbil station	MK PET mm/month	TU PET mm/month	IV PET mm/month	PT PET mm/month	Tw PET mm/month	P-M PET mm/month	FAO P-M PET mm/month
Jan	49.48	39.96	43.78	60.45	53.54	5.55	40.23	33.28
Feb	66.71	44.53	49.60	71.83	67.79	8.17	49.10	40.31
Mar	120.94	86.07	96.65	107.11	109.26	23.53	83.16	70.17
Apr	162.93	229.63	131.88	158.00	147.83	58.32	110.38	91.27
May	275.925	326.52	216.83	292.49	225.54	167.95	170.62	141.49
Jun	368.39	339.38	259.12	409.30	232.64	251.12	200.03	163.79
Jul	412	385.88	300.23	476.82	258.07	342.79	214.99	180.37
Aug	382.33	348.98	269.21	457.67	245.12	306.04	194.77	164.52
Sep	288.73	255.39	191.57	358.17	178.52	174.12	146.64	123.68
Oct	188.74	179.97	122.39	247.88	137.08	98.45	104.23	88.14
Nov	89.41	104.45	65.32	119.04	79.78	27.09	57.01	49.87
Dec	54.21	81.16	47.61	70.26	67.47	8.56	41.26	35.14

From table 1 it is clear that maximum evapotranspiration occurs during July for all study models while the minimum evapotranspiration occurs in January. The table revealed that Ivanov method has the highest value of evapotranspiration. The Pearson correlation coefficients were computed for calculated values of evapotranspiration and real measured evapotranspiration of each method of Erbil station (measured value Vs simulated value).The Pearson correlation coefficient values (R2) (table 2) were around (0.93, 0.98, 0.98, 0.96, 0.96, 0.98, and 0.98) for each of Mikkinc, Turc, and Ivanov, pristley, Thornthwait, penman, and Fao - penman method respectively. Table (2) shows Statistical parameters such as: Root Mean Square (RMSE), Mean bias error (MBE), Mean Absolute Error (MAE) for each model. The highest value of Root Mean Square, Mean bias error, Mean Absolute Error, Pearson correlation coefficients where 10.3, 2.9, 4.3, and 0.98 for Fao P-M model while the minimum value where 1.7, 0.5, 0.12, and 0.93 respectively for Mikking model.

Table (2): Statistical parameters

statistical parameters	MK	TU	IV	PT l	TW	P-M	FAO P-M
RMSE	**1.7**	**7.4**	**5.5**	**7.4**	**9.1**	**9.3**	**10.3**
MBE	**0.5**	**2.1**	**1.6**	**2.1**	**2.6**	**2.7**	**2.9**
MAE	**0.12**	**2.2**	**1.2**	**2.2**	**3.34**	**3.54**	**4.3**
R^2	**0.93**	**0.98**	**0.98**	**0.96**	**0.96**	**0.98**	**0.98**

It is obvious from fig 2 that monthly potential evapotranspiration from Makkink method is the closest one to the real evapotranspiration from Erbil station. Fig 3 clearly indicates that the Makkink method is identical to the real data of evapotranspiration from Erbil station for the periodic time (1992-2015) where the coefficient (R) is around 0.96.

Figure 4 represents the yearly evapotranspiration values from all study models, the results of the graph is consist with the measured value and support that Makking model is the best one for Erbil city. Figure 5 shows the monthly mean values of PET for the period 1992 to 2015.

Both cases reveal that makkink model is very close to the measured PET.

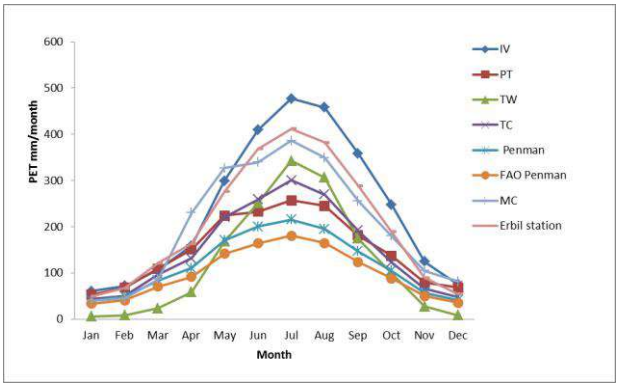

Fig 5. Monthly estimation of Potential Evapotranspiration models with month (1992-2015)

Figure 6 shows the mean annual values of evapotranspiration for each model. Frome both yearly and monthly values, Ivanove model show the highest value, while Fao model shows the minimum value. It is quite obvious from the graphs that Makking model is very close to the real value.

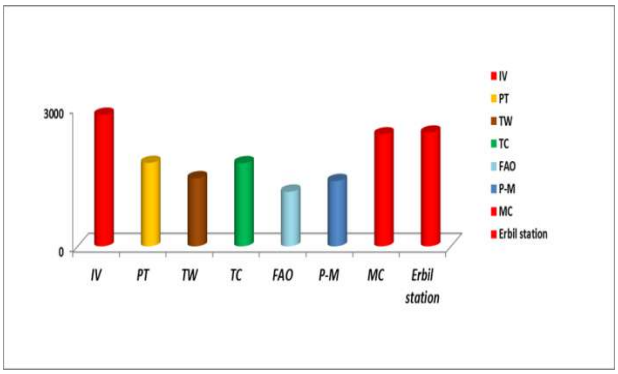

Fig 6. Yearly estimation of Potential Evapotranspiration Models (1992-2015)

6. CONCLUSION

Seven empirical methods for calculating potential evapotranspiration in Erbil governorate were evaluated by using climatological data from Erbil station. Makkink method was proven to be more desirable for estimating potential evapotranspiration (PET) in Erbil city. A less reliable result can be expected from thornthwaite (TW). All the other five empirical methods gave much less acceptable estimates for potential evapotranspiration (PET) in the region of the study. The methods of the study show a maximum potential evapotranspiration (PET) in July while the minimum value was in January.

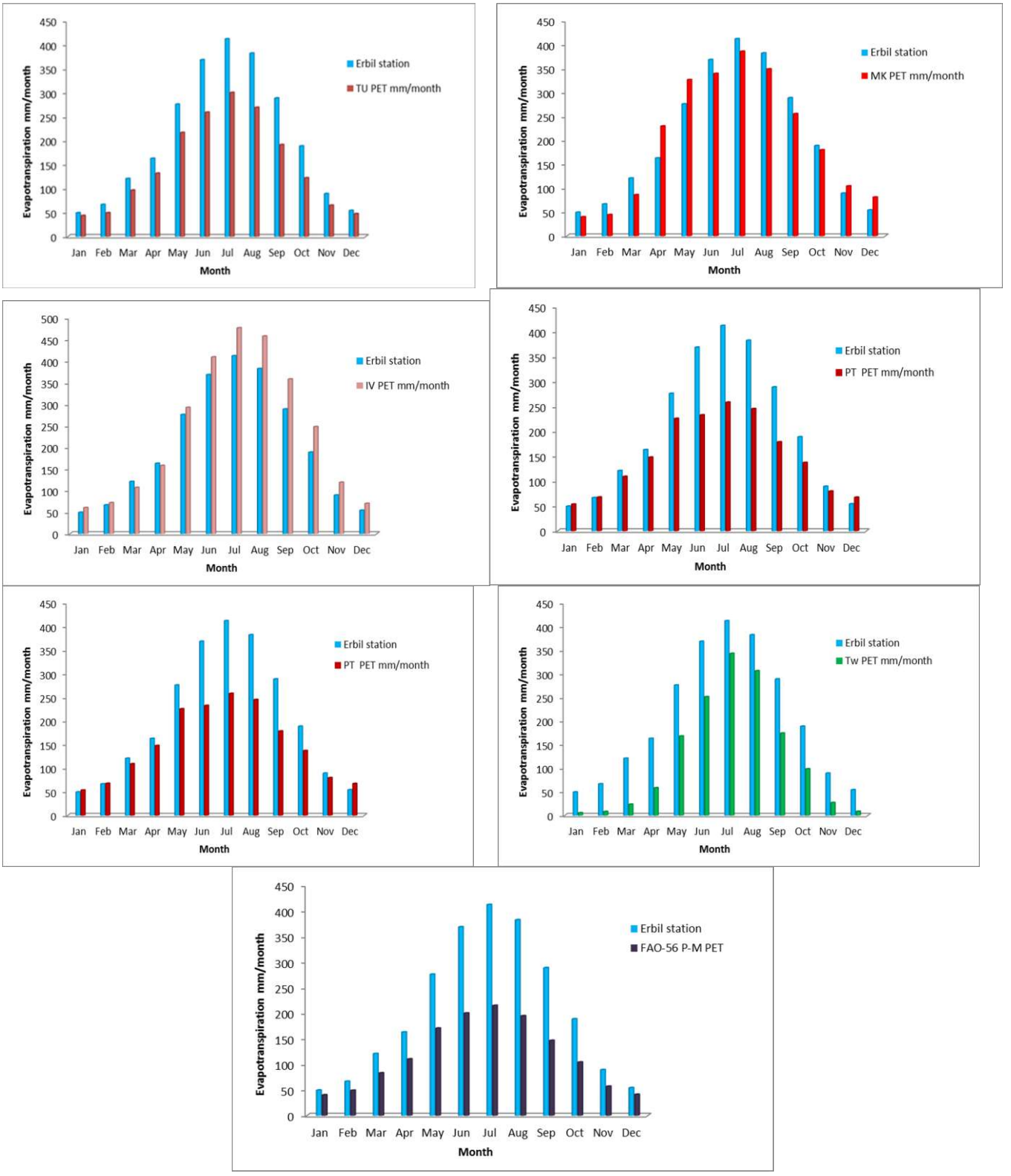

Fig 2. Average monthly Potential Evapotranspiration by seven models with measured PET in Erbil station (1992-2015)

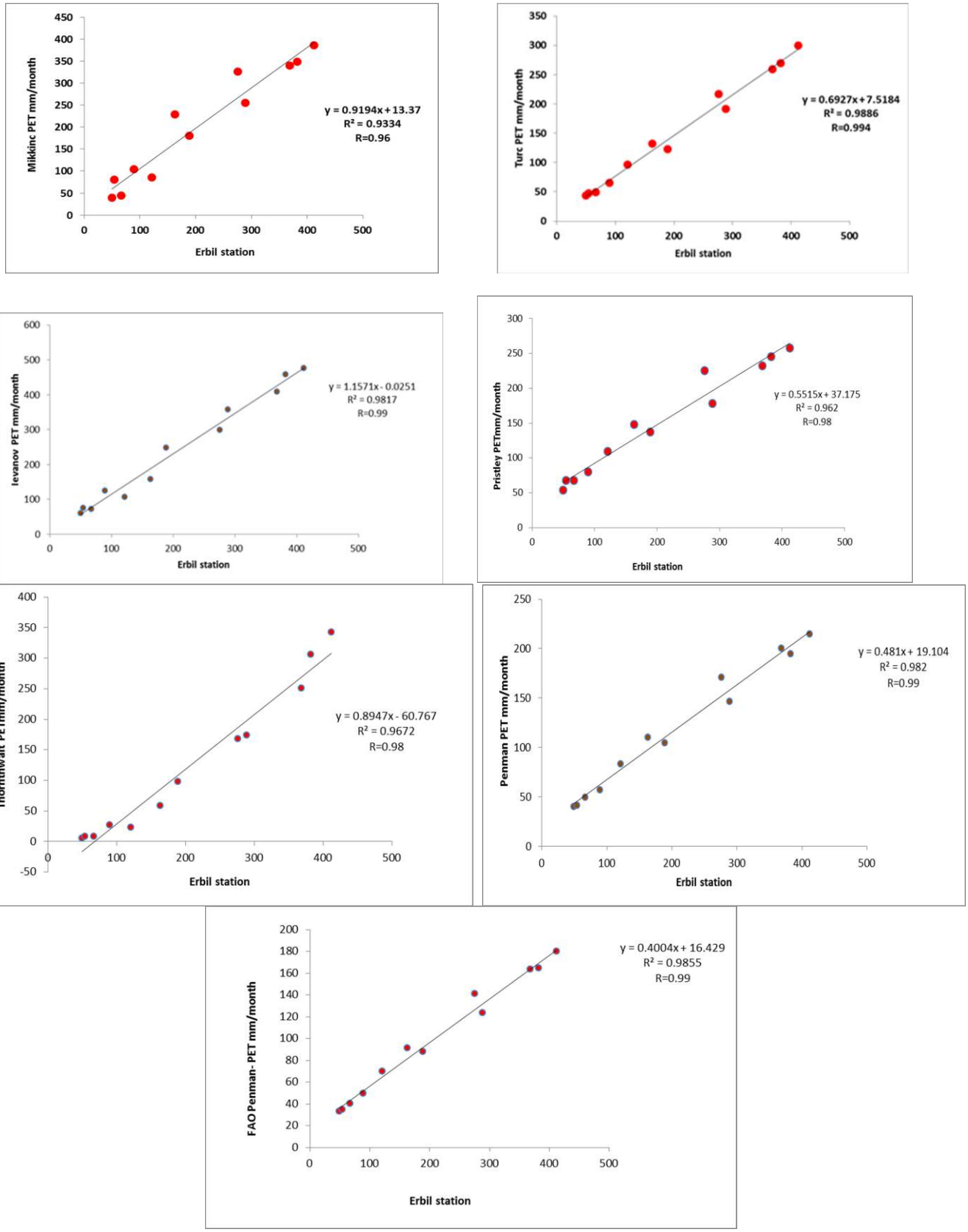

Fig3. Monthly estimation of Potential Evapotranspiration by seven models with Observer PET in Erbil station (1992-2015)

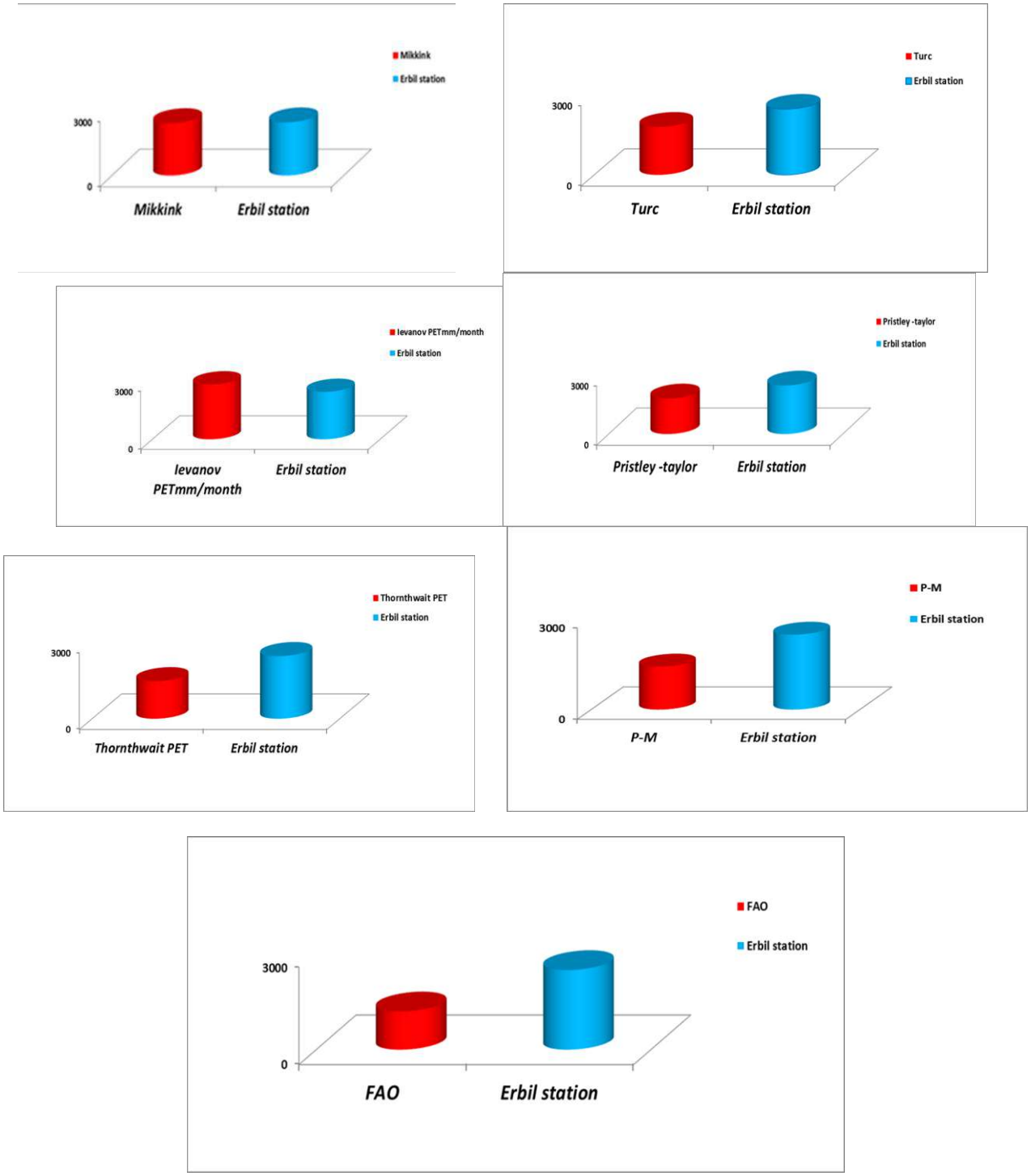

Fig4. Yearly estimation of Potential Evapotranspiration by using seven models with Observer PET in Erbil station (1992-2015)

7. REFERENCES

Allen, R.G.; Pereira, L.S.; Raes, D. & Smith, M. (1998). Crop evapotranspiration – Guidelines for computing crop water requirements. FAO Irrigation and Drainage Paper, No. 56, FAO, Rome.

Abdullah, S.S., Malek, M., Mustapha, A. and Aryanfar, A. (2014) Hybrid of Artificial Neural Network-Genetic Algorithm for Prediction of Reference Evapotranspiration (ET?) in Arid and Semiarid Regions. Journal of Agricultural Science 6(3), p191.

Ahmed Saud, Md Azlin Md Said , Rozi Abdullah and Ammar Hatem.,2014. Temporal and Spatial variability of Potential Evapotranspiration in Semi-Arid Region: Case Study the Valleys of Western Region of Iraq.6(9), 0975-5462.

Anderson, M.C. Hain, C., Pimstein, A., Mecikalski, J. R., and Kustas, W. P.: Evaluation of Drought Indices Based on Thermal Remote Sensing of Evapotranspiration over the Continental United States. J. Climate, 24, 2025-2044, doi:10.1175/2010JCLI3812.1, 2011a.

Allen, R.G., Pereira, L.S., Raes, D., Smith, M. (1998): Crop evapotranspiration – Guidelines for computing crop water requirements – FAO Irrigation and drainage paper 56. Food and Agriculture Organization of the United Nations, Rome.

Bakhtiari. S. (2011). "Microfinance And Poverty Reduction: Some International Evidence", International Business & Economics Research Journal (IBER), 5(12).

Bormann H, (2011) Sensitivity analysis of 18 different potential evapotranspiration models to observed climatic change at German climate stations. Climatic Change 104:729–753.

Efthimiou, K., Argalia, E., Kaskaba, E., & Makri, A. (2013). Economic crisis & mental health: What do we know about the current situation in Greece, 50, 22-30.

Efthimiou N, Alexandris S, Karavitis C, Mamassis N (2013) Comparative analysis of reference evapotranspiration estimation between various methods and the FAO56 penman-Monteith procedure. European Water Journal 42:19–34.

Federer, C.A., C. Vörösmarty, and B. Fekete, 1996. Intercomparison of Methods for Calculating Potential Evaporation in Regional and Global Water Balance Models. Water Resources Research 32:2315-2321.

Fennessey, N.M. and R.M. Vogel, 1996. Regional Models of Potential Evaporation and Reference ET for the Northeast USA. Journal of Hydrology 184:337-354.

Fennessey, N., Vogel, R.M., 1990. Regional flow-duration curves for ungauged sites in Massachusetts. J. Water Resour. Plan. Manag. 116 (4), 530–549.

Federer CA, Vörösmarty C, Fekete B (1996) Intercomparison of methods for calculating potential evaporation in regional and global water balance models. Water Resour Res 32(7):2315–2321.

Henderson, J. Vernon, Adam Storeygard, and David N. Weil. 2012. "Measuring Economic Growth from Outer Space: Dataset." American EconomicReview.

Ibrahim, A., A. Gilerson, T. Harmel, A. Tonizzo, J. Chowdhary, and S. Ahmed, 2012: The relationship between upwelling underwater polarization and attenuation/absorption ratio. Opt.Express,23,25662-25680, doi:10.1364/OE.20.025662.

Jahanbani, H., El-Shafie, A.H. 2011 a comparison of empirical equations of estimating potential evapotranspiration (PET) from climatological data in Erbil city, Paddy and Water Environmen, 9, Issu 2, June: 207-220.

Kijne,J.W.1974.DeterminingEvapotranspiration. In : Drainage Principles and Applications. Int. Inst. for Land Recl. and lmpr. Wageningen-The Netherlands. 111 : 53-1 11.

Lu, Jianbiao; Sun, Ge; McNulty, Steven G.; Amatya, Devendra. 2005. A comparison of six potential evapotranspiration methods for regional use in the Southeastern United States. Journal of American Water Resources Association. 41(3): 621-633.

Morton, Fl., 1983. Operational estimates of areal evapotranspiration and their significance to the science and practice of hydrology. 3. Hydrol., 66: 1 76.

MAKKINK, G.F. (1957); Testing the Penman formula by means of lysimeters. Journal of the Institution of Water Engineers and Scientists. Vol. 11. 277–288.

Monteith, J.L. 1965. Evaporation and environment. pp. 205-234. In G.E. Fogg (ed.) Symposium of the Society for Experimental Biology, The State and Movement of Water in Living Organisms, Vol. 19, Academic Press, Inc., NY.

Mokhele Edmond Moeletsi , Sue Walker b, Hamisai Hamandawana (2013), Comparison of the Hargreaves and Samani equation and the Thornthwaite equation for estimating dekadal evapotranspiration in the Free State Province, South Africa, Physics and Chemistry of the Earth 66 (2013) 4–15.

Peterson, T. C., V. S. Golubev, and P. Y. Groisman (1995), Evaporation losing its strength, Nature, 377, 687 – 688.

Priestley,C.H.B., and R.J. Taylor, 1972:on the assessment of surface heat flux and evaporation using large scale parameters.Mon.Wea.Rev., 100,81-92.

Sardar M.R. Kareem, Dilshad G.A. Ganjo, Janan J.Toma.2017. Physical and Chemical properties of rainwater and its suitability for drinking and irrigating in Erbil city. ZJPAS 29 (5); 39-50.

Sardar M. Rashed, Osama T. Al-Taai , Ali M. Al-Salihi.2017.Analysis Study of Meteorological

Parameters and their Relationship with Some Concentration of Tropospheric Gases over Erbil City. ZJPAS 29 (s4); s227-s241.

Shakeel Ahmad Bhat, Bashir Pandit, Mehraj U. Din Dar, Rehana Jan, Shafat Khan and Khanday Mehraj. 2017. Statistical Comparison of Reference Evapotranspiration Methods: A Case Study from Srinagar in J&K.Int.J.Curr.Microbiol.App.Sci. 6(9): 3731-3737.doi:https://doi.org/10.20546/ijcmas.2017.609.460 .

Thornthwaite, C. W.: Report of the Committee on Transpiration and Evaporation, 1943–1944. Trans. Amer. Geophys. Union25, 683–693 (1944).

Zohary, M.(1950). The flora of Iraq and its phytogeographical sub division. Dept. Agri. Iraq. Publ. 31:1-201.

ZANCO Journal of Pure and Applied Sciences
The official scientific journal of Salahaddin University-Erbil
https://zancojournals.su.edu.krd/index.php/JPAS

ISSN (print):2218-0230**, ISSN (online):** 2412-3986**, DOI: http://dx.doi.org/10.21271/zjpas**

RESEARCH PAPER

Genetic Similarity of two different color Local Guinea Fowl (*Numida Meleagris*) By Using RAPD-PCR Technique

Hurea S. Abdulrazaq

Department of Animal Resource ,College of Agriculture Engineering Sciences, Salahadden University -Erbil/ Kurdistan Region, Iraq.

A B S T R A C T:
The aim of present study to determine DNA polymorphism, between and within two different color (white) and (black) guinea fowl lines. Blood samples were collected about 3 ml of 30 white guinea fowl and 30 black guinea fowl, in six different local farms. DNA was isolated, the purity of the DNA samples ranged from 1.8 to 1.9. RAPD – PCR was used to evaluate genetic similarity between the lines of guinea fowl. Using eighteen primers for amplification of RAPD, from Gen Script USA. A total of (14) primers out of (18) primers gave results to find Genomic DNA complementary sites. After electrophoresis the largest number of bands were appeared with OPA-03 primers, but the smallest was obtained when OPQ-15 primer used. Determined Genetic similarity as the mean for the primers used, between the black and white guinea fowl, was 0.76. The coefficient of genetic similarity within white guinea fowl line, was 0.78 and 0.73 within black guinea fowl line.

KEY WORDS: Genetic similarity, Guinea fowl, RAPD – PCR, Polymorphisms.
DOI: http://dx.doi.org/10.21271/ZJPAS.32.2.14
ZJPAS (2020) , 32(2);140-144 .

INTRODUCTION

The most important type of poultry in Iraq is domestic fowl. The domestication of poultry was originally started from the wild types that collect the eggs from it for hatching and rearing young birds, but keeping the birds permanently in captivity later. The term poultry is used collectively for those species of birds that have been domesticated to reproduce and grow in captivity and render product of economic value such as meat, eggs manure. The term poultry is applied to birds of several species like fowls or chicken, guinea, duck, turkeys etc.

The second most exceedingly eaten globally from of meat is the birds and along with eggs, because it has high-quality protein with low proportion of fat which supply nutritionally helpful food (Fadhil et al., 2016). Around the world in different avian spices the genetic variation has been investigated, locate the degree of relatedness or to identify genes responsible for interesting traits. The molecular nature of the precise differences in the nucleotide sequences within gene is. The genetic identity is related to check relationships between species and breeds. The genetic improvement of poultry has created new possibilities because of the molecular development. Build on DNA markers (RAPD, RFLP, VNTR, CRI, SSR – PCR), they enable to be studied whole genomes or the polymorphic of DNA fragments. The rapid and simple technique is RAPD (Randomly Amplified Polymorphic DNA) to determining relatedness and to

* **Corresponding Author:**
Hurea Saber Abdulrazaq
E-mail: Hurea.Abdulrazaq@su.edu.krd
Article History:
Received: 27/06/2019
Accepted: 28/10/2019
Published:22/04/2020

identifying responsible of genes for avian advantage trait. In the study of similarity or variation the RAPD – PCR has been used repeatedly in chickens populations (Abdulrazaq and Suliaman.,2016, Dehghanzadeh, et, al., 2009, Smith, et, al., 1996, Sharma, et, al.,2001, Ali, et, al., 2003, Sharma and Singh, 2002, Semenova, et al., 2002), ducks (Dolmatova, et al., 2000a, b), turkey (Smith, et, al., 1996), animal (Abdulrazaq, et, al., 2019).guinea birds (Sharma, et, al., 1998, Nahashon, et, al., 2010, Daham and Sharma, 2007). In many countries the basis of genetic improvement in guinea birds species to improve meat production efficiency. Due to the nutritional value and the gorgeous taste of their meat, guinea birds are a valuable though undervalued species of gallinaceous poultry. Guinea birds farming was popular in the 1980s and 1990s, in Iraq, when guinea birds multiplication farms and breeding were instituted. Today, yet, there are no reproduction programmers and organized breeding for guinea bird, which are mainly kept under backyard systems in Iraq. Understanding better of guinea birds lines may help to increase their popularity. Determine the genetic similarity within and between two different color local guinea fowl are the aim of this study.

1. MATERIALS AND METHODS

1.1 SAMPLES COLLECTION

The blood samples were collected from the wing near the elbow joint into tubes contain a EDTA, and DNA analysis was performed directly in the laboratory. Blood samples were collected about 3 ml of 30 black guinea birds and 30 white guinea birds, in 6 different local farms.

1.2 GENOMIC DNA EXTRACTION

The DNA Extracted by Using Kit Promega USA (Beutler et., 1990). The laboratory analyses of DNA were performed in Erbil Medical Research Center / Hawler Medical University. The DNA quality isolated by the Nano Drop® spectrometere, purity of DNA samples ranged from 1.8 to 1.9. Were diluted the samples to 30 ng /µl for use of RAPD – PCR in the Research Center of Salahaddin University - Erbil.

1.3 RAPD- PCR ANALYSIS

Using 18 primers for amplification of RAPD, from Gen Script USA. A total of (14) Primers out of (18) Primers gave results to find Genomic DNA complementary sites, OPA-07, OPA-10, OPA-03, OPA-06, OPA-12, OPA-14, OPA-15, OPA-19, OPA-20, OPQ-10, OPA-04, OPQ-01, OPQ-12, OPQ-15, (Table 1). The DNA analyses was amplified in a T Gradient thermo cycler. At 95°C for 5 min initial denaturation double-stranded DNA was carried. This was followed by 40 cycles: 95°C for 1 min, 42°C for 1 min, 72°C for 2 min. At 75°C for 5 min the complementary strands were synthesized.
The contained of PCR reaction include: DNA 30 ng, primer 10 µM, 1x PCR buffer GoTaq® Green Master Mix, 1x, MgCl2 3 mM, Each: (dATP, dCTP, dGTP dTTP) (400µM), The volume of total reaction was 25 µl. The Gene Ruler ^{TM} 100bp DNA Ladder marker (100 – 1500 bp). In all samples 2 µl of Blue / Orange loading day was added to 10 µl of the product. The 100V power supply was performed was. Electrophoresis long was about 90 min. The products of PCR were tested with electrophoresis on 2% agarose gel in 1X TBE buffer, stained with ethidium bromide (promega, USA). The pattern was amplified by ultraviolet light and photographed.

1.4. STATISTICAL ANALYSIS

The F is genetic similarity between the white guinea birds and black guinea birds. It was computed by used the (bands) fragments amplified in PCR reaction, the formula of Nei and Li (1979) was applied: F=2x Nxy / (Nx + Ny). Data recording and statistical analysis RAPD patterns were recorded because of (1) or absence (0). The polymorphism of each primer was Calculated by use the formula: polymorphism = (Np / Nt) × 100, NP = # polymorphic forms of random primer Nt = total number of sample primer domains (Bowditch et al., 1993).The numerical data were analyses statistically. Excel software were using to calculate the arithmetic means of the analyses traits.

2. RESULTS AND DISCUSSION

The technique of RAPD was used in the present study to assess relatedness of genetic

among guinea birds line. The samples containing eighteen genotypes chosen randomly were tested. Reaction of PCR performed with fourteen selected primers in all of guinea birds of both white and black colors (Table 1). The bands number common to both of white color line and black color line was determined from the band obtained from electrophoresis (Figure 1).

Table 1. Sequences of the primers used GC content

Primer Name	Sequence 5' to 3'	%GC content
OPA-07	GAAACGGGTG	60%
OPA-10	GTGATCGCAG	60%
OPA-03	AGTCAGCCAC	60%
OPA-06	GGTCCCTGAC	70%
OPA-12	TCGGCGATAG	60%
OPA-14	TCTGTGCTGG	60%
OPA-15	TTCCGAACCC	60%
OPA-19	CAAACGTCGG	60%
OPA-20	GTTGCGATCC	60%
OPQ-10	GCTAACCGA	60%
OPA-04	AATCGGGCTG	60%
OPQ-01	GGGACGATGG	70%
OPQ-12	TCTCCGCAAC	60%
OPQ-15	GACGCTTCA	60%

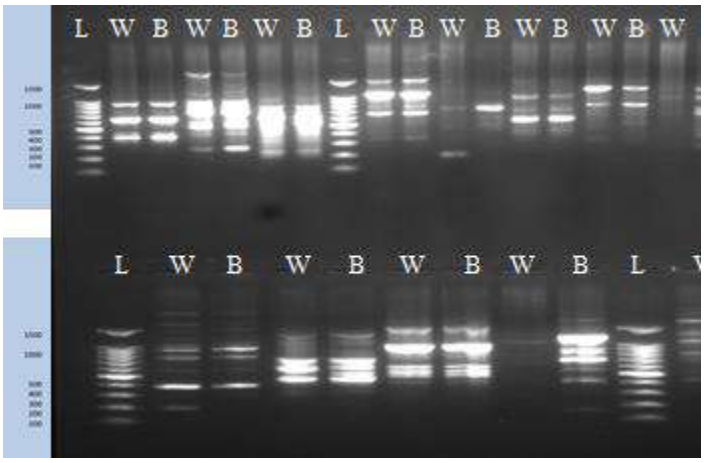

Figure 1. Electrophoretic pattern of genomic DNA amplification in white and Black guinea fowl using OPA-07; OPA-10; OPA-03;OPA-06; OPA-12; OPA-14;OPA-15; OPA-19; OPA-20; OPQ-10;OPA-04; OPQ-01;OPQ-12; OPQ-15 primer.

Table (2) is contain the PCR product from both white color guinea fowl line and black color guinea fowl line. The higher numbers of band shown in Black guinea fowl lines (47) then the white guinea fowl lines of total (92) bands. The polymorphism level detected between the both white and black phenotypes varied. The polymorphic bands showed higher number in black phenotype and the percent of Polymorphism (%6.2). A total of 206 different fragments (bands) are produced, out of them 36 bands were polymorphic, 36 Mono band, 170 Monomorphic band. It is higher than, Al_Jallad, et al. (2012), study 125 different fragments (bands) a total, out of them the polymorphic bands were 93 bands. The number of bands amplified varied from 7 (OPQ-15) to 53 (OPA-03) per Primer. The primer OPA-10 detect highest number of polymorphic bands 12 polymorphic band, while detected 1 polymorphic band with (OPA-07), and there is a lowest number of band. In this study it was found an average number 17.48 of bands, polymorphic bands per primer. The highest range of the molecular weight was (200 - 1500 bp) for the primer OPA-12, and was over in less primer OPA-14 which is (400 – 500 bp) for each primer are given in ,Table (3). The size difference average from 325 to 1325 bp reported by Fadhil, et al. (2016).

Table 2. Number of bands for different groups of guinea fowl

guinea fowl	Total number of bands	polymorphic band	% Polymorphism
white guinea fowl	45	2	4.4
Black guinea fowl	47	3	6.4
All	92	5	10.8

The genetic similarity coefficient for analysis different guinea birds line. The F values for white guinea birds and black guinea birds within each primers were the mean genetic similarity coefficients for all of fowls of a given different colors. The average of F was 0.73 for white guinea birds and 0.78 for black guinea birds. It was Strikingly lower that reported by Sharma, et, al., (1998), which was (0.95 – 0.97).Within the primers, the highest coefficient of genetic similarity between the different guinea birds lines was 0.93 in (OPQ-01) were the lowest 0.76 was in (OPA-12). Thin is similar with reported by Bawej,

Table 3. Number of bands, % Polymorphism, Size (bp),Primer efficiency and Discriminatory Value for different prime

Primer number	Total number of band	polymorphic band	Mono band	Monomorphic band	% Polymorphism	Size (bp)
PA-07	15	1	3	14	6.67	500 - 1000
OPA-10	25	12	2	13	48.00	100 - 1400
OPA-03	53	5	10	48	9.43	220 - 1200
OPA-06	15	7	4	8	46.67	100 - 800
OPA-12	35	2	8	33	5.71	200 - 1500
OPA-14	7	1	1	6	14.29	400 - 500
OPA-15	7	1	1	6	14.29	401 - 500
OPA-19	7	1	1	6	14.29	402 - 500
OPA-20	7	1	1	6	14.29	403 - 500
OPQ-10	7	1	1	6	14.29	404 - 500
OPA-04	7	1	1	6	14.29	405 - 500
OPQ-01	7	1	1	6	14.29	406 - 500
OPQ-12	7	1	1	6	14.29	407 - 500
OPQ-15	7	1	1	6	14.29	408 - 500
Sum	206	36	36	170	17.48	0

et al. (2012), who found coefficient of genetic similarity was 1 between both colors white and gray guinea birds, and it is indicative of entire similarities. The high and average genetic similarity was determined as the mean for primers, 0.97 between both colors. But I found 0.76 between white and black colors of guinea birds determined as the mean for primers used, (Table 4).

Table 4. Coefficient of genetic similarity (F) for different groups and primers

	Within groups		
Primer	white guinea fowl	Black guinea fowl	white/Black
OPA-07	0.84	1.00	0.92
OPA-10	0.93	0.82	0.87
OPA-03	0.80	0.85	0.82
OPA-06	0.86	0.92	0.89
OPA-12	0.73	0.80	0.76
OPA-14	1.00	0.82	0.91
OPA-15	0.91	0.78	0.85
OPA-19	0.80	1.00	0.90
OPA-20	0.81	0.92	0.87
OPQ-10	0.94	0.89	0.92

Nahashon, et, al., (2003) when determining the genetic similarity between guinea birds and hens it ranged from 0 - 0.46 and within guinea birds population from 0.89 – 0.98. It is a strong indicative of the lowest genetic similarity between species. In the other hand Sharma, et, al., (1998), ranged the genetic similarity from 0.95 – 0.97 within variety but between variety from 0.99 – 1,they show that genetic variation was lowest between and within varieties, when the evaluated the genetic variation from three (white, lavender and pearl) guinea birds. In the present study the coefficient of similarity, calculated among both white and black guinea birds 0.76 is lowest slightly than that reported by Sharma, et, al., (1998). In the study of Bawej, et al. (2012) study the mean value ranged from 0.92 - 1.0 within primers and 0.65 genetic similarity for white guinea birds and 0.64 for grey guinea birds within the color varieties of guinea fowl. It is know that the same primers with different poultry species may produce various results in various laboratories depending on the status of reaction, which translates into the genetic similarity coefficients. On the other hand, the various primer use in the same species gives various amounts of PCR products, which interpret in to various values of the genetic similarity coefficient.

3. CONCLUSIONS

Through the present study it was confirmed that RAPD is a valuable tool to evaluate genetic relationships. It indicated the effectiveness of RAPD markers in detecting the estimating of similarity and polymorphism between and within guinea birds lines. Genetic similarity evaluating

are useful for conservation of native guinea birds lines as a genetic resource and natural monument.

REFERENCES

Abdulrazaq,H.S., Suliaman, N. M. A.,(2016) Genetic Relationship and Similarity of Some Chicken Strains". *ZANCO Journal of Pure and Applied Sciences*, Vol. 28, no. 5, Nov. 2016, pp. 78-83.

Abdulrazaq, H. S., Chiman, H. S., Nazhad. H. Q.,(2019). Genetic Diversity Among horse Lines in Erbil Region Using RAPD Markers". *ZANCO Journal of Pure and Applied Sciences*, ZJPAS (2019) , 31(3);39-44 ..

Al_Jallad. T., Choumane. W., Hmeshe. M.,(2012). Characterization and Estimation of Genetic Diversity inTwo Syrian Chicken Phenotypes Using Molecular Markers. International Journal of Poultry Science 11 (1): 16-22.

Ali, B.A., Ahmed, M. M. M., Aly, O.M., (2003) Relationship between genetic similarity and some productive traits in local chicken strains. African Journal of Biotechnology 2(2), 46-47.

Bawej, M. B., Kokoszyński, D,. Bernacki, Z., (2012), who Evaluation Of Genetic Similarity Between White And Grey Varieties Of Guinea Fowl (*Numida Meleagris*). Journal of Central European Agriculture, 13(4), p.654-661.

Beutler,E., Gelbar, T . Aand Kuhl , W . (1990). Interfrence of heparin with the polymerase chain reaction . Bio Techniques 9,166.

Bowditch BM, Albright A, Williams J, Braun MJ (1993). The use of RAPD markers in comparative genomes studies. Meth Enzymol. 224:294–309.

Dehghanzadeh, H., Mirhoseini, S.Z., Romanov, M. N., Ghorbani, A., (2009) Evaluation of genetic variability and distances among five Iranian native chicken populations using RAPD markers. Pakistan Journal of Biology Sciences 12, 866-871.

Dolmatova, Iu. I., Saitbatalov, T.F., Gareev, F.T., (2000a) RAPD-analysis of genetic polymorphism of ducks: differences in breeds. Genetica 36, 682-687.

Dolmatova, Iu. I., Saitbatalov, T.F., Gareev, F.T., (2000b) RAPD-analysis of duck genetic polymorphisms. Interlineal differences in a Peking duck species. Genetica 36, 805-812.

Fadhil,I. A., Dakheel, M.H., Hussein, T.H., (2016) Detection of Genetic Diversity through Two Poultry Breeds by using RAPD-PCR Technique. Journal of Babylon University/Pure and Applied Sciences/ No.(9)/ Vol.(24)

Nahashon, S.N., Adefope, N., Amenyenu, A., Wright, D., Payne, L., (2003) Nutritional and genetic approaches for improving guinea fowl production efficiency. Cooperative Agricultural Research Program Seminar Series, Tennessee State University.

Nahashon, S.N., Amenyenu, A., Adefope, N., (2010) Genetic relatedness of Pearl Grey guinea fowl and Single Comb White Leghorn chickens. Journal of Poultry Science 47, 280-287.

Nei, M., Li, W.H., (1979) Mathematical model for studying genetic variation in terms of restriction endonucleases. Proceedings of the National of Academy Sciences of USA 76, 5269-5273.

Semenova S.K., Moiseeva I.G., Vasilev V.A., Filenko A.L, Nikiforov A.A., Sevestianova A.A., Ryskov A.P., (2002) Genetic polymorphism of Russian, European and Asian chicken breeds as revealed with DNA and protein markers. Genetika 38, 1304-1308.

Sharma D., Appa Rao K.B.C., Singh H. P., Totey S.M.,(1998) Randomly amplified polymorphic DNA (RAPD) for evaluating genetic relationships among varietes of guinea fowl. Genetic Anlysis: Biomolecular Engineering 14(4),125-128.

Sharma, D., Appa Rao, K.B., Singh, R.V., Totey, S.M., (2001) Genetic diversity among chicken breeds estimated through randomly amplified polymorphic DNA. Animal Biotechnology 12(2), 111-120.

Sharma, D., Dhama, K., (2007) Genetic polymorphism between guinea fowl lines with high and low antibody response to sheep red blood cells using randomly amplified polymorphic DNA (RAPD) markers. Indian Journal of Comparative Microbiology, Immunology and Infectious Diseases 28(1-2), unpaginated.

Singh, R.V., Sharma, D., (2002) Within and between-strain genetic variability in White Leghorn population detected through RAPD markers. British Poultry Science 43, 33-37.

Smith, P.J., Jones, C.P., Bartlett, J., Nestor, K.E., (1996) Use of randomly amplified polymorphic DNA markers for the genetic analysis of relatedness and diversity in chickens and turkeys. Poultry Science 75, 579-584.

ZANCO Journal of Pure and Applied Sciences
The official scientific journal of Salahaddin University-Erbil
https://zancojournals.su.edu.krd/index.php/JPAS

ISSN (print):2218-0230**, ISSN (online):** 2412-3986**, DOI: http://dx.doi.org/10.21271/zjpas**

RESEARCH PAPER

Influence of Calcium Foliar Application to Increase Growth and Yield of Two Strawberry Cultivars (*Fragaria x ananassa* Duch.)

Parween Muhammad Kareem Rozbiany[1], Shler Mahmood Taha [2]

[1,2]Department of Horticultural, College of Science of Engineering Agriculture, Salahaddin University- Erbil, Kurdistan Region, Iraq

A B S T R A C T:
There are many studies about calcium effect on strawberry plants in the world, but few studies have been devoted to investigating its effects on strawberries in Kurdistan-Iraq. Strawberry, which has around twenty documented species, is native to Asia, Europe and South and North America. In the horticulture, it is considered the most important fruits. This research investigates the effect of spray of calcium on growth, flowering and yield of two strawberry cultivars *(Fragaria X ananassa* Duch.). Three different concentrations of Ca (0, 250 and 500 ppm) were applied by foliar method on two cultivars of strawberry (Festival and Albion). The results revealed a substantial increase in all the vegetative growth parameters at the level (500 ppm) of calcium for Alboin cultivar. However, the highest number of daughter plants was recorded at the level (250 ppm). while all flowering parameters increased significantly at the level (500 ppm) of calcium for Festival cultivar, significant increases were observed in the fruit parameters such as dry weight (g), dry weight percentage and fruit length (cm) at the level (500 ppm) of calcium for Alboin cultivar. Furthermore, it is monitored that fresh weight (g), fruit diameter (cm), fruit size (cm^3), number of fruits, yield/plant (g) and yield/ha were increased significantly at the level (500 ppm) of calcium for Festival cultivar. Moreover, the highest value of fruit fall percentage was recorded at the control of Albion cultivar, conversely the lowest value was at control of Festival. The TSS and ascorbic acid were significantly elevated at the level (500 ppm) for Alboin cultivar, however, acidity percentage and sugar percentage raised significantly at the level (500 ppm) calcium for Festival cultivar. The biggest amount of vitamin C was acquired after storage of Festival cultivar that treated with (500 ppm) calcium, whereas the smallest amount was from the control group of Festival cultivar.

KEY WORDS: Ca concentration, Foliar application, Festival, Albion, Fragaria X ananassa Duch.
DOI: http://dx.doi.org/10.21271/ZJPAS.32.2.15
ZJPAS (2020) , 32(2);145-150 .

1.INTRODUCTION

Calcium plays a very important role in plant growth and nutrition, as well as in cell wall deposition. Fragaria X ananassa Duch is the periodic fruiting type of the strawberry and is a long-night plant. During this short time, limited vegetative growth happens. Consequently, according to (Asrey et al., 2004) and (Singh et al., 2007) the produced fruit has poor quality and minimum marketable yield. Thus, it fetches less price in the market. Even though fresh strawberries contain high amount of vitamin C and phenolic compounds, their quality declines straight after harvest (Sturm, 2003 and Oszmianski, 2009). Testoni (2006) expressed that strawberries fruit is a highly rich source of bioactive composites comprising vitamin E, ascorbic acid, ß-carotene and phenolic compounds (phenol acids, flavan-3-ols, flavones, and anthocyanin). In addition, to determine fruit quality in strawberry, total soluble solids (TSS), total acids (TA) and their proportion (TSS/TA) considered as vital parameters. Within the mitochondria, Ca play a vital role in the formation

* **Corresponding Author:**
Parween Muhammad Kareem Rozbiany
E-mail: Parween.kareem@su.edu.krd
Article History:
Received: 13/09/2019
Accepted: 19/11/2019
Published: 22//04 /2020

of protein and escalating the amount of protein. Because of mitochondria's role in aerobic respiration and absorbing nutrients, it can be stated that the amount of calcium directly related to nutrient uptake by plants. The uptake of calcium by the plant is utilized by the mass diffusion.

The quality and the firmness of fruit is closely associated to calcium (Ca) (Sams, 1999). Chéour (1991) demonstrated that the functions and structure of cell walls and membranes, and cell metabolism events might be impacted by the frequent application of Ca, it is considered a vital mineral element that strawberry fruit quantity. However, calcium may cause issues for the quality because of its slow movement. The transference of Ca to the plant and fruit might decrease physiological damage of fruit. The ripening presses rises DE polymerization of pectin in the strawberry fruit. Kaya (2002) reported that one of the most important constituents in the plant cell wall is Ca which leads the solidity of cell wall. According to Hernandez- Muñoz *et al.* (2008) fruit nutrition value and fruit density are positively affected by the addition of calcium. Moreover, Levent Tuna *et al.* (2007) indicated that Ca supplementation has positive impact on the growth and crop yields. The results of Andriolo *et al.,* (2010) revealed that the calcium chloride ($CaCl_2$) applications did not significantly impact plant growth, total soluble solids (TSS) and the TTS/TA proportion. The study also demonstrated that while $CaCl_2$ addition rises the leaf area index, it reduces fruit production. In addition, each of Dunn and Able (2006) and Ramezanian *et al. (*2009) stated that average size and fruit weight of strawberry fruits increased by the application of $CaCl_2$. However, the treatable acidity was not affected significantly. It was also reported that $CaCl_2$ escalates the contents of ascorbic acid. In fruits, retaining ascorbic acid content was significantly affected by $CaCl_2$ treatments. This could be related to calcium chloride concentration that suspend the quick oxidation of ascorbic acid (Ramezanian *et al.* 2009).

The effect of supplementary calcium and potassium on fruit yield and quality of strawberry (*Fragaria X ananassa* Duch.) was investigated by Khayyat *et al.* (2007) who found that while the ratio of TSS/TA was bigger in NaCl+K2SO_4 treatment, the TA, TSS and vitamin C were higher in NaCl+$CaCl_2$ treatment. It proposes that the application of $CaSO_4$ results in escalation in production and quality of strawberry in saline conditions. According to Hernandez-Muñoz *et al.* (2008), fruit nutrition value and fruit density are positively affected by the addition of calcium. Moreover, Levent Tuna *et al.* (2007) indicated that Ca supplementation has positive impact on the growth and crop yields. Calcium application caused the increased number of runner/plants significantly (Dastjerdy *et al*., 2014). It exhibits that flower number, fruit harvest and the inflorescence affected by nitrogen. The post-harvest life is enhanced and increased by calcium. Using spraying technique for calcium application positively impacted plant growth. Nitrogen addition resulted in the increase in the amount of the total soluble solids. For improving fruit production, the ideal treatment was observed when the nitrogen concentration were 240 mg/l and calcium concentration was 300 mg/l. These concentrations of nitrogen and calcium were proposed to decline production costs and increase the post-harvest life (Motamedi *et al.*, 2010).

Kazemi (2013) examined the effect of salicylic acid and calcium chloride sprays on the production parameters of strawberry. It was demonstrated that vegetative and reproductive growth were significantly impacted by the foliar application of salicylic acid and calcium chloride either alone or in mixture. It was also displayed that quality and yield of strawberry plants was enhanced in low levels of calcium chloride and salicylic acid. The study concluded that for yield enhancement and preventing yield reduction, the application of calcium chloride and salicylic is advantageous. The most effective approach for escalating calcium content in fruit is direct application of calcium to the fruit (Conway *et al.*, 2002).

Wojcik and Lewandowski (2003) stated that applying calcium chloride by foliar technique delays ripening process and retards fungal growth on strawberries. Kazemi (2014) investigated the effect of foliar application of iron, calcium and zinc sulphate on reproductive growth, yield and several qualitative characteristics of strawberry plants. The study exposed that leaf area, dry weight, length of roots of strawberry increased by the application of calcium, iron and zinc sulphate. The number of flowers, weight of primary and secondary fruits were enhanced by spraying of calcium at 10 mM. Generally, to increase the

strawberry yield, spraying calcium at 10 mM concentration is suggested. The objective of this experiment is to show the effect of calcium on the growth, flowering and fruiting of strawberry plant in different concentrations by foliar application.

2.Materials and Methods

Two strawberry cultivars; Albion and Festival were planted in plastic house with ambient sunlight. Planting date was October 15, 2016. The plants were dormant from November, 2016 to March, 2017. The treatments were applied on the plants when they completely grown after three months. Different levels of calcium were applied. The experiment comprised of three treatment groups: a control group (0 ppm calcium), and the other two groups were either treated with (250 ppm) or (500 ppm) calcium. Spraying method was utilized for supplying Ca. Standard practices of fertilizer and pesticides were applied for improving the vegetative growth and controlling insects and diseases. The experiments were performed using Complete Randomized Design (CRD) with 6 replications and results were analyzed using Statistical Analysis System (SAS) software.

3.Results

Table 1 demonstrates that most of vegetative growth parameters as fresh weigh, dry weight, crown diameter, Number of stolons (runners) and chlorophyll pigment percentage had recorded the higher values in Alboin cultivar in comparison to the Festival cultivar at the level (500 ppm) of calcium. Nevertheless, the number of daughter plants recorded the higher value at the level (250 ppm) of calcium for Alboin cultivar and this in agreement with (Levent Tuna *et al.,* 2007 and Kazemi, 2013).

In Table 2, it can be observed that there is a significant increase in all flowering parameters including number of flowers, fruit set% and available pollen grain at the level (500 ppm) calcium for Festival cultivar compared to the Alboin cultivar at the same level. This result is in agreement with (Dastjerdy *et al.,* 2014).

Table 3 displays significant increases in the fruit parameters such as fresh weight, dry weight, fruit diameter, number of fruit, fruit size, yield/plant (g) and yield/ha (kg) at the level (500 ppm) of spray calcium for Festival. Nonetheless, fruit length at the level (500 ppm) calcium for Alboin cultivar. However, the highest value of fruit fall percentage was recorded at the control treatment of Albion cultivar and the lowest value was at the control treatment of Festival. This in agreement with (Levent Tuna *et al.,* 2007; Kazemi, 2013 and 2014).

It is clearly shown in table (4) that TSS and ascorbic acid increased significantly at the level (500 ppm) calcium for Alboin cultivar, while acidity percentage and sugar percentage increased significantly at the level (500 ppm) calcium for Festival cultivar (Andriolo *et al.,* 2010; Motamedi *et al.,* 2010 and Dastjerdy *et al.,* 2014) found similar results.

Table 1. Effect of foliar calcium application on the growth of some vegetative parameters of strawberry plants (Festival and Albion cultivar).

Parameters	Festival			Albion		
	0	250 ppm	500 ppm	0	250 ppm	500 ppm
Fresh weigh (g)	59.01 f	82.79 d	90.67 b	60.67 e	87.10 c	92.11 a
Dry weight (g)	18.89 f	25.64 d	36.41 b	21.17 e	30.21c	42.57 a
Crown diameter (cm)	0.97 f	1.55 d	2.120 c	1.070 e	2.10 b	2.24 a

No. runners	7.47 f	9.33 d	11.07 b	8.020 e	10.22 c	11.92 a
No. daughter plant	9.41 e	16.36 c	20.66 b	10.22 d	21.62 a	20.66 b
Chlorophyll %	11.33 e	14.09 c	15.69 a	11.92 d	15.24 b	15.69 a

Table 2. Effect of foliar calcium application on some flowering parameters of strawberry plants (Festival and Albion cultivar).

Parameters	**Festival**			**Albion**		
	0	**250 ppm**	**500 ppm**	**0**	**250 ppm**	**500 ppm**
No. flowers	11.18 e	20.80 c	23.37 a	10.33 f	18.74 d	21.52 b
Fruit set%	57.79 e	69.95 c	83.06 a	47.39 f	65.66 d	79.78 b
Available pollen grain%	46.62 d	58.55 c	71.80 a	41.74 e	59.32 c	63.64 b

Table 3. Effect of foliar calcium application on some parameters of the strawberry fruits (Festival and Albion cultivar).

Parameters	**Festival**			**Albion**		
	0	**250 ppm**	**500 ppm**	**0**	**250 ppm**	**500 ppm**
Fresh weight (g)	6.00 e	7.28 c	8.34 a	5.73 f	7.30 c	8.04 b
Dry weight (g)	0.46 e	0.77 d	1.90 a	0.47 e	0.91 b	1.11 b
Fruit diameter (cm)	1.00 e	1.37 b	1.63 a	1.01 e	1.17 d	1.33 c
Fruit length (cm)	1.00 f	1.37 e	1.58 d	1.92 c	2.48 b	2.72 a
Fruit size (cm3)	1.35 e	2.28 c	2.63 a	1.23 f	1.94 d	2.38 b
No. fruits	12.79 f	19.31 c	24.60 a	13.9 8 e	18.87 d	24.09 b
Fruit fall%	20.19 b	15.43 c	11.99 e	20.94 a	15.34 c	12.88 d
Yield/plant (g)	67.94 e	84.52 b	87.03 a	59.78 f	70.59 d	75.79 c
Yield/ha (kg)	339.72 e	422.63 b	435.15 a	293.85 f	351.75 d	374.05 c

Table 4. Effect of foliar calcium application on some chemical substance in strawberry fruits (Festival and Albion cultivar).

Parameters	Festival			Albion		
	0	**250 ppm**	**500 ppm**	**0**	**250 ppm**	**500 ppm**
TSS	5.49 e	6.05 c	6.78 a	4.97 f	5.75 d	6.23 b
Vitamin C	24.75 e	26.24 c	27.59 a	24.91 f	26.09 d	26.81 b
Acidity%	0.79 d	0.79 d	0.84 b	0.81 c	0.79 d	0.87 a
Sugar%	0.10 d	0.12 c	0.14 b	0.10 d	0.12 c	0.15 a

4.Discussions

Calcium, in the form of calcium pectate, is responsible for holding together the cell walls of plants. Calcium is also used in activating certain enzymes and to send signals that coordinate certain cellular activities. It is a structural part of the cell walls, by forming cross-links within the pectin polysaccharide matrix. With rapid plant growth, the structural integrity of stems that hold flowers and fruit. It assists in movement of carbohydrates within the plant. Calcium insufficiency may impede plant growth and, as its function in root growth is so important, plants may suffer from other nutrient deficiencies as a result of calcium deficiency.

In strawberry cultivar Festival with foliar calcium at 500 ppm resulted in a remarkable increase of most of studied characteristics. While Albion cultivar shoed less response to foliar calcium at the same level. Wójcik and Lewandowski, (2003) examined the effects of foliar applications of calcium (Ca) and boron (B) on yield and fruit quality of 'Elsanta' strawberries grown on a sandy loam. Results showed that fruit and leaves from Ca-treated plants had increased Ca concentrations.

5.Conclusion

The results exposed that the application of calcium significantly affected vegetative and reproductive characteristics of strawberry. Furthermore, increasing the concentration of Ca increased the postharvest life. Moreover, the application of Ca by spraying method had positive effects on the growth of the plant. Generally, spraying calcium at the level (500 ppm) had the highest impact on the growth, flowering and yield of strawberry plants.

Acknowledgements

This work would not have been possible without the financial support of the College of Agricultural Engineering Sciences, University of Salahaddin-Erbil, Kurdistan Region, Iraq.

I am especially indebted to Dr. Jihad Sharif, Chairman of the Department of Horticulture, and my supervisor Dr. Shler Mahmud Taha, who have been supportive of my career goals and who worked actively to provide me with the protected academic time to pursue those goals.

I would especially like to thank Dr. Noura U. Kka. and Mr. Ali M. Ali for their supporting. I am grateful to all members of my family those with whom I have had I would like to thank all of them.

References

Andriolo, J. L., Janisch, D. I., Schmitt, O. J., Dal Picio, M., Cardoso, F. L. and Erpen, L. 2010. Potassium and calcium doses on plant growth, fruit yield and quality of strawberries in soilless cultivation. *Ciencia Rural, (40):* 237-242.

Asrey, R., Jain, R. K. and Singh, R. 2004. Effect of pre-harvest chemical treatment on shelf life of 'Chandler' strawberry (*Fragaria ananassa*). *Indian J. Agri. Sci., (74*): 485-487.

Cheour, F., Willemot, C., Arul, J., Makhlouf, J. and Desjardins, Y. 1991. Postharvest response of two strawberry cultivars to foliar application of CaCl2. *HortScience, (26):* 1186–1188.

Conway, W. S., HIckeyI, K.D., Sams, C.E. 2002. Pre- and postharvest calcium treatment of apple fruit and its effect on quality. *Acta Horticulturae, (592)*:53-58.

Dunn, J. L. and Able, A.J. 2006. Pre-harvest calcium effects on sensory quality and calcium mobility in strawberry fruit. *Acta Horticulturae, (708):* 307-312.

Dastjerdy, T. M., Jafarpour, M., Rezagolparvar, A. 2014. Effect of Applying Calcium and Zinc on vegetative Characteristics of Strawberry "Aromas". The 1st International conference on New Ideas in Agriculture. Islamic Azad University Khorasan Branch.26-27Jan.20140 Isfahan. Iran.

Hernandez-Muñoz, P., Almenar, E., Del VallE, V., Velez, D., and Gavara, R. 2008. Chitosan coating combined with postharvest calcium treatment on strawberry (*Fragria ananassa*) quality during refrigerated storage. *Food Chemistry, (110):* 428-435.

Kaya, C., Kimak, M., Higgs, D., AND Saltali, K. 2002. Supplementary calcium enhances Plants growth and fruit yield in strawberry cultivars grown at high (NaCl) salinity. *Scentia Horticulture, (93)*: 65-74.

Kazemi, M. 2013. Foliar Application of Salicylic Acid and Calcium on Yield, Yield Component and Chemical properties of Strawberry. Bull. Env. *Pharmacol. Life Sci, (2):* 19-23.

Kazemi, M. 2014. Influence of foliar application of iron, calcium and zinc sulfate on vegetative growth and reproductive characteristics of strawberry cultivar. 'pajaro'. *Trakia Journal of Sciences, (12)*: 21-26.

Khayyat, M., Tafazoli, Eshghi, E. S, Rahemi, M and Rajaee, S. 2007. Salinity, Supplementary Calcium and Potassium Effects on Fruit Yield and Quality of Strawberry (*Fragaria ananassa* Duch.). *American-Eurasian J. Agric. & Environ. Sci., (2):* 539-544.

Levent tuna A, C. K., Muhammad A, Hakan A, Ibrahim Y, and Bulent Y. 2007. The effect of calcium sulphate on growth, membrane stability and nutrient uptake of tomato plants grown under salt stress. *Environmental and Experimental Botany, (59):* 173-178.

Lieten,I F., Misotten, C. 1993. Nutrient uptake of strawberry plants (cv. Elsanta) grown on substrate. *Acta Hortic, (348):* 299-306.

Motamedi, S. Jafarpour, M. and Shams, J. 2010. Evaluation of nutrition on flower number and yield of strawberry in greenhouse. *International Journal of Agriculture and Crop Sciences, (5):* 2091-2095.

Oszmianski, J., and Wojdylo, A. 2009. Comparative study of phenolic content and antioxidant activity of strawberry puree, clear, and cloudy juices. *European Food Research and Technology, (4):*623-631

Ramezanian, A., Rahemi, M. and Vazifehshenas, M.R. 2009. Effects of foliar application of calcium chloride and urea on quantitative and qualitative characteristics of pomegranate fruits. *Sci. Hortic, (121):* 171-175.

Sams, C. E. 1999. Preharvest factors affecting postharvest texture. *Postharvest Biology and Technology, (15)*: 249-254.

Singh, R., Sharma, R.R. and Tyagi SK. 2007. Prehavest foliar application of calcium and boron influences physiological disorders, fruit yield and quality of strawberry (*Fragaria ananasa*). *Scintia Horticulture, (112):*215-220.

Sturm, K., Koron, D., and Stampar, F. 2003. The composition of fruit of different strawberry varieties depending on maturity stage. *Food Chemistry, (83):* 417-422.

Testoni, A., Lovati, F, Nuzzi, M. 2006. Evaluation of postharvest quality of strawberries in Italy. *Acta Hortic, (708):* 355-358.

Wojcik, P., Lewandowski, M. 2003. Effect of calcium and boron sprays on yield and quality of ''Elsanta" strawberry. *Journal of Plant Nutrition, (24):* 671-682.

ZANCO Journal of Pure and Applied Sciences
The official scientific journal of Salahaddin University-Erbil
https://zancojournals.su.edu.krd/index.php/JPAS

ISSN (print):2218-0230**, ISSN (online):** 2412-3986**, DOI: http://dx.doi.org/10.21271/zjpas**

RESEARCH PAPER

Determination of the Aflatoxin B1 Level in Imported Milled Rice by ELISA in Duhok Province

[1]Jaafar A. Ali, [2]Nadhim Sulaiman A. Jakhsi

[1] Food Analysis laboratory, Directorate of Preventive Health Affairs, Duhok, Kurdistan Region, Iraq

[2] Department of Microbiology and Pathology, College of Veterinary Medicine, Duhok University, Kurdistan Region, Iraq

A B S T R A C T:
Aflatoxins are fungal metabolites, toxic and carcinogenic. Aflatoxin B1 is the most common toxic mycotoxin classified as Group I carcinogen by the International Agency for Cancer Research. The purpose of this study is to determine the level of Aflatoxin B1 in different varieties of milled rice imported from different origins to Kurdistan region of Iraq between October and December 2018 by using indirect competitive enzyme-linked Immunosorbent Assay (ELISA). A total of 150 rice samples (30 each group) were collected from different sources (Thailand, Russia, India, Kurdistan and different sources from Iraqi public food distribution system), to evaluate their Aflatoxin B1. Out of 150 samples 90 (60%) have been detected with Aflatoxin B1, while the others 60 (40%) samples were not detected (under the detection limit of 0.02µg/kg). The concentrations were ranged from (0.03 to 3.12) µg/kg with an average range 0.94 µg/kg. The highest percentage of detected samples were from Russia 25 (28%) followed by a group of origins distributed through national distribution system 22 (24%), Thailand 21 (23%), Kurdish 12 (13%) and the lowest percentage was from India 10 (11%). However, out of 90 positive samples, only 4 (4%) samples from Russia were exceeded the European Union regulations limit of 2µg/kg of Aflatoxin B1 and other 86 (96%) were within the permissible levels of international legislations, these concentrations can cause a serious health issues to human because of the large amount of rice consumption per capita per year in Kurdistan region where rice is included in the daily diet, as a result, accumulation of Aflatoxin B1 in a human body will raise.

KEY WORDS: Aflatoxin B1, ELISA, Rice.
DOI: http://dx.doi.org/10.21271/ZJPAS.32.2.16
ZJPAS (2020) , 32(2);151-156 .

1. INTRODUCTION

Rice (*oryza sativa*) is the staple food grain of over 50 percent of the world population and is the second main grain consumed after wheat (Elzupir, Alamer and Dutton, 2015). Iraq ranked among top ten countries of rice importer in the world (Bedford et al., 2017). The largest amount of rice in the world in 2018 were produced by China with 208.1, followed by India with 169.5 million metric tons (FAO, 2018). It is flood resistant, dry, damp, cool and warm and grows in alkaline acid and saline soils (Eslami et al., 2015).

Mycotoxins are secondary fungal metabolites that can contaminate a broad range of foods (Ferre, 2016). In addition, the natural contaminants of important plant products (rice, wheat, barley, maize ... etc.). They created serious problems for human and animal health (Kamkar et al., 2014).

Aflatoxins are the world's leading food contaminant mycotoxins (Kamkar et al., 2014)

* **Corresponding Author:**
Jaafar Abdulmanaf Ali
E-mail: Email: jaferdhk73@gmail.com or jaferdhk73@duhokhealth.org
Article History:
Received: 16/10/2019
Accepted: 01/12/2019
Published: 22/04 /2020

which are a class of mycotoxins mainly produced by *Aspergillus flavus*, *A. parasiticus*, and seldom *A. nominus* (Alpsoy, 2010; Reddy et al., 2010). The main Aflatoxins are AFB1, AFB2, AFG1, AFG2, AFM1 and AFM2. They are harmful for human health because of their toxicity, carcinogenic, mutagenic, teratogenic and hepatotoxic characteristics. Amongst other Aflatoxins, AFB1 is the most toxic type; and also is the most powerful human cancer. AFB1 is therefore listed by the International Agency for Research Cancer (IARC) of the World Health Organization (WHO) as group I of carcinogenic chemicals compounds (Elzupir, Alamer and Dutton, 2015). There is a high risk of liver cancer for careers of hepatitis B or hepatitis C if Aflatoxin is exposed (Costanzo et al., 2015). The findings of epidemiological data indicate that liver cancer and exposure to AFB1 are in a positive correlation which may be increased by hepatitis B virus (Liu et al., 2012). The carcinogenicity of Aflatoxins is higher 30 times for populations infected by hepatitis B virus (Groopman, et al. 2008).

Aflatoxin B1 are heat-stable chemical compounds that during most food processing are not totally destroyed. Several countries have therefore developed broad law to regulate mycotoxin levels in plant products, and each has its own different limits (Tavakoli et al., 2013; Kamkar et al., 2014)**.**

The maximum tolerable limits for total Aflatoxins (B1+B2+G1+G2) and 2µg / kg for AFB1 in rice were established by the European Union as 4µg / kg for total Aflatoxins (B1+B2+G1+G2) (Commission, 2010). A joint FAO / WHO Expert Committee on food additives reviewed Afatoxins in 1987 (FAO/WHO, 1987) No daily intake was acceptable; individual intakes were advised to be reduced to the lowest executable.

Many methods, including thin-layer chromatographic (TLC) analysis, high-performance liquid chromatography (HPLC) and the enzyme-linked immunosorbent assay (ELISA), were used for analyzing Aflatoxins (Tavakoli et al., 2013; Sasan et al., 2014). Due to the adaptability, simplicity and sensitivity, ELISA is the most common method for the study of Aflatoxins (Magliulo et al., 2005), even accuracy of the study and routine diagnosis of a huge range of samples (Kamkar et al., 2014).

This work was determined the level of Aflatoxin B1 in most common consumed imported rice in Duhok province, Kurdistan region of Iraq.

2. MATERIALS AND METHODS

2.1. Sample Collection:

A total of (150) imported raw milled rice samples (250 g each) from five different sources (Thailand, India, Kurdistan, Russia and group origins distributed through national public distribution system of food) were collected randomly in Duhok governorate, Kurdistan region of Iraq during winter between October and December 2018. The samples were collected from local markets; retail stores and sampling unit of Ibrahim Khalil (border point between Iraq and Turkey). Long grain white rice (Basmati), white medium grain rice and round grain rice were evaluated for their Aflatoxins content. In addition, locally produced round grain rice (Kurdish) cultivated at a limited scale was also evaluated for Aflatoxins. The storage period of rice samples was ranged between 3-24 months. All samples were labeled then, placed in clean paper bags then, in zipped polyethylene bags. After that, the samples were shipped to the food analysis laboratory belong to directorate of preventive health affairs in Duhok governorate to be store at -20°C until analysis.

2.2. Detection of AFB1 by indirect competitive ELISA:

The quantitative detection of AFB1 and preparation of the samples were performed based on a competitive enzyme immunoassay using Helica Bio-systems, Aflatoxin B1, ELISA assay Low Matrix 69-1B10LFAB149 test kit, USA, 2018.

2.3. Extraction of AFB1 from rice samples:

The extraction procedure was carried out according to commercial ELISA kit of Helica Bio-systems, USA, 2018. The Samples (250g) were thoroughly mixed and 30g from a sub-sample were ground to powder. Twenty grams from powdered sub-sample were added to the 100ml of 80% methanol (20ml distilled water with 80ml of methanol v/v). The ratio of sample to extraction solvent is 1:5 (w/v). The samples were mixed by

shaking in a sealed container for 10 minutes then, left for 30 minutes to allow the particulate matter to settle. Ten milliliter from aliquot was centrifuged 3500 RPM for 5 minutes and the extract were diluted 1:10 in phosphate buffer saline containing 0.05% Tween20 prior to ELISA test. (The final dilution was 1:50).

2.4. ELISA test procedure:

According to manual instructions provided with Aflatoxin B1 (cat#981BAFL01LM-96) low matrix test kit, 100µl of each standard and prepared sample was gently mixed with 200µl of sample diluent in a mixing well. Then, 100µl from each mixing well was transferred to a corresponding antibody coated microtiter well, incubated at room temperature (20–25°C) for 30 minutes. Liquid was drained by firmly taping the wells against the absorbent paper; a washing buffer washing three times the wells (300 µl). After that, 100µl from horse-radish peroxidase (HRP) Aflatoxin enzyme conjugate was added to each well and incubated 30 minutes at room temperature. After a washing step repeated, 100µl of substrate solution added to each well, incubated 10 minutes at room temperature in a dark place. Finally, 100µl of the stop solution was added to each well and the optical density (OD) of the resulting color was measured at 450nm by using ELISA plate reader (BioTek-USA). To calculate the absorption percentage, the values obtained for the samples and standards were divided by the absorbance value of the 1st standard (zero standard) and then multiplied by 100 (percentage of maximal absorbance). The founded intensity of absorption in the samples was inversely proportional to AFB1 concentration. In order to create a generic curve and then measure the AFB1 concentration in every sample, Helica Bio-system was used.

2.5. Statistical Analysis:

Statistical analysis was applied using Minitab software version 17.1 (Minitab, LLC, USA, 2014). Results were given as mean ± SD to illustrate Aflatoxin B1 concentration ranges in each origin and study the differences.

3. RESULTS:

The Aflatoxin B1 contamination in different imported rice samples were presented in data sheet (Table 1). A total of 150 milled rice samples from 5 origins (Thailand, India, Russia, Kurdish and different origins from Iraqi public food distribution system), (Thirty samples each) were analyzed for Aflatoxin B1 contamination. Analytical results showed that 60% (90 out of 150) rice samples were detectable or positive (containing ≥ 0.03 µg/kg AFB1) ranged between 0.03-3.12 µg/kg of Aflatoxin B1 with an average 0.94 µg/kg , while the remaining 40% (60 out of 150) samples were undetectable or negative (containing less than 0.03µg/kg AFB1) to ELISA test (Figure 1).

Figure 1: Percentage of negative and positive samples**.**

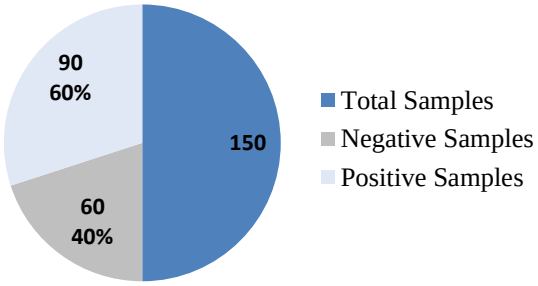

Table 1: Occurrence and level of Aflatoxin B1 in rice in different origins imported to Kurdistan region of Iraq.

			Number of samples in AFB1 concentration range, (µg/kg)				
Sample Origins	Analyzed Samples	Positive Samples	<1	1-2	>2	AFB1 ranges (µg/kg)	Average ±SD (µg/kg)
Russia	30	25 (83%)	11 (44%)	10 (40%)	4 (16%)	0.35-3.12	1.28©±0.70
Iraqi PDS*	30	22 (73%)	18 (82%)	4 (18%)	0	0.12-1.38	0.62±0.39
Thailand	30	21 (70%)	7 (33%)	14 (67%)	0	0.03-1.73	1.03±0.47
Kurdish	30	12 (40%)	9 (75%)	3 (25%)	0	0.06-1.51	0.77±0.41
India	30	10 (33%)	6 (60%)	4 (40%)	0	0.10-1.83	0.86±0.76
Total	150	90 (60%)	51 (57%)	35 (39%)	4 (4%)	0.03-3.12	0.94±0.60

* Origins selected from Iraqi Public Distribution System (Uruguay, USA, Argentina, Vietnam and Thailand).

The minimum limit of detection (LOD) for Aflatoxin B1 (low matrix) kit used was 0.02µg/kg. The (average ± SD µg/kg) ranges of Aflatoxin B1 contamination were 1.28±0.70 for Russia, 1.03±0.47 Thailand, 0.86±0.76 India, 0.77±0.41 Kurdish and 0.62±0.39 for origins (Uruguay, USA, Argentina, Vietnam and Thailand) distributed through Iraqi public food distribution system. The results showed that maximum level of AFB1 was found in rice samples originated by Russia and lowest from rice samples originated by India. Only 4 (4%) samples from all detectable (positive) samples were exceeded the European Union (EU) regulatory limit of AFB1 (2µg/kg); all of them were Russian origins while, none of the other 86 (96%) samples were passed over EU tolerance limits of AFB1.

4. DISCUSSION

AFB1 is one of the most toxic mycotoxins in various studies examined in rice samples. In this study 150 imported milled rice samples from different sources were analyzed for Aflatoxin B1 content. A total of 60% (90) samples were detected, 25 (28%) samples from Russia, 22 (24%) from sources distributed through Iraqi public food system (Uruguay, USA, Argentina, Vietnam and Thailand), 21 (23%) from Thailand, 12 (13%) from Kurdish (locally cultivated) and 10 (11%) from India. The contamination range of AFB1 in rice samples cultivated in Russia 4(4%) were out of normal ranges comparing with European regulations limit, while all other samples were in the normal ranges. The finding of highest percentage of contaminated samples in rice originated by Russia may be because of inappropriate harvesting, transporting and storage conditions. Moreover, the variety of rice cultivating in Russia (round rice) has more ability to affected by Aflatoxigenic fungi as it contain more starch and produced more broken seeds through milling process. On the other hand, the appropriate harvesting, good conditions of storage, pigmentation and flavoring, as well as quality improvement may be result from smallest percentage of contaminated samples from India because all of these processes and conditions play an important role in propagation of Aflatoxigenic fungi. Regarding in rice cultivated locally (Kurdish), although it has low level of harvesting, milling, storage and packing, it registered a small portion of positive samples in our study due to its freshness and a short time of both transporting and storage. This finding is strongly significant therefore the author strongly recommend further studies on different varieties of locally cultivated rice should be conducted.

Aflatoxin B1 contaminations in rice are reported in previous studies most of them analyzed different varieties of rice. In a study by Park et al., 2005 (Je, Lee and Kim, 2005) in Korea, they analyzed the concentration range of Aflatoxin B1 in 88 samples of polished rice and reported that 5 (5.6%) samples with mean 4.3 µg/kg were contaminated with Aflatoxin B1. Also, AFB1 found in 21 (11.2%) samples from 187 rice samples analyzed with a maximum range of (63.32µg/kg) in Brazil by Katsurayama et al., 2018. In Canada, Bansal et al., 2011 Investigated 99 different varieties of rice from retail markets and registered (56.1%) as incidence of Aflatoxin B1 and they discovered that the most contamination presence was related to AFB1 which was higher than other mycotoxins. In another study carried out by Wang and Liu, 2007 they detected AFB1 in 16 out of 84 rice samples with a range of (0.15–3.22µg/kg) which is like our study ranges. Similar incidence of AFB1 in rice samples (67.8%) to our study were reported in a survey by Reddy et al. 2009, when they found the AFB1 in 814 (68%) out of 1200 rice samples of Basmati variety collected from field and where-houses in India. In (2011), Makun et al. published a maximum incidence (100%) in Nigeria from 21 different rice samples, Also, in (2012) and (2013) a similar incidence of AFB1 in rice samples showed by (Eslami et al., 2015) in Iran.

Such concentrations of AFB1 are high and are most likely to cause acute human symptoms and are therefore disturbing and essential for experts and government bodies, producers and consumers. They would play an important role in the propagation of hepatocellular carcinoma (HCC) in rice in countries with a high intake of rice in AFB1. As a result, the outcome of these investigations places a responsibility on the member states of such populations to ensure food safety for this basic food commodity.

5. CONCLUSIONS AND RECOMENDATIONS:

To conclude, the level of Aflatoxin B1 in most varieties of consumable imported, and some locally cultivated rice are in the allowed ranges while, excessive observation should be taken by continuous screening of AFB1 in imported rice in all custom points of Iraqi borders because Aflatoxins have a negative impact on consumer health especially in rice-consumer countries such as Iraq where, rice consider as a main part of the daily food system.

ACKNOWLEDGMENTS

I would like to thanks all members of the department of microbiology and pathology and Duhok Research Center at College of Veterinary Medicine in the University of Duhok also, special thanks to all members of food laboratory at Directorate of Preventive and Health Affairs, Duhok Governorate for supporting me to complete the study work.

Conflicts of interest Statement

The authors declare that they have no conflict of interest.

FUNDING

This research was funded by individuals.

References:

Alpsoy, L. (2010) 'Inhibitory effect of essential oil on aflatoxin activities', African Journal of Biotechnology, 9(17), pp. 2474–2481.

Bansal, J. et al. (2011) 'Surveys of rice sold in canada for aflatoxins, ochratoxin a and fumonisins', Food Additives and Contaminants - Part A Chemistry, Analysis, Control, Exposure and Risk Assessment, 28(6), pp. 767–774. doi: 10.1080/19440049.2011.559279.

Bedford, D. et al. (2017) Food Outlook. [Online], Available from: www.fao.org/paublications [Accesed 12 Jun. 2019].

Commission, T. H. E. E. (2010) 'COMMISSION REGULATION (EU) No 165/2010', Official Journal of the European Union, 50/9(2009), pp. 8–12.

Costanzo, P. et al. (2015) 'Toxicity of aflatoxin B1 towards the vitamin D receptor (VDR)', Food and Chemical Toxicology. Elsevier Ltd, 76, pp. 77–79. doi: 10.1016/j.fct.2014.11.025.

Elzupir, A. O., Alamer, A. S. and Dutton, M. F. (2015) 'The occurrence of aflatoxin in rice worldwide: A review', Toxin Reviews, pp. 37–42.

doi: 10.3109/15569543.2014.984229.

Eslami, M. et al. (2015) 'Determination of aflatoxin B1 levels in Iranian rice by ELISA method', Toxin Reviews, 34(3), pp. 125–128. doi: 10.3109/15569543.2015.1074925.

Ferre, F. S. (2016) 'Worldwide occurrence of mycotoxins in rice', Food Control. Elsevier Ltd, 62, pp. 291–298.

doi: 10.1016/j.foodcont.2015.10.051.

Food and Agriculture Organization (2018) 'FAO Rice Market Monitor (RMM)', FAO. Rice market monitoring, XXI(1), p. 38 [Online] Available from:

http://www.fao.org/economic/est/publications/rice-publications/rice-market-monitor-rmm/en [Accessed 25 Sep. 2019].

Groopman, J. D., Kensler, T. W. and Wild, C. P. (2008) 'Protective Interventions to Prevent Aflatoxin-Induced Carcinogenesis in Developing Countries', Annual Review of Public Health, 29(1), pp. 187–203. doi: 10.1146/annurev.publhealth.29.020907.090859.

Je, W. P., Lee, C. and Kim, Y. B. (2005) 'Fate of aflatoxin B1 during the cooking of Korean Polished rice', Journal of Food Protection, 68(7), pp. 1431–1434.

Kamkar, A. et al. (2014) 'The review of aflatoxin M 1 contamination in milk and dairy products produced in Iran', 9543(4), pp. 160–168. doi: 10.3109/15569543.2014.922580.

Katsurayama, A. M. et al. (2018) 'Occurrence of Aspergillus section Flavi and aflatoxins in Brazilian rice: From field to market', International journal of food microbiology. Elsevier, 266, pp. 213–221.

Liu, Y. et al. (2012) 'Population attributable risk of aflatoxin-related liver cancer: Systematic review and meta-analysis', European Journal of Cancer. Elsevier Ltd, 48(14), pp. 2125–2136. doi: 10.1016/j.ejca.2012.02.009.

Magliulo, M. et al. (2005) 'Development and validation of an ultrasensitive chemiluminescent enzyme immunoassay for aflatoxin M1 in milk', Journal of agricultural and food chemistry. ACS Publications, 53(9), pp. 3300–3305.

Reddy, K. R. N. et al. (2010) 'An overview of mycotoxin contamination in foods and its implications for human health', Toxin reviews. Taylor & Francis, 29(1), pp. 3–26.

Reddy, K. R. N., Reddy, C. S. and Muralidharan, K. (2009) 'Detection of Aspergillus spp. and aflatoxin B1 in rice in India', Food Microbiology. Elsevier Ltd, 26(1), pp. 27–31. doi: 10.1016/j.fm.2008.07.013.

Sasan, A. et al. (2014) 'Determination of aflatoxin B 1 levels in Iranian and Indian spices by ELISA method', Toxin Reviews, 9543(4), pp. 151–154. doi: 10.3109/15569543.2014.942319.

Tavakoli, H. et al. (2013) 'Assessment of aflatoxin M1 levels by enzyme-linked immunosorbent assay in yoghurt consumed in Tehran, Iran', Asian J Chem, 25(5), pp. 2836–2838.

'Thirty-first report of the Joint FAO/WHO Expert Committee on Food Additives.' (1987) World Health Organization technical report series. Switzerland, 759, pp. 1–53.

Wang, J. and Liu, X.-M. (2007) 'Contamination of aflatoxins in different kinds of foods in China.', Biomedical and environmental sciences : BES. China, 20(6), pp. 483–487.

ZANCO Journal of Pure and Applied Sciences
The official scientific journal of Salahaddin University-Erbil
https://zancojournals.su.edu.krd/index.php/JPAS

ISSN (print):2218-0230**, ISSN (online):** 2412-3986**, DOI:**

RESEARCH PAPER

Molecular and Bacteriological Study of *Enterococcus faecalis* Isolated from Different Clinical Sources

Khalil H. Khdir [1], Khadija kh. Mustafa [2]

[1,2] Department of Biology, College of Education, Salahaddin University-Erbil, Kurdistan Region, Iraq

A B S T R A C T:
Enterococci are Gram-positive bacteria that cause serious nosocomial infections, including urinary tract, bloodstream infections and endocarditis. During the period of September 2018 to February 2019, forty four isolates of *E. faecalis* were isolated from 826 clinical specimens including; 35(5.07%) isolates of *E. faecalis* from urine, 7(7.60%) isolates from high vaginal swab and 2(8.69%) isolates from blood patients in different hospitals. All isolates that described above were identified depending on cultural criteria, morphological criteria, biochemical tests and further confirmed by Vitek 2 compact systems. The results of eleven antimicrobial against obtained isolates revealed that 100% of *E. faecalis* were resistant to cefotaxime, vancomycin, amoxicillin and erythromycin. While, it were 100% sensitive to doxycycline, imipenem, and nitrofurantion. Whereas, most isolates were differ in their susceptibility to amikacin, gentamycin, tetracycline and azithromycin. On the other hand, the results of biofilm found that 13.63% of isolates were produce strong biofilm, 54.54% were produce moderate biofilm and 31.81% were produce weak biofilm. The results of molecular analysis by using PCR showed that isolated *E. faecalis* were carried 97.72%, 90.90%, 63.63% of *ebpR*, *asa1*, *esp* genes respectively.

KEY WORDS: Antimicrobial resistant, Biofilm, *Enterococcus faecalis*, Virulence genes.

DOI: http://dx.doi.org/10.21271/ZJPAS.32.2.17
ZJPAS (2020) , 32(2);157-166 .

1. INTRODUCTION

Enterococcus faecalis (*E. faecalis*) is one of the most widely recognized types of enterococcus which causes 85 to 90% of enterococcal infections. Gram-positive bacteria were before classified as group D Streptococcus, because of specific antigen which is teichoic acid. The vast majority of these microbes are non-hemolytic and occasionally are alpha-hemolytic which can be catalase and oxidase enzymes, non- motile, facultative anaerobic bacteria (Van Tyne and Gilmore, 2014; Anagnostopoulos et al., 2018). Enterococci are mesophilic bacteria that could develop from 10 ^{o}C to 45 ^{o}C with ideal temperature included between 30 ^{o}C and 35^{o}C (García-Solache and Rice, 2019). *E. faecalis* develop in salt 6.5% (sodium chloride), bile salts 40% and pH=9.6 (Higuita and Huycke, 2014). It can survive in a temperature of 60 °C for 30 minutes which differentiate them from other Enterococcus species (Alipour et al., 2014). Moreover, *E. faecalis* is known to be opportunistic pathogen and is a common reason for nosocomial infections and cause some diseases in humans and these bacteria have been associated in bacteremia, endocarditis, urinary tract diseases or different infections. Lately, a role of *E. faecalis* in pancreatic and colorectal cancers has also been

* **Corresponding Author:**
Khadija Kh. Mustafa
E-mail: Khadija.mustafa@su.edu.krd
Article History:
Received: 04/09/2019
Accepted: 05/11/2019
Published: 22/04/2020

recommended but this remains questionable(O'Driscoll and Crank, 2015; de Almeida et al., 2018). The enterococci have an amazing capacity to adjust to various conditions and have an affinity to obtain antibiotic resistance, which has led to the appearance of multi-drug resistant variants, across the genus**.** The *E. faecalis* is naturally resistant to many antibiotics, for example, penicillin, ampicillin, piperacillin and vancomycin which have just bacteriostatic before bactericidal effects (Kristich et al., 2014). Furthermore, Opportunistic diseases has been related with the creation of virulence factors, adherence to cells, ability for biofilm creation and protection from antimicrobials (Bhatty et al., 2015). Many virulence factors have been recognized that are related with a wide range of *E. faecalis* diseases; in particular, aggregation substance (AS), gelatinase (GelE) and biofilm-associated Pili (Ebp), and biofilm creation (Singh et al., 2010). The purposes of this study were isolation and identification of *E. faecalis* from various clinical sources from various hospitals patients, antimicrobial sensitivity, detection of biofilm producer bacteria and detection of some virulence genes by using PCR technique.

Fritillaria zagrica Stapf. is a species very closely allied to *F. tulipifolia* and *F. armena*.

2. MATERIALS AND METHODS

2.1. Isolation of *E. faecalis* bacteria

Forty four isolates of *E. faecalis* were obtained from 826 specimens were collected from 555 female and 271 male patients in Rizgary (Erbil province) and Shahidan Qaladze teaching hospitals (Sulaimani province) within five months (September 2018 to February 2019) and from different clinical sources including; 690 specimens from urine, 92 from high vaginal swab, 23 from blood and 21 from stool. All specimens transferred to laboratory for microbiological examinations. All isolates were identified depending on cultural, morphological, and some biochemical tests, in addition to Vitek 2 Compact system (Navas et al., 2014). Also the bacterial isolates were screened for catalase, oxidase, coagulase , gelatinase , lipase, DNase, protease, urease , beta lactamase and hemolysin tests (Sharma, 2007; Cappuccino and Sherman, 2008; Stratev et al., 2015).

2.2 Antimicrobial Resistant Test

Antimicrobial resistant test was used to known the resistant of isolated *E. faecalis* against 11 antimicrobials by using Kirby Bauer method (Clinical and Institute, 2009), including amikacin (10 µg), amoxicillin (25 µg), azithromycin (15 µg), cefotaxime (30 µg), doxycycline (10 µg), erythromycin (10 µg), gentamycin (10 µg), imipenem (10 µg), nitrofurantion (100 µg), tetracycline (10 µg), and vancomycin (30 µg).

2.3 Biofilm Assay

All obtained *E. faecalis* were tested for biofilm production by using microtiter plate assay according to (Mathur et al., 2006).

2.4. Molecular Study

2.4.1. Isolation of DNA from *E. faecalis*

The way that used for isolation of DNA from bacterial cells was done by using Presto™ Mini gDNA bacteria kit. The steps includ; Sample preparation, lysis, DNA binding, washing and elution.

2.4.2. Primer

The studied primers were provided by macrogen (Table 1). Macrogen made the primer as lyophilized powder, thus the concentration defines as pmol. Primers were prepared by adding 300µl of deionized water to each lyophilized primers (forward and reverse) for each gene separately. Then 20µl from each primer put in 180µl deionized distilled water as work stock, and then used in PCR reaction and the volume of each primer stock solution was 100 pmol/µl.

2.4.3. Detection of *E. Faecalis* Genes

DNA extraction was done by the tissue buffer boiling method as defined by (Aghdam et al., 2017). Extracted DNA assisted as a template for the enlargement of virulence genes particular for *E. faecalis* includes *asa1and ebpR*. Conventional PCR was performed in 25 µl volumes reactions that contained 20–200 ng DNA, 0.5 µM of 1 µl of each specific primers for each gene, 1.5 mM MgCl2, and 200 µM of each dNTP, 1× PCR buffer and 2 U DNA Taq-polymerase (Cinnage, Tehran, Iran) as described by (Asgharzadeh et al., 2015). An initial denaturation at 94 °C for 10 min was followed by 35 cycles of 1 min denaturation at 94 °C, annealing at 58 °C for (*esp*) /52 °C (for *ebpR* and *asa1*) for 1 min and extension at 72 °C for 1 min, followed by a final extension at 72 °C for 10 min (Aghdam et al., 2017). PCR products were analyzed in 1.5% agarose gels and visualized under UV after staining with 0.5 µg × ml-1 DNA

safe stains. AccuPower PCR PreMix is the great technology and easy to do DNA amplification. It comprises DNA polymerase, dNTPs, a tracking dye and reaction buffer in a premixed format, freeze-dried into a pellet. Primer (1.3 µl) of each forward and reverse, (2.5µl) of DNA template were added to AccuPower PCR tube then 20µl of distilled water added to AccuPower PCR tubes. After that, lyophilized blue pellet dissolved by vortexing. PCR done for samples, process in the thermal cycler for 30 cycles (Table 2).

2.4.4. Detection of DNA Content by Agarose Gel Electrophoresis

The most public way to isolate DNA molecules according to size is electrophoresis technique in 1.5% agarose gel (Igeltjørn, 2009; Mishra et al., 2010). The DNA concentration and purity was determined by using Nanodrop spectrophotometer (Thermo Scientific/ United States) in agarose gel (Philippe and Deborah, 2010)

3. RESULTS AND DISCUSSIONS

3.1. Frequencies of *E. faecalis* isolates

In the present study 44(5.33%) isolates of *E. faecalis* were isolated from 826 specimens (555 females and 271 males) including (Urine, stool, High vaginal swab and Blood) during five months (September 2018 to February 2019) as illustrated in table (3). In the present study, the results showed that 35(5.07%) isolates of *E. faecalis* were obtained from urine samples, the current results similar with

Table 1. Primers sequences and their product size.

Primers	Primer sequences	Product size	References
Forward primer(*asa1*)	5'-GCA CGC TAT TAC GAA CTA TAT GA-3'	375bp	(Kafil and Mobarez, 2015).
Reverse primer(*asa1*)	5'-TAA GAA AGA ACA TCA CCA CGA-3'		
Forward primer(*ebpR*)	5'-AAA AAT GAT TCG GCT CCA GAA-3'	101bp	(Bourgogne et al., 2007).
Reverse primer (*ebpR*)	5'-TGC CAG ATT CGC TCT CAA AG-3'		
Forward primer(*esp*)	5'-GGA ACG CCT TGG TAT GCT AAC-3'	95bp	(Shankar et al., 1999).
Reverse primer (*esp*)	5'-GCC ACT TTA TCA GCC TGA ACC-3'		

Table 2. PCR protocol and thermo cycling conditions.

Gene name	Initial denaturation	Cycles	Denaturation	Annealing	Elongation	Final elongation
asa1	94°C/10min	35	94°C/1min	52°C/1min	72°C/1min	72°C/10min then 4°C→∞
ebpR	94°C/10min	35	94°C/1min	52°C/1min	72°C/1min	72°C/10min then 4°C→∞
Esp	94°C/10min	35	94°C/1min	58°C/1min	72°C/1min	72°C/10min then 4°C→∞

Table 3. Frequency of *E. faecalis* in different clinical sources.

Sources	No. of samples	No. of isolates	Percentages
Urine	690	35	5.07%
Stool	21	0	0%
High Vaginal Swab	92	7	7.60%
Blood	23	2	8.69%
Total	826	44	5.3%

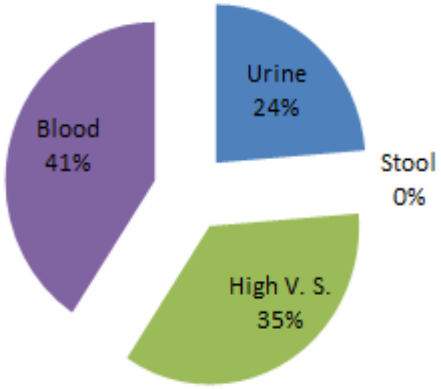

Figure 1. Distribution of E. faecalis isolates in different clinical sources.

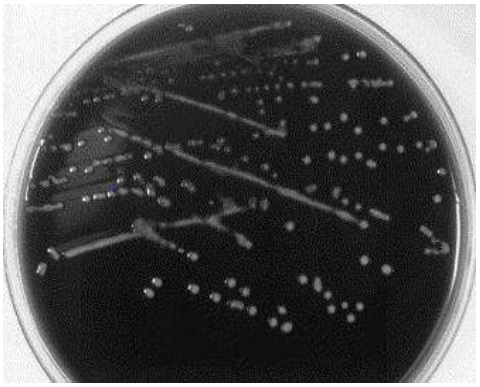

Figure 2. *E. faecalis* colonies on Bile Esculin Agar.

results of Daza et al. in (2001) and Al Sweih et al. in (2005) which they isolated (6%) and (4.2%) of *E. faecalis* from urine samples, respectively. while no isolates was isolated from stool specimens, On the other hand 7(7.60%) isolates of *E. faecalis* were isolated from high vaginal swab, this result was near with recent studies of Udo *et al.* in (2003) and Kudo et al. in (2014) which they isolated (9%) and (9.7%) of *E. faecalis* from high vaginal swab, respectively; whereas, 2(8.69%) of *E. faecalis* were isolated from the blood. These results were different with recent studies of Al-Husseiny, in (2008) and Kehinde et al. in (2013) which they isolated (16.27%) and (5%) of *E. faecalis* from blood, respectively (Figure 1). The percentages of isolation may be different and may be related to the time of collecting specimens, the number of specimens, the differences in the sources, hospital included and differences in the identification methods. All isolates identified as *E. faecalis* on bile esculin agar (Figure 2) depend on creamy color of colony which conversion of media to black, it comprise of 40% bile salt assistance in inhibition growth of Streptococci belong to group D antigen made this media valuable in determination of enterococcus from other non-enterococcus bacteria that belong to group D antigen (Hemraj et al., 2013). Additionally, the *E. faecalis* are Gram positive, do not form spore, not motile, do not produce oxidase, catalase, DNase, and urease, and ferment glucose without gas generation (Arias et al., 2010; Jayasundara, 2014; Subramanian et al., 2015; Sangeetha et al., 2016). They are facultative anaerobic bacteria, round, single, pairs or may be short chains (Silva et al., 2012).

The results of lipase showed that 4(9.09%) isolates were given positive results and 40(90.90%) isolates were gave negative and these results was close with results of (AL-Khafaji et al., 2010; Biswas et al., 2014). Moreover, 26(59.09%) of the isolates were positive for protease test and 18(40.90%) of isolates were negative and these results similar to Fuka et al. in (2017). Furthermore, out of all isolates of *E. faecalis* just 24(54.54%) hydrolyzed gelatin and the other isolates do not and these results agreed with the consequences of Mohamed and Murray, in (2005) and Zoletti et al. in (2011). However,

39(88.63%) were coagulase negative and 5(11.36%) were coagulase positive and these outcome is close that result which described by Kent in (2013) which they detected Coagulase-negative *Enterococci* represented 93%. All 44 isolates of *E. faecalis* from different sources were β-hemolysin .The current study was an endeavor to distinguish β-lactamase creation between isolated bacteria and the results found that all *E. faecais* were positive for β- lactamase creation. These results was similar with results obtained by Al-Duliami et al. in (2011) which they distinguished 76.7% of β-lactamase makers of *E. faecalis*.

3.3. Antibiotics Susceptibility Test

Antibiotic sensitivity test was conducted for 44 *E. faecalis* isolates using 11 types of antibiotics with different action, the percentage of resistance (Figure 3). The results found that 100% of *E. faecalis* were resistant to cefotaxime, vancomycin, amoxicillin and erythromycin. While, 95.45%, 86.36%, 81.81% and 68.18% of isolates were resistant to each of tetracycline, amikacin, gentamycin and azithromycin respectively.

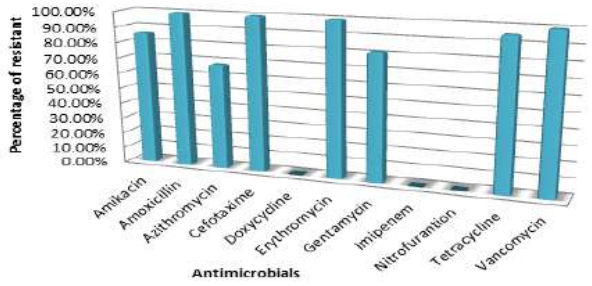

Figure 3. Percentage of antimicrobial resistant in *E. Faecalis.*

Moreover, 100% of obtained *E. feacalis* were susceptible for doxycycline, imipenem and nitrofurantion. These results similar with those results reported by Ullah et al. in (2015). and Yang and Juett, in (2016) where they detected that 100% of isolates were resisting to cefotaxime and vancomycin. Also, these results was near with results reported by AL-Gheethi et al. in (2013) where they detected that 95.23% of isolates were resistant to amoxicillin. As well as, Stępień-Pyśniak et al. in (2016) demonstrated that *E. faecalis* isolates absolute resistance 100% against erythromycin. Furthermore, Endo et al. in (2014); Talebi et al. in (2015); Samadi et al. in (2015) and Pourcel et al. in (2017) detected that 66.7% of isolates were resisting to azithromycin, 86% of isolates were resisting to tetracycline, 80% of isolates were resisting to amikacin and 77.2% of isolates were resisting to gentamicin, respectively; Also results of doxycycline, imipenem and nitrofurantion were agreed with the results reported by Yüceer and Özden Tuncer, in (2015); Sarah *et al.* in (2015) and El-Kersh *et al.* in (2016) which they detected that 100% of isolates were sensitive to doxycycline, 100% of isolates were sensitive to imipenem and 88% of isolates were sensitive to nitrofurantion, respectively.

3.4. Detection of Biofilm Producer *E. faecalis*

The results of this test showed that 6 (13.63%) of *E. faecalis* were strong biofilm producer, While, 24(54.54%) were moderate biofilm producer and 14(31.81%) isolates of *E. faecalis* were weak biofilm producer. These results was a little bit differ from results of Al-Hashimy and Alhalaby in (2016) where they detected that 20(40%) of *E. faecalis* were strong biofilm producer, 26(52%) of *E. faecalis* were moderate biofilm producer and 4(8%) were strong biofilm producer. The most dependable technique was microtiter plate method. The biofilm is a community of bacteria living with each other in an organised structure as microcolonies and it is encased in a matrix composed of an extracellular polymeric substance.

The above method was the better screening test for biofilm production than other methods for Gram positive bacteria because microtiter assay was easy to perform and assess both qualitatively and quantitatively (Abdullah and barzani, 2016). Also, Mathur et al., (2006) reported that the microtiter assay (TCP) method was an accurate and reproducible method than other methods for screening and this method can serve as a reliable quantitative tool for determining biofilm formation by clinical isolates of microorganism. However, the bacterial biofilm make the bacteria to adhere to inert materials and increased antibiotic resistance (Davies, 2003; Høiby et al., 2010).

3.4. Molecular Study

3.4.1. DNA Extraction

DNA of all isolated Gram positive bacteria effectively extracted by utilizing genomic DNA mini kit (Presto ^{TM} Mini gDNA bacteria kit), Then DNA concentration was estimated by Nanodrop spectrophotometer, and DNA concentration was among 50-90ng/µl. Proportion of tests absorbance at 260/280nm were 1.8–1.85. The proportion of tests absorbance at 260 / 230nm was between1.8-2 and commonly accepted a pure for DNA (Philippe

and Deborah, 2010). Also, DNA bands were affirmed and examined by agarose gel electrophoresis. The results revealed that all DNA successfully extracted and all isolates gave bands with molecular weight 1500bp (Yang et al., 2018) as shown in figure (4).

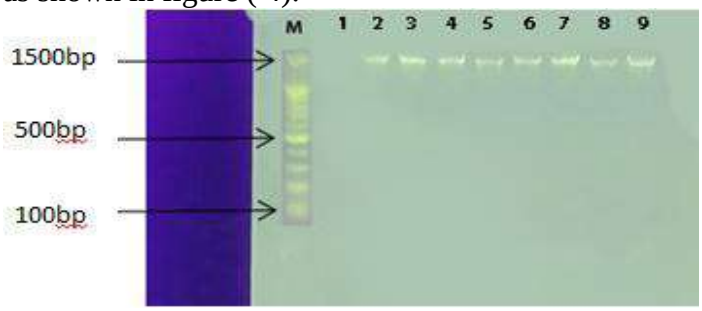

Figure 4. Genome profile of *E. faecalis* isolates performed with agarose gel electrophoresis. M: DNA ladder (100bp). Lane 1: Negative control; Lanes 2, 3, 4, 5, 6, 7, 8 and 9: Are genomes of *E. faecalis* isolates.

3.4.2. Detection of *E. faecalis* Virulence Genes

3.4.2.1. Detection of *ebpR* gene by PCR

In present study, PCR method showed that 43(97.72%) of *E. faecalis* isolates were harboring *ebpR* gene with molecular weight of 101bp as showed in figure (5). This result in agreement with Aghdam et al. in (2017) which they isolated 100 isolates of *E. faecalis* from patient's dental root canals and they examined for the occurrence of virulence genes and their results showed that 91(91%) had *ebpR* gene.

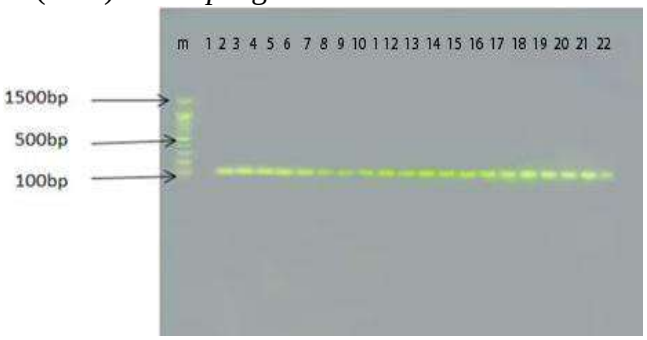

Figure 5. Polymerase chain reaction products on gel electrophoresis for *ebpR* gene. M: DNA ladder (100bp). Lane 1: Negative control; Lanes 2, 3, 4, 5 , 6, 7, 8, 9, 10, 11, 12, 13, 14, 15, 16, 17, 18, 19, 20, 21 and 22: Amplified PCR product of *ebpR* gene *(*101bp) for *E. faecalis* isolates.

On the other hand Kafil and Mobarez in (2015) isolated 196 isolate of *E. faecalis* from urinary tract infection of patients in various wards and they reported that 183 (93.36%) of isolates were harbor *ebpR* gene. Like many bacteria, *E. faecalis* encodes various adhesions involved in colonization or infection of various niches. Two well-considered *E. faecalis* adhesions, aggregation substance (AS) and endocarditis- and biofilm-related pili (Ebp), both add to biofilm development on abiotic surfaces and in endocarditis, suggesting that they may be communicated at the same time. If they are co-communicated on the same cells and what is the practical effect of co-expression on single cells and inside a population. When Ebp and AS are communicated on the same cells, pili interfere with AS-mediated clumping and impede AS-mediated conjugative plasmid move during planktonic development (Afonina et al., 2018).

3.4.2.2. Detection of *asa1*gene by PCR

In present study, PCR method indicated that 40 (90.90%) of *E. faecalis* isolates which isolated from various sources were carried *asa1* gene with molecular weight 375bp as showed in figure (6), This result in agreement with near result of various studies are available for the prevalence of *asa1* in enterococcal isolates obtained from various sources. In a study 8 out of 10(80%) of *E. faecalis* harbored *asa1* gene and majority (62.5%) of them were being isolated from urine specimen. Additionally, in other study the scientist found that 76(38.77%) isolates had *asa1* gene from 196 isolates of enterococcus species which isolated from patients with urinary tract infections. In various wards including serious care units, women particular ward, pediatrics, nephrology and internist (Kafil and Mobarez, 2015). Aggregation substance (*asa1*) is a sex pheromone plasmid-encoded surface protein, which promotes the conjugative exchange of sex pheromone plasmids by arrangement of mating aggregates among donor and recipient cells (Aspri et al., 2017) there is considerable evidence for a functional role of collection substance in the collaboration of *E. faecalis* with its mammalian host. Surface expression of aggregation substance rises adherence to host tissues and furthermore regulates the natural resistant reaction to enterococcal disease, thus increasing virulence in various models of opportunistic infection (Chuang et al., 2009). The development of biofilms *in vitro* is also greatly upgraded by aggregation substance (Bhatty et al., 2015).

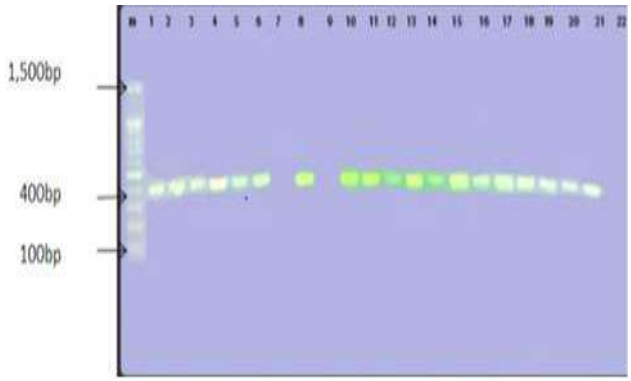

Figure 6. Polymerase chain reaction products on gel electrophoresis for *asa1* gene. M: DNA ladder (100bp). Lane 22: is negative control; Lanes 1, 2, 3, 4, 5, 6, 8, 10, 11, 12, 13, 14, 15, 16, 17, 18, 19, 20 and 21 Amplified PCR product of *asa1* gene (375bp) for *E. faecalis* isolates; Lanes 7,9: negative for *asa1* gene.

4.5.2.3. Detection of *esp* gene by PCR

In current study, the results indicated that 28(63.63%) of *E. faecalis* isolates were carried *esp* gene with molecular weight 95bp (Figure 7). This result in agreement with the results of (Strateva et al., 2016) which they found in their study that 60% of *E. faecalis* isolates carried *esp* gene. Enterococcus surface protein (esp) is a virulence factor that helps in the adhesion, but its role in biofilm formation is still opposing (Shridhar and Dhanashree, 2019). Esp is encoded on a pathogenicity island in *E. faecalis* and is involved in biofilm formation and binding to epithelial cells (Zou and Shankar, 2016). *E. faecalis* surface protein (Esp) is known to help surface attachment leading to biofilm development. It has been presented that Esp insertion-deletion mutants form unstructured and weak biofilms (Heikens et al., 2007). Percentage of positive and negative results for virulence genes showed in table (4).

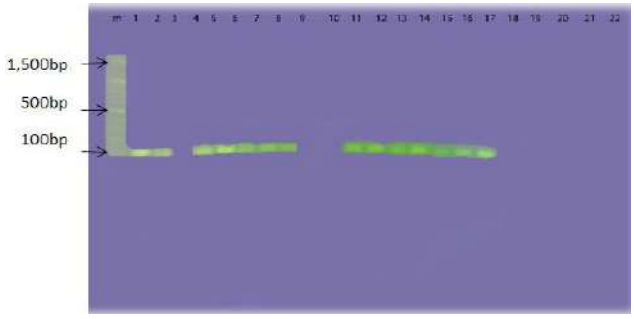

Figure 7. Polymerase chain reaction products on gel electrophoresis for *esp* gene. M: DNA ladder (500bp). Lanes 1, 2, 4, 5, 7, 6, 8, 11, 12, 13, 14, 15, 16 and 17: Amplified PCR product of *esp* gene (95bp) for *E. faecalis* isolates. Lanes 3, 9, 10, 18, 19, 20, 21 and 22: Negative for *esp* gene.

Table 4. Prevalence of virulence genes.

Virulence Genes	% Positive	% Negative
ebpR	(97.72%)	(2.27%)
asa1	(90.90%)	(9.09%)
Esp	(63.63%)	(36.36%)

4. REFERENCES

ABDULLAH, ZH. , & BARZANI, Kh. M. 2016. Bacteriological and Molecular Study of Gram Positive Bacteria Isolated From Thalassemic Patients in Erbil City. ZJPAS . 28 (5); 163-181. http://doi.org/10.21271/ZJPAS.28.5.17.

AFONINA, I., LIM, X. N., TAN, R. & KLINE, K. A. 2018. Planktonic interference and biofilm alliance between aggregation substance and endocarditis-and biofilm-associated pili in Enterococcus faecalis. *Journal of bacteriology*, 200**,** e00361-18.

AGHDAM, M. A., BARHAGHI, M. S., AGHAZADEH, M., JAFARI, F., HAGH, M. B., HAGHDOOST, M., MEMAR, M., REZAEE, M. A. & KAFIL, H. S. 2017. Virulence genes in biofilm producer *Enterococcus faecalis* isolates from root canal infections. *Cell Mol Biol (Noisy le Grand)*, 63.

AL-DULIAMI, A. A., NAUMAN, N. G., SALMAN, A. R. & HASAN, A.-R. S. 2011. Virulence factors of enterococci species isolated from nosocomial and community acquired infections. *Diyala Journal For Pure Science*, 7**,** 174-182.

AL-GHEETHI, A. A., ISMAIL, N., LALUNG, J., TALIB, A., EFAQ, A. & KADIR, M. O. A. 2013. Susceptibility for antibiotics among faecal indicators and pathogenic bacteria in sewage treated effluents. *Water Practice and Technology*, 8**,** 1-6.

AL-HASHIMY, A. B. & ALHALABY, A. H. 2016. MOLECULAR IDENTIFICATION OF (EfaA) IN ENTEROCOCCUS FECALIS AND ENTEROCOCCUS FACIUM AND THEIR ROLE IN BIOFILM FORMATION. *Basrah Journal of Veterinary Research*, 15.

AL-HUSSEINY, K. R. 2008. Bactermia and Septicemia in the ChildrenUnder three years at Al-Nasseria Province. *Al-Qadisiyah Medical Journal*, 4**,** 1-10.

AL-KHAFAJI, J. K. T., SAMAAN, S. F. & AL-SAEED, M. S. 2010. Virulence factors of Enterococcus faecalis. *Medical Journal of Babylon*, 7**,** 579-583.

AL SWEIH, N., JAMAL, W. & ROTIMI, V. 2005. Spectrum and antibiotic resistance of uropathogens isolated from hospital and community patients with urinary tract infections in two large hospitals in Kuwait. *Medical Principles and Practice*, 14**,** 401-407.

ALIPOUR, M., HAJIESMAILI, R., TALEBJANNAT, M. & YAHYAPOUR, Y. 2014. Identification and antimicrobial resistance of Enterococcus spp. isolated from the river and coastal waters in northern Iran. *The Scientific World Journal,* 2014**,** 6.

ANAGNOSTOPOULOS, D., BOZOUDI, D. & TSALTAS, D. 2018. Enterococci isolated from cypriot green table olives as a new source of technological and probiotic properties. *Fermentation*, 4**,** 48.

ARIAS, C. A., CONTRERAS, G. A. & MURRAY, B. E. 2010. Management of multidrug-resistant enterococcal infections. *Clinical microbiology and infection*, 16**,** 555-562.

ASGHARZADEH, M., SAMADI KAFIL, H. & POURASTADI, M. 2015. Mannose Binding Lectin (MBL) and Its Clinical Significance. *Journal of Babol University of Medical Sciences*, 17**,** 61-73.

ASPRI, M., BOZOUDI, D., TSALTAS, D., HILL, C. & PAPADEMAS, P. 2017. Raw donkey milk as a source of Enterococcus diversity: Assessment of their technological properties and safety characteristics. *Food Control*, 73**,** 81-90.

BHATTY, M., CRUZ, M. R., FRANK, K. L., LAVERDE GOMEZ, J. A., ANDRADE, F., GARSIN, D. A., DUNNY, G. M., KAPLAN, H. B. & CHRISTIE, P. J. 2015. E nterococcus faecalis pCF 10-encoded surface proteins PrgA, PrgB (aggregation substance) and PrgC contribute to plasmid transfer, biofilm formation and virulence. *Molecular microbiology*, 95**,** 660-677.

BISWAS, P. P., DEY, S., ADHIKARI, L. & SEN, A. 2014. Virulence markers of vancomycin resistant enterococci isolated from infected and colonized patients. *Journal of global infectious diseases*, 6**,** 157.

BOURGOGNE, A., SINGH, K. V., FOX, K. A., PFLUGHOEFT, K. J., MURRAY, B. E. & GARSIN, D. A. 2007. EbpR is important for biofilm formation by activating expression of the endocarditis and biofilm-associated pilus operon (ebpABC) of Enterococcus faecalis OG1RF. *Journal of bacteriology*, 189**,** 6490-6493.

CAPPUCCINO, J. G. & SHERMAN, N. 2008. Microbiology: a laboratory manual (Vol. 9). Pearson/Benjamin Cummings.

CHUANG, O. N., SCHLIEVERT, P. M., WELLS, C. L., MANIAS, D. A., TRIPP, T. J. & DUNNY, G. M. 2009. Multiple functional domains of Enterococcus faecalis aggregation substance Asc10 contribute to endocarditis virulence. *Infection and immunity*, 77**,** 539-548.

CLINICAL & INSTITUTE, L. S. 2009. *Performance standards for antimicrobial susceptibility testing of anaerobic bacteria: informational supplement*, Clinical and Laboratory Standards Institute (CLSI).

DAVIES, D. 2003. Understanding biofilm resistance to antibacterial agents. *Nature reviews Drug discovery*, 2**,** 114.

DAZA, R., GUTIÉRREZ, J. & PIÉDROLA, G. 2001. Antibiotic susceptibility of bacterial strains isolated from patients with community-acquired urinary tract infections. *International journal of antimicrobial agents*, 18**,** 211-215.

DE ALMEIDA, C. V., TADDEI, A. & AMEDEI, A. 2018. The controversial role of Enterococcus faecalis in colorectal cancer. *Therapeutic advances in gastroenterology*, 11**,** 1756284818783606.

EL-KERSH, T. A., MARIE, M. A., AL-SHEIKH, Y. A., AL-AGAMY, M. H. & AL BLOUSHY, A. A. 2016. Prevalence and risk factors of early fecal carriage of Enterococcus faecalis and Staphylococcus spp and their antimicrobial resistant patterns among healthy neonates born in a hospital setting in central Saudi Arabia. *Saudi Med J*, 37**,** 279-286.

ENDO, M. S., SIGNORETTI, F., KITAYAMA, V. S., MARINHO, A., MARTINHO, F. C. & GOMES, B. 2014. Culture and molecular detection of Enterococcus faecalis from patients with failure endodontic treatment and antimicrobial susceptibility of clinical isolates. *Braz Dent Sci*, 17**,** 83-91.

FUKA, M. M., MAKSIMOVIC, A. Z., TANUWIDJAJA, I., HULAK, N. & SCHLOTER, M. 2017. Characterization of enterococcal community isolated from an Artisan Istrian raw milk cheese: Biotechnological and safety aspects. *Food technology and biotechnology*, 55**,** 368.

GARCÍA-SOLACHE, M. & RICE, L. B. 2019. The Enterococcus: a model of adaptability to its environment. *Clinical microbiology reviews*, 32**,** e00058-18.

HEIKENS, E., BONTEN, M. J. & WILLEMS, R. J. 2007. Enterococcal surface protein Esp is important for biofilm formation of Enterococcus faecium E1162. *Journal of bacteriology*, 189**,** 8233-8240.

HEMRAJ, V., DIKSHA, S. & AVNEET, G. 2013. A review on commonly used biochemical test for bacteria. *Innovare J Life Sci*, 1**,** 1-7.

HIGUITA, N. I. A. & HUYCKE, M. M. 2014. Enterococcal disease, epidemiology, and implications for treatment. *Enterococci: From commensals to leading causes of drug resistant infection [Internet].* Boston: Massachusetts Eye and Ear Infirmary.

HØIBY, N., BJARNSHOLT, T., GIVSKOV, M., MOLIN, S. & CIOFU, O. 2010. Antibiotic resistance of bacterial biofilms. *International journal of antimicrobial agents*, 35**,** 322-332.

IGELTJØRN, L. 2009. *Molecular and biochemical characterisation of naturally occurring hyperexpressed and mutated extended spectrum AmpC beta-lactamases in Norwegian clinical isolates of Escherichia coli.* Master thesis in medical microbiology, Universitetet i Tromsø.

JAYASUNDARA, N. S. 2014. *An investigation of Staphylococcus aureus and related species from flood affected and other environmental sources.* Thesis submitted to Queensland University of Technology in fulfilment of the requirements for

the degree of Masters of Applied Science (Research), Queensland University of Technology.

KAFIL, H. S. & MOBAREZ, A. M. 2015. Assessment of biofilm formation by enterococci isolates from urinary tract infections with different virulence profiles. *Journal of King Saud University-Science*, 27**,** 312-317.

KEHINDE, E. O., AL-MAGHREBI, M., SHEIKH, M. & ANIM, J. T. 2013. Combined ciprofloxacin and amikacin prophylaxis in the prevention of septicemia after transrectal ultrasound guided biopsy of the prostate. *The Journal of urology*, 189**,** 911-915.

KENT, V. 2013. *Cell wall architecture and the role of wall teichoic acid in Staphylococcus aureus.* University of Sheffield.

KRISTICH, C. J., RICE, L. B. & ARIAS, C. A. 2014. Enterococcal infection—treatment and antibiotic resistance. *Enterococci: From commensals to leading causes of drug resistant infection [Internet].* Boston:Massachusetts Eye and Ear Infirmary.

KUDO, M., NOMURA, T., YOMODA, S., TANIMOTO, K. & TOMITA, H. 2014. Nosocomial infection caused by vancomycin-susceptible multidrug-resistant Enterococcus faecalis over a long period in a university hospital in Japan. *Microbiology and immunology*, 58**,** 607-614.

MATHUR, T., SINGHAL, S., KHAN, S., UPADHYAY, D., FATMA, T. & RATTAN, A. 2006. Detection of biofilm formation among the clinical isolates of staphylococci: an evaluation of three different screening methods. *Indian journal of medical microbiology*, 24**,** 25.

MISHRA, V., NAG, V. L., TANDON, R. & AWASTHI, S. 2010. Response Surface Methodology-Based Optimisation of Agarose Gel Electrophoresis for Screening and Electropherotyping of Rotavirus. *Applied biochemistry and biotechnology*, 160**,** 2322-2331.

MOHAMED, J. A. & MURRAY, B. E. 2005. Lack of correlation of gelatinase production and biofilm formation in a large collection of Enterococcus faecalis isolates. *Journal of clinical microbiology*, 43**,** 5405-5407.

MOHAMMADI, F., GHAFOURIAN, S., MOHEBI, R., TAHERIKALANI, M., PAKZAD, I., VALADBEIGI, H., HATAMI, V. & SADEGHIFARD, N. 2015. Enterococcus faecalis as multidrug resistance strains in clinical isolates in Imam Reza Hospital in Kermanshah, Iran. *British journal of biomedical science*, 72**,** 182-184.

NAVAS, M., PINCUS, D. H., WILKEY, K., SERCIA, L., LASALVIA, M., WILSON, D., PROCOP, G. W. & RICHTER, S. S. 2014. Identification of aerobic Gram-positive bacilli by use of Vitek MS. *Journal of clinical microbiology*, 52**,** 1274-1277.

O'DRISCOLL, T. & CRANK, C. W. 2015. Vancomycin-resistant enterococcal infections: epidemiology, clinical manifestations, and optimal management. *Infection and drug resistance*, 8**,** 217.

PHILIPPE, D. & DEBORAH, C. 2010. Nanodrop microvolume quantitation of nucleic acid. *Journal of Visualized Experiment*, 45**,** 2565.

POURCEL, N. G., SPARO, M. D., CORSO, A., DELPECH, G., GAGETTI, P. S., DE LUCA, M. M., BERNSTEIN, J. C., SCHELL, C. M. B., LISARRAGUE, S. & BASUALDO FARJAT, J. A. 2017. Molecular genetic profiling of clinical and foodborne strains of enterococci with high level resistance to gentamicin and vancomycin.

SAMADI, N., PAKZAD, I., SEFIDAN, A. M., HOSAINZADEGAN, H. & TANOMAND, A. 2015. Study of aminoglycoside resistance genes in Enterococcus and Salmonella strains isolated from Ilam and Milad hospitals, Iran. *Jundishapur journal of microbiology*, 8.

SANGEETHA, B. G., JAYAPRAKAS, C. A., SIJI, J. V., RAJITHA, M., SHYNI, B. & MOHANDAS, C. 2016. Molecular characterization and amplified ribosomal DNA restriction analysis of entomopathogenic bacteria associated with Rhabditis (Oscheius) spp. *3 Biotech*, 6**,** 32.

SARAH, A., SAIF, Q., RUHI, K., ASFIA, S., MEHER, R. & SHAHZAD, H. F. 2015. Semen culture in patients with chronic prostatitis syndrome: A valuable diagnostic tool. *International Journal of Current Microbiology and Applied Sciences, Special***,** 236-242.

SHANKAR, V., BAGHDAYAN, A. S., HUYCKE, M. M., LINDAHL, G. & GILMORE, M. S. 1999. Infection-derived Enterococcus faecalisstrains are enriched in esp, a gene encoding a novel surface protein. *Infection and immunity*, 67**,** 193-200.

SHARMA, K. 2007. *Manual of Microbiology*, Ane Books Pvt Ltd.

SHRIDHAR, S. & DHANASHREE, B. 2019. Antibiotic Susceptibility Pattern and Biofilm Formation in Clinical Isolates of Enterococcus spp. *Interdisciplinary perspectives on infectious diseases,* 2019.

SILVA, N., IGREJAS, G., GONÇALVES, A. & POETA, P. 2012. Commensal gut bacteria: distribution of Enterococcus species and prevalence of Escherichia coli phylogenetic groups in animals and humans in Portugal. *Annals of Microbiology*, 62**,** 449-459.

SINGH, K. V., NALLAPAREDDY, S. R., SILLANPÄÄ, J. & MURRAY, B. E. 2010. Importance of the collagen adhesin ace in pathogenesis and protection against Enterococcus faecalis experimental endocarditis. *PLoS pathogens*, 6**,** e1000716.

STĘPIEŃ-PYŚNIAK, D., MAREK, A., BANACH, T., ADASZEK, Ł., PYZIK, E., WILCZYŃSKI, J. & WINIARCZYK, S. 2016. Prevalence and antibiotic resistance of Enterococcus strains isolated from poultry. *Acta Veterinaria Hungarica*, 64**,** 148-163.

STRATEV, D., DASKALOV, H. & VASHIN, I. 2015. Characterisation and determination of antimicrobial

resistance of β-haemolytic Aeromonas spp. isolated from common carp (Cyprinus carpio L.). *Revue de médecine vétérinaire,* 166**,** 54-61.

STRATEVA, T., ATANASOVA, D., SAVOV, E., PETROVA, G. & MITOV, I. 2016. Incidence of virulence determinants in clinical Enterococcus faecalis and Enterococcus faecium isolates collected in Bulgaria. *Brazilian Journal of Infectious Diseases,* 20**,** 127-133.

SUBRAMANIAN, M. R., TALLURI, S. & CHRISTOPHER, L. P. 2015. Production of lactic acid using a new homofermentative E nterococcus faecalis isolate. *Microbial biotechnology,* 8**,** 221-229.

TALEBI, M., MOGHADAM, N. A., MAMOOII, Z., ENAYATI, M., SAIFI, M. & POURSHAFIE, M. R. 2015. Antibiotic Resistance and Biofilm Formation of Enterococcus faecalis in Patient and Environmental Samples. *Blood,* 14**,** 24.

UDO, E. E., AL-SWEIH, N., PHILLIPS, O. A. & CHUGH, T. D. 2003. Species prevalence and antibacterial resistance of enterococci isolated in Kuwait hospitals. *Journal of medical microbiology,* 52**,** 163-168.

ULLAH, O., KHATTAK, M., HASAN, F., RAJA, N., HUSSAIN, S., AKHTAR, N. & SHAH, A. A. 2015. Vancomycin Resistant Enterococcal Infections in Tertiary Care Hospitals of Islamabad and Rawalpindi, Pakistan. *Pakistan Journal of Zoology,* 47.

VAN TYNE, D. & GILMORE, M. S. 2014. Friend turned foe: evolution of enterococcal virulence and antibiotic resistance. *Annual review of microbiology,* 68**,** 337-356.

YANG, H. K. & JUETT, B. W. 2016. Preliminary Report: Prevalence of vancomycin-resistant Enterococcus faecalis in public restrooms in central Kentucky. *Bios,* 87**,** 150-154.

YANG, Y., LI, W., HOU, B. & ZHANG, C. 2018. Quorum sensing LuxS/autoinducer-2 inhibits Enterococcus faecalis biofilm formation ability. *Journal of Applied Oral Science,* 26.

YÜCEER, Ö. & ÖZDEN TUNCER, B. 2015. Determination of Antibiotic Resistance and Biogenic Amine Production of Lactic Acid Bacteria Isolated from Fermented Turkish Sausage (Sucuk). *Journal of Food Safety,* 35**,** 276-285.

ZOLETTI, G. O., PEREIRA, E. M., SCHUENCK, R. P., TEIXEIRA, L. M., SIQUEIRA JR, J. F. & DOS SANTOS, K. R. N. 2011. Characterization of virulence factors and clonal diversity of Enterococcus faecalis isolates from treated dental root canals. *Research in Microbiology,* 162**,** 151e158.

ZOU, J. & SHANKAR, N. 2016. Surface protein Esp enhances pro-inflammatory cytokine expression through NF-κB activation during enterococcal infection. *Innate immunity,* 22**,** 31-39.

ZANCO Journal of Pure and Applied Sciences
The official scientific journal of Salahaddin University-Erbil
https://zancojournals.su.edu.krd/index.php/JPAS

ISSN (print):2218-0230**, ISSN (online):** 2412-3986**, DOI: http://dx.doi.org/10.21271/zjpas**

RESEARCH PAPER

Molecular Characterization of Some Virulence Genes and Antibiotic Susceptibility Pattern among Uropathogenic *Escherichia coli* Isolated from Patient in Zakho City/Iraq

Marwa S. Ibrahim[1], Haval M. Khalid[2], Wijdan M. S. Mero[2]

[1]Department of Nursing, Zakho Technical Institute, Duhok Polytechnic University, Duhok, Iraq
[2]Department of Biology, Faculty of Science, University of Zakho, Duhok, Iraq

A B S T R A C T:

Uropathogenic *Escherichia coli* (UPEC) is one of the most causative agents which causing urinary tract infections (UTIs) in humans. This study involved the prevalence of the virulence genes among UPEC isolated from patients in various hospitals in Zakho city from July 2018 until January 2019 and their susceptibility to different commonly used antimicrobial agent against UPEC. The different culture media were used for the identification of *Escherichia coli* (*E. coli*). Out of 400 samples, 141 (35.25%) strains of UPEC were isolated from enrolled patients. The antibiotic susceptibility toward different antibiotics was varied among the isolates. Imipenem was the most potent antibiotic with a resistant rate of only 2.84%. While the isolates were resistant to most screened antibiotics, with the highest rate 96.45% to Amoxicillin/ clavulanic. The resistant rates decreased toward other antibiotics at rates varied from 93.62% for Amoxicillin to 43.97% for Norfloxacin. Fifty-seven isolates were selected for PCR analysis, according to the resistance of *E.coli* to various antibiotics. The selected samples were successfully amplified for *E. coli* identification by producing a single band of a target *uidA* gene. In this study, the virulence related genes were detected in only 35 (61.40%) isolates out of 57 isolates. The distribution of the virulence related genes that included; *afa*, *sfa*, *hly*, *cnf* and *pai* were 28.07%, 17.54%, 26.32%, 22.81% and 22.81%, respectively. The study highlight that multidrug resistance UPEC harbors multiple virulence genes circulating in this setting.

KEY WORDS: UPEC, Virulence factors, PCR, Antibiotics resistant.
DOI: http://dx.doi.org/10.21271/ZJPAS.32.2.18
ZJPAS (2020) , 32(2);167- 177 .

INTRODUCTION

The gram negative *E. coli* bacteria is an opportunistic pathogen which is naturally found in the intestinal tract of humans and other mammals, it may cause serious diseases in the intestinal tract and extraintestinal tract (Russo and Johnson, 2000; Kaper *et al.*, 2004). Among extraintestinal pathogenic *E. coli* (ExPEC), the most common strains of *E. coli* that causes UTIs in human is uropathogenic *E. coli* (UPEC) (Russo and Johnson, 2000). In ascending of the UPEC infections, colonization of the *E. coli* in the urethra leads to the spread upward that causes cystitis and pyelonephritis (Bien *et al.*, 2012). Approximately 70-95% of the community-acquired UTIs and 50% of the nosocomial UTIs are due to the UPEC infections (Wiles *et al.*, 2008; Šišková *et al.*, 2015). So, *E. coli* is considered as an important public health problem (Farell *et al.*, 2003; Zhanel *et al.*, 2006).

Several virulence factors of the UPEC play an important role in the colonization, invasion, and survival within the urinary system of the host and causing UTI (Litza and Brill, 2010; Bien *et al.*, 2012; Behzadi *et al.*, 2016). These different

* **Corresponding Author:**
Marwa Subhi Ibrahim
E-mail: marwa.3789@gmail.com
Article History:
Received:15/09/2019
Accepted: 17/11/2019
Published: 22/04/2020

virulence factors that develop the infectious process includes: adhesins (P and S fimbriae), toxins (cytotoxic necrotizing factor type 1 and α-hemolysin) and siderophores (aerobactin and yersiniabactin). Also, a fimbrial adhesin I and type 1 fimbriae are beneficial in this type of infection (Miyazaki *et al.,* 2002; Dobrindt *et al.,* 2002; Dobrindt *et al.,* 2003). The virulence-associated genes are located on transmissible genetic elements, such as plasmids, bacteriophages and pathogenicity islands (PAIs) (Dobrindt *et al.,* 2003). The PAI is located in a specific region on the chromosome (Farshad *et al.,* 2012), and has led to the coordination of the horizontal transfer of virulence genes between strains of one species or related bacterial species (Johnson and Stell, 2000; Dobrindt *et al.,* 2003). Multidrug-resistant (MDR) among *E. coli* have been increased over the years and this is a major clinical problem in treating the UTI infections caused by *E. coli* (Manikandan and Amsath, 2014). The antimicrobials resistance differs from one region to another and the rates of resistance have increased over the years (Tiwary *et al.,* 2017). Multi-drug resistance and extended spectrum beta-lactamases (ESBLs) producing gram negative bacteria are the major cause of infection of the urinary tract (Poirel *et al.,* 2005).

The limited availability of treatment for *E. coli* has particular clinical significance. Moreover, preventing and controlling the spread of UPEC infection is hampered by a misunderstanding of the population biology of these pathogens (Siu *et al.,* 2008). The spread of resistance for antimicrobial agents used for the first line treatment for uncomplicated UTI such as Ampicillin and Trimethoprim/Sulfamethoxazole lead to the use of the alternative choice of antimicrobial agents such as quinolones and cephalosporins (Hryniewicza *et al.,* 2001). The MDR rates of *E.coli* increase for aminoglycosides, fluoroquinolones and third generation cephalosporins, at rates of 63% during 2012 and further increased to 65 % in 2014 over the consecutive years (Sharma *et al.,* 2016).

The aims of this study were firstly to identify the UPEC and the rate of their distribution among patients in the various hospital in Zakho City, Kurdistan Region-Iraq. Secondly to investigate the antibiogram rates for the isolated UPEC and thirdly to perform PCR analysis of some resistant strains in order to identify the five virulence related gene; *afa*, *sfa*, *hly*, *cnf* and *pai*.

1. MATERIALS AND METHODS

1.1. Sample Collection

In this study, 400 clinical midstream urine samples were collected in clean fully labelled screw-capped containers from patients with UTI. The samples were collected from various hospitals in Zakho city namely; Zakho General hospital, Maternity hospital and Emergency hospital, from July 2018 until January 2019 (for about 6 days/week). Following collection, each sample was cultured on different culture media and UPEC was identified by cultural characters and biochemical tests: indole production, methyl red reaction, citrate utilization and sugar fermentation with gas production.

1.2. Culturing of the urine sample

After delivery of urine samples to the laboratory, a loopful of urine samples of each patient was cultured on Blood and MacConkey agars by streaking method and incubated at 37^{o}C for overnight. After overnight incubation, a single colony from the suspected UPEC was selected and sub-cultured on selected media (MacConkey agar) to obtain a pure colony. After incubation of the subcultured bacteria, the pure colonies were cultured on different culture media such as Peptone water, Methyl red broth, Simmon citrate agar and TSI agar to ensure that the isolated bacteria was *E. coli* (Alexander and Strete, 2001; Leboffe and Pierce, 2011).

1.3. Antibiotic susceptibility test

Sixteen antibiotics discs supplied by Bioanalyses (Turkey) were used for testing the susceptibility of the isolated UPEC, as most of these antibiotics were commonly prescribed by physicians to patients having UTI infection, as listed in Table 1. The disk diffusion method on the Mueller-Hinton agar was performed to detect the sensitivity and resistant of these antibiotics to the *E. coli*. After 24 hours of incubation, the diameters of inhibition zone around each disc was compared with the standard chart and interpreted as sensitive or resistant depending on the size of the inhibition zone (Coyle, 2005; Cheesbrough, 2006).

Table 1: Antibiotic discs

Antibiotics	Code	Potency (mcg)
Amikacin	AK	10 mcg
Amoxicillin	AX	25 mcg
Amoxicillin/clavulanic acid	AMC	20/10 mcg
Ampicillin	AM	20 mcg
Cefixime	CFM	5 mcg
Cefotaxime	CTX	30 mcg
Ceftriaxone	CRO	10 mcg
Chloramphenicol	C	10 mcg
Ciprofloxacin	CIP	10 mcg
Gentamicin	CN	10 mcg
Imipenem	IPM	10 mcg
Nalidixic acid	NA	30 mcg
Norfloxacin	NOR	10 mcg
Tetracycline	TE	10 mcg
Trimethoprim	TMP	10 mcg
Trimethoprim/ Sulfamethoxazole	SXT	1.25/23.75 mcg

1.4. Genomic DNA extraction and determination of the concentration

Fifty-seven of the isolated UPEC were selected for molecular identification according to the resistance rates of *E. coli* to 16 used antibiotics. Genomic DNA was extracted by using a commercial extraction kit (PrimePrep^{TM} Genomic DNA Extraction Kit) supplied by GeNet Bio (Korea). After DNA extraction, the concentration of the genomic DNA were detected by using Nanodrop spectrophotometer (Thermo scientific) and then used for PCR amplification.

1.5. Primers

Six primers were used in this study, as listed in Table 2, *uidA* primer was used for amplifying the target *uidA* gene as a species-specific primer for *E. coli*. The five other primers were used to detect the spread of five virulence-related genes including; a fimbrial adhesion, S-fimbrial adhesion, hemolysin, cytotoxic necrotizing factor-1 and pathogenicity island, and the five primers which were represented for the virulence gene were *afa*, *sfa*, *hly*, *cnf* and *pai*, respectivly.

1.6. PCR amplification and gel electrophoresis

The PCR amplification reaction was prepared in 20µl as a final volume which contained 5µl of the master mix, 2µl of each primer including forward and reverse (10 pmol/µl except for *hly* 30 pmol/µl and *afa* 20 pmol/µl), 2µl of DNA genome (25-50 ng/µl) and 9 µl of PCR grade water. The amplification condition was shown in Table 3. After amplification, the PCR products were run on gel electrophoresis using 1.2% (w/v) of agarose prepared in 1x Tris-Boric-EDTA (TBE) buffer. The running of the electrophoresis was inserted in 45V for 5 min and then changed to 80V for 1 hour. After running, the DNA bands on agarose gel was visualized using U.V. (Cleaver scientific) light source (Ausubel *et al.,* 2003).

Table 2: Primers used for detection of Species-specific gene in UPEC and their virulence genes

Method	Primer	DNA sequence 5'- 3' (forward and reverse)	Amplified product (bp)	Reference or source
Species-specific PCR	*uidA*	F-CATTACGGCAAAGTGTGGGTCAAT R-CCATCAGCACGTTATCGAATCCTT	658 bp	(Adamus-bialek *et al.,* 2009)
Virulence genes	*afa*	F-GCTGGGCAGCAAACTGATAACTCTC R-CATCAAGCTGTTTGTTCGTCCGCCG	750 bp	(Le-Bouguenec *et al.,* 1992)
	sfa	F-GTGGATACGACGATTACTGTG R-CCGCCAGCATTCCCTGTATTC	240 bp	(Chapman *et al.,* 2006)
	hyl	F-AGATTCTTGGGCATGTATCCT R-TTGCTTTGCAGACTGTAGTGT	565 bp	(Mladin *et al.,* 2009)
	cnf	F-AAGATGGAGTTTCCTATGCAGGAG R-CATTCAGAGTCCTGCCCTCATTATT	498 bp	(Adamus-bialek *et al.,* 2009; Chapman *et al.,* 2006)
	pai	F-GGACATCCTGTTACAGCGCGCA R-TCGCCACCAATCACAGCCGAAC	930 bp	(Chapman *et al.,* 2006; Oliveira *et al.,* 2011)

Table 3: The amplification condition of specific species gene and different virulence gene among *E.coli*

***uidA* primer**					**Reference**
Initial denaturation	Denaturation	Annealing	Extension	Final extension	
94 °C	92 °C	58 °C	72 °C	72 °C	(Adamus-bialek *et al.*, 2009)
10 min	1 min	1min	30 sec.	5 min	
1 cycle		35 cycles		1 cycle	
***afa* primer**					
Initial denaturation	Denaturation	Annealing	Extension	Final extension	(Le-Bouguenec *et al.*, 1992)
94 °C	94 °C	63 °C	68 °C	72 °C	
5 min	1 min	1 min	3 min	7 min.	
1 cycle		30 cycles		1 cycle	
***sfa* primer**					
Initial denaturation	Denaturation	Annealing	Extension	Final extension	(Chapman *et al.*, 2006)
95 °C	94 °C	63 °C	68 °C	72 °C	
3 min	30 sec.	30 sec.	4 min	10 min	
1 cycle		30 cycles		1 cycle	
hly primer					
Initial denaturation	Denaturation	Annealing	Extension	Final extension	(Mladin *et al.*, 2009)
94 °C	94 °C	55 °C	72 °C	72 °C	
4 min	30 sec.	30 sec.	1 min	5 min	
1 cycle		30 cycles		1 cycle	
***cnf* primer**					
Initial denaturation	Denaturation	Annealing	Extension	Final extension	(Chapman *et al.*, 2006; Adamus-bialek *et al.*, 2009)
95 °C	94 °C	68 °C	68 °C	72 °C	
3 min	30 sec.	30 sec.	4 min	10 min	
1 cycle		25 cycles		1 cycle	
***pai* primer**					
Initial denaturation	Denaturation	Annealing	Extension	Final extension	(Chapman *et al.*, 2006; Oliveira *et al.*, 2011)
94 °C	94 °C	63 °C	72 °C	72 °C	
1 min	1 min	30 sec.	1.30 min	5 min	
1 cycle		30 cycles		1 cycle	

2. RESULT AND DISCUSSION

2.1. Identification of UPEC

A total of 400 clinical urine samples were collected. Out of 400 urine samples, 141 samples (35.25%) were found positive for UPEC, that were recovered from various hospitals in Zakho city. Nearly similar findings have been reported by Muhammad and Ghareb, (2019) in Erbil City in which *E.coli* was responsible for 33.07% of uropathogenic infections. The *E. coli* was identified by the morphological and biochemical characterization on the culture media which have been able to ferment lactose on the MacConkey agar (Alexander and Strete, 2001; Engelkirk and Duben-Engelkirk, 2008). In addition, the isolated bacteria were confirmed to be *E. coli* strains by biochemical tests and the results showed: indole positive, methyl red positive, citrate utilization negative and in TSI test the sugar fermentation with acid accumulation in slant and butt, with gas production and without H_2S production (Leboffe and Pierce, 2011; M *et al.*, 2016).

2.2. Antibiotics sensitivity test

All 141 isolated UPEC were tested for their susceptibility toward 16 antibiotics discs. It was obvious from the results that not all the isolates were sensitive to all antibiotics while a wide range of them showed resistance to most of the testes antibiotics, as shown in Table 4.

The most potent antimicrobial agent against *E. coli* was Imipenem with a resistance rate of only 2.84% and this antibiotic is considers as one of the β-lactam antibiotics of carbapenem agent. This finidng was close to study performed by Polse *et al.*, (2016) who found that the sensitivity

rate toward Imipenem was 100%. Likewise, Abdulrahman *et al.,* (2016) revealed that all isolates *E. coli* was sensitive for Imipenem. It is known that carbapenems is stable against the enzymes ESBLs produced by Enterobacteriaceae and is preferred for treating serious bacterial infections caused by bacteria producing β-lactam (Rupp and Fey, 2003; Paterson, 2006).

The isolated *E. coli* were considered as resistant to the most antibiotics, and the resistant rates varied according to the antibiotics used. The resistant rate was high toward penicillin group including; Amoxicillin, Amoxicillin/ clavulanic acid and Ampicillin with rates of 93.62%, 96.45% and 91.49%, respectively. As the resistant rates of these antibiotics are high, therefore, they are limited in use, but some of these agents remain useful for the treatment of certain patients, such as Amoxicillin or Ampicillin. These antibiotics remain the preferred therapy for group B streptococcal and enterococci infection (Nicolle, 2005). The resistant rates of the third generation cephalosporins groups of β-lactam were high. This group includes; Cefixime, Ceftriaxone and Cefotaxime with resistant rates of 83.69%, 87.23% and 87.23%, respectively. The resistance of the *Enterobacteriaceae* to the cephalosporins third-generation is often due to the β-lactamase production and the ESBLs that are able to hydrolyze and disrupt cephalosporins both broad-spectrum and extended-spectrum (Rupp and Fey, 2003; Shah *et al.,* 2004). The resistant rates for Aminoglycoside agent including; Amikacin and Gentamicin with rates of 87.94% and 63.83%, respectively. Furthermore, the quinolones group including; Nalidixic acid, Ciprofloxacin and Norfloxacin with resistant rates of 79.43%, 49.65% and 43.97%, respectively. The resistance rates of Trimethoprim and Trimethoprim/ sulfamethoxazole were 61.70% and 63.12%, respectively. Aminoglycosides, quinolones and trimethoprim-sulfamethoxazole are generally not an eligible therapeutic choice for serious infections caused by *Enterobacteriaceae* producing ESBL enzymes because of ESBL producers are often resistant to those drugs (Lautenbach *et al.,* 2002; Hyle *et al.,* 2005). Moreover, multidrug resistance (MDR) is increasing among *E. coli* producing ESBL, in which *E. coli* is resistant to more than two class of antibiotic (Hyle *et al.,* 2005). The resistance rates of the two other antibiotics used were found to be 63.83% for Tetracycline and 66.67% for Chloramphenicol.

Table 4: Antibiotic sensitivity pattern of UPEC isolates in UTI patients

Antibiotics Disc	Resistance		Sensitivity	
	No.	%	No.	%
Amoxicillin	132	93.62	9	6.38
Amoxicillin/ clavulanic acid	136	96.45	5	3.55
Ampicillin	129	91.49	12	8.51
Cefixime	118	83.69	23	16.31
Ceftriaxone	123	87.23	18	12.77
Cefotaxime	123	87.23	18	12.77
Amikacin	124	87.94	17	12.06
Gentamicin	90	63.83	51	36.17
Nalidixic acid	112	79.43	29	20.57
Norfloxacin	62	43.97	79	56.03
Ciprofloxacin	70	49.65	71	50.35
Trimethoprim	87	61.70	54	38.30
Trimethoprim/ sulfamethoxazole	89	63.12	52	36.88
Imipenem	4	2.84	137	97.16
Tetracycline	90	63.83	51	36.17
Chloramphenicol	94	66.67	47	33.33
Total No. Tested	141 *E.coli* bacteria			

The resistance of UPEC toward the antibiotics in the present study was similar to other studies performed in Kurdistan Region / Iraq and in other developing countries. For example, Merza and Jubrael, (2015) in Duhok, showed that the isolated UPEC displayed high resistance to Ampicillin 92.6%, Amoxicillin 90.6%, Amoxicillin/Clavulanic acid 90%, Tetracycline 83.3%, Trimethoprim 77.3%, Trimethoprim/ sulfamethoxazole 73.3%, Nalidixic acid 78%, Cefixime 78%, Cefotaxime 78%, Ceftriaxone 71.3%, Gentamicin 70.7%, Ciprofloxacin 52.6%, Norfloxacin 48.6%, Amikacin 46%, Chloramphenicol 30% and Imipenem was 4.6%. Likewise, another study in Kurdistan region reported that UPEC showed variable resistant rates to Ampicillin 85%, Ceftriaxone 65%, Ciprofloxacin 48%, Gentamicin 38%, Amoxicillin 33% and all isolated *E. coli* were sensitive to both Imipenem and Amikacin antibiotics (Assafi *et al.,* 2015). Furthermore, Muhammad and Ghareb, (2019) in Erbil city found that the resistant rates of both Ceftriaxone and Ciprofloxacin were increased against isolates *E. coli* which were 100%. On the other hand, a recent study in Egypt, Hegazy *et al.,* (2018) showed high resistance rates

of UPEC to Ampicillin 100%, followed by Nalidixic acid 91.84%, Trimethoprim/ sulfamethoxazole 87.9%, Norfloxacin 82.65%, Amoxicillin/ clavulanic acid 81.3%, Ceftriaxone 79.60%, Cefotaxime 74.49%, Gentamicin 26.53%, Amikacin 22.45% and Imipenem 20.41%.

For many decades, Amoxicillin/clavulanate, Cephalexin, Fluoroquinolones (for example, Ciprofloxacin) or Trimethoprim/sulfamethoxazole have been used as first-line for the treatment for uncomplicated UTI (Totsika *et al.,* 2012). However, *E. coli* are resistant to typical first-line agents has become substantial and these drugs can no longer be used in many parts of the world as empiric therapy (Gupta *et al.,* 2011). Earlier, Ampicillin was reported to have no greater effect on pathogens in the urinary tract (Sahm *et al.,* 2001), and this is because of the continuous use of Ampicillin among UTIs patients for many years which led to the production of the resistant by UTI pathogens to Ampicillin (Hassan *et al.,* 2011).

It has been reported that the improper empiric antimicrobial treatment for nosocomial-acquired or community-acquired infections, contributed to significantly higher mortality rates in the intensive care unit (ICU). Also, the insufficient antimicrobial therapy of the infection was the most significant independent determinant of hospitals mortality (Kollef *et al.,* 1999). Another important mechanism that facilitates the increase in the resistance of antimicrobial agents to UTIs infections is the introduction and clonal expansion of competitive resistant strains of *E. coli* in the community (Nordstrom *et al.,* 2013).

In all cases of UTIs, the patients were starting antimicrobial therapy before the laboratory results were available for urine culture (Dash *et al.,* 2013). The misuse and self-medication of the antimicrobial agent (where antibiotics could be purchased without any medical prescription) may be a major problem in many countries, including Iraq, and these led to a general rise of resistant of the bacteria to antibiotics (Sahm *et al.,* 2001; Merza and Jubrael, 2015). Furthermore, about 95% of UTI infections were treated without bacteriological investigations (Taghizadeh *et al.,* 2013; Bari *et al.,* 2017). There is a need to introduce strict strategies for dispensing antibiotics in the community in order to prevent the emergence of more resistant isolates of pathogenic bacteria. In addition, physician should depend more on laboratory guidance, and laboratories should provide resistance pattern data for optimum patient management more rapidly (Merza and Jubrael, 2015). Many reports suggested that the resistance of *E. coli* strains to commonly used antimicrobial agents has made the clinical management of UTI complicated by increasing incidence of their infections (Van De *et al.,* 2008). Most of these studies agreed that there is a need to improve on infection control methods (Mukherjee *et al.,* 2013). Genes encoding ESBLs are often found on the same plasmids as genes that encode resistance to aminoglycosides and sulfonamides, and many *Enterobacteriaceae* species have changes that give high-level resistance to quinolones (Paterson, 2006).

2.3. PCR Analysis

Out of 141 UPEC isolates, 57 isolated were selected for PCR amplification, and typical all *E. coli* were successfully amplified for specific-species locus by producing a single band of a target *uidA* gene with molecular weight of 670 bps as shown in Figure 1.

Therefore, the amplification of the *uidA* in the selected samples confirmed that all these strains were, in fact, *E.coli.* The result in this study was similar to the study performed by Merza *et al.,* (2016) in Kurdistan region/Iraq for identification *E.coli*, they used the same *uidA* primer and produced 670 bp as molecular weight. However, this molecular weight is different from that obtained by Adamus-bialek *et al.,* (2009) by using the same primer. This might be due to the fact that genes usually contain several repeats of the coding microsatellite (1-10 bp) and minisatellite (>10 bp), which are very dynamic components of genomes and are subcategories of tandem repeats (TRs) that make up genomic repetitive regions (Merza, 2013; Vieira *et al.,* 2016). Therefore, the recombination events within these TRs led to alter in the repetition numbers, which in turn change the sequences (Merza, 2013).

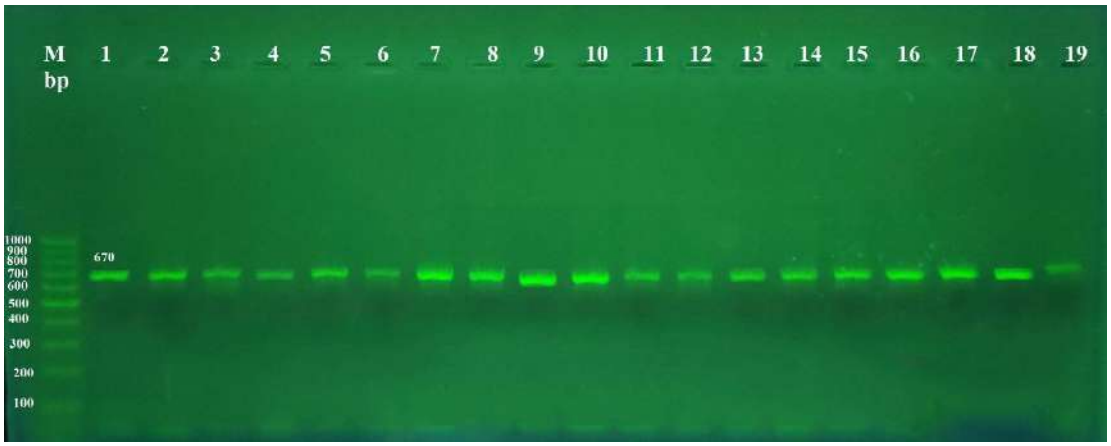

Figure 1: The amplification of PCR for *E.coli* species identification:
Using specific-species *uidA* primer with molecular weight 670bp for 57 UPEC isolated strains and the amplicons separation performed on 1.2% agarose gel electrophoresis for 1 hour. Lane M contained DNA molecular weight marker (1000-100bp).

The selected *E. coli* that had *uidA* gene were subjected for the determination of the genes related to virulence and their distribution among UPEC patients in Zakho city, which includes; *afa*, *sfa*, *hly*, *cnf* and *pai* as shown in Figure 2. The most common virulence gene among UPEC isolates was *afa* which was detected in 28.07% (16/57) of the isolates. Following by *hly* that account for 26.32% (15/57). Whereas the prevalence of both *cnf* and *pai* genes displayed among 22.81% (13/57) of the isolates. The *sfa* gene was the lowest prevalence around 17.54% (10/57). According to this study, the prevalence of the virulence related genes among 57 UPEC isolates, it was found that only 35 (61.40%) of these isolated had one of these five virulence related genes. This rate was somewhat in agreement with the related published studies, for example, a total of 59.4% of UPEC isolates contained at least one of the virulence genes (Pourzare *et al.*, 2017). Furthamore, the rates in this study are in agreement with other studies for most of the virulence genes, for example, a study in Duhok province, showed prevalence rates of virulence related genes that includes *afa*, *cnf*, *hly* and *sfa* among UPEC isolates at 32%, 28%, 24% and 16%, respectively, with the exception of the high prevalence rate (70%) of *pai* gene (Merza *et al.*, 2016). In other studies such as, Oliveira and coworkers, (2011) they also determined the virulence factors of the isolated UPEC in the Curitiba/ Brazil and their different prevalence rates as following; *pai* 32%, *sfa* 26%, *cnf*1 18%, *afa* 6% and *hly* 5%. Furthermore, Karimian *et al.*, (2012) found that the presence of difference in the prevalence rates of the virulance genes in the isolated *E. coli* from urine as following; *cnf*1 50.4%, *hly*A 50.4% and *afa* 8.13%.

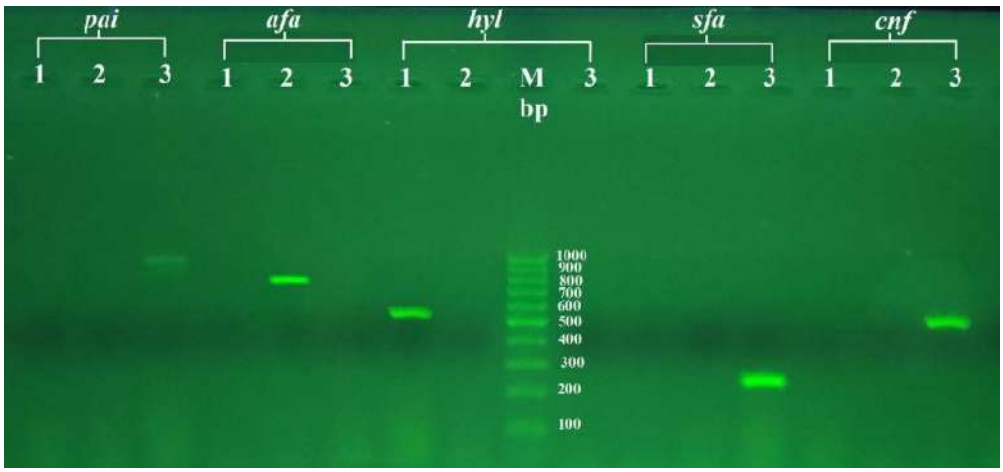

Figure (2): The PCR amplification of the five virulence gene using the five primer includes (*afa*, *sfa*, *hly*, *cnf* and *pai*) with different molecular weight.
Lane M contained DNA molecular weight marker (1000-100bp).

The reported differences in the prevalence of UPEC virulence genes might be due to geographical region or to the climatic conditions of each region (Karimian *et al.*, 2012; Firoozeh *et al.*, 2014). Most likely, habits, public health, food, hospital's health and even sampling methods have significant rules for the spread of virulence genes of UPEC strains (Karimian *et al.*, 2012). This study somewhat is giving alarming data regarding multidrug resistant with multiple virulence factors of UPEC spreading in our community. It is highly recommended to survey all UTIs patients for multidrug resistant isolates simultaneously specifying virulence factors, in addition, to limit the random prescription of antibiotics by general practitioners physician in our community.

3. CONCLUSION

The *E.coli* is the most common pathogen which causes UTI in human. Furthermore, this pathogen have developed resistance to the most used antibiotics except Imipenem which was highly sensitive against the isolates of pathogenic *E. coli.* The use of *uidA* primer gave successful identification of *uidA* gene in the tested *E. coli* isolates. It is worthwhile to mention that various virulence factors facilitate the spreading of bacteria in human urinary tract causing UTI.

Conflict of Interest: there is no conflict of interest.

References

Abdulrahman, Z.F.A., Salah, H.F. and Mohammad, M.I. 2016. Molecular study and assessment of the medicinal potential of the lepidium sativum plant extracts against antibiotic resistance *E.coli*, *ZANCO Journal of Pure and Applied Sciences*, 28 (1), 1–10.

Adamus-bialek, W., Wojtasik, A., Majchrzak, M., Sosnowski, M. and Parniewski, P. 2009. (CGG) 4-Based PCR as a Novel Tool for Discrimination of Uropathogenic *Escherichia coli* Strains : Comparison with Enterobacterial Repetitive Intergenic Consensus-PCR, *Journal of Clinical Microbiology*, 47 (12), 3937–3944.

Alexander, S.K. and Strete, D. 2001. *Microbiology: a photographic atlas for the laboratory*, USA, Daryl Fox.

Assafi, M.S.A., Ibrahim, N.M.R., Hussein, N.R., Taha, A.A. and Balatay, A.A. 2015. Urinary Bacterial Profile and Antibiotic Susceptibility Pattern among Patients with Urinary Tract Infection in Duhok City, Kurdistan Region, Iraq, *International Journal of Pure & Applied Sciences & Technology*, 30(2), 54–63.

Ausubel, F.M., Brent, R., Kingston, R.E., Moore, D.D., Seidman, J.G., Smith, J.A. and Struhl, K. 2003. *Current Protocols in Molecular Biology*, USA, John Wiley & Sons.

Bari, M.A., Arefin, M., Nessa, M., Mostofa, G. and Islam, T. 2017. Recent Antibiotic Sensitivity Pattern of *Escherichia coli* in Urinary Tract Infection, *Journal of Teachers Association*, 30(1), 61–65.

Behzadi, P., Najafi, A., Behzadi, E. and Ranjbar, R. 2016. Microarray long oligo probe designing for *Escherichia coli* : An in-silico DNA marker extraction, *Central European Journal of Urology*, 69(1), 105–111.

Bien, J., Sokolova, O. and Bozko, P. 2012. Role of Uropathogenic *Escherichia coli* Virulence Factors in Development of Urinary Tract Infection and Kidney Damage, *International Journal of Nephrology*, 2012, 1–15.

Le-Bouguenec, C.L.E., Archambaud, M. and Labigne, A. 1992. Rapid and Specific Detection of the pap , afa , and sfa Adhesin- Encoding Operons in Uropathogenic *Escherichia coli* Strains by Polymerase Chain Reaction, *Journal of Clinical Microbiology*, 30 (5), 1189–1193.

Chapman, T.A., Wu, X., Barchia, I., Bettelheim, K.A., Driesen, S., Trott, D., Wilson, M. and Chin, J.J. 2006. Comparison of Virulence Gene Profiles of *Escherichia coli* Strains Isolated from Healthy and Diarrheic Swine, *Enviromental Microbiology*, 72(7), 4782–4795.

Cheesbrough, M. 2006. *District Laboratory Practice in Tropical Countries*, United States of America New York, Cambridge University Press.

Coyle, M., B. 2005. *Manual of Antimicrobial Susceptibility Testing*, USA, Washington, DC : American Society for Microbiology.

Dash, M., Padhi, S., Mohanty, I., Panda, P. and Parida, B. 2013. Antimicrobial resistance in pathogens causing urinary tract infections in a rural community of Odisha, India, *Journal of Family and Community Medicine*, 20(1), 20–26.

Van De, S.-B.N., Grundmann, H., Verloo, D., Tiemersma, E., Monen, J., Goossens, H., Ferech, M., System,

Surveillance, E.A.R. and Groups, E.S. of A.C.P. 2008. Antimicrobial drug use and resistance in Europe, *Antimicrobial Drug Use and Resistance in Europe drug*, 14(11), 1722–1730.

Dobrindt, U., Agerer, F., Michaelis, K., Janka, A., Buchrieser, C., Samuelson, M., Svanborg, C., Gottschalk, G., Karch, H. and Hacker, J. 2003. Analysis of Genome Plasticity in Pathogenic and Commensal *Escherichia coli* Isolates by Use of DNA Arrays, *Journal of Bacteriology*, 185(6), 1831–1840.

Dobrindt, U., Blum-oehler, G., Nagy, G., Schneider, G., Johnn, A. and Gottschalk, G. 2002. Genetic Structure and Distribution of Four Pathogenicity Islands (PAI I 536 to PAI IV 536) of Uropathogenic, *American Society for Microbiology*, 70(11), 6365–6372.

Engelkirk, P.G. and Duben-Engelkirk, J. 2008. *Laboratory diagnosis of Infectious Diseases*, USA, Wolters Kluwer Health/Lippincott Williams & Wilkins.

Farell, D.J., Morrissay, I., De Rubeids, D., Robbins, M. and Felmingham, D. 2003. A UK multicenter study and the antimicrobial susceptibility of bacterial pathogens causing urinry tract infection, *Journal of Infection*, 46 (2), 94–100.

Farshad, S., Ranjbar, R., Japoni, A., Hosseini, M., Anvarinejad, M. and Mohammadzadegan, R. 2012. Microbial Susceptibility, virulence Factors, and Plasmid Profiles of Uropathogenic *Escherichia coli* Strains Isolated from children in Jahrom, Iran. *Arch Iran Med*, 15(5), 312–316.

Firoozeh, F., Saffari, M., Neamati, F. and Zibaei, M. 2014. Detection of virulence genes in *Escherichia coli* isolated from patients with cystitis and pyelonephritis, *International Journal of Infectious Diseases*, 29, 219–222.

Gupta, K., Hooton, T.M., Naber, K.G., Wullt, B., Colgan, R., Miller, L.G., Moran, G.J., Nicolle, L.E., Raz, R., Schaeffer, A.J. and Soper, D.E. 2011. Highlights from international clinical practice guidelines for the treatment of acute uncomplicated cystitis and pyelonephritis in women: A 2010 update by the infectious diseases society of America and the european society for microbiology and infectious, *Clin Infect Dis.*, 52(5), e103–e120.

Hassan, S.A., Jamal, S.A. and Kamal, M. 2011. Occurrence of multidrug resistant and ESBL producing *E. coli* causing urinary tract infections, *Journal of Basic & Applied Sciences*, 7(1), 39–43.

Hegazy, E.E., Alam El Din, R.A.E., Amin, A.M., Mahgoub, F.M. and El Gamal, S.A.E. 2018. Microbiological Profile of Urinary Tract Infections with special Reference to Antibiotic Susceptibility Pattern of *Escherichia coli* Isolates, *International Journal of Current Microbiology and Applied Sciences*, 7(2), 911–920.

Hryniewicza, K., Szczypab, K., Sulikowskab, A., Jankowskia, K., Betlejewskab, K. and Hryniewiczb, W. 2001. Antibiotic susceptibility of bacterial strains isolated from urinary tract infections in Poland, *Journal of Antimicrobial Chemotherapy*, 47(6), 773–780.

Hyle, E.P., Lipworth, A.D., Zaoutis, T.E., Nachamkin, I., Fishman, N.O., Bilker, W.B., Mao, X. and Lautenbach, E. 2005. Risk Factors for Increasing Multidrug Resistance among Extended-Spectrum-Lactamase-Producing *Escherichia coli* and *Klebsiella* Species, *Clinical Infectious Diseases*, 40(9), 1317–1324.

Johnson, J.R. and Stell, A.L. 2000. Extended Virulence Genotypes of *Escherichia coli* Strains from Patients with Urosepsis in Relation to Phylogeny and Host Compromise, *The Journal of Infectious Diseases*, 181(1), 261–272.

Kaper, J.B., Nataro, J.P. and Mobley, H.L.T. 2004. Pathogenic *Escherichia coli*, *Nature Reviews Microbiology*, 2, 123–140.

Karimian, A., Momtaz, H. and Madani, M. 2012. Detection of uropathogenic *Escherichia coli* virulence factors in patients with urinary tract infections in Iran, *African Journal of Microbiology Research*, 6(39), 6811–6816.

Kollef, M.H., Sherman, G., Ward, S. and Fraser, V.J. 1999. Inadequate Antimicrobial Treatment of Infections: A Risk Factor for Hospital Mortality Among Critically Ill Patients, *Chest*, 115(2), 462–474.

Lautenbach, E., Strom, B.L., Bilker, W.B., Patel, J.B., Edelstein, P.H. and Fishman, N.O. 2002. Epidemiological Investigation of Fluoroquinolone Resistance in Infections Due to Extended-Spectrum β-Lactamase–Producing *Escherichia coli* and Klebsiella pneumoniae, *Clinical Infectious Diseases*, 33(8), 1288–1294.

Leboffe, M.J. and Pierce, B.E. (2011). *Photographic Atlas for the microbiology laboratory*, USA, Douglas N. Morton.

Litza, J. and Brill, J. 2010. Urinary tract infections, *Prim Care*, 37(3), 491–507.

M, N.S., Jayakumar, K. and Aravazhi, A.N. 2016. The

effectiveness of antibiotics against a major uropathogen- *Escherichia coli* and its biofilm assay by phenotypic methods, *International Journal of Research in Medical Sciences*, 4(11), 4820–4828.

Manikandan, C. and Amsath, A. 2014. Antibiotic susceptibility pattern of *Escherichia coli* isolated from urine samples in Pattukkottai, Tamilnadu, *International Journal of Current Microbiology and Applied Sciences*, 3(10), 449–457.

Merza, N.S. 2013. Clonal Grouping of Uropathogenic *Escherichia coli* Using Different molecular Typing Methods in Kurdistan Region-Iraq, Ph.D Dissertation, University of Zakho. .

Merza, N.S., Fadhel Al Deen, I.S., Khalid, H.M. and Jubrael, J.M.S. 2016. Molecular Characterization of Extended Spectrum B-lactamase Producing *Escherichia coli* Isolated from Urine in Kurdistan Region-Iraq, *International Journal of Chemical and Biomolecular Science*, 2(2), 51–55.

Merza, N.S. and Jubrael, J.M.S. 2015. The Prevalence of Virulence Factors Among Uropathogenic *Escherichia coli* Strains Isolated From Different Hospitals in Kurdistan Region-Iraq, *International Journal of Bioinformatics and Biomedical Engineering*, 1(3), 338–343.

Miyazaki, J., Ba-Thein, W., Kumao, T., Obata Yasuoka, M., Akaza, H. and Hayshi, H. 2002. Type 1, P and S fimbriae, and afimbrial adhesin I are not essential for uropathogenic *Escherichia coli* to adhere to and invade bladder epithelial cells, *FEMS Immunology and Medical Microbiology*, 33(1), 23–26.

Mladin, C. Usein, C.A. Chifiriuc, M.C. Palade, A. Slavu, C. L. Negut, M. and Damian, M. 2009. Genetic analysis of virulence and pathogenicity features of uropathogenic *Escherichia coli* isolated from patietns with neurogenic bladder, *Romanian Biotechnological Letters*, 14(6), 4900–4905.

Muhammad, I.A. and Ghareb, D.J. 2019. Biofilm Forming Capability , Multidrug Resistance and Detection of Associated Genes in Uropathogenic *Escherichia coli* isolated from Catheterized Patients, *ZANCO Journal of Pure and Applied Sciences*, 31(4), 9–22.

Mukherjee, M., Basu, S., MuKherjee, S.K.M. and Majumder, M. 2013. Multidrug-resistance and extended spectrum beta-lactamase production in uropathogenic *E. coli* which were isolated from hospitalized patients in Kolkata, India, *Journal of Clinical and Diagnostic Research*, 7(3), 449–453.

Nicolle, L E. 2005. Complicated Urinary Tract Infection in Adults, *Can J Infect Dis Med Microbiol*, 16 (6), 349-60.

Nordstrom, L., Liu, C.M. and Price, L.B. 2013. Foodborne urinary tract infections: A new paradigm for antimicrobial-resistant foodborne illness, *Frontiers in Microbiology*, 4(29), 1–6.

Oliveira, F.A., Paludo, K.S., Arend, L.N.V.S., Farah, S.M.S.S., Pedrosa, F.O., Souza, E.M., Surek, M., Picheth, G. and Fadel-Picheth, C.M.T. 2011. Virulence characteristics and antimicrobial susceptibility of uropathogenic *Escherichia coli* strains, *Genetics and Molecular Research*, 10(4), 4114–4125.

Paterson, D.L. 2006. Resistance in gram-negative bacteria: Enterobacteriaceae, *American Journal of Infection Control*, 34 (5 SUPPL.), 20–28.

Poirel, L., Loo, M. Van De, Mammeri, H. and Nordmann, P. 2005. Association of Plasmid-Mediated Quinolone Resistance with Extended-Spectrum β-Lactamase VEB-1, *Antimicrobial Agents and Chemotherapy*, 49(7), 3091–3094.

Polse, R.F., Yousif, S.Y. and Assafi, M.S. 2016. Prevalence and Antimicrobial Susceptibility Patterns of Uropathogenic *E. coli* among People in Zakho, Iraq, *International Journal of Research in Medical Sciences*, 4 (4), 1219–23.

Pourzare, M., Derakhshan, S. and Roshani, D. 2017. Distribution of Uropathogenic Virulence Genes in *Escherichia coli* Isolated from Children with Urinary Tract Infection in Sanandaj, Iran, *Archives of Pediatric Infectious Diseases*, 5(3), 1–6.

Rupp, M.E. and Fey, P.D. 2003. Extended Spectrum β-Lactamase (ESBL) Producing Enterobacteriaceae, *Drugs*, 63(4), 353–365.

Russo, T.A. and Johnson, J.R. 2000. Proposal for a New Inclusive Designation for Extraintestinal Pathogenic Isolates of *Escherichia coli* : ExPEC, *The Journal of Infectious Diseases*, 181(5), 1753–1754.

Sahm, D.F., Critchley, I.A., Kelly, L.J., Karlowsky, J.A., Mayfield, D.C., Thornsberry, C., Mauriz, Y.R. and Kahn, J. 2001. Evaluation of current activities of fluoroquinolones against gram-negative bacilli using centralized in vitro testing and electronic surveillance, *Antimicrobial Agents and Chemotherapy*, 45(1), 267–274.

Shah, A.A., Hasan, F., Ahmed, S. and Hameed, A. 2004. Extended-spectrum β-lactamases (ESBLs): Characterization, epidemiology and detection, *Critical Reviews in Microbiology*, 30(1), 25–32.

Sharma, N., Gupta, A., Walia, G. and Bakhshi, R. 2016. Pattern of antimicrobial resistance of *Escherichia coli* isolates from urinary tract infection patients: A three year retrospective study, *Journal of Applied Pharmaceutical Science*, 6(1), 062–065.

Šišková, P., Černohorská, L., Mahelová, M., Turková, K. and Woznicová, V. 2015. Phenotypes of *Escherichia coli* isolated from urine: Differences between extended-spectrum β-lactamase producers and sensitive strains, *Journal of Microbiology, Immunology and Infection*, 48(3), 329–334.

Siu, H.L., Reddy, S., Cheesbrough, J., Bolton, F.J., Willshaw, G., Cheasty, T., Fox, A.J. and Upton, M. 2008. Major uropathogenic *Escherichia coli* strain isolated in the Northwest of England identified by multilocus sequence typing, *Journal of Clinical Microbiology*, 46(3), 1076–1081.

Taghizadeh, G., Kulkarni, D.K., Delbari, A.S. and Taghizadeh, R. 2013. Antimicrobial susceptibility pattern of *E. coli* among patients attending at apadana hospital in ahwaz, Iran, *International Journal of Research in Ayurveda and Pharmacy*, 4(1), 120–122.

Tiwary, S.K., Sharan, S., Kumar, R. and Kumari, K. 2017. Antimicrobial susceptibility patterns of uropathogenic *Escherichia coli* and their prevalence among people in and around Dhanbad, Jharkhand, *International Journal of Contemporary Medical Research*, 4(8), 1637–1639.

Totsika, M., Moriel, D.G., Idris, A., Rogers, B.A., Wurpel, D.J., Phan, M.-D., Paterson, D.L. and Schembri, M.A. 2012. Uropathogenic *Escherichia coli* Mediated Urinary Tract Infection, *Current Drug Targets*, 13(11), 1386–1399.

Vieira, M.L.C., Santini, L., Diniz, A.L. and Munhoz, C. de F. 2016. Microsatellite markers: What they mean and why they are so useful, *Genetics and Molecular Biology*, 39(3), 312–328.

Wiles, T.J., Kulesus, R.R. and Mulvey, M.A. 2008. Origins and virulence mechanisms of uropathogenic *Escherichia coli*, *Experimental and Molecular Pathology*, 85(1), 11–19.

Zhanel, G.G., Hisanaga, T.L., Laing, N.M., DeCorby, M.R., Nichol, K.A., Weshnoweski, B., Johnson, J. ack, Noreddin, A., Low, D.E. and Karlowsky, J.A. 2006. Antibiotic resistance in *Escherichia coli* outpatient urinary isolates: final results from the North American Urinary Tract Infection Collaborative Alliance (NAUTICA), *Int J Antimicrob Agents*, 27(6), 468–76.

ZANCO Journal of Pure and Applied Sciences
The official scientific journal of Salahaddin University-Erbil
https://zancojournals.su.edu.krd/index.php/JPAS

ISSN (print):2218-0230**, ISSN (online):** 2412-3986**, DOI: http://dx.doi.org/10.21271/zjpas**

RESEARCH PAPER

Improvement of wheat quality and soil fertility by integrates chemical fertilizer with rhizobial bacteria

Trifa Dhahir Saber[1] and Mohammed Qader Khursheed[2]

[1,2] Department of biology, College of education, Salahaddin University-Erbil, Kurdistan Region, Iraq

A B S T R A C T:

A field experiment was carried out in Erbil city at Agricultural Research Center, during winter season 2017 - 2018, to study the effect of three levels (120, 240, 360 kg.ha^{-1}) of NPK (20:20:20) fertilizer, five species of Rhizobial inoculation (Control, *Bradyrhizobium sp.* (Vigna) (B1), *Rhizobium leguminosarum bv. Viciae* (B2). *Bradyrhizobium* Mungbean (B3), *Mesorhizobium ciceri* (B4) and *Rhizobium leguminosarum bv phaseoli* (B5)) and two wheat cultivar soft (*Triticum aestivum* L.) Hawler2,and hard (*Triticum durum* L.) Seminto and their combination on leaf (Nitrogen, Phosphor, Potassium, Calcium and Iron)contents, soil nutrient (Total Nitrogen, available Phosphor, Potassium and Iron contents, leaf (Auxin IAA, Gibberellin GA and Cytokinin CK) contents, grain number.plot^{-1}, weight of 1000 grain(g), grain yield kg.hac^{-1}, biological yield kg.hac^{-1} and harvest index% by utilizing complete randomized block design (CRBD) with three replication. Rhizobial inoculation individually increased significantly all tested parameters of growth. Generally, Seminto significantly surpassed Hawler2 in most traits under study. Interaction between of chemical fertilizer with rhizobial bacteria was more evident than that of chemical fertilizer alone for all mentioned traits. The combination of chemical fertilizer, rhizobial bacteria and wheat cultivars had a synergistic effect and improved leaf (N,P,K,Ca and Fe) contents, fertility of soil, phytohormone concentration in leaves and yield components. The finding indicated that the combination between the lower levels of NPK fertilizer with *Rhizobium leguminosarum bv phaseoli* inoculation for *Triticum aestivum* increased grain yield by 114.39% over the control. We recommend using rhizobial bacteria in combination with lower levels of NPK to reduce chemical fertilizer dose and improving yield production and soil fertility because combination between mentioned factors gave the highest values of most traits under study.

KEY WORDS: Chemical fertilizer, Rhizobial bacteria, Wheat cultivars Hawler2 and Seminto.
DOI: http://dx.doi.org/10.21271/ZJPAS.32.2.19
ZJPAS (2020) , 32(2);178-191 .

1.INTRODUCTION

Nutritional value of *Triticum* sp. is extremely important as it takes a significant place among the few crop species that are extensiv ely grown as staple food sources, its grain can be ground into flour, semolina, etc., which constitute the fundamental components of bread and other bakery products, a s well as pastas, and is thus the major source of nu trients for the majority of the world's population (Šramková et al., 2009).

* **Corresponding Author:**
Trifa Dhahir Saber1
E-mail: trifa.saber@su.edu.krd
Article History:
Received: 01/09/2019
Accepted: 26/11/2019
Published: 22/04 /2020

It is common food that contributes more calories and proteins to the world diet than any other cereal crop (Biesaga-Kościelniak et al., 2014). Improving yield is satisfied by either increasing the area under cultivation or improving the yield per unit area; the first option is very limited and has helped to in crease the yield per unit area (Moradi et al., 2015).The UN predicts that the world population will grow over the next decades. For this reason, the world needs to increase crop yields through better use of water and fertilizer in order to guarantee food security and environmental protection (Foulkes et al., 2010). The total biomass is a result of the integration of metabolic reaction in the plants. Consequently, any factor

influencing the metabolic activity of the plant at any period of its growth can affect the yield. Metabolic processes in wheat plants are greatly governed by both internal i.e. genetic makeup of the plant and external conditions which namely climatic and edaphically environmental factors. Thus, increasing wheat production per unit area can be achieved by breeding and cultivating the promising wheat cultivars and applying the optimum cultural practices such as suitable fertilizer(Zaki et al., 2012).

Nutrients availability is the most limiting factor for crop growth. Nutrients removal from the field, besides their uptake by crops, was also caused by wind and water erosion, leaching to deeper soil layers and for nitrogen by ammonia volatilization and denitrification. Consequently, to avoid crop yield reduction, replenishment of nutrients through chemical and natural fertilizers is necessary. The excessive uses of mineral fertilizers have generated several environmental problems: potential pollution to soil, water and air (Stajković-Srbinović et al., 2014). One potential way to decrease negative environmental impacts resulting from continued use of chemical fertilizers is inoculation with plant growth-promoting rhizobacteria (PGPR). These bacteria exert beneficial Effect on plant growth and development, and many different genera have been commercialized for use in agriculture(Adesemoye and Kloepper, 2009). Plant growth promoting rhizobacteria (PGPR) is free-living bacterial group colonizing the rhizosphere and exert a positive effect on plant health and fertility of soil (Zahir et al., 2010). Improving yield of wheat plants by interactive influence of chemical, organic fertilizer and biofertilizer is a promising purpose in wheat production for lowering high doses of inorganic fertilizer also, get more clean yield with low undesirable high doses of heavy metals and other pollutants(Jala-Abadi et al., 2012). *Rhizobium* is an important symbiotic for legumes but it plays an important role with non-legumes by producing growth hormones. The first important step for producing growth hormone is root colonization of beneficial bacteria with plants(Akhtar et al., 2013). This experiment was planned to determine the best levels of NPK to be integrated with rhizobial bacteria for obtaining more economical, environment friendly and wheat production improvement.

2.MATERIALS AND METHODS

2.1 Describing of experiment: The experiment was performed under field condition at Agricultural Research Center in Erbil, during winter season 2017 - 2018. The experimental plants used in this investigation were soft wheat (*Triticum aestivum* L.) cultivar Hawler2 and hard wheat (*Triticum durum* Desf.) cultivar Seminto obtained from the Agricultural Research Center in Erbil. Some chemical and physical properties of the soil before treatments are shown in Table (1).

Table 1 some physical and chemical properties of soil

Physical properties		Value
Particle size distribution (%)	Sand	18.1
	Silt	43.6
	Clay	38.3
Soil texture		Silty Clay loam
Chemical properties		Value
pH		7.8
Electrical Conductivity ($dS.m^{-1}$)		0.5
Total nitrogen $mg.g^{-1}$		0.51
Available Phosphorous $mg.kg^{-1}$		4.34
Available Potassium $mg.kg^{-1}$		293.70
Available Iron ppm		1.63

2.2 Treatment and experimental design: The experiment was comprised of six levels of rhizobial inoculums (Control, *Bradyrhizobium sp.* (Vigna), *Rhizobium leguminosarum bv. viciae*, *Bradyrhizobium* Mungbean, *Mesorhizobium ciceri*

and *Rhizobium leguminosarum bv phaseoli*) and three levels of NPK (20:20:20) fertilizers (120, 240 and 360) kg.ha^{-1}. Fifty grains were planting in each plot. Thirty six treatments were tested in randomized block design with three replications. The comparisons between means were made using Tukey's's test at significant level of 5% for field experiment parameters and 1% for laboratory parameters. SPSS version 16 was used for data analysis.

2.3 Isolation of Rhizobial sp.: Five strains of rhizobia were isolated from the root nodules of (*Vigna unguiculata), (Vicia faba), (Vigna radiata L.),* (*Cicer arietinum* L) and (*Phaseoulus vulgasrous*), respectively which were growing for 2-3 months under field conditions at a different area of Erbil city. With some non-rhizospheric soil, host plants were uprooted from t he field and carried to the laboratory in polythene containers. Then estimated according to (Mehboob et al., 2011).

2.4 Preparation of inoculums: Preparation of inoculum was performed by (Mehboob, 2010).

2.5 Experimental parameters:

1- Biochemical contents: dried leaves were grinded by an electrical grinder for each replicate of the experiment; 0.3g of ground samples were digested, then total nitrogen determined by Kjeldahl method, total phosphorus and available phosphorus estimated using spectrophotometer method, total calcium, available calcium, total iron and available iron estimated by atomic absorption method, Total potassium and available potassium determined, using Flame –photometer method as described by(Ryan et al., 2001) . The total protein was calculated by multiplying the value of total nitrogen by (5.75) (Dalaly and Al-Hakim, 1987). And total soluble carbohydrate was determined by the Anthron methods(Sadasivam, 1996).

2- Determination of plant hormones: Endogenous hormones, namely auxins (IAA), gibberellic acid (GA) and cytokinins (CK) were extracted according to(Jogi et al., 2017), then plant hormones determined by HPLC. The endogenous concentration of (IAA, GA and CK) in samples was calculated from the spectra obtained using the following equation:

$$Sample\ concentration(ppm) = \frac{Concentration\ of\ standard \times Area\ of\ sample}{area\ of\ stanndard} \times \frac{Volume\ of\ sample}{Weight\ of\ sample}\ 100$$

3- Yield components: At harvest; number of grains.plant^{-1}, weight of 1000 grains (g), grain yield (kg.hac.$^{-1}$), biological yield (kg.hac.$^{-1}$), Harvest index(HI%) and increase grain yield (%) were estimated. Improving grain yield was estimated as described by (Ye et al., 2005)

$$Increase\ grain\ yield\% = \frac{(Grain\ yield\ of\ fertilized\ pot - Grain\ yield\ of\ control)}{Grain\ yield\ of\ control} \times 100$$

3.RESULTS

3.1 Nutrient content of leaves and soil

Table (2) showed progressive increases of leaf nutrient contents in response to different species of rhizobial bacteria. The highest value of total nitrogen (20395.33mg.kg^{-1}) and protein (117.27mg.g^{-1}) were recorded with B3 treatments, while maximum phosphorus (3902.50mg.kg^{-1}) content was recorded by using B5 treatment. Otherwise, the highest value of potassium (9555.00mg.kg^{-1}) and iron content (376.67mg.kg^{-1}) were obtained by B2 treatments. In contrast, the same treatments did not affect calcium and carbohydrate contents. The same table indicated that the highest value of soil total N (1.62g.kg^{-1}) and available K (462.41mg.kg^{-1}) was recorded by using B1 and B2 respectively. While B3 treatment gave highest available (P: 10.31mg.kg^{-1} and Fe: 4.25mg.kg^{-1}).

Data presented in table (3) shows that carbohydrate content of leaves significantly increased by different levels of NPK fertilizer and

significant difference was observed on protein, nitrogen and phosphorus contents of leaves. The greatest value of N, P, K, protein and carbohydrate content were obtained by adding 240kg.ha^{-1}, while calcium and iron content were obtained by adding NPK1. Also table (3) detected that the greatest value of total N (1.52g.kg^{-1}), available P (9.25mg.kg^{-1}), available K (434.51mg.kg^{-1}) and available Fe (3.94mg.kg^{-1}) was gained by adding 240kg.ha^{-1} NPK.

Data in table (4) indicated that Seminto significantly exceeded Hawler2 in all leaf composition contents under study except potassium and iron, which not affected by wheat cultivars. Data present in same table clearly showed that, wheat cultivars did not cause any significant effect on soil nutrient status.

Table (5) revealed that, the interaction among different wheat of rhizobial bacteria with different levels of NPK affected significantly some leaf nutrient contents for both wheat cultivars under study while affected non-significantly on potassium, calcium and carbohydrate leaf contents. The highest value of nitrogen (28253mg.kg^{-1}), phosphorus (5160mg.kg^{-1}) and protein content (162.45mg.g^{-1}) were achieved by combining (B3 with 120kg.ha^{-1} NPK of *Triticum durum*), while greatest value of iron content (505.00mg.kg^{-1}) was recorded by integrating (B2 with 120kg.ha^{-1} NPK of *Triticum durum*). Data present in same table shows that, combination between chemical fertilizers with rhizobial bacteria for both wheat cultivars significantly increased soil total nitrogen and available phosphorus. The highest value of total N (1.86g.kg^{-1}) was recorded by both (B1NPK1) and (B3NPK2) of *Triticum durum* respectively. While, the maximum value of available phosphorus concentration: 13.29mg.kg^{-1} was recorded by both (B3NPK1 of *Triticum aestivum*) and (B3NPK1 of *Triticum durum*) respectively. In contrast, avaialable (K and Fe) contents of soil did not affected by combining mentioned factors.

3.2 Plant hormone contents

Figure (1) revealed that rhizobium inoculation individually enhanced the phytohormone content of leaves significantly. The maximum value of CK: 21.42ppm, IAA: 29.00ppm and GA: 159.56ppm was obtained by B5 inoculation. On the other hand, figure (2) showed that the treated plants with NPK fertilizers had a significant effect on leaf phytohormone contents. The greatest value of CK: 20.56ppm, IAA: 23.77ppm and GA: 99.24ppm was achieved by applying 240kg.ha^{-1} of NPK. Data in figure (3) demonstrated that Seminto significantly surpassed Hawler2 in CK and IAA content of leaves, except GA content, where, Hawler2 overcame Seminto in this character.

Results given in table (6) generally clear that all phytohormones under this study were significantly affected by combination between wheat cultivars, chemical fertilizers and rhizobial bacteria. The maximum value of CK (31.45ppm) and IAA (69.49ppm) was obtained by using (B1 with 240kg.ha^{-1} NPK of *Triticum durum*) and (B5 with 120kg.ha^{-1} NPK of *Triticum durum*) respectively. However, the maximum value of GA (292.65ppm) was recorded by using (B5 with 120kg.ha^{-1} NPK of *Triticum aestivum*).

Table 2 Effect of different species of rhizobial bacteria on leaf composition contents and soil nutrient status at harvesting

Rhizobial species	Plant leaf							Soil			
	Protein mg.g^{-1}	Carbohydrate mg.g^{-1}	N mg.kg^{-1}	P mg.kg^{-1}	K mg.kg^{-1}	Ca mg.kg^{-1}	Fe mg.kg^{-1}	Total (N) mg.g^{-1}	Avai. (P)mg.kg^{-1}	Anai (K) mg.kg^{-1}	Avai (Fe) mg.kg^{-1}
Control	79.75	202.55	13869.83	2284.17	8065.83	8675.83	263.33	0.86	4.31	312.88	1.76
B1	114.00	220.75	19825.83	3397.50	9172.50	10121.67	348.33	1.62	7.70	402.20	3.65
B2	108.6	220.78	18889.	3408.	9555.	10417.	376.	1.44	7.87	462.	3.90

	1		33	33	00	50	67			41	
B3	117.27	225.57	20395.33	3632.50	8944.17	9764.17	339.17	1.40	10.31	390.90	4.25
B4	115.44	228.11	20076.00	3378.33	9085.83	10368.33	363.33	1.36	8.90	425.79	3.47
B5	111.43	247.09	19380.17	3902.50	9248.33	9980.83	368.33	1.26	8.36	440.12	3.80
Tukey's0.01	18.45	n.s.	3208.74	628.19	1194.38	n.s.	49.99	0.34	2.29	74.50	1.17

B1: *Bradyrhizobium sp.* (Vigna), B2: *Rhizobium leguminosarum bv. viciae*, B3: *Bradyrhizobium* Mungbean, B4: *Mesorhizobium ciceri* andB5: *Rhizobium leguminosarum bv phaseoli*

Table 3 Effect of different levels of chemical fertilizer on leaf composition contents and soil nutrient status at harvesting

Chemical fertilizer kg.ha^{-1}	Plant leaf							Soil			
	Protein mg.g^{-1}	Carbohydrate mg.g^{-1}	N mg.kg^{-1}	P mg.kg^{-1}	K mg.kg^{-1}	Ca mg.kg^{-1}	Fe mg.kg^{-1}	Total (N) mg.g^{-1}	Avai. (P)mg.kg^{-1}	Anai (K) mg.kg^{-1}	Avai (Fe) mg.kg^{-1}
NPK1	114.42	235.95	19898.58	3545.42	9186.25	11172.92	375.42	1.21	8.08	406.14	3.59
NPK2	116.52	238.00	20265.25	3750.83	9290.83	9627.50	332.08	1.52	9.25	434.51	3.94
NPK3	92.31	198.47	16054.42	2705.42	8558.75	8863.75	322.08	1.24	6.39	376.50	2.88
Tukey's0.01	11.12	38.99	1933.13	378.46	719.56	1726.05	30.12	0.20	1.38	44.88	0.71

NPK1= 120kg.ha^{-1}, NPK2= 240kg.ha^{-1}, NPK3= 360kg.ha^{-1}

Table 4 Effect of wheat cultivars on leaf composition contents and soil nutrient status at harvesting

Wheat cultivars	Plant leaf							Soil			
	Protein mg.g^{-1}	Carbohydrate mg.g^{-1}	N mg.kg^{-1}	P mg.kg^{-1}	K mg.kg^{-1}	Ca mg.kg^{-1}	Fe mg.kg^{-1}	Total (N) mg.g^{-1}	Avai. (P)mg.kg^{-1}	Anai (K) mg.kg^{-1}	Avai (Fe) mg.kg^{-1}
Hawle2	97.03	188.28	16874.89	3125.28	8910.83	9529.44	350.56	1.29	7.68	403.30	3.51
Seminto	118.47	260.00	20603.94	3542.50	9113.06	10246.67	335.83	1.36	8.14	408.14	3.43
Tukey's0.01	7.94	27.85	1380.555	270.28	n.s.	n.s.	n.s.	n.s.	n.s.	n.s.	n.s.

Table 5 Interaction effect of wheat cultivars, chemical fertilizer and rhizobial bacteria on leaf composition contents and soil nutrient status at harvesting

Wheat cultivars	Chemical fertilizer kg.ha^{-1}	Rhizobial species	Plant leaf							Soil			
			Protein mg.g^{-1}	Carbohydrate mg.g^{-1}	N mg.kg^{-1}	P mg.kg^{-1}	K mg.kg^{-1}	Ca mg.kg^{-1}	Fe mg.kg^{-1}	Total (N) mg.g^{-1}	Avai.(P) mg.kg^{-1}	Anai(K) mg.kg^{-1}	Avai(Fe) mg.kg^{-1}
Hawler 2		Control	72.49	151.81	12608	2485	7785	8185	230	0.71	4.04	301.07	1.57
	NPK1	B1	109.24	184.73	18998	3460	9640	13425	415	1.59	5.72	406.53	3.73
		B2	99.48	198.66	17300	3280	9910	9410	400	1.2	7.16	529.61	3.68
		B3	120.76	225.38	21003	3295	9020	9910	395	1.4	13.29	341.18	5.11
		B4	119.34	201.87	20755	3450	9045	12125	415	1.22	7.28	413.35	3.9
		B5	99.07	205.36	17230	4070	9050	10560	390	1.05	7.73	413.33	3.54
		Control	82.43	172.9	14335	2900	7820	9080	265	0.93	4.47	324.85	1.98
	NPK2	B1	114.09	219.11	19843	3255	9680	9090	340	1.47	10.16	415.95	4.84
		B2	107.19	178.68	18643	3835	9695	9380	375	1.49	9.75	425.74	4.78
		B3	113.58	183.92	19753	3435	9075	9770	300	1.5	8.81	491.17	4.72
		B4	115.72	212.78	20125	3375	9150	10370	340	1.75	9.67	436.78	3.29
		B5	101.42	198.64	17638	3630	9680	8450	400	1.46	12.34	502.86	4.79
		Control	74.51	169.13	12958	2490	8020	8295	315	0.92	4.16	368.74	2.01
	NPK3	B1	91.24	177.19	15868	3120	8200	8870	375	1.52	5.8	332.63	2.89
		B2	76.83	178.4	13363	2420	8455	8570	320	1.55	6.84	407.72	3.13
		B3	78.60	169.58	13670	2415	8700	8410	330	1.11	6.94	324.47	2.9
		B4	85.30	178.82	14835	2935	8745	9010	325	1.11	7.01	418.28	3.11
		B5	85.23	182.06	14823	2405	8725	8620	380	1.17	7.04	405.08	3.18
		Control	73.28	194.93	12745	1680	8105	9145	225	0.76	3.79	297.11	1.93
	NPK1	B1	120.75	261.75	21000	3455	9465	11475	360	1.86	7.56	420.04	3.5
		B2	140.	261.	24450	3660	104	1576	505	1.2	7.8	513.8	3.94

			59	15			15	5		2	9	9	
		B3	162.45	263.52	28253	5160	9270	10970	380	1.27	13.29	391.11	4.94
		B4	120.10	255.71	20888	3505	9110	10695	430	1.17	11.67	429.27	3.81
Seminto		B5	135.43	426.54	23553	5045	9420	12410	360	1.06	7.54	417.18	3.39
		Control	82.20	274.59	14295	1815	8300	9350	285	0.91	4.22	279.67	1.52
	NPK2	B1	141.18	271.32	24553	4665	9125	9435	320	1.64	11.06	469.67	4.02
		B2	136.07	293.57	23665	4365	9890	9880	335	1.65	9.13	480.11	4.78
		B3	120.26	275.25	20915	4695	9580	9995	335	1.86	12.9	436.39	4.55
		B4	137.47	293	23908	4355	9705	10935	330	1.72	10.51	441.56	3.45
		B5	146.68	282.25	25510	4685	9790	9795	360	1.84	8.01	509.31	4.61
		Control	93.60	251.91	16278	2335	8365	8000	260	0.95	5.19	305.83	1.53
	NPK3	B1	107.48	210.42	18693	2430	8925	8435	280	1.65	5.92	368.38	2.89
		B2	91.51	214.21	15915	2890	8965	9500	325	1.55	6.42	417.39	3.09
		B3	107.97	235.74	18778	2795	8020	9530	295	1.23	6.63	361.08	3.28
		B4	114.68	226.48	19945	2650	8760	9075	340	1.16	7.27	415.5	3.23
		B5	100.78	187.66	17527	3580	8825	10050	320	0.98	7.49	392.95	3.26
Tukey's0.01			59.59	n.s.	10362.61	2028.73	n.s.	n.s.	161.44	1.10	7.40	n.s.	n.s.

B1: *Bradyrhizobium sp.* (Vigna), B2: *Rhizobium leguminosarum bv. viciae*, B3: *Bradyrhizobium* Mungbean, B4: *Mesorhizobium ciceri* andB5: *Rhizobium leguminosarum bv phaseoli.*, NPK1= 120kg.hac^{-1}, NPK2= 240kg.hac^{-1}, NPK3= 360kg.hac^{-1}

Table 6 Interaction effect of wheat cultivars, chemical fertilizer and rhizobial bacteria on leaf phytohormone

Wheat cultivars	Chemical fertilizer kg.ha^{-1}	Rhizobial species	CK (ppm)	IAA (ppm)	GA (ppm)
Hawler2	NPK1	Control	6.22	4.37	12.49
		B1	12.73	13.17	51.87
		B2	8.11	11.03	45.83
		B3	11.72	12.14	159.05
		B4	8.97	11.84	66.19
		B5	20.12	17.42	292.65
		Control	6.35	4.54	12.95
		B1	7.56	14.70	56.19
		B2	10.89	12.77	102.17

	NPK2	B3	15.56	12.64	197.78
		B4	16.61	13.60	51.02
		B5	18.78	13.19	210.68
		Control	7.15	5.13	14.08
	NPK3	B1	6.82	11.44	26.56
		B2	6.79	10.88	28.85
		B3	6.99	9.06	33.30
		B4	9.40	9.00	39.15
		B5	9.11	6.99	41.17
		Control	19.14	7.93	14.33
Seminto	NPK1	B1	28.82	25.87	56.68
		B2	29.73	25.19	52.37
		B3	28.20	38.53	53.31
		B4	28.69	40.00	112.83
		B5	30.08	69.49	180.17
		Control	21.06	8.60	17.05
	NPK2	B1	31.45	58.57	44.74
		B2	30.06	33.77	181.98
		B3	29.64	29.82	53.51
		B4	30.59	28.53	70.44
		B5	28.17	54.53	192.39
		Control	21.13	10.22	15.11
	NPK3	B1	23.07	23.42	42.77
		B2	23.84	20.56	44.02
		B3	27.74	25.87	46.43
		B4	27.98	22.92	42.40
		B5	22.25	12.35	40.30
	Tukey's0.01		4.70	42.90	7.25

B1: *Bradyrhizobium sp.* (Vigna), B2: *Rhizobium leguminosarum bv. viciae*, B3: *Bradyrhizobium* Mungbean, B4: *Mesorhizobium ciceri* andB5: *Rhizobium leguminosarum bv phaseoli.*, NPK1= 120kg.hac^{-1}, NPK2= 240kg.hac^{-1}, NPK3= 360kg.hac^{-1}

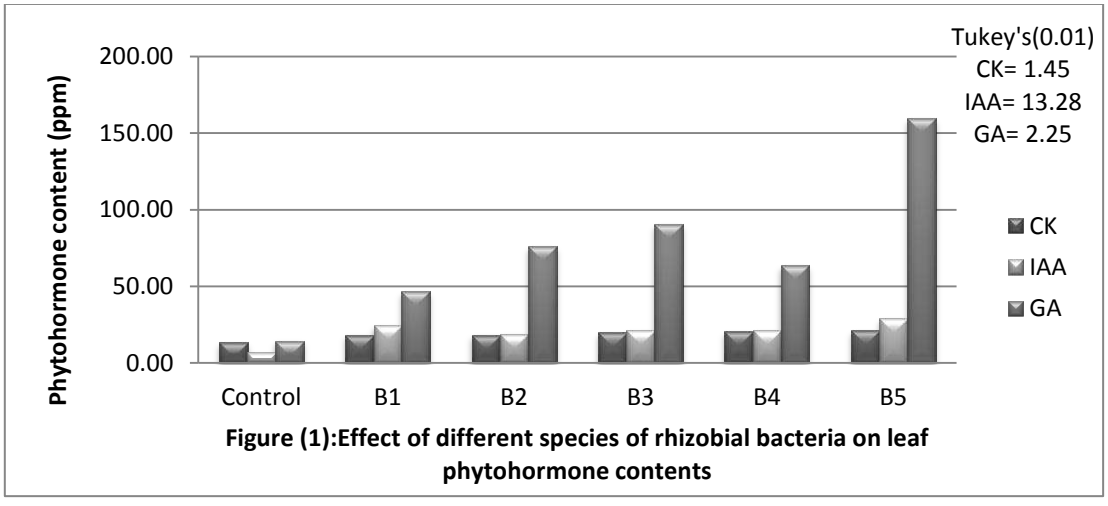

Figure (1):Effect of different species of rhizobial bacteria on leaf phytohormone contents

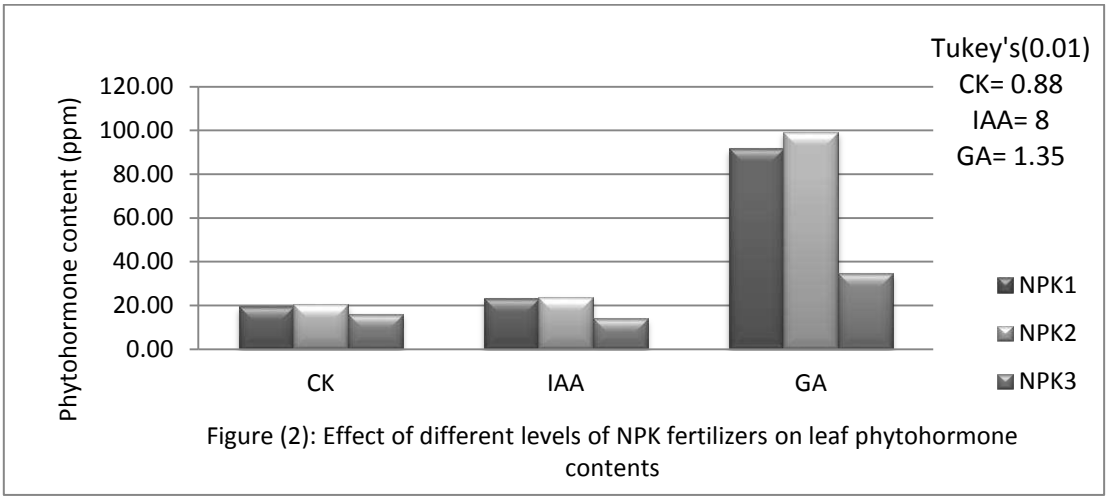

Figure (2): Effect of different levels of NPK fertilizers on leaf phytohormone contents

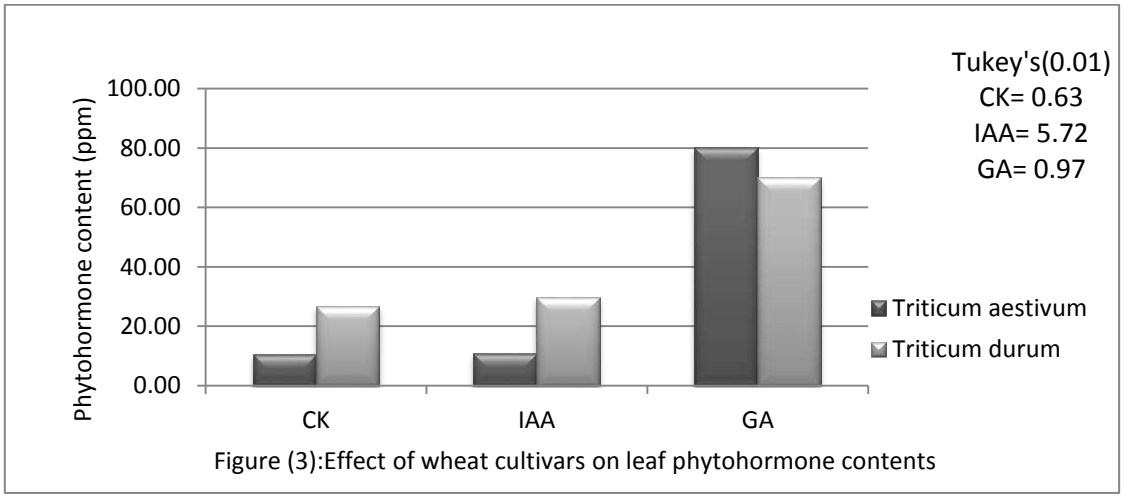

Figure (3):Effect of wheat cultivars on leaf phytohormone contents

3.3 Yield components

Table (7) showed the positive influence of rhizobial inoculation on yield components, highest grain number was 3692.22.plot^{-1}, grain yield: 854.09kg.ha^{-1} and harvest index: 29.82% were recorded by B5 inoculation. The maximum weight of 1000 grain: 50.45g and biological yield: 3009.17kg.ha^{-1} was recorded by using B1 and B2 inoculation respectively.

Data presented in table (8) indicated that, application of different levels of NPK significantly improved yield components. The maximum weight of 1000 grain (48.44g) grain yield (806.47kg.ha^{-1}) and biological yield (2984.45kg.ha^{-1}) were recorded by applying 240kg.ha^{-1} of NPK fertilizer. While, adding 120kg.ha^{-1} of NPK produced significantly higher grain number (3517.22) and harvest index (27.88%)

Table (9) showed that the effect of wheat cultivars on yield components was significant. Seminto surpassed Hawler2 for weight of 1000 grain, grain yield and biological yield, and opposite is true in case of grain number and harvest index.

Results given in table (10) showed that, interaction between wheat cultivars, chemical fertilizer and rhizobial bacteria significantly improved grain yield. As observed, application of (B5 with NPK2 in *Triticum aestivum*), (B1 with NPK2 in *Triticum durum*), (B5 with NPK1 in *Triticum aestivum*), (B4 with NPK1 in *Triticum durum*) and (B1 with NPK1 in *Triticum aestivum*) gave highest grain number 4746.67.plot^{-1}, weight of 1000 grain: 68.64g, grain yield: 991.41kg.ha^{-1}, biological yield: 3730.00kg.ha^{-1} and HI: 35.05% respectively. However figure (4) showed that NPK1 with B5 inoculation of *Triticum aestivum* enhanced grain yield by 114.39% over the control.

Table 7 Effect of different species of rhizobial bacteria on yield components

Rhizobial species	Grain number.plot^{-1}	Weight of 1000grain(g)	Grain yield kg.hac^{-1}	Biological yield kg.hac^{-1}	Harvest index%
Control	2670.17	40.99	513.74	2231.39	23.39
B1	3345.61	50.45	793.99	2836.39	28.34
B2	3394.39	48.79	789.56	3009.17	26.22
B3	3511.56	49.24	831.43	2973.39	28.03
B4	3153.28	48.86	734.64	2850.00	26.27
B5	3692.22	48.06	854.09	2889.17	29.82
Tukey's0.05	248.42	3.19	53.37	217.58	1.84

B1: *Bradyrhizobium sp.* (Vigna), B2: *Rhizobium leguminosarum bv. viciae*, B3: *Bradyrhizobium* Mungbean, B4: *Mesorhizobium ciceri* andB5: *Rhizobium leguminosarum bv phaseoli*

Table 8 Effect of different levels of NPK on yield components

Chemical fertilizer kg.ha^{-1}	Grain number.plot^{-1}	Weight of 1000grain(g)	Grain yield kg.hac^{-1}	Biological yield kg.hac^{-1}	Harvest index%
NPK1	3517.22	46.72	801.26	2904.17	27.88
NPK2	3454.39	48.44	806.47	2984.45	27.03
NPK3	2912.00	48.02	651.00	2506.14	26.12
Tukey's0.05	143.55	1.84	30.84	125.72	1.06

NPK1= 120kg.hac^{-1}, NPK2= 240kg.hac^{-1}, NPK3= 360kg.hac^{-1}

Table 9 Effect of wheat cultivars on yield components

Wheat cultivars	Grain number.plot^{-1}	Weight of 1000grain(g)	Grain yield kg.hac^{-1}	Biological yield kg.hac^{-1}	Harvest index%
Hawler2	3891.35	36.63	719.44	2523.70	28.52
Seminto	2697.72	58.83	786.37	3072.80	25.50
Tukey's0.05	97.62	1.25	20.97	85.50	0.72

Table 10 Interaction effect of wheat cultivars, chemical fertilizer and rhizobial bacteria on yield components

Wheat cultivars	Chemical fertilizer kg.ha^{-1}	Rhizobial species	Grain number.plot^{-1}	Weight of 1000grain(g)	Grain yield kg.hac^{-1}	Biological yield kg.hac^{-1}	Harvest index%
Hawler2	NPK1	Control	3316.67	27.89	462.43	1745.00	26.50
		B1	3953.33	44.32	876.13	2500.00	35.05
		B2	4053.00	38.40	778.27	3216.67	24.19
		B3	4510.00	37.23	839.55	3033.33	27.68
		B4	3810.00	37.89	721.73	2216.67	32.56
		B5	4633.33	42.79	991.41	2911.67	34.05
	NPK2	Control	3206.67	30.54	489.73	1898.33	25.80
		B1	4293.00	40.03	859.30	3045.00	28.22
		B2	4016.67	40.48	813.06	2955.00	27.51
		B3	4090.00	42.27	864.39	3093.33	27.94

		B4	3720.00	36.91	686.53	2911.67	23.58
		B5	4746.67	37.22	883.46	2623.33	33.68
		Control	3210.00	30.09	482.98	1966.67	24.56
		B1	3673.33	36.47	669.75	2256.67	29.68
	NPK3	B2	3886.67	32.08	623.36	2363.33	26.38
		B3	3640.00	37.01	673.65	2248.33	29.96
		B4	3661.67	35.33	646.76	2475.00	26.13
		B5	3623.33	32.43	587.46	1966.67	29.87
		Control	2196.00	47.91	526.08	2496.67	21.07
		B1	4007.33	48.83	978.35	3016.67	32.43
	NPK1	B2	2997.00	56.06	840.00	3150.00	26.67
		B3	3136.67	56.42	884.87	3200.00	27.65
		B4	2460.00	62.23	765.43	3730.00	20.52
		B5	3133.33	60.69	950.81	3633.33	26.17
		Control	2175.00	55.62	604.88	2783.33	21.73
		B1	2120.00	68.64	727.56	3366.67	21.61
	NPK2	B2	3293.00	59.71	983.23	3586.67	27.41
		B3	3295.00	57.45	946.49	3300.00	28.68
Seminto		B4	3033.33	59.55	903.18	3050.00	29.61
		B5	3463.33	52.89	915.82	3200.00	28.62
		Control	1916.67	53.88	516.36	2498.33	20.67
		B1	2026.67	64.43	652.86	2833.33	23.04
	NPK3	B2	2120.00	65.98	699.44	2783.33	25.13
		B3	2397.67	65.03	779.62	2965.33	26.29
		B4	2234.67	61.23	684.20	2716.67	25.19
		B5	2553.33	62.31	795.55	3000.00	26.52
	Tukey's0.05		837.77	10.76	179.98	733.74	6.20

B1: *Bradyrhizobium sp.* (Vigna), B2: *Rhizobium leguminosarum bv. viciae*, B3: *Bradyrhizobium* Mungbean, B4: *Mesorhizobium ciceri* andB5: *Rhizobium leguminosarum bv phaseoli.*, NPK1= 120kg.hac^{-1}, NPK2= 240kg.hac^{-1}, NPK3= 360kg.hac^{-1}

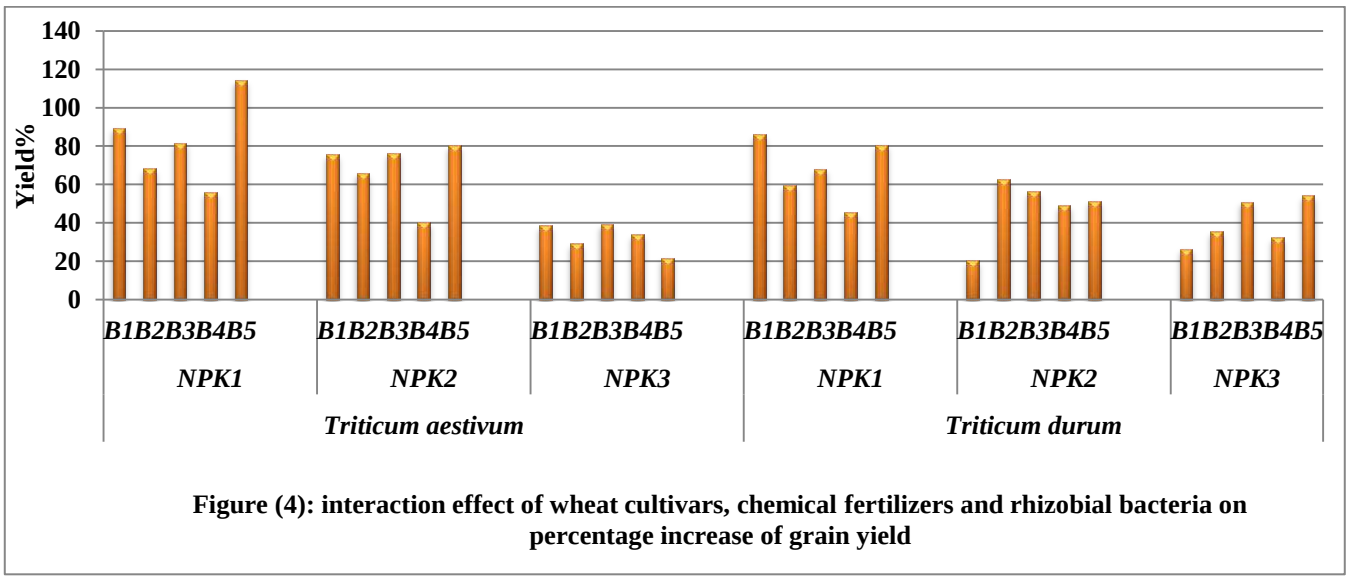

Figure (4): interaction effect of wheat cultivars, chemical fertilizers and rhizobial bacteria on percentage increase of grain yield

4.DISCUSSION

Nutrient deficiency cause significant impact on agriculture, resulting in reduced crop yield or plant quality reduction (Morgan and Connolly, 2013). (Kumar, 2015) suggested that, to overcome the problem of nutrient deficiency and to increase wheat yield, the farmers are applying chemical fertilizers. Chemical fertilizer has its benefits and disadvantages in terms of nutrient supply, quality of the soil and crop growth (Chen, 2006). Less or more plant population and insufficient cro p nutrition are the primary factors responsible for l ow yield (Khursheed and Mahammad, 2015). Chemical fertilizers improve crop yields by providing essential plant nutrients which are easily available to plants; however, their abuse can be harmful for the environment and their use implies increased production costs which reduce the economic viability of agricultural products(Kholssi et al., 2018). Application of biofertilizers became of great necessity to get a yield of high quality and to avoid the environmental pollution(Das et al., 2008). Plant growth promoting rhizobacteria are able to increase mineral and nitrogen availability in the soil as a way to augment growth(Saharan and Nehra, 2011). Increasing of leaf nutrient contents by rhizobial inoculation primarily related to the bacterial production of phytohormone, which caused changes in root morphology and physiology that resulted in increased nutrient and water uptake from the soil(Mia and Shamsuddin, 2010). However, increasing of leaf nutrient contents may be due to the role of Rhizobial bacteria in an increasing the availability of insoluble phosphorus through phosphate-solubilization (Data presented in table (5) supported this results) and siderophore production (which are compounds having low molecular weight and high affinity for iron) (Mehboob, 2010). The positive effect of rhizobial bacteria on soil fertility may be due to the fact that soil microbes are active drivers of soil nutrient cycling, being associated with the decomposition of organic matter, and the transformation and cycling of nutrients, which help to maintain crop productivity and the physical and chemical quality of the soil(Anik et al., 2017). Increasing of leaf phytohormone contents in wheat plants may be correlated to the role of rhizobial bacteria in biosynthesis of plant growth regulators, including auxins, gibberellins, cytokinins, and ABA . The microbial regulators modulate plant hormone levels in plant tissue, and they have been found to have effect that are similar to exogenous phytohormone application(Egamberdieva et al., 2017), the results achieved in the figure (1) largely confirm the positive effect of rhizobial bacteria on plant hormones. Production of phytohormones by inoculation has been suggested as one of the most plausible mechanisms of action affecting plant growth. Soil microbes are potential sources of these phytohormones(Shakhawat, 2007). Enhancing yield components by using rhizobial bacteria may be because of one or more growth promoting mechanisms which may imply that the ability of rhizobia to produce different metabolites like organic acids, vitamins, enzymes and exopolysaccharides in the rhizosphere could be responsible for improve yield production(Mehboob et al., 2011). (Etesami et al., 2009) revealed that inoculation of wheat with beneficial bacteria has the potential to increase the yield of wheat and improve the higher plant growth. (Adnan et al., 2014) suggested that rhizobial bacteria could be used as PGPR for wheat crop in prevailing soil and climatic conditions. This results partially agreed with those obtained by(Mohamed, 2000) concerning wheat plants. In general, the capacity of plant species and their genotypes to absorb and metabolize components differs genetically.

1. CONCLUSION

From the study, it might be concluded that the combination between the lower levels of NPK fertilizer with different species of rhizobial bacteria had positive effect on wheat production and soil fertility.

ACKNOWLEDGEMENT: We are thankful to staff of Agricultural Research Center in Erbil for support in doing this research. We appreciate the reviewers and editors for their exceptionally helpful comments about the manuscript

.

REFERENCES

ADESEMOYE, A. O. & KLOEPPER, J. W. 2009. Plant–microbes interactions in enhanced fertilizer-use efficiency. *Applied microbiology and biotechnology,* 85**,** 1-12.

ADNAN, M., SHAH, Z., KHAN, A., KHAN, G. A., ALI, A., KHAN, N. A., SALEEM, N., NAWAZ, S., AKBAR, S. & SAMREEN, S. 2014. Integrated Effect of Rhizobial inoculum and inorganic fertilizers on wheat yield and yield components. *American Journal of Plant Sciences,* 5**,** 2066.

AKHTAR, N., ARSHAD, I., SHAKIR, M., QURESHI, M., SEHRISH, J. & ALI, L. 2013. Co-inoculation with Rhizobium and Bacillus sp. to improve the phosphorus availability and yield of wheat (Triticum aestivum L.). *JAPS, Journal of Animal and Plant Sciences,* 23**,** 190-197.

ANIK, M. F. A., RAHMAN, M. M., RAHMAN, G. M., ALAM, M. K., ISLAM, M. S. & KHATUN, M. F. 2017. Organic amendments with chemical fertilizers improve soil fertility and microbial biomass in Rice-Rice-Rice triple crops cropping systems. *Open Journal of Soil Science,* 7**,** 87.

BIESAGA-KOŚCIELNIAK, J., OSTROWSKA, A., FILEK, M., DZIURKA, M., WALIGÓRSKI, P., MIREK, M. & KOŚCIELNIAK, J. 2014. Evaluation of spring wheat (20 varieties) adaptation to soil drought during seedlings growth stage. *Agriculture,* 4**,** 96-112.

CHEN, J.-H. (2006). The combined use of chemical and organic fertilizers and/or biofertilizer for crop growth and soil fertility. International workshop on sustained management of the soil-rhizosphere system for efficient crop production and fertilizer use, 16-20. Citeseer, 20.

DALALY, B. & AL-HAKIM, S. 1987. Food analysis. Printed in Mosel University.

DAS, K., DANG, R. & SHIVANANDA, T. 2008. Influence of bio-fertilizers on the availability of nutrients (N, P and K) in soil in relation to growth and yield of Stevia rebaudiana grown in South India. *International Journal of Applied Research in Natural Products,* 1**,** 20-24.

EGAMBERDIEVA, D., WIRTH, S. J., ALQARAWI, A. A., ABD_ALLAH, E. F. & HASHEM, A. 2017. Phytohormones and beneficial microbes: essential components for plants to balance stress and fitness. *Frontiers in microbiology,* 8**,** 2104.

ETESAMI, H., ALIKHANI, H. A., JADIDI, M. & ALIAKBARI, A. 2009. Effect of superior IAA producing rhizobia on N, P, K uptake by wheat grown under greenhouse condition. *World Appl. Sci. J,* 6**,** 1629-1633.

FOULKES, M. J., SLAFER, G. A., DAVIES, W. J., BERRY, P. M., SYLVESTER-BRADLEY, R., MARTRE, P., CALDERINI, D. F., GRIFFITHS, S. & REYNOLDS, M. P. 2010. Raising yield potential of wheat. III. Optimizing partitioning to grain while maintaining lodging resistance. *Journal of experimental botany,* 62**,** 469-486.

JALA-ABADI, A. L., SIADAT, S., BAKHSANDEH, A., FATHI, G. & SAIED, K. A. 2012. Effect of organic and inorganic fertilizers on yield and yield components in wheat (T. aestivum and T. durum) genotypes. *Advances in Environmental Biology***,** 6(2), 756-763.

JOGI, Q., KANDHRO, M. N., QURESHI, A. A. & SOLANGI, M. 2017. EFFECT OF BALANCED FERTILIZER FOR ENHANCEING WHEAT GROWTH AND YIELD. *Science International (Lahore),* 29**,** 981-984.

KHOLSSI, R., MARKS, E. A., MIÑÓN, J., MONTERO, O., DEBDOUBI, A. & RAD, C. 2018. Biofertilizing Effect of Chlorella sorokiniana Suspensions on Wheat Growth. *Journal of Plant Growth Regulation***,** 38(644),1-6.

KHURSHEED, M. Q. & MAHAMMAD, M. Q. 2015. Effect of different nitrogen fertilizers on growth and yield of wheat. *ZANCO Journal of Pure and Applied Sciences,* 27**,** 19-28.

KUMAR, M. 2015. *Effect of NPK levels and vermicompost on growth and yield of wheat (Triticum aestivum L.) under normal practice and system of wheat intensification.* MSc. thesis, Institute of Agricultural Sciences, Banaras Hindu University, Varanasi.

MEHBOOB, I. 2010. Plant growth promoting activities of rhizobium with non-legumes. *Msc. thesis, University of gricultur, Faisalabad, Pakistan*.

MEHBOOB, I., ZAHIR, Z. A., ARSHAD, M., TANVEER, A. & AZAM, F. 2011. Growth promoting activities of different Rhizobium spp. in wheat. *Pak. J. Bot,* 43**,** 1643-1650.

MIA, M. B. & SHAMSUDDIN, Z. 2010. Rhizobium as a crop enhancer and biofertilizer for increased cereal production. *African journal of Biotechnology,* 9**,** 6001-6009.

MOHAMED, S. 2000. Effect of mineral and biofertilization on growth, yield, chemical constituents and anatomical structure of wheat (Triticum aestivum L.) and broad bean (Vicia faba L.) plants grown under reclaimed soil conditions. *Annals of Agricultural Science, Moshtohor,* 38**,** 2039-2063.

MORADI, A., KORDLAGHARI, K. P. & KESHAVARZ, K. (2015). Influence of Zinc and Seed Inoculation with Rhizobium Bacteria on Yield and Yield Components of Triticum aestivum (Case study: Nurabad, Iran). Biological Forum. Citeseer, 7 (1): 185-189.

MORGAN, J. & CONNOLLY, E. 2013. Plant-soil interactions: nutrient uptake. *Nature Education Knowledge,* 4**,** 2.

RYAN, J., ESTEFON, G. & RASHID, A. 2001. Soil and Plant Analysis Laboratory Manual, 2nd edn. National Agriculture Research Center (NARC) Islamabad, Pakistan. *Bull. Fac. Sci,* 31**,** 395-303.

SADASIVAM, S. 1996. *Biochemical methods*, New age international.

SAHARAN, B. & NEHRA, V. 2011. Plant growth promoting rhizobacteria: a critical review. *Life Sci Med Res,* 21**,** 30.

SHAKHAWAT, H. M. 2007. Potential use of Rhizobium spp. to improve growth of non-nitrogen fixing plants. Msc. thesis, Department of soil science, swedish university, of agricultural science

ŠRAMKOVÁ, Z., GREGOVÁ, E. & ŠTURDÍK, E. 2009. Chemical composition and nutritional quality of wheat grain. *Acta Chimica Slovaca,* 2**,** 115-138.

STAJKOVIĆ-SRBINOVIĆ, O., DELIĆ, D., KUZMANOVIĆ, D., PROTIĆ, N., RASULIĆ, N. & KNEŽEVIĆ-VUKČEVIĆ, J. 2014. Growth and nutrient uptake in oat and barley plants as affected by rhizobacteria. *Rom. Biotechnol. Lett,* 19**,** 9429-9436.

YE, Q., ZHANG, H., WEI, H., ZHANG, Y., WANG, B.-F., XIA, K., HUO, Z.-Y., DAI, Q.-G. & XU, K. 2005. Effect of nitrogen fertilizer on nitrogen use

efficiency and yield of rice under different soil conditions. *Acta Agronomica Sinica,* 31**,** 1422.

ZAHIR, Z. A., YASIN, H., NAVEED, M., ANJUM, M. & KHALID, M. 2010. L-tryptophan application enhances the effectiveness of rhizobium inoculation for improving growth and yield of mungbean (Vigna radiata (L.) Wilczek). *Pak J Bot,* 42**,** 1771-1780.

ZAKI, N., GOMAA, M., RADWAN, F., HASSANEIN, M. & WALI, A. 2012. Effect of mineral, organic and bio-fertilizers on yield, yield components and chemical composition of some wheat cultivars. *Journal of Applied Sciences Research,* 8**,** 174-191.

ZANCO Journal of Pure and Applied Sciences
The official scientific journal of Salahaddin University-Erbil
https://zancojournals.su.edu.krd/index.php/JPAS

ISSN (print):2218-0230**, ISSN (online):** 2412-3986**, DOI: http://dx.doi.org/10.21271/zjpas**

RESEARCH PAPER

Study on the protective effect of green tea against bisphenol A- induced amyloid aggregation in the brain of male albino rats.

Dhuha Q. Kamil [1] , Khabat A. Ali [2]

[1] Department of medical lab techniques, Erbil polytechnic university,Shaqlawa technical institute, Erbil,Iraq

[2] Department of biology, college of education, Salahaddin university-Erbil , Kurdistan Region, Iraq.

A B S T R A C T:

Bisphenol A (BPA) has been used in the plastic industry and widely distributed in the environment. Green tea extract has been known for its antioxidant activity. This study was designed to investigate the protective efficacy of green tea against brain amyloid aggregation which induced by BPA. Twenty male albino rats were exposed to BPA (500 mg/kg); green tea ethanolic extracts in two dose levels 150 and 300 mg/kg respectively plus BPA. After 60 days, malondialdehyde (MDA), superoxide dismutase (SOD) in the brain were measured besides body and brain weights. BPA exposed groups showed a significant reduction ($P<0.05$) in the final body weight, with a non-significant reduction in absolute brain weight. BPA was also increased oxidative stress in the brain of the treated rats besides histological changes with amyloid deposition in the brain detected by congo red staining technique. Treatment with green tea ethanol extracts were protected animal brains against adverse effects caused by BPA and reduced oxidative stress in a dose-dependent manner. that may be related to enriched ingredients that have been found in the extract.

KEY WORDS: BPA, brain, green tea extract, oxidative stress, MDA, SOD, amyloid
DOI: http://dx.doi.org/10.21271/ZJPAS.32.2.20
ZJPAS (2020) , 32(2);192-202 .

1.INTRODUCTION

Bisphenol A (BPA) is one of the widely spread Contaminants that used in the manufacturing of polycarbonate plastic (Hernandez-Rodriguez et al., 2007). It brought extensive attention regarding the different ways of human exposure; orally by leaching from plastic containers or plastic lining of cans containing food, or by inhalation through incorporation by dust (Hugh S. Taylor, 2008).

Studies revealed that BPA causes adverse effects on the brain, reproductive system (Lang et al., 2008), and liver (Nakagawa and Tayama, 2000). BPA also brought considerable attention due to its estrogenic activity (Zuo and Zhu, 2014).

Amyloid beta(Aβ), toxic protein accumulation in the central nervous system (CNS), has been correlated with certain neurodegenerative diseases like Alzheimer's disease (Prasansuklab and Tencomnao, 2013). A previous study indicated that BPA has a direct connection to the accumulation of amyloid polypeptide in the human pancreatic islets which lead to the death of the insulin- producing cell and finally leads subsequently to type 2 Diabetes Mellitus (Gong et al., 2013). Later BPA was

* **Corresponding Author:**
Dhuha Q. Kamil
E-mail: duhaqais@epu.edu.iq
Article History:
Received: 22/07/2019
Accepted: 20/11/2019
Published: 22/04 /2020

found to disturb insulin signaling pathways and increases amyloid precursor protein in the brain cortex of mice offspring (Fang et al., 2016a). BPA considered as one of the risk factors contaminates that accelerate the appearance of Alzheimer's dementia in addition to other factors like fluoride and aluminum (Mendelson, 2009).

Green tea is a favorite beverage which first discovered and spread from China to the world, green tea is a less processed type of tea (*Camellia sinensis*) without fermentation, this type of tea contain a pharmaceutical valued ingredients contents like flavonoids, Catechins, tannin, amino acids, and vitamin C (Katiyar and Elmets, 2001, Elżbieta SIKORA, 2011). Catechins belong to the phenolic acid components of green tea, which composed of eight types and epigallocatechin- 3-gallate (EGCG) represents the most abundant catechin in the green tea (Lu and Chen, 2008).

Recently green tea has been considered as a new therapeutic approach in the treatment of several diseases like Parkinson disease as it contains a very important phenols Epigallocatechin-3-gallate (Jurado-Coronel et al., 2016). It also used in the treatment of cancer, high blood pressure, and inflammation (Riegsecker et al., 2013), With the treatment of dyslipidemia in the blood of overweight and obese people (Yuan et al., 2018).

This study is an attempt to illustrate the role of BPA in the deposition of amyloid protein in the brain. which may be in charge of accelerate aging processes in the brain and also to investigate the ameliorative effect of green tea extract on the adverse effects of BPA as green tea was known to contain unique ingredients of medical importance.

2.MATERIAL AND METHODS

Green tea (China) ethanol extract was prepared according to the way that was used by Hernandez-Perez et al., (1994). 100 g of dried plant powder was mixed with 1000 ml of ethanol (95%). Put in a horizontal shaker for 24 hours, then was separated by filter paper, and then was centrifuged for 3000 g. Crude extract was obtained by filtration followed by evaporation of the solvent in a rotatory evaporator in 40ºC under low pressure. The extraction was kept in 8ºC till usage and re-suspended with distilled water to prepare the stock solution.

This study was carried out on 20 *Wistar* male albino rats weighing between (180-200) g obtained from the college of veterinary medicine in Baghdad/Iraq. All animals were housed in polypropylene cages with mesh wire tops in a well-ventilated room and provided with balanced ration and clean water *ad libitum*, with 12:12 light /dark photoperiod at 22±4ºC. Rats were divided into four equal groups (5 animals each). First group was treated with500mg/kg BPA (Solar bio company, Beijing, China) melted in corn oil; the second group treated with a mixture of BPA (500 mg/kg) plus green tea extract 150 mg/kg; third group was treated with BPA plus green tea extract 300mg/kg; the fourth group represents the control group treated with corn oil only. Animal dosing was orally for 60 days. Treatment with green tea extract was conducted after one hour of BPA dosage.

At the end of the experiment, animals were fasted overnight and weighed then anesthetized by ketamine and xylazine. During dissection, brains of the treated rats were removed, and half of the brain was washed with cold saline. Dried and then weighed and kept in -80ºC until the preparation of tissue homogenate to measure malondialdehyde (MDA), and superoxide dismutase (SOD).

For the preparation of Brain tissue homogenate, 0.1 gm. of the brain was mixed with 1 ml of extraction solution accompanied by the commercial kits (solar bio co., Beijing, China) used for the measurement of SOD and MDA. Then the tissue was homogenized or fully ground by Dounce homogenizer in ice by 8000 rpm 4ºC and centrifuged for 10 min. The supernatant was used for the test.

Another part of the brain was fixed in 10% neutral buffered formalin. Paraffinized brain tissue blocks were processed and cut by a microtome at 5 µm thickness, then deparaffinized, and counterstained by hematoxylin and eosin (H&E) to study histological changes.

Modified Higman's Congo red was used for the detection of amyloid plaques in the brain tissue. (BANCROFT et al., 1990). Histological sections 5µm thicknesses were deparaffinized by xylene then rehydrated by ethanol, washed by distilled water (D.W.) for 1 minute. Stained with Congo red solution for 20 minutes, differentiate quickly to alkaline alcohol for 5 to 10 dips, then rinsed for 1 minute in tap water, counterstained

with Gill hematoxylin for 30 seconds. Washed for 2 minutes by running water then dehydrated by ascending serial of alcohol (95% twice,100%) each change for 3 minutes, cleared with xylene (twice each change for 3 minutes) then mounted with Canada balsam and covered. Finally, slides were examined under a polarized light microscope for the detection of amyloid protein.

Statistical analyses were conducted using GraphPad Prism software version 6.0 (GraphPad, San Diego, CA). Data are presented as means with their standard error of the mean (mean ± SEM). Normality and homogeneity of the data were confirmed before ANOVA, and differences among the experimental groups were assessed by one-way ANOVA followed by Turkey's test. A probability level of $P<0.05$ was, considered as statistically significant.

3.RESULTS

Oral administration of BPA induced significant weight reduction ($P<0.05$) in the final body weight in comparison with the control group and a non-significant decrease in brain weight (Table 1).

Green tea extract at a level dose of 150 and 300 mg/kg plus BPA were caused a gradient non-significant decrease in final body weight and brain weight when compared with BPA or control group. Although the decrease was not statistically significant, the decrease in body weight induced by BPA was slightly improved by green tea in both dose levels, but still lower than the average value when compared with the control group.

The obtained results (Table1) revealed that brain MDA levels were significantly ($P<0.05$) increased in the BPA treated group when compared to the control group. Oral administration of green tea extract shows an obvious decreasing in the MDA brain level in a dose- dependent manner. The best lowering effect was seen in 300 mg/kg of green tea extract.

In contrast, BPA administration was significantly decreased SOD activities in rat brains when compared with the control group. The best results were seen with both doses 150 and 300 mg of green tea plus BPA. This increment was statistically significant ($P<0.05$) when compared with BPA group, while it was not significant when compared with the control group (table 1).

Histologically, BPA treatment induced several changes in the brain tissue (fig.1). There was congestion in the blood vessels with shrinkage and clot formation inside the blood vessels, hyaline necrosis in the cortex layer of the brain with gliosis (inflammation), pyknosis and disarrangement of Purkinje cells in the cerebellum. In green tea dose levels 150 and 300 mg/kg there was gradient improvement in the brain tissue depending on the dose used (fig. 2).

Congo red stained section under light microscope revealed the presence of pink and red plaques in BPA, which represents amyloid deposits. The plaques were seen in both cerebrum and cerebellum of the brain. While in green tea treated groups in both dose level 150 mg/kg plus BPA, there was a noticeable reduction in amyloid plaques which completely removed in the higher dose of green tea (300) mg/kg (fig. 3).

Table 1. Effect of different treatments on final body weight, absolute brain weight, SOD and MDA levels in the brain homogenate.

Treatment	Initial body weight(g)	Final body weight(g)	absolute brain weight(g)	SOD (U/g)	MDA(nmol/L)
Control	221.8±15.79	275±7.36	1.852±0.04	649±59.29	36.38± 1.24
BPA	174.4±15.34	192±26.01[a]	1.484±0.11	383±30.79[a]	47.55±1.10[a]
BPA+green 150 mg	218.2±13.44	239±13.77	1.794±0.10	678±13.47[b]	42.19±0.42[bc]
BPA+green 300 mg	197.0±9.935	251±21.52	1.782±0.07	694±50.64 [c]	35.10±1.29[b]

Values are presented as mean ± SEM (n=5 animals/group)

a) Significantly different from control group (BPA with control) at ($P < 0.05$)

b) Significantly different from BPA group

c) Significantly different from control group (control with green tea groups)

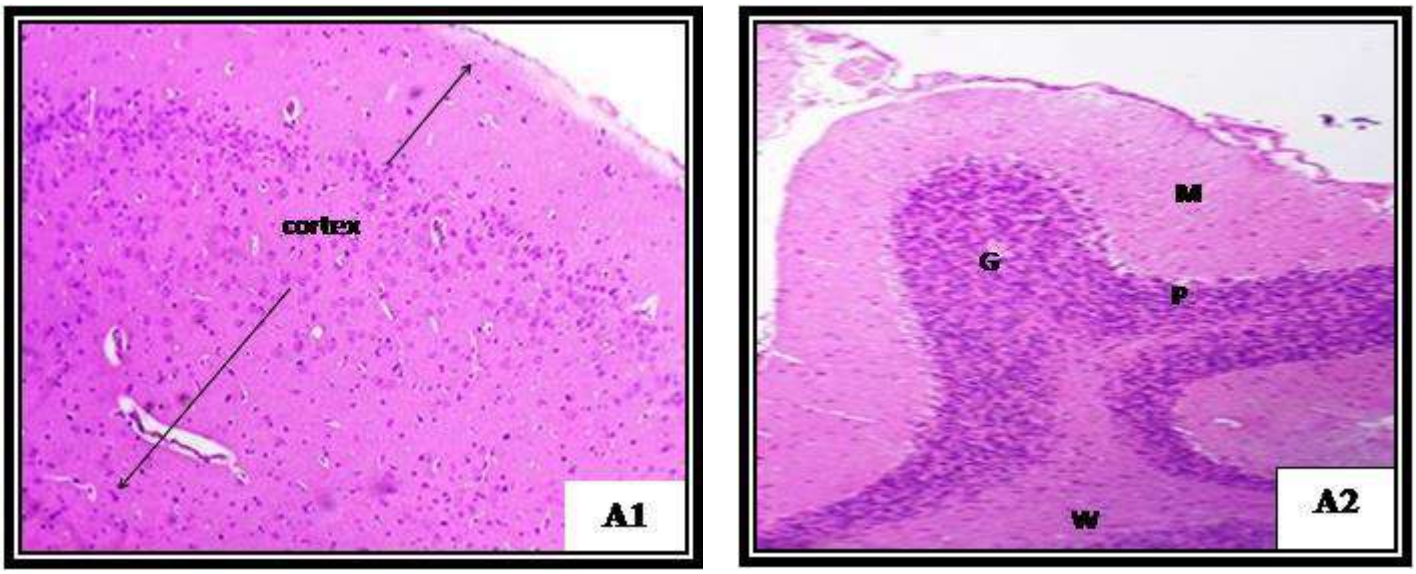

Figure 1. Cross section in the brain of control group. A1) normal cerebral cortex A2) normal cerebellum structure, granular layer (G), molecular layer (M), Purkinje cells layer (P), white matter (W).

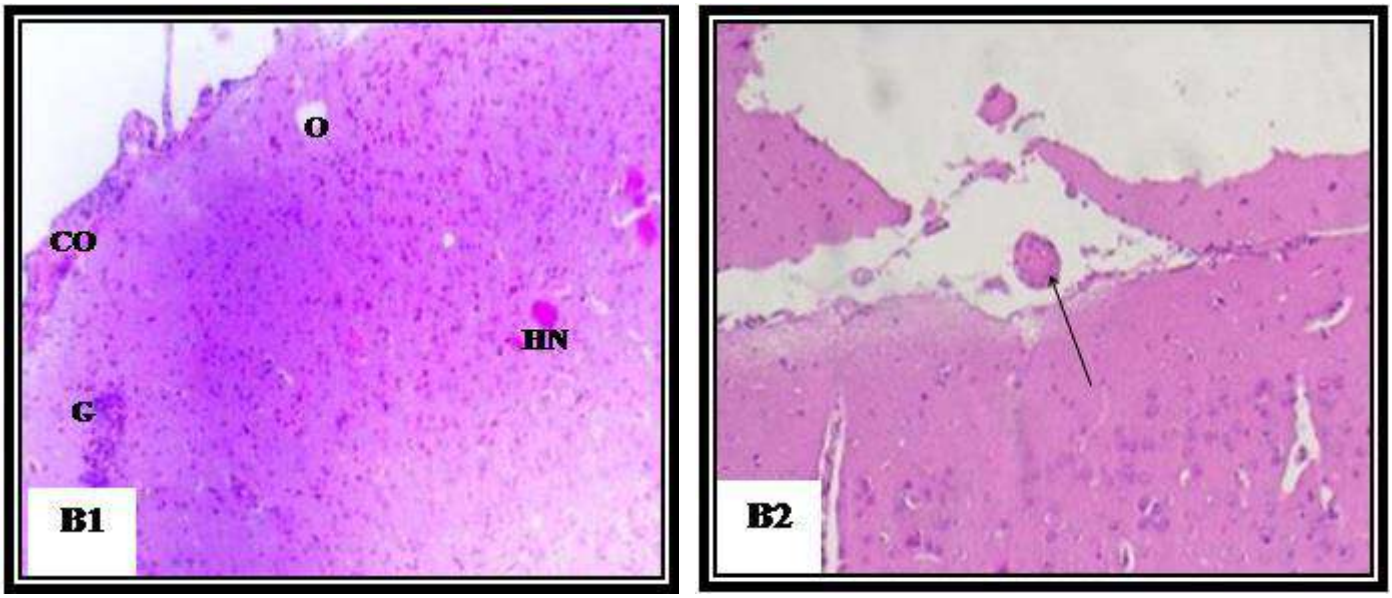

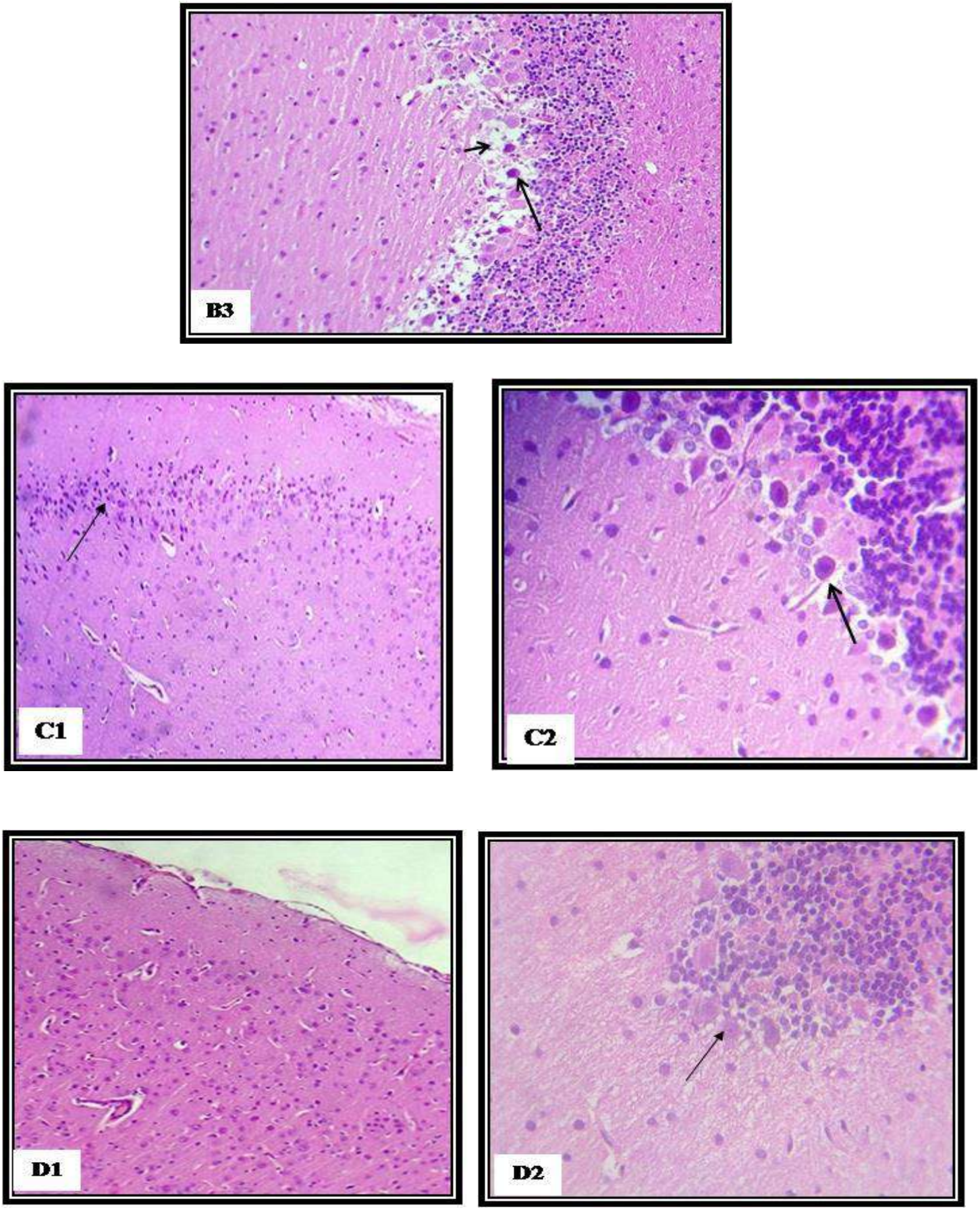

Figure 2. Cross section in the brain of the BPA treated groups B1) Cerebrum shows odema (o), Blood vessels congestion (c), Hyaline necrosis (hn), Gliosis (g) (H&E 10X). B2) Section in the cerebrum shows clot formation in the blood vessel (arrow). B3) Section in the cerebellum of BPA treated group showes

disarrangement and pyknosis of purkinje cells (H&E 10X). C1) Cerebrum of green150+BPA shows brain tissue improvement with slight gliosis and congestion in blood vessels (H&E 10X). C2) Cerebellum section shows preserved purkinje cells (H&E 10X). D1) Cerebrum section of green 300+BPA treated group shows normal cerebral cortex (H&E 10X). D2) Cerebellum of green 300+BPA treated group shows normal purkinje cells (arrow) (H&E 10X).

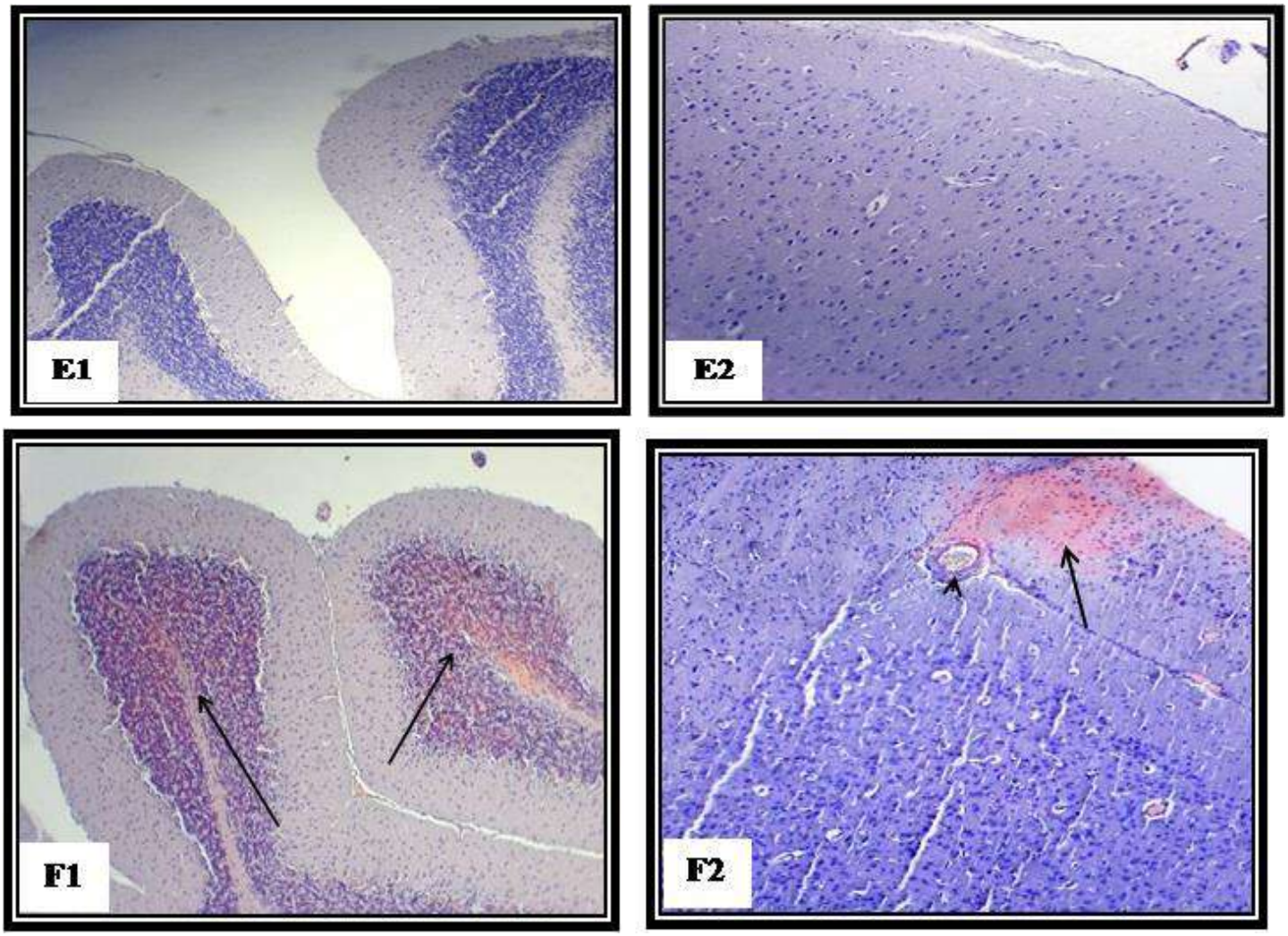

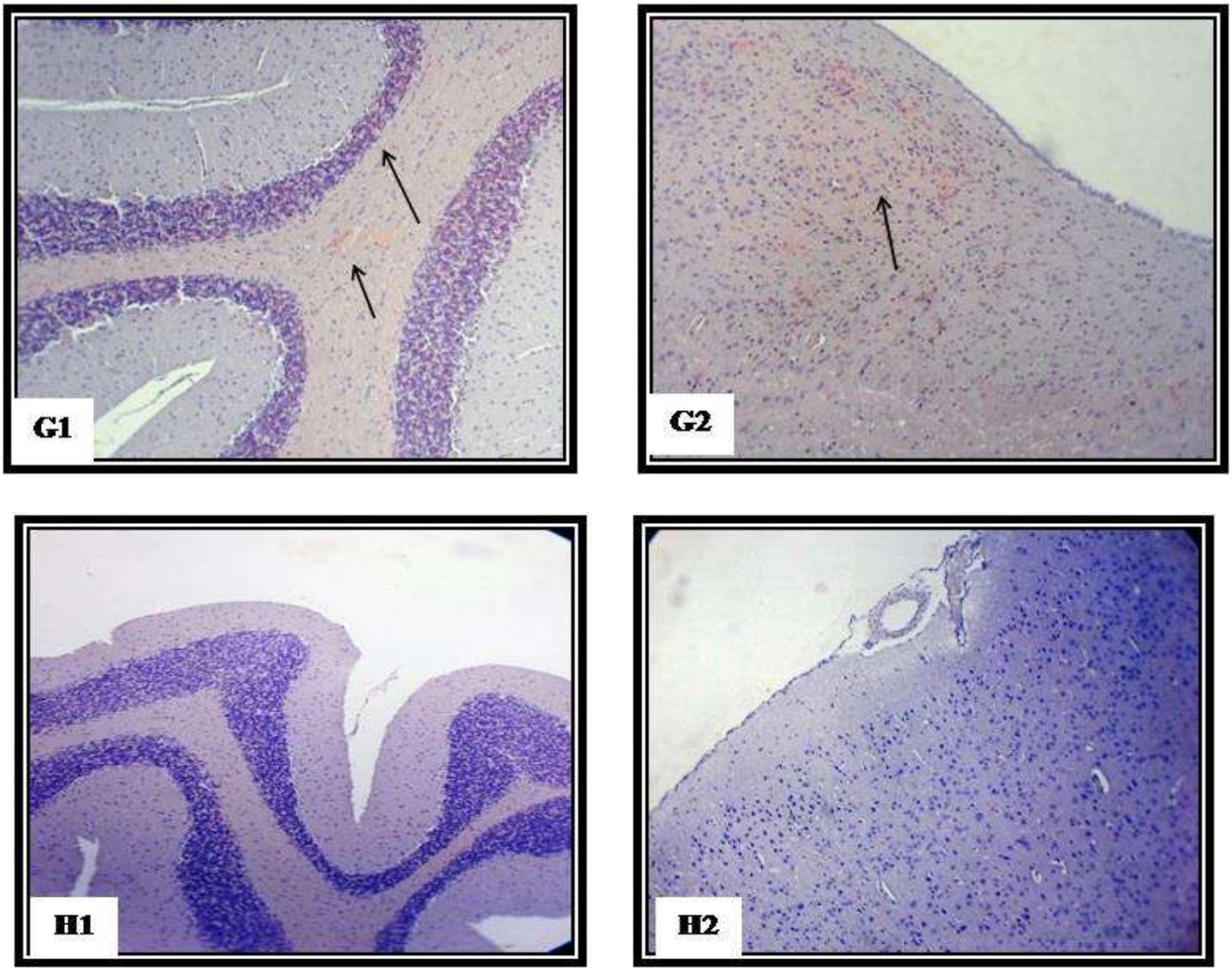

Figure3. Cross section in the brain stained with Congo red stain 10X under light microscope. E1) Normal cerebellum with no amyloid deposition in control group. E2) Normal cerebrum cortex with no amyloid deposition in control group. F1) Focal extracellular amyloid deposition (arrow) in the cerebellum taken red color under light microscope in the BPA treated group. F2) Amyloid deposition in the cerebral cortex (arrow) and wall of blood vessels (arrowhead) in BPA treated group. G1) Cerebellum of green 150+BPA treated rats shows reduced amyloid deposition. G2) Cerebrum of green 150+BPA treated rats shows reduced amyloid deposition. H1) Cerebellum of green300+BPA treated group shows no amyloid deposition. H2) Cerebrum of green300+BPA treated group shows no amyloid deposition.

4.DISCUSSION

In most cases, the etiology of BPA on the brain is completely known. Result of this study revealed a possible detrimental effect of BPA on the body and brain weight as compared to the control. The reduction in the body weight in BPA treated group may be related to the reduction in the rate of food consumption (lack of appetite); that may increase lipid mobilization and lipolysis to produce fatty acids in negative energy balance (Zechner et al., 2012). BPA has been known as xenoestrogen which works as a weak estrogen, that may alter the stimulating role of estrogen which may, in turn, increase the rate of lipolysis by suppressing food intake through a direct effect on the central nervous system (Negri-Cesi, 2015). These results concur with many previous results (2018, Perera et al., 2016). Elsewhere, some reports indicate that BPA stimulates weight gaining and cause obesity (Morgan et al., 2014).

The improvement in the final body weight and brain weight by green tea extracts may be related to the presence of antioxidant compounds catechins (GTC), which comprise four major epicatechin derivatives; namely, epicatechin (EC), epigallocatechin (EGC), epicatechin gallate (ECG), and epigallocatechin gallate (EGCG), and the extraction with ethanol ensure the highest phenolic content of the green tea extract (Setyopratomo, 2014). Other reports suggested that green tea has a lowering weight effect (Chen et al., 2011). The explanation for this disagreement with our findings, the experiment of that research was made by using healthy rats; in our study the rats were intoxicated by BPA. Related to the antioxidant properties, food intake and energy balance was improved. Body weight improvement was better seen in the higher dose of green tea with BPA. Green tea is also containing Lipids, proteins, vitamin C, and minerals (Cabrera et al., 2003).

BPA induced oxidative stress in the brain of the treated rats. Oxidative stress related to the ability of BPA to accumulate in the brain because of its lipophilic action and increase oxidative stress by increasing the activity of acetylcholinesterase in cortical and hippocampal areas of the brain (Khadrawy et al., 2016). A recent study indicated that BPA increases the gene expression of stress response genes, which increase the oxidative response and cellular damage genes (Garcia-Espineira et al., 2018). Previous studies showed that BPA has adverse effects on several organs including the developing brain, recent study indicates that BPA disrupts neural differentiation in human-derived neural progenitor cells, potentially disrupting brain development (Fujiwara et al., 2018) those changes were supposed to be mediated by stimulating oxidative damage in different organs especially for the brain (Ke et al., 2013). An earlier study showed that BPA affects CNS function in rodent and its stronger in the prenatal stage, that may be because it is easier for BPA to cross the placental barrier and blood- brain barrier (Nishikawa et al., 2010).

Our findings were shown that green tea extract was reduced oxidative stress in a dose dependent manner. Green tea extract enriched with polyphenols family (catechins) as it works as a chelating agent with high affinity for ions binding to reduce oxidative stress that mediated by low-density lipoprotein (Yoshida et al., 1999, Galleano et al., 2010, Seeram et al., 2006). The effect of green tea extracts does not appear due only for its polyphenol content, but several signaling events on cell level may be responsible for their biological actions (Mandel et al., 2004).

BPA rat exposure lead to adverse effects in the brain histology, those effects include congestion and clotting in the blood vessels of the brain, that may be related to the alteration in the concentration of some ions in the blood that contribute in blood clotting process like calcium ions, this in turn, will increase blood clotting rate (Pal et al., 2017). Besides that, BPA induced disorganization of cerebellum layers, and condensation of Purkinje cells. The changes in the brain histology that been mediated by BPA related to the oxidative stress that induced by BPA, which lead to the formation of reactive oxygen species (ROS) that may cause inflammation and cell apoptosis, finally cause neural diseases like Alzheimer disease (Mandel et al., 2004). Effect of BPA on the brain may be the same of those appeared by using pesticides (Ismail, 2017), antidepressant drugs (Rasul et al., 2016), and other plasticizers like Di-n-butylphthalate (Chawsheen and Aziz, 2013). In contrast, green tea was improved brain tissue. That related to the positive effect of flavonoids that have been attributed to the fortification of neural functioning, stimulation of neuronal recovery, and increased blood supply, and improve memory in studies that used pure flavonoids extracted from different plants (van Praag et al., 2007, Nehlig, 2013, Swinton et al., 2018).

BPA was accelerated toxic amyloid protein aggregation in the cerebrum, and cerebellum parts of the brain, obstruction in the blood vessels reduce brain blood supply, oxygen and energy and finally leading to beta- amyloid aggregation (Prasansuklab and Tencomnao, 2013). Low glucose supply to the brain induces different cellular pathways at a genetic level, resulting in overproduction of amyloid beta- protein (Bell et al., 2009). Increasing oxidative stress in the brain may be as a result of amyloid aggregation and cell damage (Behl et al., 1994). Our results come in agreement with previous studies on different organs. Gong et al. (2013) found that BPA increases the incidence of Diabetes type 2 by

increasing the accumulation of amyloid in pancreatic beta cells. A study conducted on the brain of offspring males BPA was found to increase amyloid precursor protein (Fang et al., 2016b). That may be explained by the inhibition of membrane integral protease enzyme, that is responsible for the degradation of amyloid precursor protein (Baba et al., 2009).

Our data showed that green tea extracts reduced amyloid aggregation in the brain of the treated rats. That may be related to the inhibitory effect of green tea catechins for amyloid fibril formation (aus dem Siepen et al., 2015) (Rezai-Zadeh K et al., 2005). These results came in agreement with previous studies (Mereles et al., 2008). The possible explanation that green tea catechins were worked in contrast with BPA by stimulating the alpha-secretase enzymes that are responsible for the transforming of amyloid precursor protein into non-amyloid protein rather than toxic beta - amyloid (Obregon et al., 2006).

CONCLUSION

BPA induced oxidative stress may be mediated by amyloid beta -protein accumulation. Green tea extracts ameliorate BPA neural changes by reducing oxidative stress and have a neuro-protective effect against brain amyloid toxicity.

Acknowledgement:
We appreciate the Staff of Salahaddin College/ Biology department and research center of polytechnic university for all the support they gave during the study.

Conflict of interest: there is no conflict of interest.

References

ABDEL-RAHMAN, H. G., A., H. M., ABDELRAZEK, H. M. A., ZEIDAN,D.W., MOHAMED, R. M. & ABDELAZIM,A. M. 2018. Lycopene: Hepatoprotective and Antioxidant Effects toward Bisphenol A-Induced Toxicity in Female Wistar Rats. *Oxidative Medicine and Cellular Longevity*

AUS DEM SIEPEN, F., BAUER, R., AURICH, M., BUSS, S. J., STEEN, H., ALTLAND, K., KATUS, H. A. & KRISTEN, A. V. 2015. Green tea extract as a treatment for patients with wild-type transthyretin amyloidosis: an observational study. *Drug Des Devel Ther,* 9**,** 6319-25.

BABA, K., OKADA, K., KINOSHITA, T. & IMAOKA, S. 2009. Bisphenol A disrupts Notch signaling by inhibiting gamma-secretase activity and causes eye dysplasia of Xenopus laevis. *Toxicol Sci,* 108**,** 344-55.

BANCROFT, J., STEVENS, A. & AND TURNER, D. 1990. *Theory and Practice of Histological Techniques*, Churchill-Livingstone

BEHL, C., DAVIS, J. B., LESLEY, R. & SCHUBERT, D. 1994. Hydrogen peroxide mediates amyloid beta protein toxicity. *Cell,* 77**,** 817-27.

BELL, R. D., DEANE, R., CHOW, N., LONG, X., SAGARE, A., SINGH, I., STREB, J. W., GUO, H., RUBIO, A., VAN NOSTRAND, W., MIANO, J. M. & ZLOKOVIC, B. V. 2009. SRF and myocardin regulate LRP-mediated amyloid-beta clearance in brain vascular cells. *Nat Cell Biol,* 11**,** 143-53.

CABRERA, C., GIMENEZ, R. & LOPEZ, M. C. 2003. Determination of tea components with antioxidant activity. *J Agric Food Chem,* 51**,** 4427-35.

CHAWSHEEN, M. A. H. & AZIZ, F. M. 2013 Synergistic Neurotoxic Effect of Di-n-butylphthalate on methomyl treated rats. *ZANCO Journal of Pure and Applied Sciences,* 24(2)**,** 1-10.

CHEN, Y. K., CHEUNG, C., REUHL, K. R., LIU, A. B., LEE, M. J., LU, Y. P. & YANG, C. S. 2011. Effects of green tea polyphenol (-)-epigallocatechin-3-gallate on newly developed high-fat/Western-style diet-induced obesity and metabolic syndrome in mice. *J Agric Food Chem,* 59**,** 11862-71.

ELŻBIETA SIKORA, J. O. 2011. Study of antioxidant properties of green tea extract. *CHEMIK 2011, ,* 65, 10, **,** 968-973.

FANG, SHI, Q., GUO, Y., HUA, J., WANG, X. & ZHOU, B. 2016a. Enhanced Bioconcentration of Bisphenol A in the Presence of Nano-TiO2 Can Lead to Adverse Reproductive Outcomes in Zebrafish. *Environ Sci Technol,* 50**,** 1005-13.

FANG, F., GAO, Y., WANG, T., CHEN, D., LIU, J., QIAN, W., CHENG, J., GAO, R., WANG, J. & XIAO, H. 2016b. Insulin signaling disruption in male mice due to perinatal bisphenol A exposure: Role of insulin signaling in the brain. *Toxicol Lett,* 245**,** 59-67.

FUJIWARA, Y., MIYAZAKI, W., KOIBUCHI, N. & AND KATOH, T. 2018. The Effects of Low-Dose Bisphenol A and Bisphenol F on Neural Differentiation of a Fetal Brain-Derived Neural Progenitor Cell Line. *Front Endocrinol (Lausanne),* 9**,** 24.

GALLEANO, M., VERSTRAETEN, S. V., OTEIZA, P. I. & FRAGA, C. G. 2010. Antioxidant actions of flavonoids: thermodynamic and kinetic analysis. *Arch Biochem Biophys,* 501**,** 23-30.

GARCIA-ESPINEIRA, M. C., TEJEDA-BENITEZ, L. P. & OLIVERO-VERBEL, J. 2018. Toxic Effects of Bisphenol A, Propyl Paraben, and Triclosan on Caenorhabditis elegans. *Int J Environ Res Public Health,* 15.

GONG, H., ZHANG, X., CHENG, B., SUN, Y., LI, C., LI, T., ZHENG, L. & HUANG, K. 2013. Bisphenol A accelerates toxic amyloid formation of human islet amyloid polypeptide: a possible link between bisphenol A exposure and type 2 diabetes. *PLoS One,* 8**,** e54198.

HERNANDEZ-PEREZ M., LOPEZ-GARCIA RE., RABANAL RM, DARIAS V& ARIAS A. 1994: Antimicrobial activity of Visnea mocanera leaf extracts. *J Ethnopharmacol* 41,115-119.

HERNANDEZ-RODRIGUEZ, G., ZUMBADO, M., LUZARDO, O. P., MONTERDE, J. G., BLANCO, A. & BOADA, L. D. 2007. Multigenerational study of the hepatic effects exerted by the consumption of nonylphenol- and 4-octylphenol-contaminated drinking water in Sprague-Dawley rats. *Environ Toxicol Pharmacol,* 23**,** 73-81.

HUGH S. TAYLOR, M. D. 2008. Endocrine Disruptors Affect Developmental Programming of HOX Gene Expression. *Fertil Steril* 89(2 Suppl): e57–e58.

ISMAIL, T. F. 2017. Histological Effect of Methomyl on Rat Brain and Testis. *ZANCO Journal of Pure and Applied Sciences,* 29**,** 161-7.

JURADO-CORONEL, J. C., AVILA-RODRIGUEZ, M., ECHEVERRIA, V., HIDALGO, O. A., GONZALEZ, J., ALIEV, G. & BARRETO, G. E. 2016. Implication of Green Tea as a Possible Therapeutic Approach for Parkinson Disease. *CNS Neurol Disord Drug Targets,* 15**,** 292-300.

KATIYAR, S. K. & ELMETS, C. A. 2001. Green tea polyphenolic antioxidants and skin photoprotection (Review). *Int J Oncol,* 18**,** 1307-13.

KE, C., LIU, X., ZUO, H., ZHAO, J., YANG, X. & YUAN, J. 2013. The oxidative damage of Bisphenol A on the organs of the mice. *Health,* 05**,** 1190-1194.

KHADRAWY, Y. A., NOOR, N. A., MOURAD, I. M. & EZZ, H. S. 2016. Neurochemical impact of bisphenol A in the hippocampus and cortex of adult male albino rats. *Toxicol Ind Health,* 32**,** 1711-9.

LANG, I. A., GALLOWAY, T. S., SCARLETT, A., HENLEY, W. E., DEPLEDGE, M., WALLACE, R. B. & MELZER, D. 2008. Association of urinary bisphenol A concentration with medical disorders and laboratory abnormalities in adults. *JAMA,* 300**,** 1303-10.

LU, M.-J. & CHEN, C. 2008. Enzymatic modification by tannase increases the antioxidant activity of green tea. *Food Research International,* 41**,** 130-137.

MANDEL, S., WEINREB, O., AMIT, T. & YOUDIM, M. B. 2004. Cell signaling pathways in the neuroprotective actions of the green tea polyphenol (-)-epigallocatechin-3-gallate: implications for neurodegenerative diseases. *J Neurochem,* 88**,** 1555-69.

MENDELSON, S. D. 2009. Beyond Alzheimer's How to avoid the modern epidemic of dimentia *M. evan , Lanham. Newyork.Boulder. Toronto.plymouth, UK , Rowman &littlefield publishing group,Inc.***,** 128-129.

MERELES, D., WANKER, E. E. & KATUS, H. A. 2008. Therapy effects of green tea in a patient with systemic light-chain amyloidosis. *Clin Res Cardiol,* 97**,** 341-4.

MORGAN, A. M., EL-BALLAL, S. S., EL-BIALY, B. E. & EL-BORAI, N. B. 2014. Studies on the potential protective effect of cinnamon against bisphenol A- and octylphenol-induced oxidative stress in male albino rats. *Toxicol Rep,* 1**,** 92-101.

NAKAGAWA, Y. & TAYAMA, S. 2000. Metabolism and cytotoxicity of bisphenol A and other bisphenols in isolated rat hepatocytes. *Arch Toxicol,* 74**,** 99-105.

NEGRI-CESI, P. 2015. Bisphenol A Interaction With Brain Development and Functions. *Dose-Response:An International Journal***,** 1-12.

NEHLIG, A. 2013. The neuroprotective effects of cocoa flavanol and its influence on cognitive performance. *Br J Clin Pharmacol,* 75**,** 716-27.

NISHIKAWA, M., IWANO, H., YANAGISAWA, R., KOIKE, N., INOUE, H. & YOKOTA, H. 2010. Placental transfer of conjugated bisphenol A and subsequent reactivation in the rat fetus. *Environ Health Perspect,* 118**,** 1196-203.

OBREGON, D. F., REZAI-ZADEH, K., BAI, Y., SUN, N., HOU, H., EHRHART, J., ZENG, J., MORI, T., ARENDASH, G. W., SHYTLE, D., TOWN, T. & TAN, J. 2006. ADAM10 activation is required for green tea (-)-epigallocatechin-3-gallate-induced alpha-secretase cleavage of amyloid precursor protein. *J Biol Chem,* 281**,** 16419-27.

PAL, S., SARKAR, K., NATH, P. P., MONDAL, M., KHATUN, A. & PAUL, G. 2017. Bisphenol S impairs blood functions and induces cardiovascular risks in rats. *Toxicology reports,* 4**,** 560-565.

PERERA, F., NOLTE, E. L. R., WANG, Y., MARGOLIS, A. E., CALAFAT, A. M., WANG, S., GARCIA, W., HOEPNER, L. A., PETERSON, B. S., RAUH, V. & HERBSTMAN, J. 2016. Bisphenol A exposure and symptoms of anxiety and depression among inner city children at 10–12 years of age. *Environmental Research,* 151**,** 195-202.

PRASANSUKLAB, A. & TENCOMNAO, T. 2013. Amyloidosis in Alzheimer's Disease: The Toxicity of Amyloid Beta (A β), Mechanisms of Its Accumulation and Implications of Medicinal Plants for Therapy. *Evidence-based complementary and alternative medicine : eCAM,* 2013**,** 413808-413808.

RASUL, K. H., MAHMOOD, N. M. S., HAMAD, S. H. & HASSAN, D. H. 2016. Histological Changes of Liver, Kidney and Brain in Uninephrectomized Male Rats Exposed to Fluoxetine. *ZANCO Journal of Pure and Applied Sciences,* 28 601-626.

REZAI-ZADEH K, SHYTLE D, SUN N, MORIT, HOU H, JEANNITON D, EHRHART J, TOWNSEND K, ZENG J, MORGAN D, HARDYJ, TOWN T & ., T. J. 2005. Green tea epi-gallocatechin-3-gallate (EGCG) modu-latesamyloidprecursorproteincleavage and reduces cerebral amyloi-dosis in Alzheimer transgenic mice. *JNeurosci* 25**,** 8807–8814

RIEGSECKER, S., WICZYNSKI, D., KAPLAN, M. J. & AHMED, S. 2013. Potential benefits of green tea polyphenol EGCG in the prevention and treatment of vascular inflammation in rheumatoid arthritis. *Life Sci,* 93**,** 307-12.

SEERAM, N. P., HENNING, S. M., NIU, Y., LEE, R., SCHEULLER, H. S. & HEBER, D. 2006. Catechin and caffeine content of green tea dietary supplements and correlation with antioxidant capacity. *J Agric Food Chem,* 54**,** 1599-603.

SETYOPRATOMO, P. 2014. EXTRACTION OF PHENOLIC COMPOUNDS FROM GREEN TEA USING ETHANOL *ARPN Journal of Engineering and Applied Sciences* 9**,** 1516-1521.

SWINTON, E., DE FREITAS, E., SWINTON, C., SHYMANSKY, T., HILES, E., ZHANG, J., ROTHWELL, C. & LUKOWIAK, K. 2018. Green tea and cocoa enhance cognition in Lymnaea. *Commun Integr Biol,* 11**,** e1434390.

VAN PRAAG, H., LUCERO, M. J., YEO, G. W., STECKER, K., HEIVAND, N., ZHAO, C., YIP, E., AFANADOR, M., SCHROETER, H., HAMMERSTONE, J. & GAGE, F. H. 2007. Plant-derived flavanol (-)epicatechin enhances angiogenesis and retention of spatial memory in mice. *J Neurosci,* 27**,** 5869-78.

YOSHIDA, H., ISHIKAWA, T., HOSOAI, H., SUZUKAWA, M., AYAORI, M., HISADA, T., SAWADA, S., YONEMURA, A., HIGASHI, K., ITO, T., NAKAJIMA, K., YAMASHITA, T., TOMIYASU, K., NISHIWAKI, M., OHSUZU, F. & NAKAMURA, H. 1999. Inhibitory effect of tea flavonoids on the ability of cells to oxidize low density lipoprotein. *Biochem Pharmacol,* 58**,** 1695-703.

YUAN, F., DONG, H., FANG, K., GONG, J. & LU, F. 2018. Effects of green tea on lipid metabolism in overweight or obese people: A meta-analysis of randomized controlled trials. *Mol Nutr Food Res,* 62.

ZECHNER, R., ZIMMERMANN, R., EICHMANN, T. O., KOHLWEIN, S. D., HAEMMERLE, G., LASS, A. & MADEO, F. 2012. FAT SIGNALS--lipases and lipolysis in lipid metabolism and signaling. *Cell Metab,* 15**,** 279-91.

ZUO, Y. & ZHU, A. Z. 2014. Simultaneous identification and quantification of 4-cumylphenol, 2,4-bis-(dimethylbenzyl)phenol and bisphenol A in prawn Macrobrachium rosenbergii. *Chemosphere,* 107**,** 447-453.